Photophysical and Electrochemical Studies of Naphthalimide-Phenanthroline Transition-Metal Complexes as Carbon Dioxide Reducing Catalysts



Ollscoil Chathair
Bhaile Átha Cliath
Dublin City University

This thesis is presented for the degree of

Doctor of Philosophy

By

Jack Biddulph B.Sc. (Hons)

Under the supervision of

Prof. Mary Pryce

School of Chemical Sciences

Dublin City University

August 2026

Declaration

I hereby certify that this material, which I now submit for assessment on the programme of study leading to the award of Doctor of Philosophy is entirely my own work, and that I have exercised reasonable care to ensure that the work is original and have conformed to the regulations on the use and declaration of Generative AI, and does not to the best of my knowledge breach any law of copyright, and has not been taken from the work of others save and to the extent that such work has been cited and acknowledged within the text of my work. I hereby certify that no Generative Artificial Intelligence (Gen AI) tools have been used in the creation of the thesis.

Signed: Jack Biddulph ID No.: 22267805 Date: 25-08-2026

Dedicated to my family who are my North Star; their love and support have always guided me to pursue my dreams.

Acknowledgements

Firstly, and most pertinently to this work, I would like to thank my supervisor Prof. Mary Pryce for her patience, advice, and support provided to me in conducting my research; from my first forays into research (when I completed my final year undergraduate research project with her), to completing my doctoral thesis, and everything in between. I will be eternally grateful for the opportunities you have afforded me.

I would also like to thank my collaborators who supported me throughout my studies. Particularly, Prof. František Hartl and Dr. Martin Pižl for their contributions to the time-resolved studies in Chapters 2 and 3. I will always remember our time together in RAL, particularly our time at Ridgeway House rejoicing the completion of our time-resolved experiments is what I will remember most fondly. Additionally, Prof. Jonathan Rochford who contributed the quantum chemical calculations to Chapter 4, thank you for your guidance and support.

I wish to extend my gratitude to all the Technical Staff at DCU School of Chemical Sciences; without your support, research would be astronomically more challenging. In particular, Veronica, Julie, Catherine, John, Ambrose, Damien, and Vincent, who I have had the pleasure of working with in my demonstrating duties, during my time as Chairperson of the Postgraduate Association of Chemistry, and who have supported my research throughout my time in DCU.

To the Mary Pryce Research Group (Leila, Michael, Florian, Jessica, Lauren, Ross, Stephen, Martyna, Patrick, Emily, Katelyn, Alex, and Conor), I would like to extend my thanks to all of them for their support throughout my time as a postgraduate researcher. Through many group meetings and conferences, you always encouraged me to put my best foot forward and supported me throughout my research.

Often, the highlight of my day was meeting with my friends for morning tea (or coffee as they usually preferred) before heading into the lab. Usually, our discussions involved going down the rabbit hole and some of our conversations really did run wild. This ritual was important to me, and I will be forever grateful to all of those who participated in this ritual with me. Particularly Róisín, Caoilte, Ross, Stephen, Martyna, Patrick, and Emily; our chats were always entertaining and made my time in DCU less taxing.

Outside of the lab, I owe many people my gratitude. To my friends, your humour and friendship would distract me from my endless thoughts of research. Without you, I surely would have gone

insane! Our social outings were important reminders that work must be balanced with fun. I look forward to future excursions with you all.

Finally, I extend my love and gratitude to my family; Garry, Dorothy, Kieran, and Niamh. You often listened to my ramblings about chemistry, a discipline unfamiliar to you. Despite this, your advice was always appreciated, even if it was not always possible to use in practice. Constants are as important to consider as variables in science, and you have remained constant supporters of my dreams and pursuits. I look forward to exchanging more of our experiences in the years to come.

"Wherever you are right now as you're reading this book, look around you. So much of what we humans have created and built has only been possible thanks to our understanding of the laws of nature: the forces that shape our world and the properties of the matter these forces act on."

"… if you look back at the great discoveries in science which later proved to have practical benefit, you will find that many of them were made out of a burning desire simply to understand the world and to satisfy scientists' curiosity."

The World According to Physics

Jim Al-Khalili

Research Output

Publications

Rajagopal, A., Biddulph, J., Tabrizi, L., D. Fitzgerald-Hughes, D., Pryce, M. T., in *Advances in Inorganic Chemistry*, Academic Press, London UK, 2022, **80**, *11*, 384-409. DOI: 10.1016/bs.adioch.2022.06.006

Biddulph, J., Pižl, M., Bhattacharya, S., Malakar, P., Greetham, G. M., Hartl, F., Pryce, M. T., *Nature and Dynamics of the Excited States of Ethynyl–Functionalized Naphthalimide–Phenanthroline Re(I) Complexes Studied by TA and TRIR Spectroscopies*, J. Phys. Chem. B., 2026, **130**, 6383–6398.

Biddulph, J., Cerpentier, F., Pižl, M., Bhattacharya, S., Malakar, P., Greetham, G. M., Hartl, F., Pryce, M. T., *Bottlenecks in Photocatalytic CO_2 Reduction with Naphthalimide-Phenanthroline Re(I) Complexes Probed by Spectroelectrochemistry and Time-Resolved Infrared Spectroelectrochemistry*, Submitted to Chem. Sci, 2026.

Magazine Articles

Biddulph, J., Pižl, M., Bhattacharya, S., Malakar, P., Greetham, G. M., Hartl, F., Pryce, M. T., *Photocatalytic CO_2 reduction probed by time-resolved infrared-spectro-electrochemistry for a mechanistic insight of the steps leading to the active catalyst*, in LaserLab-Europe Newsletter #39: Lasers for Catalysis, 2025, Available at: https://laserlab-europe.eu/laserlab-europe-newsletter-39-lasers-for-catalysis/

Scientific Talks

'Decarbonisation: Developing photocatalysts to convert CO_2 into valuable products' at SciFest@DCU, Dublin City University, 8th May 2025.

'Time-Resolved Infrared Studies of CO_2 Reducing Rhenium Photocatalysts' at 10th Annual DCU Chemical Research Symposium, Chemistry Day, Dublin City University, 16th May 2025.

Posters

'Photocatalytic Studies of a Pt(II)-Naphthalene Diimide Complex for Hydrogen Generation' Biddulph, J., Cerpentier, F., Pryce, M. T., 25th International Symposium on the Photochemistry and Photophysics of Coordination Compounds (ISPPCC) 2023, Ulm, Germany, 25th to 29th July 2023.

'Photocatalytic Studies of Re(I) Naphthalimide Complexes and Probing the Steps Leading to the Active Catalyst' Biddulph, J., Cerpentier, F., Pižl, M., Malakar, P., Greetham, G. M., Hartl, F., Pryce, M. T., 9th EuChemS Chemistry Congress, Dublin, Ireland, 7th to 11th July 2024; 29th PhotoIUPAC Symposium on Photochemistry, Valencia (Spain), 14th to 20th July 2024; CLF Artemis, Octopus and ULTRA User Meeting 2024, Oxford (UK), 9th to 11th September 2024.

'Time-Resolved Infrared Spectroelectrochemical Studies of Two Rhenium Naphthalimide Complexes' Biddulph, J., Cerpentier, F., Pižl, M., Bhattacharya, S., Malakar, P., Greetham, G. M., Hartl, F., Pryce, M. T., 26th International Symposium on the Photochemistry and Photophysics of Coordination Compounds (ISPPCC) 2025, Milazzo, Italy, 8th to 12th July 2025.

'Deploying Time-Resolved Infrared Spectroelectrochemistry to Study CO_2-Reducing Naphthalimide-Phenanthroline Re(I) Photocatalysts' Biddulph, J., Cerpentier, F., Pižl, M., Bhattacharya, S., Malakar, P., Greetham, G. M., Hartl, F., Pryce, M. T., CLF Artemis, Octopus and ULTRA User Meeting 2026, Oxford, UK, 24th to 26th March 2026.

Awards

Awarded Best Overall Poster at CLF Artemis, Octopus and ULTRA User Meeting 2026.

Table of Contents

Declaration ..... **i**
Acknowledgements ..... **iii**
Research Output ..... **v**
Table of Contents ..... **vii**
Table of Figures ..... **xi**
Table of Charts ..... **xxv**
Table of Schemes ..... **xxvi**
Table of Tables ..... **xxviii**
Table of Equations ..... **xxx**
Abbreviations ..... **xxxi**
Units of Measurement and Symbols ..... **xxxiv**
Thesis Publications ..... **xxxvi**
Thesis Abstract ..... **xxxvii**
Chapter 1
Introduction **1**
1.1 Abstract 2
1.2 CO_2 Reduction in the Context of Climate Change 2
1.2.1 Climate Change 2
1.2.2 Photocatalysis 4
1.2.3 Electrocatalysis 8
1.3 General Introduction to Photophysics 12
1.4 Properties of Photocatalytic Components 16
1.4.1 Properties of CO_2 Reducing Catalytic Centres 16
1.4.2 Organic Photosensitisers 19
1.4.2 Properties of Naphthalimides 21
1.5 Techniques Used to Study Photocatalysts and Electrocatalysts 26
1.5.1 Spectroelectrochemistry 26
1.5.2 Time-Resolved Spectroscopy 27
1.5.3 Time-Resolved Spectroelectrochemistry 30
1.6 Conclusions 33
1.7 Bibliography 34
Chapter 2
The Nature and Dynamics of the Excited States of Ethynyl-Functionalised Naphthalimide-Phenanthroline Re(I) Complexes Studied by TA and TRIR Spectroscopies **42**
2.1 Abstract 43
2.2 Introduction 43

2.3 Results and Discussion 46
2.3.1 Syntheses 46
2.3.2 FTIR and UV-Vis Absorption Studies 48
2.3.3 Emission Studies at RT and 77 K 53
2.3.4 TRIR Spectroscopy 54
2.3.5 TCSPC Studies 62
2.3.6 TA Spectroscopy 64
2.3.7 Triplet-Energy Gap 68
2.3.8 Excited-State Dynamics and Kinetics 70
2.4 Conclusions 72
2.5 Bibliography 73
Chapter 3
Bottlenecks in Photocatalytic CO_2 Reduction with Naphthalimide-Phenanthroline Re(I) Complexes Probed by Spectroelectrochemistry and Time-Resolved Infrared Spectroelectrochemistry 79
3.1 Abstract 80
3.2 Introduction 80
3.3 An Overview of Radical-Chromophore Systems 84
3.3.1 Introduction to Radical-Chromophore Systems 84
3.3.2 Excitation of the Chromophore 84
3.3.3 Excitation of the Radical 87
3.3.4 Studying Radical-Chromophore Systems 89
3.3.5 Conclusion to Radical-Chromophore Systems 89
3.4 Results and Discussion 90
3.4.1 Cyclic Voltammetry 90
3.4.2 Spectroelectrochemistry 93
3.4.3 TRIR Spectroscopy 103
3.4.4 Time-Resolved Infrared Spectroelectrochemical Studies 104
3.4.5 $[Re–R]^-$ as a Radical-Chromophore System 111
3.4.6 Photocatalytic Studies 113
3.4.7 Proposed Pathway to the Active Catalyst 115
3.5 Conclusions 117
3.6 Bibliography 119
Chapter 4
Electrochemical and Spectroelectrochemical Studies of Naphthalimide-Phenanthroline Mn(I) Complexes to Determine the Reduction Pathway Leading to the CO_2-Reducing Active Electrocatalyst 128
4.1 Abstract 129
4.2 Introduction 129

4.3 Results and Discussion 133
4.3.1 Syntheses and Spectral Characterisation 133
4.3.2 Cyclic Voltammetry 135
4.3.3 Spectroelectrochemistry under a N_2 Atmosphere 137
4.3.4 Infrared Spectroelectrochemistry under a CO_2 Atmosphere 143
4.3.5 Proposed Reduction Pathway to the Active Catalyst 143
4.3.6 Infrared Spectroelectrochemistry under CO_2 with H_2O 145
4.3.7 Electrocatalysis 152
4.3.8 Proposed Catalyst Activation Pathway under CO_2 with H_2O 153
4.4 Conclusions 155
4.5 Bibliography 155
Chapter 5
The Synthesis and Characterisation of Malononitrile-Appended Naphthalimide-Phenanthroline Re(I) and Ru(II) Complexes 161
2.1 Abstract 162
2.2 Introduction 162
2.3 Results and Discussion 164
2.3.1 Syntheses 164
2.3.2 FTIR Spectroscopy 166
2.3.3 UV-Vis Absorption Spectroscopy 168
2.3.4 UV-Vis Emission Spectroscopy 171
2.4 Conclusions 173
2.5 Bibliography 173
Chapter 6
Conclusions and Future Work 176
6.1 Overview 177
6.2 Concluding Remarks for Chapter 2 177
6.3 Concluding Remarks for Chapter 3 178
6.4 Concluding Remarks for Chapter 4 179
6.5 Concluding Remarks for Chapter 5 180
6.6 Bibliography 181
Appendices A – D
Appendix A A-2
S2.1 Experimental A-3
S2.2 ^{1}H NMR Spectra A-10
S2.3 Mass Spectrometry A-15
S2.4 IR Spectra A-19
S2.5 UV-Vis Absorption and Emission Spectra A-20

S2.6 TRIR Spectra and Kinetic Traces A-21
S2.7 TCSPC Studies A-25
S2.8 TA Spectra and Kinetic Traces A-28
S2.9 DFT and TDDFT Calculations A-31
S2.10 Bibliography A-60
Appendix B B-1
S3.1 Experimental B-2
S3.2 Spectral Characterisation B-4
S3.3 Cyclic Voltammetry B-6
S3.4 Spectroelectrochemistry B-8
S3.5 TRIR Spectra and Kinetic Traces B-10
S3.6 DFT and TDDFT Calculations B-17
S3.7 UV-Vis Monitoring of Photocatalysis B-42
S3.8 Bibliography B-42
Appendix C C-1
S4.1 Experimental C-2
S4.2 ^{1}H NMR Spectra C-5
S4.3 Cyclic Voltammetry C-7
S4.4 Spectroelectrochemistry C-9
S4.5 DFT Calculations C-10
S4.6 Bibliography C-13
Appendix D D-1
S5.1 Experimental D-2
S5.2 ^{1}H NMR Spectra D-5
S5.3 Mass Spectrometry D-8
S5.4 Bibliography D-10

Table of Figures

Figure 1.1. *Projected global warming arising from anthropogenic climate change.*[2] 3

Figure 1.2. *AM1.5 solar irradiance spectrum (300–2000 nm).*[13] *The grey-shaded region indicates the spectral region where photocatalytic water splitting is energetically accessible (λ ≤ 1008 nm). The rainbow-shaded region (380–750 nm) indicates the visible region coinciding with the solar maximum.* 5

Figure 1.3. *Electrochemical cells for electrocatalysis; (A) H-Cell, (B) Flow-cell, (C) MEA-Cell.*[22] .. 10

Figure 1.4. *Photoelectrochemical cell with a dye-sensitised semiconductor with a mediator redox species in the electrolyte solution.*[10] 11

Figure 1.5. *Spin-state diagram of a closed-shell system displaying the singlet ground state (S_0) and the singlet and triplet excited states (S_1 and T_1, respectively). The total spin angular momentum is given as S and the spin multiplicity as 2S+1.* 13

Figure 1.6. *Simplified Jablonski diagram outlining typical excited state processes observed in photophysical studies. Thick horizontal lines represent the electronic states, and thin horizontal lines are the vibrational states. S_0 is the singlet ground state, S_1/T_1 are the lowest-energy singlet/triplet excited states, and S_n/T_n are higher-energy singlet/triplet excited states.* 14

Figure 1.7. *Transition metal complexes commonly used as components in photocatalytic assemblies. Left – $[Ru(bpy)_3]^{2+}$ a common PS. Right – $Re(bpy)(CO)_3X$, where X = Br or Cl, a common photocatalyst for photocatalytic CO_2 reduction.* 16

Figure 1.8. *Examples of photocatalysts with $[Ru(bpy)_3]^{2+}$-like PSs incorporated into their structure.*[40–42] 17

Figure 1.9. *(Top) Structure of 1st row transition metal complexes with relatively long-lived excited state lifetimes. Left: cis-$[Fe(pdmi)_2]^{2+}$, Right: $[Mn(pbmi)_2]^{2+}$. (Bottom) Structure of a bimolecular Mn photocatalyst $[Mn_2(bpy)_2(CO)_6]$.* 18

Figure 1.10. *Structure of [ZnP-phen=Re].* 19

Figure 1.11. *Structure of N-heterocyclic organic PSs commonly used in photocatalytic assemblies.* 20

Figure 1.12. *Chemical structure of common rylene-imides.* 21

Figure 1.13. *The 10-π electron aromatic core of NI is highlighted with labels for the 1-8 positions.* 21

Figure 1.14. *The possible resonance forms arising from the push-pull effect for NIs with an amine at the 4-position.* 22

Figure 1.15. *Structure of three Rhenium tricarbonyl complexes covalently linked to an organic PS. (Top) [Re(dmb)(CO)$_3$(Py-DPA-NDI)]PF$_6$, (Bottom) [Re(bpy-C2-NDPI-R)Cl].* 24

Figure 1.16. *Structures of the NI-containing CO_2 reduction catalysts studied by Case, Spear, and Co-workers [Re(NO$_2$–NI–phen)(CO)$_3$Cl], and Franco et al. [Re(PNI–phen)(CO)$_3$Cl] and [Re(PNI–Ph–bpy)(CO)$_3$Cl].* 25

Figure 1.17. *(A) A schematic diagram of a TA pump-probe spectroscopic setup. (B) Representative TA spectrum (black) comprised of individual components ESA (red), GSB (green), and SE (blue). (C) Representative kinetic traces, positive traces are attributed to ESAs and negative traces are attributed to GSBs and SE.*[77] 28

Figure 1.18. *(a) A simplified diagram of a TCSPC setup and histogram, (b) a kinetic trace overlayed with the start-stop timing mode.*[82] 30

Figure 1.19. *(A) Illustrative diagrams of an OTTLE cell and a TRIR-OTTLE cell [CE = counter electrode, WE = working electrode, RE = pseudo-reference electrode]. (B) Simplified schematic of a TRIR SEC assembly including the TRIR-OTTLE cell.* 31

Figure 1.20. *Spin state diagram, following reduction of a singlet ground state (S_0) parent species, of the doublet ground state (D_0) and the lowest doublet excited state (D_1). The open-shell systems are contained within the red box. The total spin angular momentum is given as S and the spin multiplicity as 2S+1.* 32

Figure 2.1. *IR spectra of* ***Re–R*** *between 2250 and 1550 cm^{-1} in DCM (50, 20, 35, and 100 µM samples for* ***Re–H****,* ***Re–EB****,* ***Re–ES****, and* ***Re–ET****, respectively). Inset: Expanded IR spectra between 2225 and 2175 cm^{-1}.* 49

Figure 2.2. *UV-Vis absorption spectra of* ***Re–H*** *(50 µM),* ***Re–EB*** *(20 µM),* ***Re–ES*** *(35 µM), and* ***Re–ET*** *(50 µM) in DCM.* 50

Figure 2.3. *The key molecular orbitals involved in the MLCT and NI-based electronic transitions of* ***Re–R****.* 51

Figure 2.4. *Normalised emission spectra of* ***Re–R*** *following excitation at 385 nm (10, 5, 7.5, and 10 µM samples for* ***Re–H****,* ***Re–EB****,* ***Re–ES****, and* ***Re–ET****, respectively); [A] room-temperature emission spectra in DCM, [B] 77 K emission spectra of* ***Re–R*** *following excitation at 385 nm in 2-MeTHF. Inset: Non-normalised 77 K emission spectra.* 53

Figure 2.5. *(A) ps–TRIR spectra (10 µM) and (B) ns-TRIR spectra (12 µM) in the metal–carbonyl and organic carbonyl regions of* ***Re–H*** *in DCM, following excitation at 400 nm.*..... 56

Figure 2.6. *(A) ps-TRIR spectra (15 µM) and (B) ns-TRIR spectra (5 µM) of the metal–carbonyl and organic carbonyl regions of* ***Re–ET*** *in DCM following 420 nm excitation.*..... 57

Figure 2.7. *(A) ps-TRIR spectra of* ***Re–EB*** *(5 µM) following excitation at 420 nm in DCM. (B) ps-TRIR spectra of* ***Re–ES*** *(8 µM) following excitation at 420 nm. (C) The ethynyl stretching region of the ps-TRIR spectra of* ***Re–EB****. (D) The ethynyl stretching region of the ps-TRIR spectra of* ***Re–ES****. (E) The ns-TRIR spectra of* ***Re–EB*** *(5 µM) following excitation at 420 nm in DCM. (F) The ns-TRIR spectra of* ***Re–ES*** *(5 µM) following excitation at 420 nm.* 59

Figure 2.8. *The proposed resonance structures for* ***Re–EB*** *and* ***Re–ES****. Note that resonance structures with both imide carbonyls are possible, though only one is illustrated above.* 60

Figure 2.9. *Kinetic traces for aerated samples from ns–TA and ns–TRIR experiments of (A)* ***Re–H****, (B)* ***Re–EB****, and (C)* ***Re–ES****. The kinetic traces from the ns–TRIR experiments were selected based on the most intense signal in the respective spectra: this was the ^{3}MLCT transient at 2063 cm^{-1} for* ***Re–H****, while for* ***Re–EB*** *and* ***Re–ES*** *this was the ^{3}LC transient at 1615 cm^{-1}.* 65

Figure 2.10. *TA spectral changes recorded for a 20 µM DCM solution of* ***Re–H*** *after the 355 nm excitation. (The asterisk denotes a depletion arising from stimulated* ^{3}*MLCT emission).* 66

Figure 2.11. *TA spectral changes recorded for (A) 20 µM* ***Re–ET****, (B) 10 µM* ***Re–EB****, and (C) 14 µM* ***Re–ES*** *in DCM after the 355 nm excitation.* 67

Figure 2.12. *Jablonski diagrams displaying the excited-state dynamics from photoexcitation to ground state recovery of (A)* ***Re–H*** *and* ***Re–ET****, (B)* ***Re–EB*** *and* ***Re–ES****.* 72

Figure 3.1. *The excited state dynamics of a radical-chromophore system following excitation of the chromophore. Chromophore-based orbitals are on the left and radical-based orbitals are on the right of each box.* 85

Figure 3.2. *A diagram of the substates of the isoenergetic* D_n *and* Q_n *excited states. Mixing between the substates are shown with dashed lines.* 86

Figure 3.3. *The excited state dynamics of a radical-chromophore system following excitation of the radical. (A) When there are no chromophore-based molecular orbitals that are lower in energy than the* D_n *excited state, only ground-state recovery is possible. (B) When there is a chromophore-based molecular orbital lower in energy than the* D_n *excited state, DTET can occur.* 88

Figure 3.4. *Cyclic voltammograms of 1 mM [red]* ***H–NI–phen****, [black]* ***Re–H****, [blue]* ***EB–NI–phen****, and [green]* ***Re–EB*** *samples in the DCM/*10^{-1} *M* $TBAPF_6$ *electrolyte. Scan rate = 100 mV* s^{-1}*.* 91

Figure 3.5. *(A) IR SEC of 4 mM* ***Re–H*** *and (B) UV-Vis SEC of 2 mM* ***Re–H*** *in the THF electrolyte at T = 293 K, showing the stepwise conversion of the parent complex (black, dashed) to reduced species formed at R1 (red), R2 (blue), and R3 (green). OCP = open-circuit potential,* ● = ***Re–H***, ■ = ***[Re–H]***$^-$, ▼ = ^{3}***[Re–H]***$^{2-}$, ◆ = ^{3}***5–MA***, ▲ = ^{2}***5–DA***. 94

Figure 3.6. *(A) IR SEC of 4 mM* ***Re–EB*** *and (B) UV-Vis SEC of 1 mM* ***Re–EB*** *in DCM electrolyte solution at T = 293 K, showing the stepwise conversion of the parent complex (black, dashed) to the reduced species formed at R1 (red), R2 (blue), and R3 (green). OCP = open-circuit potential,* ● = ***Re–EB***, ■ = ***[Re–EB]***$^-$, ▼ = ^{3}***[Re–EB]***$^{2-}$, ◆ = ^{3}***5–MA***, ▲ = ^{2}***5–DA***. 97

Figure 3.7. *IR spectra from SEC experiments conducted under a CO_2 atmosphere in THF electrolyte, showing the stepwise conversion of the parent complex to reduced species formed at R1 (red), R2 (blue), and R3 (green), including an inset of the $^{13}CO_2$ satellite band. A =* ***Re–H****, B =* ***Re–EB*** *with an additional inset of the C≡C stretching region. OCP = open-circuit potential, ● =* ***Re–R****, ■ =* ***[Re–R]$^-$****, ▼ =* ***^{3}[Re–R]$^{2-}$****.* 100

Figure 3.8. *TRIR spectra collected in the THF electrolyte following optical excitation at 420 nm of (A)* ***Re–H*** *and (B)* ***Re–EB****.* 103

Figure 3.9. *TRIR spectrum of* ***[Re–H]$^-$*** *in the THF electrolyte following optical excitation at 420 nm. The rainbow sweep covers the $\nu_{C\equiv O}$ region over full experimental timescale (0.2 – 9500 ps). The blue/red sweep covers the $\nu_{C=O}$ region on a different timescale (0.2 – 80 ps).*..... 106

Figure 3.10. *TRIR spectrum of* ***[Re–EB]$^-$*** *in the THF electrolyte following optical excitation at 420 nm.* 107

Figure 3.11. *The TRIR spectra at 0.2, 1000, and 9500 ps following 420 nm excitation and the FTIR spectra in the DCM electrolyte of (left)* ***[Re–H]$^-$*** *and (right)* ***[Re–EB]$^-$****.*..... 109

Figure 3.12. *The TRIR spectra of* ***^{3}[Re–H]$^{2-}$*** *in the THF electrolyte following 420 nm excitation. The rainbow sweep covers the $\nu_{C\equiv O}$ region, the blue/red sweep covers the $\nu_{C=O}$ region.*..... 110

Figure 4.1. *(A) IR spectra of 20 µM* ***Mn–R*** *in THF with an inset of the $\nu_{C\equiv C}$ region. (B) UV-Vis absorption spectra of* ***Mn–R*** *series in THF with an inset displaying the MLCT and XLCT transitions.* 133

Figure 4.2. *The cyclic voltammograms of* ***Mn–R*** *in THF electrolyte under a N_2 atmosphere.* .. 136

Figure 4.4. *The experimental spectra from SEC studies of* ***Mn–phen*** *and its reduced species in 0.1 M $TBAPF_6$/THF electrolyte. (A) IR spectra. (B) UV-Vis absorption spectra.* 138

Figure 4.5. *The spectra from the SEC studies of* ***Mn–H*** *and its reduced species in 0.1 M $TBAPF_6$/THF electrolyte. (A) IR spectra. (B) UV-Vis absorption spectra.*..... 140

Figure 4.6. *The spectra recorded in the SEC studies of* ***Mn–EB*** *and its reduced species in 0.1 M $TBAPF_6$/THF electrolyte. (A) IR spectra. (B) UV-Vis absorption spectra.*..... 141

Figure 4.7. *IR spectra of* ***Mn–phen*** *(4 mM) for the SEC experiment conducted in 5% H_2O/THF electrolyte under CO_2.* 145

Figure 4.8. *IR spectra of* ***Mn–H*** *(4 mM) for the SEC experiment conducted in 5% H_2O/THF electrolyte under CO_2.* 147

Figure 4.9. *IR spectra of* ***Mn–EB*** *(4 mM) for the SEC experiment in 5% H_2O/ THF electrolyte under CO_2, with an inset showing the $\nu_{C\equiv C}$ bands. The $\nu_{C\equiv O}$ bands attributed to the* ***Mn–CO_2H*** *complex, indicated by the green boxes, are present in the spectra of the* ***Dimer*** *and* ***[Dimer]$^{2-}$****.* 148

Figure 5.1. FTIR spectra of **MN–NI–phen** and **M–MN** in DMSO. 168

Figure 5.2. UV-Vis absorption spectra of **MN–NI–phen** and **M–MN** in CH_3CN. 169

Figure 5.3. UV-Vis emission spectra of **MN–NI–phen** and **M–MN** upon excitation at 340 nm in CH_3CN. 172

Figure S2.1. *600 MHz ^{1}H NMR spectrum of* ***H–NI–phen*** *in $CDCl_3$*.....A-10

Figure S2.2. *600 MHz ^{1}H NMR spectrum of* ***Re–H*** *in $CDCl_3$* A-10

Figure S2.3. *600 MHz ^{1}H NMR spectrum of* ***EB–NA*** *in $CDCl_3$*.....A-11

Figure S2.4. *600 MHz ^{1}H NMR spectrum of* ***EB–NI–phen*** *in $CDCl_3$* A-11

Figure S2.5. *600 MHz ^{1}H NMR spectrum of* ***Re–EB*** *in $CDCl_3$* A-12

Figure S2.6. *600 MHz ^{1}H NMR spectrum of* ***ES–NA*** *in $CDCl_3$* A-12

Figure S2.7. *600 MHz ^{1}H NMR spectrum of* ***ES–NI–phen*** *in $CDCl_3$* A-13

Figure S2.8. *600 MHz ^{1}H NMR spectrum of* ***Re–ES*** *in $CDCl_3$* A-13

Figure S2.9. *600 MHz ^{1}H NMR spectrum of* ***Br–NI–phen*** *in $CDCl_3$* A-14

Figure S2.10. *600 MHz ^{1}H NMR spectrum of* ***Re–Br*** *in $CDCl_3$* A-14

Figure S2.11. *600 MHz ^{1}H NMR spectrum of* ***Re–ET*** *in $CDCl_3$*.....A-15

Figure S2.12. *ESI–QTOF mass spectrum of* ***Re–H*** *$[M+H]^+$ (M = 681.02 g/mol)*.....A-15

Figure S2.13. *ESI–QTOF mass spectrum of* ***EB–NI–phen*** *$[M+H]^+$ (M = 475.51 g/mol)* A-16

Figure S2.14. *ESI–QTOF mass spectrum of* ***Re–EB*** *$[M+H]^+$ (M = 781.19 g/mol)*.....A-16

Figure S2.15. *ESI–QTOF mass spectrum of* ***ES–NA*** *$[M+H]^+$ (M = 304.32 g/mol)* A-17

Figure S2.16. *ESI–QTOF mass spectrum of* ***ES–NI–phen*** *$[M+H]^+$ (M = 481.53 g/mol)* A-17

Figure S2.17. *ESI–QTOF mass spectrum of* ***Re–ES*** *[M] (M = 787.22 g/mol)* A-18

Figure S2.18. *ESI–QTOF mass spectrum of* ***Re–ET*** *$[M+Na]^+$ (M = 772.28 g/mol)* A-18

Figure S2.19. *FTIR spectra between 1750 and 1575 cm^{-1} of the* ***R–NI–phen*** *compounds in DCM. Inset: FTIR spectra between 2225 and 2175 cm^{-1} of* ***EB–NI–phen*** *and* ***ES–NI–phen*** *in DCM.* .A-19

Figure S2.20. *ATR–IR spectra between 2250 and 1500 cm^{-1} of* ***Re–ET****. The ethynyl vibration at 2162 cm^{-1} is indicated.* A-19

Figure S2.21. *UV-Vis absorption spectra of* ***R–NI–phen*** *in DCM solutions.* A-20

Figure S2.22. *(Left) (Right) Normalized emission spectra following excitation at 385 nm in DCM of* ***R–NI–phen****. (Right) The normalized 77 K emission spectra in 2–MeTHF of* ***R–NI–phen****. Inset – The non–normalized 77 K emission spectra of the same* ***R–NI–phen*** *compounds.* A-20

Figure S2.23. *ps–TRIR spectrum of the $\nu_{C=O}$ region of* ***H–NI–phen*** *in DCM following 365 nm excitation.* A-21

Figure S2.24. *ps–TRIR spectra displaying the ethynyl and organic carbonyl regions in DCM following 420 nm excitation of* ***EB–NI–phen*** *(Left) and* ***ES–NI–phen*** *(Right).* A-21

Figure S2.25. *Kinetic traces of the $\nu_{C=O}$ 1710 cm^{-1} GSB and $\nu_{C=O}$ 1644 cm^{-1} transient band of* ***H–NI–phen*** *following excitation at 365 nm.* A-22

Figure S2.26. *Kinetic traces of the $\nu_{C=O}$ 1706 cm^{-1} GSB and $\nu_{C\equiv C}$ 2103 cm^{-1} transient band of* ***EB–NI–phen*** *following excitation at 420 nm.* A-22

Figure S2.27. *Kinetic traces of the $\nu_{C=O}$ 1710 cm^{-1} GSB and $\nu_{C\equiv C}$ 2108 cm^{-1} transient band of* ***ES–NI–phen*** *following excitation at 420 nm.* A-23

Figure S2.28. *Kinetic traces of the $\nu_{C\equiv O}$ 1920 cm^{-1} GSB and $\nu_{C\equiv O}$ 1957 cm^{-1} transient band of* ***Re–H*** *following excitation at 400 nm.* A-23

Figure S2.29. *Kinetic traces of the $\nu_{C\equiv O}$ 2028 cm^{-1} GSB and $\nu_{C\equiv O}$ 2058 cm^{-1} transient band of* ***Re–ET*** *following excitation at 420 nm.* A-24

Figure S2.30. *Kinetic traces of the $\nu_{C\equiv O}$ 1921 cm^{-1} GSB and $\nu_{C\equiv O}$ 1961 cm^{-1} transient band of* ***Re–EB*** *following excitation at 420 nm.*.....A-24

Figure S2.31. *Kinetic traces of the $\nu_{C\equiv O}$ 2028 cm^{-1} GSB and $\nu_{C\equiv O}$ 2063 cm^{-1} transient band of* ***Re–ES*** *following excitation at 420 nm.* A-25

Figure S2.32. *Kinetic trace at 445 nm of* ***EB–NI–phen*** *in DCM following 375 nm excitation.*..A-25

Figure S2.33. *Kinetic trace at 485 nm of* ***ES–NI–phen*** *in DCM following 375 nm excitation.* ..A-26

Figure S2.34. *Kinetic trace at 630 nm of* ***Re–H*** *in DCM following 375 nm excitation.* A-26

Figure S2.35. *Kinetic trace at 445 nm of* ***Re–EB*** *in DCM following 375 nm excitation.* A-27

Figure S2.36. *Kinetic trace at 485 nm of* ***Re–ES*** *in DCM following 375 nm excitation.*.....A-27

Figure S2.37. *Kinetic trace at 630 nm following 355 nm excitation of* ***Re–EB*** *in DCM.* A-27

Figure S2.38. *Kinetic traces from µs-TA and µs-TRIR experiments of aerated samples of (A)* ***R–NI–phen****, (B)* ***R–NI–phen****, and (C)* ***R–NI–phen****.*.....A-28

Figure S2.39. *(Left) TA spectrum of* ***H–NI–phen*** *in DCM following excitation at 355 nm. (Right) Kinetic trace displaying biexponentially fit lifetimes and average lifetime at 480 nm.*.....A-28

Figure S2.40. *(Left) TA spectrum of* ***EB–NI–phen*** *in DCM following excitation at 355 nm. (Right) Kinetic trace displaying biexponentially fit lifetimes and average lifetime at 575 nm.*.....A-29

Figure S2.41. *(Left) TA spectrum of* ***ES–NI–phen*** *in DCM following excitation at 355 nm. (Right) Kinetic trace displaying biexponentially fit lifetimes and average lifetime at 645 nm.*.....A-29

Figure S2.42. *Kinetic traces from µs–TA experiments in DCM following excitation at 355 nm of (A)* ***Re–H****, (B)* ***Re–ET****, (C)* ***Re–EB****, and (D)* ***Re–ES****.*.....A-30

Figure S2.43. *DFT–calculated IR spectra. [Top-left]* ***Re–H*** *(black) and* ***^{3}Re–H*** *(red). [Top-right]* ***Re–EB*** *(black) and* ***^{3}Re–EB*** *(red). [Bottom-left]* ***Re–ET*** *(black) and* ***^{3}Re–ET*** *(red). [Bottom-right]* ***Re–ES*** *(black) and* ***^{3}Re–ES*** *(red).* A-31

Figure S2.44. *TDDFT–calculated UV-Vis spectra. [Top-left]* ***Re–H*** *(black) and* ***^{3}Re–H*** *(red). [Top-right]* ***Re–EB*** *(black) and* ***^{3}Re–EB*** *(red). [Bottom-left]* ***Re–ET*** *(black) and* ***^{3}Re–ET*** *(red). [Bottom-right]* ***Re–ES*** *(black) and* ***^{3}Re–ES*** *(red).* A-32

Figure S2.45. *Calculated UV-Vis spectrum of* ***Re–H****.* A-32

Figure S2.46. *Molecular orbitals involved in electronic transitions of* ***Re–H*** *(see* ***Table S2.1****).* A-34

Figure S2.47. *Calculated UV-Vis spectra of* ***Re–EB****.* A-35

Figure S2.48. *Molecular orbitals involved in transitions of* ***Re–EB*** *(see* ***Table S2.2****).* A-36

Figure S2.49. *Calculated UV-Vis spectra of* ***Re–ES****.* A-37

Figure S2.50. *Molecular orbitals involved in transition of* ***Re–ES*** *(see* ***Table S2.3****).* A-39

Figure S2.51. *Calculated UV-Vis spectra of* ***Re–ET****.* A-40

Figure S2.52. *Molecular orbitals involved in transition of* ***Re–ET*** *(see* ***Table S2.4****).* A-41

Figure S2.53. *Calculated UV-Vis spectrum of* ***^{3}Re–H****.* A-42

Figure S2.54. *Molecular orbitals involved in transition of* ***^{3}Re–H*** *(see* ***Table S2.5****).* A-44

Figure S2.55. *Calculated UV-Vis spectrum of* ***^{3}Re–EB****.* A-45

Figure S2.56. *Molecular orbitals involved in transitions of* ***^{3}Re–EB*** *(see* ***Table S2.6****).* A-49

Figure S2.57. *Calculated UV-Vis spectra of* ***^{3}Re–ES****.* A-50

Figure S2.58. *Molecular orbitals involved in transition of* ***^{3}Re–ES*** *(see* ***Table S2.7****).* A-53

Figure S2.59. *Calculated UV-Vis spectra of* ***^{3}Re–ET****.* A-54

Figure S2.60. *Molecular orbitals involved in transition of* ***^{3}Re–ET*** *(see* ***Table S2.8****).* A-57

Figure S2.61. *Calculated spin density of* ***^{3}Re–EB***, ***^{3}Re–ES***, *and* ***^{3}Re–ET****.* A-58

Figure S2.62. *Possible a–d structures of* ***Re–EB****.* A-58

Figure S2.63. *Possible a (left) and b (right) structures of* ***Re–ES****.* A-58

Figure S3.1. *UV-Vis absorption spectra collected in DCM of [A]* ***H–NI–phen*** *(red) and* ***Re–H*** *(black) and [B]* ***EB–NI–phen*** *(blue) and* ***Re–EB*** *(black).* B-4

Figure S3.2. *UV-Vis absorption spectra of [A]* ***H–NI–phen*** *(red) and* ***Re–H*** *(black) and [B]* ***EB–NI–phen*** *(blue) and* ***Re–EB*** *(black) collected in THF.* B-5

Figure S3.3. *IR spectra of [A]* ***H–NI–phen*** *and* ***Re–H****, and [B]* ***EB–NI–phen*** *and* ***Re–EB*** *with an inset of the ethynyl stretching vibration, collected in DCM.* B-5

Figure S3.4. *IR spectra of [A]* ***H–NI–phen*** *and* ***Re–H****, and [B]* ***EB–NI–phen*** *and* ***Re–EB*** *with an inset of the ethynyl stretching vibration collected in THF.* B-5

Figure S3.5. *CVs showing the reversibility of the R1 and R2 reduction waves of 1 mM [A]* ***H–NI–phen****, [B]* ***Re–H****, [C]* ***EB–NI–phen****, and [D]* ***Re–EB*** *in DCM/TBAH electrolyte solutions under N_2 atmosphere. Scan rates between 10 and 100 mV s^{-1}.* B-6

Figure S3.6. *CVs of 1 mM [red]* ***H–NI–phen****, [black]* ***Re–H****, [blue]* ***EB–NI–phen****, and [green]* ***Re–EB*** *samples in DMF/TBAH electrolyte solutions under N_2 atmosphere.* B-6

Figure S3.7. *CVs of 1 mM [black]* ***Re–H*** *and [green]* ***Re–EB*** *samples in THF/TBAH electrolyte solutions under N_2 atmosphere.* B-7

Figure S3.8. *CVs of 1 mM [black]* ***Re–H*** *and [green]* ***Re–EB*** *samples in DMF/TBAH electrolyte solution under CO_2 atmosphere.* B-7

Figure S3.9. *4 mM IR SEC (A) and 2 mM UV-Vis SEC (B) spectra of* ***H–NI–phen*** *in a DCM electrolyte solution.* B-8

Figure S3.10. *4 mM IR SEC (A) and 2 mM UV-Vis SEC (B) spectra of* ***EB–NI–phen*** *in a DCM electrolyte solution.* B-8

Figure S3.11. *4 mM IR SEC (A) and 2 mM UV-Vis SEC (B) spectra of* ***Re–H*** *in the DCM electrolyte solution.* ● = ***Re–H***, ■ = ***[Re–H]$^-$***, ▼ = ***^{3}[Re–H]$^{2-}$***, ◆ = ***^{3}5–MA***. B-9

Figure S3.12. *4 mM IR SEC (A) and 1 mM UV-Vis SEC (B) spectra of* ***Re–EB*** *in the DCM electrolyte solution.* ● = ***Re–EB***, ■ = ***[Re–EB]$^-$***, ▼ = ***^{3}[Re–EB]$^{2-}$***, ◆ = ***^{3}5–MA***. B-9

Figure S3.13. *TRIR spectrum of* ***Re–H*** *in a DCM electrolyte solution following 420 nm excitation.* B-10

Figure S3.14. *TRIR spectra of* ***EB–NI–phen*** *in a DCM electrolyte solution following 420 nm excitation.* B-10

Figure S3.15. *TRIR spectrum of* ***Re–EB*** *in a DCM electrolyte solution following 420 nm excitation. A: ethynyl and metal carbonyl regions. B: organic carbonyl region.* B-11

Figure S3.16. *TRIR spectrum of* ***[Re–H]$^-$*** *in the DCM electrolyte solution following 420 nm excitation. The metal and organic carbonyl regions are highlighted.* B-12

Figure S3.17. *TRIR spectrum of* ***[Re–EB]$^-$*** *in the DCM electrolyte solution following 420 nm excitation. The metal and organic carbonyl regions are highlighted.* B-12

Figure S3.18. *Kinetic traces of the $\nu_{C\equiv O}$ 2035 cm^{-1} GSB and $\nu_{C\equiv O}$ 2082 cm^{-1} transient band of* ***Re–H*** *in THF following excitation at 420 nm. Inset: Kinetic traces of the $\nu_{C\equiv O}$ 1921 cm^{-1} GSB and $\nu_{C\equiv O}$ 1954 cm^{-1} transient band of* ***Re–H*** *in THF following excitation at 420 nm.* B-13

Figure S3.19. *Kinetic traces of the $\nu_{C\equiv O}$ 2028 cm^{-1} GSB and $\nu_{C\equiv O}$ 2052 cm^{-1} transient band of* ***Re–H*** *in DCM following excitation at 420 nm.* B-13

Figure S3.20. *Kinetic traces of the $\nu_{C\equiv O}$ = 2026 cm^{-1} GSB and the $\nu_{C\equiv O}$ 2054 cm^{-1} transient band* ***Re–EB*** *in DCM following excitation at 420 nm.* B-14

Figure S3.21. *Kinetic traces of the $\nu_{C=O}$ 1705 cm^{-1} GSB, the $\nu_{C=O}$ 1633 cm^{-1} transient band, and $\nu_{C\equiv C}$ 2111 cm^{-1} transient band of* ***EB–NI–phen*** *in DCM following excitation at 420 nm.* B-14

Figure S3.22. *Kinetic traces of the $\nu_{C\equiv O}$ 2040 cm^{-1} GSB and the $\nu_{C\equiv O}$ 2059 and 2002 cm^{-1} transient bands (corresponding to the ^{4}MLCT and ^{4}ILCT transient features, respectively) of* ***[Re–H]$^-$*** *in THF following excitation at 420 nm. Inset: Kinetic traces of the $\nu_{C=O}$ 1621 cm^{-1} GSB and the $\nu_{C=O}$ 1612 cm^{-1} transient band of* ***[Re–H]$^-$*** *in THF following excitation at 420 nm.* B-15

Figure S3.23. *Kinetic traces of the $\nu_{C\equiv O}$ 2002 cm^{-1} GSB and the $\nu_{C\equiv O}$ 1993 cm^{-1} transient band of* ***[Re–H]$^{2-}$*** *in THF following excitation at 420 nm.* B-15

Figure S3.24. *Kinetic traces of the $\nu_{(C\equiv O)}$ 2028 cm^{-1} GSB and the $\nu_{C\equiv O}$ 2040 and 2002 cm^{-1} transient bands (corresponding to the ^{4}MLCT and ^{4}ILCT transient features, respectively) of* ***[Re–H]$^-$*** *in DCM following excitation at 420 nm.* B-16

Figure S3.25. *Kinetic traces of the $\nu_{C\equiv O}$ 2028 cm^{-1} GSB and the $\nu_{C\equiv O}$ 2064 and 2009 cm^{-1} transient bands (corresponding to the ^{4}MLCT and ^{4}ILCT transient features, respectively) of* ***[Re–EB]$^-$*** *in DCM following excitation at 420 nm.* B-16

Figure S3.26. *(A) DFT calculated IR spectra and (B) TDDFT calculated UV-Vis absorption spectra of* ***Re–H*** *(black),* ***[Re–H]$^{-}$*** *(red),* ***^{3}[Re–H]$^{2-}$*** *(blue).* B-17

Figure S3.27. *(A) DFT calculated IR spectra and (B) TDDFT calculated UV-Vis absorption spectra of the* ***Re–EB***, ***[Re–EB]$^{-}$***, ***^{3}[Re–EB]$^{2-}$***, ***^{3}[Re–EB]$^{2-}$*** *species.* B-17

Figure S3.28. *Calculated UV-Vis absorption spectrum of* ***Re–H***. B-18

Figure S3.29. *Molecular orbitals involved in electronic transitions of* ***Re–H*** *(see* ***Table S3.1****).* B-20

Figure S3.30. *Calculated UV-Vis absorption spectrum of* ***Re–EB.*** B-21

Figure S31. *Molecular orbitals involved in transitions of* ***Re–EB*** *(see* ***Table S3.2****).* B-22

Figure S3.32. *Calculated UV-Vis absorption spectrum of* ***[Re–H]$^{-}$***. B-23

Figure S3.33. *Molecular orbitals involved in electronic transitions of* ***[Re–H]$^{-}$*** *(listed in* ***Table S3.3****).* B-25

Figure S3.34. *Calculated UV-Vis absorption spectrum of* ***[Re–EB]$^{-}$***. B-26

Figure S3.35. *Molecular orbitals involved in the transitions of* ***[Re–EB]$^{-}$*** *(see* ***Table S3.4****).* B-29

Figure S3.36. *Calculated UV-Vis absorption spectrum of* ***^{3}[Re–H]$^{2-}$***. B-30

Figure S3.37. *Molecular orbitals involved in electronic transitions of* ***^{3}[Re–H]$^{2-}$*** *(see* ***Table S3.5****).* B-32

Figure S3.38. *Calculated UV-Vis absorption spectrum of* ***^{3}[Re–EB]$^{2-}$***. B-33

Figure S3.39. *Molecular orbitals involved in the transitions of* ***^{3}[Re–EB]$^{2-}$*** *(see* ***Table S3.6****).* B-37

Figure S3.40. *Frontier orbitals (and the spin densities for the biradical species) of the reduced species of* ***Re–H*** *observed in SEC studies.* B-38

Figure S3.41. *Possible structures of* ***Re–EB***. B-39

Figure S3.42. *Spin densities of doublet excited state of the 1e^{-} reduced species (****^{2}[Re–EB]$^{-}$****), the triplet excited state (****^{3}Re–EB****), and the 2e^{-} reduced biradical species (****$^{3/1}$[Re–EB]$^{2-}$****).* B-39

Figure S3.43. *Calculated IR spectra of* ***Re–H*** *and its reduced species.* B-40

Figure S3.44. *Calculated IR spectra of* ***Re–EB*** *and its reduced species including the 5-coordinate species; parent =* ***Re–EB****, m1_s2 =* ***[Re–EB]$^{-}$****, m2_s3 =* ***^{3}[Re–EB]$^{2-}$****, 5-MA trip =* ***^{3}5–MA****, 5-DA*

*Quad = **^{4}5–DA**, 5-DA doublet = **^{2}5–DA**, 5-MA_sing = **^{1}5–MA**. (A) organic carbonyl region, (B) metal carbonyl and ethynyl regions.* B-40

***Figure S3.45**. Calculated UV-Vis absorption spectra of **Re–R** in different redox states. (A) **Re–H** and its reduced species, (B) **Re–EB** and its reduced species; m1 = 1e-red = **[Re–R]$^-$**, m2 = 2e-red = **^{3}[Re–R]$^{2-}$**, 5C_m1_s1 = **^{1}5–MA**, 5C_m1_s3 = **^{3}5–MA**, 5C_m1_s2 = **^{2}5–DA**.* B-41

***Figure S3.46.** Visualisation of the orbitals involved in the Re^0-phen$^-$→CO_{ax} π→π* transition of the **^{1}5–MA** and **^{2}5–DA** of **Re–H**.* B-41

***Figure S3.47.** Frontier orbitals and spin densities of **^{3}5–MA** of **Re–EB**.* B-41

***Figure S3.48.** UV-Vis absorbance-difference spectra monitored up to 24 h under photocatalytic conditions of [A] **Re–H** and [B] **Re–EB**.* B-42

***Figure S4.1.** ^{1}H NMR spectrum of **Mn–phen** in $CDCl_3$.* C-5

***Figure S4.2.** ^{1}H NMR spectrum of **Mn–H** in $CDCl_3$.* C-6

***Figure S4.3.** ^{1}H NMR spectrum of **Mn–EB** in $CDCl_3$.* C-6

***Figure S4.4.** Reversibility studies at scan rates between 10–100 mV s^{-1} of (A) **Mn–phen**, (B) **Mn–H**, and (C) **Mn–EB**.* C-7

***Figure S4.5.** The cyclic voltammograms of **Mn–R** in the THF electrolyte under a CO_2 atmosphere and in the 5% H_2O in THF electrolyte under a CO_2 atmosphere. (A) **Mn–phen**, (B) **Mn–H**, and (C) **Mn–EB**.* C-8

***Figure S4.6.** 4 mM IR spectra from SEC experiments under CO_2 of (A) **Mn–phen** with an inset showing the CO_2 band at 1340 cm^{-1}, (B) **Mn–H**, and (C) **Mn–EB** with an inset showing the $\nu_{C\equiv C}$ bands.* C-9

***Figure S4.7.** DFT calculated IR spectra of (A) **Mn–phen** and its reduced species, (B) **Mn–H** and its reduced species, (C) **Mn–EB** and its reduced species.* C-10

***Figure S4.8.** Molecular structures of **Mn–phen** and its reduced species identified by SEC studies.* C-11

Figure S4.9. *The structures of the* ***syn-Dimer*** *and the* ***anti-Dimer*** *of* ***Mn–phen****. Only the* ***syn-Dimer*** *was observed in SEC studies of all* ***Mn–R*** *complexes.....* C-11

Figure S4.10. *Molecular structures of* ***Mn–H*** *and its reduced species identified by SEC studies.*

.....C-12

Figure S4.11. *Molecular structures of* ***Mn–EB*** *and its reduced species identified by SEC studies.*

..... C-12

Figure S4.12. *(A) DFT calculated IR spectra in CH_3CN of key intermediate species of* ***Mn–phen*** *identified in the IR SEC experiment with CO_2 and H_2O. The THF-solvated species $[Mn(phen)(CO)_3(THF)]^0$ is included to support the assignment of a new species to the* ***Mn–CO_2H*** *(B) The molecular structure of the* ***Mn–CO_2H*** *complex. .....* C-13

Figure S5.1. *^{1}H NMR spectrum of* ***MN–NI–phen*** *in $CDCl_3$.....*D-5

Figure S5.2. *^{1}H NMR spectrum of* ***Re–MN*** *in $CDCl_3$. *D-6

Figure S5.3. *^{1}H NMR spectrum of $[Ru(bpy)_2Cl_2]$ in CD_3CN. *D-6

Figure S5.4. *^{1}H NMR spectrum of* ***Ru–MN*** *in CD_3CN. *D-7

Figure S5.5. *^{1}H NMR spectrum of $[Ru(btfmb)_2Cl_2]$ in CD_3CN. *D-7

Figure S5.6. *^{1}H NMR spectrum of* ***CF_3Ru–MN*** *in CD_3CN. *D-8

Figure S5.7. *HR-MS of* ***MN–NI–phen*** *(MW = 439.43 g/mol). Top: negative mode $[M-H]^-$, Bottom: positive mode $[M+Na]^+$.....*D-8

Figure S5.8. *HR-MS of* ***Re–MN*** *(MW = 745.12 g/mol) displaying the negative mode $[M-H]^-$ ion.*

.....D-9

Figure S5.9. *HR-MS of* ***Ru–MN*** *(MW = 1142.81 g/mol). Top: negative mode $[PF_6]^-$ ion, Bottom: positive mode $[M+Na]^{2+}$. *D-9

Figure S5.10. *HR-MS of* ***CF_3Ru–MN*** *(MW = 1414.80 g/mol). Top: negative mode $[PF_6]^-$, Bottom: positive mode $[M–CN]^{2+}$. *D-10

Table of Charts

Chart 2.1. *General structure of the* ***Re–R*** *series of complexes studied in this work. R is the substituent at the 4–position on the NI core.* 45

Chart 3.1. *Molecular structures of the* ***R–NI–phen*** *ligands and the* ***Re–R*** *complexes studied in this work.* 83

Chart 4.1. *Chemical structures of the model (****Mn–phen****) and target complexes (****Mn–H*** *and* ***Mn–EB****).* 132

Table of Schemes

Scheme 1.1. *Schematics of (A) an intermolecular and (B) an intramolecular photocatalytic assembly. (BL = Bridging ligand, CC = Catalytic Centre, PS = Photosensitiser, SED = Sacrificial electron donor. 1. HER, 2. CO_2 reduction reaction into CO or HCO_2H).* 8

Scheme 1.2. *An illustration of an electrical double layer during electrocatalysis with mass transport, adsorption, and desorption steps indicated. Note that the layers, and also the particles, are not to scale. A = reactant molecules, B = product molecules, e^- = electrons, A⟶B represents a redox catalytic reaction; if an electron is added = reduction, if an electron is lost = oxidation.* 9

Scheme 2.1. *Reaction schemes for (A) general synthesis of **R–NI–phen**, (B) general synthesis of **Re–R**. R = H, EB, ES, or ET.* 47

Scheme 2.2. *Sonogashira cross-coupling reaction schemes for the formation of (A) **EB–NA** and **ES–NA** precursors, (B) **Re–ET** complex.* 47

Scheme 3.1. *The reduction pathway of **Re–R** under electrochemical conditions, based on the electrochemical studies conducted in this work. Note that while two possible 5-coordinate electrocatalysts are proposed, only the **^{2}5–DA** is observed in SEC studies.* 101

Scheme 3.2. *The excited state dynamics of the **[Re–R]$^-$** radical-chromophore upon excitation of the radical (blue) and chromophore (red) moieties, as determined from TRIR SEC studies. Spin-state diagrams of each excited state are included; Blue = R–NI$^{\bullet-}$ electrons, Red = Re–phen electrons, Grey = electrons originating from Re–phen or R–NI$^{\bullet-}$ for the ^{4}MLCT and ^{4}ILCT excited states, respectively. The relative energies of the HOMO and HOSO, and the LUMO and LUSO, do not reflect the relative energies in the **[Re–R]$^-$** complexes.* 112

Scheme 3.3. *The proposed pathway leading to the active catalyst under photocatalytic conditions based on this work. The coloured boxes indicate the experiment where that species is identified in this work (orange = TRIR, purple = SEC, green = TRIR SEC). Highlighted components*

*indicate where charge is localised within the structure of each **Re–R** species (cyan = R–NI-based, orange = phen-based, red = Re^{II} metal centre, green = Re^{0}).* 117

***Scheme 4.1.** Simplified reduction pathways for [Re(bpy)(CO)$_3$Cl] (Top) and [Mn(bpy)(CO)$_3$Br] (Bottom). The 6–coordinate monoanion (**6–MA**) in red and the manganese–manganese dimer (**Dimer**) in blue are highlighted as the key intermediates leading to the 5–coordinate monoanion (**5–MA**) in green as the active catalyst in both pathways.* 131

***Scheme 4.2.** Reduction pathway for the formation of the active catalyst of **Mn–R** under CO_2. The intermediate species identified in IR SEC experiments in the presence of CO_2 are highlighted.* 144

***Scheme 4.3.** Proposed reduction pathway of **Mn–R** in the presence of CO_2 and H^+. The intermediate species identified in IR SEC experiments in the presence of CO_2 and H^+ are highlighted. The **Mn–CO_2H** complex is only observed for **Mn–EB** in the aforementioned IR SEC experiments. The CO_2 reduction cycle (red) illustrates the reduction-first catalytic pathway.* . 154

***Scheme 5.1.** Keto-enol tautomerism in **MN–NI** compounds (R = alkyl or aryl group). The methine proton associated with the keto-form is highlighted in blue. The hydroxy proton associated with the enol-form is highlighted in red. Tautomerisation can occur with either carbonyl group in the imide.* 163

***Scheme 5.2.** The synthetic pathway for **MN–NI–phen** with reaction conditions and yields.* ... 165

***Scheme 5.3.** The **M–MN** complexes obtained by coordination reactions of Re^{I} and Ru^{II} complexes with **MN–NI–phen**. The % yields are included.*..... 166

Table of Tables

Table 2.1. *IR and UV-Vis absorption and emission spectral data for both the* ***R–NI–phen*** *and* ***Re–R*** *series in DCM and DFT/TDDFT calculated spectral features for* ***Re–R****.* 52

Table 2.2. *TRIR data following 420 nm excitation of* ***Re–R*** *and DFT-calculated IR wavenumbers of* ***Re–R****.*[a] 61

Table 2.3. *Excited-state lifetimes based on room-temperature emission, TRIR, and TA studies in DCM.*[a] 63

Table 3.1. *Redox potentials of* ***R–NI–phen*** *and* ***Re–R*** *from CV measurements.*[a] 93

Table 3.2. *Key spectroscopic data from experimental SEC studies and supporting DFT/TDDFT calculations of* ***Re–R*** *and their reduced forms in DCM and THF electrolyte solutions.* 102

Table 3.3. *Transient bands of the* ***Re–R*** *complexes and their reduced species from TRIR/TRIR SEC experiments in DCM and THF electrolytes.*[a,b] 105

Table 3.4. *Excited state lifetimes from TRIR studies of* ***Re–R*** *and TRIR SEC studies of* ***[Re–R]***$^-$ *following excitation at 420 nm in the DCM electrolyte.* 108

Table 3.5. *TONs and TOFs of CO obtained at indicated time intervals under indicated photocatalytic conditions.*[a] 114

Table 4.1. *Key spectral data of* ***Mn–R*** *from FTIR and UV-Vis absorption studies in THF.* 134

Table 4.2. *Reduction potentials of the* ***Mn–R*** *series in 0.1 M* $TBAPF_6$*/THF electrolyte solutions under* N_2 *and* CO_2 *atmospheres.*[a] 135

Table 4.3. *Key spectral features from IR and UV-Vis SEC experiments of* ***Mn–R*** *in THF electrolyte.* 142

Table 4.4. *Key IR spectral features from SEC experiments under* CO_2 *with* H_2O*.* 151

Table 4.5. *Controlled potential electrolysis results during 1 h experiments with 0.8 mM samples of catalyst in a 5%* H_2O*/THF electrolyte solution with 600 rpm stirring.* 152

Table 5.1. Key spectral data from FTIR and UV-Vis absorption and emission spectroscopy.[a] .. 170

Table S2.1. *Major electronic excitations in* ***Re–H*** *determined by TDDFT calculations.* A-33

Table S2.2. *Major electronic excitations in* ***Re–EB*** *determined by TDDFT calculations.* A-35

Table S2.3. *Major electronic excitations in* ***Re–ES*** *determined by TDDFT calculations.* A-37

Table S2.4. *Major electronic excitations in* ***Re–ET*** *determined by TDDFT calculations.* A-40

Table S2.5. *Major electronic excitations in* ^{3}***Re–H*** *determined by TDDFT calculations.* A-42

Table S2.6. *Major electronic excitations in* ^{3}***Re–EB*** *determined by TDDFT calculations.* A-45

Table S2.7. *Major electronic excitations in* ^{3}***Re–ES*** *determined by TDDFT calculations.* A-50

Table S2.8. *Major electronic excitations in* ^{3}***Re–ET*** *determined by TDDFT calculations.* A-54

Table S2.9. *Differential energies of structures a–d of* ***Re–EB*** *(see* ***Figure S2.62****).* A-58

Table S2.10. *Differential energies of the a and b structures of* ***Re–ES*** *(see* ***Figure S2.63****).* A-58

Table S2.11. *Table of triplet energy gap (*ΔE_T*) values.* A-59

Table S3.1. *Major electronic excitations in* ***Re–H*** *determined by TDDFT calculations.* B-18

Table S3.2. *Major electronic excitations in* ***Re–EB*** *determined by TDDFT calculations.* B-21

Table S3.3. *Major electronic excitations in* $\mathbf{[Re–H]^-}$ *determined by TDDFT calculations.* B-23

Table S3.4. *Major electronic excitations in* $\mathbf{[Re–EB]^-}$ *determined by TDDFT calculations.* B-26

Table S3.5. *Major electronic excitations in* $^{3}\mathbf{[Re–H]^{2-}}$ *determined by TDDFT calculations.* B-30

Table S3.6. *Major electronic excitations in* $^{3}\mathbf{[Re–EB]^{2-}}$ *determined by TDDFT calculations.* B-33

Table S3.7. *Energies of different spin states of* $\mathbf{[Re–H]^{2-}}$*.* B-38

Table S3.8. *Differential energies of structures a–d accompanying* ***Figure S3.41****.* B-39

Table S3.9. *Energies of different spin states of* $\mathbf{[Re–EB]^{2-}}$*.* B-40

Table S3.10. *Calculated IR modes of the 5-coordinate species of* ***Re–R****.* B-42

Table of Equations

Equation 1.1. *Overall water splitting (OWS) reaction.* 5

Equation 1.2. *Hydrogen evolving half-reaction (HER).* 5

Equation 1.3. *Oxygen evolving half-reaction (OER).* 5

Equation 1.4. *CO_2 reduction yielding carbon monoxide (CO) and H_2O.* 6

Equation 1.5. *CO_2 reduction yielding formic acid (HCO_2H).* 6

Equation 1.6. *CO_2 reduction yielding formaldehyde (HCHO) and H_2O.* 6

Equation 1.7. *CO_2 reduction yielding methanol (CH_3OH) and H_2O.* 6

Equation 1.8. *CO_2 reduction yielding methane (CH_4) and H_2O.* 6

Equation 1.9. *Beer-Lambert Law; A = absorbance, ε = molar extinction coefficient, c = concentration, l = path length of light through the cell.* 27

Equation 2.1. *Equation used to derive the ratio (a) between the rate constant obtained from the average emission lifetime (k_{Re-R}) and the rate constants obtained from the ^{3}MLCT and ^{3}LC excited-state lifetimes (k_{MLCT} and k_{LC}, respectively).* 69

Equation 2.2. *Equation used to derive the equilibrium constant (K_{eq}) from a.* 69

Equation 2.3. *Equation used to derive the triplet-energy gap (ΔE_T) from K_{eq}.* 69

Equation S2.1. *Equation for determining an amplitude-weighted average lifetime.*[10] A-9

Abbreviations

BL	Bridging Ligand
bpy	2,2’-bipyridine
btfmb	4,4’-bistrifluoromethyl-2,2’-bipyridine
CC	Catalytic Centre
CH_3CN	Acetonitrile
CO	Carbon Monoxide
CO_2	Carbon Dioxide
CE	Counter Electrode
CT	Charge Transfer
CV	Cyclic Voltammetry
DCM	Dichloromethane
DFT	Density Functional Theory
DMF	*N,N*-dimethylformamide
DMSO	Dimethyl sulfoxide
DTET	Dexter-like doublet-triplet energy transfer
D-π-A	Donor-π-Acceptor
EB	Ethynyl benzene
ES	Ethynyl-2-thiophene
ESCE	Excited-state Conjugation Enhancement
ET	Ethynyl trimethylsilane
Fc	Ferrocene
Fc^+	Ferrocenium
GSB	Ground-state bleach
HOMO	Highest-Occupied Molecular Orbital

HOSO	Highest-Occupied Spin Orbital
ILCT	Intra-Ligand Charge Transfer
IC	Internal Conversion
IR	Infrared
ISC	Intersystem Crossing
LC	Ligand Centred
LMCT	Metal-to-Ligand Charge Transfer
LUMO	Lowest-Unoccupied Molecular Orbital
LUSO	Lowest-Unoccupied Spin Orbital
2-MeTHF	2-methyl tetrahydrofuran
MLCT	Metal-to-Ligand Charge Transfer
ML'LCT	Metal-Ligand-to-Ligand Charge Transfer
MN	Malononitrile
Mn	Manganese
NA	1,8-naphthalic anhydride
NI	1,8-naphthalimide
PEC	Photoelectrochemical cell
PICT	Planar Intramolecular Charge Transfer
phen	1,10-phenanthroline
PS	Photosensitiser
Re	Rhenium
RE	pseudo-Reference Electrode
REISC	Radical-enhanced intersystem crossing
Ru	Ruthenium
SEC	Spectroelectrochemistry

SOC	Spin-Orbit Coupling
TA	Transient Absorption
$TBAPF_6$	n-tetrabutyl ammonium hexafluorophosphate
TCSPC	Time-Correlated Single Photon Counting
TDDFT	Time-dependent density functional theory
TEOA	Triethanolamine
THF	Tetrahydrofuran
TL-CV	Thin-layer Cyclic Voltammetry
TOF	Turnover Frequency
TON	Turnover Number
TRIR	Time-Resolved Infrared
TRIR SEC	Time-Resolved Infrared Spectroelectrochemistry
TTET	Triplet-triplet energy transfer
UV	Ultraviolet
VC	Vibrational Cooling
Vis	Visible
WE	Working Electrode
XLCT	Halide-to-Ligand Charge Transfer

Units of Measurement and Symbols

ν	Vibrational mode
cm^{-1}	Wavenumber
λ	Wavelength
O.D.	Optical Density
ΔO.D.	Change in optical density
ΔmO.D.	Change in milli(optical density)
nm	Nanometre
ε	Molar extinction coefficient
ϕ_{em}	Emission quantum yield
τ	Lifetime
fs	Femtosecond(s)
ps	Picosecond(s)
ns	Nanosecond(s)
µs	Microsecond(s)
α_{TA}	Amplitude
k	Rate Constant
K_{eq}	Equilibrium Constant
ΔE_T	Triplet energy gap
ΔG_T	Difference of free energy
°C	Degree Celsius
K	Kelvin
R	Gas Law Constant (8.314 J K^{-1} mol^{-1})
min	Minute(s)
h	Hour(s)

TON/h	Turnover numbers per hour
cm^3	Cubic centimetre
mL	Millilitre
L	Litre
v/v	Volume per volume
mmol	Millimole
mg	Milligram
g	Gram
g mol^{-1}	Gram per mole
µM	Micromolar
mM	Millimolar
M	Molar
MHz	Megahertz
J	Coupling Constant
eV	Electron volts
mV	Millivolt
V	Volt
mA	Milliampere
A	Ampere
C	Coulomb
F	Faraday Constant (96485 C mol^{-1})
Q	Charge
η_{FE}	Faradaic Efficiency

Thesis Publications

Chapter 2:

Biddulph, J., Pižl, M., Bhattacharya, S., Malakar, P., Greetham, G. M., Hartl, F., Pryce, M. T., *Nature and Dynamics of the Excited States of Ethynyl–Functionalized Naphthalimide–Phenanthroline Re(I) Complexes Studied by TA and TRIR Spectroscopies*, J. Phys. Chem. B., 2026, **130**, 6383–6398.

Chapter 3:

Biddulph, J., Cerpentier, F., Pižl, M., Bhattacharya, S., Malakar, P., Greetham, G. M., Hartl, F., Pryce, M. T., *Bottlenecks in Photocatalytic CO_2 Reduction with Naphthalimide-Phenanthroline Re(I) Complexes Probed by Spectroelectrochemistry and Time-Resolved Infrared Spectroelectrochemistry*, Submitted to Chem. Sci, 2026.

Thesis Abstract

Jack Biddulph - Photophysical and Electrochemical Studies of Naphthalimide-Phenanthroline Transition-Metal Complexes as Carbon Dioxide Reducing Catalysts

Chapter One serves as an introduction to CO_2 reduction catalysis. It includes a general introduction to the principles of photophysics used in the study of photocatalysts, and more specifically in relation to transition-metal complexes and organic chromophores. An outline of the techniques deployed in this research thesis follows including spectroelectrochemistry (SEC), transient absorption (TA) spectroscopy, time-resolved infrared (TRIR) spectroscopy, and time-resolved infrared spectroelectrochemistry (TRIR SEC).

Chapter Two involves a photophysical study of a series of ethynyl-functionalised naphthalimide-phenanthroline rhenium complexes. This chapter begins with a literature survey on the photophysics of naphthalimide-phenanthroline rhenium complexes. The synthesis of a series of ethynyl-functionalised naphthalimide-phenanthroline rhenium complexes is outlined followed by a photophysical study to discern the nature and dynamics of their excited states.

Chapter Three comprises the electrochemical, spectroelectrochemical, time-resolved infrared spectroelectrochemical, and photocatalytic studies of naphthalimide-phenanthroline rhenium complexes. The combination of these studies was utilised to propose a pathway leading to the active catalyst for photocatalytic CO_2 reduction.

Chapter Four consists of the study of two naphthalimide-phenanthroline manganese complexes. This chapter begins with a literature survey comparing the pathway leading to the active electrocatalyst for manganese complexes compared to their rhenium counterparts. This is followed by the synthesis, electrochemical and spectroelectrochemical studies of a series of naphthalimide-phenanthroline manganese complexes to determine the pathway leading to the active catalyst for CO_2 reduction.

Chapter Five pertains to the study of a series of malononitrile-appended naphthalimide-phenanthroline transition-metal complexes. This chapter begins with a literature survey of malononitrile as a substituent. The synthesis and photophysical study of a series of malononitrile-appended naphthalimide-phenanthroline transition-metal complexes follows.

Chapter Six provides a condensed review of the experimental findings of the work conducted in this thesis. Several future experiments are proposed to broaden the understanding imparted in the previous chapters about the prepared photocatalysts and electrocatalysts.

Chapter 1

Introduction

1.1 Abstract

This chapter provides context to the work presented in this thesis; initially, the case is made for why CO_2 reduction could be an effective approach to mitigating the negative impacts of greenhouse gas emissions that are driving climate change. Photocatalysis and electrocatalysis are then set out as approaches to achieve CO_2 reduction in a more sustainable manner, particularly by using renewable energy sources. A general introduction to the principles of photophysics is presented, followed by a review of common transition-metal complexes and organic chromophores employed in CO_2-reduction catalysis. Finally, an outline of the techniques used to study the photophysical and electrochemical properties throughout is discussed; including spectroelectrochemistry (SEC), time-resolved spectroscopies, and time-resolved infrared spectroelectrochemistry (TRIR SEC).

1.2 CO_2 Reduction in the Context of Climate Change

1.2.1 Climate Change

Climate change has been the focus of global attention in the last decade, particularly in the context of international commitments to limit global warming to +1.5 °C compared to preindustrial levels. Anthropogenic sources are widely accepted as the leading contributor of global warming. Fossil fuels are used for several energy intensive processes including transport, industry, and energy generation: with combustion generating potent greenhouse gases including carbon dioxide (CO_2), methane (CH_4), and nitrous oxides (NOx). These byproducts are released directly into the atmosphere where they have acted to trap heat absorbed from solar radiation in the atmosphere. Fossil fuel derived carbon dioxide (CO_2) is the leading contributor to greenhouse gas emissions, accounting for 74.5% of total global emissions in 2024, and despite the aforementioned international commitments, global emissions increased by 1.3% in 2024 compared to 2023.[1] The Earth reached +1 °C global warming compared to pre-industrial levels in 2017, with current trends indicating the Earth is on track to reach +1.5 °C global warming as soon as 2030 (Figure 1.1).[2] The consequences of reaching the +1 °C global warming milestone will be profound for the economies, populations, and ecosystems globally.[3] Continued warming beyond this will exacerbate the effects of +1 °C global warming.[2] Thus, combating global warming arising from anthropogenic climate change is at the forefront of environmental research.

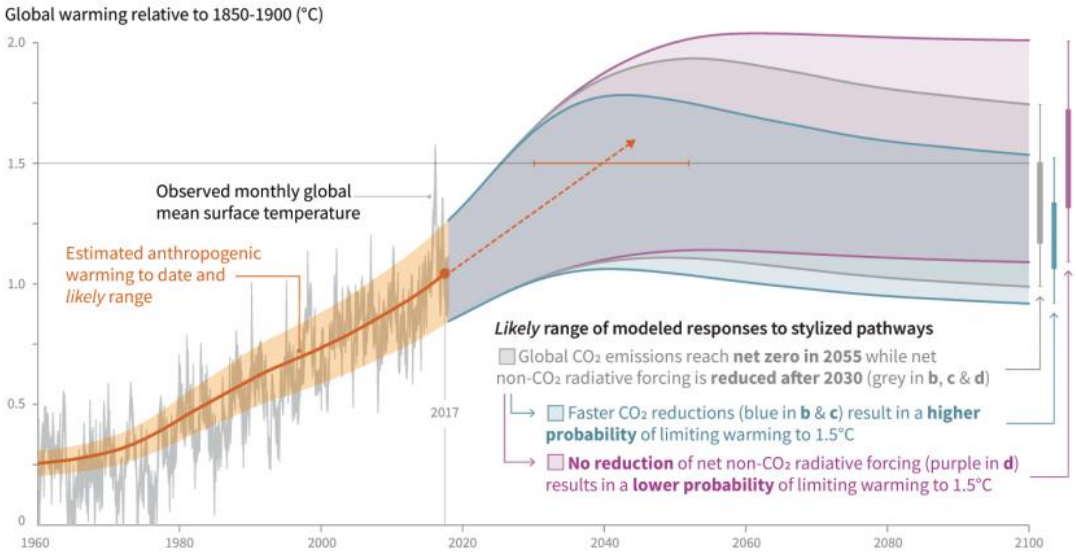


Figure 1.1. *Projected global warming arising from anthropogenic climate change.*[2]

Many approaches have been explored to combat anthropogenic climate change; carbon capture aims to prevent the release of greenhouse gas emissions into the atmosphere from anthropogenic sources, conversion to green energy sources such as wind or solar power aims to prevent the formation of those greenhouse gases in the first instance, green fuels which are energy carriers that have non-polluting byproducts have also been sought to replace fossil fuels.[4] Molecular hydrogen (H_2) has been considered as a potential green fuel to replace fossil fuels as it is a high gravimetric energy density molecule, and the byproduct of its combustion is water making it a carbon-free fuel.[5] H_2 is also a valuable industrial material as it is used in many industrial processes, the Haber process famous among these. However, due to its low abundance on Earth, H_2 must be synthesised in a sustainable manner if it is to supplement the current usage of fossil fuels.

H_2 is classified depending on how it is produced with grey, blue, and green H_2 being the most common types. Among these, grey H_2 is the most widely available and is generated from fossil fuel sources, thus, grey H_2 cannot be used as a green fuel alternative. Blue H_2 is produced in a similar manner and is therefore not referred to as a green fuel, however, carbon capture technologies can be employed to minimise the impact of this industrial process. Green H_2 is produced by water electrolysis using renewable energy sources. Green H_2 can be further categorised depending on the renewable energy source used to drive the electrolysis of water, with solar being used for yellow H_2 for instance. Solar energy is the most significant energy source available to us, with solar radiation providing 173,000 TW per hour based on the solar

minimum of 1361 W/m^2.[6] Annual energy consumption globally reached a record high of 620 EJ in 2023[7], equivalent to 172,200 TWh, thus capturing the energy from an hour of solar irradiation would supply the annual global energy demands.

Therefore, photocatalytic water splitting for H_2 generation has become a focus of research since the first dyes-sensitised solar cells (DSSCs) were developed by Grätzel et al. in 1981 followed later by the development of the photoelectrochemical cell (PEC).[8–10] There are two main energy conversion steps in the generation of yellow H_2; solar to electric, then electric to chemical energy. Each energy conversion has an associated energy loss, with the first step having a maximum energy conversion efficiency of 30.7% for a silicone-based device.[5] Thus, direct solar to chemical energy conversion, known as photocatalysis, should reduce energy loss by reducing the number of energy conversion steps. Photocatalysis has also been used to reduce CO_2 into its C1 synthons (carbon monoxide, formate, methane, methanol, etc.) since the inception of DSSCs.[11] CO_2 valorisation, that is conversion of CO_2 into another form that has value or use, is required to make CO_2 reduction catalysis an economically viable approach to combat rising greenhouse gas emissions. This is an important consideration if CO_2 reduction catalysis is to be widely adopted, particularly in developing countries which have traditionally undertaken industrialisation with relatively cheap but also heavily polluting fossil fuels.

1.1.2 Photocatalysis

Water splitting, the most widely used reaction for photocatalytic H_2 generation, is described in the overall water splitting reaction (OWS) below in Equation 1.1. The OWS can be further broken down into the H_2 evolving half reaction (HER) and the molecular oxygen (O_2) evolving half reaction (OER) (Equations 1.2 and 1.3, respectively). The OWS requires a Gibbs free energy (ΔG^0) of 237.2 kJ/mol, which equates to a potential (E^0) of 1.23 eV or 1008 nm.[12] Water does not however spontaneously decompose upon exposure to sunlight, thus, the energy for the reaction must be absorbed by another molecule and later transferred to a reaction centre. Due to radiative and non-radiative pathways associated with photoexcited species, which is discussed in more detail later, the absorption of higher energy light is required to account for energy loss arising from excited-state processes to ensure the energy supplied to the reaction centre meets the ΔG^0 requirement. As is evident from the AM1.5 solar irradiance spectrum (in Figure 1.2), a significant amount of the incident light meets this minimum energy requirement, with the solar maximum appearing in the visible region. Thus, photocatalytic materials are designed to have absorption features in the visible region to capture the available light.

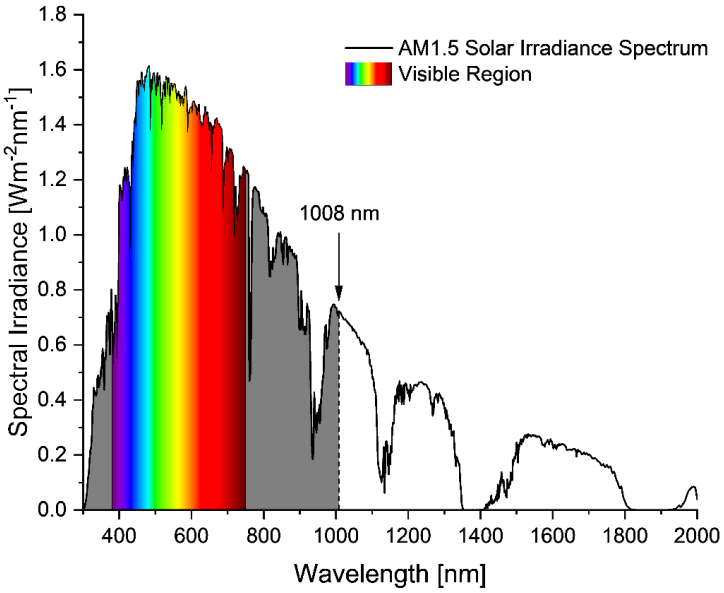


Figure 1.2. *AM1.5 solar irradiance spectrum (300–2000 nm).[13] The grey-shaded region indicates the spectral region where photocatalytic water splitting is energetically accessible (λ ≤ 1008 nm). The rainbow-shaded region (380–750 nm) indicates the visible region coinciding with the solar maximum.*

$$H_2O \longrightarrow H_2 + \frac{1}{2}O_2$$

Equation 1.1. *Overall water splitting (OWS) reaction.*

$$2H^+ + 2e^- \longrightarrow H_2$$

Equation 1.2. *Hydrogen evolving half-reaction (HER).*

$$2O^{2-} - 4e^- \longrightarrow O_2$$

Equation 1.3. *Oxygen evolving half-reaction (OER).*

For CO_2 reduction, the minimum energy requirement is dependent on the product being formed. The proton-assisted CO_2 reduction reactions (Equations 1.4–1.8) are multi-electron pathways that can be undertaken for C1 synthon formation, with CO formation requiring two electrons and CH_4 requiring eight electrons in the most extreme cases for the C1 synthons. CO and formic acid (HCO_2H) are widely encountered as reaction products in CO_2 reduction catalysis. CO is widely used in industrial processes. HCO_2H is a proposed H_2 storage material; the poor volumetric

energy density of H_2 and challenges associated its storage are overcome by combining it with CO_2 to form HCO_2H, which is more easily handled. The energy required for these reactions (reported as potentials against a standard hydrogen electrode (SHE) in water at 25 °C, pH 7, under 1 atm of gases)[14,15] are lower than that of the OWS, meaning the same spectral window determined for photocatalytic H_2 generation in Figure 1.2 can also be applied for photocatalytic CO_2 reduction into its C1 synthons. Thus, photocatalytic H_2 generation and CO_2 reduction can be performed in tandem.

$$CO_2 + 2H^+ + 2e^- \rightarrow CO + H_2O \ [\mathrm{E} = -0.53\ V]$$

Equation 1.4. *CO_2 reduction yielding carbon monoxide (CO) and H_2O.*

$$CO_2 + 2H^+ + 2e^- \rightarrow HCO_2H \ [\mathrm{E} = -0.61\ V]$$

Equation 1.5. *CO_2 reduction yielding formic acid (HCO_2H).*

$$CO_2 + 4H^+ + 4e^- \rightarrow HCHO + H_2O \ [E = -0.48\ V]$$

Equation 1.6. *CO_2 reduction yielding formaldehyde (HCHO) and H_2O.*

$$CO_2 + 6H^+ + 6e^- \rightarrow CH_3OH + H_2O \ [\mathrm{E} = -0.38\ V]$$

Equation 1.7. *CO_2 reduction yielding methanol (CH_3OH) and H_2O.*

$$CO_2 + 8H^+ + 8e^- \rightarrow CH_4 + 2H_2O \ [\mathrm{E} = -0.24\ V]$$

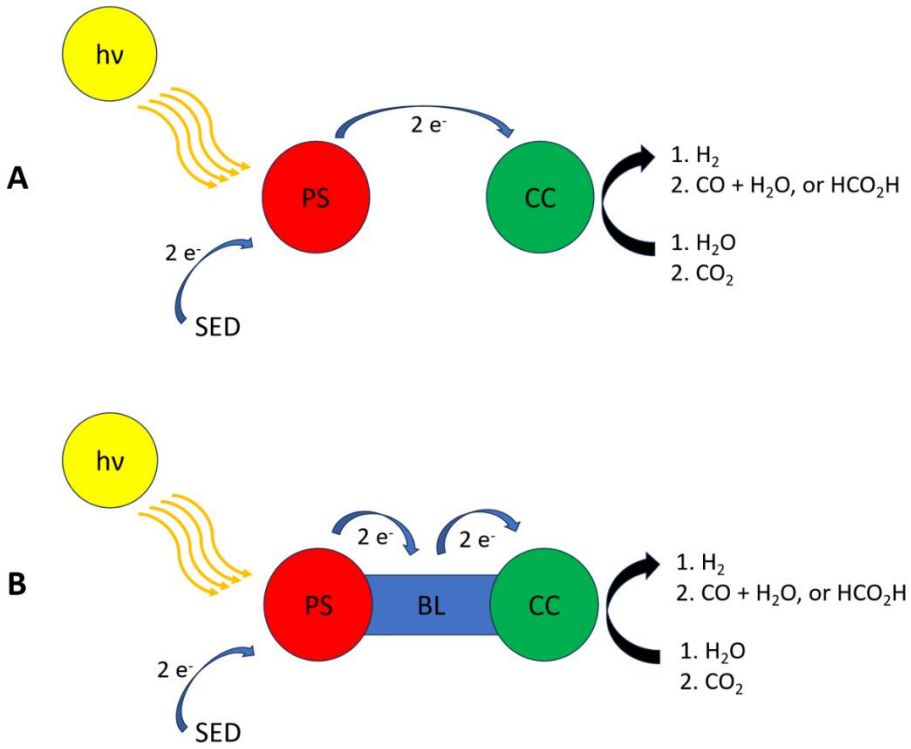
Equation 1.8. *CO_2 reduction yielding methane (CH_4) and H_2O.*

Two components are key to designing a photocatalytic assembly; a light absorbing unit called a photosensitiser (PS) and a catalytic centre (CC) which can undertake the desired reaction. It is also important that the energy absorbed by the PS upon photoexcitation is transferred to the CC by electron transfer to drive the desired photocatalytic reaction. When these assemblies are present in the same medium these are named homogeneous assemblies. Heterogenous assemblies typically involve immobilising one or both components onto a semiconductor surface

and photo-generated electrical energy to drive the desired chemical process, as discussed further in the following section on electrocatalysis. Two strategies can be employed in designing homogeneous assemblies as illustrated in Scheme 1.1. in intermolecular assemblies the PS and CC are present as separate molecules, whereas in intramolecular assemblies these components are covalently linked via a bridging ligand (BL) with the supramolecular assembly being called a photocatalyst. The ideal properties of photocatalysts are summarised below.[16]

1. Photocatalysts need suitable photophysical properties with high molar extinction coefficients (ε) and broad absorption in the visible region to benefit from solar irradiation.
2. Long-lived photoexcited species with lifetimes (τ) in milliseconds are desirable to ensure that electron transfer from the PS to the CC occurs.
3. The redox properties of the photocatalyst should allow for efficient electron transfer from the PS to the CC.
4. High photostability of the photocatalyst is necessary to guarantee its long-term operation under photocatalytic conditions.

In intermolecular assemblies, for electron transfer to occur from a photoexcited PS (PS*) to a CC a collision between PS* and CC molecules is needed**.** However, random collisions between the various components in a photocatalytic assembly can also eliminate photoexcited species before the desired reaction can occur, diminishing the performance of these assemblies. Intramolecular assemblies avoid the requirement for chance encounters by allowing for electron transfer to occur within the photocatalyst, leading to an increasing interest in their development. However, charge recombination and back electron transfer processes can impede the performance of intramolecular assemblies.[17] Overcoming these losses in efficiency requires tuning of the excited state pathway to ensure the photoexcited electron moves onto the CC and remains there for a sufficient period of time to allow the photocatalytic reaction to proceed. Accordingly, an understanding of the photophysical properties of photocatalysts is crucial to assessing the photocatalytic performance of these materials; therefore, a general introduction to photophysics is provided later in this chapter.



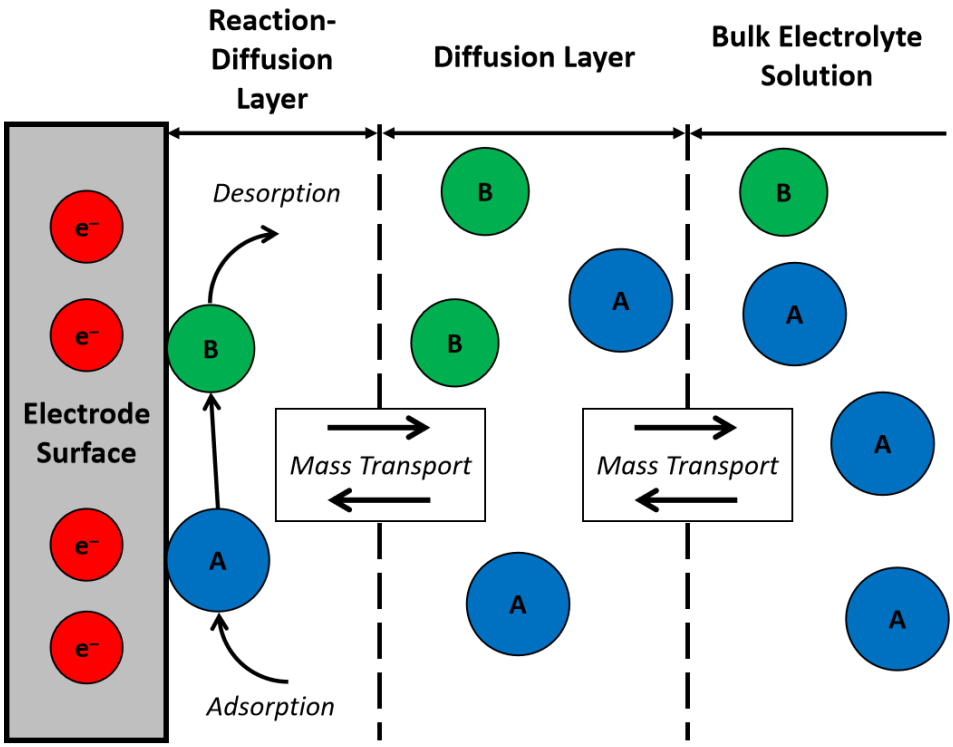
Scheme 1.1. *Schematics of (A) an intermolecular and (B) an intramolecular photocatalytic assembly. (BL = Bridging ligand, CC = Catalytic Centre, PS = Photosensitiser, SED = Sacrificial electron donor. 1. HER, 2. CO_2 reduction reaction into CO or HCO_2H).*

1.2.3 Electrocatalysis

Electrocatalysis combines electrochemistry, involving the conversion of electrical energy into chemical energy, and catalysis, which increases the rate of a chemical reaction.[18] In electrocatalysis, one overall reaction takes place within the electrochemical cell consisting of two half-reactions involving cathodic (reduction) and anodic (oxidation) processes, so named for the electrodes at which they occur. Using the example of OWS mentioned earlier (Equation 1.1), the HER half-reaction is the cathodic process and the OER half-reaction is the anodic process (Equations 1.2 and 1.3, respectively).

Electrocatalysis occurs between the electrocatalyst at the surface of an electrode and the reactants dissolved in the bulk electrolyte solution; making it a form of heterogeneous catalysis.[18] The electrical double layer, consisting of a diffusion layer and a reaction-diffusion layer as illustrated in Scheme 1.2, is key to understanding how the reactant(s) and product(s) behave near the electrode surface.[19] The diffusion layer is the region near the electrode surface where the bulk electrolyte solution can interact with the local electrode environment, but remains minimally affected by the potential applied at the electrode surface. The reaction-

diffusion layer is region of the diffusion layer in closest proximity to the electrode surface and so is the region where the desired electrocatalytic reaction occurs. Accordingly, mass transport of reactants and products between these layers significantly influences the reaction kinetics. Particularly, the diffusivity and concentration of the reactant or product in the bulk solution, the rates of adsorption (of the reactant) and desorption (of the product) to and from the electrode surface, and the kinetics of the catalytic reaction itself are all interlinked in electrocatalysis.[19,20] Stirring or flow of the electrolyte solution during electrocatalysis is employed to ensure constant diffusion of fresh electrolyte into the reaction-diffusion layer. It also supports more rapid desorption of the product, which is particularly important upon the formation of gaseous products that can reduce the total electrode surface area available for catalysis by the accumulation of bubbles at the electrode surface.



Scheme 1.2. *An illustration of an electrical double layer during electrocatalysis with mass transport, adsorption, and desorption steps indicated. Note that the layers, and also the particles, are not to scale. A = reactant molecules, B = product molecules, e^- = electrons, A⟶B represents a redox catalytic reaction; if an electron is added = reduction, if an electron is lost = oxidation.*

The electrochemical cells used for electrocatalysis take into consideration the formation of different reaction products at each electrode; accordingly, the electrodes are placed in separate compartments to maintain separation of the reaction products, but which are linked by an ion-

exchange membrane to complete the electrical circuit (see Figure 1.3). Three types of electrochemical cells are typically encountered in CO_2 reduction electrocatalysis; H-cells, Flow-cells, and membrane-electrode assemblies (MEA-cells). The H-cell is the electrochemical cell most widely used by researchers for electrocatalysis; however, H-cells are known to have slow reaction kinetics.[21] Flow-cells and MEA-cells are better candidates for the deployment of electrocatalysis on the industrial scale.[21,22] Flow cells for CO_2 reduction effectively create a tri-phasic system, with a gas phase, liquid phase, and solid phase corresponding to CO_2 gas, the electrolyte, and the electrocatalyst, respectively. This is facilitated by a gas-diffusion electrode, whereupon continuously flowing CO_2 gas can pass through a microporous electrode emersed in the electrolyte.[18,21,22] In this setup CO_2 mass transport into the diffusion layer of the electrode is avoided which greatly enhances the efficiency of Flow-cells. In MEA-cells, all components are combined into one compartment by putting each electrode into direct contact with the ion-exchange membrane. This simpler assembly minimises the distance between electrodes, which lowers the cell resistance (i.e. how much a material opposes the flow of electric current within the cell) and lowers the energy input required to conduct electrocatalysis.[21,22]

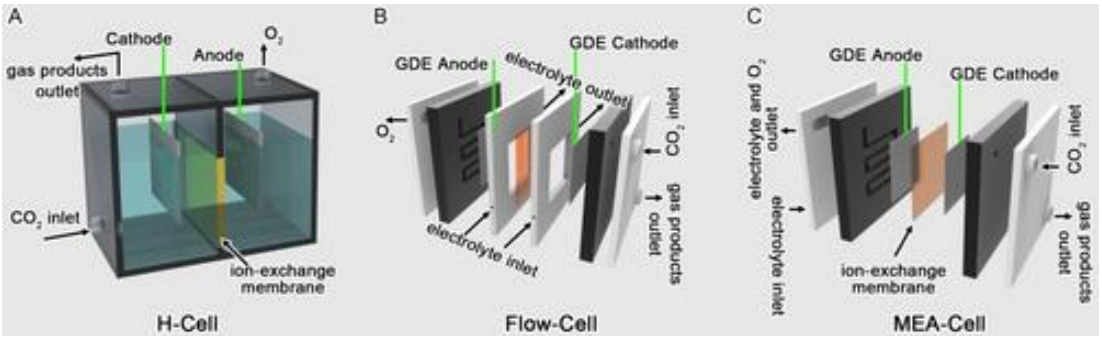


Figure 1.3. *Electrochemical cells for electrocatalysis; (A) H-Cell, (B) Flow-cell, (C) MEA-Cell.*[22]

While photocatalysis can take advantage of direct solar irradiation, electrocatalysis must drive catalysis from electricity. As previously discussed, most of the world's electricity is generated by the combustion of fossil fuels which is the leading contributor to anthropogenic climate change. Therefore, electrocatalysis using fossil fuels derived electricity does not advance the goal of limiting further greenhouse gas emissions. Instead, the use of renewable energy sources for electrocatalysis is more appropriate for CO_2 reduction. Presently, most electric grids are not separated according to the energy source used to generate the electricity that passes through them. As such, it is very challenging to perform green electrocatalysis at scale – doing so will

require significant changes to how electricity is generated. One alternative is for an electrocatalysis facility to operate its own dedicated renewable energy source that is disconnected from the wider electric grid. However, the cost associated with such an endeavour is likely prohibitive for industrial scale-up and it would take time to establish; these are incompatible with the aspirations set out by governments and international organisations in global climate goals.

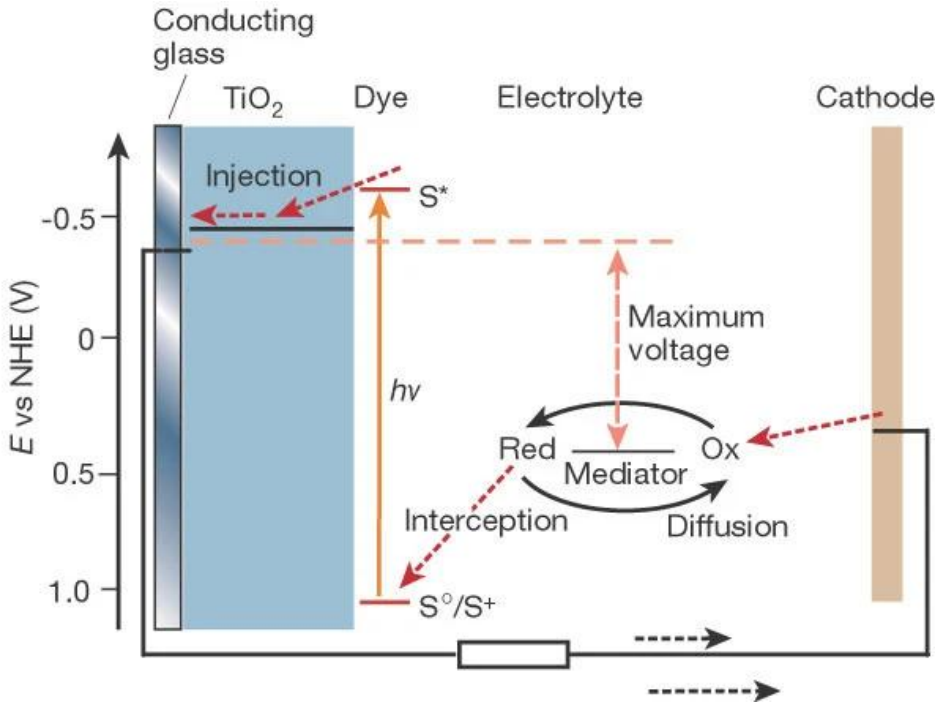


Figure 1.4. *Photoelectrochemical cell with a dye-sensitised semiconductor with a mediator redox species in the electrolyte solution.*[10]

Hence, solar energy may aid in overcoming these challenges. Particularly, the previously mentioned PEC can be used to generate electricity from solar irradiation for use in a chemical process.[10] As illustrated in Figure 1.4, a dye that is sensitised onto a semiconductor surface can absorb incident light and inject the generated charge into the semiconductor that forms part of the anode. The now oxidised dye is reductively quenched by a mediator in the electrolyte, and the oxidised mediator can then be used to perform redox chemistry; in this example an oxidation half reaction. The circuit is complete by reduction of the mediator at the cathode which restores the system to its starting conditions. A reduction half reaction can be performed in a tandem cell with a dye-sensitised semiconductor in the cathode. Since the absorption of light is critical to the activity of the PEC, it is also useful study the photophysical properties of catalysts, dyes, and

semiconductor materials employed in electrocatalysis in order to assess their suitability for use in PECs. Therefore, a general introduction to photophysics is provided in the following section which is later used to assess the catalysts studied throughout this thesis.

1.3 General Introduction to Photophysics

For any chemical process initiated by the absorption of a photon by a molecule, including photocatalysis, it is important to understand how that molecule behaves under irradiation by light. Most neutral molecules have an even number of electrons, resulting in the highest occupied molecular orbital (HOMO) being fully occupied. Such a system can be described as a closed-shell system, with a half-filled valence orbital being an open-shell system. According to the Pauli Exclusion Principle, two electrons occupying the same orbital must have opposite spin quantum numbers (i.e. m_s = ±1/2). In the case of spin-paired electrons, where the paired electrons have opposite spin quantum numbers, the opposite spins cancel out resulting in the total spin angular momentum (*S*) of the molecule being 0. The spin multiplicity of the molecule is determined using Hund's Rule of maximum multiplicity (*2S+1*)[23–25]; accordingly, for a molecule with *S* of 0, the spin multiplicity is 1 and is described as the singlet ground state (S_0) as illustrated in Figure 1.5. Upon photoexcitation, an electron is promoted to a higher energy state where it retains its opposing spin as a singlet excited state (S_n). It is also possible for the spin of the photoexcited electron to flip so that both electrons have the same spin, this results in a *S* of 1 and a spin multiplicity of 3; described as the triplet excited state (T_n). The lowest unoccupied molecular orbital (LUMO) is populated in the lowest energy excited state. The HOMO-LUMO energy gap corresponds to the lowest energy light that the molecule can absorb that results in an electronic transition.

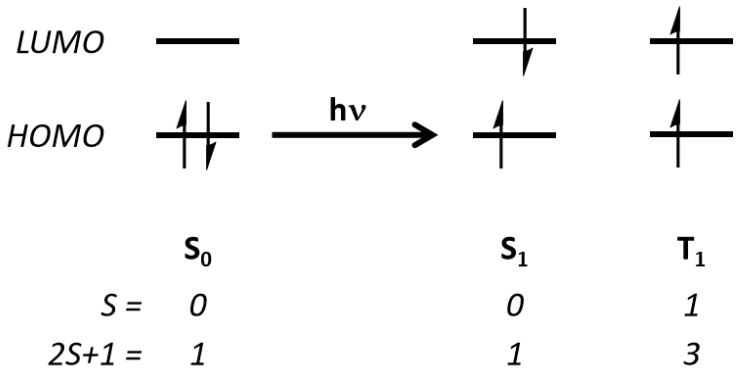


Figure 1.5. *Spin-state diagram of a closed-shell system displaying the singlet ground state (S_0) and the singlet and triplet excited states (S_1 and T_1, respectively). The total spin angular momentum is given as S and the spin multiplicity as 2S+1.*

The pathway for a photoexcited electron for larger molecular systems can be complex and so are typically represented on Jablonski diagrams[26]; a representative diagram is given in Figure 1.6 and is accompanied by the following discussion. According to the Franck-Condon principle, the lower mass of electrons compared to atomic nuclei gives rise to more rapid electronic motions ($<10^{-13}$ s) than nuclear vibrations (10^{-11}-10^{-12} s).[26] Consequently, initial photoexcitation results in the population of the Franck-Condon excited state (S_n), which retains the same nuclear geometries as the S_0 ground state. This is followed by rapid vibrational cooling (VC), which is the transition from a higher energy vibrational state to lower energy vibrational state within the same electronic state. Since multiple electronic excited states can be populated subsequent to photoexcitation, the excited state dynamics of molecules can often involve additional transitions between electronic excited states including internal conversion (IC) and intersystem crossing (ISC).[27] IC describes the conversions from a higher energy electronic state to a lower energy electronic state of the same multiplicity (i.e.: $S_n \rightarrow S_{n-1}$). ISC describes conversions from a higher energy electronic state to a lower energy electronic state of a different multiplicity (i.e.: $S_n \rightarrow T_n$). Restoration of the ground-state from the lowest energy excited state of either multiplicity occurs via radiative processes (emission) or non-radiative processes.

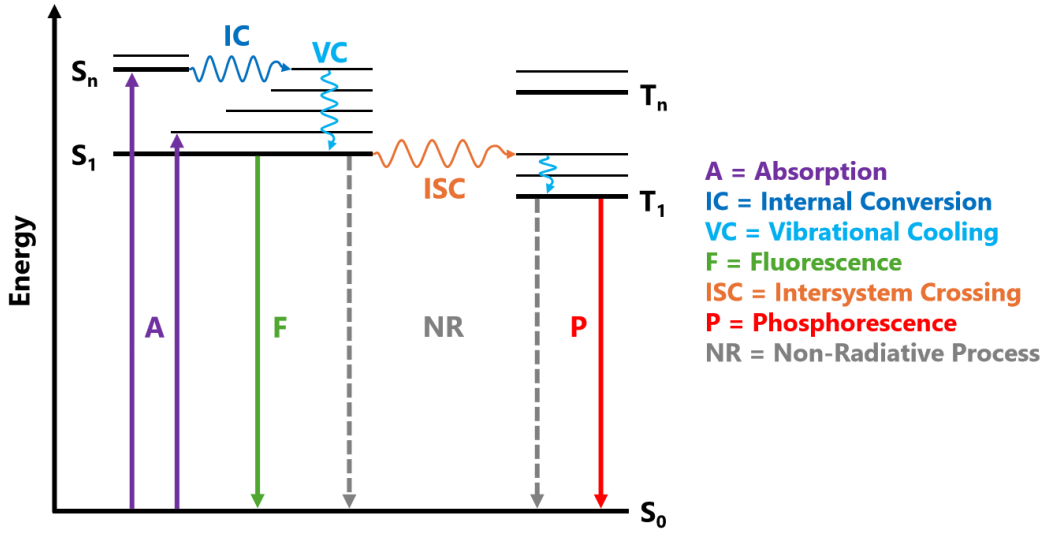


Figure 1.6. *Simplified Jablonski diagram outlining typical excited state processes observed in photophysical studies. Thick horizontal lines represent the electronic states, and thin horizontal lines are the vibrational states. S_0 is the singlet ground state, S_1/T_1 are the lowest-energy singlet/triplet excited states, and S_n/T_n are higher-energy singlet/triplet excited states.*

Molecular orbital theory can be used to describe electronic transitions in terms of the redistribution of electron density from its origin to a destination within the molecular structure.[28] In this model, the atomic orbitals involved in molecular bonding are considered; for example, combining two s-atomic orbitals yields two σ-molecular orbitals with bonding and anti-bonding character. The lower energy molecular orbital has bonding character due to the electron density being shared by both atomic orbitals, while the higher energy molecular orbital has anti-bonding character due to electron density being repelled from the atomic orbitals. Using the previous example, the σ-molecular orbitals can be considered to have bonding (σ) and anti-bonding (σ*) character. The non-bonding (n) orbitals arise from lone pairs of electrons localised on one atom that do not participate in any bonding interactions. Key electronic transitions between these molecular orbitals include metal-centred, ligand-centred (LC), and charge transfer transitions as detailed below.

1. Metal-centred electronic transitions involve the metal-based non-bonding (t_{2g}) and anti-bonding (e_g) d-orbitals.[28] Metal-centred transitions are more common amongst complexes of the 1st row transition metals; reduced octahedral-field splitting of the t_{2g} and e_g orbitals in 1st row transition metals results in a lower energy gap for metal-centred transitions compared to 2nd and 3rd row transition metals.[29,30]

2. LC electronic transitions occur between molecular orbitals within a ligand.[28] These are particularly apparent in aromatic ligands with large π-conjugated systems, which have extended π-molecular orbitals with bonding (π) and antibonding (π*) character.

3. Charge transfer electronic transitions typically invovle the transfer of an electron between metal-based and ligand-based orbitals.[28] These transitions can be further subdivided according to the directionality of electron density redistribution; namely, ligand-to-metal charge transfer (LMCT) and metal-to-ligand charge transfer (MLCT). Charge transfer excited states can have a significant impact on the oxidation state of the metal; LMCT transitions result in the reduction of the metal centre, whereas MLCT transitions increase the oxidation state of the metal as the ligand is reduced. Intraligand charge transfer (ILCT) transitions involve the redistribution of electron density between orbitals on different molecular components within the same ligand. ILCT transitions can also impact on metal-ligand interactions depending on the movement of electron density towards or away from components in close proximity to the metal centre.

These electronic transitions correlate to features in the absorption and emission profiles of molecules. The absorption of a photon can result in $S_0 \rightarrow S_n$ and $S_0 \rightarrow T_n$ transitions. However, $S_0 \rightarrow T_n$ transitions have a low probability due to the need to flip the spin of the photoexcited electron, resulting in low intensity $S_0 \rightarrow T_n$ absorption bands. Accordingly, the spin-forbidden nature of ISC results in longer T_n excited-state lifetimes (*ca*. $>10^{-7}$s) than S_n excited-state lifetimes (*ca*. $<10^{-8}$ s).[31] El-Sayed's rules allows for ISC to occur when combined with a change in the molecular orbital; for instance, a $^1\pi \rightarrow \pi^*$ excited state can readily undergo ISC to the $^3n \rightarrow \pi^*$ excited state, but not the $^3\pi \rightarrow \pi^*$ excited state.[32] Additionally, Kasha's rule states that appreciable emission only occurs from the lowest-energy electronic excited state of a given multiplicity.[33] As such, emission from the singlet excited state, called fluorescence, occurs from the lowest energy singlet excited state (S_1). Similarly, emission from the triplet excited state, called phosphorescence, occurs from the lowest energy triplet excited state (T_1). The type of emission observed for a particular molecule is dependent on the kinetics involved in the IC and ISC processes. Therefore, studying the emission lifetime can reveal both the lowest energy electronic excited state populated by a molecule and the spin-multiplicity of that excited state. Additionally, time-resolved spectroscopic studies can be implemented to monitor the evolution of the populated excited states in a photoexcited molecule.[27]

1.4 Properties of Photocatalytic Components

1.4.1 Properties of CO_2 Reducing Catalytic Centres

Transition metal complexes were originally used in the design of photocatalysts; with their visible region absorption properties, long-lived triplet excited states, multiple accessible oxidation states, and the robust photostability of many transition metal complexes. Indeed, $[Ru(bpy)_3]^{2+}$ and its derivatives have been widely used as the photosensitising component in many photocatalytic assemblies due to the MLCT transition occurring in the visible region (*ca*. 450 nm).[34–36] Additionally, the ^{3}MLCT excited state of $[Ru(bpy)_3]Cl_2$ has a lifetime of 731 ns in argon saturated DCM, while other Ru(II) polypyridyl complexes have triplet lifetimes ranging from 180–1500 ns.[37] The noble metals (Re, Ru, Os, Rh, Ir, Pd, and Pt) are typically employed as the CC in these assemblies due to their implementation as catalysts for range of reactions.[38] Re(α-diimine) tricarbonyl complexes are established CO_2 reducing photocatalysts, stemming from work on the Lehn catalyst $[Re(bpy)(CO)_3X]$ (where X = Br or Cl)[11], their visible region absorption profiles allow them to utilise solar irradiation (Figure 1.2). The ^{3}MLCT excited state of $[Re(bpy)(CO)_3Cl]$ has a lifetime of ca. 600 ns in DCM, with other Re(α-diimine) tricarbonyl complexes having lifetimes ranging from 300–650 ns.[39]

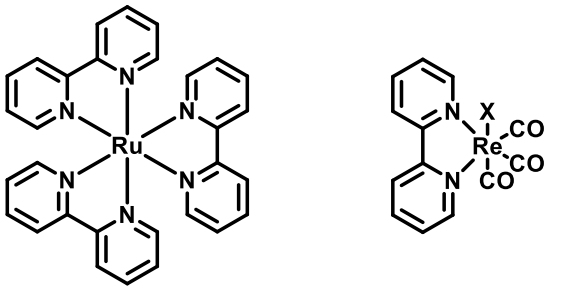


Figure 1.7. *Transition metal complexes commonly used as components in photocatalytic assemblies. Left – $[Ru(bpy)_3]^{2+}$ a common PS. Right – $Re(bpy)(CO)_3X$, where X = Br or Cl, a common photocatalyst for photocatalytic CO_2 reduction.*

Many photocatalysts use $[Ru(bpy)_3]^{2+}$ and $[Re(bpy)(CO)_3X]$ (where X = Br or Cl) as building blocks for supramolecular assemblies (Figure 1.7), resulting in the formation of polynuclear assemblies (distinguished by the number of metal centres in the assembly) allowing for the multiple photoexcited electrons needed for catalysis to be supplied to the CC by multiple PSs instead of

one PS supplying multiple photoexcited electrons. Some examples of 2nd and 3rd row transition metal photocatalysts are given below (Figure 1.8) with at least one of these building blocks present in their structure. The Ru-Rh-Ru complex studied by Rangan et al. is an example of multiple $[Ru(bpy)_3]^{2+}$ PS units covalently linked to a Rh-based CC achieving turnover numbers (TON) of 1 – 38 for H_2 generation depending on the counterion and photocatalytic conditions used.[40] Koike et al. studied a Ru-Re binuclear complex bridged by a short alkyl chain for photocatalytic CO_2 reduction under a variety of photocatalytic conditions yielding a maximum TON for CO of 3029.[41] Kowacs et al. studied a series of Ru-Pd and Ru-Pt complexes for H_2 generation with TON ranging from 69 – 650.[42]

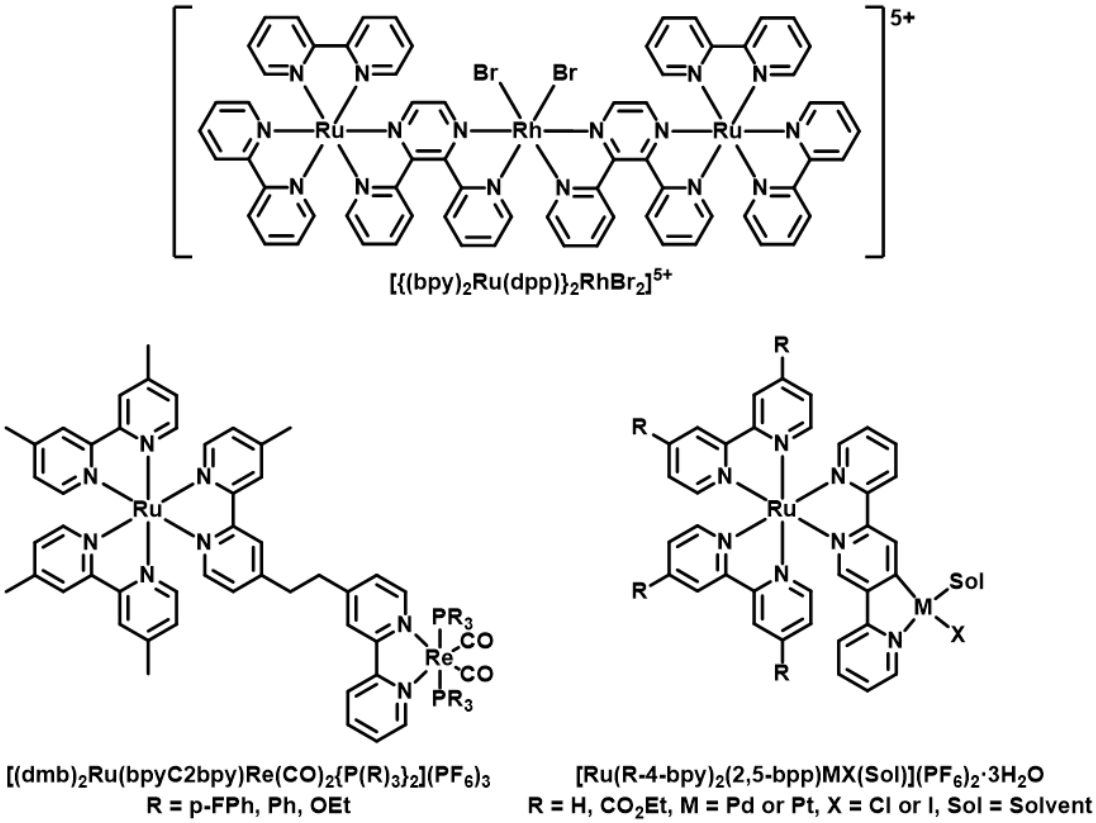


Figure 1.8. *Examples of photocatalysts with $[Ru(bpy)_3]^{2+}$-like PSs incorporated into their structure.*[40–42]

However, the noble metals have a relatively low abundance on Earth. Consequently, attempts are being made to design photocatalysts with 1st row transition metal complexes with higher abundance than their 2nd and 3rd row counterparts; particularly Mn, Fe, Co, Ni and Cu complexes which have multiple accessible oxidation states and are amongst the most abundant metals on

Earth. However, the excited-state lifetimes of 1st row transition metal complexes are known to be shorter compared to other transition metal complexes; with $[Fe(bpy)_3]^{2+}$ having a sub-picosecond triplet excited state lifetime compared to those of $[Ru(bpy)_3]^{2+}$ complexes (*ca.* 700 ns).[37,43] Additionally, the paramagnetic nature of many 1st row transition metal complexes and the increased lability of ligands in 1st row transition metal complexes are reported to limit their use as catalytic materials.[44]

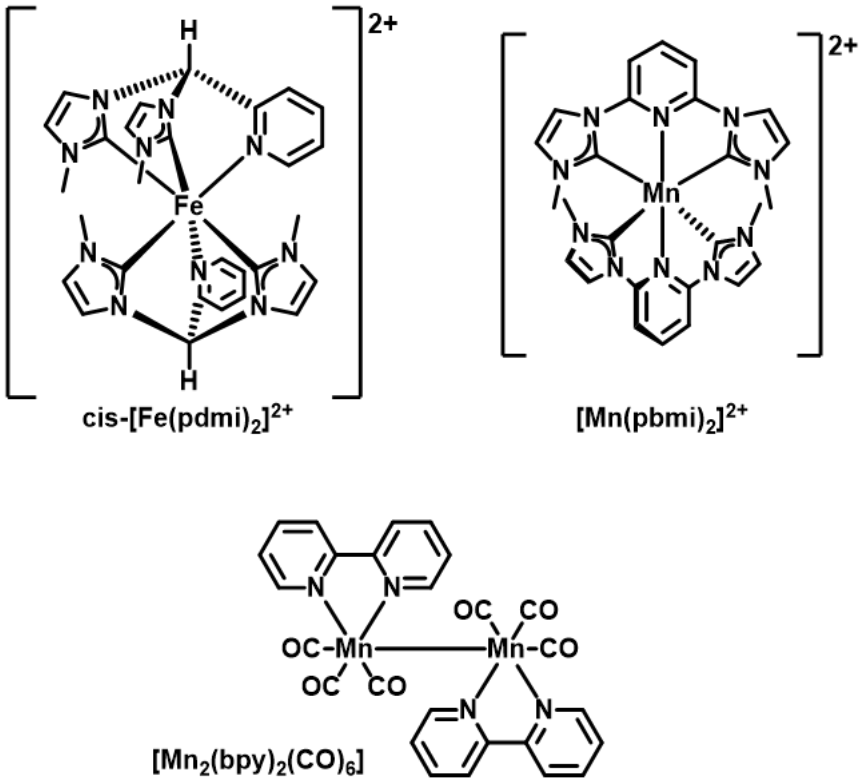


Figure 1.9. *(Top) Structure of 1st row transition metal complexes with relatively long-lived excited state lifetimes. Left: cis-$[Fe(pdmi)_2]^{2+}$, Right: $[Mn(pbmi)_2]^{2+}$. (Bottom) Structure of a bimolecular Mn photocatalyst $[Mn_2(bpy)_2(CO)_6]$.*

Recent attempts at extending the excited state lifetimes of 1st row transition metal complexes have seen some successes, utilising Fe and Mn complexes (Figure 1.9). A 1.67 ns lifetime has been reported for an Fe tetracarbene complex (cis-$[Fe(pdmi)_2]^{2+}$)[45], while the 190 ns lifetime of a related Mn tetracarbene complex ($[Mn(pbmi)_2]^{+}$)[46] is much closer to typical ^{3}MLCT lifetimes of 2nd and 3rd row transition metal complexes. However, whether the extended excited state lifetimes of these 1st row transition metal complexes correspond to improved photocatalytic activity remains to be studied by their incorporation into a photocatalytic assembly. Recently, a dimeric Mn complex, $[Mn_2(bpy)_2(CO)_6]$ was studied as a photocatalyst activated by either blue

or red light; the lower energy red light was sufficient for homolytic cleavage of the Mn-Mn bond thereby releasing the active catalyst while irradiation below 500 nm resulted in decomposition of the Mn dimer.[47]

Another approach to circumvent the use of noble metals in photocatalysts is to use organic PSs. One such example is [ZnP-phen=Re] as illustrated in Figure 1.10, where zinc porphyrin covalently linked to a [Re(phen)$(CO)_3$Br] moiety yielding a TON for CO of 1300; representing an improvement on the photocatalytic performance of [Re(phen)$(CO)_3$Br] which had a TON of 2 after 24 hours under the same conditions.[48,49] Porphyrins have long-lived T_n excited states, for example ZnTPP has a triplet lifetime of 190 μs in toluene, up to 3 orders of magnitude longer lived than that of $[Ru(bpy)_3]^{2+}$ (τ = 180–1500 ns).[37,50] Recalling that long-lived excited states are desirable for photocatalysis, the incorporation of an organic PS can enhance the photocatalytic performance of a photocatalyst compared to a purely inorganic assembly. Accordingly, the properties of organic PSs are discussed further in the following section.

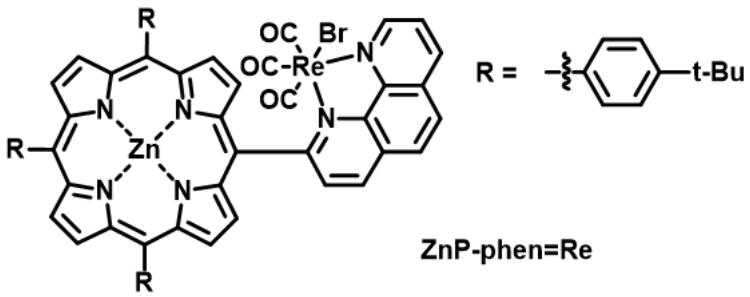


Figure 1.10. *Structure of [ZnP-phen=Re].*

1.4.2 Organic photosensitisers

As mentioned previously, PSs have been utilised to further tune the optical properties of photocatalysts into the visible region. However, the cost, both financially and environmentally, of extracting transition metals has led to the development of metal-free PSs in photocatalytic assemblies. Organic compounds with large π-conjugated systems have strong visible region absorption features and so have been sought out as metal-free PSs for photocatalytic assemblies. N-heterocycles are widely implemented as organic photosensitisers including carbazoles, boron-dipyrromethenes (BODIPYs), and porphyrins whose structures are provided in Figure 1.11.

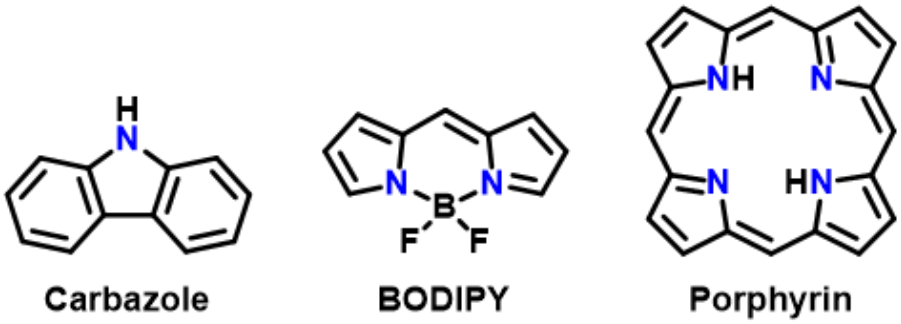


Figure 1.11. *Structure of N-heterocyclic organic PSs commonly used in photocatalytic assemblies.*

Porphyrins have seen extensive study in photocatalytic assemblies as a biomimetic system; particularly chlorophylls, whose structure contains a porphyrin, are present as the key photosensitising component in photosystem II for plant-based photosynthesis.[51] BODIPYs are structurally related to porphyrins, comprising half of a porphyrin ring. BODIPYs are typically incorporated as acceptor moieties in donor-π-acceptor (D-π-A) assemblies which exhibit ILCT properties, where the charge transfer occurs from the donor to the acceptor across a π-conjugated linker. Carbazoles are also used in D-π-A assemblies, but as the donor moiety. Many D-π-A assemblies are described as push-pull systems for their ability to direct electron density within that assembly via ILCT. These organic PSs are characterised by long-lived triplet excited states which are key to many photochemical processes, including photocatalysis as identified earlier in this chapter.[52–54] Thus, tuning of the donor and acceptor moieties can be performed to enhance ILCT; in an intramolecular photocatalytic assembly this can be used to direct electron density towards the CC.

Another family of organic-based photosensitisers are rylene-imides (Figure 1.12); whose structures compose of varying numbers of conjugated naphthalene units appended by either one imide group (monoimide) or two imide groups (diimide). Rylene diimides behave as acceptor units in D-π-A assemblies. Particularly, perylene diimides (PDI) and naphthalene diimides (NDI) have been utilised in many photo-based applications including photosensitising materials.[52,54–57] Naphthalimides (NIs) are the simplest version of a rylene-imide, containing only one naphthalene moiety in the core and one imide group. Functionalisation of NIs can be conducted at the N-imide moiety or on the aromatic core. The properties of NIs are discussed further in the following section.

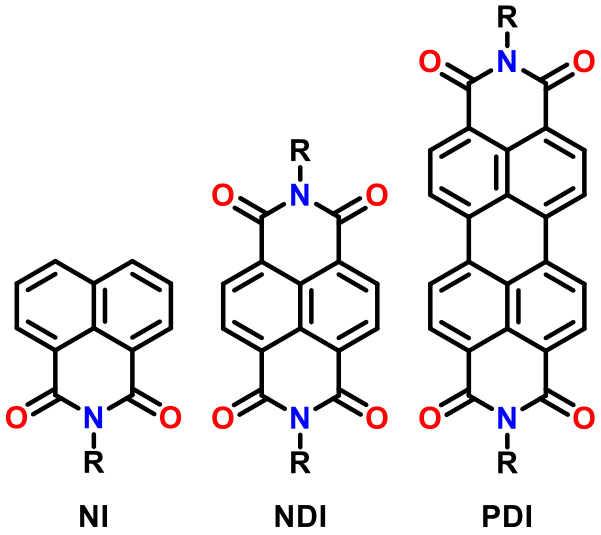


Figure 1.12. *Chemical structure of common rylene-imides.*

1.4.3 Properties of Naphthalimides

The macrocyclic core of NIs, comprising of two-fused 6-membered aromatic rings as indicated in Figure 1.13, contains 10-π electrons following Huckel's rule of aromaticity (4n+2 π-electrons, where n = 2). The substitution of alkyl or aryl groups via the imide N-atom aim to improve their solubility. Substitutions on to the aromatic core of NI via the 2, 3, and 4-positions have been carried out extensively; however, the 4-position has been favoured due to the ability to form resonance structures with the carbonyl groups of the imide moiety.[58]

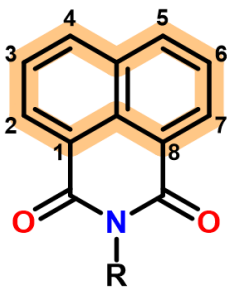


Figure 1.13. *The 10-π electron aromatic core of NI is highlighted with labels for the 1-8 positions.*

The UV-Vis absorption spectra of NIs feature a mixture of π⟶π* and n⟶π* transitions in the near-visible region (330–370 nm). In the UV-Vis absorption spectra of NIs with unsubstituted aromatic cores, vibrational structure can be seen with a n⟶π* transition at *ca.* 330 nm and a

π→π* transition at *ca.* 345 nm, accompanied by narrow and vibrationally resolved fluorescence bands appearing *ca.* 340–460 nm.[59] Substitution with an electron-donating group, such as an amine, at the 4-position of NI it is possible for two resonance structures to form via a push-pull effect in the NI moiety (Figure 1.14). This gives rise to internal charge transfer (ICT) from the electron donating amine to each of the electron withdrawing carboxy groups caused by the amine and the carboxy groups. ICT causes changes of the π→π* and n→π* transitions in the UV-Vis absorption spectra of NIs; for instance, ICT is sensitive to solvent polarity, with bathochromic shifts observed in increasingly polar solvents.[58]

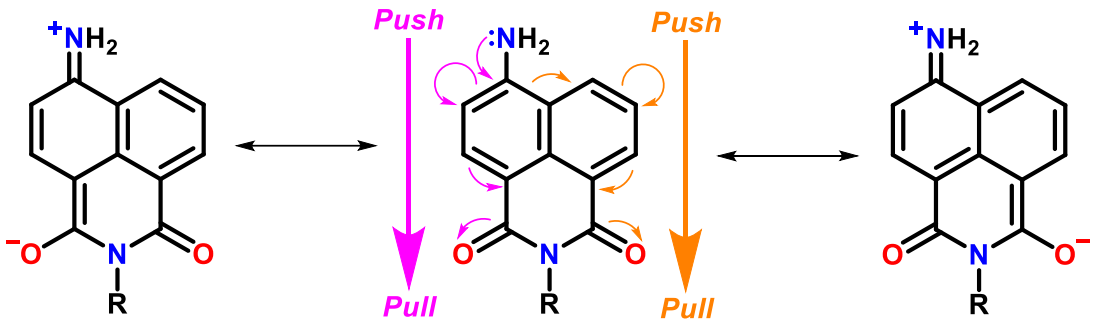


Figure 1.14. *The possible resonance forms arising from the push-pull effect for NIs with an amine at the 4-position.*

ICT in NIs results in a reduction in the π→π* energy and an increase in the n→π* energy arising from the stabilisation of the non-bonding orbitals of the carboxy groups. Consequently, broad π→π* absorption and emission features are observed that are bathochromically shifted compared to unsubstituted NIs (*ca.* 350 – 550 nm). Furthermore, the lowering of the π→π* energy increases the probability of populating the singlet π→π* excited state and thus, causes an increase in the emission intensity coupled with higher fluorescence quantum yields due to reduced rates of ISC.[59] In contrast, substitution of an electron-withdrawing group, such as a nitro group, reduces fluorescence quantum yield compared to the unsubstituted NIs. This is due to a lower n→π* energy allowing for greater population of the non-emissive triplet n→π* excited state via ISC, in-line with El-Sayed's rules.[32] Therefore, the spectral and photophysical properties of NIs are governed by the energy gap between the ^{1}π→π* and the ^{3}n→π* excited states, which can be modulated by modifying the substituent present at the 4-position.

Transition metal complexes can also be linked via the imide N-atom to adjust their photophysical properties further into the visible region.[56,60] Extending π-conjugation across the imide group is

achieved by direct conjugation of the NI moiety with an aryl substituent via an N-heterocyclic ring. Such systems have been previously prepared by linking rylene diimides to an α-diimine group via an imidazole ring.[61–64] While the absorption profiles were extended into the visible region and triplet lifetimes were observed up to 440 μs have been reported, the poor solubility of such systems in non-acidic solvents remains an issue.[63,64] Alternatively, covalently linking another molecular component to NI via the imide N-atom has a negligible impact on the spectral properties of NIs owing to the poor electronic coupling across the formed σ-bond.[59] Accordingly, a weakly coupled bichromophoric assembly is formed when NI is attached to another chromophore in this way; where the absorbance profile of the bichromophore appears as the sum of the individual chromophores.[65] While the absorption profile of the bichromophore remains largely unchanged compared to the individual chromophores, the emission profile may change drastically arising from new excited state pathways.[65] By selecting the appropriate chromophore to accompany NI, a wider spectral region may be absorbed by the bichromophore and used to access the excited state(s).

The two rhenium tricarbonyl complexes presented in Figure 1.15 illustrate some of the approaches by which a rylene core may be modified and functionalised; with [Re(dmb)$(CO)_3$(Py-DPA-NDI)]PF_6 modified via the imide groups, while [Re(bpy-C2-NPDI-R)Cl] was functionalised on the PDI core and the imide groups. In the study of [Re(dmb)$(CO)_3$(Py-DPA-NDI)]PF_6, it was reported that extending the distance from the NDI core to the rhenium metal centre with an electron accepting diphenyl anthracene moiety allowed for rapid electron transfer to the rhenium metal centre upon photoexcitation while also inhibiting back transfer to NDI resulting in the formation of a long-lived excited state species (τ = 43.2 μs).[66] While these excited state properties are ideal for photocatalysis, as discussed earlier, the photocatalytic performance of this complex has not yet been assessed. The effect of the substitution of electron donating or electron withdrawing groups onto the PDI core, in the series studied by Koenig et al., revealed that electron withdrawing groups deactivated the complex for photocatalysis while electron donating groups enhanced it; with [Re(bpy-C2-NPDI-NH_2)Cl] yielding the highest TON for CO of 234 in this series of complexes.[67]

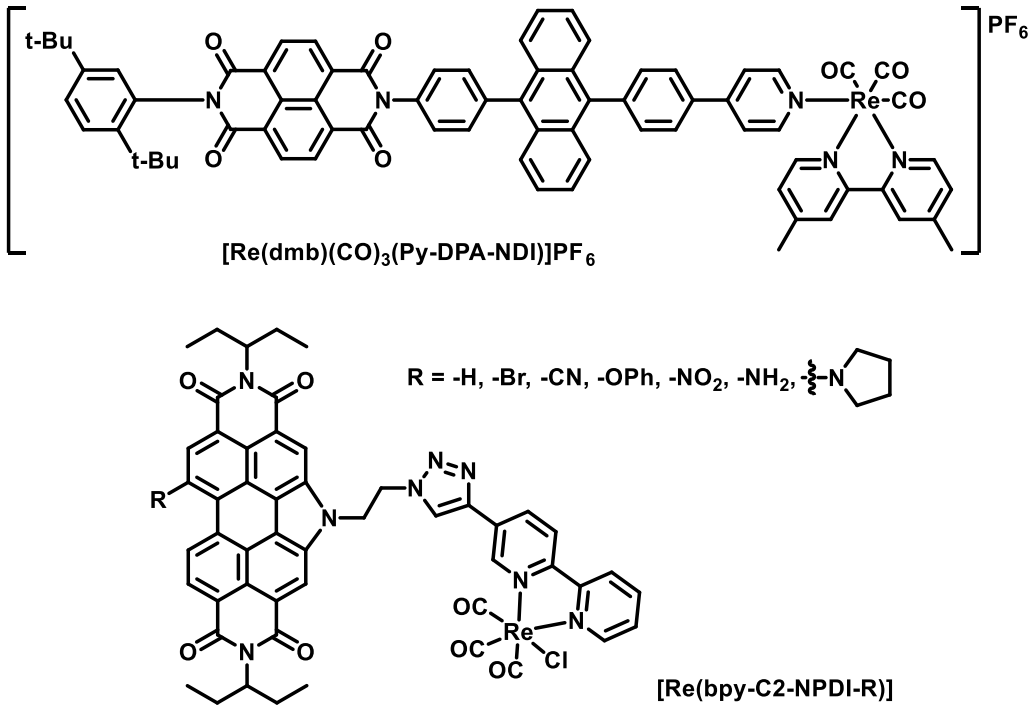


Figure 1.15. *Structure of three Rhenium tricarbonyl complexes covalently linked to an organic PS. (Top) [Re(dmb)(CO)₃(Py-DPA-NDI)]PF₆, (Bottom) [Re(bpy-C2-NDPI-R)Cl].*

Compared to their larger rylene diimide counterparts, the NIs have seen limited attention for photocatalytic and electrocatalytic systems. This may be due to the limited visible-region absorption profile of NIs, which precludes their use in setups that use solar irradiation – though as discussed earlier, their optical properties can be tuned to improve their visible-region absorption. Photocatalytic studies by Case, Spear, and co-workers showed that [Re(NO_2–NI–phen)$(CO)_3$Cl] (see Figure 1.16) can be used to reduce CO_2 to HCO_2H, yielding a maximum TON of 533 with 110 equiv. of BIH in 1:9 (v/v) DCM:MeOH and 450 – 460 nm irradiation.[68,69] A catalytic pathway is proposed in the studies by Spear et al., which involves the formation of a hydride complex whereupon CO_2 can bind via the Re-H bond.[69] While this pathway is known for other [Re(α-diimine)$(CO)_3$Cl] catalysts in the literature, and is likely the case for this complex, direct evidence for the formation of any of the intermediate species is absent. Instead, the enhancement of the photocatalytic activity in the presence of a hydride donor is used to support the proposed pathway. Furthermore, their system had a TON of 176 in the absence of light irradiation; which is significant catalytic activity to arise from no apparent stimuli.[69] Certainly, the presence of [Re(NO_2–NI–phen)$(CO)_3$Cl] is important for catalysis in their system, with only a TON of 6 in its absence; however, the proposed photo-induced mechanism cannot account for the apparent activity in the dark.

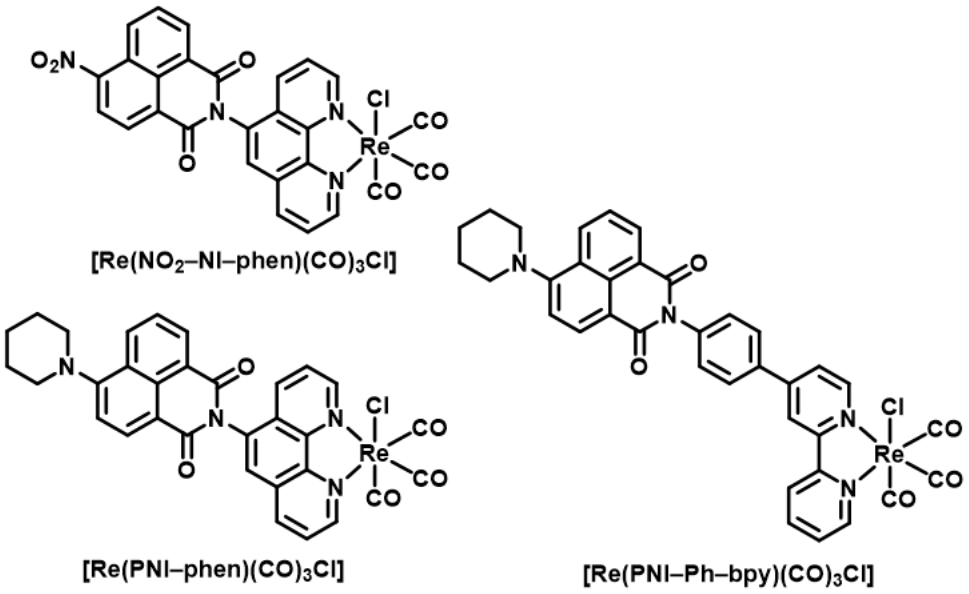


Figure 1.16. *Structures of the NI-containing CO_2 reduction catalysts studied by Case, Spear, and Co-workers [Re(NO_2–NI–phen)$(CO)_3$Cl], and Franco et al. [Re(PNI–phen)$(CO)_3$Cl] and [Re(PNI–Ph–bpy)$(CO)_3$Cl].*

Franco et al. studied the [Re(PNI–phen)$(CO)_3$Cl] and [Re(PNI–Ph–bpy)$(CO)_3$Cl] complexes illustrated in see Figure 1.16 (where PNI = 4-piperidinyl-1,8-naphthalimide) as both a photocatalyst and electrocatalyst for CO_2 reduction.[70] These structures differ from [Re(NO_2–NI–phen)$(CO)_3$Cl] by the substitution of the strongly electron-donating piperidinyl group instead of the electron withdrawing NO_2 group. Additionally, a phenyl spacer is present between the bpy and NI moieties in [Re(PNI–Ph–bpy)$(CO)_3$Cl], unlike the phen and NI moieties in Re(PNI–phen)$(CO)_3$Cl]. The results of photocatalysis and electrocatalysis with both complexes yielded CO as the main reaction product instead of HCO_2H, with enhanced electrocatalytic activity observed for both complexes. The enhanced electrocatalytic activity is attributed to electron transfer from the PNI moiety to the singly reduced Re–phen metallacycle, which occurs at less negative potentials than the second reduction of the Re–phen metallacycle typically needed to yield the active catalyst.[71] Furthermore, the greater activity of [Re(PNI–Ph–bpy)$(CO)_3$Cl] over [Re(PNI–phen)$(CO)_3$Cl] (TON = 64 and 44, respectively) is attributed to the presence of the phenyl spacer which reduces back-electron transfer.[70] However, no experimental evidence is provided that demonstrates different back-electron transfer rates, or even forward-electron transfer, between the two complexes; with only theoretical calculations indicating different electron transfer rates are possible.

The studies of the NI-containing CO_2 reducing catalysts showcase their photocatalytic and electrocatalytic activities. However, absent from these studies are direct evidence of the proposed pathways and mechanisms involved in forming the active catalyst, or their deactivation in the case of back-electron transfer. This is a significant gap in this research that makes devising improved photocatalysts and electrocatalysts challenging. If the proposed bottlenecks to the activity of these materials were identified and understood, new catalysts containing NI electron reservoirs could be devised towards improving their ability to catalytically reduce CO_2 under photochemical or electrochemical conditions.

1.5 Techniques Used to Study Photocatalysts and Electrocatalysts

1.5.1 Spectroelectrochemistry

Electrochemistry is often employed to identify the presence of redox processes; however, it is not ideal for characterising the intermediate species or products of those redox processes. Spectroelectrochemistry (SEC) combines electrochemistry with spectroscopic techniques, which are more suitable for obtaining qualitative and quantitative information about redox processes and the formed intermediate species and products. IR and UV-Vis spectroscopies are widely used in SEC and are discussed further; though combinations with Raman, NMR, and Mass spectrometry are also possible.[72]

UV-Vis spectroelectrochemistry (UV-Vis SEC) takes advantage of UV-Vis spectroscopy to study the intermediate species or products of redox processes. As explained earlier in this chapter, electronic transitions are dependent on the energy gap required to excite an electron from a lower energy occupied molecular orbital to a higher energy unoccupied molecular orbital. By adding or removing electrons from a molecule, as performed in UV-Vis SEC studies, the energy gaps change and give rise to different electronic transitions. Therefore, the UV-Vis spectra of redox species will have unique spectral features based on the redox process undertaken and its effect on the molecular orbitals.

In a similar fashion, IR spectroelectrochemistry (IR SEC) employs IR spectroscopy in the study of intermediate species or products of redox processes. When IR radiation has the same frequency as the vibrational frequency of a bond in a molecule, that radiation is absorbed by the molecule. A changing dipole moment is required for a molecule to be IR-active; typically, molecules with heteronuclear bonds are IR-active while homonuclear bonds are IR-inactive.[73] In IR SEC studies, the addition or removal of electrons from a molecule can also induce changes in the dipole

moments of bonds, with bonds that are in closer proximity to the redox centre having greater changes in their dipole moments. Therefore, the IR spectra of redox species display unique spectral features according to the proximity of molecular bonds to the region of the redox process undertaken.

$$A = \varepsilon c l$$

Equation 1.9. *Beer-Lambert Law; A = absorbance, ε = molar extinction coefficient, c = concentration, l = path length of light through the cell.*

IR studies conducted in solution can suffer from interference from the solvent, which may also interact with IR radiation; this may be overcome by using thin-layer liquid films (< 100 μm). While reducing the path length can minimise spectral features from the solvent, this also requires a higher concentration of the analyte to obtain sufficiently detectable analyte absorption readings according to the Beer-Lambert law (see Equation 1.9). This becomes a challenge when conducting IR SEC experiments, since higher sample concentrations are needed with small sample volumes. One advantage such a setup is that when the cell height is smaller than the diffusion length, total electrochemical conversion can be achieved more easily; thus, IR spectra for each redox species may be obtained.

Accordingly, an optically transparent thin-layer electrochemical (OTTLE) cell is widely used in SEC experiments.[74] In this configuration, the sample with electrolyte is loaded between IR-transparent windows such as CaF_2, with the electrode assembly contained within the space between the windows. As a result, a thin layer of liquid analyte is sandwiched between the electrode and the transparent IR windows. Such a setup can be used for transmission IR SEC and UV-Vis SEC studies; where the IR/UV-Vis beam passes through a mesh working electrode, where the local sample absorbs part of the IR/UV-Vis radiation and the rest is transmitted through the cell towards the detector. The resulting difference between the emitted light and the detected light creates the IR or UV-Vis spectrum of the redox species.

1.5.2 Time-resolved Spectroscopy

For catalytic systems, insights into their reaction mechanism can be obtained using time-resolved spectroscopy which monitors spectral changes over a period of time after excitation.[65,75–78] Certain time-resolved spectroscopic techniques use pump-probe configurations to cause

photoexcitation of a sample (i.e. pump) and then spectroscopically monitor the behaviour of the formed excited state(s) upon absorbing a secondary laser pulse (i.e. probe).[79,80] Pump-probe configurations have been developed to study excited-state processes at many timescales, generally from femtoseconds (10^{-15} s) to milliseconds (10^{-3} s). Thereby, the evolution of the populated excited states, more commonly referred to as excited-state dynamics, can be monitored form shortly after excitation until the restoration of the ground state. While many spectroscopic techniques can be combined with time-resolved spectroscopy, three are used throughout this thesis; transient absorption (TA) spectroscopy, time-correlated single photon counting (TCSPC), and time-resolved infra-red (TRIR) spectroscopy. A brief outline of these time-resolved spectroscopic techniques is provided herein.

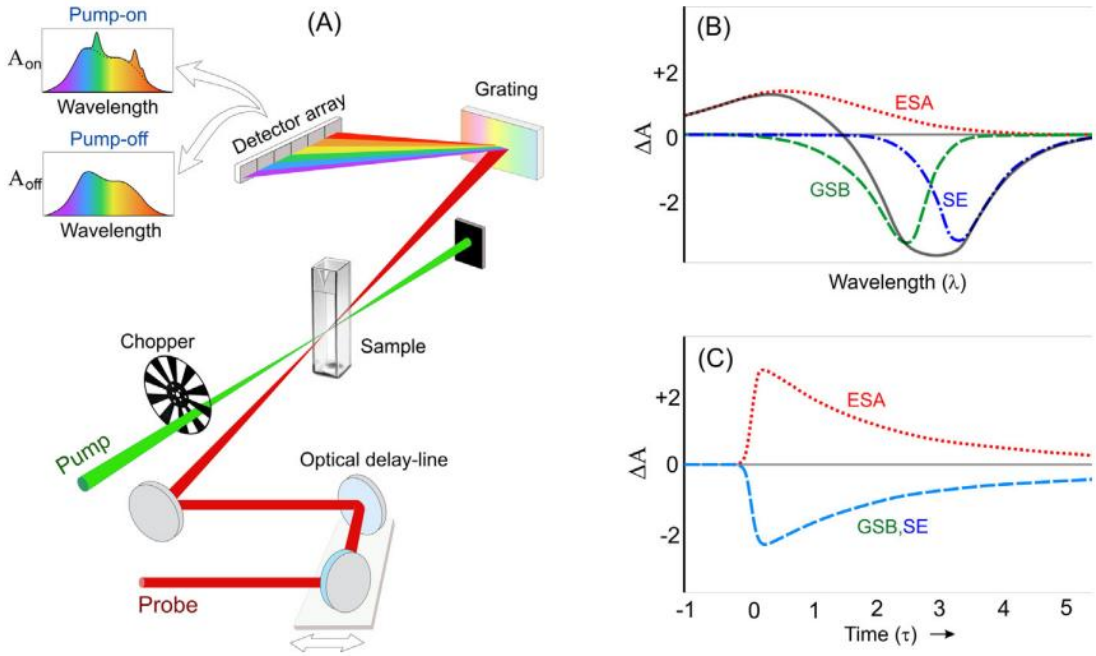


Figure 1.17. *(A) A schematic diagram of a TA pump-probe spectroscopic setup. (B) Representative TA spectrum (black) comprised of individual components ESA (red), GSB (green), and SE (blue). (C) Representative kinetic traces, positive traces are attributed to ESAs and negative traces are attributed to GSBs and SE.*[77]

TA spectroscopy monitors changes in the electronic transitions of excited-state species over time. The pump-probe TA setup, illustrated in Figure 1.17A, operates as follows.[77] The pump light causes excitation within the pump-probe cross-section within the sample; therefore, a chopper is used to alternate between pump-on and pump-off states. The probe light passes through a delay-line before the sample; this allows for the probe pulse to be temporally offset from the

pump pulse. A TA spectrum is obtained by subtracting the “pump-off” UV-Vis absorption spectrum from the “pump-on” UV-Vis absorption spectrum. The resulting difference spectrum is referred to as a TA spectrum (Figure 1.17B) which comprised of positive and negative spectral features; excited-state absorption (ESA), ground-state bleach (GSB), and stimulated emission (SE). ESAs are attributed to new absorption features populated excited state(s). GSBs arise from depleted ground-state absorption features due to the population of excited state species. SE is attributed to the emission of photons from an excited-state molecule populated subsequently to the pump pulse; this can result in the appearance of negative features in the resulting TA spectrum due to more photons reaching the detector than observed for the ground-state molecule. A TA map is comprised of multiple temporally offset TA spectra; thus, showing the spectral evolution over the timeframe of the experiment. Kinetic traces can be obtained by monitoring the change in optical density (ΔO.D.) at a particular wavelength in a TA map over the timeframe of the experiment (Figure 1.17C). The excited-state lifetimes of optically populated excited states can be obtained from exponential fitting of the kinetic traces.

TCSPC is a form of time-resolved fluorescence spectroscopy, although it can be used to detect phosphorescence as well, that records the time between an excitation pulse and the emission of a photon by an excited-state species.[77,81] Accordingly, a sample must be emissive in order to study it by TCSPC. A simplified diagram of a TCSPC assembly is provided in Figure 1.18 and accompanies the brief explanation that follows.[82] When a sample emits a photon, it is counted by a detector and converted into an electric pulse. Correlation with the excitation electric pulse gives the time delay of the counted photon. A histogram sorts the counted photon by arrival time, which allows for a kinetic trace to be obtained. Exponential fitting of kinetic traces yields the emission lifetimes of the optically populated excited state(s).

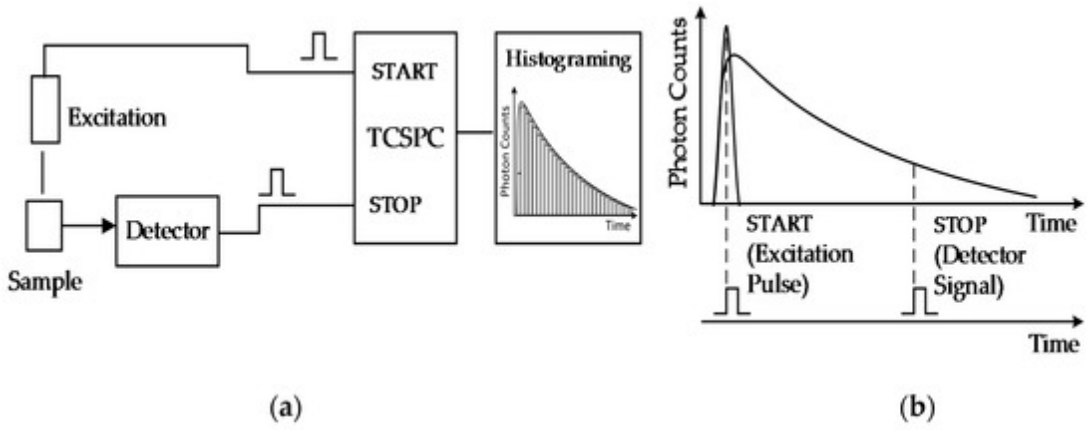


Figure 1.18. *(a) A simplified diagram of a TCSPC setup and histogram, (b) a kinetic trace overlayed with the start-stop timing mode.*[82]

TRIR spectroscopy uses a similar pump-probe setup as used in TA spectroscopy (Figure 1.17). The key difference between these spectroscopies is the use of an IR probe in TRIR, which monitors changes in the vibrational transitions of a sample.[77] Since molecular vibrations are related to the bonds present in a molecule, this technique provides insights into the redistribution of electron density within the molecular structure upon excitation. Therefore, a more detailed account of the excited-state dynamics can be obtained by adopting a combination of time-resolved spectroscopies in a complete photophysical study. Photophysical studies are often carried out along with photocatalytic studies, where the excited-state dynamics contribute to the activation of the catalyst. Therefore, the combination of TA, TCSPC, and TRIR spectroscopies used in this thesis provides insights into the character, kinetics, and molecular structure of the populated excited state(s) of the studied samples which can be used to understand their relevance to the activation pathways of the catalysts presented in subsequent chapters.

1.5.3 Time-resolved Infrared Spectroelectrochemistry

In this thesis, the TRIR and SEC techniques are combined into a new time-resolved infrared spectroelectrochemistry (TRIR SEC) experiment. In TRIR SEC, an electrochemically produced redox species can be generated in-situ within a pump-probe TRIR assembly as illustrated in Figure 1.19A. An adaptation of a standard OTTLE cell, a slit in the working electrode, is made so that the pump-probe beams of a TRIR assembly can pass through it (Figure 1.19B). The electrochemical species present in the beam path is irradiated at an appropriate excitation wavelength, determined from UV-Vis SEC studies, so that the electrochemical species is

promoted into an excited state. Thereby, the photophysical properties of the electrochemical species can be analysed. Such a study becomes relevant when secondary absorption is possible under irradiation conditions, making it important to understand the photophysical properties of the redox species in addition to those of the parent species.

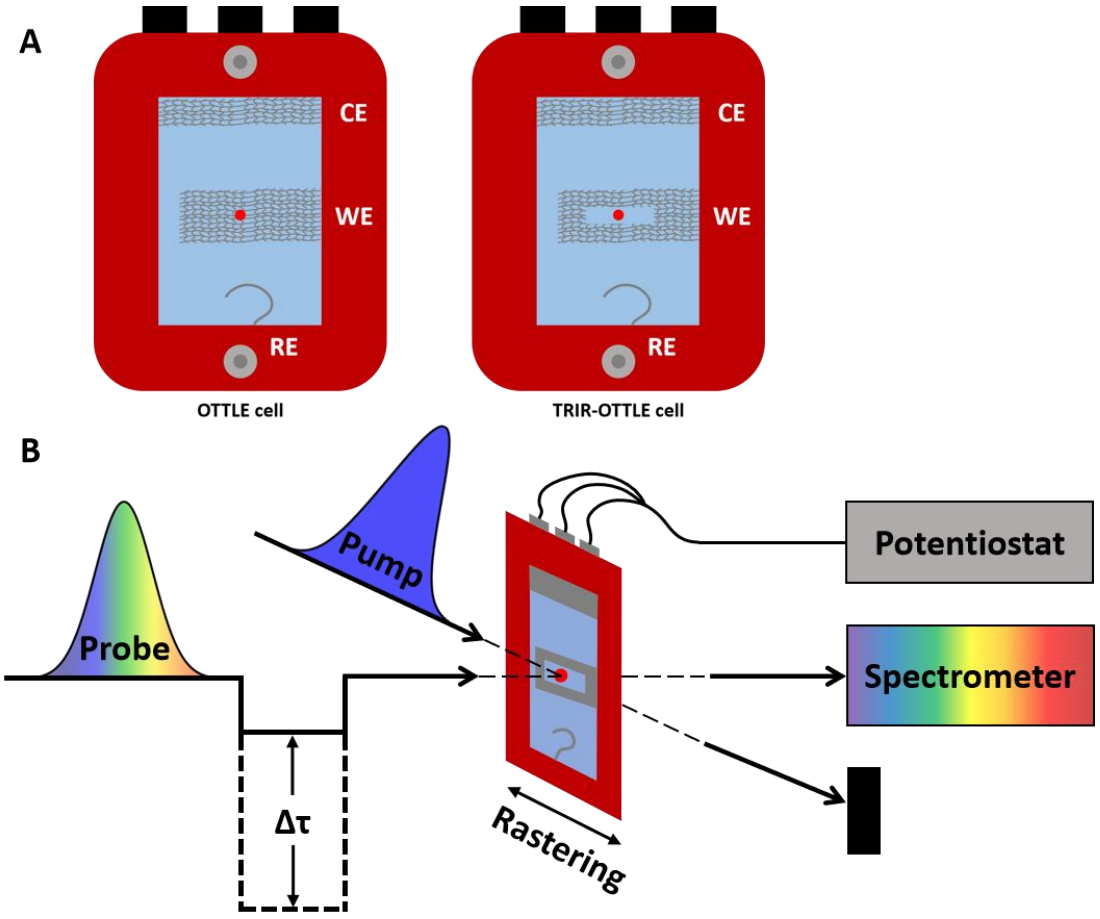


Figure 1.19. *(A) Illustrative diagrams of an OTTLE cell and a TRIR-OTTLE cell [CE = counter electrode, WE = working electrode, RE = pseudo-reference electrode]. (B) Simplified schematic of a TRIR SEC assembly including the TRIR-OTTLE cell.*

The electrochemical reduction or oxidation of a closed-shell system transforms it into an open-shell system, that is a molecule where the outermost orbital is half-filled. In the case of a reduction, the redox species is a radical anion and in the case of an oxidation this is a radical cation. Accordingly, different terminology is used when discussing the excited states of redox species. For instance, the HOMO and LUMO terminology associated with closed-shell systems are replaced with new terminology associated with open-shell systems; the highest-occupied spin-orbital (HOSO) and the lowest-unoccupied spin-orbital (LUSO) terms. For any open-shell

system, only one electron is present in the HOSO regardless of redox process undertaken, though the energy of the HOSO orbital may be higher or lower depending on whether reduction or oxidation has occurred. Accordingly, the singlet and triplet spin states are no longer representative of the total spin angular momentum, *S*; for an open-shell system this is 1/2. According to Hund's rule of maximum multiplicity the corresponding spin-multiplicity is 2 and is described as a doublet (D_n) spin state. Figure 1.20 below shows the evolution of a singlet ground state species to the doublet ground state (D_0) upon electrochemical reduction, with subsequent photoexcitation to the lowest energy doublet excited state (D_1).

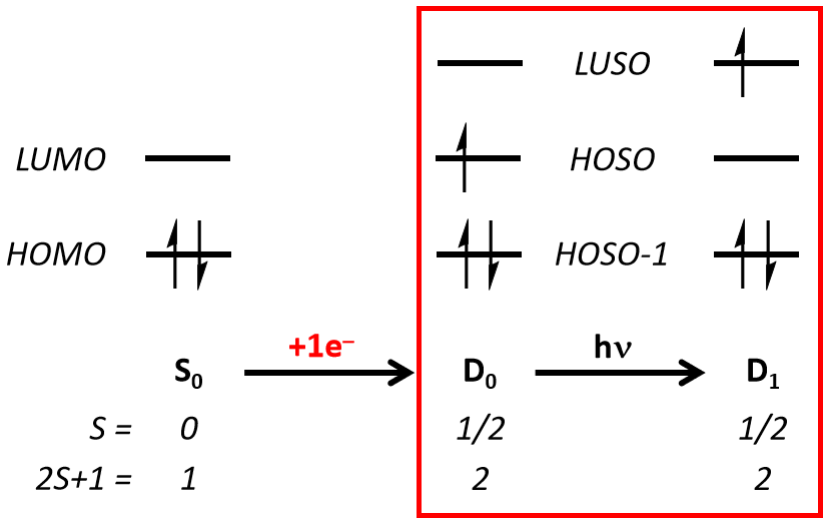


Figure 1.20. *Spin state diagram, following reduction of a singlet ground state (S_0) parent species, of the doublet ground state (D_0) and the lowest doublet excited state (D_1). The open-shell systems are contained within the red box. The total spin angular momentum is given as S and the spin multiplicity as 2S+1.*

Excited state interactions with doublet spin states can be complicated; often manifesting as interactions between two doublet states, or between a doublet state and a singlet or triplet state. The photophysics of many organic photosensitisers, including rylenes and rylene diimides, have been manipulated by linking them to stable free radicals to create radical-chromophore systems. In doing so, doublet and quartet excited states can be utilised to populate the triplet excited states of organic photosensitisers that are not accessible by typical photoexcitation in closed-shell systems.[83] The greater reactivity of T_n excited states makes radical-chromophore systems a useful design approach for many photochemical applications requiring the population of T_n excited states. The challenge with such systems is the design of radical-chromophore

systems that populate the T_n excited states required for these applications and is a growing area of research.

1.6 Conclusions

As demonstrated in the study by Franco et al., incorporating electron reservoirs onto transition-metal catalysts can positively influence electrocatalytic CO_2 reduction.[70] To fully realise the promise of these electron reservoirs in other materials, and to extend this ability to photocatalysis, a better understanding of the NI-based electron reservoirs is needed. Roth and co-workers provide an interesting assessment of current limitations in photocatalytic efficiencies; a surface of 370 km^2 coated by the best known photocatalysts would be needed to convert the CO_2 emitted by one cement plant in a year, whereas an equivalent capacity is provided by a 200 km^2 forest using photosynthesis.[84] Therefore, further advances in photocatalyst design are needed so that improved efficiencies are attained. Identifying the pathway leading to the active catalyst is important in understanding the catalytic activity of these materials and is needed to recognise bottlenecks in these pathways during catalysis. In doing so, one may bring the acquired knowledge to new catalyst materials with the aim of enhancing their performance under catalytic conditions.

This thesis studies the photophysical and electrochemical properties of a series of CO_2 reducing catalysts, consisting of NI moieties covalently linked to transition-metal catalytic centres, as CO_2 reducing photo- and electrocatalysts. NIs were identified as ideal candidates for the studies entailed in this thesis on account of their facile synthesis, tuneable optical and electronic properties, and the poor understanding of their activation pathways under electrochemical and photochemical conditions for CO_2 reduction catalysis. Three novel NI moieties are presented in Chapter 2, with ethynyl-containing substituents appended onto the 4-position of the aromatic of NI, which are linked to a $[Re(phen)(CO)_3Cl]$ catalytic centre. Detailed photophysical studies of this series of precursor catalysts are outlined which provide an account of the excited-state dynamics of the ethynyl-appended complexes. Thereafter, the electrochemical, SEC, and TRIR SEC studies of two precursor catalysts are exhibited in Chapter 3 to establish the activation pathway under photocatalytic conditions. In doing so, bottlenecks in the activation pathway are identified which account for the poor photocatalytic activity of these photocatalysts.

To support the movement of research with transition-metal catalysts to more Earth-abundant metals, the Mn^I analogues of the Re^I complexes, studied in Chapter 3, were prepared. The electrochemical and SEC studies of these Mn complexes are presented in order to determine the

activation pathways leading to the active catalyst under electrochemical conditions. With these studies it is also possible to identify the catalytic cycle by which these complexes are able to electrocatalyse CO_2 reduction. Finally, a novel series of transition-metal complexes, containing NI moiety appended with a malononitrile substituent, are characterised in Chapter 5. These complexes are prepared for future work stemming from this thesis, as outlined in Chapter 6.

To conclude, the principles of photophysics and the overviews of key spectroscopic techniques in the study of photo- and electrocatalysts are summarised in this chapter. These are considered throughout this thesis, with the insights afforded by this research aimed at improving the design of future CO_2 reducing photo- and electrocatalysts. The designed complexes take into consideration the need to move to more sustainable materials by incorporating organic-based PSs into their structure and by moving towards more Earth-abundant transition metals. Time-resolved techniques and spectroelectrochemical studies are implemented to study the effect of modifying the organic-based PS and eliciting the pathway leading to the formation of the active catalyst in those photocatalytic assemblies. The performance of these complexes as CO_2 reducing photo- and electrocatalysts are assessed. Despite their poor catalytic performance, the insights gained into their activation pathways and catalytic cycles will lead to improved designs of future photo- and electrocatalysts.

1.7 Bibliography

1 Crippa, M, Guizzardi, D, Pagani, F, Banja, M, Muntean, M, Schaaf, E, Quadrelli, R, Risquez Martin, A, Taghavi-Moharamli, P, Köykkä, J, Grassi, G, Melo, J, Suárez-Moreno, M, Sedano, F, San-Miguel, J, Manca, G, Pisoni, E, and Pekar, F, *GHG emissions of all world countries: 2025*, Publications Office of the European Union, 2025.

2 M. R. Allen, O. P. Dube, W. Solecki, F. Aragón-Durand, W. Cramer, S. Humphreys, M. Kainuma, J. Kala, N. Mahowald, Y. Mulugetta, R. Perez, M. Wairiu and K. Zickfeld, in *An IPCC Special Report on the impacts of global warming of 1.5°C above pre-industrial levels and related global greenhouse gas emission pathways, in the context of strengthening the global response to the threat of climate change, sustainable development, and efforts to eradicate poverty*, Cambridge University Press, Cambridge, UK and New York, NY, USA, 2018.

3 O. Hoegh-Guldberg, D. Jacob, M. Taylor, M. Bindi, S. Brown, I. Camilloni, A. Diedhiou, R. Djalante, K. L. Ebi, F. Engelbrecht, J. Guiot, Y. Hijioka, S. Mehrotra, A. Payne, S. I. Seneviratne, A. Thmoas, R. Warren and G. Zhou, in *An IPCC Special Report on the impacts of global warming of 1.5°C above pre-industrial levels and related global greenhouse gas emission*

pathways, in the context of strengthening the global response to the threat of climate change, sustainable development, and efforts to eradicate poverty, Cambridge University Press, Cambridge, UK and New York, NY, USA, 2018, pp. 175–312.

4 J. Rogelj, D. Shindell, K. Jiang, S. Fifita, P. Forster, V. Ginzburg, C. Handa, H. Kheshgi, S. Kobayashi, E. Kriegler, L. Mundaca, R. Séférian and M. V. Vilariño, in *An IPCC Special Report on the impacts of global warming of 1.5°C above pre-industrial levels and related global greenhouse gas emission pathways, in the context of strengthening the global response to the threat of climate change, sustainable development, and efforts to eradicate poverty*, Cambridge University Press, Cambridge, UK and New York, NY, USA, 2018.

5 N. D. McDaniel and S. Bernhard, Solar fuels: thermodynamics, candidates, tactics, and figures of merit, *Dalton Trans.*, 2010, **39**, 10021–10030.

6 G. Kopp and J. L. Lean, A new, lower value of total solar irradiance: Evidence and climate significance, *Geophys. Res. Lett.*, DOI:10.1029/2010GL045777.

7 *Statistical Review of World Energy*, Energy Institute, 2024.

8 M. Grätzel, Artificial photosynthesis: water cleavage into hydrogen and oxygen by visible light, *Acc. Chem. Res.*, 1981, **14**, 376–384.

9 B. O'Regan and M. Grätzel, A low-cost, high-efficiency solar cell based on dye-sensitized colloidal TiO_2 films, *Nature*, 1991, **353**, 737–740.

10 M. Gratzel, Photoelectrochemical cells, *Nature*, 2001, **414**, 338–344.

11 J. Hawecker, J.-M. Lehn and R. Ziessel, Efficient photochemical reduction of CO_2 to CO by visible light irradiation of systems containing $Re(bipy)(CO)_3X$ or $Ru(bipy)_3^{2+}$–Co^{2+} combinations as homogeneous catalysts, *J Chem Soc Chem Com*, 1983, **0**, 536–538.

12 A. Mazzeo, S. Santalla, C. Gaviglio, F. Doctorovich and J. Pellegrino, Recent progress in homogeneous light-driven hydrogen evolution using first-row transition metal catalysts, *Inorganica Chimica Acta*, 2021, **517**, 119950.

13 C. Gueymard, *SMARTS2, A Simple Model of the Atmospheric Radiative Transfer of Sunshine: Algorithms and performance assessment*, Florida Solar Energy Centre, 1995.

14 J. Schneider, H. Jia, J. T. Muckerman and E. Fujita, Thermodynamics and kinetics of CO_2, CO, and H^+ binding to the metal centre of CO_2 reduction catalysts, *Chem. Soc. Rev.*, 2012, **41**, 2036–2051.

15 Y. Matsubara, D. C. Grills and Y. Kuwahara, Thermodynamic Aspects of Electrocatalytic CO_2 Reduction in Acetonitrile and with an Ionic Liquid as Solvent or Electrolyte, *ACS Catal.*, 2015, **5**, 6440–6452.

16 Y.-J. Yuan, Z.-T. Yu, D.-Q. Chen and Z.-G. Zou, Metal-complex chromophores for solar hydrogen generation, *Chem. Soc. Rev.*, 2017, **46**, 603–631.

17 S. Kar and E. Reisner, Solar Air-to-Fuel Technologies for a Circular Carbon Economy, *J. Am. Chem. Soc.*, 2026, **148**, 10267–10285.

18 X. Zhang, S.-X. Guo, K. A. Gandionco, A. M. Bond and J. Zhang, Electrocatalytic carbon dioxide reduction: from fundamental principles to catalyst design, *Materials Today Advances*, 2020, **7**, 100074.

19 P. Banoth, C. Kandula and P. Kollu, in *Noble Metal-Free Electrocatalysts: New Trends in Electrocatalysts for Energy Applications. Volume 2*, American Chemical Society, 2022, vol. 1432, pp. 1–37.

20 M. Dunwell, Y. Yan and B. Xu, Understanding the influence of the electrochemical double-layer on heterogeneous electrochemical reactions, *Current Opinion in Chemical Engineering*, 2018, **20**, 151–158.

21 V. V. Mundada, M. Devi, B. Das, V. T and R. Thangavel, Review on Electrocatalytic CO_2 Reduction: From Molecular Mechanisms to Scalable Systems, *Energy Fuels*, 2025, **39**, 17192–17233.

22 X. She, Y. Wang, H. Xu, S. Chi Edman Tsang and S. Ping Lau, Challenges and Opportunities in Electrocatalytic CO_2 Reduction to Chemicals and Fuels, *Angewandte Chemie International Edition*, 2022, **61**, e202211396.

23 F. Hund, *Linienspektren*, Springer, Berlin, Heidelberg, 1927.

24 J. C. Slater, The theory of complex spectra, *Physical Review*, 1929, **34**, 1293–1322.

25 K. Hongo, T. Oyamada, Y. Maruyama, Y. Kawazoe and H. Yasuhara, Correct interpretation of Hund's multiplicity rule for atoms and molecules, *Journal of Magnetism and Magnetic Materials*, 2007, **310**, e560–e562.

26 J. R. Lakowicz, Ed., *Principles of Fluorescence Spectroscopy*, Springer US, Boston, MA, 2006.

27 L. G. Franca, D. G. Bossanyi, J. Clark and P. L. dos Santos, Exploring the Versatile Uses of Triplet States: Working Principles, Limitations, and Recent Progress in Phosphorescence, TADF, and TTA, *ACS Appl. Opt. Mater.*, 2024, **2**, 2476–2500.

28 B. Wardle, *Principles and Applications of Photochemistry*, John Wiley & Sons, 2009.

29 D. M. Roundhill, in *Photochemistry and Photophysics of Metal Complexes*, ed. D. M. Roundhill, Springer US, Boston, MA, 1994, pp. 25–65.

30 T. J. Meyer, Photochemistry of metal coordination complexes: metal to ligand charge transfer excited states, *Pure and Applied Chemistry*, 1986, **58**, 1193–1206.

31 J. R. Lakowicz, Ed., in *Principles of Fluorescence Spectroscopy*, Springer US, Boston, MA, 2006, pp. 1–26.

32 M. A. El-Sayed, Triplet state. Its radiative and nonradiative properties, *Acc. Chem. Res.*, 1968, **1**, 8–16.

33 M. Kasha, Characterization of electronic transitions in complex molecules, *Discuss. Faraday Soc.*, 1950, **9**, 14–19.

34 C. Creutz and N. Sutin, Reaction of tris(bipyridine)ruthenium(III) with hydroxide and its application in a solar energy storage system, *Proceedings of the National Academy of Sciences*, 1975, **72**, 2858–2862.

35 F. Vögtle, M. Plevoets, M. Nieger, G. C. Azzellini, A. Credi, L. De Cola, V. De Marchis, M. Venturi and V. Balzani, Dendrimers with a Photoactive and Redox-Active $[Ru(bpy)_3]^{2+}$-Type Core: Photophysical Properties, Electrochemical Behavior, and Excited-State Electron-Transfer Reactions, *J. Am. Chem. Soc.*, 1999, **121**, 6290–6298.

36 E. Deponti and M. Natali, Photocatalytic hydrogen evolution with ruthenium polypyridine sensitizers: unveiling the key factors to improve efficiencies, *Dalton Trans.*, 2016, **45**, 9136–9147.

37 W. E. Jones, R. A. Smith, M. T. Abramo, M. D. Williams and J. Van Houten, Photochemistry of hetero-tris-chelated ruthenium(II) polypyridine complexes in dichloromethane, *Inorg. Chem.*, 1989, **28**, 2281–2285.

38 K. P. S. Cheung, S. Sarkar and V. Gevorgyan, Visible Light-Induced Transition Metal Catalysis, *Chem. Rev.*, 2022, **122**, 1543–1625.

39 M. Wrighton and D. L. Morse, Nature of the lowest excited state in tricarbonylchloro-1,10-phenanthrolinerhenium(I) and related complexes, *J. Am. Chem. Soc.*, 1974, **96**, 998–1003.

40 K. Rangan, S. M. Arachchige, J. R. Brown and K. J. Brewer, Solar energy conversion using photochemical molecular devices: photocatalytic hydrogen production from water using mixed-metal supramolecular complexes, *Energy Environ. Sci.*, 2009, **2**, 410–419.

41 K. Koike, D. C. Grills, Y. Tamaki, E. Fujita, K. Okubo, Y. Yamazaki, M. Saigo, T. Mukuta, K. Onda and O. Ishitani, Investigation of excited state, reductive quenching, and intramolecular electron transfer of Ru(II)–Re(I) supramolecular photocatalysts for CO_2 reduction using time-resolved IR measurements, *Chem. Sci.*, 2018, **9**, 2961–2974.

42 T. Kowacs, L. O'Reilly, Q. Pan, A. Huijser, P. Lang, S. Rau, W. R. Browne, M. T. Pryce and J. G. Vos, Subtle Changes to Peripheral Ligands Enable High Turnover Numbers for Photocatalytic Hydrogen Generation with Supramolecular Photocatalysts, *Inorg. Chem.*, 2016, **55**, 2685–2690.

43 C. Creutz, M. Chou, T. L. Netzel, M. Okumura and N. Sutin, Lifetimes, spectra, and quenching of the excited states of polypyridine complexes of iron(II), ruthenium(II), and osmium(II), *J. Am. Chem. Soc.*, 1980, **102**, 1309–1319.

44 M. Albrecht, R. Bedford and B. Plietker, Catalytic and Organometallic Chemistry of Earth-Abundant Metals, *Organometallics*, 2014, **33**, 5619–5621.

45 T. Reuter, D. Zorn, R. Naumann, J. Klett, C. Förster and K. Heinze, A Tetracarbene Iron(II) Complex with a Long-lived Triplet Metal-to-Ligand Charge Transfer State due to a Triplet-Triplet Barrier, *Angewandte Chemie International Edition*, 2024, **63**, e202406438.

46 S. Kronenberger, R. Naumann, C. Förster, N. East, J. Klett and K. Heinze, A manganese(I) complex with a 190 ns metal-to-ligand charge transfer lifetime, *ChemRxiv*, 2024, preprint, DOI: 10.26434/chemrxiv-2024-gzvbj.

47 H. Koizumi, Y. Tamaki, K. Kamogawa, M. Nicaso, Y. Suzuki, Y. Yamazaki, H. Takeda and O. Ishitani, Development of a Highly Durable Photocatalytic CO_2 Reduction Using a Mn-Complex Catalyst: Application of Selective Photosplitting of a Mn(0)–Mn(0) Bond, *J. Am. Chem. Soc.*, 2025, **147**, 6236–6248.

48 Y. Kuramochi, Y. Fujisawa and A. Satake, Photocatalytic CO_2 Reduction Mediated by Electron Transfer via the Excited Triplet State of Zn(II) Porphyrin, *J. Am. Chem. Soc.*, 2020, **142**, 705–709.

49 Y. Kuramochi and A. Satake, Photocatalytic CO_2 Reductions Catalyzed by meso-(1,10-Phenanthrolin-2-yl)-Porphyrins Having a Rhenium(I) Tricarbonyl Complex, *Chemistry – A European Journal*, 2020, **26**, 16365–16373.

50 R. Yabuki, K. Nishimura, Y. Sawada, M. Fuki, Y. Kobori and N. Yanai, Dynamic electron and nuclear spin polarization in solution using porphyrin and tris(2,4,6-trichlorophenyl)-methyl (TTM) radical derivatives, *Journal of Magnetic Resonance Open*, 2025, **22**, 100181.

51 D. R. Whang and D. H. Apaydin, Artificial Photosynthesis: Learning from Nature, *ChemPhotoChem*, 2018, **2**, 148–160.

52 M. R. Wasielewski, Energy, Charge, and Spin Transport in Molecules and Self-Assembled Nanostructures Inspired by Photosynthesis, *J. Org. Chem.*, 2006, **71**, 5051–5066.

53 X. Zhao, Y. Hou, L. Liu and J. Zhao, Triplet Photosensitizers Showing Strong Absorption of Visible Light and Long-Lived Triplet Excited States and Application in Photocatalysis: A Mini Review, *Energy Fuels*, 2021, **35**, 18942–18956.

54 X. Zhang, Z. Wang, Y. Hou, Y. Yan, J. Zhao and B. Dick, Recent development of heavy-atom-free triplet photosensitizers: molecular structure design, photophysics and application, *J. Mater. Chem. C*, 2021, **9**, 11944–11973.

55 X. Zhan, A. Facchetti, S. Barlow, T. J. Marks, M. A. Ratner, M. R. Wasielewski and S. R. Marder, Rylene and Related Diimides for Organic Electronics, *Advanced Materials*, 2011, **23**, 268–284.

56 F. N. Castellano, Transition metal complexes meet the rylenes, *Dalton Trans.*, 2012, **41**, 8493–8501.

57 S. Banerjee, E. B. Veale, C. M. Phelan, S. A. Murphy, G. M. Tocci, L. J. Gillespie, D. O. Frimannsson, J. M. Kelly and T. Gunnlaugsson, Recent advances in the development of 1,8-naphthalimide based DNA targeting binders, anticancer and fluorescent cellular imaging agents, *Chem. Soc. Rev.*, 2013, **42**, 1601.

58 R. M. Duke, E. B. Veale, F. M. Pfeffer, P. E. Kruger and T. Gunnlaugsson, Colorimetric and fluorescent anion sensors: an overview of recent developments in the use of 1,8-naphthalimide-based chemosensors, *Chem. Soc. Rev.*, 2010, **39**, 3936–3953.

59 L. D. Patsenker and Y. Y. Artyukhova, Molecular structure and spectral properties of thionaphthalimides, *Journal of Molecular Structure*, 2003, **655**, 311–320.

60 M. Z. Bartusiak, R. J. McGarry, L. Varvarezos, M. P. Brandon and M. T. Pryce, Incorporation of perylene and naphthalene like ligands into ruthenium complexes: Synthesis, photophysical properties and electrochemistry, *Coord. Chem. Rev.*, 2023, **495**, 215365.

61 Y. Yang, F. Doettinger, C. Kleeberg, W. Frey, M. Karnahl and S. Tschierlei, How the Way a Naphthalimide Unit is Implemented Affects the Photophysical and -catalytic Properties of Cu(I) Photosensitizers, *Front. Chem.*, DOI:10.3389/fchem.2022.936863.

62 K. A. Wells, J. E. Yarnell, S. Sheykhi, J. R. Palmer, D. T. Yonemoto, R. Joyce, S. Garakyaraghi and F. N. Castellano, Accessing the triplet manifold of naphthalene benzimidazole–phenanthroline in rhenium(I) bichromophores, *Dalton Trans.*, 2021, **50**, 13086–13095.

63 Y. Yang, J. Brückmann, W. Frey, S. Rau, M. Karnahl and S. Tschierlei, Electron Storage Capability and Singlet Oxygen Productivity of a RuII Photosensitizer Containing a Fused Naphthaloylenebenzene Moiety at the 1,10-Phenanthroline Ligand, *Chemistry – A European Journal*, 2020, **26**, 17027–17034.

64 M. A. Argüello Cordero, P. J. Boden, M. Rentschler, P. Di Martino-Fumo, W. Frey, Y. Yang, M. Gerhards, M. Karnahl, S. Lochbrunner and S. Tschierlei, Comprehensive Picture of the Excited State Dynamics of Cu(I)- and Ru(II)-Based Photosensitizers with Long-Lived Triplet States, *Inorg. Chem.*, 2022, **61**, 214–226.

65 R. Horvath, G. S. Huff, K. C. Gordon and M. W. George, Probing the excited state nature of coordination complexes with blended organic and inorganic chromophores using vibrational spectroscopy, *Coord. Chem. Rev.*, 2016, **325**, 41–58.

66 J. F. Martinez, N. T. L. Porte, C. M. Mauck and M. R. Wasielewski, Photo-driven electron transfer from the highly reducing excited state of naphthalene diimide radical anion to a CO_2 reduction catalyst within a molecular triad, *Faraday Discuss.*, 2017, **198**, 235–249.

67 J. D. B. Koenig, W. E. Piers and G. C. Welch, Promoting photocatalytic CO_2 reduction through facile electronic modification of N-annulated perylene diimide rhenium bipyridine dyads, *Chem Sci*, 2021, **13**, 1049–1059.

68 D. R. Case, A. Spear, A. F. Henwood, M. Nanao, S. Dampf, T. M. Korter, T. Gunnlaugsson, J. Zubieta and R. P. Doyle, [Re(CO)$_3$(5-PAN)Cl], a rhenium(I) naphthalimide complex for the visible light photocatalytic reduction of CO_2, *Dalton Trans.*, 2021, **50**, 3479–3486.

69 A. Spear, R. L. Schuarca, J. Q. Bond, T. M. Korter, J. Zubieta and R. P. Doyle, Photocatalytic turnover of CO_2 under visible light by [Re(CO)$_3$(1-(1,10) phenanthroline-5-(4-nitro-naphthalimide))Cl] in tandem with the sacrificial donor BIH, *RSC Adv.*, 2022, **12**, 5080–5084.

70 F. Franco, C. Cometto, C. Garino, C. Minero, F. Sordello, C. Nervi and R. Gobetto, Photo- and Electrocatalytic Reduction of CO_2 by [Re(CO)$_3$α,α′-Diimine-(4-piperidinyl-1,8-naphthalimide)Cl] Complexes, *Eur. J. Inorg. Chem.*, 2015, **2015**, 296–304.

71 C. Riplinger, M. D. Sampson, A. M. Ritzmann, C. P. Kubiak and E. A. Carter, Mechanistic Contrasts between Manganese and Rhenium Bipyridine Electrocatalysts for the Reduction of Carbon Dioxide, *J. Am. Chem. Soc.*, 2014, **136**, 16285–16298.

72 J. J. A. Lozeman, P. Führer, W. Olthuis and M. Odijk, Spectroelectrochemistry, the future of visualizing electrode processes by hyphenating electrochemistry with spectroscopic techniques, *Analyst*, 2020, **145**, 2482–2509.

73 B. H. Stuart, *Infrared Spectroscopy: Fundamentals and Applications*, John Wiley & Sons, Incorporated, Newark, UNITED KINGDOM, 2004.

74 M. Krejčik, M. Daněk and F. Hartl, Simple construction of an infrared optically transparent thin-layer electrochemical cell: Applications to the redox reactions of ferrocene, $Mn_2(CO)_{10}$ and Mn(CO)$_3$(3,5-di-t-butyl-catecholate)$^-$, *Journal of Electroanalytical Chemistry and Interfacial Electrochemistry*, 1991, **317**, 179–187.

75 A. El Nahhas, C. Consani, A. M. Blanco-Rodríguez, K. M. Lancaster, O. Braem, A. Cannizzo, M. Towrie, I. P. Clark, S. Záliš, M. Chergui and A. Jr. Vlček, Ultrafast Excited-State Dynamics of Rhenium(I) Photosensitizers [Re(Cl)(CO)$_3$(N,N)] and [Re(imidazole)(CO)$_3$(N,N)]$^+$: Diimine Effects, *Inorg. Chem.*, 2011, **50**, 2932–2943.

76 J. M. Jr. Favale, E. O. Danilov, J. E. Yarnell and F. N. Castellano, Photophysical Processes in Rhenium(I) Diiminetricarbonyl Arylisocyanides Featuring Three Interacting Triplet Excited States, *Inorg. Chem.*, 2019, **58**, 8750–8762.

77 V. Kumar, S. Schlücker and E. Hasselbrink, in *Molecular and Laser Spectroscopy*, Elsevier, 2020, vol. 2, pp. 563–594.

78 J. Palion-Gazda, K. Choroba, M. Penkala, P. Rawicka and B. Machura, Further Insights into the Impact of Ligand-Localized Excited States on the Photophysics of Phenanthroline-Based Rhenium(I) Tricarbonyl Complexes, *Inorg. Chem.*, 2024, **63**, 1356–1366.

79 K. Arora, N. Kondal and A. Kumar, Ultrafast charge dynamics in molecular thin films, *Materials Today: Proceedings*, 2022, **48**, 1652–1660.

80 M. Maiuri, M. Garavelli and G. Cerullo, Ultrafast Spectroscopy: State of the Art and Open Challenges, *J. Am. Chem. Soc.*, 2020, **142**, 3–15.

81 D. V. O'Connor and D. Phillips, in *Time-Correlated Single Photon Counting*, Academic Press, 1984, pp. 36–54.

82 L. Wei, W. Yan and D. Ho, Recent Advances in Fluorescence Lifetime Analytical Microsystems: Contact Optics and CMOS Time-Resolved Electronics, *Sensors*, 2017, **17**, 2800.

83 X. Zhang, X. Chen, Y. Sun and J. Zhao, Radical enhanced intersystem crossing mechanism, electron spin dynamics of high spin states and their applications in the design of heavy atom-free triplet photosensitizers, *Org. Biomol. Chem.*, 2024, **22**, 5257–5283.

84 S. Roth, A. Bonduelle-Skrzypczak, C. Legens and P. Raybaud, Meeting the Industrial Challenges of CO_2 Photocatalytic Reduction: Moving From Molybdenum Disulfides to Oxysulfides Based Materials?, *ChemSusChem*, 2025, **18**, e202400572.

Chapter 2

The Nature and Dynamics of the Excited States of Ethynyl-Functionalised Naphthalimide-Phenanthroline Re(I) Complexes Studied by TA and TRIR Spectroscopies

---

Jack Biddulph[1], Martin Pižl[2,3], Sayantan Bhattacharya[4], Partha Malakar[4], Gregory M. Greetham[4], František Hartl[2] and Mary T. Pryce[1], *J. Phys. Chem. B*, 2026, **130**, 6383–6398.

[1] *School of Chemical Sciences, Dublin City University, Glasnevin, Dublin, D09 V289, Ireland*

[2] *Department of Chemistry, University of Reading, Whiteknights, Reading, RG6 6DX, UK*

[3] *Department of Inorganic Chemistry, University of Chemistry and Technology Prague, Technická 5, 166 28 Prague 6, Czech Republic*

[4] *Central Laser Facility, Science & Technology Facilities Council, Research Complex at Harwell, Rutherford Appleton Laboratory, Didcot, OX11 0QX, UK*

Author Contributions:

Jack Biddulph prepared all materials and conducted all experimental studies and writing for this chapter. Martin Pižl performed quantum chemical calculations and contributed to TRIR studies.

2.1 Abstract

The synthesis and photophysical properties of four [Re(R–NI–phen)$(CO)_3$Cl] complexes (**Re–R**), where NI = 1,8-naphthalimide and phen = 1,10-phenanthroline, are reported. The R–NI chromophores were substituted at their 4-positions with R = H (**Re–H**), ethynyl benzene (**Re–EB**), ethynyl thiophene (**Re–ES**), ethynyl trimethylsilane (**Re–ET**), yielding a series of metal–organic bichromophores. The **R–NI–phen** organic chromophores were investigated in parallel to better understand the photophysical properties exhibited in the **Re–R** complexes. The excited-state processes of these molecules were studied by transient absorption and time-resolved infrared spectroscopies, to unravel the kinetics of the energy transfer processes occurring in the **Re–R** series. Namely, the interplay between the singlet ligand-centred (^{1}LC), the triplet metal-to-ligand charge-transfer (^{3}MLCT), and the triplet ligand-centred (^{3}LC) excited states were studied using these time-resolved spectroscopic techniques, supported by quantum chemical calculations, to monitor the changing excited-state dynamics in the **Re–R** series. These studies reveal that the thermal equilibrium between the ^{3}MLCT and ^{3}LC excited states present in **Re–H** is modulated in favour of the ^{3}LC excited state in the remaining **Re–R** series, giving rise to increasingly ligand-like photophysics as the electron-donating strength of the R-group increases.

2.2 Introduction

In the last two decades, rylene diimides have emerged as organic photosensitising units, due to their visible-region absorption bands and typically long-lived triplet excited states when attached to transition-metal complexes.[1,2] Particularly, perylene and naphthalene diimides have extensively been studied for many photo-based applications, including photocatalysis and OLED design.[3–6] When employed in photocatalysis, these dyes are covalently attached to transition-metal complexes, leading to intramolecular assemblies.[1,7,8] The naphthalimide (NI) moiety is one of the simplest structures in this series of compounds; however, the smaller π-delocalised system of NI compounds results in absorption bands shifted predominantly to the UV spectral region. The presence of only one imide group in NI, as opposed to two in the rylene diimide family, allows for further functionalisation on the NI core, which can modulate the UV-Vis absorption spectra.[9,10] Additionally, when covalently linked to 1,10-phenanthroline (phen), as in NI–phen, the phen unit can be utilised for coordination to transition metals. Thus, a bichromophore is created with the (Cl)Re–phen π-system as a ligated metal chromophore and the NI moiety as an organic chromophore.[11] Despite being covalently linked, these chromophores behave as electronically distinct units in the ground state.[12]

Photophysical studies of transition-metal NI–phen complexes, including those typically prepared for photocatalytic applications (Cu^{+}, Ir^{3+}, Re^{+}, Ru^{2+}), have predominantly utilised transient absorption (TA) spectroscopy to probe the excited-state dynamics in these systems.[13–16] Yarnell et al. reported TA studies for a series of [Re(R–NI–phen)$(CO)_3$(dmap)](PF_6) complexes (where R = H, Br, phenoxy, phenylthiol, or piperidinyl groups and dmap = 4-dimethylaminopyridine) proposing a "ping-pong" effect when describing the populated excited states.[17] Initially, optical excitation results in the population of the NI-based singlet ligand-centred (^{1}LC) excited state and concomitant population of the ^{3}MLCT excited state that persists on the nanosecond timescale. Subsequently, a NI-based triplet ligand-centred (^{3}LC) excited state forms and decays to the ground state on the microsecond timescale.

Metal–carbonyl ligands display unique stretching patterns and wavenumbers in both the IR and TRIR spectra, which can easily be monitored, depending on the metal centre and its oxidation state, the number of bonded carbonyls, the molecular structure, the symmetry point group, and any (non-innocent) auxiliary ligands present.[18] Accordingly, TRIR spectroscopy has widely been implemented to study the excited states of transition-metal carbonyls.[19–23] By comparison, the organic-carbonyl vibrations ($\nu_{C=O}$) can be more challenging to detect, being approximately 20 times weaker than metal–carbonyl vibrations ($\nu_{C\equiv O}$). In the NI-containing rhenium carbonyl compounds presented here, inclusion of both metal–carbonyl (C≡O) and organic carbonyl (C=O) bonds within the same molecule enables monitoring of the excited states involving both moieties in a relatively silent IR region (2400–1700 cm^{-1}) by TRIR spectroscopy.[18] Generally, IR $\nu_{C\equiv O}$ absorption features are intense owing to the nature of π-back-bonding through the C≡O bonds, thus resulting in a large change in the dipole moment, which enables monitoring of excited-state processes near the metal centre, such as metal-to-ligand charge transfer (MLCT).[24] Time-resolved infrared spectroscopy (TRIR) has also been used to study a number of transition-metal NI–phen complexes, including [Re(PNI–phen)$(CO)_3$Cl] and [Ir$(ppy)_2$(PNI–phen)](PF_6) (where PNI = 4-piperidinyl-1,8-naphthalimide).[14,15] For [Re(PNI–phen)$(CO)_3$Cl], the incorporation of a strong electron-donating group (EDG) onto the NI core resulted in a 3000-fold increase of the triplet excited-state lifetime compared to [Re(phen)$(CO)_3$Cl], from a 0.2 μs ^{3}MLCT excited-state lifetime to a 651 μs ^{3}LC excited-state lifetime with significant ligand-like photophysics.

While carbonyl ligands have been used extensively as IR-active tags for TRIR studies, other triple bonds, namely ethynyl (C≡C) and nitrile (C≡N) groups, have come to be more widely used for this purpose.[25–30] Their ground-state vibrations occur in the IR multiple-bond stretching region; *ca.* 2240 cm^{-1} for C≡N bonds[27] and *ca.* 2200 cm^{-1} for C≡C bonds[31]. Additionally, transient enhancement has previously been observed for C≡X (where X = C, N, O) functionalised

compounds, making these vibrations more readily detectable. Previous TRIR studies of C≡N groups as IR-active tags have reported significant enhancement of the C≡N vibrational modes in the excited state, similarly to the enhancement observed for the reduced species in IR-SEC studies.[27,32,33] Recently, Vauthey et al. used TRIR spectroscopy to study the excited-state dynamics of ethynyl-bridged donor-acceptor systems and reported excited-state symmetry breaking in the ethynyl transient features observed.[25,26,34] In such systems, a donor–acceptor dyad can undergo a transition from a symmetrical "dipolar" excited state to an asymmetric "dipolar" excited state.[25]

While ethynyl groups are known electron-withdrawing groups, this character is influenced by the molecular components they bridge.[35] Trimethylsilane, benzene, and thiophene[36] are known to weakly donate electron density onto aromatic ring systems via induction. Hence, when attached to the electron-accepting NI–phen moiety, the ethynyl-substituents should exhibit behaviour akin to an EDG. Consequently, the triplet–triplet state equilibrium in the rhenium(I) complexes can be modulated in favour of the ^{3}LC excited state, giving rise to more ligand-like photophysics, as in the case of the series appended with EDGs, studied by Yarnell et al.[17] Indeed, in our experimental studies, complemented with TDDFT calculations, indicate that the triplet–triplet energy gap between the ^{3}MLCT and ^{3}LC excited states increases in the explored series of [Re(R–NI–phen)(CO)$_3$Cl] complexes (**Re–R**, where **R** = **H**, ethynyl trimethylsilane (**ET**), ethynyl benzene (**EB**), and ethynyl thiophene (**ES**), see Chart 2.1); [**Re–H** < **Re–ET** < **Re–EB** < **Re–ES**].

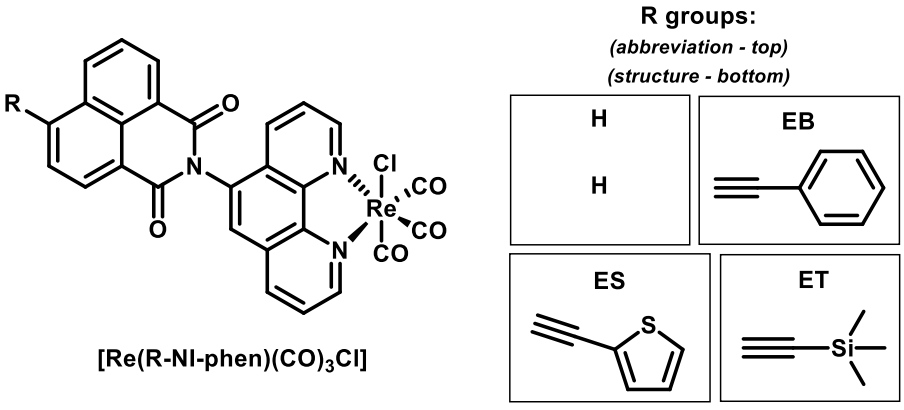


Chart 2.1. *General structure of the* ***Re–R*** *series of complexes studied in this work. R is the substituent at the 4–position on the NI core.*

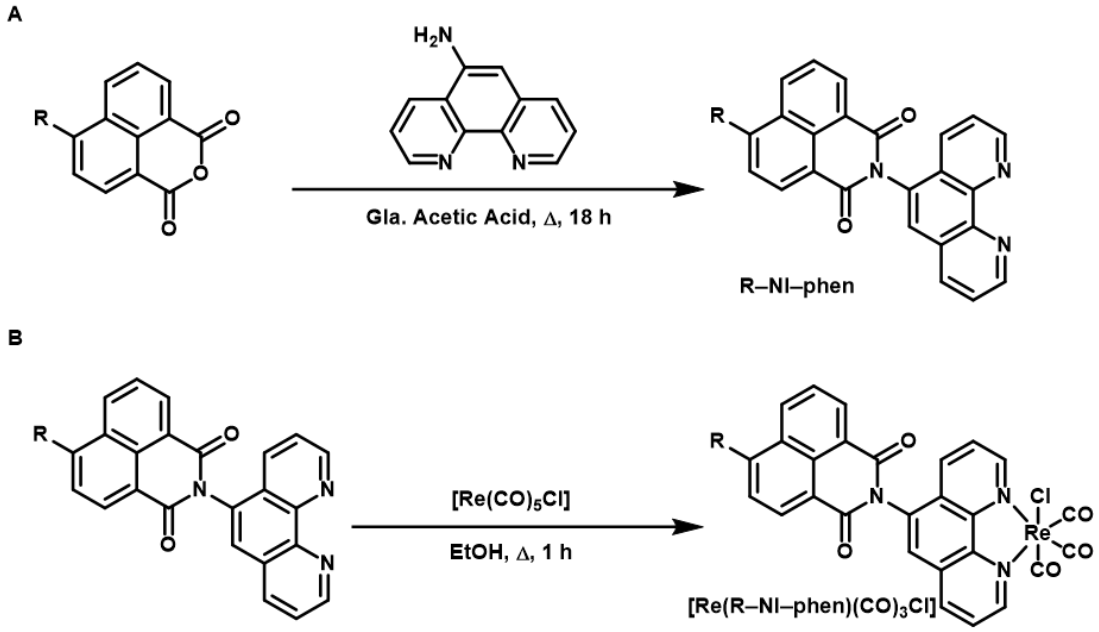
The [Re(H–NI–phen)(CO)$_3$Cl] (**Re–H**) complex with the unsubstituted NI core was studied as a reference complex in tandem with three novel **Re–R** complexes incorporating ethynyl benzene

(**Re–EB**), ethynyl thiophene (**Re–ES**), and ethynyl trimethylsilane (**Re–ET**) groups attached onto the NI core at the 4-position. The impact of the weak electron-donating effect associated with the ethynyl substituents on the triplet–triplet equilibrium between the ^{3}MLCT and ^{3}LC excited states was assessed using steady-state and time-resolved spectroscopic techniques. Additionally, the presence of C≡O, C=O, and C≡C bonds as IR-active tags enables taking advantage of TRIR studies for gaining a deeper understanding of the photophysics of this **Re–R** series. The insights gained may lead to the design of photocatalysts or as materials for use in other photo-based applications.

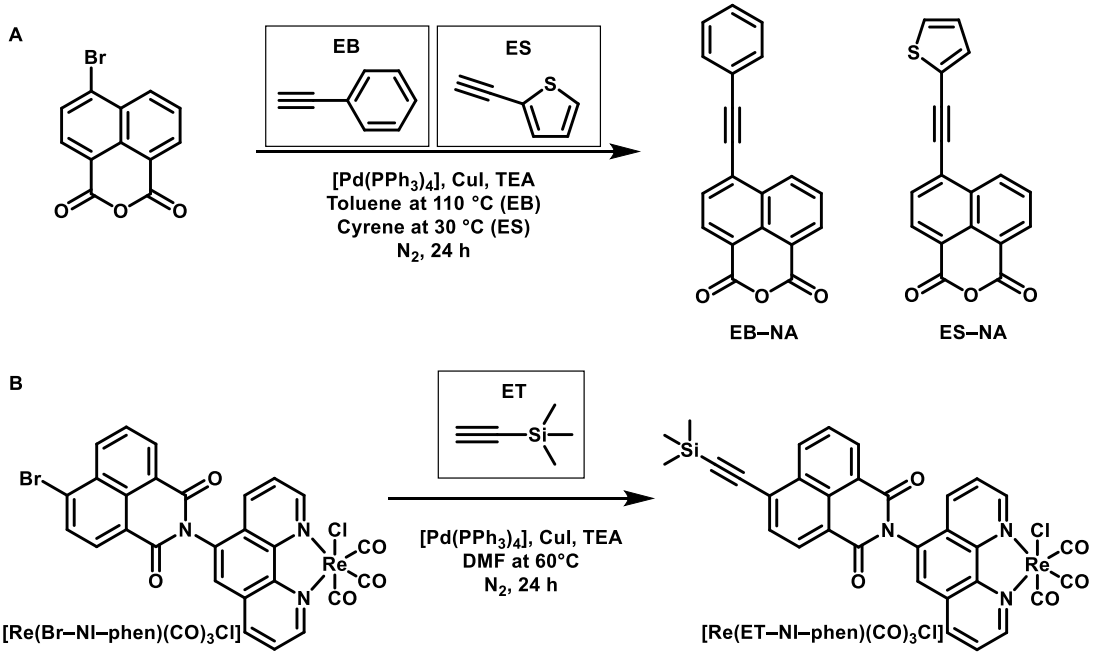
2.3 Results and Discussion

2.3.1 Syntheses

The literature-based syntheses of **H–NI–phen** and **Re–H** were modified to develop the general reaction scheme for the target materials of this study (Scheme 2.1).[13,17] Briefly, the naphthalimide chromophores were prepared from the corresponding naphthalic anhydride (NA) (either unsubstituted or substituted with Br, 2-ethynyl benzene or 2-ethynyl thiophene in the 4-position of NA) by reacting with 5-amino-1,10-phenanthroline according to published protocols to generate the series of **R–NI–phen** compounds. Subsequently, **R–NI–phen** were brought to reflux temperature with [Re(CO)$_5$Cl], yielding the [Re(R–NI–phen)(CO)$_3$Cl] complexes. For **Re–EB** and **Re–ES**, the starting anhydrides were synthesised according to Scheme 2.2a. The Br group in [Re(Br–NI–phen)(CO)$_3$Cl] was substituted with 2-ethynyl trimethylsilane, using the Sonogashira cross-coupling reaction, to make the last target complex, **Re–ET** (Scheme 2.2b). All products were characterised using ^{1}H NMR spectroscopy (Figures S2.1–S2.11), high resolution mass spectroscopy, and elemental analyses (Figures S2.12–S2.18).



Scheme 2.3. *Reaction schemes for (A) general synthesis of* ***R–NI–phen****, (B) general synthesis of* ***Re–R****. R = H, EB, ES, or ET.*



Scheme 2.4. *Sonogashira cross-coupling reaction schemes for the formation of (A)* ***EB–NA*** *and* ***ES–NA*** *precursors, (B)* ***Re–ET*** *complex.*

NI-containing compounds, including those linked to metal centres, are known to undergo aggregation via π-π stacking interactions.[14,37–41] Though aggregation is not the focus of this work, the effect of aggregation on the spectral and photophysical properties of **R–NI–phen** and **Re–R**

are briefly outlined. In terms of the spectral properties, blue/red-shifts and signal broadening/narrowing are associated with the formation of such aggregates in solution. Additionally, aggregation-induced emission and aggregation-induced self-quenching have been reported for NI's which can impact on the photophysical properties of these materials. Sample concentrations are reported for all spectra, and where aggregation does affect the studies performed in this work, specific mention of their impact is outlined in the relevant sections.

Finally, many of the reactants and reaction products involved in preparation of the **R–NI–phen** and **Re–R** samples contain π-conjugated systems. It is well known that π-π stacking interactions makes it very difficult to remove all starting materials, and in this case resulted in trace amounts of the reactants in the product materials. This is apparent in the ^{1}H NMR spectra of the **EB–NI–phen** and **ES–NI–phen** samples (Figure S2.4 and S2.7). However, these impurities are not observed in the **Re–EB** and **Re–ES** complexes which form part of the main **Re–R** series studied in this work.

2.3.2 FTIR and UV-Vis Absorption Studies

The FTIR and UV-Vis absorption spectra of **Re–R** are presented in Figures 2.1 and 2.2, respectively. The FTIR and UV-Vis absorption spectra of **R–NI–phen** are available in Figures S2.19–2.21. Key spectral data from the IR and UV-Vis absorption spectra are given in Table 2.1. The calculated electronic absorption and vibrational properties of **Re–R** (Figures S2.43 and S2.44) are in a good agreement with the recorded experimental spectral data. The key molecular orbitals involved in the main electronic transitions of **Re–R**, as determined by the TDDFT calculations, are presented in Figure 2.3.

The IR $\nu_{C=O}$ wavenumbers are identical for **Re–R** (Figure 2.1) and **R–NI–phen** (Figure S2.19), proving the electronically independent nature of NI in free and complexed **R–NI–phen**. For all **Re–R** complexes, the $\nu_{C\equiv O}$ band pattern supports their fac-configuration.[17,19,42,43] For ethynyl-bearing **Re–EB** and **Re–ES**, the ethynyl stretching vibration ($\nu_{C\equiv C}$) is observed at 2206 and 2195 cm^{-1}, respectively. For **Re–ET**, it was not possible to detect the IR $\nu_{C\equiv C}$ band; instead, ATR IR technique was used to observe the $\nu_{C\equiv C}$ band at 2162 cm^{-1} (Figure S2.20). The DFT-calculated IR spectra are in good agreement with the experimental IR spectra (Figure S2.43).

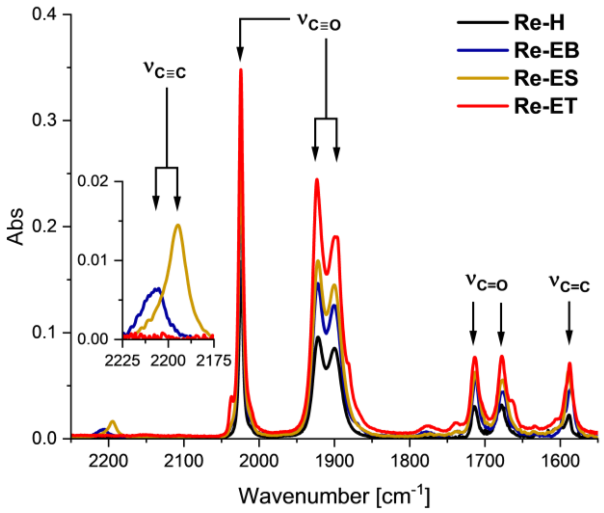


Figure 2.1. *IR spectra of **Re–R** between 2250 and 1550 cm^{-1} in DCM (50, 20, 35, and 100 µM samples for **Re–H**, **Re–EB**, **Re–ES**, and **Re–ET**, respectively). Inset: Expanded IR spectra between 2225 and 2175 cm^{-1}.*

The UV-Vis absorption spectra of the **Re–R** series in Figure 2.2 feature absorption bands corresponding to electronic transitions arising from the (Cl)Re–phen π-system and the NI chromophore, consistent with a bichromophoric system showing negligible electronic communication between the subunits.[12] The phen π→π* transition at 265 nm was observed for all **Re–R** complexes. In the UV-Vis absorption spectrum of **Re–H**, a transition with a maximum at 385 nm appeared as a shoulder in the spectrum of **Re–ET**. This transition was attributed to a mixture of dπ(Re)→π*(phen) MLCT and π(Cl)→π*(phen) halide-to-ligand charge transfer (XLCT), a so-called "metal-ligand-to-ligand charge transfer" (ML'LCT) transition. However, when the halide is Cl, as is the case with the **Re–R** series in this work, the MLCT character predominates over the XLCT character.[24,44,45] As such, this transition is referred to as a MLCT transition herein. The MLCT transition was expected for **Re–EB** and **Re–ES**, as the (Cl)Re–phen π-system chromophore is retained in those complexes; however, it was obscured by the transitions from the NI chromophore. The intra-ligand NI transitions were expected to differ the most in the **Re–R** series owing to the substitutions made at the 4-position of the NI core. For **Re–H**, the transitions belonging to the NI chromophore display vibrational fine structure; with a π→π* transition at 352 nm, and a n→π* transition at 338 nm.[37,46] These assignments are supported by TDDFT calculations of **Re–H** in Figure 2.3; where the NI-based transitions correspond with the HOMO–3 to LUMO transition, while the MLCT transition corresponds with the HOMO–1 localised on the Re(CO)$_3$Cl moiety and the LUMO+1 localised on the phen moiety (Figures S2.45 and S2.46 and Table S2.1).

The intraligand NI transitions are bathochromically shifted relative to those seen for **Re–H**, with the smallest shift of the n→π* transition of 26 nm (2110 cm^{-1}) being observed for **Re–ET** followed by **Re–EB** with a shift of 47 nm (3610 cm^{-1}) and **Re–ES** seeing the largest shift of 70 nm (5080 cm^{-1}). Previously, similar shifts have been assigned to an increasing charge-transfer character in a series of transition-metal complexes with ligated **R–NI–phen**[11,14–16], and becomes more noticeable as the electron-donating character of the R-group increases.[17,36] The UV-Vis absorption spectrum of **Re–ET** retained the vibrational fine structure of the NI transitions; the n→π* transition appears at 364 nm and the π→π* transition appears at 381 nm. The π→π* transition of the **ET–NI** unit has the largest ε value among the NI-based transitions in **Re–ET** compared to the n→π* transition in **Re–H**; but this is most likely due to an additive effect of the underlying MLCT transition rather than a true hyperchromic shift of the π→π* transition. This indicates that extended π-conjugation is responsible for the bathochromic shift and the retention of the vibrational fine structure, in the absorption profile of **Re–ET**, rather than an electron-donating effect. TDDFT calculations of **Re–ET** provided in Figure 2.3 show the NI-based transitions correspond to HOMO–2→LUMO and the MLCT transition involves the HOMO–1 and LUMO+1 molecular orbitals localised on the $Re(CO)_3Cl$ moiety and the phen moiety, respectively (Figures S2.51 and S2.52 and Table S2.4).

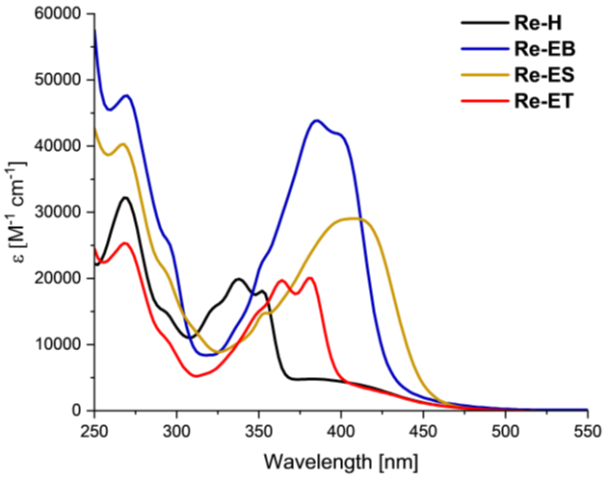


Figure 2.2. *UV-Vis absorption spectra of* ***Re–H*** *(50 µM),* ***Re–EB*** *(20 µM),* ***Re–ES*** *(35 µM), and* ***Re–ET*** *(50 µM) in DCM.*

In the UV-Vis absorption spectrum of **Re–EB**, a bathochromic and hyperchromic shift of the NI transitions are observed, while the vibrational fine structure is less pronounced than that seen for **Re–H** and **Re–ET**. The n→π* transition is observed at 385 nm and the π→π* transition at 398

nm. The UV-Vis absorption spectrum of **Re–ES** shows a further bathochromic shift of the NI transitions though the hyperchromic shift was less than that observed for **Re–EB**. Broadening of the NI transitions resulted in a complete loss of the vibrational fine structure such that one peak is observed at 408 nm. The TDDFT calculations presented in Figure 2.3 support these spectral assignments for **Re–EB** and **Re–ES**; where the HOMO is distributed across the extended π-conjugated system of the NI moiety and the LUMO is localised on the NI core, while the MLCT transition involves the HOMO–2 and LUMO+1 molecular orbitals (Figures S2.47–S2.50 and Tables S2.2 and S2.3). Thus, the lowest-energy transition in **Re–EB** and **Re–ES** arises from a R–NI→NI π→π* intra-ligand charge transfer (ILCT) transition within the NI moiety, with a close-lying MLCT transition.

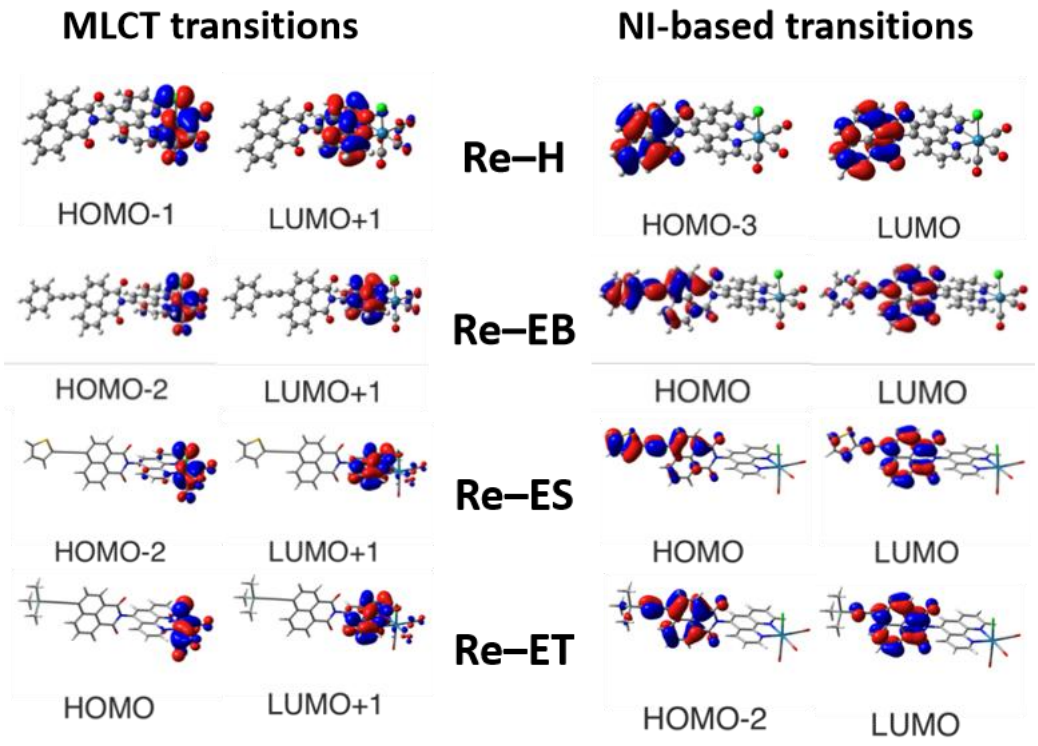


Figure 2.3. *The key molecular orbitals involved in the MLCT and NI-based electronic transitions of* ***Re–R****.*

Table 2.1. *IR and UV-Vis absorption and emission spectral data for both the* ***R–NI–phen*** *and* ***Re–R*** *series in DCM and DFT/TDDFT calculated spectral features for* ***Re–R****.*

Sample	λ_{max} (nm) [ε (M^{-1} cm^{-1})]	calc. λ_{max} (nm)	λ_{em} (nm) 298 K	λ_{em} (nm) 77 K[b]	$\nu_{C=O}$ (cm^{-1})	calc. $\nu_{C=O}$[a] (cm^{-1})	$\nu_{C\equiv O}$ (cm^{-1})	calc. $\nu_{C\equiv O}$[a] (cm^{-1})	$\nu_{C\equiv C}$ (cm^{-1})	calc. $\nu_{C\equiv C}$[a] (cm^{-1})
H–NI–phen	336 [12500]	–	374	449, 539, 587	1712, 1675	–	–	–	–	–
EB–NI–phen	381 [30790]	–	442	410, 432	1711, 1673	–	–	–	2208	–
ES–NI–phen	406 [16680]	–	483	434, 456	1710, 1672	–	–	–	2195	–
Re–H	338 [19900]	353	628	451, 539, 588	1712, 1678	1678, 1630	2024, 1921, 1900	1998, 1872, 1853	–	–
Re–EB	385 [43040]	446	447	446, 611	1713, 1677	1678, 1630	2024, 1921, 1900	1998, 1872, 1853	2206	2220
Re–ES	408 [29030]	473	487	453, 593	1713, 1676	1678, 1630	2024, 1922, 1900	1998, 1872, 1853	2195	2212
Re–ET	381 [20010]	397	412, 624	453, 591	1714, 1677	1678, 1630	2024, 1923, 1899	1998, 1872, 1853	2162[c]	2183

[a]A proportionality factor of 0.983 was used to multiply the DFT-calculated IR spectra.[47] [b]2-Me-THF was used as the solvent glass for 77 K emission studies with excitation at 385 nm for all samples except ***H–NI–phen*** *which used 330 nm excitation. [c]* $\nu_{C\equiv C}$ *for* ***Re–ET*** *is only observed using ATR IR.*

2.3.3 Emission studies at RT and 77 K

The RT emission spectra of **Re–R** are presented in Figure 2.4A. The 77 K emission spectra of **Re–R** in 2-MeTHF were also recorded and are displayed in Figure 2.4B. The RT and 77 K emission spectra of **R–NI–phen** are provided in Figure S2.22. All emission maxima (λ_{em}) were recorded above in Table 2.1.

The emission profile of **Re–H** (Figure 2.4A) reaches a maximum at 628 nm, which closely matches that of other Re(α-diimine) complexes with emissive ^{3}MLCT excited states.[17,43,48,49] A second emission band with a maximum below 400 nm occurs at a similar wavelength to fluorescence of **H–NI–phen** (λ_{em} = 374 nm) and was previously assigned to the ^{1}LC excited state.[17] Dual emission was previously reported for **H–NI–phen** in polar solvents such as THF, which displayed short-wavelength and long-wavelength components.[17,50,51] This behaviour is attributed to excited-state conjugation enhancement (ESCE), where the orthogonal geometry of the NI and phen moieties undergoes planarisation and is stabilised by polar solvent environments.[50] Thus, ESCE is likely inhibited in DCM due to the non-polar solvent environment, resulting in only a single emissive feature. Fluorescence from the ^{1}LC excited state (λ_{em} = 374 nm for **H–NI–phen**) has a good overlap with the MLCT absorption band of **Re–H** (λ_{MLCT} = 385 nm); thus, the population of the ^{1}MLCT excited state can occur by energy transfer from the ^{1}LC excited state of **Re–H**, with subsequent population of the emissive ^{3}MLCT excited state. Indeed, Förster-like resonance energy transfer has been reported for the related series of complexes studied by Yarnell et al.[17]

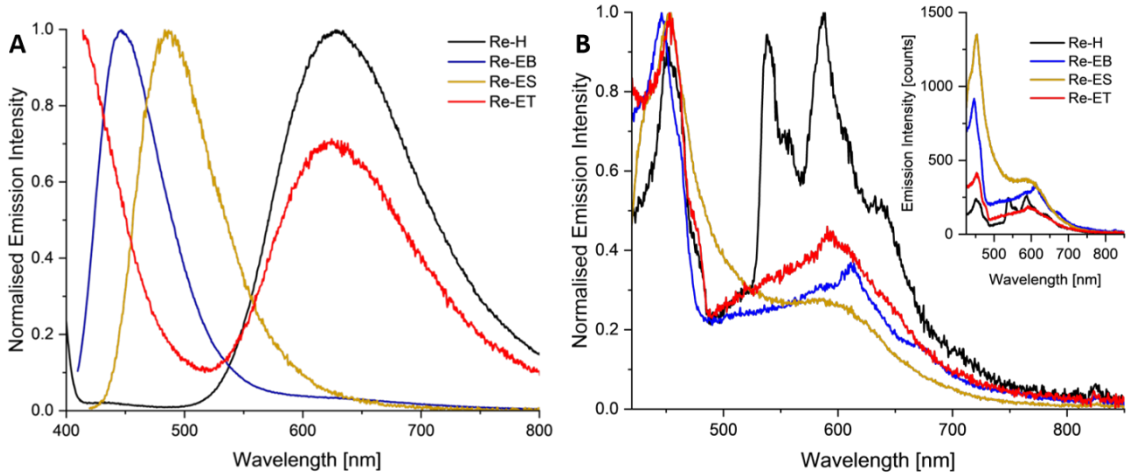


Figure 2.4. *Normalised emission spectra of **Re–R** following excitation at 385 nm (10, 5, 7.5, and 10 μM samples for **Re–H**, **Re–EB**, **Re–ES**, and **Re–ET**, respectively); [A] room-temperature emission spectra in DCM, [B] 77 K emission spectra of **Re–R** following excitation at 385 nm in 2-MeTHF. Inset: Non-normalised 77 K emission spectra.*

Re–ET displayed a similar emission profile as **Re–H**, with an emissive ^{3}MLCT excited state centred at 624 nm and the higher-energy ^{1}LC excited-state emission near the edge of the spectroscopic window (λ_{em} = 412 nm). The relative intensity of these emission features shifts from **Re–H** to **Re–ET**, with the ^{1}LC emission appearing more prominently than the ^{3}MLCT emission in **Re–ET**. This may be explained by the bathochromically shifted ^{1}LC fluorescence of **Re–ET** (λ_{em} = 412 nm), having reduced overlap with the MLCT absorption band at *ca.* 385 nm and consequently reducing energy transfer in **Re–ET**. In contrast to the notable changes in the emission profiles of **H–NI–phen** and **Re–H**, there was little difference in the emission profiles of **Re–EB** and **Re–ES** compared with their **R–NI–phen** counterparts (Figure S2.22). Intense ^{1}LC emission bands were observed for **Re–EB** and **Re–ES** at 447 and 487 nm respectively. These ^{1}LC emission bands have poor overlap with the MLCT absorption band at *ca.* 385 nm. Accordingly, the bathochromic shifts associated with substitution of the NI core in the **Re–R** series inhibit population of the ^{3}MLCT excited state via energy transfer, leading to significant quenching of the ^{3}MLCT emission in **Re–EB**, with an extremely weak tail extending beyond 700 nm. The ^{3}MLCT emission is entirely quenched in **Re–ES**. This quenching of the ^{3}MLCT excited state matched the bathochromic shift of the NI absorption bands in the following trend: **Re–H** < **Re–ET** < **Re–EB** < **Re–ES**.

The 77 K emission spectra (Figure 2.4B) were collected to monitor the population of the ^{3}LC excited states in 2-MeTHF, following the excitation at 385 nm. The 77 K emission spectra of the **R–NI–phen** displayed similar emissive profiles to those in the **Re–R** series (Figure S2.22); and as such, only the spectra of **Re–R** are discussed. The 77 K emission spectrum for **Re–H** displayed vibrationally structured emission bands *ca*. 550–600 nm, similarly to [Re(NI–phen)$(CO)_3$(dmap)](PF_6), which Yarnell et al. attributed to the population of the ^{3}LC excited state.[17] For the remaining **Re–R** complexes in this work, a broad emission band was observed *ca*. 600 nm closely resembling the ^{3}LC excited state at 77 K for [Re(R–NI–phen)$(CO)_3$(dmap)](PF_6) with increasingly electron-donating R groups (R = phenoxy, phenylthiol, or piperidinyl).[17] In the 77 K emission spectra of all **Re–R**, a band near 450 nm was observed with minimal shifts in energy throughout the series. However, the relative intensity between the 450 nm band and the 600 nm band in the **Re–R** series shifted from a 1:1 ratio in **Re–H** to 3.5:1 ratio for **Re–ES**, following the previously established trend for this series: **Re–H** < **Re–ET** < **Re–EB** < **Re–ES**.

2.3.4 TRIR Spectroscopy

The TRIR spectra of **Re–R** on the picosecond (ps) and nanosecond (ns) timescales (Figures 2.5–2.8) were collected in DCM following excitation at 420 nm, except for **Re–H** that was excited at

400 nm. The TRIR spectra of the **R–NI–phen** series are presented in Figures S2.23 and S2.24. The kinetic traces from TRIR studies are shown in Figures S2.25–S2.31. All transient features ($\nu_{C=O}$, $\nu_{C\equiv O}$, $\nu_{C\equiv C}$) from the TRIR spectra of the **Re–R** series are summarised in Table 2.2, with the lifetimes (τ_{TRIR}) reported in Table 2.3. The calculated vibrational data obtained for the ^{3}LC excited states (Figure S2.43) are in a good agreement with the experimental spectra (Table 2.2).

Following excitation at 400 nm, the TRIR spectrum of **Re–H** (Figure 2.5A) displayed an excited-state transient formed within the laser pulse (< 0.2 ps). Femtosecond processes are known for Re(α-diimine) complexes, particularly ultrafast intersystem-crossing (ISC) processes, resulting in the formation of a triplet excited state, typically the ^{3}MLCT excited state.[19] For **Re–H**, $\nu_{C\equiv O}$ ground-state bleaches (GSBs) were observed at 2030, 1920, and 1898 cm^{-1}, accompanied by three transient $\nu_{C\equiv O}$ bands at 2058 , 1975 and 1957 cm^{-1}. The transient bands at 1975 and 1957 cm^{-1}, which arises from a mixture of the ^{3}LC (phen π→π*) and ^{3}MLCT excited states[52,53], shift to larger wavenumbers ($\nu_{C\equiv O}$ = 1993 and 1965 cm^{-1}) with a lifetime τ_{TRIR} of 7.2 ps. This coincided with a blue shift of the $\nu_{C\equiv O}$ transient band at 2058 cm^{-1} to 2082 cm^{-1}, which has been attributed to vibrational cooling of the vibrationally hot ^{3}MLCT excited state.[19] The $\nu_{C\equiv O}$ transient signal at 2082 cm^{-1} did not reach maximum absorbance until about 200 ps after excitation, with a doubling of the ΔO.D. in this time domain compared to the other $\nu_{C\equiv O}$. In the ns-TRIR experiments (Figure 2.5B), these signals returned to the baseline with a lifetime of 258 ns, which is in agreement with the literature ^{3}MLCT lifetime for Re(α-diimine) complexes.[43,54]

On the ps-timescale (Figure 2.5A), weak $\nu_{C=O}$ GSBs were observed at 1706 and 1670 cm^{-1} with transient bands at 1695 and 1655 cm^{-1} assigned to the ^{1}LC excited state. However, unlike that observed for **H–NI–phen** (Figure S2.34), no transient band was detected *ca*. 1620 cm^{-1} for the NI-based radical anion.[55] Ultrafast ISC from the ^{1}LC excited state to the ^{3}MLCT excited state of **Re–H** leads to significant depletion of electron density on the NI moiety in the ^{1}LC excited state, as the ^{3}MLCT excited state is populated. The $\nu_{C=O}$ features remain unchanged up to 9.5 ns. In the ns-TRIR experiment, displayed in Figure 2.5B, the ^{3}LC excited state was first detected at 10 ns as two new $\nu_{C=O}$ transient features at 1642 and 1599 cm^{-1} that reached a maximum between 30–35 ns, coinciding with the decay of the ^{1}LC $\nu_{C=O}$ transient bands. This is in agreement with previous studies in the literature, which indicated that the ^{3}LC excited state forms over *ca*. 10–30 ns.[14,17]

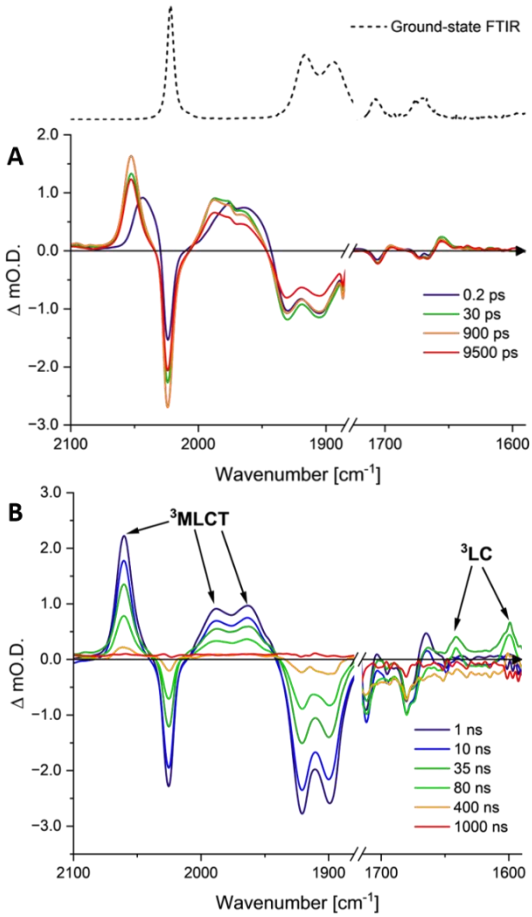


Figure 2.5. *(A) ps–TRIR spectra (10 µM) and (B) ns-TRIR spectra (12 µM) in the metal–carbonyl and organic carbonyl regions of* ***Re–H*** *in DCM, following excitation at 400 nm.*

The ps-TRIR spectra of **Re–ET** in Figure 2.6A displayed the same $\nu_{C\equiv O}$ and $\nu_{C=O}$ transient features and excited state processes as observed for the **Re–H** reference. Despite the incorporation of the ethynyl moiety into **Re–ET**, no $\nu_{C\equiv C}$ were detected likely due to the limited redistribution of spin density across the ethynyl moiety in the triplet excited state according to TDDFT calculations (Figure S2.61). The main difference between the TRIR spectra of **Re–H** and **Re–ET** were the lifetimes determined for the observed excited-state processes. While the formation of the ^{3}LC excited state was not observed in the picosecond experiment for **Re–H**, in **Re–ET** the two new $\nu_{C=O}$ transient features at 1655 and 1606 cm^{-1} with a τ_{TRIR} of 3.3 ns were attributed to the concurrent decay of the ^{1}LC excited and the formation of the ^{3}LC excited state in **Re–ET**. Additionally, all $\nu_{C\equiv O}$ bands associated with the ^{3}MLCT excited state had decayed to the baseline within the 9.5 ns. In the ns-TRIR experiments (Figure 2.6B), the ^{3}LC $\nu_{C=O}$ bands were poorly resolved; although, it was possible to confirm rapid depopulation of the ^{3}MLCT excited state (τ_{TRIR} = 3.3 ns). Thus, the population of the ^{3}LC excited state of **Re–ET** was faster than observed for **Re–**

H (τ_{TRIR} = 30–35 ns) and was similar to the lifetimes reported by Yarnell et al. for complexes substituted with EDGs (2.1 and 5.4 ns).[17]

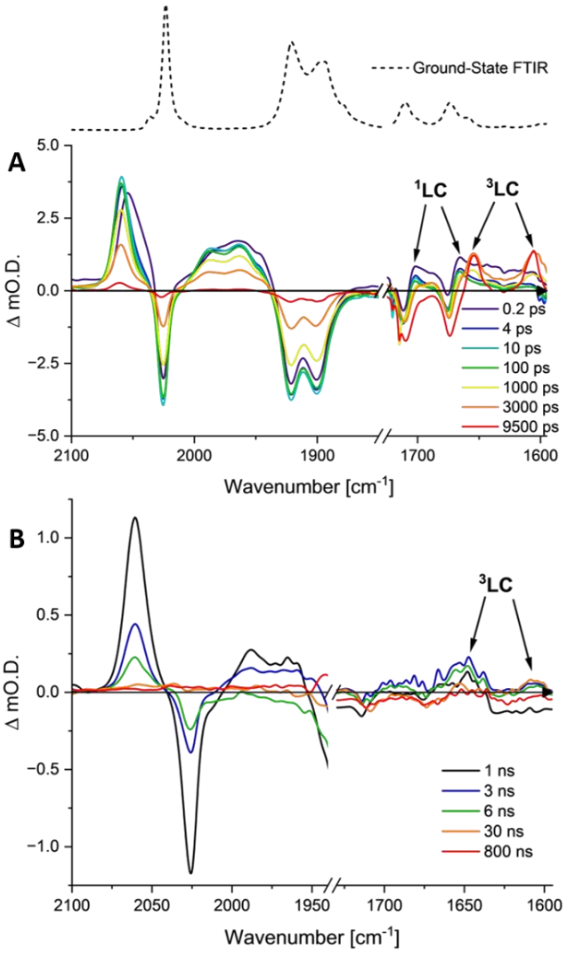


Figure 2.6. *(A) ps-TRIR spectra (15 µM) and (B) ns-TRIR spectra (5 µM) of the metal–carbonyl and organic carbonyl regions of* ***Re–ET*** *in DCM following 420 nm excitation.*

The ps-TRIR spectra of **Re–EB** and **Re–ES** (Figures 2.7A and 2.7B) displayed $\nu_{C\equiv O}$ and $\nu_{C=O}$ GSBs that closely matched all vibrations in the ground-state IR spectra; additionally, they revealed the same transient features and excited state processes as observed for **Re–ET**. Population of the ^{3}LC excited state in **Re–EB** was more rapid (τ_{TRIR} = 2.2 ns) than that of **Re–H** (τ_{TRIR} < 400 ns). Likewise, the population of the ^{3}LC excited state of **Re–ES** was the fastest in the **Re–R** series studied here (τ_{TRIR} = 1.7 ns). The $\nu_{C=O}$ transient bands associated with the ^{1}LC excited state were observed within the laser pulse at 1688 and 1633 cm^{-1}, and at 1686 and 1638 cm^{-1} for **Re–EB** and **Re–ES**, respectively. A broad transient signal at *ca*. 1645 cm^{-1} was observed within the laser pulse for **Re–EB** and **Re–ES** and was also observed for **EB–NI–phen** and **ES–NI–phen** (Figure S2.35), which

was attributed to the NI-based radical anion. New $\nu_{C=O}$ transients were observed at 1658 and 1610 cm^{-1} for **Re–EB** and at 1661 and 1614 cm^{-1} for **Re–ES**, which formed concurrently with the decay of the ^{3}MLCT and ^{1}LC transient bands. These new $\nu_{C=O}$ transients appeared similarly to those for the ^{3}LC excited state of **Re–ET**. The two ^{3}LC $\nu_{C=O}$ transient bands were monitored in the ns-TRIR experiment (Figure 2.6) and up to 1400 ns in both complexes. The similarities between these TRIR spectra show that these **Re–R** complexes have more ligand-like photophysics. These processes were also observed for the **EB–NI–phen** and **ES–NI–phen** counterparts (Figure S2.24).

The inclusion of ethynyl-bearing substituents in **Re–EB** and **Re–ES** allowed for the ethynyl stretching region to be monitored in the ps-TRIR studies as presented in Figures 2.7C and 2.7D, respectively. A broad transient signal was observed throughout the ethynyl stretching region of both complexes, which decayed to the baseline within 5 ns, in agreement with the nanosecond lifetimes arising from the $S_{n+}\leftarrow S_n$ electronic transition in organic compounds containing ethynyl bridges.[34] A weak $\nu_{C\equiv C}$ GSB at 2207 cm^{-1} and a transient signal at 2106 cm^{-1} were formed within 0.2 ps for **Re–EB**, similarly to the **EB–NI–phen** analogue. For **Re–ES**, the $\nu_{C\equiv C}$ GSB at 2196 cm^{-1} and a transient band at 2109 cm^{-1} were observed within 0.2 ps, as in the **ES–NI–phen** analogue. These features are attributed to the partial oxidation of the C≡C bond upon 420 nm excitation of the $\pi\rightarrow\pi^*$ HOMO-LUMO transition (Figure 2.3) discussed previously in the UV-Vis absorption spectra of **Re–EB** and **Re–ES**.

The $\nu_{C\equiv C}$ GSBs for **Re–EB** and **Re–ES** persisted onto the nanosecond time scale (Figures 2.7E and 2.7F, respectively), with the growth of new transient bands at 1997 and 1976 cm^{-1} for **Re–EB** and **Re–ES**, respectively. Similar $\nu_{C\equiv C}$ transient features were observed between 1–9 ns in the TRIR spectra of the **R–NI–phen** analogues (Figure S2.24). However, TRIR studies at longer time intervals were not performed for **R–NI–phen**. For **Re–EB** and **Re–ES**, the transient bands at 1997 and 1976 cm^{-1} produced a similar ΔO.D. as the ^{3}LC $\nu_{C=O}$ transient bands which coexist on the same nanosecond timeframe. Indeed, the long-lived $\nu_{C\equiv C}$ modes decayed to the baseline over 1.4 μs, together with the ^{3}LC $\nu_{C=O}$ transient bands. Tentatively, the transient bands at 1997 and 1976 cm^{-1} are assigned to long-lived $\nu_{C\equiv C}$ transient features associated with the ^{3}LC excited state and involve a redistribution of electron density across the ethynyl bridge, as further detailed below.

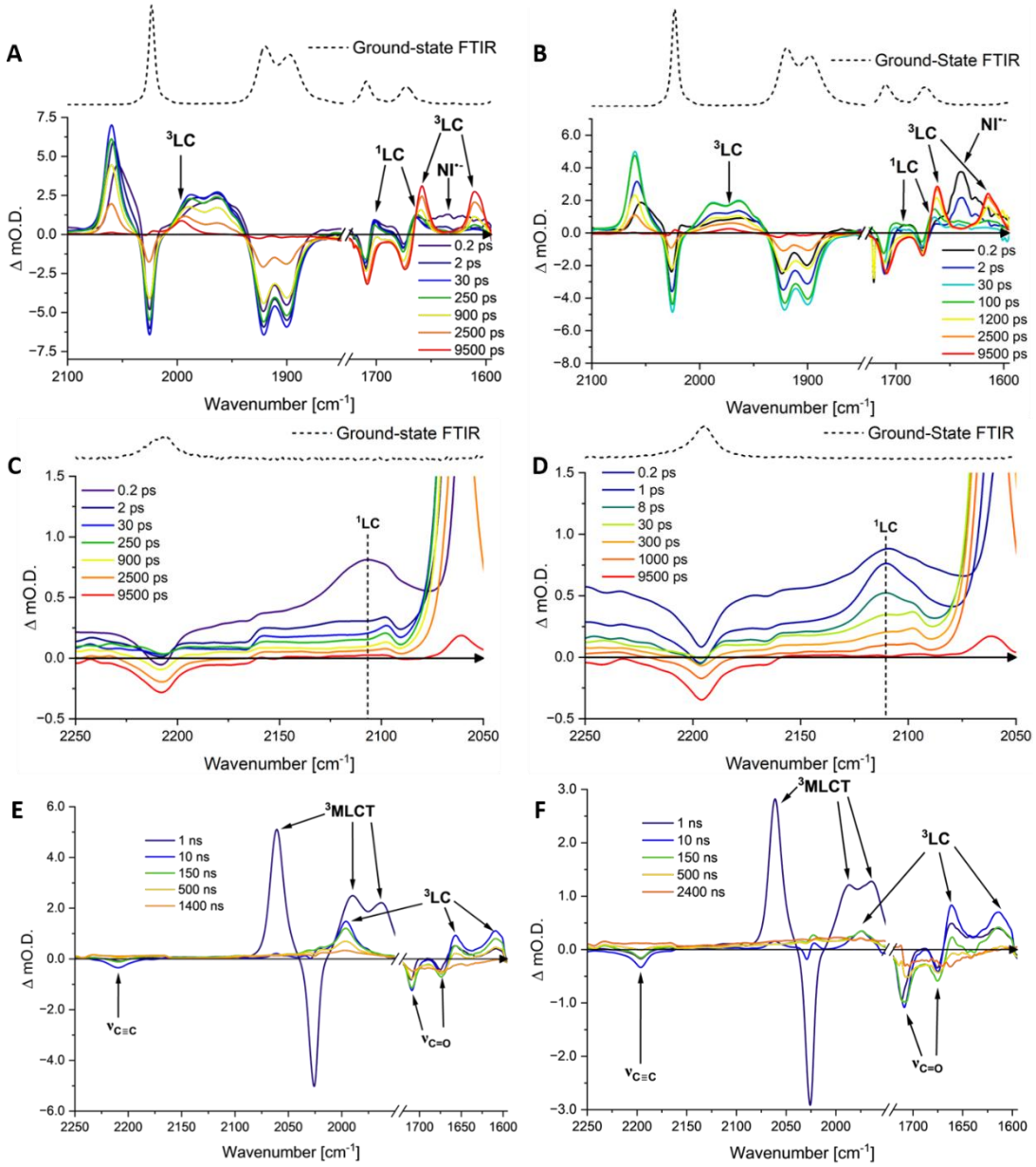


Figure 2.7. *(A) ps-TRIR spectra of* ***Re–EB*** *(5 µM) following excitation at 420 nm in DCM. (B) ps-TRIR spectra of* ***Re–ES*** *(8 µM) following excitation at 420 nm. (C) The ethynyl stretching region of the ps-TRIR spectra of* ***Re–EB****. (D) The ethynyl stretching region of the ps-TRIR spectra of* ***Re–ES****. (E) The ns-TRIR spectra of* ***Re–EB*** *(5 µM) following excitation at 420 nm in DCM. (F) The ns-TRIR spectra of* ***Re–ES*** *(5 µM) following excitation at 420 nm.*

Pt–acetylide complexes with ethynyl-appended NI groups have recently been reported to generate similar $\nu_{C\equiv C}$ transients *ca*. 1950 cm^{-1} in the ^{3}LC excited state.[55,56] Adams et al. propose a change in the bond order of the ethynyl bridge in the excited state, resulting in a partial cumulene bridge.[57] These results indicate that a redistribution of the electron density across the ethynyl bridge occurs in the ^{3}LC excited state of **Re–EB** and **Re–ES**. Indeed, the calculated spin densities of the **^{3}Re–EB** and **^{3}Re–ES** complexes support this explanation, showing that a

redistribution of the spin densities occurs between the NI moiety and the phenyl or thiophene rings via the ethynyl bridge (Figure S2.61). We suggest that in the ^{3}LC excited states of **Re–EB** and **Re–ES**, the bond order of the C≡C bond is closer to a partial C=C bond (corresponding to the cumulene chain "aryl=C=C=NI"), with new stretching vibrations at 1997 and 1976 cm^{-1} for **Re–EB** and **Re–ES**, respectively. Such a rearrangement can be stabilised by resonance with the imide carbonyls, as illustrated in Figure 2.8; which is known to occur for NIs with EDGs present at the 4-position on the NI core.[58] Furthermore, the lone pair on the sulphur atom can participate in this resonance, accounting for the greater electron-donating effect seen for **Re–ES**.

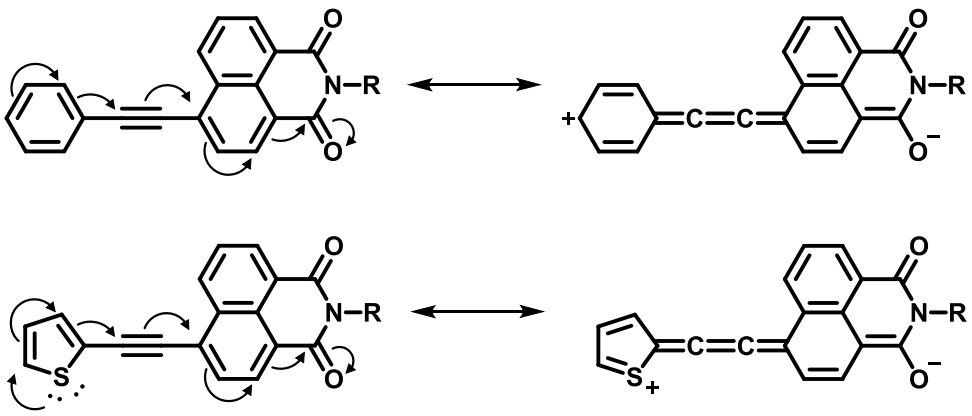


Figure 2.8. *The proposed resonance structures for* ***Re–EB*** *and* ***Re–ES****. Note that resonance structures with both imide carbonyls are possible, though only one is illustrated above.*

Table 2.2. *TRIR data following 420 nm excitation of* ***Re–R*** *and DFT-calculated IR wavenumbers of* ***Re–R****.*[a]

Complex	Excited State(s)	$\nu_{C=O}$ (cm^{-1})	Calc. $\nu_{C=O}$[c] (cm^{-1})	$\nu_{C\equiv O}$[b] (cm^{-1})	Calc. $\nu_{C\equiv O}$[c] (cm^{-1})	$\nu_{C\equiv C}$ (cm^{-1})	Calc. $\nu_{C\equiv C}$[c] (cm^{-1})
Re–H	^{1}LC and ^{3}MLCT	1703, 1665	–	2060, 1988, 1964	–	–	–
	^{3}LC	1641, 1599	1625, 1615	–	1998, 1872, 1853	–	–
Re–EB	^{1}LC and ^{3}MLCT	1702, 1664	–	2059, 1987, 1963	–	2106	–
	^{3}LC	1658, 1610	1634, 1625	–	1998, 1872, 1853	1996	2037
Re–ES	^{1}LC and ^{3}MLCT	1699, 1664	–	2060, 1987, 1963	–	2109	–
	^{3}LC	1662, 1615	1634, 1625	–	1998, 1872, 1853	1972	2032
Re–ET	^{1}LC and ^{3}MLCT	1702, 1665	–	2059, 1987, 1964	–	–[d]	–
	^{3}LC	1654, 1606	1634, 1625	–	1998, 1872, 1853	–[d]	2018

[a]*TRIR studies in DCM following excitation at 420 nm. All GSBs were in good agreement with the ground-state IR spectra of the corresponding* ***Re–R*** *species (see Table 2.1).* [b]*The $\nu_{C\equiv O}$ signals are attributed to the ^{3}MLCT excited state.* [c]*A proportionality factor of 0.983 was used to multiply the DFT-calculated IR spectra.*[47] *The ^{1}LC and ^{3}MLCT excited states are reported together as both are populated within the laser pulse (< 0.2 ps) in the ps-TRIR experiments; the $\nu_{C\equiv O}$ and calc. $\nu_{C\equiv O}$ values are attributed to the ^{3}MLCT excited state only. The long-lived ^{3}LC excited state is populated on the nanosecond timescale and is reported separately; no $\nu_{C\equiv O}$ modes are observed for the ^{3}LC excited state.* [d]*No $\nu_{C\equiv C}$ signal was observed for* ***Re–ET*** *in DCM.*

2.3.5 TCSPC studies

The kinetic traces obtained from the time-correlated single photon counting (TCSPC) studies are displayed in Figures S2.32–S2.37, with experimental data in Table 2.3.

For **Re–H**, a bi-exponential fit was obtained, resulting in 31.6 ns and 233 ns components. The former one coincides with the maximum ΔO.D. observed in the organic carbonyl region of the ns-TRIR experiment, associated with formation of the ^{3}LC excited state living between 30–35 ns. The longer component of 233 ns is assigned to emissions from the ^{3}MLCT excited state.[17] As emission signals for **Re–ET** were weak, no lifetimes could be determined. Indeed, the low fluorescence quantum yields in the **Re–R** series (ϕ_{em} = 0.1–4.9%), compared to the **R–NI–phen** ligands, indicates that there is efficient ISC from the ^{1}LC excited state to the triplet manifold in these complexes.

Emission lifetimes in the nanosecond time domain were determined for **Re–EB** and **Re–ES** (τ_{em} = 2.2 and 1.0 ns, respectively). They closely correspond to those obtained for **EB–NI–phen** and **ES–NI–phen** (τ_{em} = 2.1 and 1.2 ns, respectively). Additionally, these values are in good agreement with the ^{1}LC excited-state lifetime determined from the ps-TRIR studies of **Re–EB** and **Re–ES** (τ_{TRIR} = 2.2 and 1.7 ns, respectively). An emission lifetime from experimental data at 630 nm was also obtained for **Re–EB** (τ_{em} = 242.3 ns), corresponding to the weak ^{3}MLCT emission observed in the emission profile. **Re–ES** was also studied at 630 nm, but no lifetime associated with the emission from the ^{3}MLCT state was obtained. Due to the lower energy of the ^{3}LC excited state of **Re–EB** and **Re–ES**, the there is no evidence for a thermal equilibrium and the ^{3}MLCT emission is effectively quenched in these complexes.

Table 2.3. *Excited-state lifetimes based on room-temperature emission, TRIR, and TA studies in DCM.*[a]

Sample	λ_{em} (nm)	ϕ_{em} (%)	τ_{em} (ns)	τ_{TRIR} (ns)	λ_{TA} (nm)	τ_{TA} (μs) [α_{TA}][f]	Relative Contributions	τ_{avg} (μs)
H–NI–phen	374	0.3	–[b]	1.8	480	16.7 [0.01], 93.7 [0.01]	(15%, 85%)	56
EB–NI–phen	442	54.9	2.1	0.7	575	16.9 [0.027], 104 [0.018]	(20%, 80%)	52
ES–NI–phen	483	30.1	1.2	0.9	645	14.3 [0.036], 75.7 [0.032]	(18%, 82%)	43
Re–H	628	2.6	31.6, 233.4	30–35[e]	480	0.35 [0.026], 18.5 [0.002]	(20%, 80%)	1.6
Re–EB	447, 630[b]	4.9	2.1, 242.3[c]	2.2	600	13.1 [0.036], 60.3 [0.026]	(23%, 77%)	33
Re–ES	487	1.0	1.1	1.7	660	16.9 [0.026], 65.9 [0.028]	(19%, 81%)	42
Re–ET	412, 624	0.1	–[d]	3.3	510	0.26 [0.059], 20.0 [0.00612], 62.3 [0.00835][f]	(3%, 18%, 79%)	8.1[g]

*[a]All τ_{em} values correspond to excitation at 375 nm for all samples. All τ_{TRIR} values were determined following excitation at 420 nm (except for **H–NI–phen**, λ_{ex} = 365nm). The τ_{TA} values were determined upon excitation at 355 nm for all samples. [b]No τ_{em} could be obtained following excitation at 375 nm. [c]The ^{3}MLCT τ_{em} was obtained at 630 nm, following excitation at 375 nm. [d]The **Re–ET** emission was too weak for τ_{em} to be obtained. [e]The reported lifetime range for the formation of the ^{3}LC excited state based on the ns-TRIR experiment. [f]Amplitudes (α_{TA}) used to calculate the amplitude-weighted average lifetime. [g]The τ_{avg} for **Re–ET** was calculated using the tri–exponentially fitted τ_{TA} and α_{TA}.*

2.3.6 TA Spectroscopy

Kinetic traces for aerated samples of **Re–R** from ns-TA and ns-TRIR experiments are presented in Figure 2.9 and for **R–NI–phen** in Figure S2.38. The TA spectra for the **Re–R** complexes under an N_2 atmosphere were collected on the microsecond (μs) timescale, following excitation at 355 nm (Figures 2.10 and 2.11). The **R–NI–phen** ligands were also studied upon 355 nm excitation (Figures S2.39–S2.41). The kinetic traces of **Re–R** are reported in Figure S2.42. All TA lifetimes (τ_{TA}) are presented in Table 2.3. The calculated electronic spectra obtained for the **^{3}Re–R** excited states (Figures S2.53–S2.60 and Tables S2.5–S2.8) are in good agreement with the recorded experimental spectra.

Rylene diimides and their transition-metal complexes are known to form aggregates; with the kinetics of the long-lived species following progressively more second-order character with increasing sample concentration.[14,37–39] It was not possible to prepare sufficiently dilute solutions and obtain the mono-exponential fits of non-aggregated samples. As such, the amplitude-weighted average lifetimes (τ_{avg}) were calculated[59] and used for further discussion. This approach has been implemented previously in systems where an aggregation-induced self-quenching effect is present.[17,38,39]

Kinetic traces were collected for **Re–R** in aerated solutions to mimic conditions used in the ns-TRIR experiments. Figure 2.9 shows an overlay of the closely matched kinetic traces from the aerated ns-TRIR and ns-TA experiments of **Re–H**, **Re–EB**, and **Re–ES**. The long-lived signals in the ns-TRIR spectra of **Re–ET** were poorly resolved, preventing their exploration. An excited-state lifetime of 267 ns for **Re–H** in an aerated solution closely matched the ^{3}MLCT lifetime determined by TCSPC (τ_{em} = 233 ns). Slightly longer excited-state lifetimes of 655 and 538 ns were obtained for **Re–EB** and **Re–ES**, respectively. These extended lifetimes probably arise from the ^{3}LC excited state of **R–NI–phen** living *ca*. 1 μs under the same conditions (Figure S2.38).

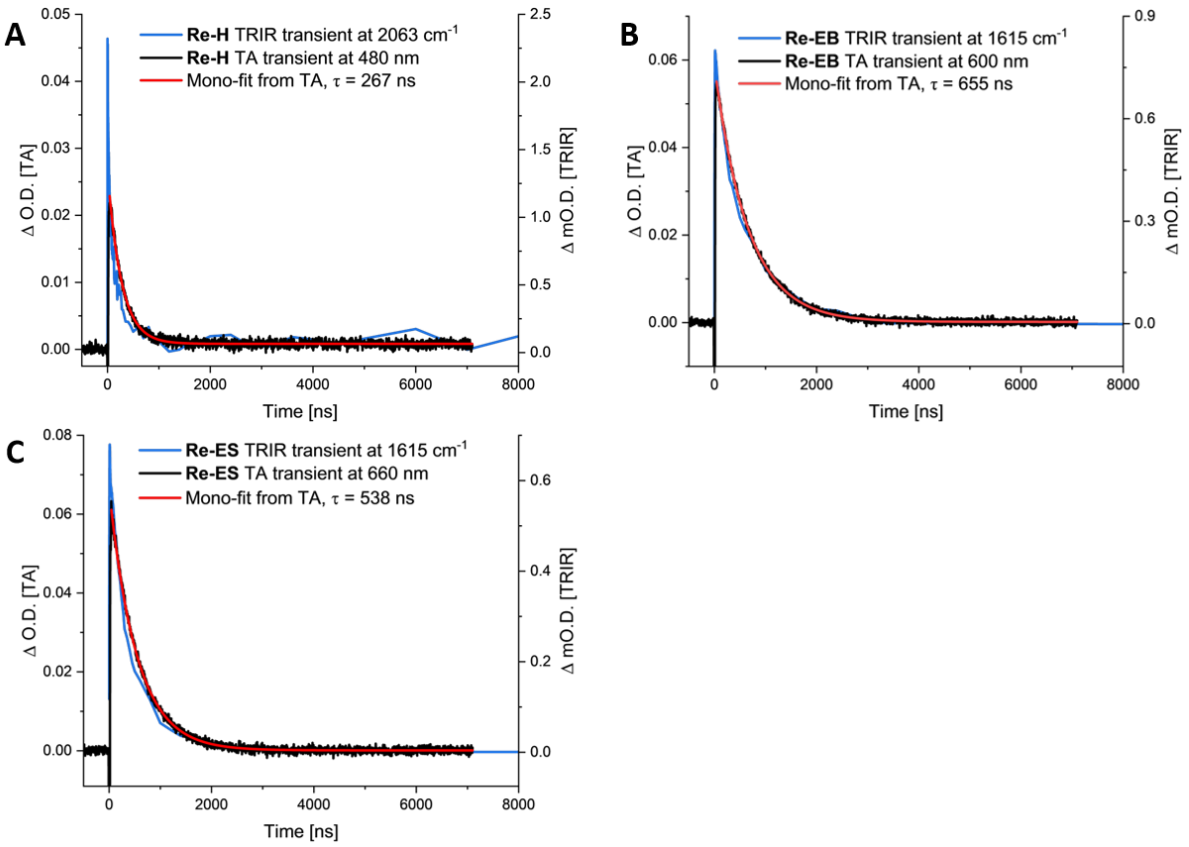


Figure 2.9. *Kinetic traces for aerated samples from ns–TA and ns–TRIR experiments of (A)* ***Re–H****, (B)* ***Re–EB****, and (C)* ***Re–ES****. The kinetic traces from the ns–TRIR experiments were selected based on the most intense signal in the respective spectra: this was the* ^{3}*MLCT transient at 2063 cm*$^{-1}$ *for* ***Re–H****, while for* ***Re–EB*** *and* ***Re–ES*** *this was the* ^{3}*LC transient at 1615 cm*$^{-1}$*.*

Additional TA studies were performed under an N_2 atmosphere to further confirm the ^{3}LC excited state lifetime. In all instances, the excited-state features in the µs-TA spectra of **R–NI–phen** (Figures S2.39–S2.41) closely match those of the **Re–R** counterparts; these transients were attributed to the ^{3}LC excited state known for NI-containing complexes.[14,17] The µs-TA spectra of **Re–H** in Figure 2.10 display two excited-state absorption (ESA) bands at 370 nm and 480 nm. Stimulated emission was also apparent, with a negative feature at *ca*. 650 nm arising from ^{3}MLCT emission. TDDFT calculations of **^{3}Re–H** document that the ESA at 370 nm arises from Re→phen HOSO-to-LUSO transitions, whereas the ESA at 480 nm arises from NI-based HOSO-to-LUSO transitions (Figures S2.53 and S2.54 and Table S2.5). The TA spectra of **Re–R** indicate that the ^{3}LC excited states have formed within the laser pulse (< 50 ns), closely matching observations from previous studies, where the ^{3}LC excited states were populated in *ca*. 31 ns, as determined by the TCSPC experiments.[14,17]

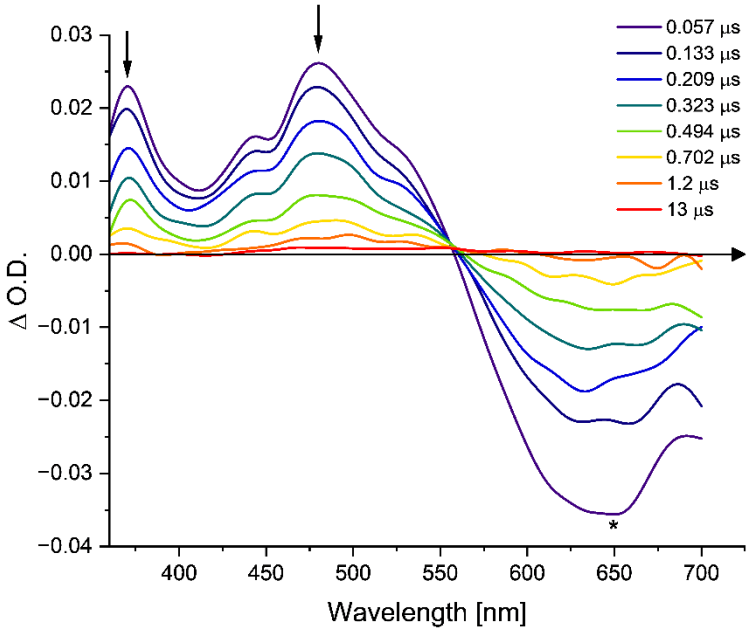


Figure 2.10. *TA spectral changes recorded for a 20 μM DCM solution of* ***Re–H*** *after the 355 nm excitation. (The asterisk denotes a depletion arising from stimulated* ^{3}*MLCT emission).*

In the TA spectra of **Re–ET** (Figure 2.11A), two ^{3}LC ESA bands are evident at 410 and 510 nm, which are red shifted compared to the corresponding bands observed for **Re–H**. Unlike **Re–H**, a GSB was detected for **Re–ET** at *ca*. 375 nm, approximately matching the NI transitions in the electronic absorption spectrum. From TDDFT calculations performed on **^{3}Re–ET**, the ESA at 410 nm is assigned to a mixture of Re→phen and NI-based HOSO-to-LUSO transitions, while the ESA at 510 nm arises solely from NI-based HOSO-to-LUSO transitions (Figures S2.59 and S2.60 and Table S2.8). Similar observations were made in the TA spectra of **Re–EB** and **Re–ES** in Figures 2.11B and 2.11C, respectively. The GSB was observed at 380 nm and the two ^{3}LC ESA bands at 435 and 600 nm for **Re–EB**, while for **Re–ES** the GSB was observed at 400 nm and the two ^{3}LC ESA bands at 465 and 660 nm. Similarly to **Re–ET**, the GSBs approximately match the NI-based transitions in the absorption spectra of **Re–EB** and **Re–ES**. However, TDDFT calculations performed on **^{3}Re–EB** and **^{3}Re–ES** indicate that the higher-energy ESA bands (λ_{TA} = 435 and 465 nm, respectively) and the lower-energy ESA bands (λ_{TA} = 600 and 660 nm, respectively) arise solely from NI-based HOSO-to-LUSO transitions (Figures S2.55–S2.58 and Tables S2.6 and S2.7). These results suggest that the thermal equilibrium between the close triplet excited states of **Re–H** is less established for **Re–ET** and does not occur in **Re–EB** and **Re–ES**, shifting in favour of population of the NI-based ^{3}LC excited state.

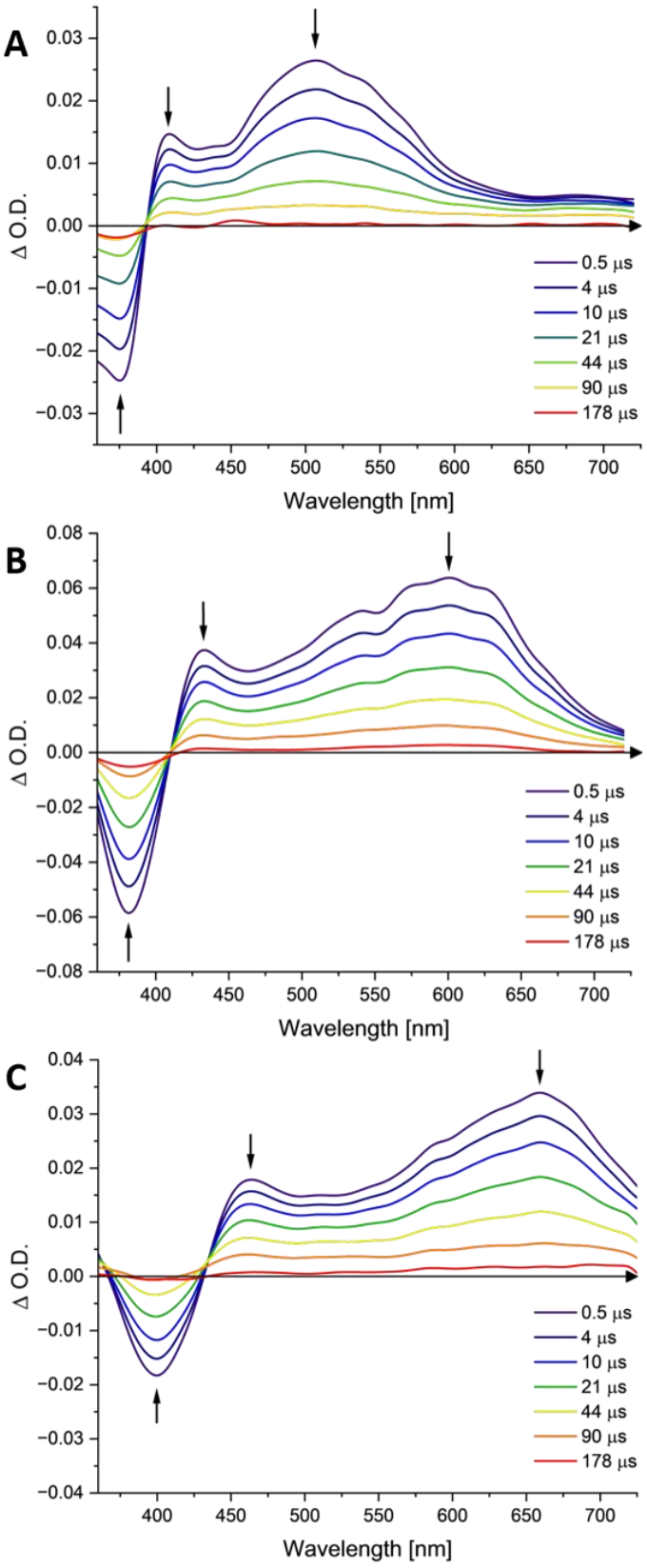


Figure 2.11. *TA spectral changes recorded for (A) 20 μM* ***Re–ET****, (B) 10 μM* ***Re–EB****, and (C) 14 μM* ***Re–ES*** *in DCM after the 355 nm excitation.*

A bi-exponential fit of the ns-TA spectra of **Re–H** was obtained. The first component has been attributed to the population of the ^{3}MLCT excited state (τ_1 = 350 ns), which closely matched the ^{3}MLCT emission lifetime of **Re–H** (τ_{em} = 233 ns). The second component (τ_2 = 21 µs) resembles the ^{3}LC excited state lifetime for [Re(NI–phen)(CO)$_3$(dmap)](PF$_6$) (τ = 19.6 µs).[17] Due to the planar nature of the NI moiety, as discussed earlier, aggregation occurs for all the NI compounds studied; thus, lifetime averaging is used to simplify the analysis of the ^{3}LC excited states. This approach has been reported in the literature previously.[14,16,17]

The τ_{avg} for **Re–H** of 1.6 µs, lies between the ^{3}MLCT emission lifetime of **Re–H** (τ_{em} = 233 ns) and the ^{3}LC lifetime of **H–NI–phen** (τ_{TA} = 36 µs); representing a value lying between the ^{3}MLCT and ^{3}LC lifetimes indicative of the thermal equilibrium between these triplet excited states. For **Re–ET,** a tri-exponential fit was required; in addition to the two microsecond components attributed to aggregation, a 255 ns component was also observed similarly to the ^{3}MLCT emission lifetime of **Re–H** (τ_{em} = 233 ns). Averaging of the tri-exponentially fitted lifetimes gave τ_{avg} of 8.1 µs for **Re–ET**. For **Re–EB** and **Re–ES**, no ^{3}MLCT component was observed in the kinetic traces obtained from the TA studies. This resulted in the average ^{3}LC excited-state lifetimes of **Re–EB** and **Re–ES** (τ_{avg} = 33 and 42 µs, respectively) being closer to those of their **R–NI–phen** counterparts (viz. τ_{avg} = 52 and 43 µs, for **EB–NI–phen** and **ES–NI–phen**, respectively). The ligand-like photophysics of **Re–EB** and **Re–ES** indicates that there is a significant deviation from a triplet–triplet equilibrium in favour of the ^{3}LC excited state. **Re–ES** displayed the most pronounced ligand-like photophysics in the series; matching the trend in the **Re–R** series established earlier in this work (**Re–H** < **Re–ET** < **Re–EB** < **Re–ES**).

2.3.7 Triplet Energy Gap

The triplet energy gap (ΔE_T) between the ^{3}MLCT and ^{3}LC excited states determines the (non-)existence of a thermal equilibrium between the triplet excited states of each **Re–R** complex. In the first approach, an equilibrium constant (K_{eq}) was calculated from Equations 2.1 and 2.2, comparing the rate constant of **Re–R** ($k_{Re–R}$) obtained from their τ_{avg}, to the rate constants from the ^{3}MLCT and ^{3}LC models (k_{MLCT} and k_{LC}, respectively).[17] The equilibrium approach then utilises K_{eq} in Equation 2.3 to determine the difference of free energy (ΔG_T) which is used to approximate ΔE_T. Another approach uses recorded ^{3}MLCT emission (at room temperature) and ^{3}LC emission (at 77 K), where the high-energy side of the respective emission bands at 25% of the maximum intensity are used to determine ΔE_T.[14] The ultimate approach taken in this work determines a value of ΔE_T by comparing the TDDFT calculated energies of the ^{3}MLCT and ^{3}LC excited states

(Table S2.11). The ΔE_T values obtained for each **Re–R** complex, using the equilibrium, emission, and the TDDFT approaches, are presented below in Table 2.4.

$$a = \frac{k_{\mathrm{Re-R}}}{k_{\mathrm{MLCT}} + k_{\mathrm{LC}}}$$

Equation 2.10. *Equation used to derive the ratio (a) between the rate constant obtained from the average emission lifetime (k_{Re-R}) and the rate constants obtained from the ^{3}MLCT and ^{3}LC excited-state lifetimes (k_{MLCT} and k_{LC}, respectively).*

$$K_{\mathrm{eq}} = \frac{[a]}{[1-a]}$$

Equation 2.11. *Equation used to derive the equilibrium constant (K_{eq}) from a.*

$$\Delta E_{\mathrm{T}} \cong \Delta G_{\mathrm{T}} = -RT(\ln K_{\mathrm{eq}})$$

Equation 2.12. *Equation used to derive the triplet-energy gap (ΔE_T) from K_{eq}.*

Table 2.4. *Key values for ΔE_T calculations of **Re–R**.*

Re–R	ΔE_T based on K_{eq} [a] (cm^{-1})	ΔE_T based on emission spectra (cm^{-1})	ΔE_T based on TDDFT (cm^{-1})
Re–H	370	850	530
Re–EB	1030	1760	3480
Re–ES	1080	1840	4410
Re–ET	740 [b]	1180	2470

*[a]The value for k_{MLCT} was determined from the emission lifetime of the ^{3}MLCT excited state of **Re–H** and the value for k_{LC} was determined from the ^{3}LC lifetime of the corresponding **R–NI–phen** ligands. [b]In lieu of the corresponding **R–NI–phen** ligand, **H–NI–phen** was used as the ^{3}LC model in the calculations for **Re–ET**.*

In the case of **Re–H**, ΔE_T = 370 cm^{-1} was determined from the equilibrium approach, which indicates that a thermal equilibrium exists between the two triplet excited states. Using the same approach for **Re–ET**, ΔE_T = 740 cm^{-1} suggests that some thermal equilibrium between the two

triplet excited states may also exist. There was a minimal difference between the ΔE_T values obtained for **Re–EB** and **Re–ES** (ΔE_T = 1060 and 1080 cm^{-1}, respectively). This represents a significant increase in ΔE_T, indicating that thermal equilibrium between the two triplet excited states is unlikely. While the magnitude of the ΔE_T values were greater using the emission and TDDFT approaches, the same trend is observed for all three approaches for ΔE_T (**Re–H** < **Re–ET** < **Re–EB** < **Re–ES**). Our results are in agreement with previous reports in the literature, where the trends in ΔE_T values are maintained despite the different approaches taken in calculating those values.[17] The ΔE_T values calculated using the emission data is a better representation of the true ΔE_T value for these **Re–R** complexes, as the concentration used in these experiments is substantially lower compared to the TA studies and so is less affected by aggregation. The higher ΔE_T for **Re–EB** and **Re–ES** of 1760 and 1840 cm^{-1}, determined by the emission approach, reflect the absence of a thermal equilibrium in these complexes.

2.3.8 Excited-State Dynamics and Kinetics

Based on the photophysical studies conducted in this work, the Jablonski diagrams in Figure 2.12 illustrate the excited state dynamics and kinetics of the **Re–R** series in DCM following photoexcitation.

In the case of **Re–H**, the electronic excitation at 365 nm leads to initial population of the Franck-Condon excited state (S_n), followed by vibrational cooling to form the fluorescent ^{1}LC excited state. The first electron transfer process is the population of the ^{1}MLCT excited state by energy transfer. Excitation at either 400 nm or 420 nm directly populates the ^{1}MLCT excited state. Therefore, the excitation between 365 and 420 nm results in the same excited-state dynamics after the population of the ^{1}MLCT excited state. Ultrafast intersystem crossing from the ^{1}MLCT excited state yields the vibrationally hot ^{3}MLCT excited state (< 0.2 ps). Subsequently, vibrational cooling of the hot ^{3}MLCT excited state occurs with τ_{TRIR} of 7.2 ps to yield the emissive ^{3}MLCT excited state (τ_{em} = 233.4 ns). The next electron transfer process is the formation of an equilibrium between the ^{3}MLCT and ^{3}LC excited states (τ_{em} = 31 ns). Finally, a ground-state recovery from the ^{3}MLCT and ^{3}LC excited states occurs with a τ_{avg} of 1.3 µs, as determined by TA spectroscopy.

For **Re–ET**, the same energy-transfer pathway occurs as in **Re–H** (Figure 2.12A), with slight variations in the kinetics. Energy transfer from the ^{1}LC excited state to the ^{1}MLCT excited state is retained as the first energy-transfer step for **Re–ET**. However, a reduced spectral overlap between the ^{1}LC excited-state fluorescence and the MLCT absorption bands, and therefore

reduced mixing of the excited-state energies, results in a reduced energy transfer efficiency for **Re–ET**. Vibrational cooling from the hot ^{3}MLCT excited state with a τ_{TRIR} = 3.2 ps yields the ^{3}MLCT excited state (τ_{TA} = 0.26 μs). The second electron transfer process results in population of the ^{3}LC excited state, with a shorter lifetime (τ_{TRIR} = 3.3 ns) compared to **Re–H** (τ_{em} = 31 ns). The extended conjugation due to the ethynyl trimethylsilane on the NI moiety lowered the energy of the ^{3}LC excited state in **Re–ET** compared to in **Re–H**. As a result, the population redistribution of the ^{3}MLCT and ^{3}LC excited states shifts in favour of the ^{3}LC excited state, representing a deviation from the triplet–triplet equilibrium observed for **Re–H**. This observation is reflected in the ground-state recovery lifetime (τ_{avg} = 8.1 μs), which is closer to the ^{3}LC lifetimes determined for the other two ethynyl-substituted **Re–R** complexes (**R** = **EB** and **ES**) and all **R–NI–phen** compounds.

Identical pathways are proposed for both **Re–EB** and **Re–ES** complexes (Figure 2.12B). Due to the large bathochromic shifts of the NI-based electronic transitions in the absorption spectra of **Re–EB** and **Re–ES**, the excitation at 420 nm results in the simultaneous population of the ^{1}LC and ^{1}MLCT excited states. However, unlike **Re–H** and **Re–ET**, energy transfer from the ^{1}LC excited state to the ^{1}MLCT excited state is negligible for **Re–EB**, with a significantly quenched ^{3}MLCT emission band. The lack of any ^{3}MLCT emission band or an associated lifetime, which would be indicative of delayed MLCT photoluminescence, suggests that this energy transfer process does not occur for **Re–ES**. The ^{1}LC excited state had a fluorescent lifetime of 2.2 and 1.7 ns for **Re–EB** and **Re–ES**, respectively, closely resembling the fluorescent lifetimes of **EB–NI–phen** and **ES–NI–phen**.

Following the ^{1}MLCT pathway, population of the vibrationally hot ^{3}MLCT excited state from the ^{1}MLCT excited state occurs subsequently on sub-picosecond timescales (< 0.2 ps) as observed in the TRIR experimental data (Figure 2.7). Vibrational cooling of the hot ^{3}MLCT excited state follows with a τ_{TRIR} of 2.1 and 4.9 ps, for **Re–EB** and **Re–ES**, respectively. The resulting ^{3}MLCT excited state observed in the TRIR experiments is short-lived for both complexes. Indeed, the ^{3}LC excited state of **Re–EB** and **Re–ES** is populated from both the ^{1}LC and ^{3}MLCT excited states ($\tau_{em} \approx \tau_{TRIR}$ = 2.2 and 1.7 ns, respectively). Additionally, the lower energy of the ^{3}LC excited state of **Re–EB** and **Re–ES**, the lowest in the **Re–R** series, prevents the formation of a thermal equilibrium between the ^{3}LC and ^{3}MLCT excited states. This is supported by the relatively large ΔE_T calculated for **Re–EB** and **Re–ES**, which indicates that a thermal equilibrium between the triplet excited states is unlikely. Consequently, the photophysics of **Re–EB** and **Re–ES** more closely resembles that of the corresponding **R–NI–phen** ligands; with τ_{avg} = 33 μs for **Re–EB** compared to 52 μs for **EB–NI–phen** and for **Re–ES** τ_{avg} = 42 μs compared to 43 μs for **ES–NI–phen**.

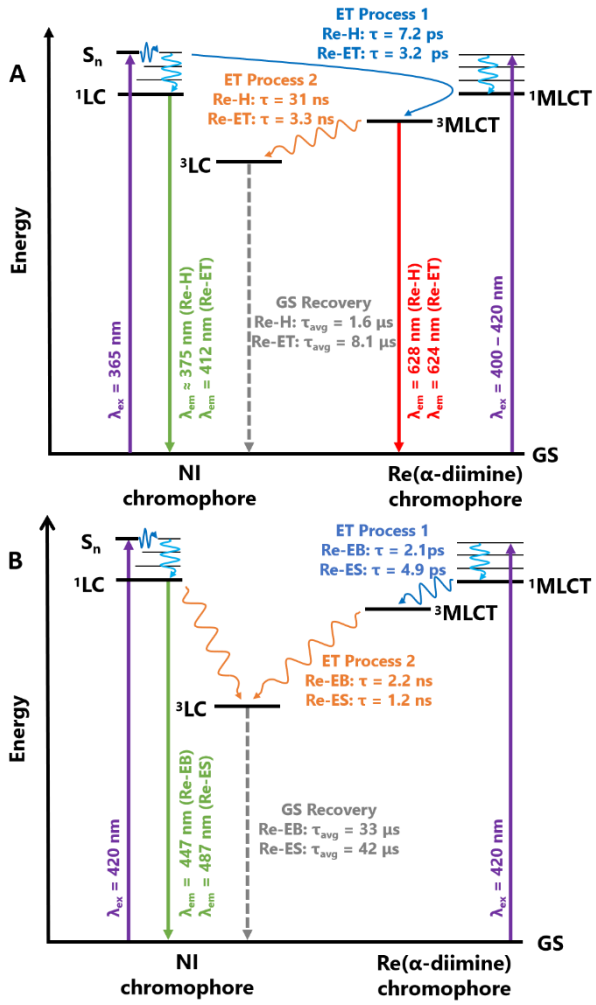


Figure 2.12. *Jablonski diagrams displaying the excited-state dynamics from photoexcitation to ground state recovery of (A)* ***Re–H*** *and* ***Re–ET****, (B)* ***Re–EB*** *and* ***Re–ES****.*

2.4 Conclusions

The incorporation of a C≡C group as an IR-active tag within the **R–NI–phen** moiety was successful. The $\nu_{C\equiv C}$ GSBs and transient bands were particularly useful for understanding the ^{1}LC excited state on the picosecond time regime. Fluorescent lifetimes were determined for the **Re–EB**, **Re–ES**, and **Re–ET** complexes which were attributed to the ^{1}LC excited state (τ_{TRIR} = 1.7, 2.2, and 3.3 ns respectively), closely matching the fluorescent lifetimes of the **EB–NI–phen** and **ES–NI–phen** compounds in this study. New $\nu_{C\equiv C}$ transients were also detected in the ns-TRIR experiments which were associated with a partially oxidised C≡C bond in the ^{3}LC excited state of the **EB–NI–phen** and **ES–NI–phen** compounds and the **Re–EB** and **Re–ES** complexes.

The triplet excited state lifetime for the **Re–EB**, **Re–ES**, and **Re–ET** complexes were extended (τ_{avg} = 45, 49, and 54 µs respectively) compared to the **Re–H** complex (τ_{avg} = 1.3 µs). This demonstrated

that the substitution of weak EDGs (ethynyl benzene, ethynyl thiophene, and ethynyl trimethylsilane, respectively) onto the NI core affected the excited-state dynamics of the **Re–R** complexes. Particularly, the thermal equilibrium between the ^{3}MLCT and ^{3}LC excited states present for **Re–H** shifted in favour of the ^{3}LC excited state in the following series: **Re–H** < **Re–ET** < **Re–EB** < **Re–ES**. Thus, the ethynyl group can be used to study the triplet excited states of organic compounds and transition-metal complexes key to electron transfer pathways in many photo–based applications, including photocatalysis.

2.5 Bibliography

1 M. Z. Bartusiak, R. J. McGarry, L. Varvarezos, M. P. Brandon and M. T. Pryce, Incorporation of perylene and naphthalene like ligands into ruthenium complexes: Synthesis, photophysical properties and electrochemistry, *Coord. Chem. Rev.*, 2023, **495**, 215365.

2 V. L. Gunderson, E. Krieg, M. T. Vagnini, M. A. Iron, B. Rybtchinski and M. R. Wasielewski, Photoinduced Singlet Charge Transfer in a Ruthenium(II) Perylene-3,4:9,10-bis(dicarboximide) Complex, *J. Phys. Chem. B*, 2011, **115**, 7533–7540.

3 H. Li and O. S. Wenger, Photophysics of Perylene Diimide Dianions and Their Application in Photoredox Catalysis, *Angew. Chem., Int. Ed.*, 2022, **61**, e202110491.

4 J. E. Yarnell, A. Chakraborty, M. Myahkostupov, K. M. Wright and F. N. Castellano, Long-lived triplet excited state in a platinum(II) perylene monoimide complex, *Dalton Trans.*, 2018, **47**, 15071–15081.

5 Y. Shi, H. Tang, S. Jiang, L. V. Kayser, M. Li, F. Liu, F. Ji, D. J. Lipomi, S. P. Ong and Z. Chen, Understanding the Electrochemical Properties of Naphthalene Diimide: Implication for Stable and High-Rate Lithium-Ion Battery Electrodes, *Chem. Mater.*, 2018, **30**, 3508–3517.

6 L. G. Franca, D. G. Bossanyi, J. Clark and P. L. dos Santos, Exploring the Versatile Uses of Triplet States: Working Principles, Limitations, and Recent Progress in Phosphorescence, TADF, and TTA, *ACS Appl. Opt. Mater.*, 2024, **2**, 2476–2500.

7 N. El Harakeh, A. C. P. de Morais, N. Rani, J. A. G. Gomez, A. Cousino, M. Lanznaster, S. Mazumder and C. N. Verani, Reactivity and Mechanisms of Photoactivated Heterometallic [$Ru^{II}Ni^{II}$] and [$Ru^{II}Ni^{II}Ru^{II}$] Catalysts for Dihydrogen Generation from Water, *Angew. Chem., Int. Ed.*, 2021, **60**, 5723–5728.

8 F. Franco, C. Cometto, C. Garino, C. Minero, F. Sordello, C. Nervi and R. Gobetto, Photo- and Electrocatalytic Reduction of CO_2 by [$Re(CO)_3$α,α′-Diimine-(4-piperidinyl-1,8-naphthalimide)Cl] Complexes, *Eur. J. Inorg. Chem.*, 2015, **2015**, 296–304.

9 S. Banerjee, E. B. Veale, C. M. Phelan, S. A. Murphy, G. M. Tocci, L. J. Gillespie, D. O. Frimannsson, J. M. Kelly and T. Gunnlaugsson, Recent advances in the development of 1,8-naphthalimide based DNA targeting binders, anticancer and fluorescent cellular imaging agents, *Chem. Soc. Rev.*, 2013, **42**, 1601.

10 A. Saini, K. R. Justin Thomas, K. R. J. Thomas, Abhay Sachdev, A. Sachdev, P. Gopinath and P. Gopinath, Photophysics, Electrochemistry, Morphology, and Bioimaging Applications of New 1,8-Naphthalimide Derivatives Containing Different Chromophores., *Chem. Asian J.*, 2017, **12**, 2612–2622.

11 K. A. Wells, J. E. Yarnell, J. R. Palmer, T. S. Lee, C. M. Papa and F. N. Castellano, Energy Migration Processes in Re(I) MLCT Complexes Featuring a Chromophoric Ancillary Ligand, *Inorg. Chem.*, 2020, **59**, 8259–8271.

12 R. Horvath, G. S. Huff, K. C. Gordon and M. W. George, Probing the excited state nature of coordination complexes with blended organic and inorganic chromophores using vibrational spectroscopy, *Coord. Chem. Rev.*, 2016, **325**, 41–58.

13 Y. Yang, F. Doettinger, C. Kleeberg, W. Frey, M. Karnahl and S. Tschierlei, How the Way a Naphthalimide Unit is Implemented Affects the Photophysical and -catalytic Properties of Cu(I) Photosensitizers, *Front. Chem.*, DOI:10.3389/fchem.2022.936863.

14 J. E. Yarnell, J. C. Deaton, C. E. McCusker and F. N. Castellano, Bidirectional “Ping-Pong” Energy Transfer and 3000-Fold Lifetime Enhancement in a Re(I) Charge Transfer Complex, *Inorg. Chem.*, 2011, **50**, 7820–7830.

15 J. E. Yarnell, C. E. McCusker, A. J. Leeds, J. M. Breaux and F. N. Castellano, Exposing the Excited-State Equilibrium in an Ir^{III} Bichromophore: A Combined Time Resolved Spectroscopy and Computational Study, *Eur. J. Inorg. Chem.*, 2016, **2016**, 1808–1818.

16 D. S. Tyson, C. R. Luman, X. Zhou and F. N. Castellano, New Ru(II) Chromophores with Extended Excited-State Lifetimes, *Inorg. Chem.*, 2001, **40**, 4063–4071.

17 J. E. Yarnell, K. A. Wells, J. R. Palmer, J. M. Breaux and F. N. Castellano, Excited-State Triplet Equilibria in a Series of Re(I)-Naphthalimide Bichromophores, *J. Phys. Chem. B*, 2019, **123**, 7611–7627.

18 A. M. Ricks, Z. E. Reed and M. A. Duncan, Infrared spectroscopy of mass-selected metal carbonyl cations, *J. Mol. Spectrosc.*, 2011, **266**, 63–74.

19 A. El Nahhas, C. Consani, A. M. Blanco-Rodríguez, K. M. Lancaster, O. Braem, A. Cannizzo, M. Towrie, I. P. Clark, S. Záliš, M. Chergui and A. Jr. Vlček, Ultrafast Excited-State Dynamics of Rhenium(I) Photosensitizers $[Re(Cl)(CO)_3(N,N)]$ and $[Re(imidazole)(CO)_3(N,N)]^+$: Diimine Effects, *Inorg. Chem.*, 2011, **50**, 2932–2943.

20 R. Fernández-Terán and L. Sévery, Living Long and Prosperous: Productive Intraligand Charge-Transfer States from a Rhenium(I) Terpyridine Photosensitizer with Enhanced Light Absorption, *Inorg. Chem.*, 2021, **60**, 1334–1343.

21 R. J. Fernández-Terán and L. Sévery, Coordination Environment Prevents Access to Intraligand Charge-Transfer States through Remote Substitution in Rhenium(I) Terpyridinedicarbonyl Complexes, *Inorg. Chem.*, 2021, **60**, 1325–1333.

22 K. Koike, D. C. Grills, Y. Tamaki, E. Fujita, K. Okubo, Y. Yamazaki, M. Saigo, T. Mukuta, K. Onda and O. Ishitani, Investigation of excited state, reductive quenching, and intramolecular electron transfer of Ru(II)–Re(I) supramolecular photocatalysts for CO_2 reduction using time-resolved IR measurements, *Chem. Sci.*, 2018, **9**, 2961–2974.

23 I. E. Pomestchenko, D. E. Polyansky and F. N. Castellano, Influence of a Gold(I)−Acetylide Subunit on the Photophysics of $Re(Phen)(CO)_3Cl$, *Inorg. Chem.*, 2005, **44**, 3412–3421.

24 M. W. George and J. J. Turner, Excited states of transition metal complexes studied by time-resolved infrared spectroscopy, *Coordination Chemistry Reviews*, 1998, **177**, 201–217.

25 E. Vauthey, Watching Excited-State Symmetry Breaking in Multibranched Push–Pull Molecules, *J. Phys. Chem. Lett.*, 2022, **13**, 2064–2071.

26 E. Balanikas, M. Reymond-Joubin and E. Vauthey, Excited-State Symmetry Breaking in Solvent Mixtures, *J. Phys. Chem. Lett.*, 2024, **15**, 2447–2452.

27 E. Sumner, M. Pižl, K. T. McQuaid and F. Hartl, Nitrile Substituents at the Conjugated Dipyridophenazine Moiety as Infrared Redox Markers in Electrochemically Reduced Heteroleptic Ru(II) Polypyridyl Complexes, *Inorg. Chem.*, 2024, **63**, 2460–2469.

28 J. G. Löffler, E. Deniz, C. Feid, V. G. Franz and J. Bredenbeck, Versatile Vibrational Energy Sensors for Proteins, *Angew. Chem., Int. Ed.*, 2022, **61**, e202200648.

29 A. A. Cullen, K. Heintz, L. O'Reilly, C. Long, A. Heise, R. Murphy, J. Karlsson, E. Gibson, G. M. Greetham, M. Towrie and M. T. Pryce, A Time-Resolved Spectroscopic Investigation of a Novel BODIPY Copolymer and Its Potential Use as a Photosensitiser for Hydrogen Evolution, *Front. Chem.*, DOI:10.3389/fchem.2020.584060.

30 A. A. Cullen, A. Rajagopal, K. Heintz, A. Heise, R. Murphy, I. V. Sazanovich, G. M. Greetham, M. Towrie, C. Long, D. Fitzgerald-Hughes and M. T. Pryce, Exploiting a Neutral BODIPY Copolymer as an Effective Agent for Photodynamic Antimicrobial Inactivation, *J. Phys. Chem. B*, 2021, **125**, 1550–1557.

31 C. Jiang, P. J. Young, S. E. Brown-Xu, W. T. Kender, E. J. M. Hamilton, J. C. Gallucci and M. H. Chisholm, Probing Interligand Electron Transfer in the ^{1}MLCT S_1 Excited State of trans-$Mo_2L_2L'_2$ Compounds: A Comparative Study of Auxiliary Ligands and Solvents, *Inorg. Chem.*, 2017, **56**, 9660–9668.

32 M. E. Smith, E. L. Flynn, M. A. Fox, A. Trottier, E. Wrede, D. S. Yufit, J. A. K. Howard, K. L. Ronayne, M. Towrie, A. W. Parker, F. Hartl and P. J. Low, Facile photoinduced charge separation through a cyanoacetylide bridge in a heterobimetallic Fe(II)–Re(I) complex, *Chem. Commun.*, 2008, 5845–5847.

33 A. M. Brown, C. E. McCusker, M. C. Carey, A. M. Blanco-Rodríguez, M. Towrie, I. P. Clark, A. Vlček and J. K. McCusker, Vibrational Relaxation and Redistribution Dynamics in Ruthenium(II) Polypyridyl-Based Charge-Transfer Excited States: A Combined Ultrafast Electronic and Infrared Absorption Study, *J. Phys. Chem. A*, 2018, **122**, 7941–7953.

34 Z. Szakács, M. Tasior, D. T. Gryko and E. Vauthey, Change of Quadrupole Moment upon Excitation and Symmetry Breaking in Multibranched Donor-Acceptor Dyes, *ChemPhysChem*, 2020, **21**, 1718–1730.

35 X. Lucas, D. Quiñonero, A. Frontera and P. M. Deyà, Counterintuitive Substituent Effect of the Ethynyl Group in Ion−π Interactions, *J. Phys. Chem. A*, 2009, **113**, 10367–10375.

36 J. R. W. McLay, J. J. Sutton, G. E. Shillito, C. B. Larsen, G. S. Huff, N. T. Lucas and K. C. Gordon, Transitioning from Intraligand π,π* to Charge-Transfer Excited States Using Thiophene-Based Donor–Acceptor Systems, *Inorg. Chem.*, 2021, **60**, 130–139.

37 V. Wintgens, P. Valat, J. Kossanyi, L. Biczok, A. Demeter and T. Bérces, Spectroscopic properties of aromatic dicarboximides. Part1.—N—H and N-methyl-substituted naphthalimides, *J. Chem. Soc., Faraday Trans.*, 1994, **90**, 411–421.

38 B. M. Aveline, S. Matsugo and R. W. Redmond, Photochemical Mechanisms Responsible for the Versatile Application of Naphthalimides and Naphthaldiimides in Biological Systems, *J. Am. Chem. Soc.*, 1997, **119**, 11785–11795.

39 I. V. Sazanovich, M. A. H. Alamiry, J. Best, R. D. Bennett, O. V. Bouganov, E. S. Davies, V. P. Grivin, A. J. H. M. Meijer, V. F. Plyusnin, K. L. Ronayne, A. H. Shelton, S. A. Tikhomirov, M. Towrie and J. A. Weinstein, Excited State Dynamics of a Pt^{II} Diimine Complex bearing a Naphthalene-Diimide Electron Acceptor, *Inorg. Chem.*, 2008, **47**, 10432–10445.

40 Y. J. Wang, Z. Li, J. Tong, X. Y. Shen, A. Qin, J. Z. Sun and B. Z. Tang, The fluorescence properties and aggregation behavior of tetraphenylethene–perylenebisimide dyads, *J. Mater. Chem. C*, 2015, **3**, 3559–3568.

41 S. Misra, P. Singh, A. Das, P. Brandão, P. Sahoo, N. Sepay, G. Bhattacharjee, P. Datta, A. K. Mahapatra, B. Satpati and J. Nanda, Supramolecular assemblies of a 1,8-naphthalimide conjugate and its aggregation-induced emission property, *Mater. Adv.*, 2020, **1**, 3532–3538.

42 P. Kurz, B. Probst, B. Spingler and R. Alberto, Ligand Variations in [ReX(diimine)$(CO)_3$] Complexes: Effects on Photocatalytic CO_2 Reduction, *Eur. J. Inorg. Chem.*, 2006, **2006**, 2966–2974.

43 V. Komreddy, K. Ensz, H. Nguyen, D. P. Rillema and C. E. Moore, Design, synthesis, and photophysical properties of Re(I) tricarbonyl 1,10-phenanthroline complexes, *J. Mol. Struct.*, 2021, **1223**, 128739.

44 B. D. Rossenaar, D. J. Stufkens and A. Vlček, Halide-Dependent Change of the Lowest-Excited-State Character from MLCT to XLCT for the Complexes $Re(X)(CO)_3(\alpha\text{-diimine})$ (X = Cl, Br, I; α-diimine = bpy, iPr-PyCa, iPr-DAB) Studied by Resonance Raman, Time-Resolved Absorption, and Emission Spectroscopy, *Inorg. Chem.*, 1996, **35**, 2902–2909.

45 K. Choroba, J. Palion-Gazda, A. Kryczka, E. Malicka and B. Machura, Push–pull effect – how to effectively control photoinduced intramolecular charge transfer processes in rhenium(I) chromophores with ligands of D–A or D–π–A structure, *Dalton Transactions*, 2025, **54**, 2209–2223.

46 L. D. Patsenker and Y. Y. Artyukhova, Molecular structure and spectral properties of thionaphthalimides, *Journal of Molecular Structure*, 2003, **655**, 311–320.

47 I. M. Alecu, J. Zheng, Y. Zhao and D. G. Truhlar, Computational Thermochemistry: Scale Factor Databases and Scale Factors for Vibrational Frequencies Obtained from Electronic Model Chemistries, *J. Chem. Theory Comput.*, 2010, **6**, 2872–2887.

48 J. Palion-Gazda, K. Choroba, M. Penkala, P. Rawicka and B. Machura, Further Insights into the Impact of Ligand-Localized Excited States on the Photophysics of Phenanthroline-Based Rhenium(I) Tricarbonyl Complexes, *Inorg. Chem.*, 2024, **63**, 1356–1366.

49 A. V. Müller, L. A. Faustino, K. T. de Oliveira, A. O. T. Patrocinio and A. S. Polo, Visible-Light-Driven Photocatalytic CO_2 Reduction by Re(I) Photocatalysts with N-Heterocyclic Substituents, *ACS Catal.*, 2023, **13**, 633–646.

50 S. K. Behera, S. Y. Park and J. Gierschner, Dual Emission: Classes, Mechanisms, and Conditions, *Angew. Chem., Int. Ed.*, 2021, **60**, 22624–22638.

51 A. Demeter, T. Bérces, L. Biczók, V. Wintgens, P. Valat and J. Kossanyi, Comprehensive Model of the Photophysics of N-Phenylnaphthalimides: The Role of Solvent and Rotational Relaxation, *J. Phys. Chem.*, 1996, **100**, 2001–2011.

52 J. Bredenbeck, J. Helbing and P. Hamm, Labeling Vibrations by Light: Ultrafast Transient 2D-IR Spectroscopy Tracks Vibrational Modes during Photoinduced Charge Transfer, *J. Am. Chem. Soc.*, 2004, **126**, 990–991.

53 A. Vlček, in *Photophysics of Organometallics*, ed. A. J. Lees, Springer Berlin Heidelberg, Berlin, Heidelberg, 2009, vol. 29, pp. 115–158.

54 H. Takeda, K. Koike, T. Morimoto, H. Inumaru and O. Ishitani, in *Advances in Inorganic Chemistry*, Elsevier, 2011, vol. 63, pp. 137–186.

55 P. A. Scattergood, M. Delor, I. V. Sazanovich, O. V. Bouganov, S. A. Tikhomirov, A. S. Stasheuski, A. W. Parker, G. M. Greetham, M. Towrie, E. S. Davies, A. J. H. M. Meijer and J. A. Weinstein, Electron transfer dynamics and excited state branching in a charge-transfer platinum(II) donor–bridge-acceptor assembly, *Dalton Trans.*, 2014, **43**, 17677–17693.

56 A. J. Auty, P. A. Scattergood, T. Keane, T. Cheng, G. Wu, H. Carson, J. Shipp, A. Sadler, T. Roseveare, I. V. Sazanovich, A. J. H. M. Meijer, D. Chekulaev, P. I. P. Elliot, M. Towrie and J. A. Weinstein, A stronger acceptor decreases the rates of charge transfer: ultrafast dynamics and on/off switching of charge separation in organometallic donor–bridge–acceptor systems, *Chem. Sci.*, 2023, **14**, 11417–11428.

57 C. J. Adams, N. Fey, Z. A. Harrison, I. V. Sazanovich, M. Towrie and J. A. Weinstein, Photophysical Properties of Platinum(II)−Acetylide Complexes: the Effect of a Strongly Electron-Accepting Diimine Ligand on Excited-State Structure, *Inorg. Chem.*, 2008, **47**, 8242–8257.

58 R. M. Duke, E. B. Veale, F. M. Pfeffer, P. E. Kruger and T. Gunnlaugsson, Colorimetric and fluorescent anion sensors: an overview of recent developments in the use of 1,8-naphthalimide-based chemosensors, *Chem. Soc. Rev.*, 2010, **39**, 3936–3953.

59 V. Q. Dang and T. S. Teets, A practical guide to measuring and reporting photophysical data, *Dalton Trans.*, 2025, **54**, 16268–16284.

Chapter 3

Bottlenecks in Photocatalytic CO_2 Reduction with Naphthalimide-Phenanthroline Re(I) Complexes Probed by Spectroelectrochemistry and Time-Resolved Infrared Spectroelectrochemistry

---

Jack Biddulph[1], Florian Cerpentier[1], Martin Pižl[2,3], Sayantan Bhattacharya[4], Partha Malakar[4], Gregory M. Greetham[4], František Hartl[2] and Mary T. Pryce[1], Submitted, *Chem. Sci.*, 2026.

[1] *School of Chemical Sciences, Dublin City University, Glasnevin, Dublin, D09 V289, Ireland*

[2] *Department of Chemistry, University of Reading, Whiteknights, Reading, RG6 6DX, UK*

[3] *Department of Inorganic Chemistry, University of Chemistry and Technology Prague, Technická 5, 166 28 Prague 6, Czech Republic*

[4] *Central Laser Facility, Science & Technology Facilities Council, Research Complex at Harwell, Rutherford Appleton Laboratory, Didcot, OX11 0QX, UK*

Author Contributions:

Jack Biddulph conducted all experimental studies and writing for this chapter. Florian Cerpentier contributed to the SEC, TRIR, and TRIR-SEC studies. Martin Pižl performed quantum chemical calculations and contributed to the TRIR and TRIR-SEC studies. Note that sections 3.3 and 3.4.5 regarding radical-chromophore systems are not included in the content submitted for publication.

3.1 Abstract

UV-Vis and infrared spectroelectrochemistry were employed to investigate the CO_2 reduction pathway of electro- and photocatalyst precursors, [Re(R–NI–phen)$(CO)_3$Cl] (**Re–R**), with R–NI electron reservoirs; where R = H (**Re–H**), and EB = 4-ethynylbenzene (**Re–H**). Three reduction steps are reported (R1–R3); a/ R–NI-based, yielding **[Re–R]$^-$** (R1), b/ phen-based, yielding **[Re–R]$^{2-}$** biradical (R2), and c/ [R–NI]$^-$-based (R3), inducing concomitant Cl^- dissociation and yielding [Re(R–NI–phen)$(CO)_3]^{2-}$ (**^{2}5–DA**). Complementary quantum chemical calculations reveal a spin-flip in **^{1}[Re–R]$^{2-}$** to **^{3}[Re–R]$^{2-}$** allows partial Cl^- dissociation near R2, producing [Re(R–NI–phen)$(CO)_3]^-$ (**^{3}5–MA**). Subsequent intramolecular electron transfer [R–NI]$^-$→[Re–phen$^-$] in **^{3}5–MA** produces **^{1}5–MA**. Both **$^{1/3}$5–MA** are reducible between R2 and R3 to give [Re(R–NI–phen)$(CO)_3]^{2-}$ (**^{2}5–DA**). Theoretical calculations reveal that both **^{1}5–MA** and **^{2}5–DA** featuring {Re^0–phen$^-$} are the active electrocatalysts; although, catalysis accelerates from **^{2}5–DA** formed at R3. Spectroelectrochemistry combined with ps–ns time-resolved infrared spectroscopy (TRIR SEC) probed the excited state(s) populated upon 420-nm excitation of **[Re–R]$^-$** and **^{3}[Re–H]$^{2-}$**, mimicking the intermediates formed under photocatalysis. TRIR SEC with **[Re–R]$^-$** revealed the concurrent population of Re→phen ^{4}MLCT and NI^-→phen ^{4}ILCT excited states. Re^I→Re^{II} photooxidation in the ^{4}MLCT excited state triggers the formation of **[Re–R]$^{2-}$** by reductive quenching from TEOA under photocatalytic conditions. Additionally, the ^{4}ILCT excited state indicates that [R–NI]$^-$→Re–phen intramolecular electron transfer can be achieved photochemically. The Cl^- dissociation from **[Re–R]$^{2-}$** has been identified as the bottleneck in the photocatalytic pathway.

3.2 Introduction

There is an urgent need to devise solutions to curb the current trajectory of climate change to limit global warming to an additional 1.5 °C in the coming years.[1] Since the invention of the first dye-sensitised solar cells by Grätzel et al., there has been a growing interest in developing photo-driven processes to mitigate climate change.[2,3] One such application is photocatalytic CO_2 reduction; this approach converts CO_2, a major greenhouse gas, into another form such as its C_1-synthons (CO, HCO_2H, CH_3OH, and CH_4).[4] These C_1-synthons can be further utilised in industrial processes beyond simply capturing carbon. The classical Lehn catalyst, [Re(bpy)$(CO)_3$Cl] (bpy = 2,2'-bipyridine), has been extensively studied as a CO_2-reducing photocatalyst due to its facile synthesis and its ability act as both the photosensitiser and catalytic centre, being often viewed as a benchmark in CO_2 reduction chemistry.[5,6] Re^I(α-diimine) tricarbonyl complexes are widely

known for their ability to photocatalyse CO_2 reduction to CO and/or formate, stemming from the seminal work by Hawecker, Ishitani, and co-workers who proposed the underlying photocatalytic cycles.[7–11]

Various α-diimine ligands have been used to tune the photophysical properties of [Re^{I}(α-diimine)$(CO)_3$X] (X = Cl or Br) complexes towards improved photocatalytic activity, where 2,2'-bipyridine (bpy) is replaced by 1,10-phenanthroline (phen) or dipyrido[3,2-a:2',3'-c]phenazine (dppz) ligands.[11–14] Another approach is to tune the ground-state properties and the excited state dynamics of the [Re^{I}(α-diimine)$(CO)_3$X] complexes; this can be achieved by varying the substituents on the α-diimine ligand. For instance, substitution at the phen core with electron-rich *N*-donors including carbazole, phenoxazine, phenothiazine, or pyrrole creates a push-pull organic chromophore, with phen acting as an electron acceptor. The excited-state properties are then modulated by the degree of conjugation and electron-donating ability of the appended substituents.[15–17]

Rylenes form a family of organic chromophores with tuneable electronic and optical properties that are significantly affected by the extent of conjugation in their delocalized π-systems, by substitution at the rylene core, and by functionalisation through the imide groups.[18] Of the rylene family, naphthalimide (NI) is amongst the simplest forms, featuring naphthalene as the core with a single imide group. The small π-conjugated system of NI exhibits relatively high-energy n→π* and π→π* electronic transitions at *ca*. 340 nm, but lower-lying compared to phen absorbing at *ca*. 270 nm. The number of substitution sites on the NI core facilitates the potential to tune the optical and electronic properties of the NI chromophore.[19,20] By linking NI and α-diimine moieties, as in naphthalimide-phenanthroline (NI–phen), a visible/near-UV region organic chromophore can be appended to a metal(α-diimine) chromophore, thereby creating a bichromophoric system.[21–24] Furthermore, linking these chromophores through the imide group has little impact on the electronic properties of the NI motif, while allowing for a charge-transfer processes via the formation of radical species.[25]

The photophysical properties of [Re(PNI–phen)$(CO)_3$Cl] (where PNI = 4-piperidinyl-1,8-naphthalimide) were reported by Yarnell et al.[22] This Re^{I}(α-diimine) complex displayed a 3000-fold increase in the triplet excited-state lifetime (651 μs) compared to [Re(phen)$(CO)_3$Cl] (197 ns), due to a bidirectional "ping-pong" energy transfer proposed between the triplet metal-to-ligand charge-transfer (^{3}MLCT) excited state of the Re^{I}(α-diimine) chromophore and the triplet ligand-centred (^{3}LC) excited state of the NI chromophore.[22] Sub-microsecond TRIR spectroscopy was employed to analyse the intense and distinct metal carbonyl stretching vibrations associated

with *fac*-rhenium tricarbonyl motif, typically observed between 2100–1800 cm^{-1}.[26] Additionally, the stretching vibrations arising from the imide organic carbonyls of NI were simultaneously monitored to locate the populated excited states within the complex. Later, Yarnell et al. varied the substituents on the NI unit in [Re(R–NI–phen)$(CO)_3$(dmap)](PF_6) (where R = H, Br, phenoxy, phenylthiol, or piperidinyl groups and dmap = 4-dimethylaminopyridine) to further study the nature of the bidirectional "ping-pong" energy transfer in these complexes.[27] The latter studies revealed that the triplet–triplet equilibrium is dependent on the electron-donating ability of the R-group; with stronger electron-donating groups lowering the energy of the ^{3}LC excited state and thereby preventing the formation of a triplet–triplet equilibrium in those complexes.[27]

While some [Re(R–NI–phen)$(CO)_3$X] complexes (where R = 4-piperidinyl and nitro groups, and X = Cl) have been deployed as CO_2 reducing photocatalysts, the study by Franco et al. showed that CO_2 conversion is relatively low upon the addition of the R–NI moiety as an electron reservoir when conducted by photocatalysis compared to electrocatalysis.[28–30] In designing new photocatalysts, it is essential to provide a rationale for why some systems give poor conversion. Spectroelectrochemistry (SEC) can aid in identifying the nature of the intermediates in redox catalytic cycles and mimic the formation of photoreduced species and their intermediates.[31] SEC has been combined with time-resolved techniques including transient absorption, 2D-electronic, and 2D-ATR-IR spectroscopic techniques.[32–34] Recently, time-resolved infrared spectroelectrochemistry (TRIR SEC), achieved by using a semi-stopped-flow optically transparent thin-layer electrochemical (OTTLE) cell, was adopted for probing the excited-state dynamics of intermediates formed during photocatalytic CO_2 reduction in a proof-of-concept study using [Re(bpy)$(CO)_3$X] (where X = Cl or Br), with the excited-state lifetimes obtained for several *in situ* reduced species.[35] This combination of techniques provides a powerful approach to identify the active catalyst formed from the precursor.

In this study, two [Re(R–NI–phen)$(CO)_3$Cl] complexes, denoted as **Re–R** hereinafter, were prepared as potential CO_2 reducing photocatalysts featuring R–NI electron reservoirs (where R = H or ethynyl benzene (EB)) appended to the phen ligand, as illustrated in Chart 3.1. The syntheses and spectral characterisation of **Re–R** are already discussed in Chapter 2[36], and therefore a brief synopsis of their spectral characterisation in THF is provided here. The UV-Vis absorption spectra of **Re–R** (Figures S3.1 and S3.2) have distinct features arising from the Re–phen metallacycle and the R–NI moiety. Particularly, a metal–ligand-to-ligand charge-transfer (ML'LCT) transition at *ca*. 380 nm has a dual character arising from π(Cl)→π*(phen) halide-to-ligand charge transfer (XLCT) and dπ(Re)→π*(phen) metal-to-ligand charge-transfer (MLCT) transitions; hereinafter, this is for simplicity referred to as an MLCT transition.[37–39] Different electronic transitions arising from the

R–NI moiety are apparent for each **Re–R** complex, also involving the differing R-groups attached at the NI core; with vibrationally structured n→π* and π→π* transitions for **Re–H** at *ca*. 340 nm, while a new EB–NI→NI π→π* intraligand charge-transfer (ILCT) transition is observed at *ca*. 385 nm. The IR spectra (see Figures S3.3 and S3.4) of **Re–R** reveal the typical *fac*-band pattern of the metal tricarbonyl vibrational modes ($\nu_{C\equiv O}$) in the C_s point group associated with the [Re^{I}(R–NI–phen)$(CO)_3$Cl] complexes[26,40], with additional organic carbonyl bands ($\nu_{C=O}$) from the NI moiety. In the case of **Re–EB**, the ethynyl bridge is an additional IR-active reporter group, with the C≡C stretching mode ($\nu_{C\equiv C}$) observed at 2206 cm^{-1}. The experimental IR and UV-Vis absorption spectra are closely matched by DFT/TDDFT calculated spectra (Table 3.2 and Figures S3.26 and S3.27).

In this work, electrochemical techniques (CV, SEC) were employed to elucidate the reduction pathway leading to the active catalyst of **Re–R**. Further to these, TRIR SEC studies were conducted to gain a more detailed account of the excited-state dynamics of some of the reduced intermediates leading to the formation of the active catalyst for photocatalytic CO_2 reduction. This approach uses a OTTLE cell adapted with a working electrode bearing a wide rectangular aperture enabling *in situ* TRIR SEC studies upon cell-rastering to avoid local overheating.[41] The results of the experimental electrochemical (CV, SEC), TRIR and TRIR SEC studies, together with the investigation of the photocatalytic CO_2 reduction mechanism, of **Re–R** are discussed and analysed with insightful data obtained from DFT and TDDFT calculations.

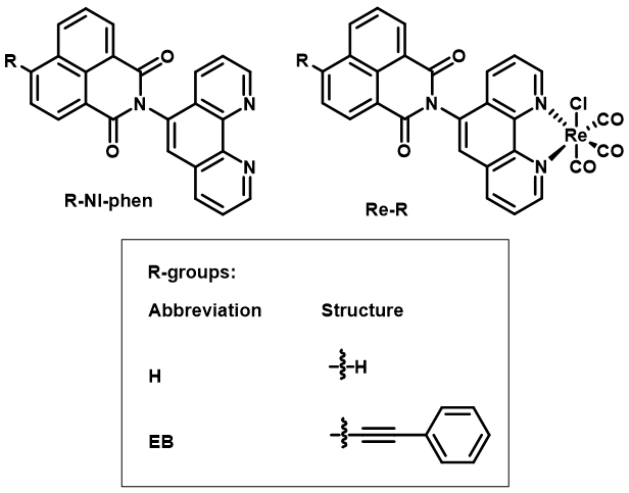


Chart 3.2. *Molecular structures of the* ***R–NI–phen*** *ligands and the* ***Re–R*** *complexes studied in this work.*

3.3 Radical-Chromophore Systems

3.3.1 Overview

Upon the electrochemical reduction of the **Re–R** complexes, as undertaken later in this chapter, the R–NI moiety becomes a radical species while the Re–phen chromophore remains unperturbed; thereby establishing a radical-chromophore system. Studies of radical-chromophore systems typically involve stable-free radicals, air-stable organic compounds that have unpaired π-spin systems that are delocalised through π-conjugation[42], linked to organic chromophores. However, radicals can also be formed by redox and excited-state processes, although these are not typically air-stable and must be formed during *in situ* studies. Regardless of how they are formed, radicals exist in the doublet ground state (D_0) and populate doublet excited states (D_n, where $n \geq 1$) upon optical excitation, as illustrated in Figure 1.20 in Chapter 1. When linked to an organic chromophore, these radicals can modify the excited-state dynamics of the appended chromophore.[43]

In the TRIR SEC experiments presented later in this chapter, **Re–R** is first electrochemically reduced, and the formed radical-chromophore system is then excited at 420 nm. Two scenarios can be considered upon excitation of a radical-chromophore system; namely, excitation of the chromophore or excitation of the radical. The processes arising from each excitation pathway can be complicated and requires some examination prior to discussing the results of the TRIR SEC studies presented in this chapter. As such, a brief overview of radical-chromophore systems follows.

3.3.2 Excitation of the Chromophore

Excitation of the chromophore in a radical-chromophore system typically results in the population of the same locally excited state(s) obtained by excitation of the isolated chromophore. However, the presence of a covalently linked radical changes the nature of the excited-state dynamics subsequent to the populated of the locally excited state(s). Since there are two valence electrons in the chromophore HOMO, and the radical characteristically possess one unpaired electron in the HOSO, the spin-pairing of all three valence electrons in the covalently linked radical-chromophore system must be considered. Consequently, there are three possible configurations as outlined below:

1. Where a singlet chromophore (↑,↓) is linked to a doublet radical (↓) a sing-doublet is formed. The ground state of radical-chromophore systems are sing-doublets, with an overall doublet spin multiplicity.
2. When two of the three valence electrons are spin-paired, i.e. chromophore (↑,↑) and radical (↓), a trip-doublet is formed. This is the case upon excitation of the chromophore to a triplet excited state with a doublet on the radical. The overall spin multiplicity in this case remains as a doublet spin state.
3. When all unpaired electrons are spin-aligned, i.e. chromophore (↑,↑) and radical (↑), a trip-quartet is formed. In this case, the overall spin state changes to a quartet (Q_n) arising from Hund's rule (2S+1, where S = 3/2).

The local spin state of the chromophore differs in the first two configurations, being either a singlet or triplet in the sing-doublet and trip-doublet, respectively. However, when the chromophore is linked to a radical it cannot be simply considered as an isolated system. When the overall spin multiplicity of the radical-chromophore system is considered, by correlating the individual spin states of the radical and chromophore components, a doublet spin state is obtained in both of first two configurations.[44] This creates an unusual situation where ISC on the chromophore becomes spin-allowed in the presence of a radical as the overall spin multiplicity of the radical-chromophore system is unchanged; so-called radical-enhanced ISC (REISC). In REISC, ISC from the chromophore S_n to T_n excited state is enhanced by a spin-exchange mechanism with the radical, where the valence electrons of the chromophore and of the radical are coupled allowing for their spin to be exchanged; this preserves the overall spin multiplicity of the radical-chromophore, as illustrated in Figure 3.1.

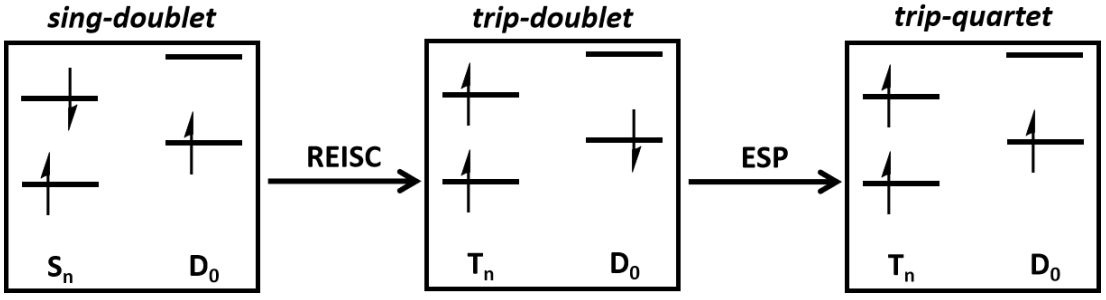


Figure 3.13. *The excited state dynamics of a radical-chromophore system following excitation of the chromophore. Chromophore-based orbitals are on the left and radical-based orbitals are on the right of each box.*

The $D_0 \rightarrow D_n$ and $D_n \rightarrow D_0$ transitions are spin-allowed processes. Accordingly, high ISC efficiencies can be attained in radical-chromophore systems at the cost of shorter-lived T_n excited state lifetimes compared to the isolated chromophore.[45] Increasing the distance between the radical and chromophore with a spacer reduces coupling between these components; this can extend the lived T_n excited state lifetime, but also reduces the efficiency of ISC in these systems. This effect was studied by Wang et al. using a 2,2,6,6-tetramethyl-1-piperidinyloxyl radical linked to a BODIPY chromophore; a high triplet state quantum yield of 80% and an triplet excited state lifetime of 62 µs were reported with a shorter spacer (1,4-dimethyl-1*H*-1,2,3-triazole), while a longer spacer (4-methyl-1-(2-phenoxyethyl)-1*H*-1,2,3-triazole) had a lower ISC efficiency of 14% but a longer triplet state lifetime of 190 µs.[46]

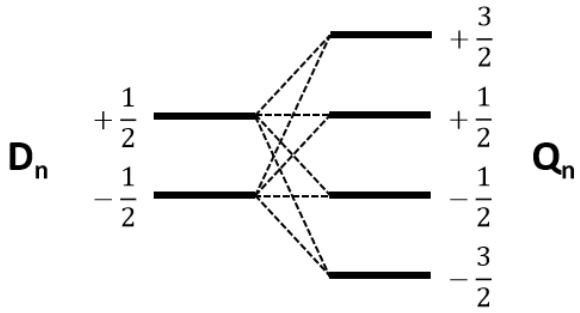


Figure 3.14. *A diagram of the substates of the isoenergetic D_n and Q_n excited states. Mixing between the substates are shown with dashed lines.*

To access long-lived excited states in radical-chromophore systems spin-forbidden transitions are required; this is achieved by populating quartet (Q_n) excited states. The Q_n excited states in covalently linked radical-chromophore systems are populated by electron spin polarisation (ESP), where the spin of the radical valence electron becomes aligned with those of the T_n excited chromophore as illustrated in Figure 3.1.[47,48] While the overall spin state changes from the trip-doublet to trip-quartet state, the spin-states of the individual components remain unchanged; this results in the two excited states having very similar energies. Under the influence of a magnetic field, the spin magnetic quantum number (m_s) causes the energy levels of D_n and Q_n excited states to undergo hyperfine splitting into substates (for $S = 1/2$; $m_s = \pm 1/2$ for D_n, and $S = 3/2$; $m_s = \pm 1/2, \pm 3/2$), as shown in Figure 3.2. If the D_n and Q_n excited states are isoenergetic an equilibrium between their substates is established with a 1:2 probability ratio in favour of the Q_n excited states.[49] This equilibrium has been shown to form over an 80 ps timescale for oxoverdazyl-perylene radical-chromophore systems studied with fs-TAS.[42,50] Zero-field splitting

interactions also allow for the hyperfine splitting of the D_n and Q_n substates even in the absence of an external magnetic field due to the mixing of the unpaired electrons in the radical-chromophore system.[51,52] If the D_n and Q_n excited states have different energies, the Q_n excited state can be populated so long as the Q_n substates have a lower energy than the D_n substates or the energy difference between the substates remains sufficient small for mixing to occur. [42,45,50]

Ground-state recovery involves ISC from the T_n excited state on the chromophore to its S_0 ground state, similarly to $T_n \rightarrow S_0$ transitions seen for the isolated chromophore. However, two pathways are possible in radical-chromophore systems; one is the spin-forbidden $Q_n \rightarrow D_0$ transition from the trip-quartet state and the other is the spin-allowed $D_n \rightarrow D_0$ transition from the trip-doublet state. The latter is the more likely pathway due to the spin-allowed nature of the $D_n \rightarrow D_0$ transition, and the equilibrium between the trip-quartet and trip-doublet states makes this transition accessible.

3.3.3 Excitation of the Radical

The excitation of a radical species was previously described in Chapter 1. However, the relevant characteristics of the subsequently populated D_n excited states that are pertinent to this discussion are described here. Upon populating a D_n excited state, the formerly occupied D_0 ground state HOSO is vacated. This creates an unstable species where the valence electron occupies a high energy molecular orbital, while a lower energy molecular orbital is empty. As described above, $D_0 \rightarrow D_n$ and $D_n \rightarrow D_0$ transitions are spin-allowed processes; consequently, D_n excited states are short-lived. However, interactions between an excited radical and a chromophore are still possible in a radical-chromophore system. This requires the linked chromophore to have an excited state lower in energy than the initially populated D_n excited state of the radical.[42] Without this, ground state recovery proceeds via a $D_n \rightarrow D_0$ transition as illustrated in Figure 3.3A, which is also the only situation where fluorescence from a D_n excited state occurs in radical-chromophore systems.[42,53]

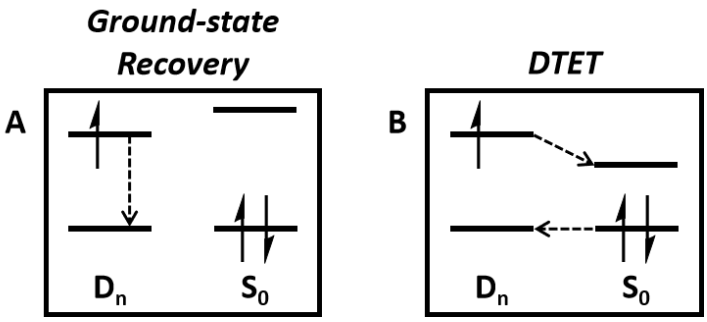


Figure 3.15. *The excited state dynamics of a radical-chromophore system following excitation of the radical. (A) When there are no chromophore-based molecular orbitals that are lower in energy than the D_n excited state, only ground-state recovery is possible. (B) When there is a chromophore-based molecular orbital lower in energy than the D_n excited state, DTET can occur.*

One possible interaction between an excited radical and a chromophore involves electron-exchange based Dexter-like doublet-triplet energy transfer (DTET; see Figure 3.3B), which has many common attributes with triplet-triplet energy transfer (TTET). TTET involves an energy donor in the T_n excited state that transfers its energy to an acceptor through electron exchange via a Dexter mechanism; this produces a T_n excited state on the acceptor and restores the donor to the S_0 ground state.[54] However, TTET involves spin-forbidden transitions and so spin-orbit coupling (SOC) interactions are required to obtain high efficiency ISC, widely attained from the triplet excited states of transition metal complexes.[52] In DTET, the radical species in the D_n excited state is the energy donor; consequently, the overall spin multiplicity of the radical-chromophore system remains a doublet despite ISC within the chromophore. Therefore, the advantage of DTET over TTET is that ISC can be achieved without using a heavy atom, such as the use of transition metal complexes in TTET.[55] DTET is also a form of REISC, driven by an electron-exchange mechanism in this case rather than the spin-exchange mechanism described earlier.

Separate studies by Han et al. and Wei et al. used DTET to achieve triplet-triplet annihilation photon up-conversion (TTA-UC), where two T_n excited states produce a higher energy acceptor S_n excited state that subsequently displays upconverted delayed fluorescence.[55,56] In doing so, they could use near-IR light to excite the radical while attaining high UC quantum yields of 6.8%, reportedly close to the highest UC quantum yield of 7% with a heavy-metal complexes as photosensitsers.[56] An excited state radical can also populate the chromophore triplet excited state via an intermediate excited state. The intermediate excited state can be populated by a number of excited state processes including electron transfer, energy transfer, or ISC, and subsequently the trip-doublet and trip-quartet states are then populated from the intermediate excited state by SOC-ISC or radical-pair intersystem crossing (RP-ISC).[42] Once the trip-doublet and

trip-quartet states are populated, the same excited state pathways can occur as outlined for these states identified by excitation of the chromophore.

3.3.4 Studying Radical-Chromophore Systems

Electron paramagnetic resonance (EPR) spectroscopy is the most widely adopted technique to study the spin states of open-shell systems ($S \geq 1/2$).[52] EPR is related to nuclear magnetic resonance (NMR) spectroscopy in that both techniques study the splitting of spin states under an applied magnetic field.[57] However, while NMR is concerned with nuclear spin (i.e. the spin of the neutrons and protons in the nuclei of atoms), EPR analyses electronic spin (i.e. the spin of electrons) which is relevant to this discussion of radical-chromophore systems. The EPR spectra of systems with multiple unpaired electrons, such as the trip-doublet and trip-quartet state (S = 1/2 and 3/2, respectively), can be difficult to interpret due to the multiple possible processes involved in the interconversion of these states.[57–59] These spectra are often accompanied by theoretical calculations which aid in assigning the absorption and emission signals by unpaired electrons to D_n or Q_n excited states.

Time-resolved EPR (TREPR) spectroscopy can be employed to study the spin-state dynamics of open-shell systems, which includes photocatalysts.[52,57–61] This technique could be very beneficial to studying radical-chromophore systems that undergo optical excitation, particularly due to its ability to distinguish between the many mechanisms that ESP can proceed by.[42,57,59] However, TREPR spectroscopy experiments face difficulties with data interpretation, which require sophisticated data analysis systems, and complex setups that require precise synchronisation of microwave pulses, magnetic fields, and time-resolved detection systems.[61] Accordingly, most systems are studied as solids at low temperatures (*ca.* 77 K) which prolongs their excited-state dynamics, allowing for the excited-state processes to be monitored on longer time regimes.[43]

3.3.5 Conclusion to Radical-Chromophore Systems

Photocatalytic systems are often overlooked as radical-chromophore systems despite the creation of radical species upon optical excitation during photocatalysis, including photosynthesis.[62] In this chapter, a radical-chromophore system is created following electrochemical reduction of the **Re–R** photocatalyst precursors, mimicking the formation of radical species during photocatalysis. This is unlike the studies presented in this overview of radical-chromophore systems, which primarily use stable-free radicals. However, the same

analyses can be applied to those radical-chromophore systems as the electrochemically generated radical-chromophores in this work.

To conclude, the studies presented in this chapter are used to determine the excited-state dynamics of a photocatalyst precursor by creating an electrochemically generated radical-chromophore system; the first that uses TRIR SEC to do so. Furthermore, there are many reports of radical-chromophore systems incorporating rylenes, rylene monoimides, and rylene diimides.[44,48,50,56,58,63–65] However, these organic compounds are typically incorporated as the chromophore, or in larger radical-chromophore systems as donor or acceptor moieties. As such, the formation of a R–NI$^{\bullet-}$ upon the electrochemical reduction of **Re–R** also presents an interesting opportunity to study a rylene monoimide as the radical component in a radical-chromophore system.

3.4 Results and Discussion

3.4.1 Cyclic Voltammetry

Cyclic voltammetry of **H–NI–phen**, **EB–NI–phen**, **Re–H**, and **Re–EB** conducted in DCM/10^{-1} M $TBAPF_6$ under a N_2 atmosphere is presented in Figure 3.4. The reversibility of the R1 and R2 reduction waves for all samples is assessed at various scan rates between 10–100 mV s^{-1} (Figure S3.5). Complementary cyclic voltammograms were recorded in DMF/10^{-1} M $TBAPF_6$ under N_2 and CO_2 (**Re–R**) atmospheres, and in THF/10^{-1} M $TBAPF_6$ under a N_2 atmosphere (Figures S3.6–S3.8). The reduction potentials against Fc^+/Fc (used as the internal standard) are listed in Table 3.1.

The first reduction wave, R1, seen in the cyclic voltammogram of **H–NI–phen** at $E_{1/2}$ = –1.83 V, appeared reversible and closely matched the literature electrode potential for generating the NI radical anion, **[H–NI–phen]$^{\bullet-}$**.[66] For **EB–NI–phen**, the R1 reduction forms the corresponding radical anion, **[EB–NI–phen]$^{\bullet-}$**, at a less negative potential, viz. $E_{1/2}$ = –1.60 V, indicating that binding EB onto NI stabilises the LUMO of the NI moiety. In both **R–NI–phen**, the uncoordinated phen moiety has a higher-lying LUMO compared to that of NI and reduces more negatively. For free phen, $E_{p,c}$ = –2.53 V vs. Fc^+/Fc in CH_3CN[67], which is comparable with the second reduction wave (R2) in **[H–NI–phen]$^{\bullet-}$** but more negative than the R2 wave in **[EB–NI–phen]$^{\bullet-}$** (Table 3.1). However, upon complexation of **R–NI–phen** in **Re–R**, the phen LUMO becomes strongly stabilised and chelating phen reduces at much less negative potentials. In [Re(PNI–phen)$(CO)_3$Cl] (where PNI = 4-piperidinyl-1,8-naphthalimide), an analogue of the **Re–R** complexes in this study,

the phen complexation even results in a reversed situation, where the R1 wave at $E_{1/2}$ = –1.59 V has been attributed to the population of the stabilised phen-based LUMO and the more negative R2 wave at $E_{1/2}$ = –1.71 V is localised on the PNI moiety bearing the strongly donating 4–piperidinyl substituent.[28] Especially in **Re–EB**, **EB–NI** has its LUMO significantly more stabilised compared to chelating phen.

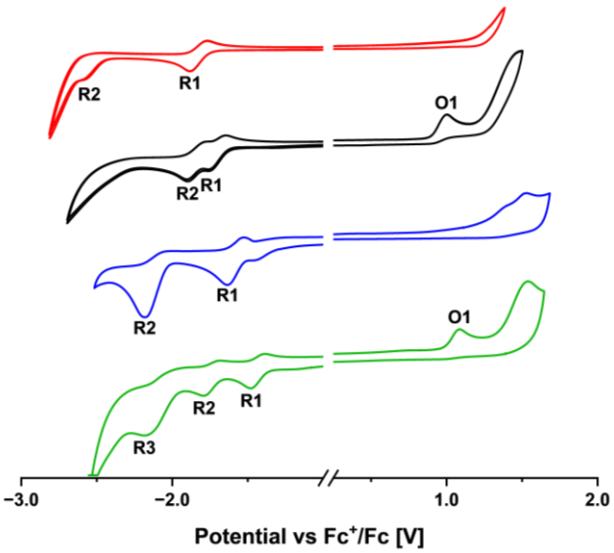


Figure 3.16. *Cyclic voltammograms of 1 mM [red]* ***H–NI–phen****, [black]* ***Re–H****, [blue]* ***EB–NI–phen****, and [green]* ***Re–EB*** *samples in the DCM/10^{-1} M $TBAPF_6$ electrolyte. Scan rate = 100 mV s^{-1}.*

Two close-lying reversible reduction waves, R1 and R2, are localised in the CV of **Re–H** in DCM (Figure 3.4) at $E_{1/2}$ = –1.70 V and –1.84 V, respectively. The R1 reduction producing the **[Re–H]**$^{-}$ species corresponds to reduced NI in coordinated **[H–NI**$^{\bullet-}$**–phen]**. This is confirmed by TDDFT calculations showing the LUMO of **Re–H** entirely localised on the NI moiety, while the LUMO+1 of **Re–H** is predominantly distributed across the phen moiety (Figure S3.29). Accordingly, the R2 reduction wave can be attributed to the reduction of the phen moiety forming **[H–NI**$^{\bullet-}$**–phen**$^{\bullet-}$**]** as a biradical species named **[Re–H]**$^{2-}$ herein. DFT calculations reveal that two biradical species are formed by the **Re–R** complexes (Table S3.7 and S3.9); the open-shell singlet, ^{1}**[Re–R]**$^{2-}$, and the slightly lower energy open-shell triplet, ^{3}**[Re–R]**$^{2-}$. Both have added electrons in the R–NI and phen moieties but vary by being spin-paired and spin-unpaired in ^{1}**[Re–R]**$^{2-}$ and ^{3}**[Re–R]**$^{2-}$, respectively. Further details of these biradical species are discussed in the following section.

The reversible R1 and R2 reduction waves observed in the CV of **Re–EB** (Figure 3.4) resembles those of **Re–H**, but R1 is much less negatively shifted: $E_{1/2}$ = –1.51 V and –1.81 V, respectively.

The R1 and R2 reductions are assigned to the formation of **[Re–EB]**$^{-}$ and **[Re–EB]**$^{2-}$, respectively. Accordingly, **[Re–EB]**$^{-}$ arises from the formation of chelated **[EB–NI**$^{\bullet-}$**–phen]**, while **[Re–EB]**$^{2-}$ is formed by a phen-based reduction with chelated **[EB–NI**$^{\bullet-}$**–phen**$^{\bullet-}$**]**. This assignment is supported by DFT calculations showing the LUMO almost entirely localised on the NI moiety, while the LUMO+1 of **Re–EB** is predominantly distributed across the phen moiety (Figure S3.31). Thus, the greater separation of the R1 and R2 reduction waves for **Re–EB** (ΔE_{R2-R1} ≈ 300 mV) compared to **Re–H** (ΔE_{R2-R1} ≈ 140 mV) arises from the greater stabilisation of the NI LUMO in **Re–EB**. The reduction potential of phen in chelating **R–NI–phen** is clearly much less affected by the R-substituent, reflecting the limited electronic communication between NI and phen as independent redox centres.

An irreversible oxidation (O1) wave is observed for both **Re–R** complexes at $E_{p,a}$ = +1.01 V and +1.09 V, respectively. For **Re–H,** the DFT calculations indicate that the HOMO and HOMO–1 are based on the Re–phen metallacycle (Figure S3.29); therefore, O1 is attributed oxidation of the Re(I) (or, more precisely, the Re–Cl) centre. However, the HOMO is localised on the EB–NI moiety for **Re–EB**, with a close-lying HOMO–1 assigned to oxidation of the Re(I) centre (Figure S3.31); therefore, O1 is attributed oxidation of the EB–NI moiety which precedes the oxidation of the Re(I) centre in **Re–EB**.

The continued negative CV scan of **Re–H** and **Re–EB** in DCM (for **Re–EB** only), DMF and THF electrolytes (Figure 3.4, S3.6, and S3.7) displayed a separate irreversible third reduction wave (R3) as indicated in Table 3.1. The β-LUSO of **[Re–R]**$^{2-}$ (Figures S3.37 and S3.39) are localised on the R–NI moiety, therefore the reduction at R3 likely creates the R–NI dianion initially. This is sufficient to labilise and break the Re-Cl bond to obtain uncommon **^{3}5–MA**, with the **[R–NI^{-}–phen^{-}]** biradical coordinated to a 5-coordinate Re^{I} metal centre. Concomitant reduction at R3 then yields the formally Re^{0} metal centre, establishing the 5-coordinate dianion (**^{2}5–DA**) as the electrochemically formed active catalyst. Indeed, the diamagnetic 5-coordinate monoanion, [Re^{0}(α-diimine)(CO)$_3$]$^{-}$ (**^{1}5–MA**), formed from double reduced Re^{I}(α-diimine) precursors, has been reported as the CO_2 reducing active catalyst.[35,68] The **^{1}5–MA** of **Re–EB** could be formed from the **^{3}5–MA** by intramolecular electron transfer from [R–NI]$^{-}$ to the [Re–phen^{-}] metallacycle; however, R–NI is easily reduced at this potential to spontaneously form the **^{2}5–DA**. A weak catalytic effect is observed at the R3 reduction wave for both **Re–R** complexes in DMF under a CO_2 atmosphere associated with the binding of CO_2 to a Re^{0} metal centre (Figure S3.8).[21,69] Accordingly, the R3 reduction waves are formally assigned to a [R–NI]$^{-}$-based reduction with concomitant Cl^{-} dissociation resulting in the formation of **^{3}5–MA**, followed by a subsequent [R–NI]$^{-}$-based reduction which yields the **^{2}5–DA** active catalyst. This complex electrochemical-

chemical-electrochemical (*ECE*) process is further detailed by the corresponding IR and UV-Vis SEC studies outlined in the following section.

Table 3.4. *Redox potentials of* ***R–NI–phen*** *and* ***Re–R*** *from CV measurements.*[a]

Sample	Solvent	R1 (V)	R2 (V)	R3 (V)	O1 (V)
H–NI–phen	DCM	–1.83	–2.60[b]	–	–
	DMF	–1.70	–	–	–
EB–NI–phen	DCM	–1.60	–2.18[b]	–	–
	DMF	–1.55	–	–	–
Re–H	DCM	–1.70	–1.84	–	+1.01[b]
	DMF	–1.57	–1.70	–2.74[b]	+1.06[b]
	THF	–1.85	–1.95	–2.87[b]	+0.99[b]
Re–EB	DCM	–1.51	–1.81	–2.19[b]	+1.08[b]
	DMF	–1.46	–1.75	–2.17[b]	+1.06[b]
	THF	–1.55	–1.84	–2.29[b]	+0.96[b]
[Re(PNI–phen)$(CO)_3$Cl][c]	CH_3CN	–1.59	–1.71	–2.40[b]	–

[a]*All potentials (V) are reported versus ferrocene internal standard (Fc^+/Fc). $E_{1/2}$ values for reversible redox processes.* [b]*$E_{p,c}$ values for irreversible reduction and $E_{p,a}$ values for irreversible oxidation processes.* [c]*See Ref. 28.*[28]

3.4.2 Spectroelectrochemistry

IR and UV-Vis SEC experiments were performed in DCM/$TBAPF_6$ and THF/$TBAPF_6$ electrolytes. The reduction paths of **Re–H** and **Re–EB** encompassed three steps at the R1–R3 reduction waves identified in the parallel thin-layer CV (TL-CV) scans. The corresponding IR and UV-Vis spectral changes in THF/$TBAPF_6$ under an inert N_2 atmosphere are presented in Figure 3.5 (**Re–H**) and Figure 3.6 (**Re–EB**), and the IR spectral changes in THF/$TBAPF_6$ under a CO_2 atmosphere in Figure 3.7 (**Re–H** and **Re–EB**). The IR and UV-Vis spectral changes in DCM/$TBAPF_6$ for free **R–NI–phen**

and **Re–R** are presented in Figures S3.9–S3.12. The key IR and UV-Vis spectroscopic characteristics from the SEC experiments in THF and DCM, complemented by supporting DFT and TDDFT calculated data (Figures S3.28–S3.42 and Tables S3.1–S3.6), are summarised in Table 3.2.

For **[H–NI–phen]$^{\bullet-}$**, the IR spectrum (Figure S3.9A) features two $\nu_{C=O}$ absorption bands at 1635 and 1618 cm^{-1}, which are shifted to smaller wavenumbers compared to the parent, **H–NI–phen** ($\nu_{C=O}$ at 1713 and 1675 cm^{-1}). Similarly, the two $\nu_{C=O}$ absorption bands of the parent **EB–NI–phen** at 1710 and 1673 cm^{-1} shifted to smaller wavenumbers ($\nu_{C=O}$ = 1638 and 1621 cm^{-1}) upon the 1e$^-$ reduction at R1 (Table 3.1) to **[EB–NI–phen]$^{\bullet-}$** (Figure S3.10A). This change is coupled with a red shift of the parent $\nu_{C\equiv C}$ absorption band at 2207 cm^{-1}, associated with weaking of the C≡C bond, with two $\nu_{C\equiv C}$ absorption maxima being observed at 2157 and 2136 cm^{-1}. Depletion of the parent NI π→π* transition at 335 nm in the UV-Vis absorption spectrum of **[H–NI–phen]$^{\bullet-}$** coincided with the formation of a new electronic transition at 417 nm (Figure S3.9B), corresponding to the NI-based radical anion.[66] Similarly, the UV-Vis SEC monitoring of the formation of **[EB–NI–phen]$^{\bullet-}$** displayed the gradual growth of two new absorption bands at 444 and 487 nm, which accompanied the depletion of the parent NI π→π* transition at 385 nm (Figure S3.10B).

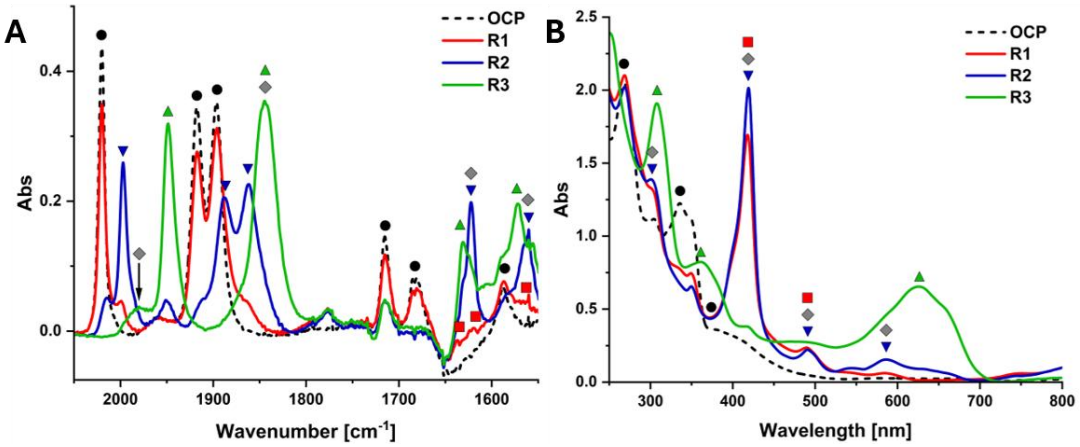


Figure 3.17. *(A) IR SEC of 4 mM **Re–H** and (B) UV-Vis SEC of 2 mM **Re–H** in the THF electrolyte at T = 293 K, showing the stepwise conversion of the parent complex (black, dashed) to reduced species formed at R1 (red), R2 (blue), and R3 (green). OCP = open-circuit potential, ● = **Re–H**, ■ = **[Re–H]$^-$**, ▼ = **^{3}[Re–H]$^{2-}$**, ◆ = **^{3}5–MA**, ▲ = **^{2}5–DA**.*

The IR SEC experiments indicated that there is almost complete conversion of the parent **Re–H** at the R1 reduction wave (partially overlapping with R2 in Figure 3.4) to **[Re–H]$^-$** with minimal

appearance of **[Re–H]$^{2-}$** (Figure 3.5A). New $\nu_{C=O}$ bands at 1637 and 1621 cm^{-1}, associated with the formation of **[H–NI$^{\bullet-}$–phen]**, are shifted to a smaller wavenumber for **[Re–H]$^{-}$** by *ca*. 70 cm^{-1} compared to **Re–H** at the open circuit potential (OCP). A slight red shift of the $\nu_{C\equiv O}$ bands of **[Re–H]$^{-}$** (by *ca*. 2 cm^{-1}) further indicates that the first reduction is remote from the tricarbonyl Re centre, supporting the assignment of the R1 reduction wave to the NI→NI$^{\bullet-}$ reduction step. The DFT-calculated IR spectrum corroborates with the experimental IR spectrum of **[Re–H]$^{-}$** (Table 3.2) and further supports the reduction of the NI moiety at the R1 reduction wave (Figure S3.40).

The UV-Vis spectral changes accompanying the reduction of **Re–H** at R1 (Figure 3.5B) are similar in appearance to those of **H–NI–phen** (Figure S3.9); showing the growth of a band at 417 nm upon the formation of **[Re–H]$^{-}$** with the concurrent depletion of the NI π→π* transition in **Re–H** at 338 nm. The TDDFT-calculated UV-Vis spectrum of **[Re–H]$^{-}$** agrees with the experimental spectra (Table 3.2); with the new transition at 417 nm attributed to a NI$^{\bullet-}$→phen π→π* ILCT transition which overlies the MLCT transition unperturbed by the NI-based reduction (Figures S3.32 and S3.33 and Table S3.3). These spectral changes are consistent with the formation of chelated **[H–NI$^{\bullet-}$–phen]** and is in agreement with the NI–based radical anion in the literature.[66] Similar features are observed for **[Re–H]$^{-}$** in the IR SEC and UV-Vis SEC experiments conducted in the DCM electrolyte (Figure S3.11).

For **Re–EB**, the greater separation of the R1 and R2 reduction waves ensured reduction to **[Re–EB]$^{-}$** without the formation of **[Re–EB]$^{2-}$**. In the IR spectrum of **[Re–EB]$^{-}$** in THF (Figure 3.6A), the $\nu_{C=O}$ and $\nu_{C\equiv O}$ bands underwent similar shifts as observed for **[Re–H]$^{-}$** associated with the formation of the NI-based radical anion. Inclusion of the ethynyl group in **Re–EB**, with $\nu_{C\equiv C}$ = 2207 cm^{-1}, enabled monitoring of bands in the C≡C IR region. Indeed, two new bands at smaller wavenumbers ($\nu_{C\equiv C}$ = 2156 and 2140 cm^{-1}) are observed for **[Re–EB]$^{-}$**, representing a red shift of *ca*. 60 cm^{-1}. DFT calculations support the experimental data for **[Re–EB]$^{-}$** (Table 3.2) and the reduction of the EB–NI moiety at R1 (Figure S3.41).

In the UV-Vis spectrum of **[Re–EB]$^{-}$** (Figure 3.6B), the reduction at R1 resulted in a depletion of the EB–NI→NI π→π* ILCT transition at 385 nm and coincided with the growth of two new bands at 443 and 488 nm. The TDDFT-calculated UV-Vis spectra of **[Re–EB]$^{-}$** agreed with the experimental spectra (Table 3.2); the band at 443 nm arises entirely from an EB–NI$^{\bullet-}$-based π→π* LC transition, while the band at 488 nm is attributed to a mixture of EB–NI$^{\bullet-}$-based π→π* LC and EB–NI$^{\bullet-}$→phen π→π* ILCT transitions (Figures S3.34 and S3.35 and Table S3.4). The IR and UV-Vis spectra of **[Re–EB]$^{-}$** matched the spectral profiles of **[EB–NI–phen]$^{\bullet-}$** (Figure S3.10);

further supporting that the first reduction in both **Re–R** complexes is localised on the NI moiety. Similar features are observed for **[Re–EB]**$^{-}$ in the IR SEC and UV-Vis SEC experiments conducted in the DCM electrolyte (Figure S3.12).

Upon the subsequent phen-based reduction of [**Re–H**]$^{-}$ at R2, new $\nu_{C\equiv O}$ bands are observed at 1997, 1888, and 1862 cm^{-1} (see Figure 3.5A). These are assigned to the 6-coordinate biradical [Re^{I}(H–NI^{-}–phen^{-})(CO)$_3$Cl]$^{2-}$, ^{3}**[Re–H]**$^{2-}$; the assignment of the triplet biradical is based on it being lower in energy ($\Delta E \approx 0.65$ kcal mol^{-1}) compared to the singlet biradical (Tables S3.7–S3.9). This assignment is also supported by the calculated IR spectrum of ^{3}**[Re–H]**$^{2-}$ in Figure S3.40. These $\nu_{C\equiv O}$ bands retained the *fac*-Re-tricarbonyl pattern in the local C_s symmetry, being red-shifted by ~30 cm^{-1} compared to the $\nu_{C\equiv O}$ bands of **Re–H** (Table 3.2), in line with the phen-based reduction increasing the Re→C≡O π-back-donation.[70] Trace amounts of the ^{3}**5–MA** may be present at *ca*. 1990 cm^{-1} on account of the slight asymmetry of the 1997 cm^{-1} band. The UV-Vis spectrum of ^{3}**[Re–H]**$^{2-}$ (Figure 3.5B) displayed new transitions at 307 and 580 nm with concurrent depletion of the phen π→π* transition at 265 nm. The calculated UV-Vis spectra of ^{3}**[Re–H]**$^{2-}$ agreed with the experimental spectra (Table 3.2); the transition at 307 nm arises from both NI^{-}–phen^{-}-based and Re→phen^{-} transitions, while the transition at 580 nm is attributed solely to a NI^{-}–phen^{-}-based transition redistributing onto the Re–phen metallacycle (Figures S3.36 and S3.37 and Table S3.5).

The IR spectra collected in DCM provide more detail about the species formed at R2. Two species were observed in the IR spectrum collected at R2 (Figure S3.11A). The ^{3}**[Re–H]**$^{2-}$ species with $\nu_{C\equiv O}$ bands at 1998, 1893, 1869 cm^{-1} closely matched the same species in THF. A second, minor species with $\nu_{C\equiv O}$ at 1989, 1869 and 1846 cm^{-1} is attributed to the formation of ^{3}**5–MA** of **Re–H**. The ^{3}**[Re–H]**$^{2-}$ and ^{3}**5–MA** species were also identified in UV-Vis absorption spectrum recorded at R2 (Figure S3.11B). The three absorption bands at 287, 457, and 580 nm are assigned to ^{3}**[Re–H]**$^{2-}$. The band at 287 nm is red shifted to 313 nm for ^{3}**5–MA**, but the longer wavelength features were largely unchanged. Upon applying a *ca*. 150 mV more negative potential beyond R2, complete conversion to ^{3}**5–MA** occurred. The TDDFT calculations of the electronic transition at 287 nm of ^{3}**[Re–H]**$^{2-}$ indicates the involved orbitals are localised on the Re–phen^{-} metallacycle (Figures S3.36 and S3.37 and Table S3.5). This transition shifted to lower energy in ^{3}**5–MA**, in line with the calculated UV-Vis spectra in Figure S3.40A, indicating that the Re–phen^{-} metallacycle is stabilised upon Cl^{-} dissociation.

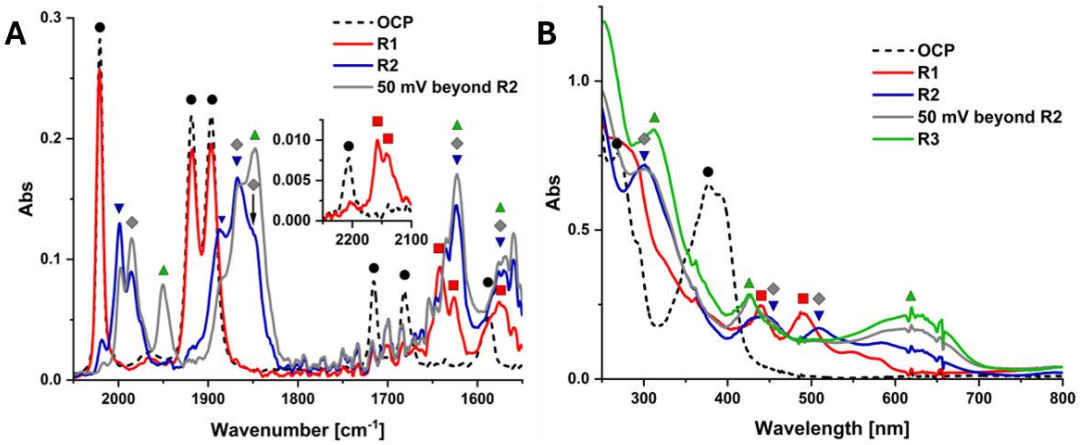


Figure 3.18. *(A) IR SEC of 4 mM* ***Re–EB*** *and (B) UV-Vis SEC of 1 mM* ***Re–EB*** *in DCM electrolyte solution at T = 293 K, showing the stepwise conversion of the parent complex (black, dashed) to the reduced species formed at R1 (red), R2 (blue), and R3 (green). OCP = open-circuit potential,* ● *=* ***Re–EB****,* ■ *=* ***[Re–EB]***$^{-}$*,* ▼ *=* ***^{3}[Re–EB]***$^{2-}$*,* ◆ *=* ***^{3}5–MA****,* ▲ *=* ***^{2}5–DA****.*

In the IR spectrum recorded beyond the R2 reduction wave of **Re–EB** (Figure 3.6A), the $\nu_{C\equiv O}$ vibrations remained largely unchanged, and no $\nu_{C\equiv C}$ vibrations are observed. New $\nu_{C\equiv O}$ bands attributed to the **^{3}[Re–EB]**$^{2-}$ species are apparent at 1998, 1890, and 1862 cm^{-1}; which are shifted by *ca.* 15 cm^{-1} to higher frequency compared to the $\nu_{C\equiv O}$ bands of **[Re–H]**$^{2-}$. An additional set of $\nu_{C\equiv O}$ bands are observed at 1983, 1858, and 1842 cm^{-1}; and agree with the calculated IR spectrum of the **^{3}5–MA** of **Re–EB** in Figure S3.41. Thus, two reduced species are formed from the second reduction localised on the phen moiety, which are easily identified in the IR spectrum recorded at R2 in the DCM electrolyte (Figure S3.12); with $\nu_{C\equiv O}$ stretching wavenumber at 1998, 1889, 1862 cm^{-1} and 1983, 1858, 1842 cm^{-1} for **^{3}[Re–EB]**$^{2-}$ and **^{3}5–MA**, respectively. The 2e^{-} reduction products typically formed by [Re(α-diimine)(CO)$_3$Cl] complexes are diamagnetic, particularly the **^{1}5–MA** active catalyst.[71] The addition of the R–NI moiety enables larger delocalisation of the added electrons after Cl^{-} dissociation. This is visualised in the spin-density distribution of **^{3}5–MA** of **Re–EB** in Figure S3.47; where the extended delocalisation of **Re–EB** further stabilises the **^{3}5–MA**. This also accounts for the increased absorption of the **^{3}5–MA** $\nu_{C\equiv O}$ bands in the IR spectrum of **Re–EB** at R2 compared to that seen in the IR spectrum of **Re–H**.

In the UV-Vis absorption spectrum recorded at the R2 reduction wave of **Re–EB**, the two absorption bands associated with the EB–NI$^{\bullet-}$ were marginally red-shifted compared to that of **[Re–EB]**$^{-}$; they appeared at 443 and 509 nm in THF (Figure 3.6B), and at 430 and 506 nm in DCM (Figure S3.12B). The transition at 430 nm in DCM is attributed to EB–NI^{-}→phen^{-} based transitions based on TDDFT calculations (Figures S3.38 and S3.39 and Table S3.6). The new

absorption band observed at 585 nm in THF, and at 539 nm in DCM, is attributed to both ^{3}**[Re–EB]**$^{2-}$ and ^{3}**5–MA** species as observed in the IR spectra in both electrolytes. The TDDFT-calculated UV-Vis spectrum of ^{3}**[Re–EB]**$^{2-}$ at 506 nm is attributed to transitions entirely localised on the EB–NI^{-} moiety, while the 539 nm band is assigned to redistribution of electron density from phen^{-} to the Re(CO)$_3$ moiety (Figures S3.38 and S3.39 and Table S3.6). The bands at 509 and 585 nm in THF are red shifted compared to those in DCM; this indicates that the more polar THF environment stabilises these species which lowers the energy of their transitions. For the ^{3}**5–MA**, this may be facilitated by forming the more stable, weakly THF-solvated complex, which would account for the larger red-shift of its transition from 539 nm in DCM to 585 nm in THF.

The doubly reduced **[Re–R]**$^{2-}$ species can exist in two biradical open-shell spin-states; the spin-singlet biradical (^{1}**[Re–R]**$^{2-}$), with added electrons in the R–NI(↑) and phen(↓) moieties, and the spin-triplet biradical (^{3}**[Re–R]**$^{2-}$), with added electrons in the R–NI(↑) and phen(↑) moieties. Theoretical calculations of ^{1}**[Re–R]**$^{2-}$ and ^{3}**[Re–R]**$^{2-}$ (Figures S3.40–S3.42) revealed that these species are very close in energy, with Δ*E* of *ca*. 0.65 kcal mol^{-1} (Tables S3.7–S3.9). The increased electron density on the Re–phen metallacycle of $^{1/3}$**[Re–R]**$^{2-}$ is sufficient to induce Cl^{-} dissociation, which yields the more stable ^{3}**5–MA** detected in the SEC experiments; particularly apparent for **Re–EB** reduced at R2. However, only trace amounts of the ^{3}**5–MA** of **Re–H** is observed in the SEC experiments at the R2 reduction wave, and a small quantity is detected at R3 as discussed later in this section. Again, the supporting TDDFT calculations provide an explanation for this as follows.

For ^{3}**[Re–H]**$^{2-}$, α-HOSO is delocalised over phen and β-HOSO on H–NI and are reducible at the LUSOs delocalised over the corresponding π*–system (α-LUSO on phen and β-LUSO on H–NI; Figure S3.40). The α-HOSO and β-HOSO of ^{3}**[Re–EB]**$^{2-}$ are delocalised over EB–NI and are reducible at the LUSOs delocalised over the π*–system of EB–NI (Figure S3.39). As such, **[Re–EB]**$^{2-}$ appears to be stabilised by the presence of the EB substituent on the NI moiety, likely due to stabilisation of the π-system as shown in structure "c" which has a lower energetic barrier of 0.38 kcal mol^{-1} (Figure S3.41 and Table S3.8). Accordingly, the ^{3}**5–MA** is more easily obtained from ^{3}**[Re–EB]**$^{2-}$ at R2, and is reduced to the ^{2}**5–DA** before R3. While the ^{3}**5–MA** of **Re–H** may be obtained from the ^{3}**[Re–H]**$^{2-}$ by intramolecular electron transfer, it requires a more negative potential to do so; likely much closer to R3 where electrochemical reduction of ^{3}**[Re–H]**$^{2-}$ to the ^{2}**5–DA** occurs. The 5-coordinate dianion with a quartet spin multiplicity (^{4}**5–DA**), with all added electrons being spin unpaired, has larger calculated wavenumbers than the ^{2}**5–DA** and is not observed in the experimental data (Figure S3.44).

No further reduced species are observed in the SEC experiments in the DCM electrolyte due to its limited negative potential window. However, the **^{2}5–DA** formed at the R3 reduction wave of **Re–R** is investigated in THF. In the IR spectrum of **Re–H** collected at the R3 reduction wave (Figure 3.5A), strongly red-shifted $\nu_{C\equiv O}$ vibrations are observed at 1948 and 1844 cm^{-1} matching the A_1 + E pattern associated with a local C_{3v} symmetry due to the rotation of a Re^0 tricarbonyl unit.[72–74] Weak shoulders are observed at 1980, 1862, 1844 cm^{-1} corresponding to the **^{3}5–MA** of **Re–H**, which supports that the **^{3}5–MA** is formed at a lower potential closer to R3. The $\nu_{C\equiv O}$ vibrations are essentially unchanged compared to **^{3}[Re–H]$^{2-}$**. In the UV-Vis spectrum (Figure 3.5B), depletion of the H–NI$^{\bullet-}$ transition at 418 nm is observed, with concurrent growth of a strong electronic absorption band at 625 nm with Re^0-phen$^-$→CO_{ax} π→π* character as visualised in Figure S3.45; characteristic of the 5-coordinate active catalyst.[73,74] Similar spectral features are observed in both the IR and UV-Vis spectra at the R3 reduction wave of **Re–EB** (Figure 3.6). Two strongly red-shifted $\nu_{C\equiv O}$ bands are observed at 1950 and 1845 cm^{-1} with a local C_{3v} symmetry, with residual $\nu_{C\equiv O}$ bands from **^{3}[Re–EB]$^{2-}$** and **^{3}5–MA** apparent in this spectrum. A strong π→π* (Re^0–phen$^-$) electronic absorption at 620 nm in the UV-Vis spectrum is observed together with the depleted EB–NI$^{\bullet-}$ transitions at 443 and 509 nm. TDDFT calculations of the **^{3}5–MA** of **Re–EB** reveal that the HOSOs are localised on EB–NI$^-$, with LUSOs reducible on the Re–phen$^-$ metallacycle (Figure S3.47). Therefore, reduction of **^{3}[Re–R]$^{2-}$** with concomitant Cl^- dissociation at R3 reduction, or reduction of **^{3}5–MA** before R3, produces the [$Re^0(CO)_3$(R–NI$^-$–phen$^-$)]$^{2-}$ complex as the **^{2}5–DA** species as the electrochemically generated active catalyst.

Presented in Figure 3.7 are the reference IR SEC experiments with **Re–R** performed in THF under a CO_2 atmosphere, with both **[Re–R]$^-$** and **^{3}[Re–R]$^{2-}$** being observed. At more negative potentials, significant CO gas evolution is observed in the OTTLE cell preventing further monitoring. New bands between 1700-1600 cm^{-1} correspond to the formation of bicarbonate species, which begins at R2 but accelerates at more negative potentials.[72,75,76] This is particularly evident in the spectra collected at an approximately 300 mV more negative potential than R2, where the absorbance of the bicarbonate species in the spectrum of **Re–EB** drastically increase (Figure 3.7B). In contrast, there is only a slight increase in the absorbance of the bicarbonate species in the spectrum of **Re–H** at a 300 mV more negative potential than R2 (Figure 3.7A); this indicates that **Re–EB** is activated at less negative potentials than **Re–H**. This is supported by the slow decrease of the $^{13}CO_2$ satellite band at R2, found at *ca.* 2330 cm^{-1}, followed by a further depletion approaching R3. These results indicate that CO_2 binding with **^{3}5–MA**, followed by intramolecular electron transfer and subsequent reduction, produces **^{2}5–DA** before R3 and reduces CO_2 to CO and bicarbonate species under electrochemical conditions.

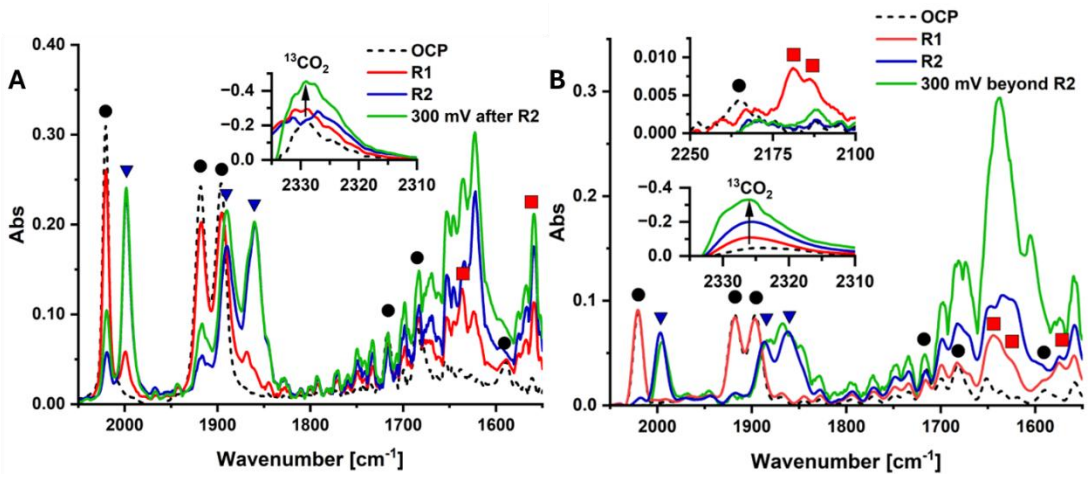
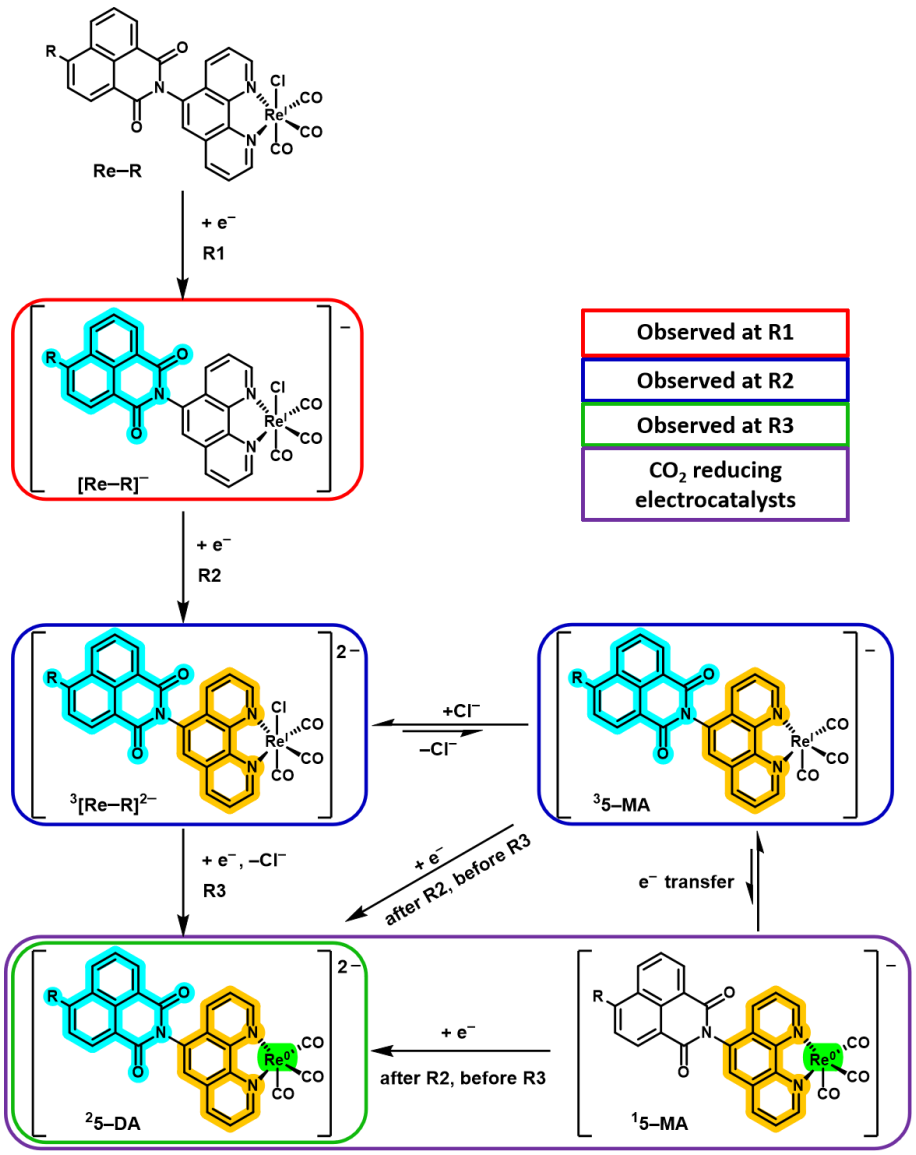


Figure 3.19. *IR spectra from SEC experiments conducted under a CO_2 atmosphere in THF electrolyte, showing the stepwise conversion of the parent complex to reduced species formed at R1 (red), R2 (blue), and R3 (green), including an inset of the $^{13}CO_2$ satellite band. A =* ***Re–H****, B =* ***Re–EB*** *with an additional inset of the C≡C stretching region. OCP = open-circuit potential, ● =* ***Re–R****, ■ =* ***[Re–R]$^{-}$****, ▼ =* ***^{3}[Re–R]$^{2-}$****.*

The absence of the **^{3}5–MA** from the IR SEC experiments under CO_2 atmosphere indicates its involvement in catalysis. However, catalysis directly from the **^{3}5–MA** is unlikely due to the Re–phen metallacycle in the **^{3}5–MA** being only singly reduced. Instead, reduction of the **^{3}5–MA** would yield the R–NI dianion, as indicated by the β-LUSO of **[Re–R]$^{2-}$** which are localised on the R–NI moiety (Figure S3.37 and S3.39), and subsequent intramolecular electron transfer to the Re–phen metallacycle induces Cl^- dissociation to give **^{2}5–DA**. Alternatively, intramolecular electron transfer from the reduced R–NI moiety of **^{3}5–MA** to the Re–phen metallacycle would produce $[Re^0(CO)_3(R–NI–phen^-)]^-$ **^{1}5–MA**. The calculated UV-Vis spectra of **^{1}5–MA** and **^{2}5–DA** in Figure S3.45 have a common π→π* transition within the {Re^0–$phen^-$} moiety at *ca.* 650 nm in both species, as shown in Figure S3.46. This transition is reported for the active 5-coordinate catalyst of other related Re(α-diimine) complexes[35,73,74,77]; a strong indication the electron density on the Re–phen metallacycle has increased sufficiently for CO_2 reduction catalysis to proceed with either **^{1}5–MA** and **^{2}5–DA**, as illustrated in Scheme 3.1.

Of the two 5-coordinate monoanions formed from **Re–R**, only **^{3}5–MA** is observed in the SEC experiments under a N_2 atmosphere due to the **^{1}5–MA** being more reactive (reducible). An equilibrium between **$^{1/3}$5–MA** is possible under these conditions leading to the gradual accumulation of the **^{2}5–DA** before R3 by reduction of the **^{1}5–MA** (Scheme 3.1). However, the absence of any **^{3}5–MA** under CO_2 indicates that CO_2 binding shifts this equilibrium in favour of **^{1}5–MA**. This may account for the catalytic activity observed between R2 and R3 during the SEC

experiments under a CO_2 atmosphere. Although the **^{1}5–MA** and **^{2}5–DA** have very similar calculated IR and UV-Vis spectra (Figure S3.44 and S3.45 and Table S3.10), they are distinguished by the region where neutral and reduced R–NI absorb. The retention of reduced R–NI features in the IR and UV-Vis absorption spectra between R2 and R3 supports **^{2}5–DA** being the active electrocatalyst. Thus, upon the formation of **^{3}5–MA** between R2 and R3, intramolecular electron transfer from reduced R–NI to the [Re–phen$^-$] metallacycle produces the **^{1}5–MA**. While **^{1}5–MA** has the prerequisite doubly reduced {Re^0–phen$^-$} metallacycle for CO_2 reduction, spontaneous reduction of the R–NI moiety yields **^{2}5–DA** as the CO_2-reducing active electrocatalyst.



Scheme 3.5. *The reduction pathway of* ***Re–R*** *under electrochemical conditions, based on the electrochemical studies conducted in this work. Note that while two possible 5-coordinate electrocatalysts are proposed, only the* ***^{2}5–DA*** *is observed in SEC studies.*

Table 3.5. *Key spectroscopic data from experimental SEC studies and supporting DFT/TDDFT calculations of* ***Re–R*** *and their reduced forms in DCM and THF electrolyte solutions.*

Compound	Solvent	UV-Vis SEC		IR SEC					
		λ_{max} (nm)	λ_{max} (calc.) (nm)	$\nu_{C\equiv O}$ (cm^{-1})	$\nu_{C\equiv O}$ (calc.)[a] (cm^{-1})	$\nu_{C=O}$ (cm^{-1})	$\nu_{C=O}$ (calc.)[a] (cm^{-1})	$\nu_{C\equiv C}$ (cm^{-1})	$\nu_{C\equiv C}$ (calc.)[a] (cm^{-1})
Re–H	DCM	269, 339, 382	353	2025, 1921, 1901	2019, 1911, 1887	1715, 1682	1710, 1666	–	–
	THF	336, 377	–	2020, 1918, 1896	–	1715, 1682	–	–	–
[Re–H]$^-$	DCM	417, 488	400	2022, 1916, 1897	2014, 1901, 1882	1636, 1623	1646, 1617	–	–
	THF	418, 490	–	2020, 1917, 1896	–	1637, 1621	–	–	–
^{3}[Re–H]$^{2-}$	DCM	287, 457, 580	299, 606	1998, 1893, 1869	1984, 1857, 1838	1636, 1623	1631, 1612	–	–
	THF	301, 491, 580	–	1997, 1888, 1862	–	1631, 1622	–	–	–
^{3}5–MA of Re–H	DCM	313, 454, 578	300, 395, 830	1989, 1869, 1846	1967, 1848, 1839	1636, 1624	1636	–	–
	THF	301, 491, 586	–	1980, 1862, 1844	–	1631, 1622	–	–	–
^{2}5–DA of Re–H	THF	307, 362, 626	305, 390, 670	1948, 1844	1936, 1812, 1807[b]	1631, 1622	1635	–	–
Re–EB	DCM	270, 385	446	2023, 1920, 1901	2019, 1911, 1887	1712, 1676	1710, 1666	2207	2254
	THF	269, 378	–	2021, 1918, 1896	–	1715, 1682	–	2204	–
[Re–EB]$^-$	DCM	441, 488	427, 502	2022, 1915, 1899	2014, 1901, 1882	1640, 1623	1646, 1617	2158, 2140	2181
	THF	440, 491	–	2021, 1917, 1896	–	1642, 1626	–	2156, 2143	–
^{3}[Re–EB]$^{2-}$	DCM	289, 430, 506	427, 508	1997, 1889, 1862	1980, 1852, 1842	1656, 1621	1631, 1612	–[c]	2176
	THF	301, 443, 509	–	1999, 1887, 1868	–	1622	–	–[c]	–
^{3}5–MA of Re–EB	DCM	304, 430, 539	325, 495, 820	1983, 1858, 1842	1968, 1849, 1840	1656, 1621	1642, 1635	–[c]	2230
	THF	301, 443, 585	–	1985, 1866, 1848	–	1622	–	–[c]	–
^{2}5–DA of Re–EB	THF	312, 426, 620	340, 505, 650	1950, 1848	1937, 1814, 1808[b]	1620	1641, 1633	–[c]	2225

[a]The calculated values were multiplied by a 0.983 proportionality factor.[78] [b]The multiplication of the DFT data by 0.983 is not needed here because of the strongly delocalised π-bonding in the 2e$^-$ reduced Re^0–phen$^-$ metallacycle that does not change the dipole moment upon electronic excitation (Figure S3.46). [c]No IR $\nu_{C\equiv C}$ bands are observed.

3.4.3 TRIR Spectroscopy

TRIR spectroscopic investigations were performed on both **Re–R** complexes to establish their excited-state dynamics in the electrolyte solutions, with 420-nm excitation used to replicate the photocatalytic conditions (λ_{irr} = 450 ± 50 nm) used later in this study. For both **Re–R** complexes, the excitation at 420 nm populates the ^{3}MLCT excited state in both complexes, and for **Re–EB** it also directs to the EB–NI→NI π→π* ILCT transition. The results obtained in the THF electrolyte are briefly outlined below, though similar excited-state dynamics were observed in the ps-TRIR spectra collected in DCM electrolyte prepared in this work (Figures S3.13 and S3.14) and in studies previously reported in organic solvents.[36]

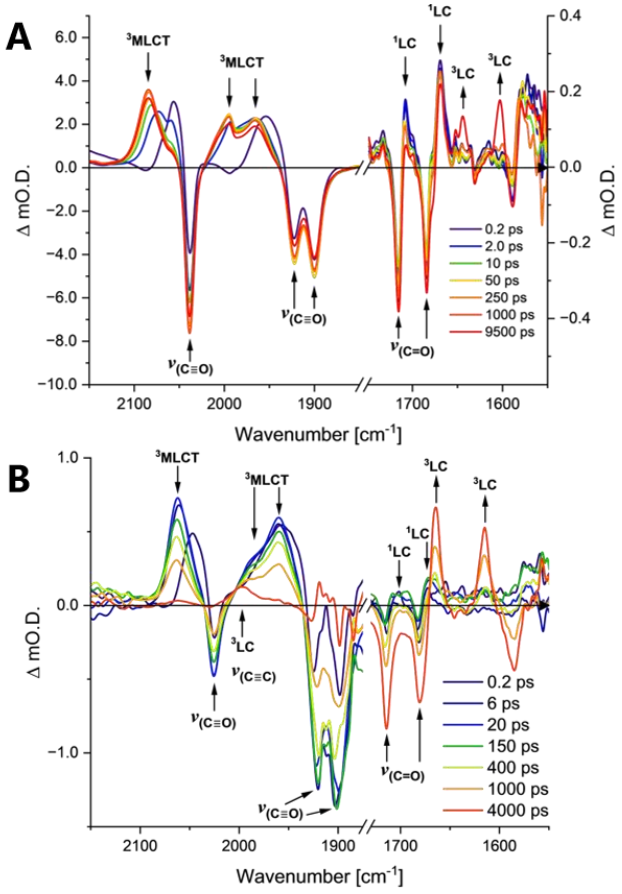


Figure 3.20. *TRIR spectra collected in the THF electrolyte following optical excitation at 420 nm of (A)* ***Re–H*** *and (B)* ***Re–EB****.*

Excitation of **Re–H** (Figure 3.8A) initially populates a vibrationally hot-^{3}MLCT excited state within the laser pulse (<0.2 ps) with $\nu_{C\equiv O}$ at 2058 and 1954 cm^{-1}.[79] Subsequent vibrational cooling yields

the ^{3}MLCT excited state with $\nu_{C\equiv O}$ at 2084, 1995 and 1965 cm^{-1}, in agreement with the literature for other Re^{I}(α-diimine) complexes, and is assigned to the ^{3}MLCT excited state.[80–82] Weak $\nu_{C=O}$ transient bands at 1708 and 1669 cm^{-1}, attributed to the ^{1}LC excited state were also evident. At longer time delays (from τ > 1 ns), new bands formed ($\nu_{C=O}$ = 1644 and 1603 cm^{-1}) and were assigned to the ^{3}LC excited state.[22] In the ps-TRIR spectrum of **Re–EB** (Figure 3.8B), excitation results in population of both the ^{3}MLCT ($\nu_{C\equiv O}$ = 2062, 1985, 1960 cm^{-1}) and the ^{1}LC ($\nu_{C=O}$ = 1702 and 1672 cm^{-1}) excited states. The reduced solubility of **Re–EB** in THF electrolyte inhibited the detection of the ^{1}LC $\nu_{C\equiv C}$ transient bands. However, a $\nu_{C\equiv C}$ band at 2110 cm^{-1}, associated with the ^{1}LC excited state, is observed in the DCM electrolyte (Figure S3.15). The bands assigned to the ^{3}MLCT and ^{1}LC excited states decayed (τ of 2.2 ns) with concomitant population of the ^{3}LC excited state ($\nu_{C=O}$ = 1664 and 1615 cm^{-1} and $\nu_{C\equiv C}$ = 1997 cm^{-1}), with the ^{3}LC excited state persisting on the microsecond timescale.[36]

3.4.4 Time-Resolved Infrared Spectroelectrochemical Studies

The TRIR SEC studies were conducted on the reduced species of **Re–R** to determine the character of the populated excited state(s), and their lifetimes, following excitation at 420 nm to replicate the photocatalytic conditions used later in this study. The rationale for this study is that the reduced species formed under these pseudo-photocatalytic conditions can provide additional insights into the photoreduced species involved in the pathway leading to the active catalyst. The same excitation source (420 nm) as used in the TRIR studies is used to excite the **[Re–R]**$^-$ and **[Re–R]**$^{2-}$ species owing to the presence of absorption features in this region as confirmed in the UV-Vis SEC studies discussed previously (Figures 3.5 and 3.6). Specifically, both Re→phen MLCT and H–NI$^{\bullet-}$→phen π→π* ILCT transitions are populated by excitation of **[Re–H]**$^-$, while the Re→phen MLCT and H–NI$^{\bullet-}$-based π→π* LC transitions are populated by excitation of **[Re–EB]**$^-$. The TRIR spectra were collected in THF electrolyte, while later in this work DMF is used as the solvent in photocatalytic studies, as is the norm.[83] However, the TRIR spectra of **EB–NI–phen**, **Re–R** and **[Re–R]**$^-$ in the DCM electrolyte, presented in Figures S3.13–S3.17, displayed similar excited-state dynamics as those measured in THF electrolyte. The kinetic traces from all TRIR spectra are provided in Figures S3.18–S3.25. The transient features observed in the TRIR spectra of **Re–R**, **[Re–R]**$^-$, and **[Re–R]**$^{2-}$ are summarised in Table 3.3.

Table 3.6. *Transient bands of the **Re–R** complexes and their reduced species from TRIR/TRIR SEC experiments in DCM and THF electrolytes.*[a,b]

Complex	^{3}MLCT/^{4}MLCT $\nu_{C\equiv O}$ (cm^{-1})	^{4}ILCT$\nu_{C\equiv O}$ (cm^{-1})	$\nu_{C=O}$ (cm^{-1})	$\nu_{C\equiv C}$ (cm^{-1})
Re–H	2060, 1988, 1964	–[c]	1705, 1665[d]	–[c]
	[2084, 1995, 1965]	[–][c]	[1708, 1669][d]	[–][c]
[Re–H]$^-$	2061, 1964, 1954	2001, 1868	–[c]	–[c]
	[2074, 1975, 1957]	[2002, 1872, 1849]	[1628, 1610]	[–][c]
^{3}[Re–H]$^{2-}$ [e]	[–][c]	[1993, 1838]	[1611]	[–][c]
Re–EB	2065, 1990, 1964	–[c]	1698, 1662[d]	2114, 1997
	[2062, 1985, 1960]	[–][c]	[1702, 1672][d]	[–][c]
[Re–EB]$^-$	2060, 1980, 1954	2001, 1870	–[c]	–[c]
	[2058, 1973, 1958]	[1996][f]	[1633, 1610]	[–][c]

[a]*All GSBs are in good agreement with the calculated and experimental spectra of the corresponding complex (see Table 3.2).* [b]*All $\nu_{C\equiv O}$, $\nu_{C=O}$, and $\nu_{C\equiv C}$ values from experiments in THF electrolyte solutions are given in square brackets.* [c]*No transient bands associated with that vibrational mode/excited state are observed.* [d]*The $\nu_{C=O}$ values for **Re–R** are given for the ^{1}LC excited state, which is populated concurrently with the ^{3}MLCT excited state for which the $\nu_{C\equiv O}$ values are reported.* [e]*The **[Re–H]$^{2-}$** complex is only studied in the THF electrolyte.* [f]*Only the high frequency transient is captured within the experimental window.*

Following excitation of **[Re–H]$^-$**, ground-state bleaches (GSBs) of the $\nu_{C\equiv O}$, $\nu_{C=O}$, and $\nu_{C\equiv C}$ vibrations occurred within the laser pulse (Figure 3.9); the GSBs closely match the experimental IR spectra observed in the IR SEC studies of **Re–R** (Table 3.2) and the associated DFT-calculated IR spectra (Figures S3.26A and S3.27A). Several new $\nu_{C\equiv O}$ transient features are formed concurrently and are attributed to the population of two excited states. One group of $\nu_{C\equiv O}$ transient bands are shifted to higher wavenumber compared to the GSBs ($\nu_{C\equiv O}$ = 2058 and 1954 cm^{-1}), similarly to the vibrationally hot ^{3}MLCT transient bands observed in the TRIR spectra for **Re–H** (Figure 3.8A). These blue-shifted bands underwent vibrational cooling resulting in new bands at 2075, 1975, and 1954 cm^{-1}; resembling the local C_s symmetry of fac-$Re(CO)_3$ in a pseudo-octahedral

environment, similar to the bands for the ^{3}MLCT excited state observed in the TRIR spectra of **Re–H**. Accordingly, the bands at 2075, 1975, and 1954 cm^{-1} are attributed to a Re→phen ^{4}MLCT excited state. The transient bands at lower wavenumber, 2002, 1872, and 1849 cm^{-1}, are assigned to a [H–NI]$^-$→phen π→π* ^{4}ILCT excited state. The ^{4}ILCT transient bands exhibit similar stretching wavenumber as the IR spectrum of **^{3}[Re–H]$^{2-}$** ($\nu_{C\equiv O}$ = 1989, 1869, and 1846 cm^{-1}) previously observed in the IR SEC experiment coinciding with the phen-localised R2 reduction wave.

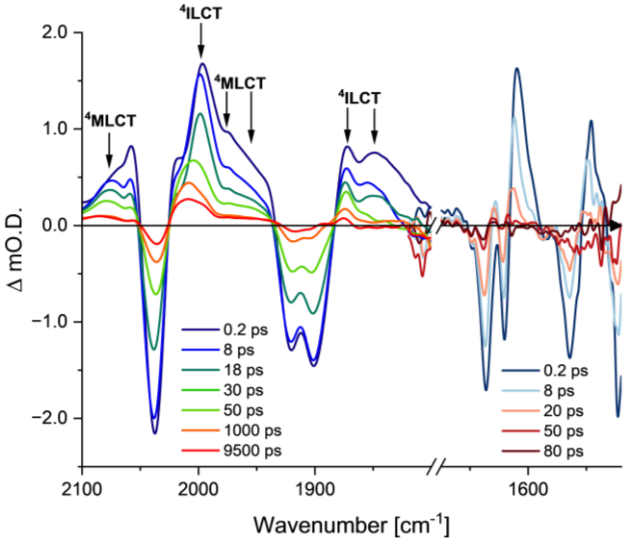


Figure 3.21. *TRIR spectrum of* ***[Re–H]$^-$*** *in the THF electrolyte following optical excitation at 420 nm. The rainbow sweep covers the $\nu_{C\equiv O}$ region over full experimental timescale (0.2 – 9500 ps). The blue/red sweep covers the $\nu_{C=O}$ region on a different timescale (0.2 – 80 ps).*

The TRIR spectra of **[Re–H]$^-$** collected in DCM electrolyte (Figure S3.16) displayed similar $\nu_{C\equiv O}$ transient bands; with the bands at higher wavenumber assigned to the ^{4}MLCT excited state, while those at lower wavenumber are assigned to the ^{4}ILCT excited state. All $\nu_{C\equiv O}$ transient bands persisted beyond the runtime of this experiment (>9.5 ns). Notably, in the DCM electrolyte no new $\nu_{C=O}$ bands are observed. However, two $\nu_{C=O}$ GSBs are observed at 1636 and 1620 cm^{-1} in the THF electrolyte that formed within the laser pulse, with one $\nu_{C=O}$ transient band at 1609 cm^{-1} that has a similar ΔmO.D. as the $\nu_{C\equiv O}$ transient bands. Recent TRIR studies have shown that excited states impacting the strength of C≡X bonds (where X = C, N, or O) frequently result in a significant enhancement in intensity of these vibrational responses[84–90]; a similar process may account for the observed enhancement of the $_{C\equiv O}$ transient bands in this work. The transient band at 1609 cm^{-1} decayed to the baseline with a τ of 14 ps. This feature may be evidence for

the initial population of a NI^{-}-based ^{2}LC excited state, formed within the laser pulse, which undergoes rapid electron exchange with the phen moiety to populate the ^{4}ILCT [H–NI]$^{-}$→phen π→π* excited state. Electron-exchange based Dexter-like doublet-triplet energy transfer (DTET) has previously been reported for radical-chromophore systems where excitation of a stable π-radical can be used to populate a covalently linked acceptor.[55,56] **[Re–H]$^{-}$** , consisting of the H–NI$^{\bullet-}$ and Re–phen moieties, closely resembles such a radical-chromophore system. However, no observed spectral changes in the ^{4}ILCT $\nu_{C\equiv O}$ transient bands coincide with the decay of the 1609 cm^{-1} transient band and this does not account for the absence of $\nu_{C=O}$ features in DCM. While an interesting observation, we do not believe this has an effect on photocatalysis and so is not discussed further.

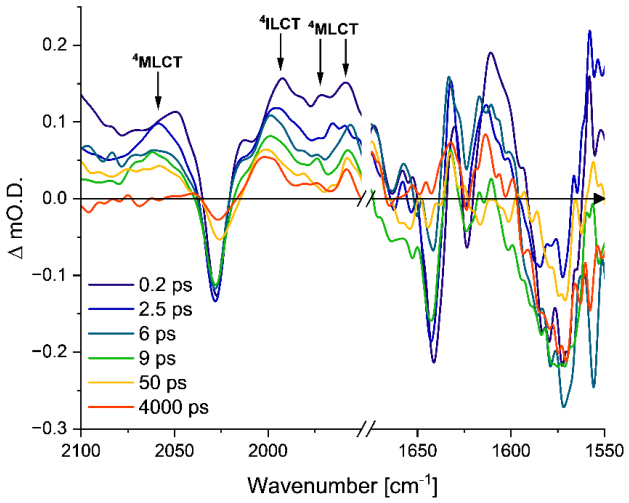


Figure 3.22. *TRIR spectrum of* ***[Re–EB]$^{-}$*** *in the THF electrolyte following optical excitation at 420 nm.*

Excitation of **[Re–EB]$^{-}$** leads to GSBs and new transient bands in the TRIR spectrum (Figure 3.10); however, poor solubility of **[Re–EB]$^{-}$** in the THF electrolyte resulted in small ΔmO.D. values for all transient features. Similarly to the TRIR SEC experiment for **[Re–H]$^{-}$**, the $\nu_{C\equiv O}$ transient bands corresponding to the population of two species are observed following excitation of **[Re–EB]$^{-}$**. A vibrationally hot ^{3}MLCT-like excited state is formed within the laser pulse with $\nu_{C\equiv O}$ transient bands at 2053 and 1954 cm^{-1}; which subsequently underwent vibrational cooling to a ^{4}MLCT excited state with $\nu_{C\equiv O}$ at 2060, 1969, and 1954 cm^{-1}. The lower frequency $\nu_{C\equiv O}$ transient band assigned to the ^{4}ILCT excited state were observed at 1996 cm^{-1} (the other ILCT vibrational modes were not captured within the spectroscopic window) and have similar wavenumber to the bands

in the IR spectrum of ^{3}**[Re–EB]**$^{2-}$ associated with the phen-based R2 reduction wave in the IR SEC studies (Table 3.2). Similar $\nu_{C\equiv O}$ spectral features are also observed in the DCM electrolyte (Figure S3.17). The improved separation of the R1 and R2 reduction waves for **Re–EB** compared to those of **Re–H** facilitated complete reduction to the **[Re–EB]**$^{-}$ species. This confirms that population of a MLCT excited state does not arise from excitation of unreduced **Re–R**, thereby verifying that concurrent population of the ^{4}MLCT and ^{4}ILCT excited states is possible upon 420 nm irradiation of both **[Re–R]**$^{-}$ complexes. Similarly to **[Re–H]**$^{-}$, only the TRIR spectra collected in THF electrolyte displayed $\nu_{C=O}$ GSBs at 1641 and 1623 cm^{-1}, and $\nu_{C=O}$ transient bands at 1633 and 1610 cm^{-1}. All $\nu_{C=O}$ bands decayed to the baseline with a τ of 4 ps, which is faster than the lifetime obtained for the $\nu_{C=O}$ transient band of **[Re–H]**$^{-}$ at 1609 cm^{-1} (τ = 14 ps). No vibrations associated with the C≡C bond were observed for **[Re–EB]**$^{-}$ in either electrolyte.

Table 3.7. *Excited state lifetimes from TRIR studies of **Re–R** and TRIR SEC studies of **[Re–R]**$^{-}$ following excitation at 420 nm in the DCM electrolyte.*

Complex	MLCT $\nu_{C\equiv O}$ probe ~2060 cm^{-1}		ILCT $\nu_{C\equiv O}$ probe ~2000 cm^{-1}
	τ_1 [ps]	τ_2 [ps]	τ_1' [ps]
^{3}**Re–H**	2.7	> 9500	–
^{4}**[Re–H]**$^{-}$	33.0	> 9500	> 9500
^{3}**Re–EB**	4.9	2500	–
^{4}**[Re–EB]**$^{-}$	26.7	3000	> 9500

*τ_1 is attributed to vibrational cooling of the hot-^{3}MLCT/^{4}MLCT excited states. τ_2 is attributed to the decay of the ^{3}MLCT/^{4}MLCT excited states. τ_1' is attributed to the decay of the ^{4}ILCT excited state and so is only reported for the **[Re–R]**$^{-}$ complexes.*

The lifetimes obtained for the ^{4}MLCT and ^{4}ILCT $\nu_{C\equiv O}$ species for both **[Re–R]**$^{-}$ complexes were obtained in DCM (Figure 3.11 and Table 3.4). Two lifetimes are obtained for the ^{4}MLCT vibrational mode ($\nu_{C\equiv O}$ ≈ 2060 cm^{-1}) of both **[Re–R]**$^{-}$ complexes. The τ_1 of 26.7 and 33.0 ps (for **[Re–H]**$^{-}$ and **[Re–EB]**$^{-}$, respectively) arises from vibrational cooling of the vibrationally hot ^{4}MLCT excited state in both complexes. The τ_2 arises from the decay of ^{4}MLCT excited state in both **[Re–R]**$^{-}$ complexes. For **[Re–H]**$^{-}$, the τ_2 is greater than the runtime of this experiment (>9500 ps) and appears similar to the decay of the analogous ^{3}MLCT transient band in the TRIR spectrum of **Re–**

H (Figure 3.8A). For **[Re–EB]**$^{-}$, a τ_2 of 3000 ps is obtained for the decay of the ^{4}MLCT transient band; this lifetime is very similar to the τ_2 of 2500 ps for the analogous ^{3}MLCT transient band in the TRIR spectrum of **Re–EB** (Table 3.4). The ^{4}ILCT vibrational mode ($\nu_{C\equiv O} \approx 2000$ cm^{-1}) for both **[Re–R]**$^{-}$complexes persisted beyond the 9500 ps timeframe of these experiments.

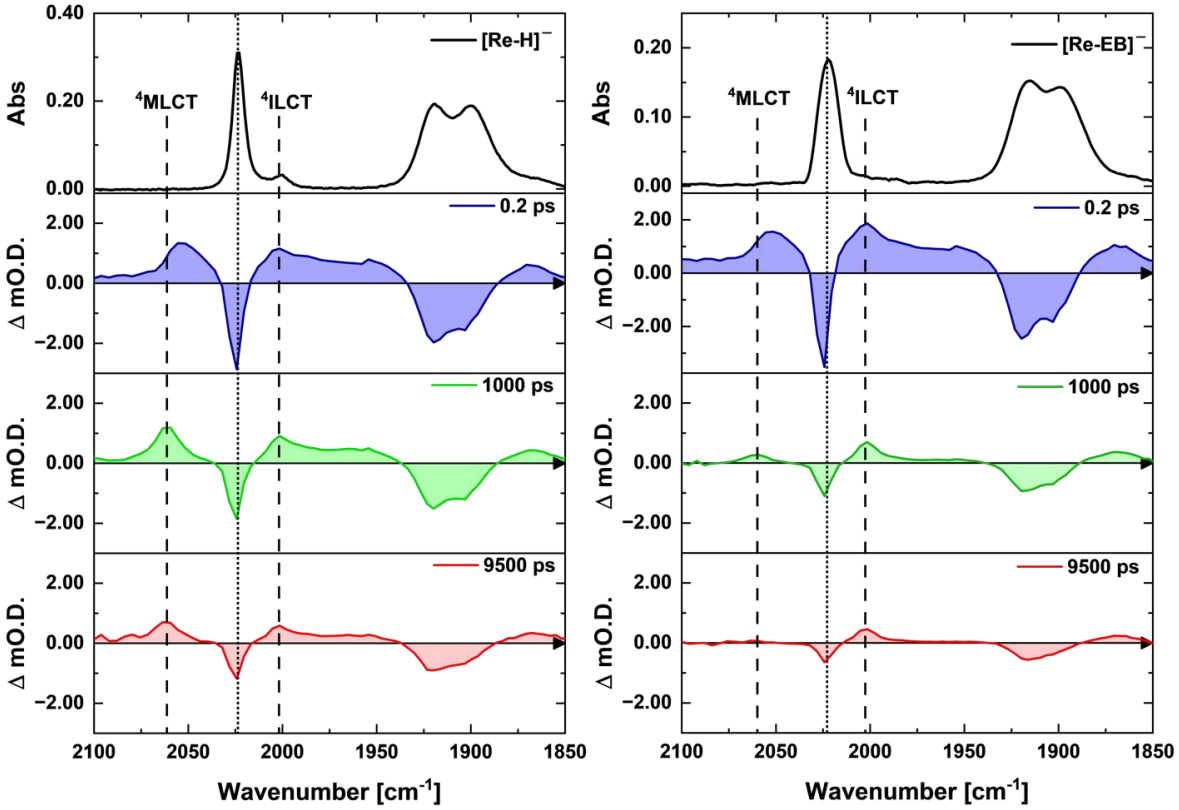


Figure 3.23. *The TRIR spectra at 0.2, 1000, and 9500 ps following 420 nm excitation and the FTIR spectra in the DCM electrolyte of (left)* ***[Re–H]***$^{-}$ *and (right)* ***[Re–EB]***$^{-}$.

Accordingly, the excited state dynamics of the **[Re–R]**$^{-}$ complexes can be summarised as follows. Upon photoexcitation, electron density is redistributed towards the phen moiety via two distinct excited-state pathways. Re^{I}→Re^{II} photooxidation results in the ^{4}MLCT excited state, analogous to the ^{3}MLCT excited state of **Re–R**, giving rise to the low-spin d^5 [Re^{II}(R–NI^{-}–phen^{-})(CO)$_3$Cl]$^{-}$ species. The ^{4}MLCT excited-state species resembles **^{3}[Re–R]$^{2-}$** observed in the SEC studies (Table 3.2), with the added electrons localised on the NI and phen moieties. A major difference is the formation of a Re^{II} metal centre following excitation that can undergo reductive quenching in the presence of a sacrificial electron-donor under photocatalytic conditions.[91] Concurrently, excitation of the NI-based electron of **[Re–R]**$^{-}$ yields a ^{2}LC excited state localised on [R–NI]$^{-}$. This photoexcited electron can exchange with an electron on the phen moiety via DTET[55,56], ultimately

resulting in the population of the [R–NI]$^{-}$→phen ^{4}ILCT excited state. The resulting [Re^{I}(R–NI–phen^{-})(CO)$_3$Cl]$^{-}$ excited-state species is analogous to the radical anionic [Re(α-diimine^{-})(CO)$_3$Cl]$^{-}$ complexes that have previously been reported as the precursors to the active catalyst.[68]

Interestingly, the [H–NI]$^{-}$→phen ^{4}ILCT excited state resembles the intramolecular electron transfer step from [H–NI]$^{-}$ to phen, as proposed in the reduction pathway for **^{1}5–MA** from the **^{3}5–MA** (as shown in Scheme 3.1). While the formation of a **5–MA** species from the ^{4}ILCT excited state is unlikely, population of a similar ILCT excited state in **^{3}[Re–R]$^{2-}$** supports formation of **^{1}5–MA** from the **^{3}5–MA** under photocatalytic conditions. For **[Re–EB]$^{-}$**, the shorter ^{4}MLCT lifetime of 3 ns allows for the redistribution of electron density towards the phen moiety to be dominated by the ^{4}ILCT excited state at longer time intervals. Therefore, formation of **^{1}5–MA** from the **^{3}5–MA** under photocatalytic conditions may be more accessible for **Re–EB** than for **Re–H**.

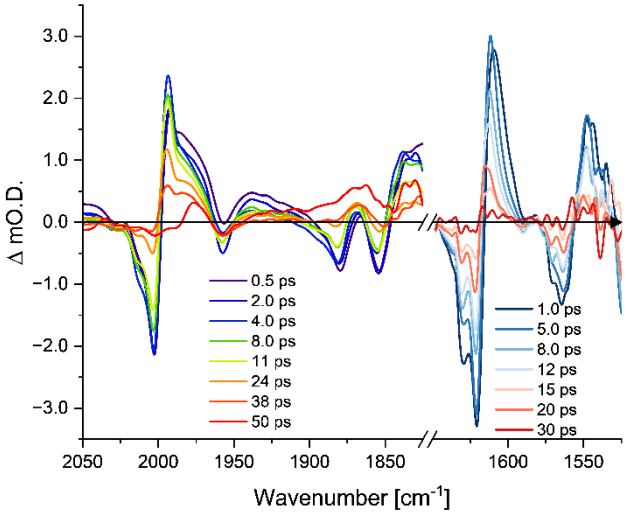


Figure 3.24. *The TRIR spectra of* ***^{3}[Re–H]$^{2-}$*** *in the THF electrolyte following 420 nm excitation. The rainbow sweep covers the* $\nu_{C\equiv O}$ *region, the blue/red sweep covers the* $\nu_{C=O}$ *region.*

The TRIR spectra collected at R2 of **Re–H** (Figure 3.12) displayed $\nu_{C\equiv O}$ and $\nu_{C=O}$ GSBs that correspond to **^{3}[Re–H]$^{2-}$** as observed in the IR SEC experiment (Figure 3.5). The $\nu_{C=O}$ region closely resembles that observed during the the TRIR SEC experiments of **[Re–H]$^{-}$**; and as such is assigned to a short-lived LC excited state localised on the R–NI^{-} moiety (τ = 14 ps). Additionally, $\nu_{C\equiv O}$ transient bands at 1993 and 1838 cm^{-1} reveal the population of a short-lived [H–NI]$^{-}$→[Re–phen^{-}] partial ligand-to-metal charge transfer (LMCT) excited state (τ = 22 ps). The assignment of [H–NI]$^{-}$-based LC and [H–NI]$^{-}$→[Re–phen^{-}] LMCT excited states are supported by TDDFT calculations of the **^{3}[Re–H]$^{2-}$** complex, showing that the α-HOSO–1 orbital involved in the transition excited

at 420 nm is localised on the [H–NI]$^{-}$moiety while the α-LUSO+11 and α-LUSO+12 are distributed on the H–NI moiety and the Re(CO)$_3$ moiety, involving increased density on the axial Re-CO bond (Figures S3.36 and S3.37 and Table S3.5).

The LMCT excited state of **^{3}[Re–H]$^{2-}$** resembles the [H–NI]$^{-}$→phen ^{4}ILCT excited state observed in the TRIR spectrum of **[Re–H]$^{-}$** (Figure 3.8). However, the partial LMCT excited state of **^{3}[Re–H]$^{2-}$** is short-lived (τ = 22 ps) due to the presence of the phen^{-} moiety, which impedes electron redistribution towards the Re metal centre. Although a GSB is observed at 1957 cm^{-1}, which indicates limited formation of a 5-coordinate species, it is unclear if it is formed photochemically or due to a slight overreduction during the TL-CV scan. Consequently, it is not possible to determine if the GSB at 1957 cm^{-1} can be assigned to the **^{1}5–MA** or **^{2}5–DA**; especially since they have very similar IR spectra based on their calculated IR modes being within 10 cm^{-1} of each other (Table S3.10).

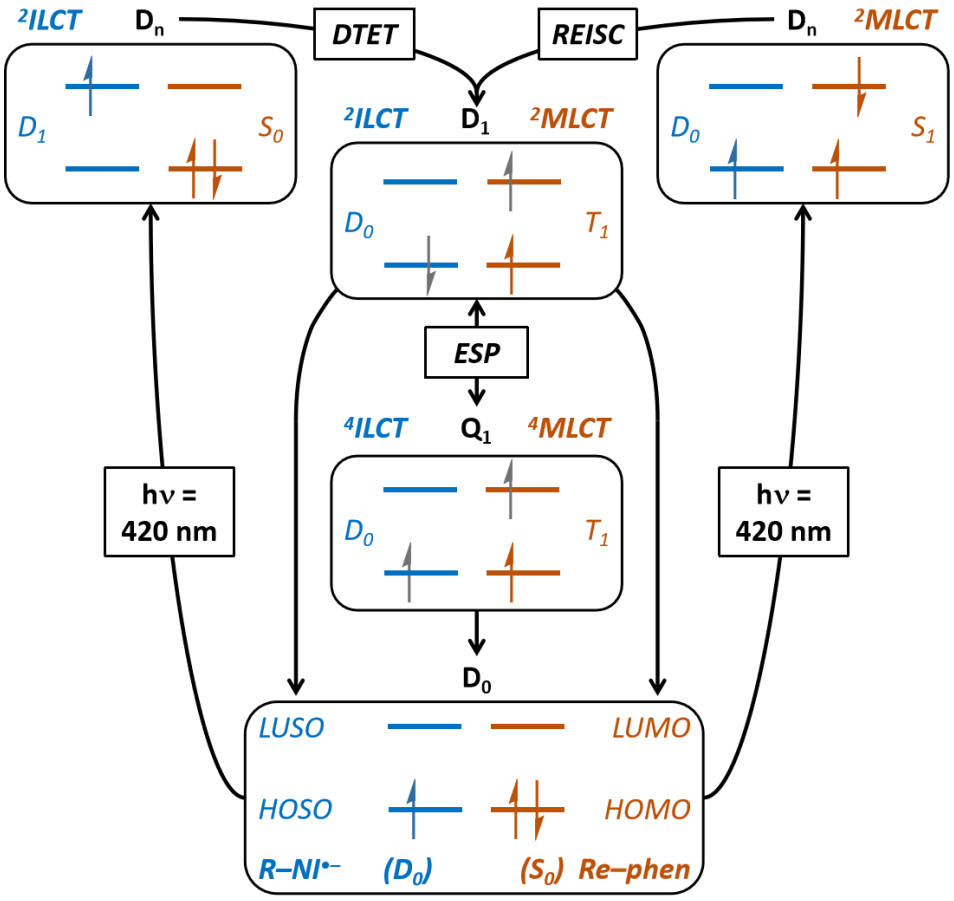
3.4.5 [Re–R]$^{-}$ as a Radical-Chromophore System

The excited-state dynamics of the **[Re–R]$^{-}$** complexes were studied by TRIR SEC and supported by quantum chemical calculations as described in the previous section. Importantly, the results demonstrate that it is possible to simultaneously excite both the chromophore, [Re(phen)(CO)$_3$Cl], and the radical, R–NI$^{\bullet-}$, in **[Re–R]$^{-}$** at 420 nm. This leads to the concurrent population of two excited states as observed in the TRIR SEC studies. The proposed excited-state dynamics of **[Re–R]$^{-}$** are illustrated in Scheme 3.2 and are described below.

Excitation of [Re(phen)(CO)$_3$Cl] initially results in population of the ^{1}MLCT excited state locally on the chromophore, which corresponds to the ^{2}MLCT excited state of the whole **[Re–R]$^{-}$** complex. Subsequent population of the local ^{3}MLCT excited state proceeds via REISC in the presence of the appended R–NI$^{\bullet-}$.[44,45] The ^{2}MLCT excited state of **[Re–R]$^{-}$** complex, persists as the trip-doublet configuration upon REISC. The ^{4}MLCT excited state of **[Re–R]$^{-}$** has a similar profile to that of the ^{3}MLCT excited state observed upon excitation of **Re–R** (Figures 3.8 – 3.10), supporting the hypothesis that a local ^{3}MLCT excited state is present on the [Re(phen)(CO)$_3$Cl] chromophore in both **[Re–R]$^{-}$** complexes.

Separately and simultaneously, excitation of R–NI$^{\bullet-}$ populates the doublet ligand centred (^{2}LC) excited state locally, which coincidentally is also the ^{2}LC excited state for the 'whole' **[Re–R]$^{-}$** complex. The unstable configuration of the ^{2}LC excited state decays by way of two possible pathways; it either undergoes ground-state recovery from the ^{2}LC excited state, or DTET with the

phen moiety of the [Re(phen)(CO)$_3$Cl] chromophore.[42,55] In the TRIR spectra of **[Re–R]$^-$** the red-shifted $\nu_{C\equiv O}$ transient bands are attributed to an R–NI$^{\bullet-}$→phen ^{4}ILCT excited state; this indicates that there is limited ground-state recovery from the ^{2}LC excited state. The ^{2}ILCT excited state has the same trip-doublet configuration as the ^{2}MLCT excited state, with a D_0 ground state on the radical and a T_n excited state on the chromophore most likely localised on the phen moiety.



Scheme 3.6. *The excited state dynamics of the* ***[Re–R]$^-$*** *radical-chromophore upon excitation of the radical (blue) and chromophore (red) moieties, as determined from TRIR SEC studies. Spin-state diagrams of each excited state are included; Blue = R–NI$^{\bullet-}$ electrons, Red = Re–phen electrons, Grey = electrons originating from Re–phen or R–NI$^{\bullet-}$ for the ^{4}MLCT and ^{4}ILCT excited states, respectively. The relative energies of the HOMO and HOSO, and the LUMO and LUSO, do not reflect the relative energies in the* ***[Re–R]$^-$*** *complexes.*

Accordingly, 420 nm excitation of **[Re–R]$^-$** proceeds via two excited state pathways leading to population of near-identical trip-doublet excited states, but their character is distinguished by the origin of the excited-state electron; for the ^{2}MLCT excited state this electron originates from the [Re(phen)(CO)$_3$Cl] chromophore and for the ^{2}ILCT excited state this electron originates from

the R–NI$^{\bullet-}$ radical. Hereafter, the excited-state pathways converge, and the following excited state processes apply to both ^{2}MLCT and ^{2}ILCT excited states. The ^{4}MLCT and ^{4}ILCT excited states are subsequently populated by ESP, involving a spin-flip of the radical-based valence electron.[47,48] Vibrational cooling of the hot ^{4}MLCT excited-state lifetimes of **[Re–R]**$^-$ ($\tau \approx 30$ ps) may be longer than for the hot ^{3}MLCT excited-state lifetime of **Re–R** ($\tau \approx 2$–5 ps) due to a contribution from interconversion or equilibration between the trip-doublet and trip-quartet states in **[Re–R]**$^-$. An interconversion or equilibration process between D_n and Q_n excited states over a 80 ps time range has been reported in oxoverdazyl-perylene radical-chromophores.[50]

The relatively long excited lifetimes attributed to the ^{4}MLCT and ^{4}ILCT excited states (see Table 4) mostly likely arise from the trip-quartet excited states, which are only depopulated by spin-forbidden transitions ($Q_1 \rightarrow D_0$ or $Q_1 \rightarrow D_1$). While ground-state recovery can occur by a $Q_1 \rightarrow D_0$ transition, the main pathway likely proceeds from the trip-doublet ^{2}MLCT and ^{2}ILCT excited states via the spin-allowed $D_1 \rightarrow D_0$ transition. Accordingly, the TRIR SEC studies and the supporting quantum chemical calculations presented within this chapter were able to identify the character of the excited states and reasonable assignments of the spin multiplicities are proposed in accordance with the literature of radical-chromophore systems.

3.4.6 Photocatalytic Studies

Photocatalytic studies focused on detecting the conversion of CO_2 to CO, with key results presented in Table 3.5. UV-Vis absorbance-difference spectra of the **Re–R** complexes under photocatalytic conditions (0.1 mM **Re–R** in a DMF/TEOA (5:1 v/v) solution, with λ_{irr} = 450 nm) were collected over a 24 h period (Figure S3.48). Note that in the IR SEC and TRIR SEC studies, DMF was not used due to potential interference in the $\nu_{C=O}$ region in those experiments.

In the absorbance-difference spectra of **Re–H** (Figure S3.48A), a negative feature at λ_{max} = 353 nm, attributed to the depletion of the NI-based $n \rightarrow \pi^*$ and $\pi \rightarrow \pi^*$ transitions, reached a maximum after 5 min. Simultaneously, the formation of the **[Re–H]**$^-$ species with a increasing absorption at λ_{max} = 432 nm assigned to the NI radical anion in the **[Re–H]**$^-$ complex (Table 3.2). After 10 mins this band underwent a blue shifted to 423 nm and decreased in absorbance. Concurrently, a new band grew in with a λ_{max} at 579 nm and is assigned to **^{3}[Re–H]$^{2-}$**, based on the similarity of the spectral profile with that discussed previously in the UV-Vis SEC experiment (Table 3.2).

In the absorbance-difference spectra of **Re–EB** (Figure S3.48B), a depletion at 380 nm (NI π→π* transition) is evident within 10 s of the onset of irradiation. Simultaneously, new bands formed at 440 and 485 nm, closely matching the UV-Vis spectrum of **[Re–EB]**$^{-}$ in the SEC experiments (Table 3.2). After 1 minute, these features decayed with a new band at 573 nm, assigned to the formation of ^{3}**[Re–EB]**$^{2-}$ based on the similar spectral profile observed in the UV-Vis SEC studies (Table 3.2).

The continual growth (over 2 hours) of the bands assigned to the ^{3}**[Re–R]**$^{2-}$ complexes in the photocatalysis experiments indicates that the Cl^{-} dissociation step to yield the $^{1/3}$**5–MA**, is likely the rate limiting step in the pathway leading to the formation of the active catalyst. Previously, Cl^{-} dissociation from $[Re^{I}(\alpha\text{-diimine}^{\bullet})(CO)_3Cl]^{-}$ complexes has been reported to be slower than other processes in the photocatalytic cycles for CO_2 reduction.[72,80,92] Müller et al. also showed that it is not possible to exactly distinguish between the spectra of other reduction adducts related to the $[Re^{I}(\alpha\text{-diimine}^{\bullet})(CO)_3Cl]^{-}$ complex, including the DMF-solvated adduct and the TEOA/CO_2-bound adducts.[17] The calculated IR and UV-Vis spectra of the 5-coordinate species of **Re–EB** support this observation (Figures S3.44 and S3.45), with subtle differences in the spectral profiles of the ^{1}**5–MA** and ^{2}**5–DA** of **Re–EB**. Additionally, marginal decomposition occurs for both of the ^{3}**[Re–R]**$^{2-}$ complexes after 24 h of irradiation (Figure S3.48B).

Table 3.8. *TONs and TOFs of CO obtained at indicated time intervals under indicated photocatalytic conditions.*[a]

Irradiation Time (h)	**Re–H**		**Re–EB**	
	TON	*TOF* (*TON*/h)	*TON*	*TOF* (*TON*/h)
1	4.2	4.2	6.1	6.1
2	4.9	2.5	6.6	3.3
24	6.6	0.3	8.8	0.4

[a]*Photocatalytic conditions: 0.1 mM **Re–R** in a DMF/TEOA (5:1, v/v) solution, λ_{irr} = 450 nm.*

After 1 h of irradiation of **Re–H** and **Re–EB**, CO is detected in the headspace of the reaction vessel with a turnover frequency (*TOF*) of 4.2 and 6.1, respectively. However, CO evolution decreased

to a *TOF* of 2.5 and 3.3 after 2 h. After 24 h irradiation CO evolution had further decreased (*TOF* = 0.3 and 0.4). The turnover number (*TON*) for CO at the end of the photocatalytic experiments are 6.6 and 8.8 for **Re–H** and **Re–EB** respectively; these *TON* are lower than those reported for [Re(phen)$(CO)_3$Cl] under similar photocatalytic conditions (10 mL of a solution containing 1 M TEOA and 1 mM of the catalyst in DMF. *TON* = 12 after 2 h).[11]

The poor photocatalytic activity of **Re–R** reflects the weak catalytic effect at the R3 reduction wave under a CO_2 atmosphere as discussed in the electrochemical studies earlier (Figure S3.8). However, the *TON* obtained in this study are slightly higher than those for the related [Re(PNI–phen)$(CO)_3$Cl] complex (PNI = 4-piperidinyl-1,8-naphthalimide) with a *TON* = 3 after 4 h under identical photocatalytic conditions.[28] Furthermore, the marginally higher TONs determined for **Re–EB** than **Re–H** may be explained by the formation of the **^{3}5–MA** occurring close to R2 for **Re–EB** (only 50 mV more negative potential), while a 150 mV more negative potential is required for **Re–H** (Figures S3.11 and S3.12). This suggests that **^{3}5–MA** is more accessible under photocatalytic conditions for **Re–EB** and the reason for the marginal increase in photocatalytic activity.

3.4.7 Proposed pathway to the active catalyst

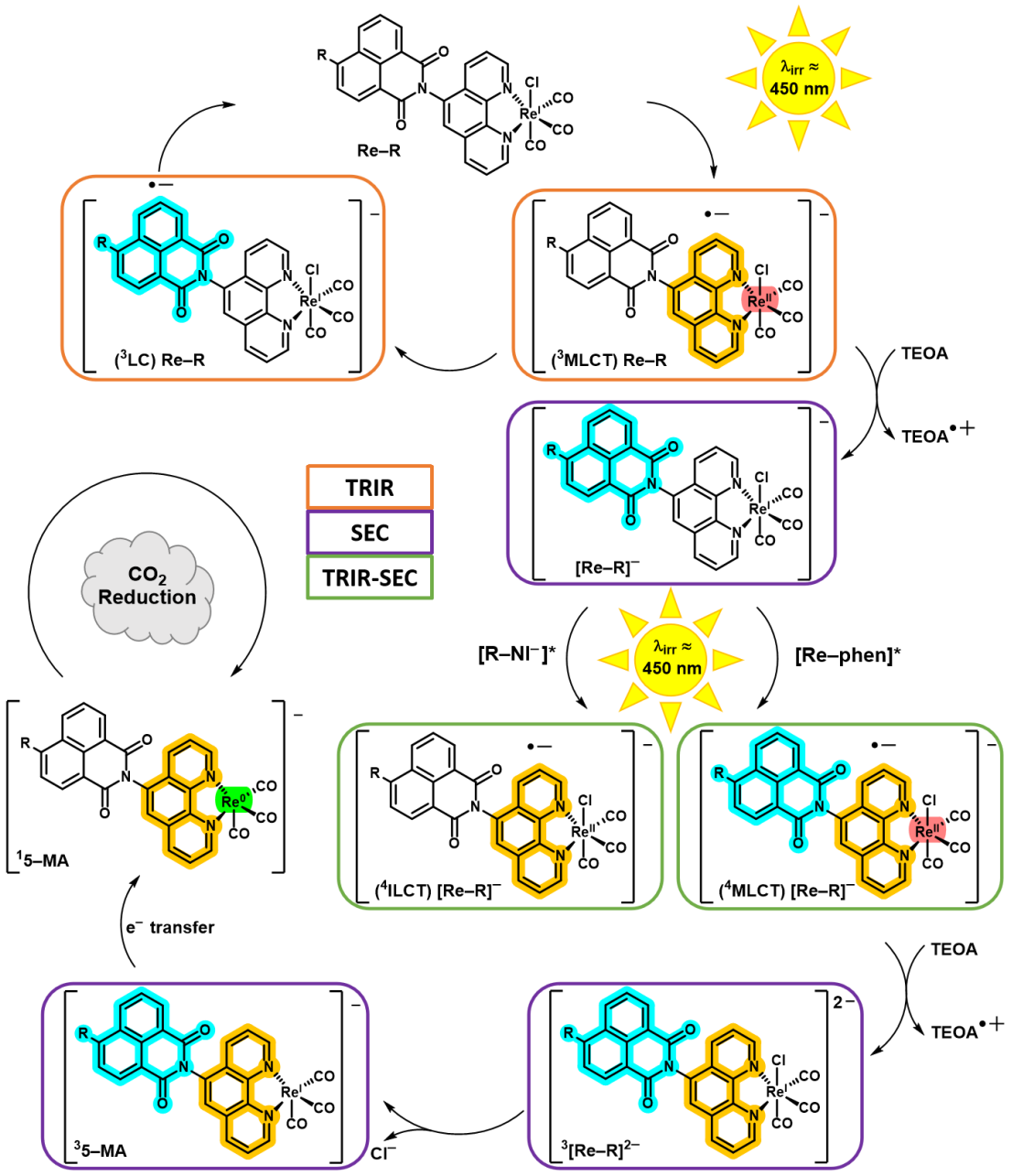
From the combined studies; CV, SEC, TRIR, TRIR SEC, and DFT/TDDFT the pathway shown in Scheme 3.3 is proposed for the generation of the active catalyst. Excitation of **Re–R** at 450 nm leads to population of a ^{3}MLCT excited state corresponding to the phen-localised radical anion [Re^{II}(R–NI–$phen^{-}$)] (**^{3}MLCT Re–R**). As described in the TRIR studies, the ^{3}LC excited state with a NI-localised radical anion [Re^{II}($R–NI^{-}$–phen)] (**^{3}LC Re–R**) is populated subsequently to the ^{3}MLCT excited state (Figure 3.8). A triplet-triplet equilibrium exists for **Re–H**, but only the ^{3}LC excited state of **Re–EB** is populated at long time intervals (>3 ns). Recovery of the ground-state **Re–R** complex occurs on the microsecond time scale based on the TRIR experiments of the **Re–R** complexes and previous time-resolved studies of related complexes. [21,22,24,27,36]

Under photocatalytic conditions, the **^{3}MLCT Re–R** complexes undergo reductive quenching by the sacrificial electron-donor, TEOA, to form the singly reduced complex localised on the phen moiety which subsequently undergoes intramolecular electron transfer onto the LUMO localised on the R–NI moiety. The resulting **[Re–R]$^-$** complex is observed in the SEC experiments (Figures 3.5 and 3.6) and the UV-Vis absorption-difference spectra recorded for the photocatalytic solutions confirmed the rapid formation of the **[Re–R]$^-$** species (Figure S3.48). Subsequent irradiation of **[Re–R]$^-$** results in the concurrent population of two distinct quadruplet excited

states; specifically, the ^{4}MLCT and ^{4}ILCT excited states observed in the TRIR SEC experiments (Figures 3.8–3.10). Similar to the **^{3}MLCT Re–R** excited state species, **^{4}MLCT [Re–R]$^-$** undergoes reductive quenching in the presence of TEOA to form the doubly reduced species **^{3}[Re–R]$^{2-}$** observed in the SEC experiments (Figures 3.5 and 3.6). The gradual formation of the **^{3}[Re–R]$^{2-}$** species is observed throughout the photocatalytic experiment, as shown in the UV-Vis absorption-difference spectra collected under photocatalytic conditions (Figure S3.48).

Following conversion of biradical **^{3}[Re–R]$^{2-}$** to **^{3}[Re–R]$^{2-}$**, the added unpaired electrons on the R–NI and phen moieties differ by being spin-unpaired and spin-paired, respectively. Subsequent Cl^- dissociation from **^{3}[Re–R]$^{2-}$** forms the **^{3}5–MA**, with the added electrons remaining on the R–NI and phen moieties. Subsequently, the **^{3}5–MA** intermediate undergoes intramolecular electron transfer, where the electron on the R–NI moiety can transfer on to the phen$^-$ unit, to yield **^{1}5–MA**. The **^{1}5–MA** has a neutral R–NI moiety and the doubly reduced {Re^0–phen$^-$} metallacycle; therefore, this is the active photocatalyst under these conditions. While CO_2 can coordinate to both the **^{3}5–MA** and **^{1}5–MA**, IR SEC proved that CO_2 binds to **^{3}5–MA** (Figure 3.7), only **^{1}5–MA** reduces CO_2 as it has the prerequisite doubly reduced {Re^0–phen$^-$} metallacycle.[30] This is only obtained photochemically upon forming the **^{1}5–MA**. Accordingly, Scheme 3.3 illustrates CO_2 binding and with subsequent catalysis proceeding from **^{1}5–MA**, although it should be noted that CO_2 binding to **^{3}5–MA** is also possible.

Based on the changes in the absorbance-difference spectra during photocatalysis (Figure S3.48), the Cl^- dissociation is tentatively assigned to the bottleneck in the catalytic pathway leading to formation of the active catalyst; as noted by the continual increase in concentration of **^{3}[Re–R]$^{2-}$** throughout the photocatalytic studies. Under photocatalytic conditions, **$^{1/3}$5–MA** may also form a solvated species with DMF, which is a moderately coordinating solvent.[93,94] Morimoto et al. have shown that TEOA can displace the DMF adduct and CO_2 binding can then proceed from the TEOA adduct.[95] However, the inclusion of additional steps to activation pathway under photocatalytic conditions, where conversion to the active catalyst is already poor, likely exacerbates the poor catalytic activity of the **Re–R** complexes further.



Scheme 3.7. *The proposed pathway leading to the active catalyst under photocatalytic conditions based on this work. The coloured boxes indicate the experiment where that species is identified in this work (orange = TRIR, purple = SEC, green = TRIR SEC). Highlighted components indicate where charge is localised within the structure of each* ***Re–R*** *species (cyan = R–NI-based, orange = phen-based, red = Re^{II} metal centre, green = Re^{0}).*

3.5 Conclusions

A detailed photophysical study is presented that probes the intermediates leading to CO_2 reduction using two rhenium photocatalysts **Re–H** and **Re–EB.** The SEC studies, in combination with theoretical calculations, identified a three-step reduction pathway to form the active catalyst for both **Re–R** complexes. This is unlike many [Re(α-diimine)$(CO)_3$X] complexes where

catalysis has been reported to occur via a two-step reduction pathway, forming [Re(α-diimine)$^{-}$(CO)$_3$]$^{-}$ as the active catalyst. The **[Re–R]$^{-}$** species which formed at R1 has a radical anion on the R–NI moiety, representing the reduction of the electron reservoir. At R2, **^{3}[Re–R]$^{2-}$** is formed consisting of a dianion with one electron on each of the R–NI and phen moieties. The **^{3}5–MA**, ^{3}[Re^{I}(R–NI–phen)$^{2-}$(CO)$_3$]$^{-}$, is formed from **^{3}[Re–R]$^{2-}$** upon Cl^{-} dissociation between R2 and R3. The **^{1}5–MA**, ^{1}[Re^{0}(R–NI–phen)$^{-}$(CO)$_3$]$^{-}$, can be formed from **^{3}5–MA** by intramolecular electron transfer from a reduced-NI to the Re–phen metallacycle. However, only **^{3}5–MA** is observed in the SEC studies due to stabilisation by solvation in the presence of coordinating solvents like THF or DMF. For **Re–EB**, the extended π-system associated with the EB–NI moiety further stabilises the **^{3}5–MA** allowing for it to be formed closer to R2 than **Re–H**. At R3, reduction of **^{3}[Re–R]$^{2-}$** and subsequent Cl^{-} dissociation results in the formation of the **^{2}5–DA** ^{2}[Re^{0}(R–NI–phen)$^{2-}$(CO)$_3$]$^{2-}$ as the active catalyst. The **^{2}5–DA** can also be formed by reducing **$^{1/3}$5–MA** before R3. The two possible active catalysts, **^{1}5–MA** and **^{2}5–DA**, can be formed from **^{3}5–MA** – making it a key precursor in the reduction pathway of **Re–R**. Indeed, the different stabilities of the ^{3}**5–MA** of **Re–R** may account for the marginally enhanced photocatalytic activity of **Re–EB** (*TON* = 9 after 24 h) over **Re–H** (*TON* = 7 after 24h).

Pioneering TRIR SEC studies of **Re–H** and **Re–EB** were successfully conducted to gain insights into the pathways leading to the formation of the active catalyst for photocatalytic CO_2 reduction. The key contribution of TRIR SEC in elucidating this pathway is the documented photooxidation of Re^{I}→Re^{II} in the ^{4}MLCT excited state of the singly reduced **[Re–R]$^{-}$** complex, which permits the second intramolecular electron transfer from TEOA to form **^{3}[Re–R]$^{2-}$**. Additionally, excitation of the radical leads to the population of the relatively long-lived NI^{-}→phen ^{4}ILCT excited state; demonstrating that intramolecular electron transfer from the reduced-NI electron reservoir to the Re–phen metallacycle can be facilitated photochemically. Implicitly, photoexcitation of ^{3}**5–MA** may also induce intramolecular electron transfer from the reduced-NI electron reservoir to the Re–phen metallacycle to produce the **^{1}5–MA** active catalyst under photocatalytic conditions. These key insights highlight the importance of studying the optically populated excited states of redox products and modelling the intermediates formed under photocatalytic conditions. Furthermore, it showcases the benefits of using TRIR SEC experiments to understand and tailor photocatalytic systems.

The accumulation of **^{3}[Re–R]$^{2-}$** during the photocatalytic studies is a strong indicator that the Cl^{-} dissociation step is a key bottleneck in the activation pathway of **Re–R**. The **^{3}[Re–R]$^{2-}$** complex is relatively inert compared to the **$^{1/3}$5–MA**, with Cl^{-} dissociation occurring at R3 or only proceeding thermally between R2 and R3; this is likely a significant barrier to the formation of the active

catalyst. Furthermore, any 5-coordinate species that are produced can rapidly interact with many components present during photocatalysis; with only the CO_2-bound adduct needed for the desired photocatalytic reaction. To conclude, the successful incorporation of an electron reservoir onto a [Re(α-diimine)$(CO)_3$X] photocatalyst requires that intramolecular electron transfer from the electron reservoir to the catalytic centre is sufficient to produce a 5-coordinate active catalyst under photocatalytic conditions. How electron reservoirs are incorporated into the photocatalysts, and what electron reservoirs are used, should be considered. Alternatively, alterations to the catalytic centre could be a successful strategy; halide dissociation could be achieved more easily by using a metal such as Mn^{I} or by using cationic $[Re(\alpha\text{-diimine})(CO)_3]^+$ photocatalysts, where the halide dissociation step is entirely circumvented.

3.6 Bibliography

1 J. Rogelj, D. Shindell, K. Jiang, S. Fifita, P. Forster, V. Ginzburg, C. Handa, H. Kheshgi, S. Kobayashi, E. Kriegler, L. Mundaca, R. Séférian and M. V. Vilariño, in *An IPCC Special Report on the impacts of global warming of 1.5°C above pre-industrial levels and related global greenhouse gas emission pathways, in the context of strengthening the global response to the threat of climate change, sustainable development, and efforts to eradicate poverty*, Cambridge University Press, Cambridge, UK and New York, NY, USA, 2018.

2 M. Grätzel, Artificial photosynthesis: water cleavage into hydrogen and oxygen by visible light, *Acc. Chem. Res.*, 1981, **14**, 376–384.

3 B. O'Regan and M. Grätzel, A low-cost, high-efficiency solar cell based on dye-sensitized colloidal TiO_2 films, *Nature*, 1991, **353**, 737–740.

4 S. Monticelli, A. Talbot, P. Gotico, F. Caillé, O. Loreau, A. Del Vecchio, A. Malandain, A. Sallustrau, W. Leibl, A. Aukauloo, F. Taran, Z. Halime and D. Audisio, Unlocking full and fast conversion in photocatalytic carbon dioxide reduction for applications in radio-carbonylation, *Nat Commun*, 2023, **14**, 4451.

5 Y. Kuramochi, O. Ishitani and H. Ishida, Reaction mechanisms of catalytic photochemical CO_2 reduction using Re(I) and Ru(II) complexes, *Coordination Chemistry Reviews*, 2018, **373**, 333–356.

6 L. Kearney, M. P. Brandon, A. Coleman, A. M. Chippindale, F. Hartl, R. Lalrempuia, M. Pižl and M. T. Pryce, Ligand−Structure Effects on N−Heterocyclic Carbene Rhenium Photo− and Electrocatalysts of CO_2 Reduction, *Molecules*, 2023, **28**, 4149.

7 J. Hawecker, J.-M. Lehn and R. Ziessel, Efficient photochemical reduction of CO 2 to CO by visible light irradiation of systems containing $Re(bipy)(CO)_3X$ or $Ru(bipy)_3^{2+}$–Co^{2+} combinations as homogeneous catalysts, *J Chem Soc Chem Com*, 1983, **0**, 536–538.

8 H. Takeda, K. Koike, H. Inoue and O. Ishitani, Development of an Efficient Photocatalytic System for CO_2 Reduction Using Rhenium(I) Complexes Based on Mechanistic Studies, *J. Am. Chem. Soc.*, 2008, **130**, 2023–2031.

9 G. Sahara and O. Ishitani, Efficient Photocatalysts for CO_2 Reduction, *Inorg. Chem.*, 2015, **54**, 5096–5104.

10 U. Shee, B. Khutia, S. Ray, S. Ghosh and K. K. Rajak, Highly efficient photocatalytic reduction of CO_2 to CO under visible light using rhenium benzo[d]oxazole complexes, *Dalton Trans.*, 2025, **54**, 7294–7305.

11 P. Kurz, B. Probst, B. Spingler and R. Alberto, Ligand Variations in $[ReX(diimine)(CO)_3]$ Complexes: Effects on Photocatalytic CO_2 Reduction, *Eur. J. Inorg. Chem.*, 2006, **2006**, 2966–2974.

12 A. El Nahhas, C. Consani, A. M. Blanco-Rodríguez, K. M. Lancaster, O. Braem, A. Cannizzo, M. Towrie, I. P. Clark, S. Záliš, M. Chergui and A. Jr. Vlček, Ultrafast Excited-State Dynamics of Rhenium(I) Photosensitizers $[Re(Cl)(CO)_3(N,N)]$ and $[Re(imidazole)(CO)_3(N,N)]$+: Diimine Effects, *Inorg. Chem.*, 2011, **50**, 2932–2943.

13 H. Takeda, K. Koike, T. Morimoto, H. Inumaru and O. Ishitani, in *Advances in Inorganic Chemistry*, Elsevier, 2011, vol. 63, pp. 137–186.

14 P. A. Summers, B. S. Adams, N. Ibrahim, K. E. A. Reynolds, K. L. Fow, E. S. Davies, M. Towrie and M. W. George, Photophysical and electrochemical properties of $[Re(CO)_3Cl(NN)]$ (NN = dppp3, dppp2, dppp2Br) complexes functionalised with pendant pyridyl ligands, *Vib. Spectrosc.*, 2019, **100**, 86–92.

15 J. Palion-Gazda, K. Choroba, M. Penkala, P. Rawicka and B. Machura, Further Insights into the Impact of Ligand-Localized Excited States on the Photophysics of Phenanthroline-Based Rhenium(I) Tricarbonyl Complexes, *Inorg. Chem.*, 2024, **63**, 1356–1366.

16 J. Palion-Gazda, B. Machura, A. Szłapa-Kula, A. M. Maroń, J. E. Nycz, P. Ledwon, E. Schab-Balcerzak, M. Siwy, J. Grzelak and S. Maćkowski, Effect of carbazole and pyrrolidine functionalization of phenanthroline ligand on ground- and excited-state properties of rhenium(I) complexes. Interplay between ^{3}MLCT and ^{3}IL/^{3}ILCT, *Dyes Pigm.*, 2022, **200**, 110113.

17 A. V. Müller, L. A. Faustino, K. T. de Oliveira, A. O. T. Patrocinio and A. S. Polo, Visible-Light-Driven Photocatalytic CO_2 Reduction by Re(I) Photocatalysts with N-Heterocyclic Substituents, *ACS Catal.*, 2023, **13**, 633–646.

18 M. Z. Bartusiak, R. J. McGarry, L. Varvarezos, M. P. Brandon and M. T. Pryce, Incorporation of perylene and naphthalene like ligands into ruthenium complexes: Synthesis, photophysical properties and electrochemistry, *Coord. Chem. Rev.*, 2023, **495**, 215365.

19 D. Jacquemin, E. A. Perpète, G. Scalmani, I. Ciofini, C. Peltier and C. Adamo, Absorption and emission spectra of 1,8-naphthalimide fluorophores: A PCM-TD-DFT investigation, *Chemical Physics*, 2010, **372**, 61–66.

20 C. Queffélec, P. B. Pati and Y. Pellegrin, Fifty Shades of Phenanthroline: Synthesis Strategies to Functionalize 1,10-Phenanthroline in All Positions, *Chem. Rev.*, 2024, **124**, 6700–6902.

21 Y. Yang, F. Doettinger, C. Kleeberg, W. Frey, M. Karnahl and S. Tschierlei, How the Way a Naphthalimide Unit is Implemented Affects the Photophysical and -catalytic Properties of Cu(I) Photosensitizers, *Front. Chem.*, DOI:10.3389/fchem.2022.936863.

22 J. E. Yarnell, J. C. Deaton, C. E. McCusker and F. N. Castellano, Bidirectional “Ping-Pong” Energy Transfer and 3000-Fold Lifetime Enhancement in a Re(I) Charge Transfer Complex, *Inorg. Chem.*, 2011, **50**, 7820–7830.

23 J. E. Yarnell, A. Chakraborty, M. Myahkostupov, K. M. Wright and F. N. Castellano, Long-lived triplet excited state in a platinum(II) perylene monoimide complex, *Dalton Trans.*, 2018, **47**, 15071–15081.

24 J. E. Yarnell, C. E. McCusker, A. J. Leeds, J. M. Breaux and F. N. Castellano, Exposing the Excited-State Equilibrium in an Ir^{III} Bichromophore: A Combined Time Resolved Spectroscopy and Computational Study, *Eur. J. Inorg. Chem.*, 2016, **2016**, 1808–1818.

25 A. Saini, K. R. Justin Thomas, K. R. J. Thomas, Abhay Sachdev, A. Sachdev, P. Gopinath and P. Gopinath, Photophysics, Electrochemistry, Morphology, and Bioimaging Applications of New 1,8-Naphthalimide Derivatives Containing Different Chromophores., *Chem. Asian J.*, 2017, **12**, 2612–2622.

26 A. Vlček, in *Photophysics of Organometallics*, ed. A. J. Lees, Springer Berlin Heidelberg, Berlin, Heidelberg, 2009, vol. 29, pp. 115–158.

27 J. E. Yarnell, K. A. Wells, J. R. Palmer, J. M. Breaux and F. N. Castellano, Excited-State Triplet Equilibria in a Series of Re(I)-Naphthalimide Bichromophores, *J. Phys. Chem. B*, 2019, **123**, 7611–7627.

28 F. Franco, C. Cometto, C. Garino, C. Minero, F. Sordello, C. Nervi and R. Gobetto, Photo- and Electrocatalytic Reduction of CO_2 by [$Re(CO)_3$α,α′-Diimine-(4-piperidinyl-1,8-naphthalimide)Cl] Complexes, *Eur. J. Inorg. Chem.*, 2015, **2015**, 296–304.

29 D. R. Case, A. Spear, A. F. Henwood, M. Nanao, S. Dampf, T. M. Korter, T. Gunnlaugsson, J. Zubieta and R. P. Doyle, [$Re(CO)_3$(5-PAN)Cl], a rhenium(I) naphthalimide complex for the visible light photocatalytic reduction of CO_2, *Dalton Trans.*, 2021, **50**, 3479–3486.

30 A. Spear, R. L. Schuarca, J. Q. Bond, T. M. Korter, J. Zubieta and R. P. Doyle, Photocatalytic turnover of CO_2 under visible light by [$Re(CO)_3$(1-(1,10) phenanthroline-5-(4-nitro-naphthalimide))Cl] in tandem with the sacrificial donor BIH, *RSC Adv.*, 2022, **12**, 5080–5084.

31 F. J. R. Cerpentier, J. Karlsson, R. Lalrempuia, M. P. Brandon, I. V. Sazanovich, G. M. Greetham, E. A. Gibson and M. T. Pryce, Ruthenium Assemblies for CO_2 Reduction and H_2 Generation: Time Resolved Infrared Spectroscopy, Spectroelectrochemistry and a Photocatalysis Study in Solution and on NiO, *Front. Chem.*, DOI:10.3389/fchem.2021.795877.

32 D. Lotti, P. Hamm and J. P. Kraack, Surface-Sensitive Spectro-electrochemistry Using Ultrafast 2D ATR IR Spectroscopy, *J. Phys. Chem. C*, 2016, **120**, 2883–2892.

33 J. Heitmüller, K. Eckstein, R. Renner, M. Stolte, T. Hertel, F. Würthner and T. Brixner, Coherent two-dimensional electronic spectroelectrochemistry, *Spectrochimica Acta Part A: Molecular and Biomolecular Spectroscopy*, 2021, **253**, 119567.

34 S. Goia, M. A. P. Turner, J. M. Woolley, M. D. Horbury, A. J. Borrill, J. J. Tully, S. J. Cobb, M. Staniforth, N. D. M. Hine, A. Burriss, J. V. Macpherson, B. R. Robinson and V. G. Stavros, Ultrafast transient absorption spectroelectrochemistry: femtosecond to nanosecond excited-state relaxation dynamics of the individual components of an anthraquinone redox couple, *Chemical Science*, 2022, **13**, 486–496.

35 K. T. Oppelt and P. Hamm, FullThrOTTLE-TrIR: Time-Resolved IR Spectroscopy of Electrochemically Generated Species Using a Full Throughput Optically Transparent Thin-Layer Electrochemical Cell, *J. Phys. Chem. C*, 2024, **128**, 16040–16049.

36 J. Biddulph, M. Pižl, S. Bhattacharya, P. Malakar, G. M. Greetham, F. Hartl and M. T. Pryce, Nature and Dynamics of the Excited States of Ethynyl-Functionalized Naphthalimide–Phenanthroline Re(I) Complexes Studied by TA and TRIR Spectroscopies, *J. Phys. Chem. B*, 2026, **130**, 6383–6398.

37 B. D. Rossenaar, D. J. Stufkens and A. Vlček, Halide-Dependent Change of the Lowest-Excited-State Character from MLCT to XLCT for the Complexes $Re(X)(CO)_3$(α-diimine) (X = Cl, Br, I; α-diimine = bpy, iPr-PyCa, iPr-DAB) Studied by Resonance Raman, Time-Resolved Absorption, and Emission Spectroscopy, *Inorg. Chem.*, 1996, **35**, 2902–2909.

38 M. W. George and J. J. Turner, Excited states of transition metal complexes studied by time-resolved infrared spectroscopy, *Coord. Chem. Rev.*, 1998, **177**, 201–217.

39 K. Choroba, J. Palion-Gazda, A. Kryczka, E. Malicka and B. Machura, Push–pull effect – how to effectively control photoinduced intramolecular charge transfer processes in rhenium(I) chromophores with ligands of D–A or D–π–A structure, *Dalton Transactions*, 2025, **54**, 2209–2223.

40 J. A. Timney and J. J. Turner, The calculation of energy-factored force constants for *fac*-Re(CO)$_3$(N-N)(X) molecules and related complexes, *Vibrational Spectroscopy*, 2022, **120**, 103374.

41 M. Krejčik, M. Daněk and F. Hartl, Simple construction of an infrared optically transparent thin-layer electrochemical cell: Applications to the redox reactions of ferrocene, $Mn_2(CO)_{10}$ and $Mn(CO)_3$(3,5-di-t-butyl-catecholate)$^-$, *Journal of Electroanalytical Chemistry and Interfacial Electrochemistry*, 1991, **317**, 179–187.

42 Y. Teki, Excited-State Dynamics of Non-Luminescent and Luminescent π-Radicals, *Chemistry – A European Journal*, 2020, **26**, 980–996.

43 M. Imran, X. Zhang, Z. Wang, X. Chen, J. Zhao, A. Barbon and V. K. Voronkova, Electron spin dynamics in excited state photochemistry: recent development in the study of intersystem crossing and charge transfer in organic compounds, *Phys. Chem. Chem. Phys.*, 2021, **23**, 15835–15868.

44 M. Franz, F. Neese and S. Richert, Calculation of exchange couplings in the electronically excited state of molecular three-spin systems, *Chem. Sci.*, 2022, **13**, 12358–12366.

45 X. Zhang, X. Chen, Y. Sun and J. Zhao, Radical enhanced intersystem crossing mechanism, electron spin dynamics of high spin states and their applications in the design of heavy atom-free triplet photosensitizers, *Org. Biomol. Chem.*, 2024, **22**, 5257–5283.

46 Z. Wang, J. Zhao, A. Barbon, A. Toffoletti, Y. Liu, Y. An, L. Xu, A. Karatay, H. G. Yaglioglu, E. A. Yildiz and M. Hayvali, Radical-Enhanced Intersystem Crossing in New Bodipy Derivatives and Application for Efficient Triplet–Triplet Annihilation Upconversion, *J. Am. Chem. Soc.*, 2017, **139**, 7831–7842.

47 J. Fujisawa, K. Ishii, Y. Ohba, M. Iwaizumi and S. Yamauchi, Electron Spin Polarization Transfer from Excited Triplet Porphyrins to a Nitroxide Radical via a Spin Exchange Mechanism, *J. Phys. Chem.*, 1995, **99**, 17082–17084.

48 E. M. Giacobbe, Q. Mi, M. T. Colvin, B. Cohen, C. Ramanan, A. M. Scott, S. Yeganeh, T. J. Marks, M. A. Ratner and M. R. Wasielewski, Ultrafast Intersystem Crossing and Spin Dynamics of Photoexcited Perylene-3,4:9,10-bis(dicarboximide) Covalently Linked to a Nitroxide Radical at Fixed Distances, *J. Am. Chem. Soc.*, 2009, **131**, 3700–3712.

49 E. Sartori, A. Toffoletti, C. Corvaja, L. Moroder, F. Formaggio and C. Toniolo, An oligopeptide doubly labelled with an azulene chromophore and a TEMPO radical. Azulene triplet generation by enhanced ISC from S_2, *Chemical Physics Letters*, 2004, **385**, 362–367.

50 M. Imran, M. Taddei, A. A. Sukhanov, L. Bussotti, W. Ni, P. Foggi, G. G. Gurzadyan, J. Zhao, M. Di Donato and V. K. Voronkova, Radical-Enhanced Intersystem Crossing in Perylene-Oxoverdazyl Radical Dyads, *ChemPhysChem*, 2022, **23**, e202100912.

51 C. Blättler, F. Jent and H. Paul, A novel radical-triplet pair mechanism for chemically induced electron polarization (CIDEP) of free radicals in solution, *Chemical Physics Letters*, 1990, **166**, 375–380.

52 J. Telser, in *eMagRes*, John Wiley & Sons, Ltd, 2017, vol. 6, pp. 207–234.

53 F. Li, A. J. Gillett, Q. Gu, J. Ding, Z. Chen, T. J. H. Hele, W. K. Myers, R. H. Friend and E. W. Evans, Singlet and triplet to doublet energy transfer: improving organic light-emitting diodes with radicals, *Nat Commun*, 2022, **13**, 2744.

54 F. Strieth-Kalthoff and F. Glorius, Triplet Energy Transfer Photocatalysis: Unlocking the Next Level, *Chem*, 2020, **6**, 1888–1903.

55 J. Han, Y. Jiang, A. Obolda, P. Duan, F. Li and M. Liu, Doublet–Triplet Energy Transfer-Dominated Photon Upconversion, *J. Phys. Chem. Lett.*, 2017, **8**, 5865–5870.

56 Y. Wei, K. An, X. Xu, Z. Ye, X. Yin, X. Cao and C. Yang, Π-Radical Photosensitizer for Highly Efficient and Stable Near-Infrared Photon Upconversion, *Advanced Optical Materials*, 2024, **12**, 2301134.

57 M. M. Roessler and E. Salvadori, Principles and applications of EPR spectroscopy in the chemical sciences, *Chem. Soc. Rev.*, 2018, **47**, 2534–2553.

58 A. Kawai, T. Okutsu and K. Obi, Spin polarization generated in the triplet-doublet interaction: hyperfine-dependent chemically induced dynamic electron polarization, *J. Phys. Chem.*, 1991, **95**, 9130–9134.

59 N. Hirota and S. Yamauchi, Short-lived excited triplet states studied by time-resolved EPR spectroscopy, *Journal of Photochemistry and Photobiology C: Photochemistry Reviews*, 2003, **4**, 109–124.

60 G. Kothe, S. S. Kim and S. I. Weissman, Transient magnetic resonance of a photoexcited quartet state, *Chemical Physics Letters*, 1980, **71**, 445–447.

61 S. De Kreijger, M. Gillard, B. Elias and L. Troian-Gautier, Spectroscopic Techniques to Unravel Mechanistic Details in Light-Induced Transformations and Photoredox Catalysis, *ChemCatChem*, 2024, **16**, e202301100.

62 Haim. Levanon and J. R. Norris, The photoexcited triplet state and photosynthesis, *Chem. Rev.*, 1978, **78**, 185–198.

63 G. P. Wiederrecht, W. A. Svec, M. R. Wasielewski, T. Galili and H. Levanon, Novel Mechanism for Triplet State Formation in Short Distance Covalently Linked Radical Ion Pairs, *J. Am. Chem. Soc.*, 2000, **122**, 9715–9722.

64 Z. Wang, Y. Gao, M. Hussain, S. Kundu, V. Rane, M. Hayvali, E. A. Yildiz, J. Zhao, H. G. Yaglioglu, R. Das, L. Luo and J. Li, Efficient Radical-Enhanced Intersystem Crossing in an NDI-

TEMPO Dyad: Photophysics, Electron Spin Polarization, and Application in Photodynamic Therapy, *Chemistry – A European Journal*, 2018, **24**, 18663–18675.

65 X. Zhang, A. A. Sukhanov, E. A. Yildiz, Y. E. Kandrashkin, J. Zhao, H. G. Yaglioglu and V. K. Voronkova, Radical-Enhanced Intersystem Crossing in a Bay-Substituted Perylene Bisimide−TEMPO Dyad and the Electron Spin Polarization Dynamics upon Photoexcitation, *ChemPhysChem*, 2021, **22**, 55–68.

66 D. Gosztola, M. P. Niemczyk, W. Svec, A. S. Lukas and M. R. Wasielewski, Excited Doublet States of Electrochemically Generated Aromatic Imide and Diimide Radical Anions, *J. Phys. Chem. A*, 2000, **104**, 6545–6551.

67 H. Ferreira, M. M. Conradie, K. G. von Eschwege and J. Conradie, Electrochemical and DFT study of the reduction of substituted phenanthrolines, *Polyhedron*, 2017, **122**, 147–154.

68 C. Riplinger, M. D. Sampson, A. M. Ritzmann, C. P. Kubiak and E. A. Carter, Mechanistic Contrasts between Manganese and Rhenium Bipyridine Electrocatalysts for the Reduction of Carbon Dioxide, *J. Am. Chem. Soc.*, 2014, **136**, 16285–16298.

69 D. R. Case, A. Spear, A. F. Henwood, M. Nanao, S. Dampf, T. M. Korter, T. Gunnlaugsson, J. Zubieta and R. P. Doyle, $[Re(CO)_3(5\text{-PAN})Cl]$, a rhenium(I) naphthalimide complex for the visible light photocatalytic reduction of CO_2, *Dalton Trans.*, 2021, **50**, 3479–3486.

70 P. Christensen, A. Hamnett, A. V. G. Muir and J. A. Timney, An in situ infrared study of CO_2 reduction catalysed by rhenium tricarbonyl bipyridyl derivatives, *J. Chem. Soc., Dalton Trans.*, 1992, 1455–1463.

71 C. W. Machan, M. D. Sampson, S. A. Chabolla, T. Dang and C. P. Kubiak, Developing a Mechanistic Understanding of Molecular Electrocatalysts for CO_2 Reduction using Infrared Spectroelectrochemistry, *Organometallics*, 2014, **33**, 4550–4559.

72 F. P. A. Johnson, M. W. George, F. Hartl and J. J. Turner, Electrocatalytic Reduction of CO2 Using the Complexes $[Re(bpy)(CO)_3L]n$ (n = +1, L = $P(OEt)_3$, CH_3CN; n = 0, L = Cl^-, Otf^-; bpy = 2,2‘-Bipyridine; Otf^- = CF_3SO_3) as Catalyst Precursors: Infrared Spectroelectrochemical Investigation, *Organometallics*, 1996, **15**, 3374–3387.

73 G. J. Stor, F. Hartl, J. W. M. Van Outersterp and D. J. Stufkens, Spectroelectrochemical (IR, UV/Vis) Determination of the Reduction Pathways for a Series of $[Re(CO)_3$(.alpha.-diimine)$L']^{0/+}$ (L’ = Halide, OTf^-, THF, MeCN, n-PrCN, PPh_3, $P(OMe)_3$) Complexes, *Organometallics*, 1995, **14**, 1115–1131.

74 E. E. Benson, K. A. Grice, J. M. Smieja and C. P. Kubiak, Structural and spectroscopic studies of reduced $[Re(bpy\text{-}R)(CO)_3]^{-1}$ species relevant to CO_2 reduction, *Polyhedron*, 2013, **58**, 229–234.

75 S. C. Cheng, C. A. Blaine, M. G. Hill and K. R. Mann, Electrochemical and IR Spectroelectrochemical Studies of the Electrocatalytic Reduction of Carbon Dioxide by $[Ir_2(dimen)_4]^{2+}$ (dimen = 1,8-Diisocyanomenthane), *Inorg. Chem.*, 1996, **35**, 7704–7708.

76 A. Barbero, L. Rotundo, C. Reviglio, R. Gobetto, R. Sokolova, J. Fiedler and C. Nervi, New Spectroelectrochemical Insights into Manganese and Rhenium Bipyridine Complexes as Catalysts for the Electrochemical Reduction of Carbon Dioxide, *Molecules*, 2023, **28**, 7535.

77 E. E. Benson, M. D. Sampson, K. A. Grice, J. M. Smieja, J. D. Froehlich, D. Friebel, J. A. Keith, E. A. Carter, A. Nilsson and C. P. Kubiak, The Electronic States of Rhenium Bipyridyl Electrocatalysts for CO_2 Reduction as Revealed by X-ray Absorption Spectroscopy and Computational Quantum Chemistry, *Angewandte Chemie International Edition*, 2013, **52**, 4841–4844.

78 I. M. Alecu, J. Zheng, Y. Zhao and D. G. Truhlar, Computational Thermochemistry: Scale Factor Databases and Scale Factors for Vibrational Frequencies Obtained from Electronic Model Chemistries, *J. Chem. Theory Comput.*, 2010, **6**, 2872–2887.

79 J. Bredenbeck, J. Helbing and P. Hamm, Labeling Vibrations by Light: Ultrafast Transient 2D-IR Spectroscopy Tracks Vibrational Modes during Photoinduced Charge Transfer, *J. Am. Chem. Soc.*, 2004, **126**, 990–991.

80 M. W. George, F. P. A. Johnson, J. R. Westwell, P. M. Hodges and J. J. Turner, Excited-state properties and reactivity of $[ReCl(CO)_3(2,2'\text{-bipy})](2,2'\text{-bipy} = 2,2'\text{-bipyridyl})$ studied by time-resolved infrared spectroscopy, *J. Chem. Soc., Dalton Trans.*, 1993, 2977–2979.

81 H. Kvapilová, A. Jr. Vlček, V. Barone, M. Biczysko and S. Záliš, Anharmonicity Effects in IR Spectra of $[Re(X)(CO)_3(\alpha\text{-diimine})]$ (α-diimine = 2,2′-bipyridine or pyridylimidazo[1,5-a]pyridine; X = Cl or NCS) Complexes in Ground and Excited Electronic States, *J. Phys. Chem. A*, 2015, **119**, 10137–10146.

82 A. Jr. Vlček, H. Kvapilová, M. Towrie and S. Záliš, Electron-Transfer Acceleration Investigated by Time Resolved Infrared Spectroscopy, *Acc. Chem. Res.*, 2015, **48**, 868–876.

83 J. Lin, B. Qin and G. Zhao, Effect of solvents on photocatalytic reduction of CO_2 mediated by cobalt complex, *Journal of Photochemistry and Photobiology A: Chemistry*, 2018, **354**, 181–186.

84 M. Stitch, M. Pižl, N. Lehane, G. M. Greetham, F. Hartl, M. Towrie and S. J. Quinn, Eyes on the Prize: Tracking Electron Transfer in G-Rich Duplex and Quadruplex DNA Using Enantiopure Ruthenium Polypyridyl Infrared Redox Probes, *J. Am. Chem. Soc.*, 2025, **147**, 29801–29814.

85 E. Sumner, M. Pižl, K. T. McQuaid and F. Hartl, Nitrile Substituents at the Conjugated Dipyridophenazine Moiety as Infrared Redox Markers in Electrochemically Reduced Heteroleptic Ru(II) Polypyridyl Complexes, *Inorg. Chem.*, 2024, **63**, 2460–2469.

86 E. Balanikas, M. Reymond-Joubin and E. Vauthey, Excited-State Symmetry Breaking in Solvent Mixtures, *J. Phys. Chem. Lett.*, 2024, **15**, 2447–2452.

87 M. Stitch, D. Avagliano, D. Graczyk, I. P. Clark, L. González, M. Towrie and S. J. Quinn, Good Vibrations Report on the DNA Quadruplex Binding of an Excited State Amplified Ruthenium Polypyridyl IR Probe, *J. Am. Chem. Soc.*, 2023, **145**, 21344–21360.

88 E. Vauthey, Watching Excited-State Symmetry Breaking in Multibranched Push–Pull Molecules, *J. Phys. Chem. Lett.*, 2022, **13**, 2064–2071.

89 A. A. Cullen, K. Heintz, L. O'Reilly, C. Long, A. Heise, R. Murphy, J. Karlsson, E. Gibson, G. M. Greetham, M. Towrie and M. T. Pryce, A Time-Resolved Spectroscopic Investigation of a Novel BODIPY Copolymer and Its Potential Use as a Photosensitiser for Hydrogen Evolution, *Front. Chem.*, DOI:10.3389/fchem.2020.584060.

90 A. A. Cullen, A. Rajagopal, K. Heintz, A. Heise, R. Murphy, I. V. Sazanovich, G. M. Greetham, M. Towrie, C. Long, D. Fitzgerald-Hughes and M. T. Pryce, Exploiting a Neutral BODIPY Copolymer as an Effective Agent for Photodynamic Antimicrobial Inactivation, *J. Phys. Chem. B*, 2021, **125**, 1550–1557.

91 H. Takeda, K. Koike, H. Inoue and O. Ishitani, Development of an Efficient Photocatalytic System for CO_2 Reduction Using Rhenium(I) Complexes Based on Mechanistic Studies, *J. Am. Chem. Soc.*, 2008, **130**, 2023–2031.

92 Y. Hayashi, S. Kita, B. S. Brunschwig and E. Fujita, Involvement of a Binuclear Species with the Re−C(O)O−Re Moiety in CO_2 Reduction Catalyzed by Tricarbonyl Rhenium(I) Complexes with Diimine Ligands: Strikingly Slow Formation of the Re−Re and Re−C(O)O−Re Species from $Re(dmb)(CO)_3S$ (dmb = 4,4'-Dimethyl-2,2'-bipyridine, S = Solvent), *J. Am. Chem. Soc.*, 2003, **125**, 11976–11987.

93 R. Díaz-Torres and S. Alvarez, Coordinating ability of anions and solvents towards transition metals and lanthanides, *Dalton Trans.*, 2011, **40**, 10742–10750.

94 J. Mukherjee and I. Siewert, Manganese and Rhenium Tricarbonyl Complexes Equipped with Proton Relays in the Electrochemical CO_2 Reduction Reaction, *Eur. J. Inorg. Chem.*, 2020, **2020**, 4319–4333.

95 T. Morimoto, T. Nakajima, S. Sawa, R. Nakanishi, D. Imori and O. Ishitani, CO_2 Capture by a Rhenium(I) Complex with the Aid of Triethanolamine, *J. Am. Chem. Soc.*, 2013, **135**, 16825–16828.

Chapter 4

The Electrochemical and Spectroelectrochemical Studies of Naphthalimide-Phenanthroline Mn(I) Complexes to Determine the Reduction Pathway Leading to the CO_2-reducing Active Electrocatalyst

---

Jack Biddulph[1], Jonathan Rochford[2], and Mary T. Pryce[1], *Manuscript in progress*.

[1] *School of Chemical Sciences, Dublin City University, Glasnevin, Dublin, D09 V289, Ireland*

[2] *Department of Chemistry, University of Massachusetts Boston, 100 Morrissey Boulevard, Boston, MA 02125, USA*

Author Contributions:

Jack Biddulph performed all of the synthesis, experimental studies, and writing in this chapter. Jonathan Rochford performed quantum chemical calculations.

4.1 Abstract

The synthesis and photophysical properties of two [Mn(R–NI–phen)$(CO)_3$Br] complexes (**Mn–R**), where NI = 1,8-naphthalimide and phen = 1,10-phenanthroline, are reported. The **R–NI** electron reservoirs were substituted at their 4-positions, with R = H (**Mn–H**) or ethynyl benzene (**Mn–EB**). [Mn(phen)$(CO)_3$Br] (**Mn–phen**) was prepared as a model complex to aid in the mechanistic studies of the **Mn–R** complexes. Electrochemical and spectroelectrochemical (SEC) studies were conducted to elucidate the reduction pathway leading to the CO_2 reducing active catalyst and were supported by quantum chemical calculations. Catalytic CO_2 reduction yielding CO and bicarbonate products is achieved at negative potentials (–3 V vs Fc^+/Fc), with SEC studies revealing that the **Mn–R** complexes form the five-coordinate dianion (**5–DA**) as the active catalyst. However, with the addition of a weak Brønsted acid, H_2O, catalytic CO_2 reduction was achieved at less negative potentials to yield CO as the reaction product (*ca.* –2.3 V vs Fc^+/Fc). Furthermore, homogenous electrocatalysis in the presence of CO_2 and H_2O showed higher selectivity for CO production with **Mn–H** and **Mn–EB** as the catalyst (η_{FE} = 75% and 73%, respectively) compared to the **Mn–phen** model (η_{FE} = 65%). IR SEC studies of **Mn–EB** with CO_2 and H_2O showed evidence for the formation of the [Mn(EB–NI–phen)$(CO)_3(CO_2H)$] complex (**Mn–CO_2H**). Intramolecular electron transfer, from the reduced R–NI electron reservoir to the **Mn–phen** metallacycle, is key to forming the five-coordinate monoanion (**5–MA**) at less negative overpotentials. Only in the presence of CO_2 and H_2O, does CO_2 binding occur readily at less negative overpotentials to yield **Mn–CO_2H**; a key intermediate in the catalytic CO_2 reduction cycle.

4.2 Introduction

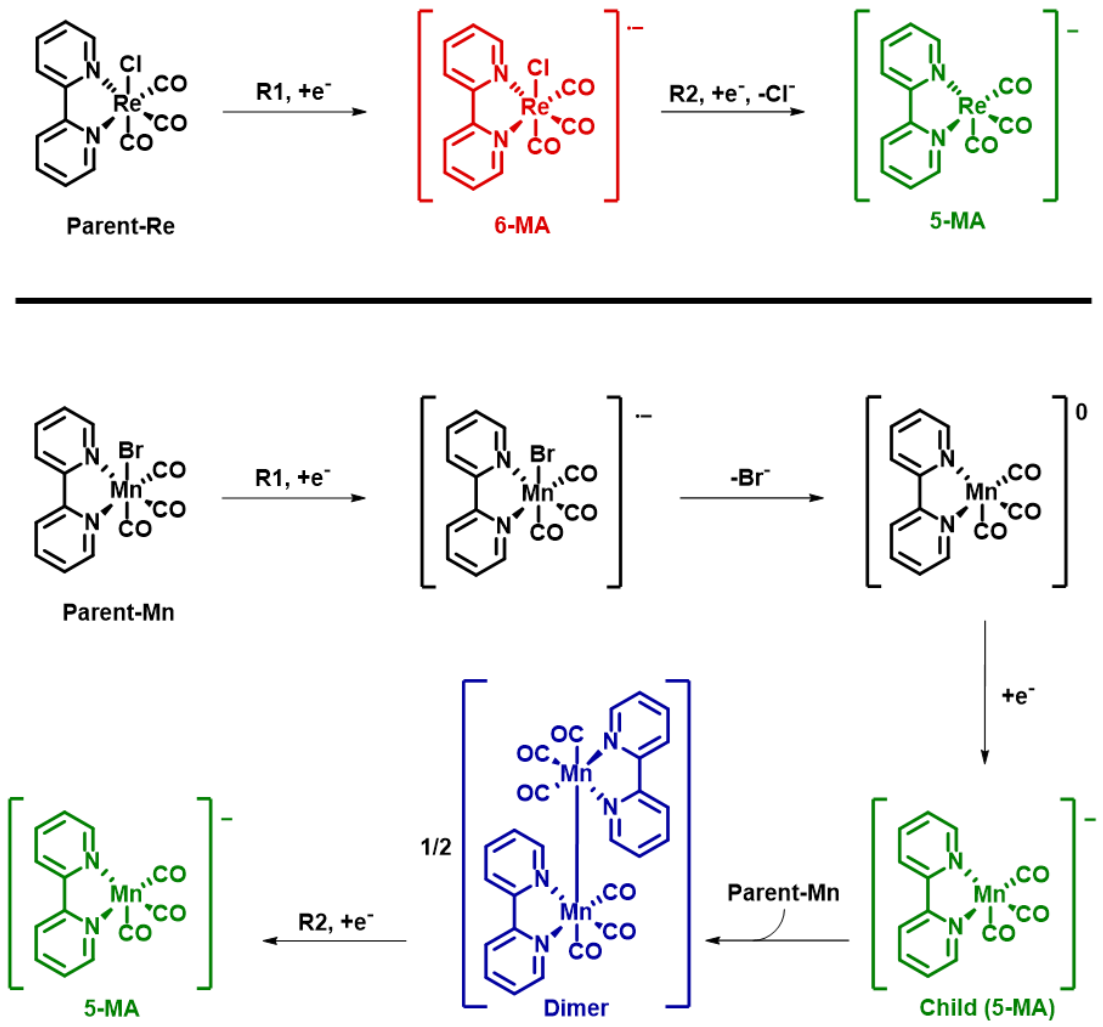
Electrocatalysis and photocatalysis are some approaches that can utilise renewable energy sources to convert captured atmospheric CO_2 into other forms to address the ongoing anthropogenic climate crisis. The development of CO_2 reducing electrocatalysts and photocatalysts derives from the seminal work by Hawecker et al. on [Re(bpy)$(CO)_3$Cl] (where bpy = 2,2'-bipyridine), later known as the Lehn catalyst.[1] Subsequently, studies of CO_2 reducing electro- and photocatalysts have focused on transition-metal α–diimine tricarbonyl complexes, with rhenium complexes being extensively studied due to their stability under the conditions employed for electrocatalysis and photocatalysis.

Manganese is an Earth-abundant alternative to rhenium; it is the first-row transition-metal analogue of rhenium and it has a vastly greater abundance in the Earth's crust (9.5×10^2 mg

Mn/kg) than that of rhenium (7.0×10^{-4} mg Re/kg).[3] While manganese and rhenium α–diimine tricarbonyls are structurally similar, much of the chemistry relevant for CO_2 reduction catalysis differs between the two metals. Chiefly, manganese α–diimine tricarbonyl complexes are known to have poor photostability in comparison to their rhenium counterparts and they have short-lived excited states; which is common for many first-row transition-metal complexes.[4] As such, rhenium α–diimine tricarbonyl complexes remain the preeminent CO_2 reduction photocatalysts, while manganese α–diimine tricarbonyl complexes are typically explored as CO_2 reducing electrocatalysts.

Early electrocatalytic studies showed no activity towards CO_2 reduction with manganese α–diimine tricarbonyl complexes under the same conditions as their rhenium counterparts.[5] Bourrez et al. determined that a weak Brønsted acid is needed for manganese complexes to elicit any CO_2 reducing activity, subsequently also demonstrated by Smieja et al.[6,7] This has been attributed to the need for a proton source to stabilise bound CO_2 in a metallocarboxylic acid complex.[8] The differences between the manganese and rhenium α–diimine tricarbonyl complexes extend to their electrochemistry, causing electrocatalysis to proceed via different activation pathways as outlined in Scheme 4.1.

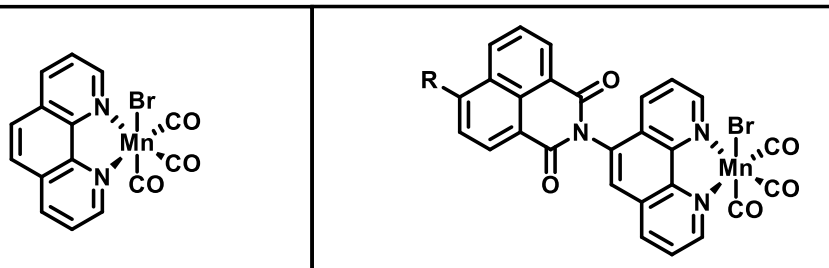
The initial reduction of the parent rhenium complex (**Parent–Re**) forms the 6–coordinate monoanion (**6–MA**) with a subsequent reduction inducing halide dissociation to form the 5–coordinate monoanion (**5–MA**) as the active catalyst for CO_2 reduction.[8] For manganese, the initial reduction causes rapid halide dissociation, thereby generating the $[Mn]^0$ intermediate within the electrochemical double-layer. As this causes potential inversion, i.e. reduction of $[Mn]^0$ is anodic of the parent Mn-Br complex, this first reduction wave is a concerted two-electron (*ECE*) process resulting in the formation of the "child" **5–MA**. Subsequently, rapid formation of a manganese-manganese dimer (**Dimer**) ensues via a bimolecular parent-child comproportionation chemical reaction; between the "parent" manganese complex (**Parent–Mn**) and the "child" **5–MA**.[6–12] Thus, unless sterically hindered[13], **Dimer** formation can compete with CO_2 and H^+ binding to the **5–MA** active catalyst at an applied potential of this first reduction of manganese α-diimine tricarbonyl complexes. Subsequent reduction of the **Dimer** causes homolytic cleavage of the Mn–Mn bond which regenerates the **5–MA** as the active catalyst available for CO_2 reduction.[8,10,14] While this does introduce a slight overpotential for quantitative generation of the five-coordinate two-electron reduced **5–MA**, relative to the initial concerted two-electron activation, the dimer reduction typically does not increase the overpotential for electrocatalytic CO_2 reduction to CO as this is often dictated by reduction of the Mn^{I}-CO_2H catalytic intermediate along the so-called 'reduction-first' pathway.



Scheme 4.8. *Simplified reduction pathways for [Re(bpy)(CO)$_3$Cl] (Top) and [Mn(bpy)(CO)$_3$Br] (Bottom). The 6–coordinate monoanion (**6–MA**) in red and the manganese–manganese dimer (**Dimer**) in blue are highlighted as the key intermediates leading to the 5–coordinate monoanion (**5–MA**) in green as the active catalyst in both pathways.*

Despite the additional steps in the activation pathway of manganese α-diimine tricarbonyl complexes, a lower potential is required to form the active catalyst for manganese complexes than rhenium complexes; making manganese an attractive catalyst to use at larger scales.[7,15] Structural adjustments to the α-diimine ligand have been incorporated to Mn electrocatalysts to avoid **Dimer** formation. Sampson et al. used the bulky 6,6'-dimesityl-2,2'-bipyridine ligand to sterically inhibit formation of the **Dimer**.[5] However, these attempts at avoiding formation of the **Dimer** resulted in more negative potentials being required to initiate catalytic CO_2 reduction, formation of the Mn(I)-CO_2H intermediate (formed upon CO_2 binding in the presence of a proton source) occurs more negatively.[5,13]

Previously, naphthalimide has been linked to [Re(phen)(CO)$_3$Cl] (where phen= 1,10-phenanthroline) by substitution onto the aromatic core of phen and studied as CO_2 reducing photocatalysts; with the NI moieties having dual functionality as a photosensitiser and electron reservoir in these assemblies. However, this did not improve the ability of the NI-bearing complexes to photocatalytically reduce CO_2 compared to [Re(phen)(CO)$_3$Cl].[16–18] Franco et al. compared [Re(PNI-phen)(CO)$_3$Cl] and [ReCl(bpy-Ph-PNI)(CO)$_3$Cl] (where PNI = 4-piperidinyl-1,8-naphthalimide) as photocatalysts and electrocatalysts; revealing they efficiently reduce CO_2 to CO electrocatalytically (TON_{CO} = 44 and 64, respectively) compared to photocatalytic CO_2 reduction (TON_{CO} = 3 and 9, respectively).[16] Furthermore, their electrocatalytic activity was achieved at less negative overpotentials (–1.96 V vs Fc^+/Fc) than [Re(bpy)(CO)$_3$Cl] (–2.26 V vs Fc^+/Fc). However, this paper did not focus on the mechanism by which electrocatalysis proceeds, which is key to understanding the behaviour of the electron reservoir in these electrocatalysts.



Model Complex:

Chemical Formula	**Abb.**
[Mn(phen)(CO)$_3$Br]	**Mn–phen**

Target Complexes:

Chemical Formula	**Abb.**	R-group structure
[Mn(H-NI-phen)(CO)$_3$Br]	**Mn–H**	**H**
[Mn(EB-NI-phen)(CO)$_3$Br]	**Mn–EB**	

Chart 4.3. *Chemical structures of the model (**Mn–phen**) and target complexes (**Mn–H** and **Mn–EB**).*

As such, a series of manganese-naphthalimide complexes [Mn(R–NI–phen)(CO)$_3$Br] (**Mn–R**) were prepared as CO_2-reducing electrocatalysts incorporating different NI-based electron reservoirs. [Mn(H–NI–phen)(CO)$_3$Br] [**Mn–H**] and [Mn(EB–NI–phen)(CO)$_3$Br] [**Mn–EB**] (where **R–NI** = 1,8-naphthalimide and 4-ethynylbenzene-1,8-naphthalimide, respectively) were studied using electrochemical and spectroelectrochemical (SEC) techniques to study the effect of implementing these electron reservoirs into manganese-based electrocatalysts.

[Mn(phen)(CO)$_3$Br] (**Mn–phen** herein) was selected as the model complex in these studies as the target **Mn–R** complexes contain the **Mn–phen** metallacycle within their structure as illustrated in Chart 4.1. Based on the results of electrochemical and SEC studies, with supporting DFT calculations, the reduction pathways leading to the active catalysts of **Mn–R** are proposed. For the design of future electrocatalysts for CO_2, this study aims to provide mechanistic insights into how intramolecular electron reservoirs can participate in the formation of the active catalyst at lower overpotentials.

4.3 Results and Discussion

4.3.1 Syntheses and Spectral Characterisation

The NI ligands were synthesised according to literature procedures and are described in Chapter 2.[19,20] The **Mn–R** complexes were synthesised according to an adaptation of the literature procedure for [Mn(phen)(CO)$_3$Br] using THF as the reaction solvent (Figures S4.1–S4.3).[21] FTIR and UV-Vis absorption spectroscopies are presented in Figure 4.1, with key spectroscopic data recorded in Table 4.1.

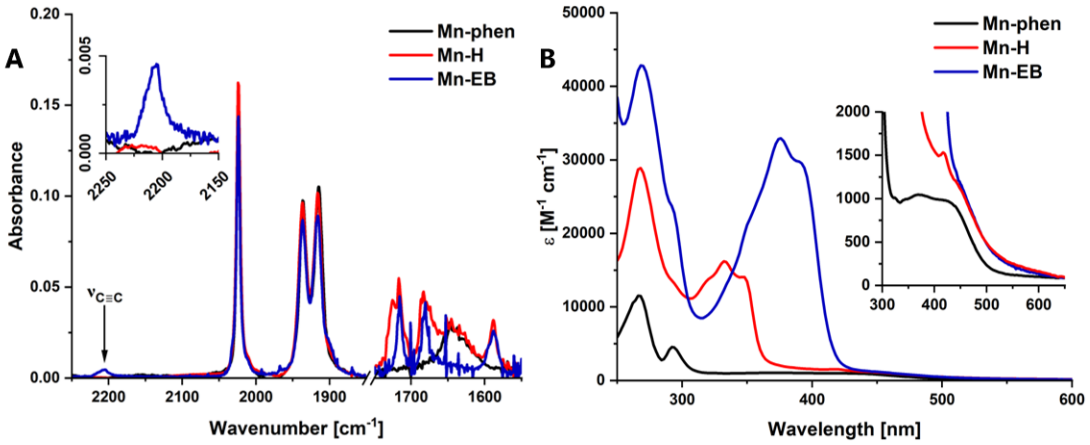


Figure 4.1. *(A) IR spectra of 20 µM* ***Mn–R*** *in THF with an inset of the* $\nu_{C\equiv C}$ *region. (B) UV-Vis absorption spectra of* ***Mn–R*** *series in THF with an inset displaying the MLCT and XLCT transitions.*

Three strong metal carbonyl stretching vibrations ($\nu_{C\equiv O}$) are observed in the IR spectra of **Mn–R** (Figure 4.1A); with $\nu_{C\equiv O}$ at 2024, 1937, and 1915 cm^{-1} corresponding to the vibrational modes associated with *fac*–[Mn(α–diimine)(CO)$_3$Br] complexes.[21,22] The spectra for **Mn–H** and **Mn–EB** also contained organic carbonyl vibrational bands ($\nu_{C=O}$) arising from the imide functionality on

the **R–NI** moiety. In **Mn–H**, the $\nu_{C=O}$ bands are observed at 1717 and 1683 cm^{-1}, while for **Mn–EB** they are observed at 1715 and 1684 cm^{-1}. Additionally, an ethynyl stretching vibration ($\nu_{C\equiv C}$) is observed for **Mn–EB** at 2206 cm^{-1}.

The UV-Vis absorption spectra for the **Mn–R** complexes, presented in Figure 4.1B, differ substantially to that of the **Mn–phen** model system due to the R–NI moieties. This is attributed to the weakly coupled bichromophoric system with both the R–NI moiety and the **Mn–phen** metallacycle acting as chromophores.[19,23] Accordingly, the UV-Vis spectra for the **Mn–H** and **Mn–EB** complexes appear as a composition of both the NI and **Mn–phen** chromophores. As such, the transitions associated with the **Mn–phen** chromophore, which are common to all of the **Mn–R** UV-Vis absorption spectra, are described first. The UV-Vis absorption spectrum of **Mn–phen** displayed characteristic phen π→π* transitions at 268 nm.[24] Additionally, two weak absorption features were observed at 369 and 420 nm corresponding to the Mn→phen dπ→π* (MLCT) transition and the Br→phen π→π* (XLCT) transition, respectively.[22,25–27]

Table 4.9. *Key spectral data of* ***Mn–R*** *from FTIR and UV-Vis absorption studies in THF.*

Sample	λ (nm) [ε (M^{-1} cm^{-1})]	$\nu_{C\equiv O}$ (cm^{-1})	$\nu_{C=O}$ (cm^{-1})	$\nu_{C\equiv C}$ (cm^{-1})
Mn–phen	268, 369, 420 [11530, 1050, 980]	2024, 1937, 1915	–	–
Mn–H	268, 332, 348, 417 [28860, 16450, 14080, 1530]	2024, 1937, 1915	1717, 1683	–
Mn–EB	269, 376, 390 [42810, 32990, 29750]	2024, 1936, 1915	1715, 1684	2206

In UV-Vis spectrum for **Mn–H**, contains a number of sharper bands than that of **Mn–phen** with a maximum at 332 nm attributed to a NI-based n→π* transition, and a shoulder at 348 nm assigned to NI-based π→π* transition.[28] The NI-based transitions overlap with the MLCT transition at 368 nm. However, the XLCT transition was observed at 417 nm, appearing as a weak shoulder on the NI π→π* transition. In the **Mn–EB** spectrum the NI n→π* and π→π* transitions have a maximum at 375 nm and 390 nm, respectively, resulting in significant overlap with the MLCT and XLCT transitions, effectively obscuring those transitions. The bathochromic and hyperchromic shifts of the NI-based transitions has been previously attributed to the increased

π-conjugation on the EB–NI moiety[29], and an increase in the charge-transfer character of the NI-based transitions with increasingly electron-donating substituents on the NI core.[19,30–32]

4.3.2 Cyclic Voltammetry

Cyclic voltammetry experiments were performed on **Mn–R** in 0.1 M $TBAPF_6$/THF electrolyte solutions under a N_2 atmosphere (Figure 4.2) to establish their behaviour under electrolysis. Reversibility studies of **Mn–R** are presented in Figure S4.4. Additional cyclic voltammograms collected under a CO_2 atmosphere, in the absence and presence of H_2O, are presented in Figure S4.5. The redox potentials of observed redox features from all electrochemical studies of the **Mn–R** series are presented in Table 4.2. The redox potentials (E_0) for reversible waves were determined at the half-wave potential ($E_{1/2}$) and for irreversible waves by noting the cathodic peak potential ($E_{p,c}$) of reduction waves or the anodic peak potential ($E_{p,a}$) of oxidation waves.

Table 4.10. *Reduction potentials of the **Mn–R** series in 0.1 M $TBAPF_6$/THF electrolyte solutions under N_2 and CO_2 atmospheres.*[a]

Sample	Atmosphere	O1 [V]	R1 [V]	R2 [V]	R3 [V]	R4 [V]
Mn–phen	N_2	–0.61[c]	–1.88[c]	–2.09[c]	–[d]	–[d]
	CO_2	–0.60[c]	–1.92[c]	–2.16[c]	–3.07[c]	–[d]
	$CO_2 + H_2O$	–0.66[c]	–1.93[c]	–2.17[c]	–[d]	–[d]
Mn–H	N_2	–0.57[c]	–1.71[c]	–1.94[b]	–2.34[c]	–[d]
	CO_2	–0.54[c]	–1.68[c]	–1.77[b]	–2.20[c]	–3.05[c]
	$CO_2 + H_2O$	–0.58[c]	–1.70[c]	–1.84[c]	–2.25[c]	–[d]
Mn–EB	N_2	–0.61[c]	–1.74[b]	–1.92[c]	–2.39[c]	–[d]
	CO_2	–0.55[c]	–1.64[b]	–1.94[c]	–2.32[c]	–3.05[c]
	$CO_2 + H_2O$	–0.64[c]	–1.67[c]	–1.94[c]	–2.30[c]	–[d]

[a]All potentials are reported versus a Fc^+/Fc internal standard. [b]The $E_{1/2}$ values are given for reversible redox processes. [c]The $E_{p,c}$ values and $E_{p,a}$ values are given for irreversible reduction for oxidation processes, respectively. [d]No E_0 value is reported for these reductions in under the experimental conditions used.

The cyclic voltammograms of **Mn–phen** appeared similar under both N_2 and CO_2 atmospheres (Figures 4.5); displaying three reduction features as reported in the literature.[22] The first

reduction wave (R1) at –1.88 V arises from reduction of the metal centre inducing Br^- dissociation followed by rapid formation of $[Mn(phen)(CO)_3]_2$, referred to as the **Dimer** herein. An accompanying oxidative wave (O1) at ca. –0.60 V arises from oxidation of the **Dimer**. A second reduction wave (R2) at –2.09 V is observed upon the reduction of the **Dimer**, leading to homolytic cleavage of the Mn–Mn bond to form $[Mn(CO)_3(phen)]^-$ as the **5–MA** active catalyst. Under CO_2, a third reduction wave (R3) is observed at –3.07 V is attributed to the addition of a second electron to the **Mn–phen** metallacycle, whereupon rapid CO_2 binding and subsequent catalysis proceeds. In the presence of, 5% H_2O in THF electrolyte, under a CO_2 atmosphere, the catalytic wave is observed at the R2 reduction wave. This is consistent with the literature reports of a catalytic response at less negative potentials when in the presence of a weak Brønsted acid.[6,7,33]

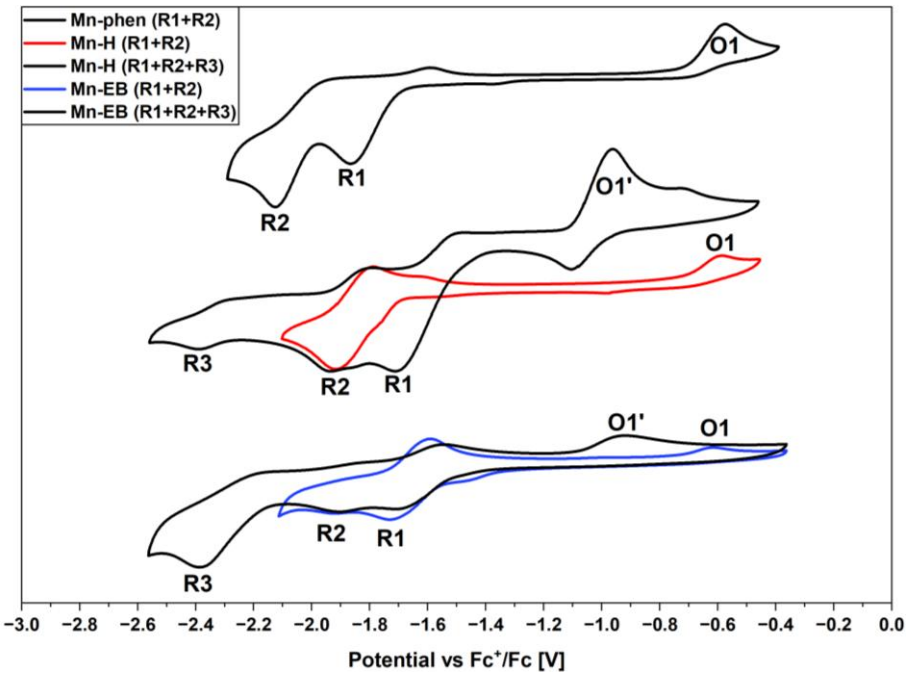


Figure 4.2. *The cyclic voltammograms of* ***Mn–R*** *in THF electrolyte under a* N_2 *atmosphere.*

Mn–H and **Mn–EB** displayed additional redox features in their cyclic voltammograms, further to those of **Mn–phen** model, which are attributed to the presence of the R–NI moiety. For **Mn–H**, the R1 reduction wave ($E_{p,c}$ = –1.88 V) appeared as a shoulder on the reversible R2 reduction wave at –1.98 V. A reversible reduction at *ca.* –2 V versus the Fc^+/Fc redox couple is characteristic of the first reduction based on the H–NI moiety.[34] Thus, **Dimer** formation precedes reduction of the H–NI moiety in **Mn–H**. For **Mn–EB**, the R1 reduction wave at –1.74 V appeared reversible, similarly to the reversible NI-based reduction in **Mn–H**. The irreversible R2 reduction wave is

cathodically shifted relative to the first reduction ($E_{p,c}$ = –1.92 V); consequently, the reduction of the EB–NI moiety precedes the formation of the **Dimer** in **Mn–EB**. Therefore, the NI-reduced dimer **[Dimer]$^{2-}$** is obtained at the R2 reduction wave of both complexes.

For **Mn–H** and **Mn–EB**, the third reduction wave (R3) is observed at –2.34 and –2.39 V, respectively. These potentials are cathodically shifted compared to the R2 reduction wave in **Mn–phen** ($E_{p,c}$ = –2.09 V), corresponding with homolytic cleavage of the **Dimer**. The separation of the reduction waves corresponding to the formation of the **Dimer** and the **5–DA** was 470 mV, significantly greater than the separation for **Mn–phen** (ΔE_{5C} = 240 mV). Therefore, this reduction is assigned to the formation of [Mn(CO)$_3$(R–NI–phen)]$^{2-}$, the 5-coordinate dianion (**5–DA**); with one reduction localised on the **Mn–phen** metallacycle and another based on the R–NI moiety. Thus, by incorporating a R–NI moiety into the structure, a significantly more negative potential is required to generate the 5–coordinate active catalyst of the NI-substituted **Mn–R** complexes. Additionally, the O1 oxidation wave, previously attributed to oxidation of the **Dimer** was not observed for the NI-rhenium complexes. A new oxidation wave however, labelled O1' in Figure 4.2, is observed at more negative potentials ($E_{p,a}$ = –0.96 and –0.91 V for **Mn–H** and **Mn–EB**, respectively). This likely arises from oxidation of the **5–DA** species, possibly including an interaction with the reduced R–NI moiety an account of the pseudo-reversibility of the R–NI redox band, upon cycling the CV scan to R3 and subsequently affecting oxidation of the **Dimer**.

Catalytic responses were observed at *ca*. –3 V under a CO_2 atmosphere, corresponding to the fourth reduction wave (R4) for both **Mn–H** and **Mn–EB**. In the presence of CO_2 and H_2O, the R3 reduction waves of **Mn–H** and **Mn–EB** at *ca*. –2.3 V undergo a cathodic current enhancement. These catalytic responses are similar to those seen for **Mn–phen** at the R2 reduction wave in the presence of CO_2 and H_2O, respectively. These results highlight the importance of having a proton source to enable CO_2 binding at less negative potentials than in the absence of a Brønsted acid.

4.3.3 Spectroelectrochemistry under a N_2 atmosphere

IR and UV-Vis SEC experiments of the **Mn–R** series were performed under a N_2 atmosphere to help identify the species formed at the reduction potentials displayed in Table 4.2. IR and UV-Vis absorption spectra are presented in Figures 4.4–4.6, with the DFT calculated IR spectra presented in Figure S4.7. Summarised in Table 4.3 are the key spectral features observed during the SEC experiments under a N_2 atmosphere for **Mn–R**. The calculated structures of the reduced species identified by the SEC experiments are presented in Figures S8–S11. The spectral evolution of the **Mn–phen** model complex under a N_2 atmosphere is described in full, followed

by a stepwise account of the spectral evolution of the target **Mn–R** complexes under the same conditions.

The parent species of **Mn–phen** in the electrolyte solution (Figure 4.4) displayed identical spectral profiles to those observed in the electrolyte-free IR and UV-Vis spectroscopic studies discussed earlier (Figure 4.1). In the IR spectrum of the R1 species of **Mn–phen** (Figure 4.4A), new $\nu_{C\equiv O}$ vibrations were observed at 1979, 1938, 1885, and 1864 cm^{-1}. The DFT-calculated IR spectrum of the **Dimer** (Figure S4.7A) closely matched the experimental spectra (Table 4.3). DFT calculations supports that the ***syn*-Dimer** is observed experimentally and that the anti-conformation is not (Figure S4.9). In the UV-Vis absorption spectrum, two new transitions are detected at 657 and 787 nm for the R1 species (Figure 4B). From the literature, the $[Mn(phen)(CO)_3]_2$ dimer has a similar spectral profile, with electronic transitions at 740 and 840 nm in THF.[35]

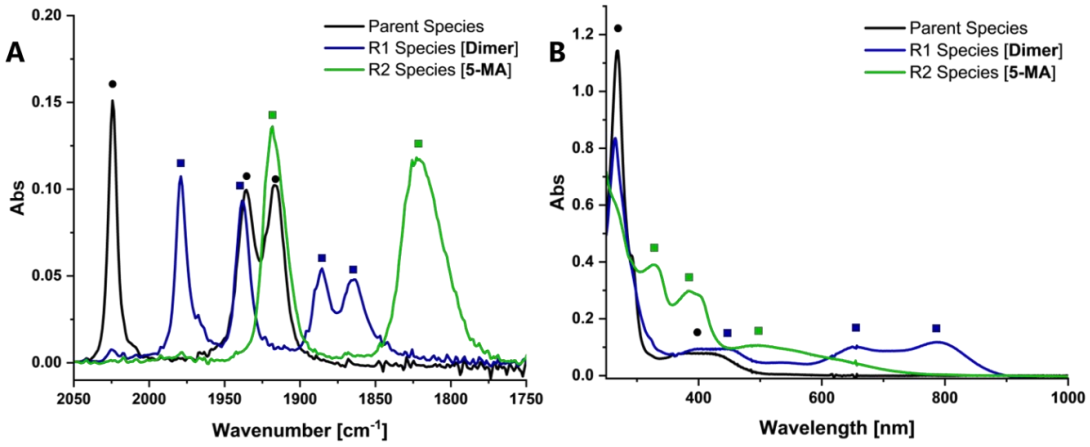


Figure 4.3. *The experimental spectra from SEC studies of* ***Mn–phen*** *and its reduced species in 0.1 M $TBAPF_6$/THF electrolyte. (A) IR spectra. (B) UV-Vis absorption spectra.*

In the IR SEC experiments following reduction of **Mn–phen** at the R2 reduction wave, two new $\nu_{C\equiv O}$ vibrations are observed at 1919 and 1822 cm^{-1}. The IR spectral features of the R2 species closely aligned with the calculated spectra (Table 4.3) and the literature IR spectrum of the $[Mn(bpy)(CO)_3]^-$.[35,10] In the corresponding UV-Vis absorption spectrum of the same species, the disappearance of the **Dimer** transitions at 657 and 787 nm coincided with the formation of a new transition at 500 nm. These differences in the UV-Vis absorption spectra were previously reported following SEC studies for $[Mn(bpy)(CO)_3X]$ (where X = Cl, Br, I) and were attributed to the $[Mn(bpy)(CO)_3]^-$.[35] Therefore, the spectral features seen at the R2 reduction wave are

attributed to the $[Mn(phen)(CO)_3]^-$ species, herein referred to as the 5-coordinate monoanion (**5–MA**). In our SEC studies a reduction pathway for **Mn–phen** is proposed that is typical of $[Mn(\alpha\text{-diimine})(CO)_3Br]$ complexes, with distinct $\nu_{C\equiv O}$ vibrational modes and electronic transitions associated with the **Dimer** and **5–MA** complexes in both the IR and UV-Vis spectra, respectively.

For the **Mn–R** complexes the main focus of this chapter, many of the spectral features that were observed are similar to that described for the model complex. However, as outlined earlier in the electrochemistry section, the inclusion of the R–NI moieties result in additional reduction processes and spectral features specific to the R–NI moieties. The parent **Mn–R** complexes in the electrolyte solution displayed identical spectral profiles to those observed in the electrolyte-free IR and UV-Vis absorption spectra discussed earlier (Figure 4.1). As such, the following discussion focuses on the reduced species of **Mn–H** and **Mn–EB**.

The IR spectrum for the species formed at the R1 reduction wave of **Mn–H** (Figure 4.5A) displayed $\nu_{C\equiv O}$ bands at 1980, 1940, 1888 and 1867 cm^{-1}, similar in appearance to those seen for the R1 species of **Mn–phen** (Table 4.3) and are in close agreement with the calculated IR spectrum of the **Dimer** (Figure S4.7B). Additionally, electronic transitions in the UV-Vis absorption spectrum (Figure 4.5B) associated with the formation of the **Dimer** are observed at 659 and 812 nm. The near-IR transition at 812 nm is red-shifted by 25 nm compared to the lowest energy transition for **Mn–phen**. Accordingly, the R1 reduction wave of **Mn–H** is assigned to the formation of the **Dimer** as previously observed for **Mn–phen**.

For **Mn–EB**, the IR and UV-Vis spectra for the R1 species could only be recorded at the onset of the R1 reduction wave due to the close reduction potentials between the R1 and the R2 reduction waves. As a result, complete conversion to the species formed at R1 was not possible; however, new spectral features associated the species formed at R1 are evident. In the IR spectrum of the R1 species (Figure 4.6A), new $\nu_{C=O}$ bands are formed at 1634 and 1622 cm^{-1} with new $\nu_{C\equiv C}$ vibrations at 2155 and 2139 cm^{-1}. These spectral features are indicative of a reduction localised on the EB–NI moiety, and formation of the EB–NI radical anion ($EB–NI^{\bullet-}$). In the UV-Vis spectrum of the R1 species (Figure 4.6B), new transitions were observed at 440 and 491 nm and were attributed to the $EB–NI^{\bullet-}$. Importantly, these spectral features are observed without any of the spectral changes associated with the formation of the **Dimer**. Therefore, the $\mathbf{[Mn–EB]^-}$ species, formed at the R1 reduction wave of **Mn–EB**, is designated to EB–NI localised reduction.

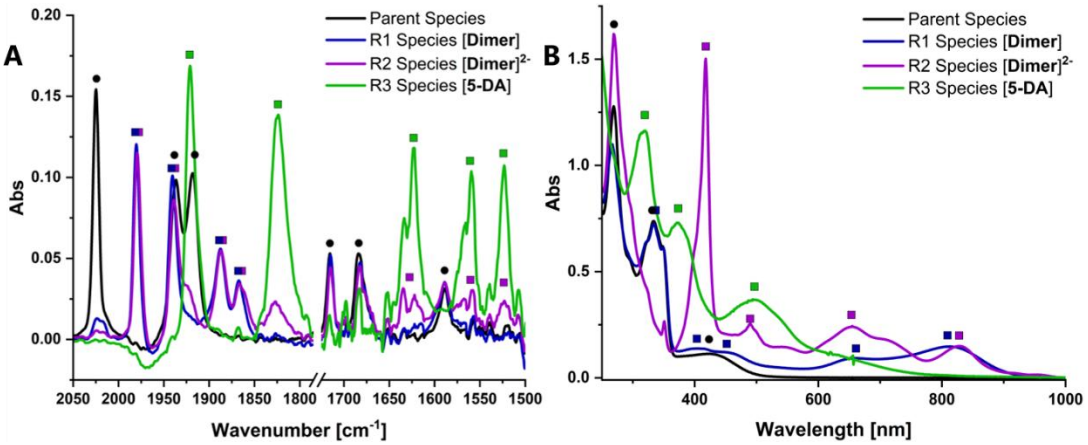


Figure 4.4. *The spectra from the SEC studies of* ***Mn–H*** *and its reduced species in 0.1 M* $TBAPF_6$*/THF electrolyte. (A) IR spectra. (B) UV-Vis absorption spectra.*

At the R2 reduction wave of **Mn–H**, two new $\nu_{C=O}$ vibrations were observed in the IR spectrum at 1634 and 1622 cm^{-1} and are attributed to a reduction localised on the **H–NI** moiety. The $\nu_{C\equiv O}$ vibrations associated with the **Dimer** remained unchanged, though weak $\nu_{C\equiv O}$ vibrations for a 5-coordinate species are seen likely due to an overpotential applied to observe the formation of the $\nu_{C=O}$ bands of the H–$NI^{\bullet-}$. In the UV-Vis absorption spectrum, the growth of a new transition at 418 nm is similar in appearance to literature reports of the H–$NI^{\bullet-}$.[34] Additional spectral changes to the transitions associated to the **Dimer** are observed; the transition at 659 nm increases in absorbance and the maximum shifts to 655 nm, and the near-IR transition undergoes a further redshift and narrowing with a peak at 828 nm. Therefore, the species formed at the R2 reduction wave of **Mn–H** is assigned to the NI-reduced dimer, labelled **$[Dimer]^{2-}$** herein.

At the R2 reduction wave of **Mn–EB**, the IR and UV-Vis spectral features associated with the **$[Mn–EB]^{-}$** complex reach their maximum absorbance. Additionally, the parent $\nu_{C\equiv O}$ vibrations is observed to decay in the IR spectrum in Figure 4.6A. This is coupled with the growth of new $\nu_{C\equiv O}$ vibrations at 1977, 1936, 1886, and 1860 cm^{-1} that closely match the **Dimer** seen for **Mn–phen**. The calculated IR spectrum of the **Dimer** of **Mn–EB** (Figure S4.7C) closely matches the experimental IR spectrum recorded at the R2 reduction wave (Table 4.3). Additionally, new near-IR transitions are observed at 800 and 898 nm in the UV-Vis absorption spectrum which have a similar absorbance profile to that of the **Dimer** of the **Mn–phen** complex (Figure 4.4). Thus, the appearance of spectral features attributed to a Mn-Mn dimer, together with the retention of the

[Mn–EB]$^{-}$ spectral features attributed to a NI-based reduction, indicates that the **[Mn–EB]**$^{2-}$ is observed at the R2 reduction wave.

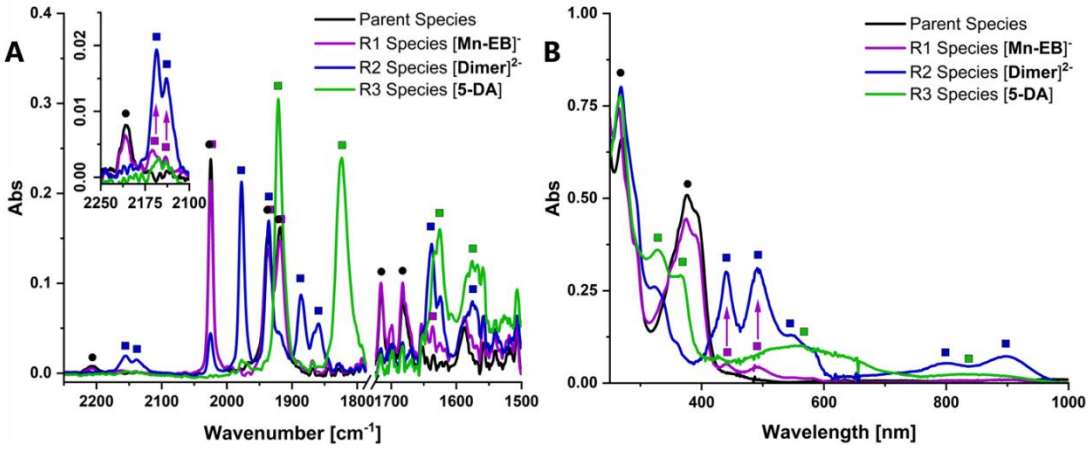


Figure 4.5. *The spectra recorded in the SEC studies of* ***Mn–EB*** *and its reduced species in 0.1 M $TBAPF_6$/THF electrolyte. (A) IR spectra. (B) UV-Vis absorption spectra.*

Based on the IR and UV-Vis spectra recorded at the R2 reduction wave of both **Mn–R** complexes, the **[Dimer]**$^{2-}$ species is formed for both complexes even though they form different species at the R1 reduction wave. Accordingly, **Mn–H** and **Mn–EB** undergo similar spectral changes at the R3 reduction wave (Table 4.3). Particularly, the appearance of two new $\nu_{C\equiv O}$ vibrations at 1920 and 1824 cm^{-1} in the IR spectra coincides with the decay of the **[Dimer]**$^{2-}$ $\nu_{C\equiv O}$ vibrations. The $\nu_{C=O}$ bands between 1650 – 1600 cm^{-1}, associated with the reduced R–NI moiety, are retained. Furthermore, the UV-Vis absorption spectra displayed new transitions at 497 and 552 nm for **Mn–H** and **Mn–EB**, respectively. These new IR and UV-Vis spectral features, which form concurrently with the decay of the **[Dimer]**$^{2-}$ spectral features, closely resemble the **5–MA** of the **Mn–phen** model (Figure 4.4). As such, the [Mn(R–NI–phen)$^{2-}$(CO)$_3$]$^{2-}$ species (**5–DA** herein) is formed at R3, with the added electrons on the R–NI moiety and another on the **Mn–phen** metallacycle. The **5–MA** could also be formed by electron transfer from the reduced R–NI moiety to the **Mn–phen** metallacycle, similarly to electron transfer proposed in the reduction pathway of the **Re–R** complexes discussed in the previous chapter (Scheme 3.1). This leads to the formation of the **5–MA** with the two added electrons localised on the **Mn–phen** metallacycle similarly to active catalyst reported for the **Mn–phen** model. However, it is challenging to discern the **5–DA** from the **5–MA** spectrally as indicated in the previous chapter for the **^{2}5–DA** from the **^{1}5–MA**.

Table 4.11. *Key spectral features from IR and UV-Vis SEC experiments of* ***Mn–R*** *in THF electrolyte.*

Complex	λ_{max} (nm)	$\nu_{C\equiv O}$ (cm^{-1})	Calc. $\nu_{C\equiv O}$ (cm^{-1})	$\nu_{C=O}$ (cm^{-1})	Calc. $\nu_{C=O}$ (cm^{-1})	$\nu_{C\equiv C}$ (cm^{-1})	Calc. $\nu_{C\equiv C}$ (cm^{-1})
Mn–phen	269, 382, 420	2024, 1937, 1917	2024, 1956, 1946	–	–	–	–
Dimer	265, 400, 447, 657, 787	1979, 1938, 1885, 1864	1973, 1927, 1902, 1883	–	–	–	–
5–MA	328, 384, 500	1919, 1822	1915, 1853	–	–	–	–
Mn–H	269, 334, 425	2025, 1937, 1918	2015, 1947, 1937	1716, 1684	1726, 1695	–	–
Dimer	267, 334, 404, 449, 659, 812	1980, 1940, 1888, 1867	1965, 1923, 1891, 1875	1715, 1682	1720, 1687	–	–
[Dimer]$^{2-}$	269, 418, 490, 655, 828	1980, 1939, 1888, 1866	1965, 1923, 1891, 1875[b]	1635, 1622	–[a]	–	–
5–DA	320, 372, 497	1921, 1824	1909, 1847	1633, 1623	–[a]	–	–
Mn–EB	270, 376	2025, 1937, 1919	2015, 1947, 1937	1715, 1682	1725, 1693	2207	2197
[Mn–EB]$^{-}$	265, 440, 491	2025, 1937, 1919	–[a]	1637, 1625	–[a]	2162, 2140	–[a]
[Dimer]$^{2-}$	268, 440, 491, 546, 800, 898	1977, 1936, 1886, 1860	1965, 1924, 1892, 1875[b]	1638, 1624	–[a]	2155, 2139	2197
5–DA	329, 365, 552, 836	1920, 1824	1959, 1878	1626	–[a]	–	–[a]

The calculated $\nu_{C\equiv O}$, $\nu_{C=O}$, and $\nu_{C\equiv C}$ values were adjusted by a 0.94 correction factor. [a]The DFT calculations do not simulate the NI-based reductions, thus, no calculated $\nu_{C=O}$, and $\nu_{C\equiv C}$ values are reported for this species. [b]The calculated $\nu_{C\equiv O}$ bands for the $[Mn(R\text{-}NI\text{-}phen)(CO)_3]_2$ are reported instead of ***[Mn–R]$^{2-}$****.*

4.3.4 Infrared Spectroelectrochemistry under a CO_2 atmosphere

IR SEC studies were recorded for the **Mn–R** series to identify the species formed under a CO_2 atmosphere. The same reduced species were observed in the IR spectra under N_2 (Figures 4.4A–4.6A) and CO_2 atmospheres (Figure S4.6). Accordingly, a brief account of electrocatalysis observed during this experiment is provided below.

The formation of the same reduced species under both atmospheres indicates that CO_2 binding does not readily occur upon the formation of the 5-coordinate species. CO_2 binding only occurs at R3 for **Mn–phen** and at R4 for **Mn–R**, coinciding with a further reduction of the **Mn–phen** metallacycle. At the R3, the **Mn–phen** reduces CO_2 to form CO gas, which rapidly evolves from solution, and the carbonate species are detected between 1700–1600 cm^{-1}.[33,36] These carbonate species may also form at the R4 reduction wave of **Mn–R**; however, the carbonate spectral features appear in the same region as that of the NI-based $\nu_{C=O}$ bands, making assignments in this region more challenging. Thus, the **Mn–phen** model complex is used to interpret the features associated with the formation of the carbonate species, although it is likely that the same catalytic processes take place for all **Mn–R** complexes.

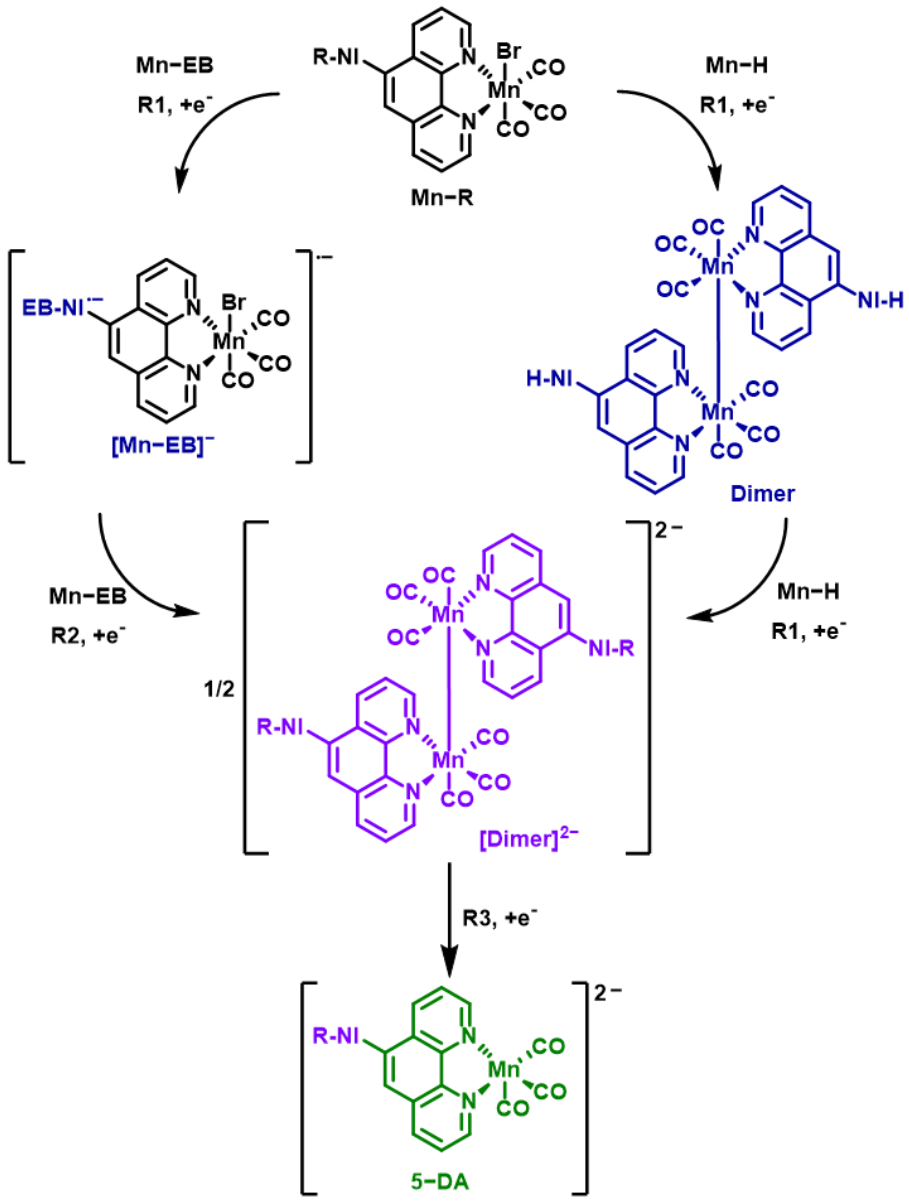
Two organic carbonyl vibrations at 1682 and 1636 cm^{-1} are observed in the IR spectra of **Mn–phen** (Figure S4.6A), tentatively assigned to the formation of bicarbonate species.[33,37,38] These bands were initially observed with the **Dimer** and slowly increase in absorbance upon the formation of the **5–MA**. At the R3 reduction wave, the bicarbonate $\nu_{C=O}$ bands are notably higher in absorbance than the $\nu_{C\equiv O}$ bands (1919 and 1826 cm^{-1}) for the **5–MA**, which had a lower absorbance compared to the spectrum of the **5–MA** at the R2 reduction wave. This is indicative of a slow catalytic response, and likely decomposition of the catalyst at very negative potentials (*ca*. –3 V vs Fc^+/Fc).

4.3.5 Proposed Reduction Pathway to the Active Catalyst

Herein, the reduction pathways of the **Mn–R** complexes leading to the active catalyst are outlined according to the experimental work and the supporting DFT calculations presented in this work.

The R1 reductions of the two **Mn–R** complexes are different (Scheme 4.2). For **Mn–H**, SEC studies revealed that the initial reduction leads to formation of the **Dimer** as is observed for **Mn–phen**. This is followed by the reversible R2 reduction wave resulting in a NI-based reduction of the dimeric species, forming the so-called NI-reduced dimer **[Dimer]$^{2-}$**. For **Mn–EB**, the initial

reduction results in a reduction localised on the EB–NI moiety, with the subsequent reduction at the R2 reduction wave resulting in the formation of **[Mn–EB]$^{2-}$**. While the R1→R2 reduction sequence differs between the two **Mn–R** complexes, both produce the **[Dimer]$^{2-}$** at the R2 reduction wave.



Scheme 4.9. *Reduction pathway for the formation of the active catalyst of **Mn–R** under CO_2. The intermediate species identified in IR SEC experiments in the presence of CO_2 are highlighted.*

At the R3 reduction wave of both **Mn–R** complexes, homolytic cleavage of **[Dimer]$^{2-}$** produces the **5–DA**. Homolytic cleavage of the **[Dimer]$^{2-}$** occurs at a more negative potential than cleavage

of the **Dimer** of **Mn–phen**; attributed to the presence of the R–NI moieties. However, the more negative potential required for homolytic cleavage prolongs the existence of the more stable dimeric species, which may be beneficial to the longevity of these complexes. The presence of the R–NI moiety does not alter the potential required for CO_2 binding compared to **Mn–phen**, occurring at ca. –3 V vs Fc^+/Fc. This overpotential was required for all **Mn–R** complexes to electrocatalytically reduce CO_2 under these conditions. A bimolecular mechanism which consumes two equivalents of CO_2 to yield CO and bicarbonate species could explain the appearance of the IR spectra collected in this experiment (Figure S4.6.[36,48]

4.3.6 Infrared Spectroelectrochemistry under a CO_2 atmosphere with H_2O

IR SEC experiments for the **Mn–R** series were conducted under a CO_2 atmosphere in a 5% H_2O/THF electrolyte solution to assess the effect of adding a Brønsted acid on electrocatalytic CO_2 reduction. The IR spectra collected from these experiments are presented in Figures 4.7–4.9, with the key IR spectral features recorded in Table 4.4. The behaviour of the **Mn–R** complexes differed in the SEC experiments in the presence of a Brønsted acid; as such, a more detailed account of the observations is provided below.

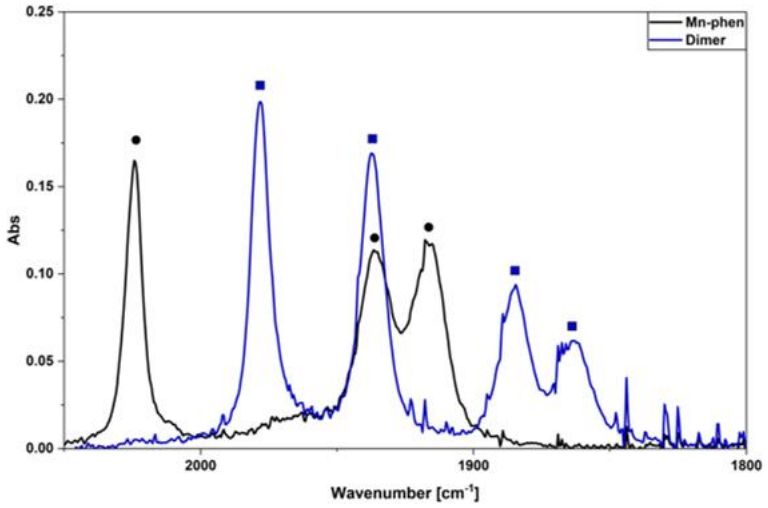


Figure 4.6. *IR spectra of **Mn–phen** (4 mM) for the SEC experiment conducted in 5% H_2O/THF electrolyte under CO_2.*

For the **Mn–phen** model complex, conversion to the **Dimer** is observed at the R1 reduction wave as described previously. Unlike the previous SEC experiments, slow evolution of a gas, likely CO

gas, was observed upon the formation of the **Dimer**. Additionally, no further spectral changes were observed at more negative potentials, though the evolution of CO gas is more rapid at the R2 reduction wave and at more negative potentials. The different rates of CO gas evolution between the R1 and R2 reduction waves is a known phenomenon for Mn(α-diimine) tricarbonyl complexes, distinguished by the progression from the protonation-first pathway at R1 to the reduction-first pathway at R2.[11]

The presence of CO_2 and H^+ in solution enables the formation of the 18e$^-$ metallocarboxylic acid complex, [Mn(α-diimine)$(CO)_3(CO_2H)$], with a hydroxycarbonyl ligand inserted into the vacant sixth coordination site of the **5–MA** active catalyst.[11] While the **Dimer** is primarily formed at R1, a small amount of the "child" **5–MA** active catalyst can bind with CO_2 to form [Mn(phen)$(CO)_3(CO_2H)$] as the metallocarboxylic acid (**Mn–CO_2H**) species (Figure S4.12B) and enters the protonation-first pathway. Similarly, upon cleavage of the **Dimer**, the **5–MA** rapidly enters the reduction-first pathway. The **5–MA** and **Mn–CO_2H** complexes are not observed for **Mn–phen** in this study, as any **Mn–CO_2H** formed rapidly enters the catalytic CO_2 reduction pathways.

Reduction at the R1 reduction wave of **Mn–H** leads to the formation of the **Dimer** $\nu_{C\equiv O}$ bands, as observed in the SEC studies earlier in this work, together with slow CO evolution. Monitoring the $\nu_{C=O}$ bands associated with the NI-based reduction is challenging in the 5% H_2O/THF electrolyte due to a significant solvent absorption between 1700 – 1600 cm^{-1} arising from the ν_{O-H} bending mode of H_2O.[39] However, the $\nu_{C=O}$ band at 1715 cm^{-1} can be monitored during the course of the SEC experiment. Indeed, at the R2 reduction wave this $\nu_{C=O}$ band is red shifted by 3 cm^{-1} and a new band at 1623 cm^{-1} is observed, however this band overlaps with the aforementioned solvent band. Concurrently, a *ca*. 5 cm^{-1} red shift was observed for the $\nu_{C\equiv O}$ bands of the **Dimer**. These may indicate that **[Dimer]$^{2-}$** is formed, which would match the earlier SEC studies of **Mn–H** at R2 without a proton source.

Rapid CO evolution occurs at the R2 reduction wave and no further spectral changes are observed, similarly to the evolution to the reduction-first pathway determined for **Mn–phen**. This suggests that a 5-coordinate species is formed from the **[Dimer]$^{2-}$** at the R2 reduction wave; involving the transfer of an electron from the H–NI moiety to the **Mn–phen** metallacycle to induce homolytic cleavage and producing the **5–MA** active catalyst. Due to the presence of CO_2 and H^+ in solution, CO_2 binding can readily occur to produce the [Mn(H–NI–phen)$(CO)_3(CO_2H)$] complex, analogous to the **Mn–CO_2H** complex proposed for **Mn–phen**. Thus, the product of the electron transfer process, the **5–MA**, is in a sense stabilised. The **Mn–CO_2H** formed at the R2

reduction wave rapidly enters the catalytic CO_2 reduction pathway and so is not observed in this study. This may explain the apparent decay of the **[Dimer]$^{2-}$** $\nu_{C\equiv O}$ bands compared to those of the **Dimer**, which was not observed in the SEC experiments under N_2 or CO_2 atmospheres. Significantly, **Mn–H** and **Mn–phen** both enter the more efficient reduction-first pathway at R2, but R2 is *ca*. 300 mV lower for **Mn–H** than **Mn–phen** (Table 4.2).

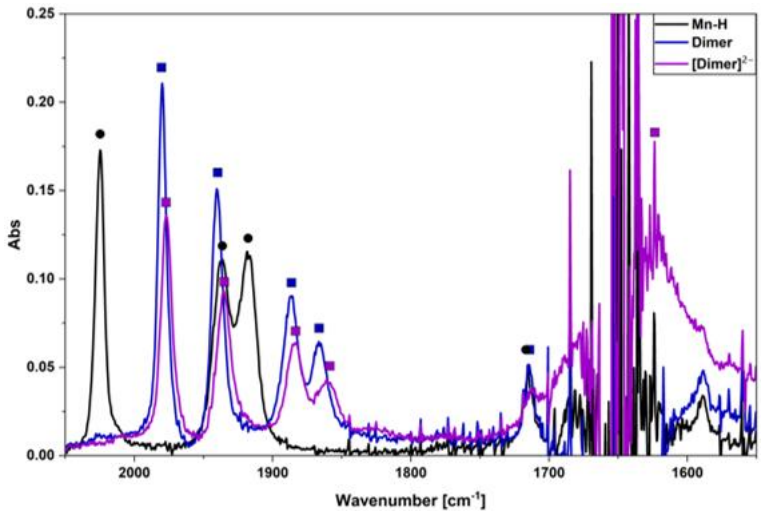


Figure 4.7. *IR spectra of* ***Mn–H*** *(4 mM) for the SEC experiment conducted in 5% H_2O/THF electrolyte under CO_2.*

The experiments conducted for **Mn–EB** in the 5% H_2O/THF electrolyte highlight significant differences in its reduction pathway in the presence of H^+ compared to the earlier SEC studies. At the R1 reduction wave, no spectral features were observed for the formation of **[Mn–EB]$^-$** as expected, associated with the formation of the **EB–NI$^{\bullet-}$**. Instead, $\nu_{C\equiv O}$ bands matching the **Dimer** are observed at 1978, 1938, 1889, and 1866 cm^{-1}, together with two new $\nu_{C\equiv O}$ bands at 1997 and 1895 cm^{-1}. These spectral changes coincide with slow CO evolution at this potential.

The new $\nu_{C\equiv O}$ bands at 1997 and 1895 cm^{-1} were only observed for **Mn–EB** in the presence of CO_2 and H^+. A THF-solvated species can be ruled out as the DFT-calculated IR spectrum of the solvated species [Mn^0(EB–NI–phen)(CO)$_3$(THF)] does not match with the $\nu_{C\equiv O}$ bands at 1997 and 1895 cm^{-1} (Figure S4.12A), and such a complex was not observed in the previously discussed SEC studies. Similar $\nu_{C\equiv O}$ bands have been reported for manganese diphosphine tricarbonyl complexes with an ester ligand instead of Br ([Mn(PP)(CO)$_3$(CO$_2$R)]BF$_4$ where PP = diphenylphosphino ethane or diphenylphosphino propane, and R = Me or Et).[40]

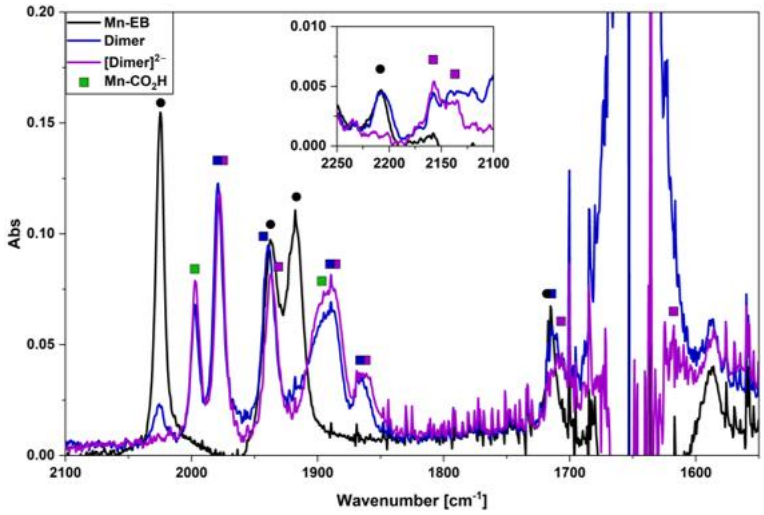


Figure 4.8. *IR spectra of* ***Mn–EB*** *(4 mM) for the SEC experiment in 5% H_2O/ THF electrolyte under CO_2, with an inset showing the $\nu_{C\equiv C}$ bands. The $\nu_{C\equiv O}$ bands attributed to the* ***Mn–CO_2H*** *complex, indicated by the green boxes, are present in the spectra of the* ***Dimer*** *and* ***[Dimer]$^{2-}$****.*

Manganese and rhenium metallocarboxylic acid complexes have been reported; the [Mn(mesbpy)(CO)$_3$(CO$_2$H)] complex (mesbpy = 6,6'-dimesityl-2,2'-bipyridine) with $\nu_{C\equiv O}$ bands at 2006 and 1907 cm^{-1} in CH_3CN with 80 mM MeOH resembles the profile of the observed bands at 1997 and 1895 cm^{-1} in this work.[5,41] Furthermore, the DFT-calculated IR spectrum of the **Mn–CO_2H** complex (Figure S4.12A) displays $\nu_{C\equiv O}$ bands at 1994, 1916, and 1908 cm^{-1}, which are a good match for the observed bands at 1997 and 1895 cm^{-1} with an additional band underlying the **Dimer** $\nu_{C\equiv O}$ band at 1889 cm^{-1}. Furthermore, the formation of a metallocarboxylic acid complex agrees with the proposed reduction pathways of **Mn–phen** and **Mn–H** under these experimental conditions.

In the absence of a proton source, the EB–NI moiety is reduced at the R1 reduction wave; this reduction step is expected to occur in the presence of a proton source. Therefore, the initial reduction of the EB–NI moiety in the **[Mn–EB]**$^-$ species likely undergoes rapid electron transfer on to the **Mn–phen** metallacycle inducing Br$^-$ dissociation and producing the **5–MA**. This mechanism is the same as that proposed for the homolytic cleavage of the **Dimer** of **Mn–H** at the R2 reduction wave under the same conditions. While the **5–MA** can undergo dimerisation to yield the **Dimer**, this typically occurs at R2 for **Mn–EB** which is *ca*. 250 mV more negative (Table 4.2). Thus, dimerisation is likely slower at R1. In combination with the slow protonation-first pathway at R1, this allows for the 18e$^-$ **Mn–CO_2H** complex [Mn(EB–NI–phen)(CO)$_3$(CO$_2$H)] to accumulate in solution at the R1 reduction wave.

A Re–Re dimer, and the corresponding heterobimetallic Re–Mn dimer, have been reported to undergo intramolecular electron transfer in their reduction pathways for electrocatalytic CO_2 reduction.[36,42] In the Re–Mn dimer, the singly reduced Re metal centre undergoes intramolecular electron transfer to the **Mn–CO_2H** component allowing for CO_2 reduction at a lower overpotential than for either of the individual components.[42] With the Re analogues of the **Mn–EB** complexes in this work, detailed time-resolved spectroscopic studies have shown that excitation of the R–NI$^{\bullet-}$ moiety results in charge transfer to the Re–phen metallacycle. Thus, an intramolecular electron transfer mechanism from the reduced R–NI moiety to the **Mn–phen** metallacycle is possible.

At the R2 reduction wave of **Mn–EB**, new $\nu_{C\equiv C}$ bands are observed at 2157 and 2141 cm^{-1} provide evidence for a NI-based reduction. Additionally, a new $\nu_{C=O}$ band at 1618 cm^{-1} is observed, with a concurrent red shift of the 1715 cm^{-1} $\nu_{C=O}$ band to 1707 cm^{-1}, likely arising from the formation of **EB–NI$^{\bullet-}$**. The **Dimer** $\nu_{C\equiv O}$ bands undergo a *ca*. 5 cm^{-1} red shift, similarly to that observed upon the proposed formation of **[Dimer]$^{2-}$** in the experiment with **Mn–H**. Therefore, the new spectral features observed at the R2 reduction wave of **Mn–EB** are attributed to **[Dimer]$^{2-}$**. The **[Dimer]$^{2-}$** $\nu_{C\equiv O}$ bands decayed slightly compared to those of the **Dimer**, while a slight rise in the absorbance of the **Mn–CO_2H** $\nu_{C\equiv O}$ bands being observed. A similar decay of the **[Dimer]$^{2-}$** $\nu_{C\equiv O}$ bands was observed for **Mn–H** in Figure 4.8, although the concurrent rise of **Mn–CO_2H** $\nu_{C\equiv O}$ bands is not observed. The accumulation of **Mn–CO_2H** in solution at the R2 reduction wave of **Mn–EB** supports the proposed electron transfer mechanism in the **[Dimer]$^{2-}$** species; with electron transfer from the reduced **R–NI** moiety to the **Mn–phen** metallacycle resulting in the formation of **Mn–CO_2H** in the presence of CO_2 and H^+. Rapid CO evolution occurs at this potential and no further spectral changes are observed at more negative potentials, representing progression to the reduction-first catalytic pathway.

This study indicates that electron transfer from the reduced R–NI moiety to the **Mn–phen** metallacycle plays a key role in the reduction pathway of the **Mn–R** complexes in the presence of CO_2 and H^+. The **Mn–EB** complex is particularly insightful in this regard; due to the reduction of the R–NI moiety preceding the formation of the **Dimer**, it was possible to accumulate the **Mn–CO_2H** complex in solution via electron transfer mechanism at the R1 reduction wave. Both **Mn–R** complexes likely form the **Mn–CO_2H** complex upon cleavage of the **[Dimer]$^{2-}$** at the R2 reduction wave, via the same electron transfer mechanism. Thus, the **Mn–R** complexes produce the **5–MA** as the active catalyst at the R2 reduction wave in the presence of CO_2 and H^+, instead of at the R3 reduction wave under N_2 and CO_2. Furthermore, the R2 reduction waves of **Mn–R** are less negative (–1.84 and –1.94 V, for **Mn–H** and **Mn–EB**, respectively) than that of **Mn–phen**

(–2.17 V), indicating electrocatalytic CO_2 reduction can be achieved at lower overpotentials for **Mn–R** than **Mn–phen**. The electrocatalytic performance of **Mn–R** in the presence of CO_2 and H^+, is assessed in the following section.

Table 4.12. *Key IR spectral features from SEC experiments under CO_2 with H_2O.*

Complex	$\nu_{C\equiv O}$ (cm^{-1})	Calc. $\nu_{C\equiv O}$[b] (cm^{-1})	$\nu_{C=O}$[a] (cm^{-1})	Calc. $\nu_{C=O}$[b] (cm^{-1})	$\nu_{C\equiv C}$ (cm^{-1})
Mn–phen	2024, 1936, 1916	2024, 1949, 1941	–	–	–
Dimer	1978, 1937, 1884, 1864	1950, 1899, 1874, 1858	–	–	–
Mn–H	2025, 1937, 1918	2024, 1949, 1941	1715	–	–
Dimer	1980, 1940, 1886, 1867	1950, 1899, 1874, 1858	1715	–	–
[Dimer]$^{2-}$	1977, 1935, 1883, 1861	–	1712, 1623	–	–
Mn–EB	2025, 1937, 1917	2024, 1949, 1941	1715	–	2208
Dimer	1979, 1939, 1888, 1865	1950, 1899, 1874, 1858	1715	–	2208
Mn–CO_2H	1997, 1895	1994, 1916, 1908	1715	1647[c]	2208
[Dimer]$^{2-}$	1977, 1937, 1889, 1863	–	1707, 1618	–	2157, 2135

*[a]The **R–NI** $\nu_{C=O}$ bands between 1700 – 1600 cm^{-1} are obscured by a band arising from the 5% H_2O in THF electrolyte mixture. [b]The calculated $\nu_{C\equiv O}$ and $\nu_{C=O}$ values are for the **Mn–phen** metallacycle and its reduced species in CH_3CN; thus, no $\nu_{C=O}$ or $\nu_{C\equiv C}$ bands based on the R–NI moiety are calculated. [c]The calculated $\nu_{C=O}$ value arises from the hydroxycarbonyl ligand (CO_2H) bound to the **Mn–phen** metallacycle.*

4.3.7 Electrocatalysis

Controlled Potential Electrolysis (CPE) experiments were conducted on **Mn–R** to assess their ability to electrocatalytically reduce CO_2. The results of the CPE experiments are summarised in Table 4.5.

The CPE experiments were performed for 1 h at a potential of -2.30 V (vs Fc^+/Fc), at which the **5–MA** active catalyst of **Mn–phen** is formed. A blank CPE experiment, with CO_2 saturated 5% H_2O in THF electrolyte at -2.30 V vs Fc^+/Fc, produced no detectable amount of H_2 and a minimal amount of CO (2.46 µmol). All samples produced detectable amounts of CO and H_2; specifically, the TON_{CO} ranged from 4–6 across all samples and a TON_{H2} of 2 was obtained for all samples (Table 4.5). This supports that the samples in this study electrocatalyse CO_2 reduction in the presence of a Brønsted acid.

The faradaic efficiency (η_{FE}) of **Mn–phen** at -2.30 V (vs Fc^+/Fc) is 65%:32% ($CO:H_2$); showing a greater selectivity for CO over H_2. This is in agreement with previous electrocatalytic experiments with **Mn–phen**, producing η_{FE} of 57% and 33% ($CO:H_2$) under optimised conditions (at -1.90 V vs Ag^+/Ag, with 15% H_2O in a 0.1 M $TBAPF_6/CH_3CN$ electrolyte over 7 h).[22] For **Mn–H** and **Mn–EB**, the **[Dimer]$^{2-}$** species are formed at this potential as outlined in the SEC section. **Mn–H** and **Mn–EB** had a reduced selectivity for H_2 (η_{FE} = 27% and 21%, respectively) compared to that of **Mn–phen**, while retaining a high selectivity for CO. These results indicate that a 5-coordinate species is produced from the **[Dimer]$^{2-}$** species in the presence of a Brønsted acid.

Table 4.13. *Controlled potential electrolysis results during 1 h experiments with 0.8 mM samples of catalyst in a 5% H_2O/THF electrolyte solution with 600 rpm stirring.*

Catalyst	Potential [V vs Fc^+/Fc]	Charge Passed (C)	TON_{CO}	TON_{H2}	η_{FE} ($CO:H_2$)
Mn–phen	–2.30	0.6557	4	2	65%:32%
Mn–H	–2.30	0.6277	5	2	75%:25%
Mn–EB	–2.30	0.8337	6	2	73%:24%

All experiments were carried out in triplicate and the averages are reported.

4.3.8 Proposed Catalyst Activation Pathway under CO_2 with H_2O

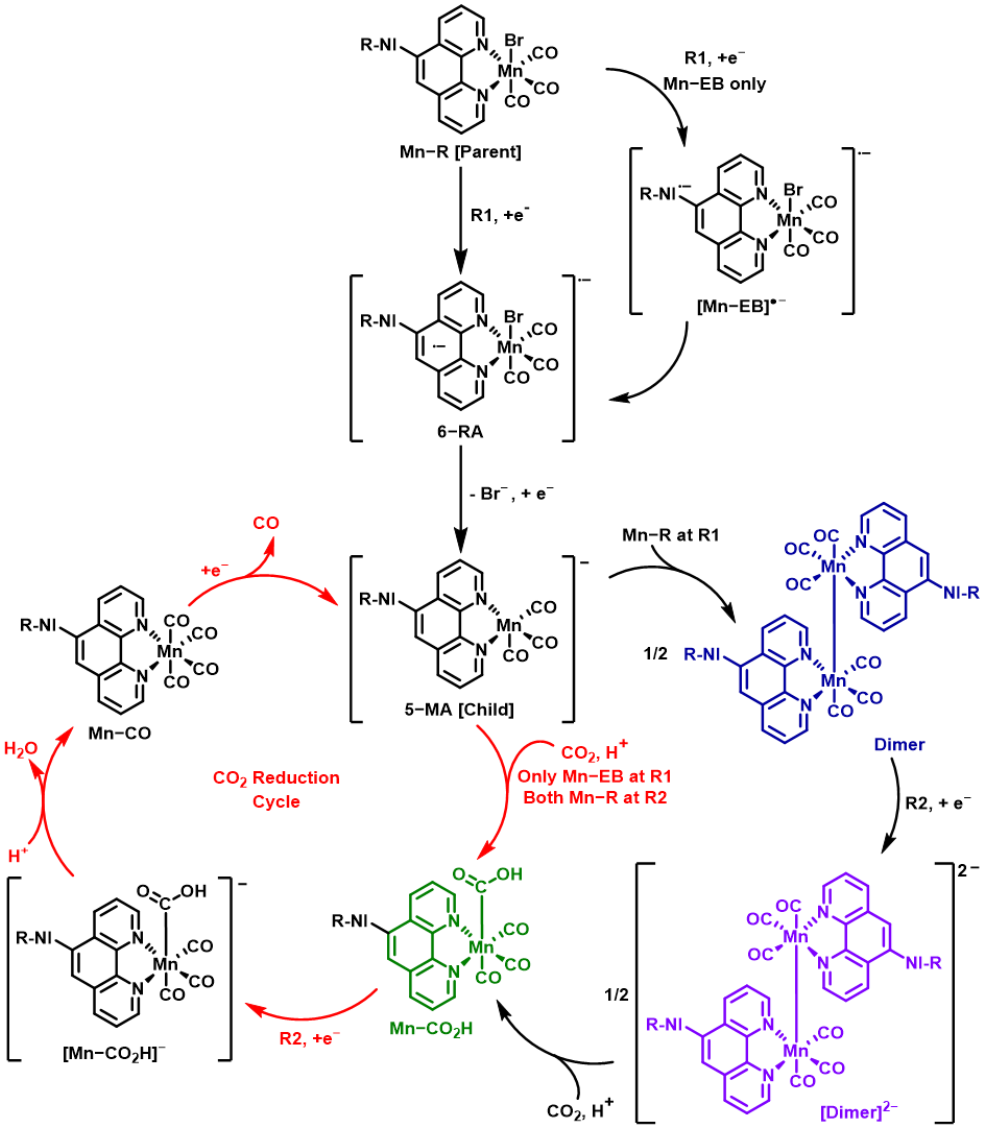
The catalyst activation pathways for the **Mn–R** complexes are presented in Scheme 4.3 according to the experimental work, and the supporting DFT calculations, outlined in this chapter. Additionally, the literature mechanisms for electrocatalytic CO_2 reduction by [Mn(α-diimine)$(CO)_3$X] complexes (where X = a halide, pseudo-halide, or solvent molecule) in the presence of a Brønsted acid were considered when proposing the reduction pathways of **Mn–R**.[7,10,13–15,47–50]

In the presence of CO_2 and H^+, the catalytic response of the **Mn–R** complexes occurs at less negative potentials than in the absence of H^+ (Figure S4.5). In the case of **Mn–H**, the **Dimer** is formed at the initial reduction step (Scheme 4.3). For **Mn–EB**, as the first reduction is based on the EB–NI moiety as observed in the SEC experiments (Figure 4.6), it is likely that electron transfer from the reduced EB–NI onto the **Mn–phen** metallacycle inducing Br^- dissociation; producing the **5–MA** active catalyst already at R1. Typically, the **5–MA** would rapidly react with parent **Mn–EB** in a parent-child comproportionation chemical reaction to produce the **Dimer**. However, formation of the **Dimer** is typically observed for **Mn–EB** at the R2 reduction wave; thus, the **5–MA** is produced at a less negative potential in the presence of H^+. Therefore, dimerisation is slower at the R1 reduction wave which allows for the concurrent formation of the stable complex **Mn–CO_2H** in the presence of a Brønsted acid. Slow CO evolution is observed at the R1 reduction wave of both **Mn–R** complexes, indicating that electrocatalysis may proceed via the kinetically slow protonation-first pathway (not shown in Scheme 4.3).

At the R2 reduction wave of both **Mn–R** complexes, the **[Dimer]$^{2-}$** is produced but undergoes electron transfer from the reduced R–NI moiety onto the **Mn–phen** metallacycle. Electron transfer to induce homolytic cleavage of **[Dimer]$^{2-}$** can occur at less negative potentials than R3 under CO_2, producing the **5–MA**. Furthermore, the stable **Mn–CO_2H** complex is only formed from the **5–MA** in the presence of a Brønsted acid. This is supported by the slow accumulation of the **Mn–CO_2H** complex is seen in the IR spectrum of **Mn–EB** at the R2 reduction wave (Figure 4.9), with the concurrent decay of the $\nu_{C\equiv O}$ bands associated with the **[Mn–R]$^{2-}$**. The **Mn–CO_2H** complex proceeds down the reduction-first pathway at the R2 reduction wave as illustrated in Scheme 4.3.

Electrocatalytic CO_2 reduction ensues after the formation of the **Mn–CO_2H** complex at the R2 reduction wave of both **Mn–R** complexes. While direct evidence for the species involved in this part of the catalytic cycle are not observed in this work, a pathway is proposed based on the reduction-first pathway widely reported in the literature as follows. Further reduction of **Mn–**

CO_2H produces the 19e⁻ $[Mn(R–NI–phen)(CO)_3(CO_2H)]^-$ complex (**$[Mn–CO_2H]^-$** in Scheme 4.3). This may occur via direct reduction of the **Mn–phen** metallacycle or a further reduction of the R–NI moiety and repeats the previously described electron transfer step onto the **Mn–phen** metallacycle. Either way, the hydroxycarbonyl ligand on the **$[Mn–CO_2H]^-$** complex rapidly decomposes to CO and OH^-, the latter of which reacts with H^+ to release H_2O, leaving the tetracarbonyl complex $[Mn(R–NI–phen)(CO)_4]$ (**Mn–CO** in Scheme 4.3).[45] CO release from **Mn–CO** is spontaneous at this potential allowing for the regeneration of the **5–MA** following reduction, which can participate in further catalytic cycles.[8]



Scheme 4.10. *Proposed reduction pathway of* ***Mn–R*** *in the presence of CO_2 and H^+. The intermediate species identified in IR SEC experiments in the presence of CO_2 and H^+ are highlighted. The* ***Mn–CO_2H*** *complex is only observed for* ***Mn–EB*** *in the aforementioned IR SEC experiments. The CO_2 reduction cycle (red) illustrates the reduction-first catalytic pathway.*

4.4 Conclusion

The **Mn–H** and **Mn–EB** complexes, with **R–NI** moieties appended onto the **Mn–phen** model complex, were synthesised and successfully employed in electrochemical and spectroelectrochemical studies. SEC studies were key to discerning the pathway leading to the CO_2-reducing active catalyst of **Mn–H** and **Mn–EB**. Under CO_2, the **5–DA** is obtained as the active catalyst with CO_2 reduction at negative potentials *ca*. -3 V vs Fc^+/Fc. In the presence of CO_2 and a proton source, the **5–MA** is the active catalyst and follows a different catalytic pathway involving the formation of a metallocarboxylic acid complex **Mn–CO_2H**.

Compared to **Mn–phen**, the **R–NI** moieties of **Mn–H** and **Mn–EB** play a key role in the reduction pathway in the presence of CO_2 and H^+. The IR SEC study of **Mn–EB** confirms that the reductions localised on the **R–NI** moieties can undergo intramolecular electron transfer to the **Mn–phen** metallacycle, inducing phen-based reductions at lower potentials. For **Mn–EB**, this results in the formation of the **Mn–CO_2H** complex at R1. Notably, this enables formation of the **5–MA** active catalyst from the dimeric species at less negative potentials than is typically required to induce homolytic cleavage. Thereby forming the active catalyst at a lower potential than in the absence of an electron reservoir as is the case with **Mn–phen**.

Homogenous electrocatalytic studies at –2.30 V vs Fc^+/Fc demonstrated that the **Mn–R** electrocatalysts have greater selectivity for CO production (η_{FE} = 75% and 74% for **Mn–H** and **Mn–EB**, respectively) than **Mn–phen** (η_{FE} = 65%). Furthermore, CO_2 reduction was achieved with **Mn–R** at a lower potential, at which **Mn–phen** was unable to electrocatalytically reduce CO_2, while retaining high selectivity for CO production. Thus, the R–NI moieties were successfully implemented as electron reservoirs in these manganese complexes, allowing for electrocatalytic CO_2 reduction at less negative potentials than conventional [Mn(α-diimine)$(CO)_3$X] complexes. These insights can be used in the future design of CO_2-reducing electrocatalysts that incorporate R–NI moieties as electron reservoirs.

4.5 Bibliography

1 Crippa, M, Guizzardi, D, Pagani, F, Banja, M, Muntean, M, Schaaf, E, Quadrelli, R, Risquez Martin, A, Taghavi-Moharamli, P, Köykkä, J, Grassi, G, Melo, J, Suárez-Moreno, M, Sedano, F, San-Miguel, J, Manca, G, Pisoni, E, and Pekar, F, *GHG emissions of all world countries: 2025*, Publications Office of the European Union, 2025.

2 J. Hawecker, J.-M. Lehn and R. Ziessel, Efficient photochemical reduction of CO_2 to CO by visible light irradiation of systems containing $Re(bipy)(CO)_3X$ or $Ru(bipy)_3^{2+}$–Co^{2+} combinations as homogeneous catalysts, *J Chem Soc Chem Com*, 1983, **0**, 536–538.

3 W. M. Haynes, D. R. Lide and T. J. Bruno, *CRC Handbook of Chemistry and Physics*, CRC Press, Boca Raton, USA, 97th edn., 2016.

4 G. Morselli, C. Reber and O. S. Wenger, Molecular Design Principles for Photoactive Transition Metal Complexes: A Guide for "Photo-Motivated" Chemists, *J. Am. Chem. Soc.*, 2025, **147**, 11608–11624.

5 M. D. Sampson, A. D. Nguyen, K. A. Grice, C. E. Moore, A. L. Rheingold and C. P. Kubiak, Manganese Catalysts with Bulky Bipyridine Ligands for the Electrocatalytic Reduction of Carbon Dioxide: Eliminating Dimerization and Altering Catalysis, *J. Am. Chem. Soc.*, 2014, **136**, 5460–5471.

6 M. Bourrez, F. Molton, S. Chardon-Noblat and A. Deronzier, $[Mn(bipyridyl)(CO)_3Br]$: An Abundant Metal Carbonyl Complex as Efficient Electrocatalyst for CO_2 Reduction, *Angewandte Chemie International Edition*, 2011, **50**, 9903–9906.

7 J. M. Smieja, M. D. Sampson, K. A. Grice, E. E. Benson, J. D. Froehlich and C. P. Kubiak, Manganese as a Substitute for Rhenium in CO_2 Reduction Catalysts: The Importance of Acids, *Inorg. Chem.*, 2013, **52**, 2484–2491.

8 C. Riplinger, M. D. Sampson, A. M. Ritzmann, C. P. Kubiak and E. A. Carter, Mechanistic Contrasts between Manganese and Rhenium Bipyridine Electrocatalysts for the Reduction of Carbon Dioxide, *J. Am. Chem. Soc.*, 2014, **136**, 16285–16298.

9 C. W. Machan, M. D. Sampson, S. A. Chabolla, T. Dang and C. P. Kubiak, Developing a Mechanistic Understanding of Molecular Electrocatalysts for CO_2 Reduction using Infrared Spectroelectrochemistry, *Organometallics*, 2014, **33**, 4550–4559.

10 F. Hartl, B. D. Rossenaar, G. J. Stor and D. J. Stufkens, Role of an electron-transfer chain reaction in the unusual photochemical formation of five-coordinated anions $[Mn(CO)_3(\alpha\text{-diimine})]^-$ from fac-$[Mn(X)(CO)_3(\alpha\text{-diimine})]$ (X = halide) at low temperatures, *Recueil des Travaux Chimiques des Pays-Bas*, 1995, **114**, 565–570.

11 L. Suntrup, V. Blasczak, R. Saeedi, M. Z. Ertem and J. Rochford, The impact of second coordination sphere functional group extension on product selectivity for manganese bipyridyl CO_2 reduction electrocatalysts, *Dalton Transactions*, DOI:10.1039/D5DT00157A.

12 L. Tatarashvili, N. von Fellenberg, K. Oppelt and P. Hamm, Monomer and dimer pathways of earth-abundant manganese tricarbonyl pre-catalysts for CO_2 reduction studied by time-resolved IR spectroscopy, *Physical Chemistry Chemical Physics*, 2026, **28**, 2281–2293.

13 V. Blasczak, M. McKinnon, L. Suntrup, N. A. Aminudin, B. Reed, S. Groysman, M. Z. Ertem, D. C. Grills and J. Rochford, Steric and Lewis Basicity Influence of the Second Coordination Sphere on Electrocatalytic CO_2 Reduction by Manganese Bipyridyl Complexes, *Inorg. Chem.*, 2022, **61**, 15784–15800.

14 J. O. Taylor, Y. Wang and F. Hartl, Photo-Assisted Electrocatalytic Reduction of CO_2: A New Strategy for Reducing Catalytic Overpotentials, *ChemCatChem*, 2020, **12**, 386–393.

15 M. D. Sampson and C. P. Kubiak, Manganese Electrocatalysts with Bulky Bipyridine Ligands: Utilizing Lewis Acids To Promote Carbon Dioxide Reduction at Low Overpotentials, *J. Am. Chem. Soc.*, 2016, **138**, 1386–1393.

16 F. Franco, C. Cometto, C. Garino, C. Minero, F. Sordello, C. Nervi and R. Gobetto, Photo- and Electrocatalytic Reduction of CO_2 by [$Re(CO)_3$α,α'-Diimine-(4-piperidinyl-1,8-naphthalimide)Cl] Complexes, *Eur. J. Inorg. Chem.*, 2015, **2015**, 296–304.

17 D. R. Case, A. Spear, A. F. Henwood, M. Nanao, S. Dampf, T. M. Korter, T. Gunnlaugsson, J. Zubieta and R. P. Doyle, [$Re(CO)_3$(5-PAN)Cl], a rhenium(I) naphthalimide complex for the visible light photocatalytic reduction of CO2, *Dalton Trans.*, 2021, **50**, 3479–3486.

18 A. Spear, R. L. Schuarca, J. Q. Bond, T. M. Korter, J. Zubieta and R. P. Doyle, Photocatalytic turnover of CO_2 under visible light by [$Re(CO)_3$(1-(1,10) phenanthroline-5-(4-nitro-naphthalimide))Cl] in tandem with the sacrificial donor BIH, *RSC Adv.*, 2022, **12**, 5080–5084.

19 J. E. Yarnell, K. A. Wells, J. R. Palmer, J. M. Breaux and F. N. Castellano, Excited-State Triplet Equilibria in a Series of Re(I)-Naphthalimide Bichromophores, *J. Phys. Chem. B*, 2019, **123**, 7611–7627.

20 Z. Liu, Z. Zhang, Y. Liu, Y. Mei, E. Feng, Y. Liu, T. Zheng, J. Chen, S. Zhang and Y. Tian, Raman Fiber Photometry for Understanding Mitochondrial Superoxide Burst and Extracellular Calcium Ion Influx upon Acute Hypoxia in the Brain of Freely Moving Animals, *Angew. Chem., Int. Ed.*, 2022, **61**, e202111630.

21 J. R. Wagner and D. G. Hendricker, Coordination of Mn(I) and Re(I) carbonyls with nitrogen heterocyclic ligands, *Journal of Inorganic and Nuclear Chemistry*, 1975, **37**, 1375–1379.

22 M. Stanbury, J.-D. Compain, M. Trejo, P. Smith, E. Gouré and S. Chardon-Noblat, Mn-carbonyl molecular catalysts containing a redox-active phenanthroline-5,6-dione for selective electro- and photoreduction of CO_2 to CO or HCOOH, *Electrochimica Acta*, 2017, **240**, 288–299.

23 R. Horvath, G. S. Huff, K. C. Gordon and M. W. George, Probing the excited state nature of coordination complexes with blended organic and inorganic chromophores using vibrational spectroscopy, *Coord. Chem. Rev.*, 2016, **325**, 41–58.

24 C. Queffélec, P. B. Pati and Y. Pellegrin, Fifty Shades of Phenanthroline: Synthesis Strategies to Functionalize 1,10-Phenanthroline in All Positions, *Chem. Rev.*, 2024, **124**, 6700–6902.

25 R. M. Carlos, I. Ap. Carlos, B. S. L. Neto and M. G. Neumann, Spectroscopic and electrochemical properties of [Mn(phen)(CO)$_3$(imidazole)](SO$_3$CF$_3$) complexes, *Inorganica Chimica Acta*, 2000, **299**, 231–237.

26 C. Pereira, H. G. Ferreira, M. S. Schultz, J. Milanez, M. Izidoro, P. C. Leme, R. H. A. Santos, M. T. P. Gambardella, E. E. Castellano, B. S. Lima-Neto and R. M. Carlos, Probing the electronic factors responsible for the cyclic electron-transfer induced isomerism *fac* ⇄ *mer*: Synthesis, electrochemical and spectroscopic studies of *fac*-[Mn(CO)$_3$(L'–L')L]$^{0/+}$ complexes, *Inorganica Chimica Acta*, 2005, **358**, 3735–3744.

27 D. A. Kurtz, B. Dhakal, R. J. Hulme, G. S. Nichol and G. A. N. Felton, Correlations between photophysical and electrochemical properties for a series of new Mn carbonyl complexes containing substituted phenanthroline ligands, *Inorganica Chimica Acta*, 2015, **427**, 22–26.

28 V. Wintgens, P. Valat, J. Kossanyi, L. Biczok, A. Demeter and T. Bérces, Spectroscopic properties of aromatic dicarboximides. Part1.—N—H and N-methyl-substituted naphthalimides, *J. Chem. Soc., Faraday Trans.*, 1994, **90**, 411–421.

29 J. Biddulph, M. Pižl, S. Bhattacharya, P. Malakar, G. M. Greetham, F. Hartl and M. T. Pryce, Nature and Dynamics of the Excited States of Ethynyl-Functionalized Naphthalimide–Phenanthroline Re(I) Complexes Studied by TA and TRIR Spectroscopies, *J. Phys. Chem. B*, 2026, **130**, 6383–6398.

30 D. S. Tyson, C. R. Luman, X. Zhou and F. N. Castellano, New Ru(II) Chromophores with Extended Excited-State Lifetimes, *Inorg. Chem.*, 2001, **40**, 4063–4071.

31 J. E. Yarnell, J. C. Deaton, C. E. McCusker and F. N. Castellano, Bidirectional "Ping-Pong" Energy Transfer and 3000-Fold Lifetime Enhancement in a Re(I) Charge Transfer Complex, *Inorg. Chem.*, 2011, **50**, 7820–7830.

32 J. R. W. McLay, J. J. Sutton, G. E. Shillito, C. B. Larsen, G. S. Huff, N. T. Lucas and K. C. Gordon, Transitioning from Intraligand π,π* to Charge-Transfer Excited States Using Thiophene-Based Donor–Acceptor Systems, *Inorg. Chem.*, 2021, **60**, 130–139.

33 A. Barbero, L. Rotundo, C. Reviglio, R. Gobetto, R. Sokolova, J. Fiedler and C. Nervi, New Spectroelectrochemical Insights into Manganese and Rhenium Bipyridine Complexes as Catalysts for the Electrochemical Reduction of Carbon Dioxide, *Molecules*, 2023, **28**, 7535.

34 D. Gosztola, M. P. Niemczyk, W. Svec, A. S. Lukas and M. R. Wasielewski, Excited Doublet States of Electrochemically Generated Aromatic Imide and Diimide Radical Anions, *J. Phys. Chem. A*, 2000, **104**, 6545–6551.

35 G. J. Stor, S. L. Morrison, D. J. Stufkens and A. Oskam, The Remarkable Photochemistry of fac-XMn(CO)$_3$(.alpha.-diimine) (X =Halide): Formation of Mn$_2$(CO)$_6$(.alpha.-diimine)$_2$ via the

mer Isomer and Photocatalytic Substitution of X^- in the Presence of PR_3, *Organometallics*, 1994, **13**, 2641–2650.

36 C. W. Machan, S. A. Chabolla, J. Yin, M. K. Gilson, F. A. Tezcan and C. P. Kubiak, Supramolecular Assembly Promotes the Electrocatalytic Reduction of Carbon Dioxide by Re(I) Bipyridine Catalysts at a Lower Overpotential, *J. Am. Chem. Soc.*, 2014, **136**, 14598–14607.

37 F. P. A. Johnson, M. W. George, F. Hartl and J. J. Turner, Electrocatalytic Reduction of CO_2 Using the Complexes [Re(bpy)$(CO)_3$L]n (n = +1, L = $P(OEt)_3$, CH_3CN; n = 0, L = Cl^-, OTf^-; bpy = 2,2'-Bipyridine; OTf^- = CF_3SO_3) as Catalyst Precursors: Infrared Spectroelectrochemical Investigation, *Organometallics*, 1996, **15**, 3374–3387.

38 S. C. Cheng, C. A. Blaine, M. G. Hill and K. R. Mann, Electrochemical and IR Spectroelectrochemical Studies of the Electrocatalytic Reduction of Carbon Dioxide by $[Ir_2(dimen)^4]^{2+}$ (dimen = 1,8-Diisocyanomenthane), *Inorg. Chem.*, 1996, **35**, 7704–7708.

39 T. Seki, K.-Y. Chiang, C.-C. Yu, X. Yu, M. Okuno, J. Hunger, Y. Nagata and M. Bonn, The Bending Mode of Water: A Powerful Probe for Hydrogen Bond Structure of Aqueous Systems, *J Phys Chem Lett*, 2020, **11**, 8459–8469.

40 S. K. Mandal, D. M. Ho and M. Orchin, The synthesis of alkoxycarbonyl, carbamoyl and isocyanato complexes, *fac*-M$(CO)_3$(P-P)Z [M = Mn, Re; P-P = dppe, dppp; Z = C(O)OMe, C(O)OEt, C(O)NHPrn, NCO]. The single crystal structures of *fac*-Mn$(CO)_3$(dppp)C(O)OEt and *fac*-Mn$(CO)_3$(dppe)NCO, *Polyhedron*, 1992, **11**, 2055–2063.

41 M. D. Sampson, J. D. Froehlich, J. M. Smieja, E. E. Benson, I. D. Sharp and C. P. Kubiak, Direct observation of the reduction of carbon dioxide by rhenium bipyridine catalysts, *Energy Environ. Sci.*, 2013, **6**, 3748–3755.

42 C. W. Machan and C. P. Kubiak, Interrogating heterobimetallic co-catalytic responses for the electrocatalytic reduction of CO_2 using supramolecular assembly, *Dalton Trans.*, 2016, **45**, 15942–15950.

43 P. L. Cheung, C. W. Machan, A. Y. S. Malkhasian, J. Agarwal and C. P. Kubiak, Photocatalytic Reduction of Carbon Dioxide to CO and HCO_2H Using fac-Mn(CN)(bpy)$(CO)_3$, *Inorg. Chem.*, 2016, **55**, 3192–3198.

44 C. W. Machan, C. J. I. Stanton, J. E. Vandezande, G. F. Majetich, H. F. I. Schaefer, C. P. Kubiak and J. Agarwal, Electrocatalytic Reduction of Carbon Dioxide by Mn(CN)(2,2'-bipyridine)$(CO)_3$: CN Coordination Alters Mechanism, *Inorg. Chem.*, 2015, **54**, 8849–8856.

45 K. T. Ngo, M. McKinnon, B. Mahanti, R. Narayanan, D. C. Grills, M. Z. Ertem and J. Rochford, Turning on the Protonation-First Pathway for Electrocatalytic CO_2 Reduction by Manganese Bipyridyl Tricarbonyl Complexes, *J. Am. Chem. Soc.*, 2017, **139**, 2604–2618.

46 D. C. Grills, M. Z. Ertem, M. McKinnon, K. T. Ngo and J. Rochford, Mechanistic aspects of CO_2 reduction catalysis with manganese-based molecular catalysts, *Coordination Chemistry Reviews*, 2018, **374**, 173–217.

47 V. Blasczak, A. Murphy, L. Suntrup, K. T. Ngo, B. Reed, S. Groysman, D. C. Grills and J. Rochford, Structure Activity Relationships for Second-Coordination Sphere Functional Group Dependent CO_2 Reduction by Manganese Bipyridyl Electrocatalysts, *ChemCatChem*, 2024, **16**, e202301388.

48 B. P. Sullivan, C. M. Bolinger, D. Conrad, W. J. Vining and T. J. Meyer, One- and two-electron pathways in the electrocatalytic reduction of CO_2 by fac-Re(bpy)$(CO)_3$Cl (bpy = 2,2'-bipyridine), *J. Chem. Soc., Chem. Commun.*, 1985, 1414–1416.

Chapter 5

The Synthesis and Characterisation of Malononitrile-Appended Naphthalimide-Phenanthroline Transition-Metal Complexes

---

5.1 Abstract

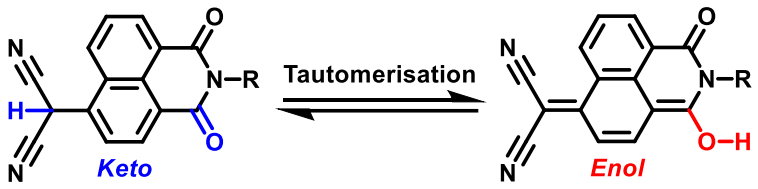
The syntheses of 4-malononitirle-1,8-naphthalimide-1,10-phenanthroline (**MN–NI–phen**) and a number of transition-metal complexes (**M–MN**) are outlined. The [Re(MN–NI–phen)$(CO)_3$Cl] (**Re–MN**) complex continues the **Re–R** series studied in Chapter 2 and 3 in this work. Additionally, two Ru^{II} complexes are also prepared, [Ru(MN–NI–phen)$(bpy)_2$]$(PF_6)_2$ (**Ru–MN**) and [Ru(MN–NI–phen)$(btfmb)_2$]$(PF_6)_2$] (**CF_3Ru–MN**), where the peripheral ligands are bpy = 2,2'-bipyridine and btfmb = 4,4'-bistrifluoromethyl-2,2'-bipyridine respectively. Structural characterisation of **MN–NI–phen** and **M–MN**, by ^{1}H NMR spectroscopy and high-resolution mass spectrometry, is presented. Additionally, preliminary IR and UV-Vis spectroscopic studies in CH_3CN further support their successful synthesis. These materials are envisaged to be employed in future spectroscopic, photophysical, and catalytic CO_2 reduction studies.

5.2 Introduction

In the previous chapters, the Re^I and Mn^I complexes of the **R–NI–phen** ligands (where R = H, ethynyl benzene, ethynyl thiophene, and ethynyl trimethylsilane) have been studied. The ethynyl-bearing R-groups display electron donating characteristics as demonstrated in Chapter 2, where detailed photophysical studies revealed the excited state dynamics of the **Re–R** complexes. Particularly, upon incorporating electron donating ethynyl moieties onto the NI core, the **Re–EB** and **Re–ES** complexes displayed increasingly ligand-like photophysics.[1] In Chapters 3 and 4, the R–NI moieties behaved as an electron reservoir when integrated in photocatalysts and electrocatalysts for CO_2 reduction studies. The addition of the R–NI electron reservoirs proved to play a key role in forming the active catalyst; involving charge transfer or electron transfer as key mechanisms to forming the active catalyst under photocatalytic and electrocatalytic conditions, respectively.

In contrast, the effect of introducing an electron withdrawing R-group to a NI moiety has received little attention in the literature. The [Re(NO_2–NI–phen)$(CO)_3$Cl] complex has been studied as a photocatalyst by Spear et al., but little is understood about its photophysical properties and limited studies into the reduction pathway are provided.[2,3] Considering the utility of the C≡C bond in the electron donating R-group of the **Re–R** complexes in the previous TRIR studies in this thesis, an electron withdrawing R-group containing a C≡X bond (X = C, N, O) could be used for future TRIR studies to determine the photophysical properties. The C≡N bond is itself electron withdrawing, therefore directly appending a nitrile-containing group to a NI moiety would be a simple way introduce an electron withdrawing IR tag.

Malononitrile has been successfully incorporated to the 4-position of NI-based fluorophores.[4–6] The resulting malononitrile-naphthalimide (**MN–NI**) compounds have absorption and emission profiles that extend into the visible region (λ_{abs} = 500–550 nm, λ_{em} = 600–650 nm).[5] For photocatalysis, the extended visible region absorption profile of **MN–NI** overlaps to a greater extent with the solar irradiance spectrum than any of the other R–NI moieties in this thesis, which only absorb light below 450 nm. Another advantage of the **MN–NI** compounds is their broad solubility range in non-polar, polar aprotic and polar protic solvents, which is attributed to keto-enol tautomerism in these compounds as outlined below in Scheme 5.1.



Scheme 5.11. *Keto-enol tautomerism in **MN–NI** compounds (R = alkyl or aryl group). The methine proton associated with the keto-form is highlighted in blue. The hydroxy proton associated with the enol-form is highlighted in red. Tautomerisation can occur with either carbonyl group in the imide.*

Typically, R–NI moieties exist in the keto-form, with the imide functional group containing two organic carbonyl (C=O) bonds. Internal charge transfer (ICT) is known to occur in NIs with electron-donating substituents at the 4-position, allowing for resonance structures where conjugation is extended to the C=O bonds. In **MN–NI** compounds, the methine proton is electron deficient due to its position within the dicyano substituent, making it susceptible to proton transfer. Indeed, ground-state intramolecular proton transfer (GSIPT) has been reported for MN–NI–R compounds (where morpholinyl, phenyl, n-butyl, and cyclopentyl R-groups are linked to the NI moiety via the N-atom of the imide).[4,5] This results in the formation of the enol-tautomer (Scheme 5.1), where one of the imide C=O bonds is transformed into a hydroxy (O–H) bond. GSIPT is sensitive to the solvent polarity, with the keto-form preferred in non-polar solvents and enol-form becoming increasingly favoured as the solvent polarity increases; accounting for the extended solubility profile of **MN–NI** compounds. Excited-state intramolecular proton transfer (ESIPT) can also occur in compounds with GSIPT, resulting in fluorescence from the normal state (the keto-form for **MN–NI**) and from the tautomer state (the enol-form for **MN–NI**).[7] In these compounds the tautomer state has a higher energy ground state than the normal state,

therefore emission from the excited state tautomer is of lower energy and appears in the red region.

The extended solubility profile and visible-region absorption features can be beneficial for photocatalysis. To create an intramolecular photocatalyst with a transition-metal catalytic centre, malononitrile can be substituted onto the **R–NI–phen** ligand. The presence of a labile proton in close proximity to the metal centre, as in the enol-tautomer, could be beneficial to CO_2 reduction catalysis. Specifically, protons in the second coordination sphere have been demonstrated to stabilise CO_2 in the vacant coordination site in Mn-based catalysts; lowering the thermodynamic barrier to CO_2 binding.[8,9] Additionally, computational studies have shown that malononitrile carbanion $[CH(CN)_2]^-$ can bind up to two CO_2 molecules and has been proposed for CO_2 capture with $[CH(CN)_2]^-$ -based ionic liquids.[10] The extended π-conjugation of the enol-form of **MN–NI** is formed from the $[CH(CN)_2]^-$ upon IPT; thereby, enabling CO_2 binding to that moiety without the need for an ionic liquid. Subsequent intermolecular interactions may enable a catalytic centre to bind with a captured CO_2 molecule, a process potentially reinforced by the enol proton in the second coordination sphere of the catalytic centre.

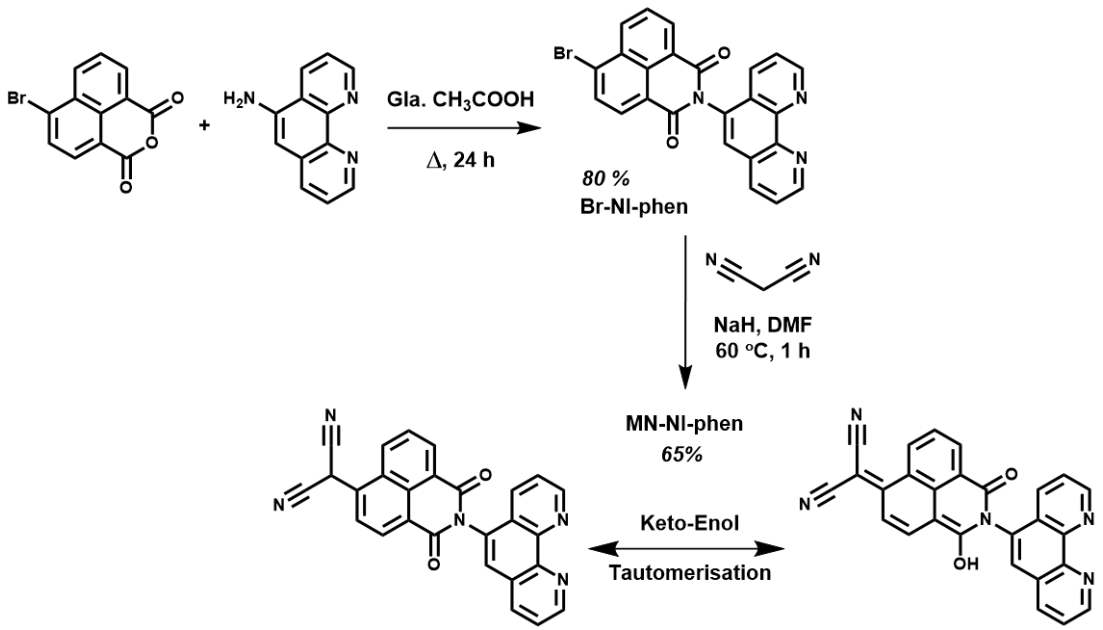
Accordingly, the syntheses of a series of transition-metal complexes (**M–MN**, where M = Re^{I}, and Ru^{II}) with the 4-malononitrile-1,8-naphthalimide-phenanthroline (**MN–NI–phen**) ligand are reported with characterisation. Preliminary spectroscopic studies of **MN–NI–phen** and the **M–MN** complexes is provided for purpose of spectral characterisation. The Re^{I} complex [Re(MN–NI–phen)$(CO)_3$Cl] (**Re–MN**) is a continuation of the **Re–R** series studied earlier in this thesis. Two Ru^{II} complexes, with peripheral 2,2-bipyridine (bpy) or 4,4'-bistrifluoromethyl-2,2'-bipyridine (btfmb) ligands, were also modulate the electron withdrawing effect of the **MN–NI–phen** ligand. Specifically, [Ru(MN–NI–phen)$(bpy)_2$]$(PF_6)_2$ (**Ru–MN**) should model the pull effect of **MN–NI–phen** alone, while [Ru(MN–NI–phen)$(btfmb)_2$]$(PF_6)_2$ (**CF_3Ru–MN**) should have a pull effect from the **MN–NI–phen** and btfmb ligands. Further spectroscopic and photophysical studies will be outlined in the Future Works section of Chapter 6 to ascertain the influence of the electron-withdrawing malononitrile group on the **M–MN** complexes.

5.3 Results and Discussion

5.3.1 Syntheses

Synthesis of **MN–NI–phen** was performed according to the synthesis illustrated in Scheme 5.2. Initially, a condensation reaction of 4-bromo,-1,8-naphthalic anhydride with 1,10-phenanthrolin-

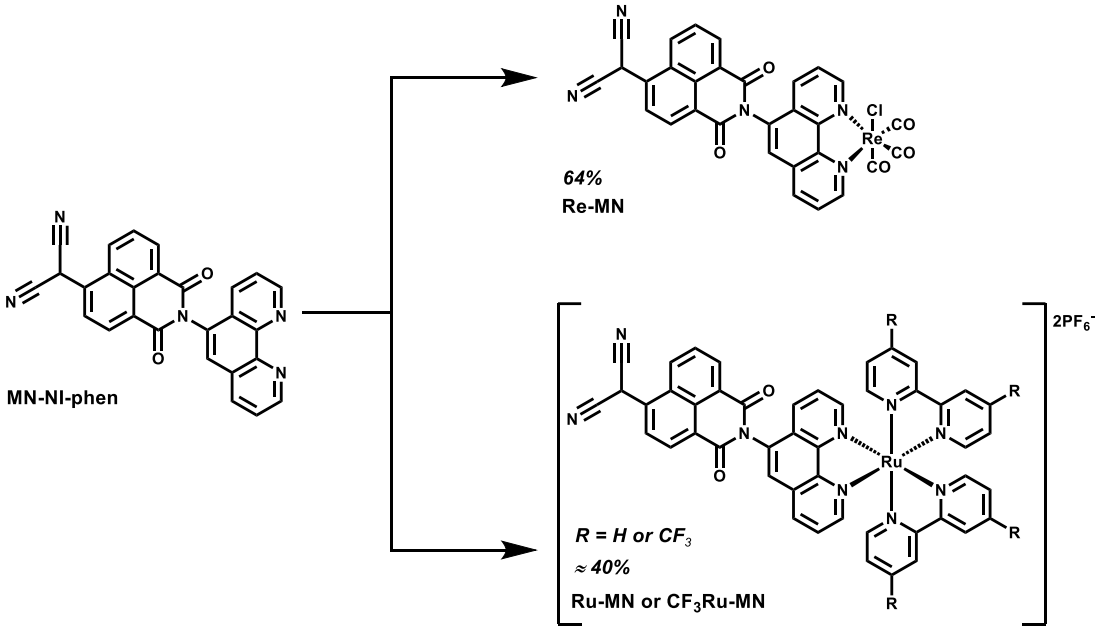
5-amine yielded 4-bromo-1,8-naphthalimide-1,10-phenanthroline (**Br–NI–phen**).[11] Subsequently, **Br–NI–phen** was reacted with malononitrile in an aromatic nucleophilic substitution reaction, using a modified literature procedure with DMF as the reaction solvent, to yield the target **MN–NI–phen** compound.[5] The ^{1}H NMR spectrum of **MN–NI–phen** is presented in Figure S5.1. Note the ^{1}H NMR spectra of **MN–NI–phen** and the **M–MN** complexes do not display a signal for the proton highlighted in the keto or enol forms indicated in Scheme 5.1, accordingly it is not possible to comment on the tautomer present during the NMR experiments. High-resolution mass spectrometry (HR-MS) detected the $[M+Na]^+$ and $[M–H]^–$ ions (Figure S5.7).



Scheme 5.12. *The synthetic pathway for* ***MN–NI–phen*** *with reaction conditions and yields.*

The **M–MN** complexes, (with M = Re^I or Ru^{II}) were prepared following literature procedures as outlined in Scheme 5.3. For **Re–MN**, $[Re(CO)_5Cl]$ was reacted with **MN–NI–phen** in EtOH.[11–13] The ^{1}H NMR spectrum of **Re–MN** is presented in Figure S5.2 and the $[M–H]^–$ ion was detected by HR-MS (Figure S5.8). For **Ru–MN** and **CF_3Ru–MN**, the $[Ru(bpy)_2Cl_2]$ and $[Ru(btfmb)_2Cl_2]$ precursors were prepared by literature procedures, and characterised by their ^{1}H NMR spectra (Figures S5.3 and S5.5).[14,15] Subsequent reaction of **MN–NI–phen** with the $[Ru(bpy)_2Cl_2]$ and $[Ru(btfmb)_2Cl_2]$ precursors was performed according to the literature procedure for tris-heteroleptic Ru^{II} complexes, using ethylene glycol in a microwave reactor at 180 °C for 15 min.[16] Extensive workup is required to extract the product as the PF_6 salt. The ^{1}H NMR spectra of **Ru–MN** and **CF_3Ru–MN** are presented in Figures S5.4 and S5.6. High-resolution mass spectrometry for both Ru^{II}

complexes revealed the presence of a PF_6 salt, while the $[M+Na]^{2+}$ and $[M–CN]^{2+}$ ions were detected for the respective Ru^{II} complexes (Figures S5.9 and S5.10).



Scheme 5.13. *The **M–MN** complexes obtained by coordination reactions of Re^{I} and Ru^{II} complexes with **MN–NI–phen**. The % yields are included.*

5.3.2 FTIR Spectroscopy

IR spectroscopy was employed to confirm the presence of specific vibrational modes in the complexes; namely the C=O, C≡O, and C≡N bonds as presented in Figure 5.1. DMSO is the only solvent where **MN–NI–phen** and **M–MN** were sufficiently concentrated for the $\nu_{C\equiv N}$ vibrational modes to be detected by the liquid-film IR technique. The key vibrational modes detected by IR spectroscopy are presented in Table 5.1

In Chapter 2, the organic carbonyl stretching vibrations ($\nu_{C=O}$) for **R–NI–phen** are observed at *ca.* 1710 and 1675 cm^{-1}.[1] However, the strongest absorbing $\nu_{C=O}$ bands in the IR spectrum of **MN–NI–phen** are observed at 1686 and 1649 cm^{-1}. Additionally, a strong and sharp feature at 1569 cm^{-1} is recorded, which is absent in the IR spectra of the previously studied **R–NI–phen** compounds. Therefore, this is attributed to the likely formation of the enol tautomer in the polar DMSO solvent. In the region of the $\nu_{C\equiv N}$ vibrational modes (2100 – 2250 cm^{-1} in Figure 5.1), two sharp $\nu_{C\equiv N}$ bands are observed at 2176 and 2137 cm^{-1}, which are similarly attributed to the enol-form. A broad and weak $\nu_{C\equiv N}$ band is detected at 2150 cm^{-1}, likely arising from trace amounts of

the keto tautomer and is linked to the weak $\nu_{C=O}$ bands also detected at 1715 and 1672 cm^{-1}. Therefore, both tautomers are observed in the IR spectrum of **MN–NI–phen** in DMSO, with the enol-form being the main tautomer formed in this polar solvent.

In the IR spectrum of **Re–MN**, the $\nu_{C=O}$ bands are observed at 1713 and 1673 cm^{-1}, which indicates that the keto-form is the main tautomer present in DMSO. Similarly, a broad and weak $\nu_{C\equiv N}$ band is detected at 2153 cm^{-1}, with two additional $\nu_{C\equiv N}$ bands at 2225 and 2176 cm^{-1}. The band at 2176 cm^{-1} is attributed to the enol-form of the **MN–NI–phen**, but any feature at 2225 cm^{-1} is too weak to detect if present at all in the IR spectrum of **MN–NI–phen**. Therefore, the $\nu_{C\equiv N}$ bands at 2225 and 2153 cm^{-1} are attributed to the keto-form in the IR spectrum of **Re–MN**, while the $\nu_{C\equiv N}$ band at 2176 cm^{-1} indicates that some of the enol tautomer is present in solution. Further to these features, the metal carbonyl vibrational modes ($\nu_{C\equiv O}$) observed at 2020, 1915, and 1894 cm^{-1}, which are associated with *fac*-[Re(α-diimine)$(CO)_3$Cl] complexes, provides strong evidence that **MN–NI–phen** is coordinated to a Re$(CO)_3$Cl moiety. As such, the presence of the Re$(CO)_3$Cl moiety influences keto-enol tautomerism in the coordinated **MN–NI–phen** ligand; appearing to restrict the formation of the enol-form even in moderately polar solvents such as DMSO.

The IR spectrum of **Ru–MN** displays two intense $\nu_{C=O}$ bands at 1667 and 1647 cm^{-1}, with these features in a similar region to the enol-form of the **MN–NI–phen** ligand (1686 and 1649 cm^{-1}). A weak $\nu_{C=O}$ band is observed at 1716 cm^{-1} which can be attributed to the keto-form. However, in the region of the $\nu_{C\equiv N}$ vibrational modes the only features observed are the broad features at 2233 and 2149 cm^{-1} previously attributed to the keto-form. While additional features are observed at 2065, 1990, and 1969 cm^{-1}, these are not observed in any of other IR spectra in Figure 5.1 and so cannot be attributed to the enol-form. Accordingly, it is challenging to verify if the C=O and C≡N bonds of the **MN–NI–phen** ligand are present in the IR spectrum of **Ru–MN**. This is more easily answered in the IR spectrum of **CF_3Ru–MN**; with $\nu_{C=O}$ bands at 1713 and 1673 cm^{-1}, and the $\nu_{C\equiv N}$ bands at 2233 and 2149 cm^{-1}. These features indicate that only the keto-form of the **MN–NI–phen** ligand is present. This is similar to the behaviour of displayed by **Re–MN**, where the metal centre appears to restrict the formation of the enol tautomer even in moderately polar DMSO.

In summary, the IR features arising from the C=O and C≡N bonds are observed in the IR spectra of **MN–NI–phen** and **M–MN** (Figure 5.1). For **Re–MN**, appearance of the *fac*-configuration of the $\nu_{C\equiv O}$ bands verify the *fac*-configuration of this complex and supports successful coordination of **MN–NI–phen** with a Re$(CO)_3$Cl moiety. DFT calculations of **MN–NI–phen** and **M–MN** would

support the assignments made here. In the case of **Ru–MN**, DFT calculations would allow for a better understanding of the observed IR spectral features.

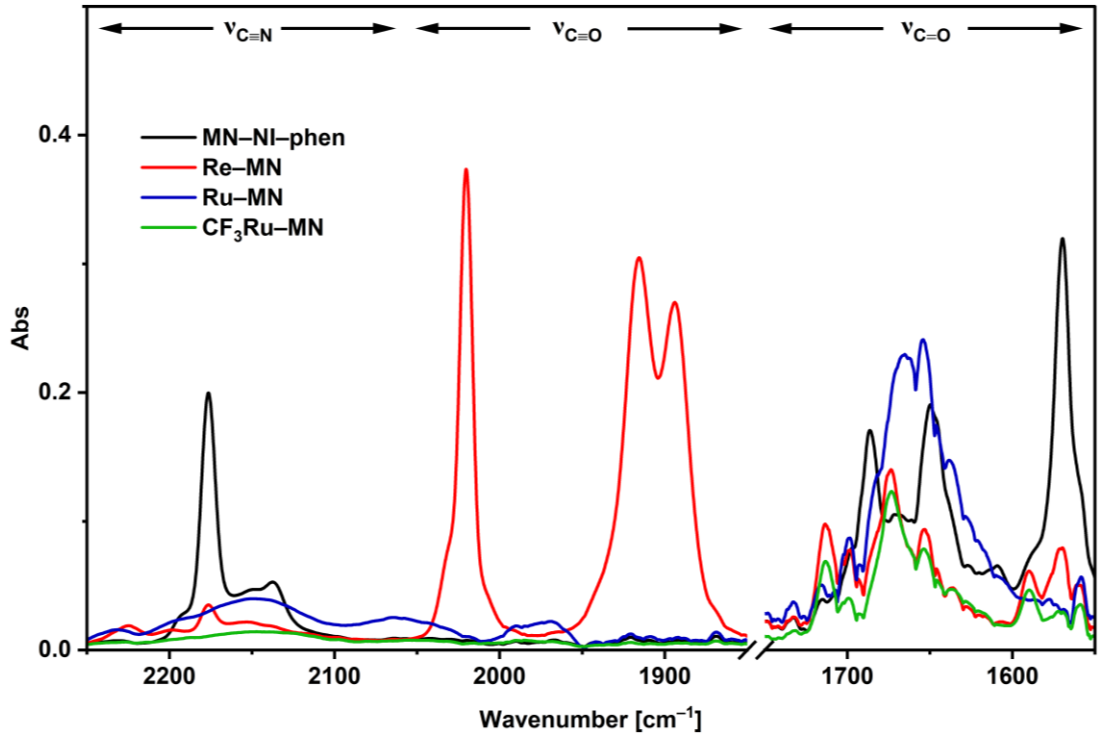


Figure 5.1. *FTIR spectra of* ***MN–NI–phen*** *and* ***M–MN*** *in DMSO.*

5.3.3 UV-Vis Absorption Spectroscopy

Upon complexation of **MN–NI–phen**, a weakly coupled bichromophoric system forms; distinguished by the absorption profile of the bichromophore appearing as a combination of the absorption profiles of the individual chromophores.[17] Therefore, the UV-Vis absorption spectra of **MN–NI–phen** and **M–MN**, presented in Figure 5.2, are used to identify key electronic transitions, summarised in Table 5.1, to support the formation of the **M–MN** bichromophores.

In the UV-Vis absorption spectrum of **MN–NI–phen** the near-UV region is distinguished by a phen-based π⟶π* transition (λ_{abs} = 262 nm) and vibrationally structured NI-based transitions in the region of 340 nm. The NI-based transitions are attributed to a mixture of n⟶π* and π⟶π* transitions, with the n⟶π* transition attributed to the maximum in this region at 342 nm, similarly to other NI-containing compounds.[18,19] The extended π-conjugated system of the enol-form results in an additional transition observed at 535 nm.[5]

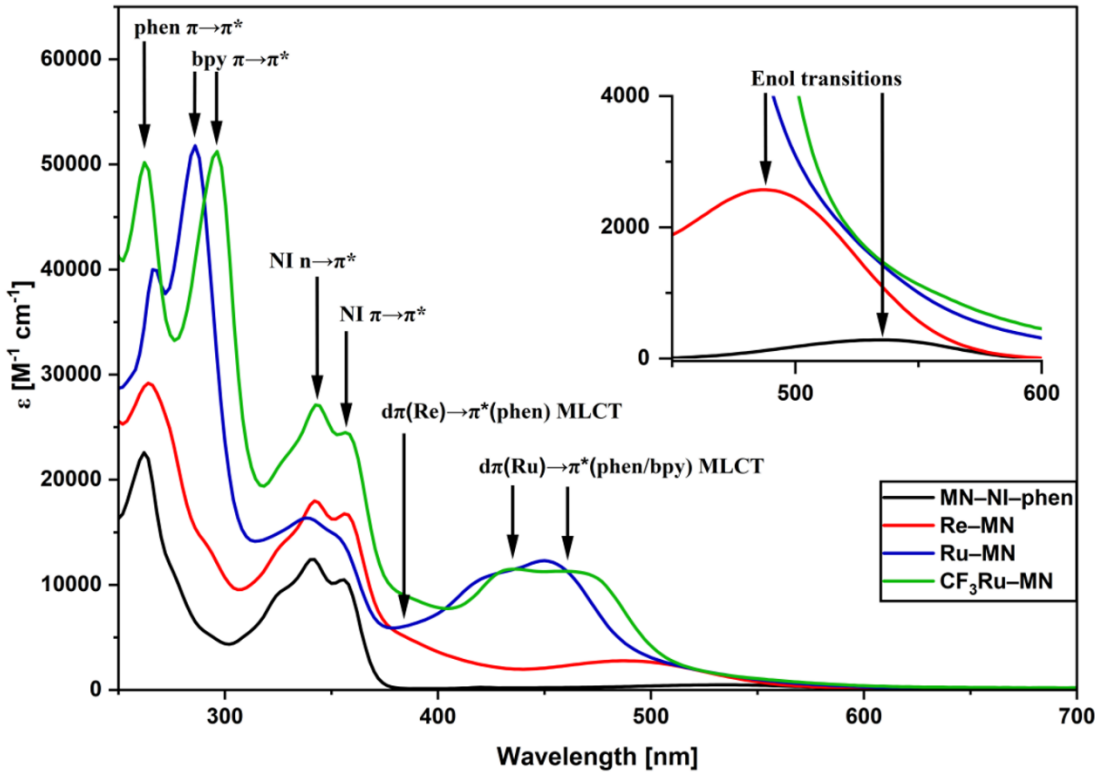


Figure 5.2. *UV-Vis absorption spectra of* ***MN–NI–phen*** *and* ***M–MN*** *in CH_3CN.*

In the UV-Vis absorption spectrum of **Re–MN**; the phen-based π→π* and vibrationally structured NI-based transitions were unchanged, though their extinction coefficients (ε) were increased, and a tail on the vibrationally structured NI-based transitions coincides with a mixture of MLCT and XLCT transitions. This so-called "metal-ligand-to-ligand charge transfer" (ML'LCT) transition is referred to as the MLCT transition herein for simplicity.[20–22] These electronic transitions closely match the appearance of [Re(H–NI–phen)$(CO)_3$Cl] studied in Chapter 2. An additional transition is apparent at 487 nm and is attributed to the enol-form, similarly to **MN–NI–phen**.

In the UV-Vis absorption spectra of the **Ru–MN** and **CF_3Ru–MN**, absorption bands are apparent below 300 nm which match the $[Ru(phen)(bpy)_2]^{2+}$ and $[Ru(phen)(btfmb)_2]^{2+}$ complexes in the literature.[16,23–25] Specifically, the phen-based π→π* transition (λ_{abs} = 266 and 262 nm for **Ru–MN** and **CF_3Ru–MN**, respectively) is associated with the **MN–NI–phen** ligand. For **Ru–MN**, the bpy-based π→π* transition is apparent at 286 nm. However, the inclusion of the electron-withdrawing CF_3 groups lowers the energy level of the π* orbitals of the bpy-based orbitals in **CF_3Ru–MN**,[25]; resulting in a red-shift of the btfmb π→π* transition (λ_{abs} = 296 nm) by 10 nm compared to that of the bpy π→π* transition (λ_{abs} = 286 nm). Additional features are observed at longer wavelengths; (Ru^{II})dπ→(bpy)π* MLCT transitions are observed in the UV-Vis absorption

spectrum of **Ru–MN** at 427 and 450 nm, as typically observed for Ru^{II} polypyridyl complexes.[23,24] The (Ru^{II})dπ→(btfmb)π* MLCT transitions are observed at 435 nm and 460 nm for **CF_3Ru–MN**; again, the electron-withdrawing CF_3 groups on the peripheral btfmb ligands results in lower energy electronic transitions compared to **Ru–MN**. The presence of a transition arising from the enol-form is not apparent in the UV-Vis absorption spectra of **Ru–MN** or **CF_3Ru–MN**; if present, it would underly the relatively intense MLCT transitions in both Ru^{II} complexes.

Table 5.14. *Key spectral data from FTIR and UV-Vis absorption and emission spectroscopy.*[a]

Compound	λ_{abs} (nm) [ε (M^{-1} cm^{-1})]	λ_{em}[b] (nm)	$\nu_{C\equiv N}$ (cm^{-1})	$\nu_{C=O}$ (cm^{-1})	$\nu_{C=O}$ (cm^{-1})
MN–NI–phen	262 [22680], 342 [12152], 535 [583]	391, 530	2176, 2150[c], 2137	–	1686, 1649
Re–MN	265 [29209], 342 [17852], 487 [2848]	385, 634	2225, 2176, 2153[c]	2020, 1915, 1894	1713, 1673
Ru–MN	266 [39850], 286 [51690], 339 [16386], 427 [11060], 450 [12340]	378, 616	2233[c], 2149[c]	–	1667, 1647
CF_3Ru–MN	262 [50091], 296 [51314], 343 [27142], 435 [11557], 460 [11290]	440, 654	2233[c], 2149[c]	–	1713, 1673

[a]In CH_3CN for UV-Vis absorption and emission studies; in DMSO for FTIR spectroscopy. [b]All emission spectra were collected upon 340 nm excitation. [c]These features are weak and broad.

The assignment of the electronic transitions of **M–MN** supports the successful coordination of the **MN–NI–phen** ligand to the respective Re^{I} and Ru^{II} precursors. For **Re–MN**, the phen and NI-based π→π* transitions closely resemble those of [Re(H–NI–phen)$(CO)_3$Cl] studied in Chapter 2. The additional transition at 487 nm also supports the occurrence of keto-enol tautomerism in **Re–MN**, which is specific to the presence of the malononitrile substituent on the NI moiety. For

Ru–MN and **CF_3Ru–MN**, the appearance of the MLCT transitions is in agreement with literature values for tris-heteroleptic Ru^{II} complexes[16,23–25]; supporting the coordination of **MN–NI–phen** to a Ru^{II} metal centre. The red-shift of the MLCT transitions in **CF_3Ru–MN** compared to **Ru–MN** shows that the btfmb ligands have a greater ability to pull electron density from the Ru^{II} metal centre than the bpy ligands. Thus, the pull of the btfmb ligands can oppose the pull of the malononitrile substituent in the **MN–NI–phen** ligand.

5.3.4 UV-Vis Emission Spectroscopy

The emission spectra of **MN–NI–phen** and the **M–MN** complexes are presented in Figure 5.3, with the emission maxima (λ_{em}) presented in Table 5.1. All samples were excited at 340 nm, corresponding to excitation of the NI-based n→π* transition. This spectral feature is common to all samples and provides an insight into the excited state dynamics of these samples subsequent to the excitation of the **MN–NI** chromophore.

The emission spectrum of **MN–NI–phen** displays two emissive features at 391 and 530 nm. This spectral profile appears similar to previous studies of **Br–NI–phen**, with emission features at 387 and 537 nm in CH_3CN.[11] The similarity of these emission spectra likely arises from the electron withdrawing character of the bromo and malononitrile substituents on the NI moiety of both compounds. These emissive features were attributed to dual emission, which has been previously reported for NIs.[11,26–28] The "short wavelength" band, with a maximum at 391 nm, arises from the fluorescent ^{1}LC excited state. The ^{1}LC excited state has a Franck-Condon-like structure, where the NI and phen moieties have a near-orthogonal configuration similar to the ground state configuration. The "long wavelength" band at 530 nm is attributed to a so-called planar intramolecular charge transfer (PICT) excited state.[26] The PICT excited state is formed from the Franck-Condon excited state where the NI and phen moieties become co-planar via excited-state conjugation enhancement (ESCE).[27,28]

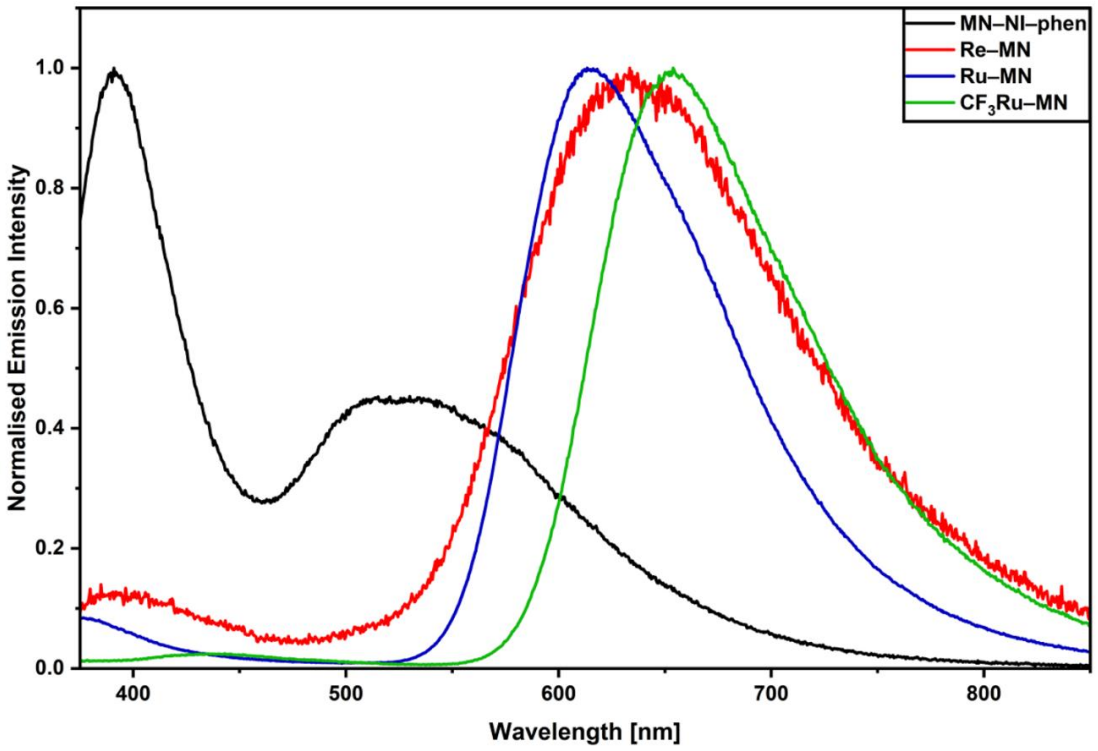


Figure 5.3. *UV-Vis emission spectra of* ***MN–NI–phen*** *and* ***M–MN*** *upon excitation at 340 nm in* CH_3CN.

Two distinct emission bands are apparent in the emission profile of **Re–MN**. The ^{1}LC excited state fluorescence of **MN–NI–phen** is observed at 385 nm, while the lower wavelength emission band associated with the PICT excited state is not detected. However, the most intense emission feature arises from the ^{3}MLCT excited state, with phosphorescence apparent at 634 nm. The emission profile of **Re–MN** most closely resembles that of **Re–H** in Chapter 2 and the related series studied by Yarnell et al., where an equilibrium between the ^{3}LC and ^{3}MLCT excited states is present in that complex.[1,11] Accordingly, the introduction of an electron withdrawing group onto the NI core, as in **MN–NI–phen**, does not appear to significantly affect the energy of the ^{3}LC excited state and thus, a triplet-triplet equilibrium between the ^{3}LC and ^{3}MLCT excited states is likely retained in **Re–MN**.

In the emission profiles of **Ru–MN** and **CF_3Ru–MN**, weak ^{1}LC emissive features were detected at 378 and 440 nm, respectively. However, as is the case for **Re–MN**, the ^{3}MLCT emission bands dominate the emission spectra of both complexes (λ_{em} = 616 and 654 nm, respectively). The maxima of ^{3}MLCT emission bands of structurally related Ru^{II} polypyridyl complexes occurs in this region, with λ_{em} of 601 nm for $[Ru(phen)(bpy)_2]^{2+}$ and 660 nm for $[Ru(phen)(btfmb)_2]^{2+}$ (as the PF_6 salt in MeOH and CH_3CN, respectively).[16,23] The similarities in the emission profiles of **Ru–**

MN and **CF_3Ru–MN** with that of **Re–MN** suggests that a triplet-triplet equilibrium between the ^{3}LC and ^{3}MLCT excited states may also present in the Ru^{II} complexes. However, the ^{3}LC excited is not observable by this spectroscopic study and so further studies are needed to establish the presence of a triplet-triplet equilibrium in all **M–MN** complexes.

5.4 Conclusion

The syntheses of the **MN–NI–phen** compound and the **M–MN** complexes are outlined with structural characterisation by ^{1}H NMR, HR-MS, and IR spectroscopy. In the UV-Vis spectroscopic studies in CH_3CN, the presence of electronic transitions attributed to the metal chromophores and the **MN–NI** chromophore further supports the successful synthesis of the bichromophoric **M–MN** complexes. Preliminary emission studies indicate that a triplet-triplet equilibrium between the ^{3}LC and ^{3}MLCT excited states may be present in the **M–MN** complexes analogous to the studies reported in Chapter 2. These materials are suitable for further spectroscopic and photophysical studies; specifically, to discern the electron withdrawing effect of the malononitrile substituent on their excited state dynamics of **M–MN** and to probe their suitability for CO_2 reduction catalysis as outlined in the following chapter.

5.5 Bibliography

1 J. Biddulph, M. Pižl, S. Bhattacharya, P. Malakar, G. M. Greetham, F. Hartl and M. T. Pryce, Nature and Dynamics of the Excited States of Ethynyl-Functionalized Naphthalimide–Phenanthroline Re(I) Complexes Studied by TA and TRIR Spectroscopies, *J. Phys. Chem. B*, 2026, **130**, 6383–6398.

2 A. Spear, R. L. Schuarca, J. Q. Bond, T. M. Korter, J. Zubieta and R. P. Doyle, Photocatalytic turnover of CO_2 under visible light by [$Re(CO)_3$(1-(1,10) phenanthroline-5-(4-nitro-naphthalimide))Cl] in tandem with the sacrificial donor BIH, *RSC Adv.*, 2022, **12**, 5080–5084.

3 D. R. Case, A. Spear, A. F. Henwood, M. Nanao, S. Dampf, T. M. Korter, T. Gunnlaugsson, J. Zubieta and R. P. Doyle, [$Re(CO)_3$(5-PAN)Cl], a rhenium(I) naphthalimide complex for the visible light photocatalytic reduction of CO_2, *Dalton Trans.*, 2021, **50**, 3479–3486.

4 H. Lan, Q. Li, Y. Li, S. Xiao, Y. Li, X. Yan, S. Yuan and P. Zhu, Solvent-controlled tautomerism of malononitrile-naphthalimide via intramolecular proton transfer, *Dyes and Pigments*, 2018, **155**, 121–125.

5 C.-H. Jeong, A. Ahmad, H. C. Schmitz and H. Cao, Synthesis and Investigation of Derivatives of 1,8-Naphthalimide with a Red Emission via an Aromatic Nucleophilic Substitution Reaction, *J Fluoresc*, 2022, **32**, 427–433.

6 M. G. Choi, J. M. Han, H. Lim, S. Ahn and S.-K. Chang, Colorimetric pH-sensing of artificial gastric fluid using naphthalimide-based CH acids, *Spectrochimica Acta Part A: Molecular and Biomolecular Spectroscopy*, 2025, **326**, 125166.

7 H. C. Joshi and L. Antonov, Excited-State Intramolecular Proton Transfer: A Short Introductory Review, *Molecules*, 2021, **26**, 1475.

8 V. Blasczak, M. McKinnon, L. Suntrup, N. A. Aminudin, B. Reed, S. Groysman, M. Z. Ertem, D. C. Grills and J. Rochford, Steric and Lewis Basicity Influence of the Second Coordination Sphere on Electrocatalytic CO_2 Reduction by Manganese Bipyridyl Complexes, *Inorg. Chem.*, 2022, **61**, 15784–15800.

9 L. Suntrup, V. Blasczak, R. Saeedi, M. Z. Ertem and J. Rochford, The impact of second coordination sphere functional group extension on product selectivity for manganese bipyridyl CO_2 reduction electrocatalysts, *Dalton Transactions*, DOI:10.1039/D5DT00157A.

10 Y. Fu, X. Suo, Z. Yang, S. Dai and D. Jiang, Computational Insights into Malononitrile-Based Carbanions for CO_2 Capture, *J. Phys. Chem. B*, 2022, **126**, 6979–6984.

11 J. E. Yarnell, K. A. Wells, J. R. Palmer, J. M. Breaux and F. N. Castellano, Excited-State Triplet Equilibria in a Series of Re(I)-Naphthalimide Bichromophores, *J. Phys. Chem. B*, 2019, **123**, 7611–7627.

12 J. R. Wagner and D. G. Hendricker, Coordination of Mn(I) and Re(I) carbonyls with nitrogen heterocyclic ligands, *Journal of Inorganic and Nuclear Chemistry*, 1975, **37**, 1375–1379.

13 J. E. Yarnell, J. C. Deaton, C. E. McCusker and F. N. Castellano, Bidirectional “Ping-Pong” Energy Transfer and 3000-Fold Lifetime Enhancement in a Re(I) Charge Transfer Complex, *Inorg. Chem.*, 2011, **50**, 7820–7830.

14 B. P. Sullivan, D. J. Salmon and T. J. Meyer, Mixed phosphine 2,2’-bipyridine complexes of ruthenium, *Inorg. Chem.*, 1978, **17**, 3334–3341.

15 S. A. McFarland, F. S. Lee, K. A. W. Y. Cheng, F. L. Cozens and N. P. Schepp, Picosecond Dynamics of Nonthermalized Excited States in Tris(2,2-bipyridine)ruthenium(II) Derivatives Elucidated by High Energy Excitation, *J. Am. Chem. Soc.*, 2005, **127**, 7065–7070.

16 H. D. Cole, A. Vali, J. A. I. Roque, G. Shi, A. Talgatov, G. Kaur, A. Francés-Monerris, M. E. Alberto, C. G. Cameron and S. A. McFarland, Ru(II) Oligothienyl Complexes with Fluorinated Ligands: Photophysical, Electrochemical, and Photobiological Properties, *Inorg. Chem.*, 2024, **63**, 9735–9752.

17 R. Horvath, G. S. Huff, K. C. Gordon and M. W. George, Probing the excited state nature of coordination complexes with blended organic and inorganic chromophores using vibrational spectroscopy, *Coord. Chem. Rev.*, 2016, **325**, 41–58.

18 V. Wintgens, P. Valat, J. Kossanyi, L. Biczok, A. Demeter and T. Bérces, Spectroscopic properties of aromatic dicarboximides. Part1.—N—H and N-methyl-substituted naphthalimides, *J. Chem. Soc., Faraday Trans.*, 1994, **90**, 411–421.

19 L. D. Patsenker and Y. Y. Artyukhova, Molecular structure and spectral properties of thionaphthalimides, *Journal of Molecular Structure*, 2003, **655**, 311–320.

20 B. D. Rossenaar, D. J. Stufkens and A. Vlček, Halide-Dependent Change of the Lowest-Excited-State Character from MLCT to XLCT for the Complexes $Re(X)(CO)_3$(α-diimine) (X = Cl, Br, I; α-diimine = bpy, iPr-PyCa, iPr-DAB) Studied by Resonance Raman, Time-Resolved Absorption, and Emission Spectroscopy, *Inorg. Chem.*, 1996, **35**, 2902–2909.

21 M. W. George and J. J. Turner, Excited states of transition metal complexes studied by time-resolved infrared spectroscopy, *Coordination Chemistry Reviews*, 1998, **177**, 201–217.

22 K. Choroba, J. Palion-Gazda, A. Kryczka, E. Malicka and B. Machura, Push–pull effect – how to effectively control photoinduced intramolecular charge transfer processes in rhenium(I) chromophores with ligands of D–A or D–π–A structure, *Dalton Transactions*, 2025, **54**, 2209–2223.

23 J. V. Caspar and T. J. Meyer, Photochemistry of MLCT excited states. Effect of nonchromophoric ligand variations on photophysical properties in the series cis-Ru(bpy)2L22+, *Inorg. Chem.*, 1983, **22**, 2444–2453.

24 A. Juris, S. Campagna, V. Balzani, G. Gremaud and A. Von Zelewsky, Absorption spectra, luminescence properties, and electrochemical behavior of tris-heteroleptic ruthenium(II) polypyridine complexes, *Inorg. Chem.*, 1988, **27**, 3652–3655.

25 M. Furue, K. Maruyama, T. Oguni, M. Naiki and M. Kamachi, Trifluoromethyl-substituted 2,2'-bipyridine ligands. Synthetic control of excited-state properties of ruthenium(II) tris-chelate complexes, *Inorg. Chem.*, 1992, **31**, 3792–3795.

26 S. K. Behera, S. Y. Park and J. Gierschner, Dual Emission: Classes, Mechanisms, and Conditions, *Angew. Chem., Int. Ed.*, 2021, **60**, 22624–22638.

27 A. Demeter, T. Bérces, L. Biczók, V. Wintgens, P. Valat and J. Kossanyi, Comprehensive Model of the Photophysics of N-Phenylnaphthalimides: The Role of Solvent and Rotational Relaxation, *J. Phys. Chem.*, 1996, **100**, 2001–2011.

28 H. Cao, V. Chang, R. Hernandez and M. D. Heagy, Matrix Screening of Substituted N-Aryl-1,8-naphthalimides Reveals New Dual Fluorescent Dyes and Unusually Bright Pyridine Derivatives, *J. Org. Chem.*, 2005, **70**, 4929–4934.

Chapter 6

Conclusions and Future Work

6.1 Overview

This thesis focussed on investigating transition-metal complexes of **R–NI–phen** ligands as catalysts towards photochemically and electrochemically driven CO_2 reduction. In the following concluding remarks, the experimental findings from the studies undertaken in this thesis are summarised. Additionally, further experiments are suggested, where appropriate, that could be completed to better understand how to implement NI moieties in catalysts for photochemically and electrochemically driven CO_2 reduction.

In terms of the catalytic performances of the catalysts studied in this thesis, the highest TON of 9 is reported for **Re–EB** in Chapter 3. While this represents a greater number of CO molecules than are present in the tricarbonyl-containing complexes studied in this body of work, in the best case 3 times more CO is produced than are present in the catalytic material, these are poor catalysts. Ideally, these catalytic materials would have a TON in the millions to be used at scale; as such, it is unlikely that this family of catalysts will be used beyond a research setting. Nonetheless, the catalysts studied in this thesis were useful systems to study, particularly to gain insights into the limitations in various catalyst activation pathways. A key step to improving the performance of any catalyst is to overcome bottlenecks in such activation pathways and so their identification is critical. This thesis demonstrates useful spectroscopic, photophysical, and electrochemical studies for identifying the bottlenecks in these naphthalimide-containing catalysts. Such studies can be conducted on many other catalysts to gain a better understanding of how those systems behave during catalysis, and how they can be adjusted or redesigned so that their catalytic performance is improved.

6.2. Concluding Remarks for Chapter 2

Chapter 2 aimed to establish the effect of the ethynyl-functionalised NI moieties on the photophysics of the Re^{I} tricarbonyl chloride complexes. An in-depth photophysical study was undertaken, including the use of time-resolved techniques from the ultrafast picosecond timescale to the microsecond time regime. This study revealed that a triplet-triplet equilibrium between the ^{3}LC and ^{3}MLCT excited states, present in the **Re–H** complex, was not present in the ethynyl-functionalised **Re–R** complexes. This was attributed to the electron-donating character of the ethynyl substituents and manifested as increasingly ligand-like photophysics in the ethynyl-functionalised **Re–R** complexes. This effect is strongest in the **Re–EB** and **Re–ES** complexes, which showed no triplet-triplet equilibrium and therefore had long-lived ^{3}LC excited

states similar to those of the corresponding **R–NI–phen** ligands. Population of the ^{3}LC excited state in these complexes leads to a resonance-type structure due to the electron-rich aromatic rings being conjugated to the electron-deficient NI core via an ethynyl bridge. In the TRIR spectroscopic studies, the resonance structures are associated with a large red shift of the ^{3}LC $\nu_{C\equiv C}$ transients (at 1997 and 1976 cm^{-1}, respectively) compared to the $\nu_{C\equiv C}$ ground state bleaches (at 2207 and 2196 cm^{-1}, respectively); indicating the formation of a partially oxidised ethynyl bridge in the ^{3}LC excited state of these complexes.[1]

6.3. Concluding Remarks for Chapter 3

In Chapter 3, the **Re–H** and **Re–EB** complexes were further studied for their ability to photocatalytically reduce CO_2. Photocatalysis with these complexes revealed that they are poor photocatalysts, with TON_{CO} of 7 and 9, respectively (0.1 mM **Re–R** in a DMF/TEOA (6:1 v/v) solution, λ_{irr} = 450 nm, after 24h). The poor photocatalytic performance of the **Re–R** complexes is attributed to the presence of the R–NI electron reservoir in their structure. Indeed, the [Re(phen)(CO)$_3$Br] photocatalyst, which differs from **Re–R** by the absence of the R–NI electron reservoir and Br as the coordinated halide, has a TON_{CO} of 12 under similar photocatalytic conditions (10 mL of a solution containing 1 M TEOA and 1 mM of the catalyst in DMF after 2 h).[2]

To better understand the effect of the R–NI electron reservoirs on photocatalysis, detailed electrochemical, SEC, and time-resolved studies were undertaken to help establish the pathway leading to the active photocatalyst. The reduction sequence of the **Re–R** complexes is as follows: reduction of the R–NI moiety first, followed by a phen-based reduction, and finally reduction of the Re–phen metallacycle which induces Cl^- dissociation yielding the 5-coordinate active catalyst. Thus, the typical two reduction-step activation pathway for [Re(α-diimine)(CO)$_3$Cl] catalysts evolve into a three-reduction step activation pathway upon the introduction of the R–NI electron reservoirs. The photocatalytic studies indicated that the **[Re–R]$^{2-}$** complexes accumulated during photocatalysis, indicating intramolecular electron transfer from the R–NI electron reservoirs only causes slow halide dissociation under those conditions.

Pioneering TRIR SEC experiments were also performed on the **Re–R** complexes. When the **[Re–R]$^-$** complexes are considered as radical-chromophore systems, generated electrochemically *in situ,* rationale for the concurrent population of two excited states could be applied based on the literature. A ^{4}MLCT excited state is populated analogous to the ^{3}MLCT excited state populated by excitation of **Re–R** parent complexes. Additionally, a ^{4}ILCT excited state is populated arising from

charge transfer from R–NI^{-}→phen; highlighting that the R–NI electron reservoir can transfer an electron to the Re–phen metallacycle upon excitation. However, charge transfer from R–NI^{-} →phen^{-} in **[Re–H]$^{2-}$** is short-lived. When considered with the observed accumulation of **[Re–H]$^{2-}$** during photocatalysis, these results indicate that back transfer to the R–NI^{-} moiety is favoured over halide dissociation in the **[Re–R]$^{2-}$** complexes.

Future work from Chapter 3 could involve further studies to better understand the activation pathway of the **Re–R** photocatalysts. TRIR SEC studies of the **[Re–R]$^{2-}$** complexes would be beneficial in this regard; yielding more direct information about the bottleneck in the pathway leading to the active catalyst. Additionally, further optimisation of the photocatalytic conditions could be performed by testing other reaction conditions including the use of other solvents, sacrificial agents, and light sources. Another approach is to modify the Cl ligand to one that forms a weaker bond with the Re^{I} metal centre, such as a Br, a pseudo-halide, or a solvent ligand, allowing for the 5-coordinate species to be formed more readily. These changes to the photocatalytic system may enable halide dissociation to occur more readily upon charge transfer from the electron reservoir.

6.4. Concluding Remarks for Chapter 4

Chapter 4 focused on studying the Mn^{I} tricarbonyl bromide counterparts of the **Re–R** complexes, studied in Chapter 3, as electrocatalysts for CO_2 reduction. Again, the R–NI moieties act as electron reservoirs in the Mn-R complexes. Therefore, detailed electrochemical and SEC studies were undertaken to determine the pathway leading to the active electrocatalyst. The reduction sequence of the **Mn–R** complexes differ from the one established for the **Re–R** complexes. In fact, **Mn–H** and **Mn–EB** also displayed different reduction sequences from each other. For **Mn–H**, the first reduction causes halide dissociation with a subsequent parent-child comproportionation reaction forming the **Dimer**, the H–NI moiety is reduced next while remaining as a dimeric species. For **Mn–EB**, the EB–NI moiety is reduced first reduce, with the NI-reduced dimer formed at the second reduction wave. For both **Mn–R** complexes, the final reduction step involves the cleavage of the NI-reduced dimer to yield a 5-coordinate species as the active catalyst.

The **Mn–R** complexes were able to reduce CO_2 at a less negative overpotential under a CO_2 atmosphere with 5% H_2O added as a Bronsted acid compared to under a CO_2 atmosphere alone. IR SEC studies under these conditions allows for intramolecular electron transfer from the R–NI

moiety to the **Mn–phen** metallacycle at the second reduction wave, inducing homolytic cleavage of the NI-reduced dimer to yield the 5-coordinate monoanion **5–MA** active catalyst. Additionally, the study of **Mn–EB** confirmed formation of the metallocarboxylic acid complex **[Mn–CO_2H]** and the **Dimer** at the first reduction. The **[Mn–CO_2H]** complex is a key intermediate species in the catalytic cycle of many CO_2 reducing [Mn(α-diimine)$(CO)_3$Br] electrocatalysts.[3] Its formation at the first reduction of **Mn–EB** is only possible by intramolecular electron transfer from the reduced EB–NI moiety to the **Mn–phen** metallacycle, with rapid CO_2 binding occurring in the presence of the Bronsted acid yielding the stable **[Mn–CO_2H]** complex.

Future work from Chapter 4 would involve assessing the suitability of the **Mn–R** complexes photo-based CO_2 reduction catalysis. This could be achieved by conducting photocatalysis similarly to that performed with the **Re–R** complexes in Chapter 3. Alternatively, photo-assisted electrocatalysis could be attempted involving electrochemically producing the dimeric species and subsequently irradiating it with low energy light to induce homolytic cleavage. Recently, Taylor et al. used photo-assisted electrocatalysis on [Mn(bpy)$(CO)_3$Br] to generate the **5–MA** by photoinduced homolytic cleavage of the Mn–Mn dimer at the potential of the first reduction with 405 nm light.[4] Koizumi et al. were able to induce homolytic cleavage of the [Mn_2(bpy)$_2(CO)_6$] dimer using lower energy light (λ ≥ 620 nm), and showed that higher energy light (λ ≥ 480 nm) resulted in photodegradation of the manganese species via decarbonylation.[5] Either approach to photo-based CO_2 reduction catalysis would require photophysical studies, similarly to those conducted in Chapter 2, to determine the behaviour of the **Mn–R** complexes upon irradiation.

6.5. Concluding Remarks for Chapter 5

In Chapter 5, malononitrile was appended on to a NI–phen compound to form **MN–NI–phen**. Subsequently, a Re^{I} tricarbonyl chloride complex was prepared (**Re–MN**), continuing the series studied in Chapter 2, in addition to two Ru^{II} polypyridyl complexes (**Ru–MN** and **CF_3Ru–MN**). **MN–NI–phen** and the **M–MN** complexes are structurally and spectrally characterised; confirming the successful preparation of these materials for further studies.

There are many possibilities for future studies of the samples prepared in Chapter 5. The most relevant to this thesis would be a detailed photophysical studies similar to those performed in Chapter 2. Malononitrile introduces an electron-withdrawing group to the NI moiety, in contrast to the electron-donating substituents used in the previous chapters. For the Ru^{II} polypyridyl complexes, the electron withdrawing nature of the MN–NI moiety is modulated by the presence

of different peripheral ligands, with the btfmb ligands of **CF_3Ru–MN** being more electron withdrawing than the bpy ligands **Ru–MN**. Therefore, the photophysics associated with the MN–NI moiety may differ between **Ru–MN** and **CF_3Ru–MN**, as the pull of MN–NI moiety is more effectively opposed by the pull of the btfmb peripheral ligands. Accordingly, time-resolved studies would be appropriate to study the photophysical properties of **MN–NI–phen** and **M–MN**. TCSPC and TA spectroscopy would reveal the lifetimes of the populated emissive and non-emissive excited states, respectively. Additionally, the presence of C≡N bonds as IR tags in the malononitrile substituent makes these samples ideal candidates for TRIR studies.

The keto-enol tautomerism introduced upon to addition of the malononitrile substituent also provides an opportunity to conduct studies in both polar and non-polar solvents. The aforementioned photophysical studies may provide insights into the occurrence of ESIPT in these materials under a broad range of solvent polarities. Additionally, the presence of an acidic proton in either tautomer (the methine proton in the keto-form and the hydroxyl proton in the enol-form) allows for pH-dependent studies to be conducted. Choi et al. showed a pH dependence for keto-enol tautomerism in their MN–NI fluorophore which could be used to detect artificial gastric acids.[6] Finally, Fu et al. proposed that the malononitrile carbanion could be used for CO_2 capture, based on their detailed modelling of CO_2 binding with malononitrile.[7]

Therefore, malononitrile could provide many functions in the **M–MN** complexes; it can modulate the photophysical properties of the MN–NI electron reservoir, its improved solubility in polar solvents and likely pH-sensitivity provide more options for optimisation of catalytic conditions, and it can act as a CO_2 capture component which may support binding with the active catalyst via an intermolecular mechanism. However, the interplay of all of these functions becomes complicated quickly and the improvement of one function may diminish another. Thus, the **M–MN** complexes may be assessed as the catalytic components in photochemically and electrochemically driven CO_2 reduction, but understanding their behaviour during catalysis requires extensive studies as outlined above.

6.6 Bibliography

1 J. Biddulph, M. Pižl, S. Bhattacharya, P. Malakar, G. M. Greetham, F. Hartl and M. T. Pryce, Nature and Dynamics of the Excited States of Ethynyl-Functionalized Naphthalimide–Phenanthroline Re(I) Complexes Studied by TA and TRIR Spectroscopies, *J. Phys. Chem. B*, 2026, **130**, 6383–6398.

2 P. Kurz, B. Probst, B. Spingler and R. Alberto, Ligand Variations in [ReX(diimine)$(CO)_3$] Complexes: Effects on Photocatalytic CO_2 Reduction, *Eur. J. Inorg. Chem.*, 2006, **2006**, 2966–2974.

3 C. Riplinger, M. D. Sampson, A. M. Ritzmann, C. P. Kubiak and E. A. Carter, Mechanistic Contrasts between Manganese and Rhenium Bipyridine Electrocatalysts for the Reduction of Carbon Dioxide, *J. Am. Chem. Soc.*, 2014, **136**, 16285–16298.

4 J. O. Taylor, Y. Wang and F. Hartl, Photo-Assisted Electrocatalytic Reduction of CO_2: A New Strategy for Reducing Catalytic Overpotentials, *ChemCatChem*, 2020, **12**, 386–393.

5 H. Koizumi, Y. Tamaki, K. Kamogawa, M. Nicaso, Y. Suzuki, Y. Yamazaki, H. Takeda and O. Ishitani, Development of a Highly Durable Photocatalytic CO_2 Reduction Using a Mn-Complex Catalyst: Application of Selective Photosplitting of a Mn(0)–Mn(0) Bond, *J. Am. Chem. Soc.*, 2025, **147**, 6236–6248.

6 M. G. Choi, J. M. Han, H. Lim, S. Ahn and S.-K. Chang, Colorimetric pH-sensing of artificial gastric fluid using naphthalimide-based CH acids, *Spectrochimica Acta Part A: Molecular and Biomolecular Spectroscopy*, 2025, **326**, 125166.

7 Y. Fu, X. Suo, Z. Yang, S. Dai and D. Jiang, Computational Insights into Malononitrile-Based Carbanions for CO_2 Capture, *J. Phys. Chem. B*, 2022, **126**, 6979–6984.

Appendices A – D

Appendix A

Supplementary information associated with Chapter 2

S2.1 Experimental

Materials

1,8–naphthalic anhydride was purchased from TCI. 1,10–phenanthrolin–5–amine, 4–bromo–1,8–naphthalic anhydride, trimethylsilyl acetylene, $[Pd(PPh_3)_4]$, TEA, and $[Re(CO)_5Cl]$ were purchased from Fluorochem. CuI was purchased from BLD Pharm. All other reagents and solvents were purchased from Sigma–Aldrich. Synthesis of the **R–NI–phen** compounds and the target **Re–R** complexes were achieved by adopting the literature syntheses of **H–NI–phen** and **Re–H** as outlined below in General Synthesis A and B, respectively.[1–4] The novel **R–NI–phen** compounds and **Re–R** complexes were characterized by FTIR spectroscopy, ^{1}H NMR spectroscopy, and high–resolution mass spectrometry.

*General Synthesis A – **R–NI–phen** (R = H, Br, EB, ES, ET)*

The synthesis was based on published procedures of related compounds.[1,3,4] 4–R–1,8–naphthalic anhydride (1.00 equiv.) and 1,10–phenanthrolin–5–amine (1.1 equiv.) were dissolved in a minimum of glacial acetic acid. The reaction solution was heated to reflux and left for 16 h. After this time, the reaction solution was allowed to cool to RT before the addition of aq. Na_2CO_3 solution (50 mL), resulting in the formation of a precipitate that was collected by vacuum filtration and washed with 2x 10 mL EtOH and 1x 10 mL Et_2O before air–drying.

*General Synthesis B – $[Re(R–NI–phen)(CO)_3Cl]$ (**Re–R**, R = H, Br, EB, ES, ET)*

Published procedures of related complexes were followed to synthesize the complexes.[1,2] $[Re(CO)_5Cl]$ (1 eq.) and **R–NI–phen** (1 eq.) were dissolved in a minimum of EtOH. The reaction solution was heated to reflux and left for 2–4 h. After this time, the reaction solution was allowed to cool to RT which resulted in the formation of a precipitate. This precipitate was collected by vacuum filtration and washed with 3x 10 mL Et_2O before air–drying.

*Synthesis of naphthalimide–5–phenanthroline (**H–NI–phen**)*

Using General Synthesis A, 1,8–naphthalic anhydride (0.1982 g, 1.00 mmol) and 1,10–phenanthrolin–5–amine (0.1962 g, 1.01 mmol) were used. The resulting white solid was collected by vacuum filtration followed by recrystallisation from EtOH and again collected by

vacuum filtration to obtain the purified product. Yield: 0.1680 g (45%), ^{1}H NMR ($CDCl_3$, 600 MHz): *δ* 9.28 (s, 1H), 9.23 (s, 1H), 8.71(s, 2H), 8.37 (s, 2H), 8.29 (s, 1H), 8.05 (s, 1H), 7.88 (d, *J* = 9.45 Hz, 3H), 7.70 (s, 1H), 7.58 (s, 3H). Elem. Anal. calcd (found) for $C_{24}H_{13}N_3O_2$: C, 76.79 (76.31); H, 3.49 (3.61); N, 11.19 (10.37).

*Synthesis of [Re(H–NI–phen)(CO)$_3$Cl] (**Re–H**)*

Using General Synthesis B, $[Re(CO)_5Cl]$ (0.0902 g, 0.25 mmol) and **H–NI–phen** (0.0951 g, 0.25 mmol) were used. The resulting yellow precipitate was collected by vacuum filtration and washed with a minimum amount of EtOH followed by 10 mL Et_2O before finally air–drying the product. The product was further purified by recrystallisation from EtOH yielding a fine yellow powder. Yield: 0.1009 g (59%). ^{1}H NMR (600MHz $CDCl_3$) *δ* 9.46 (dd, *J* = 5.23, 1.01 Hz, 1H), 9.43 (dd, *J* = 5.12, 1.11 Hz, 1H), 8.74 (dd, *J* = 7.18, 0.77 Hz, 1H), 8.71 (d, *J* = 6.84Hz, 1H), 8.56 (dd, *J* = 8.19, 1.11 Hz, 1H), 8.41 (dd, *J* = 8.27, 4.29 Hz, 2H), 8.31 (dd, *J* = 8.41, 1.07 Hz, 1H), 8.13 (s, 1H), 7.90 (m, 3H), 7.79 (dd, *J* = 8.50, 4.92 Hz, 1H). MS [ESI–QTOF (DCM) m/z] 682.0166 $[M+H]^+$, calcd ($C_{27}H_{13}ClN_3O_5Re$) 681.01. Elem. Anal. calcd (found) for $C_{27}H_{13}ClN_3O_5Re$: C, 47.62 (48.38); H, 1.92 (2.08); N, 6.17 (6.17).

*Synthesis of 4–ethynylbenzene naphthalic anhydride (**EB–NA**)*

Based on the literature synthesis[5], 4–bromo–1,8–naphthalic anhydride (1.0032 g, 3.62 mmol), phenylacetylene (600 µL, 5.46 mmol), $Pd(PPh_3)_4$ (0.0653 g, 0.57 mmol), CuI (0.0660 g, 0.35 mmol), and triethylamine (500 µL, 0.36 mmol) were first dissolved in toluene (10 mL), the mixture was heated at 110 °C under N_2 atmosphere for 22 h. After cooling, the reaction solution was filtered, the yellow solid was further washed with water and then recrystallised from toluene to obtain the pure product. Yield: 0.5540 g (55%), ^{1}H NMR ($CDCl_3$, 600 MHz): *δ* 8.85 (dd, *J* = 8.32, 1.15 Hz, 1H), 8.68 (dd, *J* = 7.30, 1.15 Hz, 1H), 8.59 (d, *J* = 7.56 Hz, 1H), 8.01 (d, *J* = 7.56 Hz, 1H), 7.92 (dd, *J* = 8.46, 7.30 Hz, 1H), 7.69 (m, 2H), 7.46 (m, 3H). Elem. Anal. calcd (found) for $C_{20}H_{10}O_3$: C, 80.53 (77.04); H, 3.38 (3.60).

*Synthesis of 4–ethynylbenzene naphthalimide–5–phenanthroline (**EB–NI–phen**)*

Using Synthesis A, **EB–NA** (0.2994 g, 1.00 mmol) and 1,10–phenanthrolin–5–amine (0.2164 g, 1.11 mmol) were used. The resulting yellow solid was collected by vacuum filtration and further

purified by recrystallisation from EtOH. Yield: 0.3189 g (67%), ^{1}H NMR ($CDCl_3$, 600 MHz): δ 9.29 (s, 1H), 9.24 (s, 1H), 8.90 (d, *J* = 8.15 Hz , 1H), 8.73 (d, *J* = 7.13 Hz, 1H), 8.65 (d, *J* = 7.72 Hz, 1H), 8.29 (d, *J* = 6.94 Hz, 1H), 8.05 (m, 2H), 7.94 (dd, *J* = 8.14, 7.85 Hz, 1H), 7.91 (m, 1H), 7.72 (dd, *J* = 6.88, 3.33 Hz, 1H), 7.69 (m, 1H), 7.59 (s, 1H), 7.47 (m, 3H). MS [ESI–QTOF (DCM) m/z] 476.1481 $[M+H]^+$, calcd ($C_{32}H_{18}N_3O_2$) 475.51. Elem. Anal. calcd (found) for $C_{32}H_{18}N_3O_2$: C, 80.83 (75.18); H, 3.60 (3.79); N, 8.84 (7.81).

*Synthesis of [Re(EB–NI–phen)(CO)$_3$Cl] (**Re–EB**)*

Using Synthesis B, $[Re(CO)_5Cl]$ (0.0506 g, 0.14 mmol) and **EB–NI–phen** (0.0669 g, 0.14 mmol) were used. The resulting yellow precipitate was collected by vacuum filtration followed by recrystallisation from MeOH to obtain the final product. Yield: 0.0723 g (66%). ^{1}H NMR ($CDCl_3$, 600 MHz): δ 9.46 (d, *J* = 5.45 Hz, 1H), 9.43 (d, *J* = 5.02 Hz, 1H), 8.94 (dd, *J* = 9.20, 8.34 Hz, 1H), 8.75 (dd, *J* = 7.91, 7.75 Hz, 1H), 8.66 (dd, *J* = 7.39, 5.30 Hz, 1H), 8.54 (dd, *J* = 8.07, 4.38 Hz, 1H), 8.32 (dd, *J* = 8.36, 0.97 Hz, 1H), 8.13 (s, 1H), 8.07 (dd, *J* = 11.06, 7.53 Hz, 1H), 7.96 (dd, *J* = 16.88, 8.37 Hz, 1H), 7.89 (dd, *J* = 8.09, 5.02 Hz, 1H), 7.80 (dd, *J* = 8.44, 4.91 Hz, 1H), 7.73 (m, 2H), 7.49 (m, 3H). MS [ESI–QTOF (DCM) m/z] 782.0134 $[M+H]^+$, calcd ($C_{35}H_{18}ClN_3O_5Re$) 781.19. Elem. Anal. calcd (found) for $C_{35}H_{18}ClN_3O_5Re$: C, 53.81 (54.17); H, 2.19 (2.40); N, 5.38 (5.50).

*Synthesis of 4–ethynylthiophene naphthalic anhydride (**ES–NA**)*

Adapted from the literature synthesis of 2–(phenylethynyl) thiophene[6]; 4–Bromo–1,8–naphthalic anhydride (0.1385 g, 0.50 mmol), $Pd(PPh_3)_4$ (0.006 g, 0.005 mmol), and CuI (0.004 g, 0.02 mmol) were vacuum dried in a Schlenk reaction flask for 15 min. Under N_2 atmosphere, dihydrolevoglucosenone (cyrene, 1 mL) was added to the reaction flask to dissolve the solid reagents, followed by 2–ethynyl thiophene (50 µL, 0.53 mmol) and triethylamine (80 µL, mmol 5.19 mmol). The reaction mixture was heated to 30 °C under N_2 atmosphere for 3 h. 10 mL EtOAc was added to the reaction solution forming a beige precipitate. The precipitate washed by organic extraction with 2 x 10 mL H_2O washings, with the precipitate now located in the aqueous layer. The precipitate was collected by vacuum filtration, washed with 2 x 10 mL Et_2O and air dried. Yield: 0.0843 g, (55%). ^{1}H NMR ($CDCl_3$, 600 MHz): δ 8.79 (dd, *J* = 8.27, 1.02 Hz, 1H), 8.69 (dd, *J* = 7.48, 1.26 Hz, 1H), 8.59 (d, *J* = 7.87 Hz, 1H), 7.99 (d, *J* = 7.56 Hz, 1H), 7.92 (dd, *J* = 8.35, 7.24 Hz, 1H), 7.51 (dd, *J* = 3.76, 1.08 Hz, 1H), 7.28 (dd, *J* =5.00, 1.13 Hz, 1 H), 7.13 (dd, *J* = 5.33, 3.64 Hz, 1H). MS [ESI–QTOF (DCM) m/z] 305.0267 $[M+H]^+$, calcd ($C_{18}H_8O_3S$) 304.02.

*Synthesis of 4–ethynylthiophene naphthalimide–5–phenanthroline (**ES–NI–phen**)*

ES–NA (0.0500 g, 0.16 mmol) and 1,10–phenanthrolin–5–amine (0.0351 g, 0.18 mmol) was used according to Synthesis A. The resulting yellow solid was collected by vacuum filtration followed by recrystallisation from toluene and again collected by vacuum filtration to obtain the purified product. Yield: 0.0505 g (64%), ^{1}H NMR ($CDCl_3$, 600 MHz): δ 9.27 (dd, J = 4.61, 1.64 Hz, 1H), 9.23 (dd, J = 4.30, 1.64 Hz, 1H), 8.83 (dd, J = 8.61, 1.13 Hz, 1H), 8.73 (dd, J = 7.38, 1.02 Hz, 1H), 8.63 (d, J = 7.58 Hz, 1H), 8.28 (dd, J = 8.10, 1.54 Hz, 1H), 8.05 (dd, J = 8.40, 1.64 Hz, 1H), 8.02 (d, J = 7.48 Hz, 1H), 7.94 (dd, J = 8.91, 7.48 Hz, 1H), 7.89 (s, 1H), 7.68 (dd, J = 8.09, 4.30 Hz, 1H), 7.58 (dd, J = 8.30, 4.20 Hz, 1H), 7.52 (dd, J = 3.59, 0.92 Hz, 1H), 7.48 (dd, J = 5.33, 1.13 Hz, 1H), 7.13 (dd, J = 5.33, 3.59 Hz, 1H). MS [ESI–QTOF (DCM) m/z] 482.0958 $[M+H]^+$, calcd ($C_{30}H_{15}N_3O_2S$) 481.09. Elem. Anal. calcd (found) for $C_{30}H_{15}N_3O_2S$: C, 74.83 (64.99); H, 3.14 (3.02); N, 8.73 (7.71); S, 6.66 (6.02).

*Synthesis of [Re(ES–NI–phen)(CO)$_3$Cl] (**Re–ES**)*

Using Synthesis B, $[Re(CO)_5Cl]$ (0.0379 g, 0.11 mmol) and **ES–NI–phen** (0.0505 g, 0.11 mmol) were refluxed in EtOH. Upon cooling the resulting yellow precipitate was collected by vacuum filtration and further drying with Et_2O. The crude material was recrystallised from toluene before further vacuum filtration and drying with Et_2O to obtain the final product. Yield: 0.0561 g (68%). ^{1}H NMR ($CDCl_3$, 600 MHz): δ 9.47 (dd, J = 5.12, 0.95 Hz, 1H), 9.44 (dd, J = 4.96, 1.21 Hz, 1H), 8.87 (dd, J = 7.21, 1.01 Hz, 1H), 8.75 (dd, J = 13.07, 1.35 Hz, 1H), 8.66 (dd, J = 11.83, 7.66 Hz, 1H), 8.56 (d, J = 7.97 Hz, 1H), 8.32 (dd, J = 8.56, 1.24 Hz, 1H), 8.12 (s, 1H), 8.04 (dd, J = 7.75, 3.13 Hz, 1H), 7.97 (dd, J = 7.92, 3.13 Hz, 1H), 7.90 (dd, J = 8.41, 5.44 Hz, 1H), 7.81 (dd, J = 8.91, 4.95 Hz, 1H), 7.53 (dd, J = 4.90, 2.24 Hz, 1H), 7.50 (m, 1H), 7.15 (dd, J = 7.56, 3.78 Hz, 1H). MS [ESI–QTOF (DCM) m/z] 786.9966 [M], calcd ($C_{33}H_{15}ClN_3O_5SRe$) 787.00. Elem. Anal. calcd (found) for $C_{33}H_{15}ClN_3O_5SRe$: C, 50.35 (48.08); H, 1.92 (1.96); N, 5.34 (5.15); S, 4.07 (4.04).

Synthesis of 4–bromo naphthalimide–5–phenanthroline

Using Synthesis A, 4–bromo–1,8–naphthalic anhydride (0.5544 g, 2.00 mmol) and 1,10–phenanthrolin–5–amine (0.4296g, 2.20 mmol) were used. The resulting brown solid was collected by vacuum filtration and dried with Et_2O to obtain the final crude product which was used without further purification. Yield: 0.8805 g (97%). ^{1}H NMR (d–DMSO, 600 MHz): δ 9.27 (s, 1H), 9.22 (s, 1H), 8.68 (dd, J = 8.22, 7.75 Hz, 2H), 8.44 (d, J = 7.56 Hz, 1H), 8.27 (d, J = 6.57 Hz,

1H), 8.09 (d, J = 7.56 Hz, 1H), 7.99 (d, *J* = 8.55 Hz, 1H), 7.90 (dd, *J* = 8.88, 7.89 Hz, 1H), 7.85 (s, 1H), 7.68 (s, 1H) 7.56 (s, 1H).

Synthesis of [Re(Br–NI–phen)(CO)$_3$Cl]

Using Synthesis B, [Re(CO)$_5$Cl] (0.1087 g, 0.30 mmol) and Br–NI–phen (0.1348 g, 0.30 mmol) were refluxed in EtOH. Upon cooling the resulting yellow precipitate was collected by vacuum filtration, with minimal EtOH and Et$_2$O washings and air–drying. Yield: 0.1565 g (69%). ^{1}H NMR (CDCl$_3$, 600 MHz): δ 9.41 (dd, *J* = 4.97, 1.28 Hz, 1H), 9.37 (dd, *J* = 5.14, 1.12 Hz, 1H), 8.71 (m, 2H), 8.47 (m, 2H), 8.21 (d, *J* = 8.67 Hz, 1H), 8.12 (dd, *J* = 8.51, 5.94 Hz, 1H), 8.05 (s, 1H), 7.92 (m, 1H), 7.84 (dd, *J* = 7.70, 5.14 Hz, 1H), 7.73 (dd, *J* = 8.67, 4.97 Hz, 1H). Elem. Anal. calcd (found) for $C_{27}H_{12}BrClN_3O_5Re$: C, 42.67 (43.47); H, 1.59 (1.77); N, 5.53 (5.84).

*Synthesis of [Re(ET–NI–phen)(CO)$_3$Cl] (**Re–ET**)*

Based on literature synthesis for 4–ethynyl trimethylsilane–1,8–naphthalic anhydride.[7] [Re(Br–NI–phen)(CO)$_3$Cl] (0.2186 g, 0.29 mmol), Pd(PPh$_3$)$_4$ (0.0901 g, 0.08 mmol), and CuI (0.0246 g, 0.13 mmol) were vacuum dried in a Schlenk reaction flask for 15 min. Under N$_2$ atmosphere, DMF (2 mL) was added to the reaction flask to dissolve the solid reagents, followed by 2–ethynyl trimethylsilane (1520 µL, 11.14 mmol) and triethylamine (760 µL, 5.41 mmol). The reaction mixture was heated to 60 °C under N$_2$ atmosphere for 24 h. Following cooling of the reaction solution, the solvents were removed in vacuo to yield a dried crude mass. The crude was recrystallised from EtOAc before being collected by vacuum filtration, washed with Et$_2$O (2x 10 mL) and air–dried. Yield: 0.0943 g (55%). ^{1}H NMR (CDCl$_3$, 600 MHz): δ = 9.47 (d, *J* = 4.96 Hz, 1H), 9.43 (d, *J* = 4.96 Hz, 1H), 8.83 (dd, *J* = 8.51, 4.39 Hz, 1H), 8.74 (dd, *J* = 18.67, 7.14 Hz, 1H), 8.63 (dd, *J* = 23.07, 7.69 Hz, 1H), 8.57 (d, *J* = 8.24 Hz, 1H), 8.31 (d, *J* = 8.79 Hz, 1H), 8.12 (s, 1H), 8.01 (dd, *J* = 8.25, 7.50 Hz, 1H), 7.95 (dd, *J* = 12.38, 7.12 Hz, 1H), 7.90 (dd, *J* = 8.44, 5.25 Hz, 1H), 7.80 (dd, *J* = 8.25, 4.88 Hz, 1H), 0.41 (s, 9H). MS [ESI–QTOF (DCM) m/z] 800.0506 $[M+Na]^+$, calcd ($C_{32}H_{21}ClN_3O_5ReSi$) 777.28. Elem. Anal. calcd (found) for $C_{32}H_{21}ClN_3O_5ReSi$: C, 49.45 (47.74); H, 2.72 (3.57); N, 5.41 (5.11).

FTIR and UV-Vis Absorption and Emission Studies

All IR spectra were recorded on a PerkinElmer Spectrum65 FTIR Spectrometer. Samples were prepared in spectroscopic grade DCM and loaded into a liquid–film IR cell with CaF_2 windows. ATR-IR spectra were recorded on a Thermoscientific Nicolet Summit FT-IR with the Everest ATR accessory. All UV-Vis absorption and emission spectra were recorded on a Horiba Duetta Fluorescence and Absorbance Spectrometer. Samples were analyzed in a quartz cuvette with a 1 cm path length and prepared in spectroscopy grade DCM. 2–MeTHF was used as the solvent glass for 77 K emission studies, with samples prepared to an optical density of ~1 at the maximum absorbance at room temperature.

Time Correlated Single Photon Counting

Emission lifetimes were measured using an Edinburgh Instruments FLS1000 photoluminescence spectrometer, using a 375 nm picosecond pulsed diode laser. Samples were prepared in spectroscopy grade DCM to an absorbance of 0.2 at 375 nm in a fluorescence quartz cuvette with 1 cm path length. The optical density of the samples was compared before and after the measurement to ensure that no photodegradation had occurred.

Emission Quantum Yields

Absolute emissive quantum yields were determined using an Edinburgh Instruments FLS1000 photoluminescence spectrometer equipped with an integrating sphere coupled with a XeArc lamp. All samples were prepared in a fluorescence quartz cuvette with a 1 cm path length, made to an absorbance of 0.2 at 375 nm in spectroscopic grade DCM. The samples were purged with N_2 for ~20 min prior to the experiment.

Time-Resolved IR studies

Time-resolved Infrared (TRIR) spectroscopy experiments were conducted using the ULTRA apparatus at the Central Laser Facility (CLF), which is described in detail elsewhere.[8] Samples were excited at 365, 400, and 420 nm using spectroscopic grade DCM in a Harrick cell. The measurements were performed with rastering to minimize photodamage and re–excitation effects. Different samples were used for the ps-TRIR and ns-TRIR experiments. All spectra were

processed using the in–house ULTRAview software provided by the CLF. Samples were calibrated from pixels into wavenumbers using the in–house ULTRAcal software provided by the CLF. The ethynyl, metal carbonyl, and organic carbonyl regions (2300 – 1600 cm^{-1}) were calibrated by fitting the absorption bands of polystyrene. All experiments were carried out at 298 K and samples were checked before and after the experiment for photodegradation by UV-Vis spectroscopy in a PerkinElmer Lambda 950 spectrophotometer and FTIR in a Nicolet Avatar spectrometer. Kinetic fitting of all TRIR spectra was conducted with global fit analysis using the Glotaran 1.5.1 software.[9]

Transient Absorption (TA) Spectroscopy

Nanosecond transient absorption spectra were measured using an Edinburgh Instruments LP980 coupled with a Quantel Qsmart 450, tuned to the third harmonic (355 nm). Samples were prepared to an absorbance of 0.4 at 355 nm in spectroscopic grade DCM. Three freeze–pump–thaw cycles were used to degas the solution before placing under a nitrogen environment prior to the experiment. The optical density of the samples was compared before and after to ensure no photodegradation occurred. The average lifetimes were calculated using Equation S1.1.[10]

$$\tau_{\mathrm{avg}} = \frac{\sum_{i=1}^{n} \alpha_i \tau_i}{\sum_{i=1}^{n} \alpha_i}$$

Equation S2.13. *Equation for determining an amplitude-weighted average lifetime.[10]*

DFT/TDDFT Calculations

DFT calculations were performed in Gaussian 16, Revision C01 (G16)[11], together with the three–parameterized Becke, Lee, Yang, and Park (B3LYP) functional.[12,13] For the Re atom, a quasi–relativistic effective–core pseudopotential and a corresponding optimized basis set[14] was used, and for non–metal atoms, the 6–31+G(d) basis set.[15] Solvent effects (DCM) were described by the conductor–like polarisable continuum model (CPCM).[16] The DFT calculations of **Re–EB** revealed four possible structures (a–d) with similar energies (Figure S2.62 and Table S2.9). The calculated electronic and vibrational spectra of the possible structures appeared identical; with the a and c versions of **Re–EB** being optical isomers, b and d behaved likewise. Two possible

structures were calculated for **Re–ES** (a and b) with the lower–energy a–structure being used in further calculations (Figure S2.63 and Table S2.10).

S2.2 ^{1}H NMR Spectra

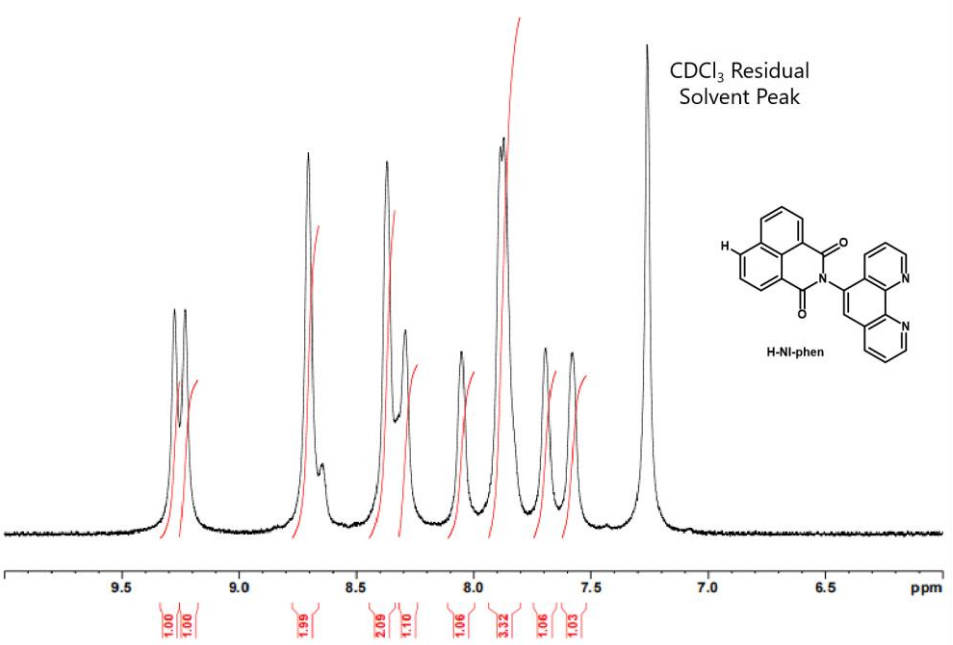


Figure S2.1. *600 MHz ^{1}H NMR spectrum of* ***H–NI–phen*** *in $CDCl_3$*

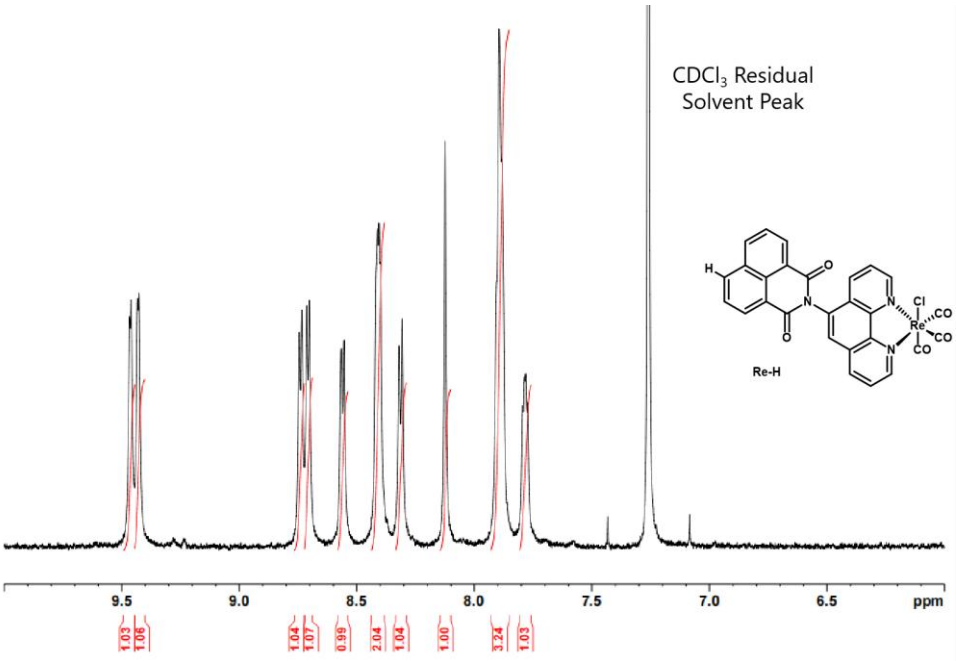


Figure S2.2. *600 MHz ^{1}H NMR spectrum of* ***Re–H*** *in $CDCl_3$*

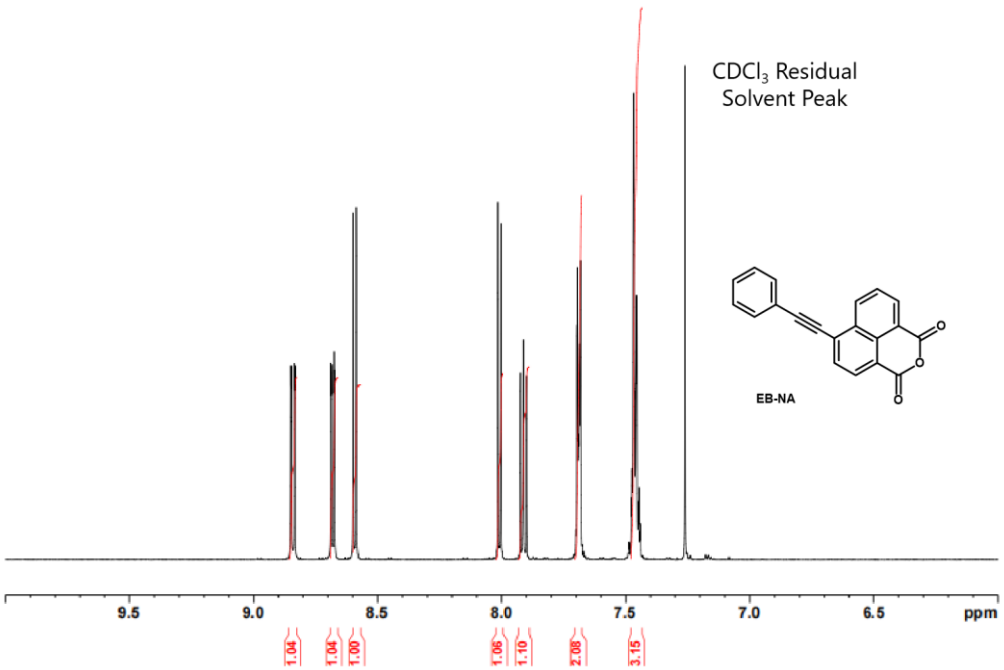


Figure S2.3. *600 MHz ^{1}H NMR spectrum of* ***EB–NA*** *in $CDCl_3$*

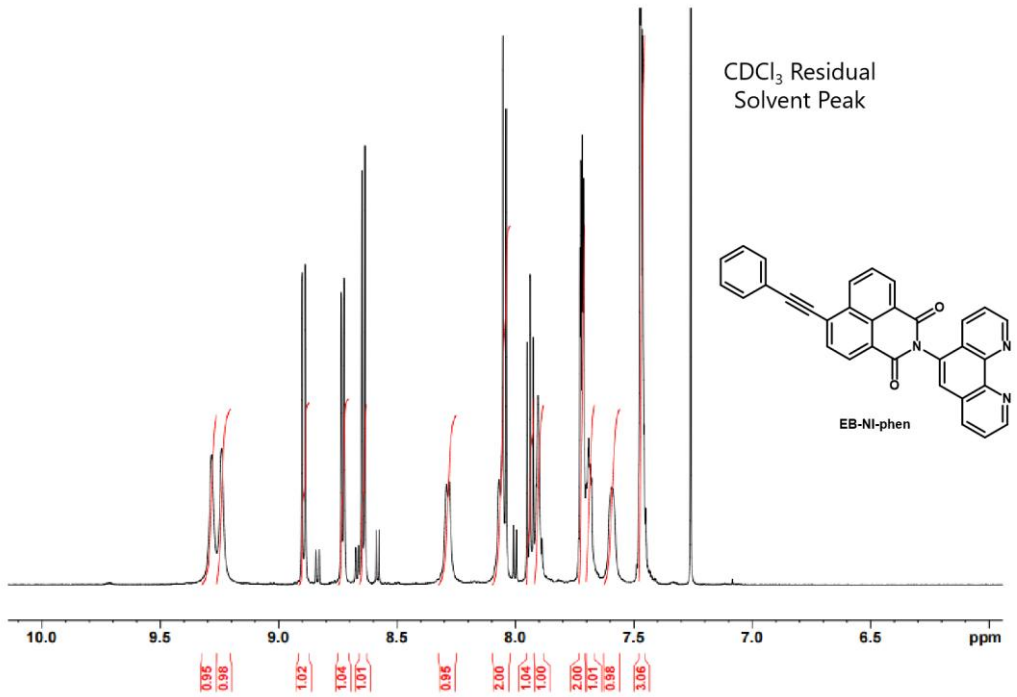


Figure S2.4. *600 MHz ^{1}H NMR spectrum of* ***EB–NI–phen*** *in $CDCl_3$*

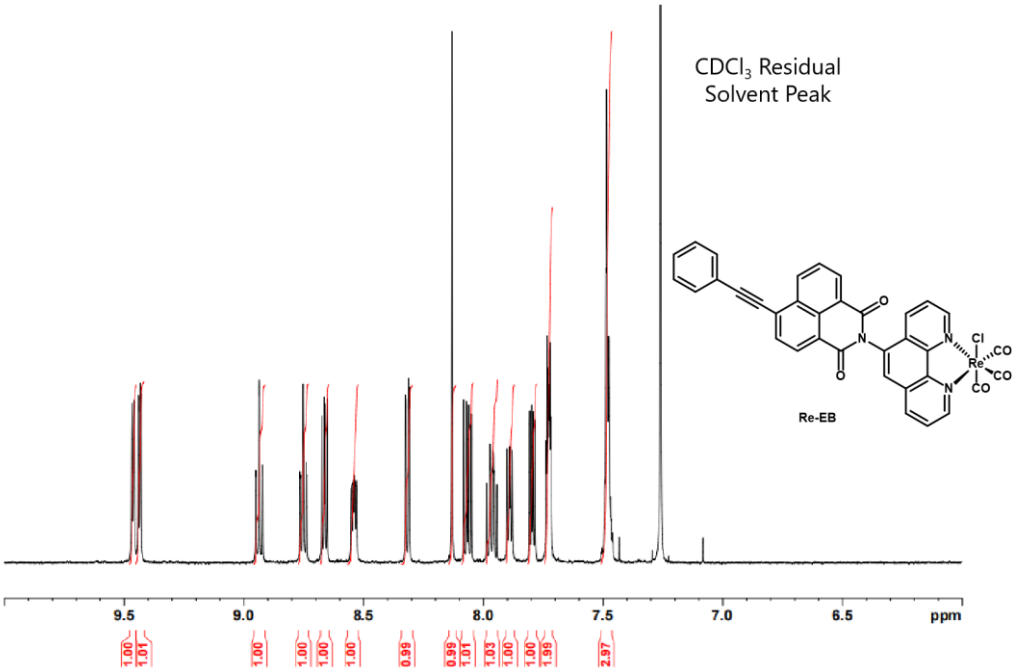


Figure S2.5. *600 MHz ^{1}H NMR spectrum of* ***Re–EB*** *in $CDCl_3$*

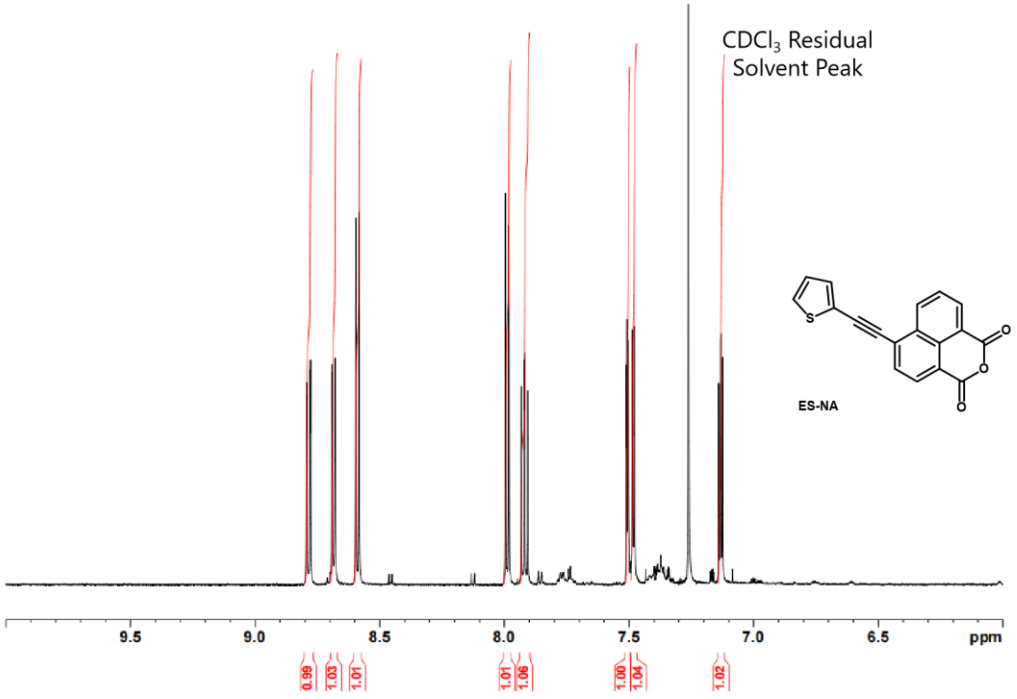


Figure S2.6. *600 MHz ^{1}H NMR spectrum of* ***ES–NA*** *in $CDCl_3$*

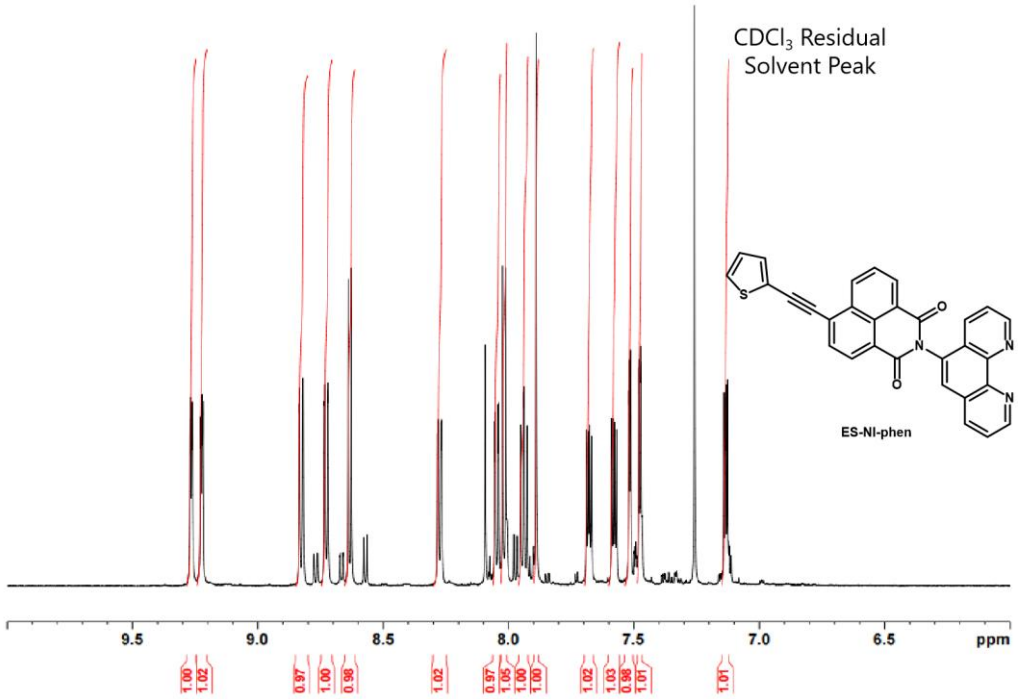


Figure S2.7. *600 MHz ^{1}H NMR spectrum of* ***ES–NI–phen*** *in $CDCl_3$*

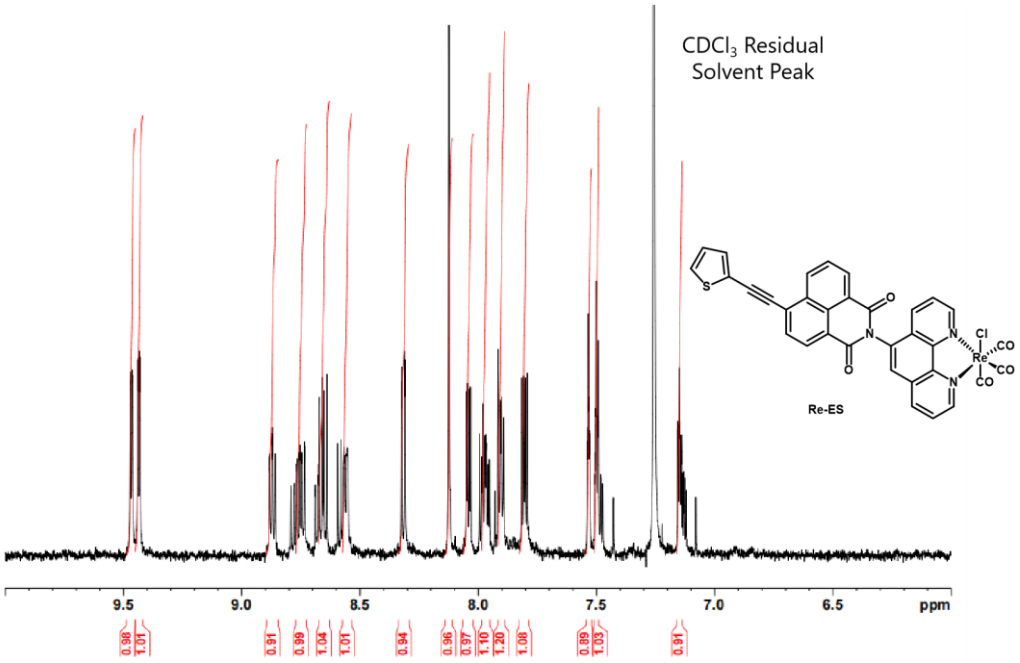


Figure S2.8. *600 MHz ^{1}H NMR spectrum of* ***Re–ES*** *in $CDCl_3$*

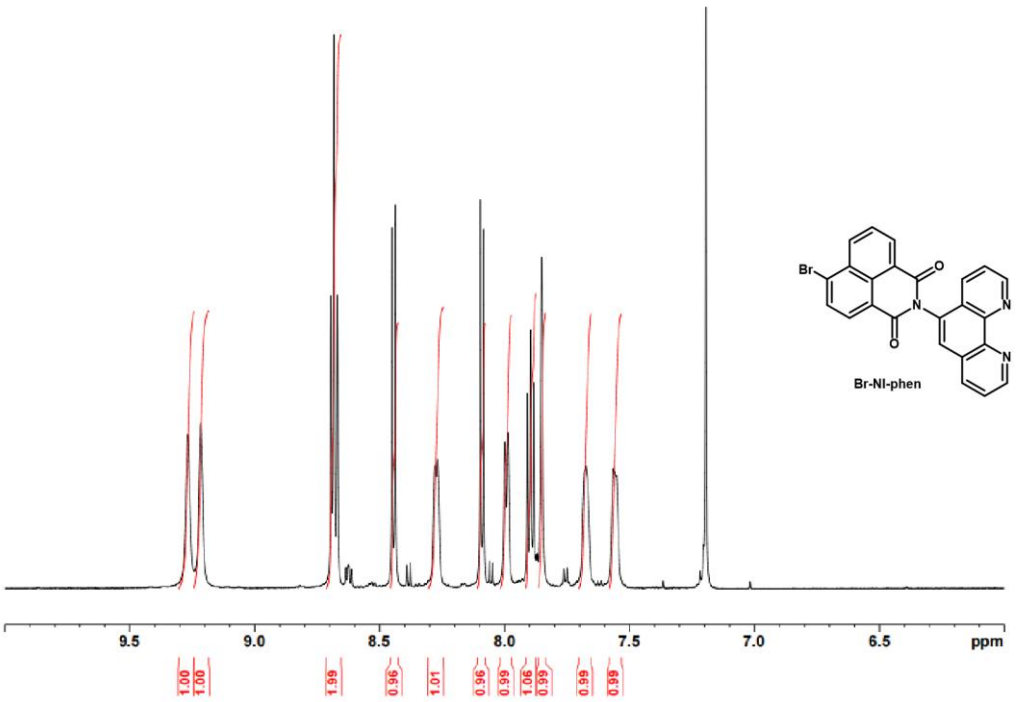


Figure S2.9. *600 MHz ^{1}H NMR spectrum of* ***Br–NI–phen*** *in $CDCl_3$*

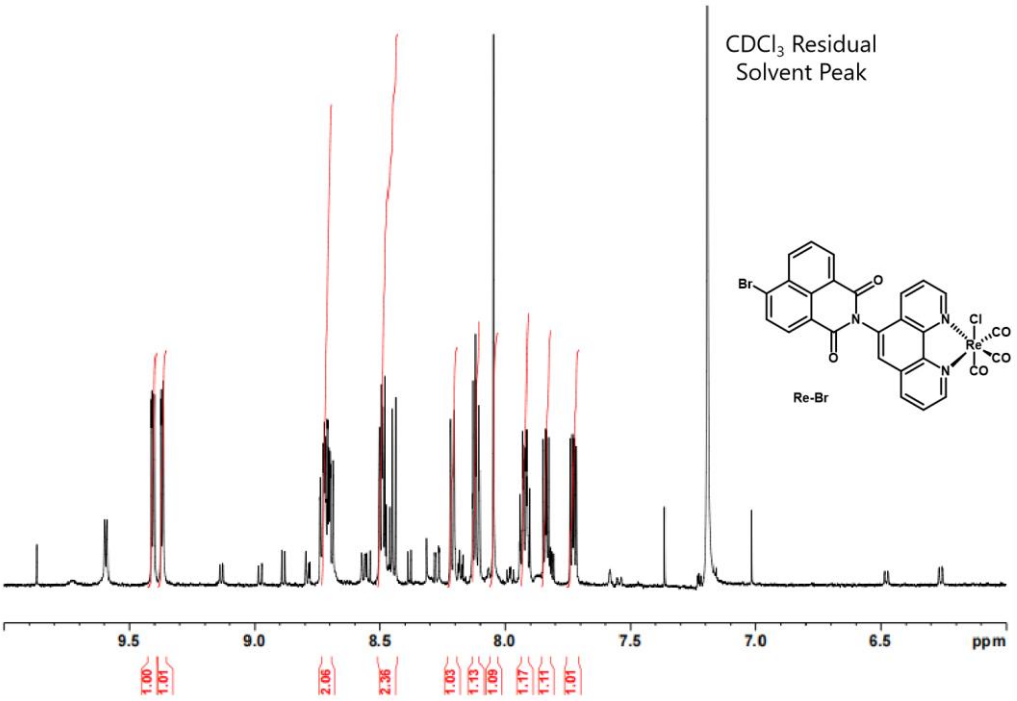


Figure S2.10. *600 MHz ^{1}H NMR spectrum of* ***Re–Br*** *in $CDCl_3$*

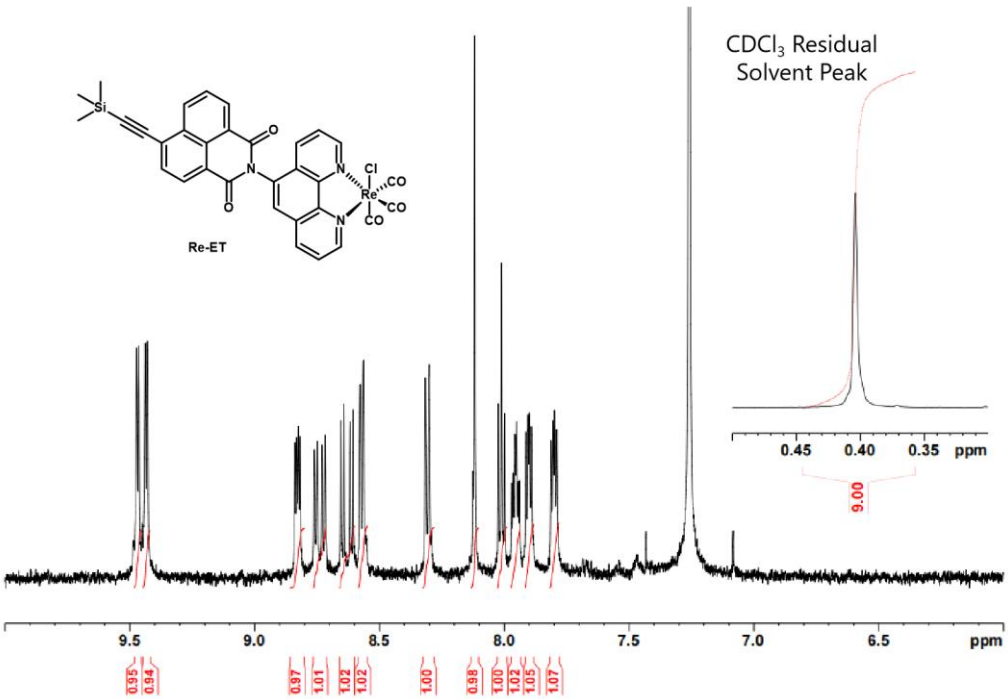


Figure S2.11. *600 MHz ^{1}H NMR spectrum of* ***Re–ET*** *in $CDCl_3$*

S2.3 Mass Spectrometry

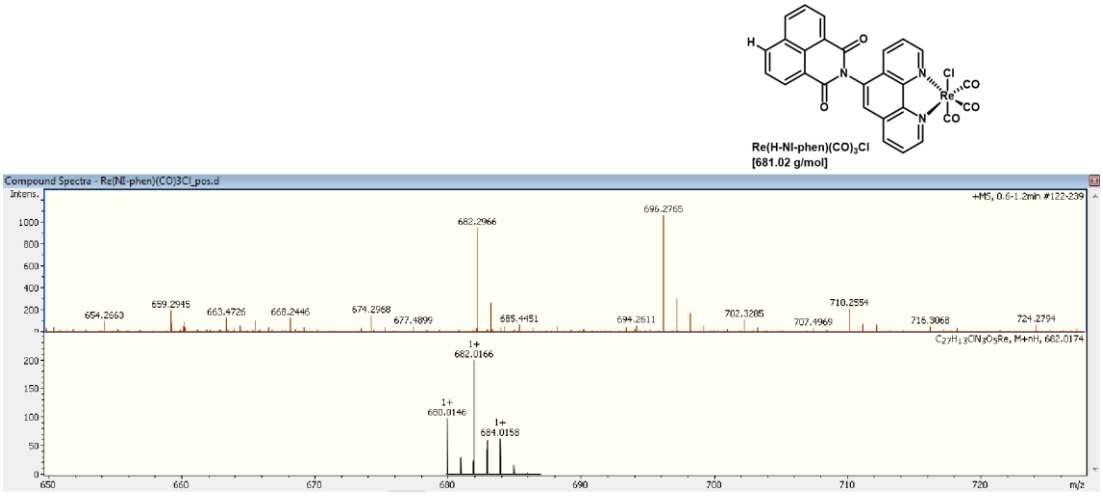


Figure S2.12. *ESI–QTOF mass spectrum of* ***Re–H*** *$[M+H]^{+}$ (M = 681.02 g/mol)*

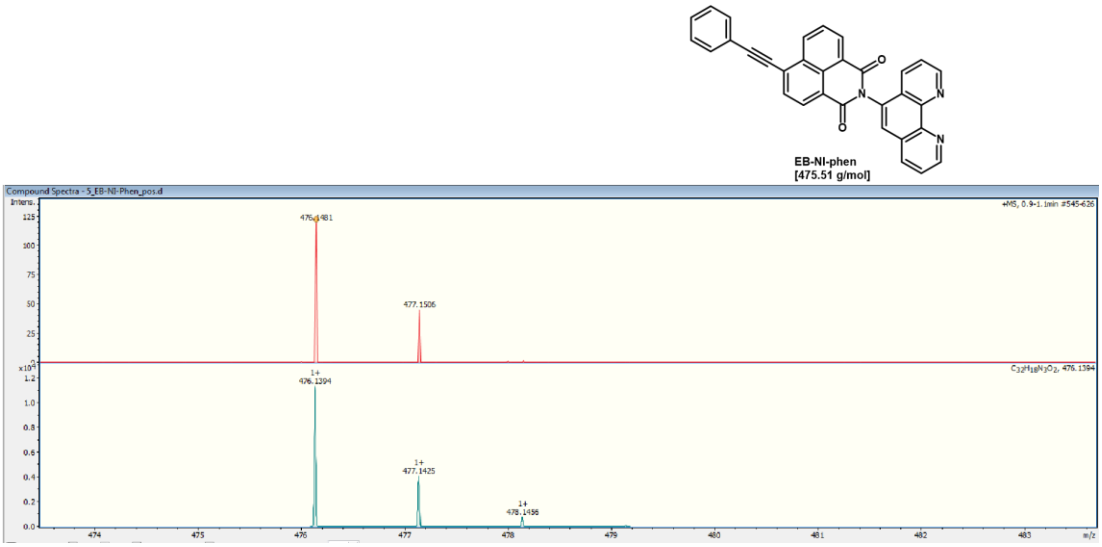


Figure S2.13. *ESI–QTOF mass spectrum of* ***EB–NI–phen*** *$[M+H]^+$ (M = 475.51 g/mol)*

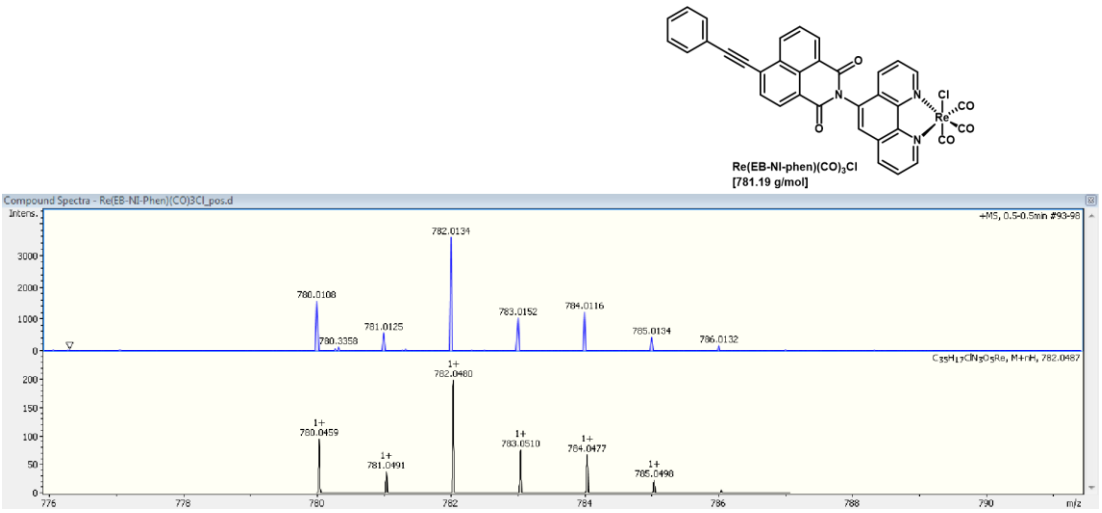


Figure S2.14. *ESI–QTOF mass spectrum of* ***Re–EB*** *$[M+H]^+$ (M = 781.19 g/mol)*

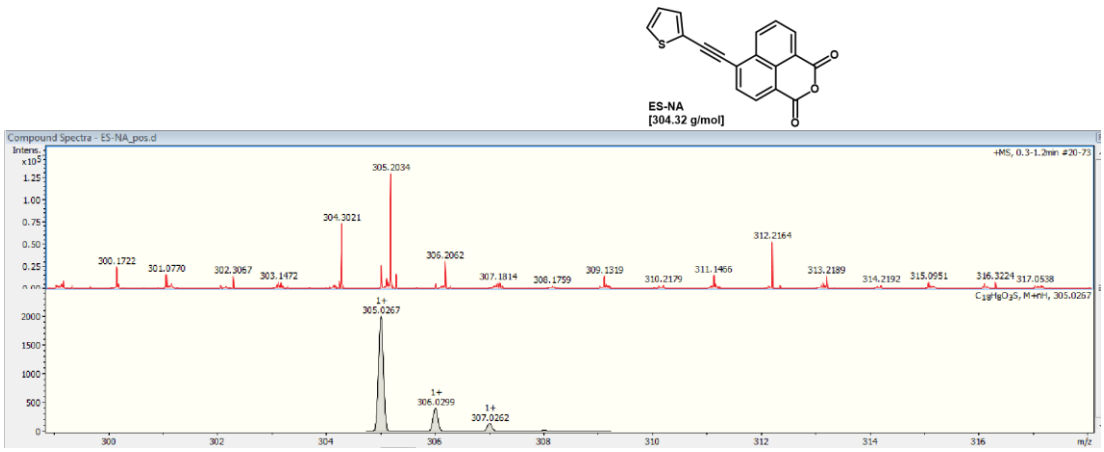


Figure S2.15. *ESI–QTOF mass spectrum of* ***ES–NA*** *$[M+H]^+$ (M = 304.32 g/mol)*

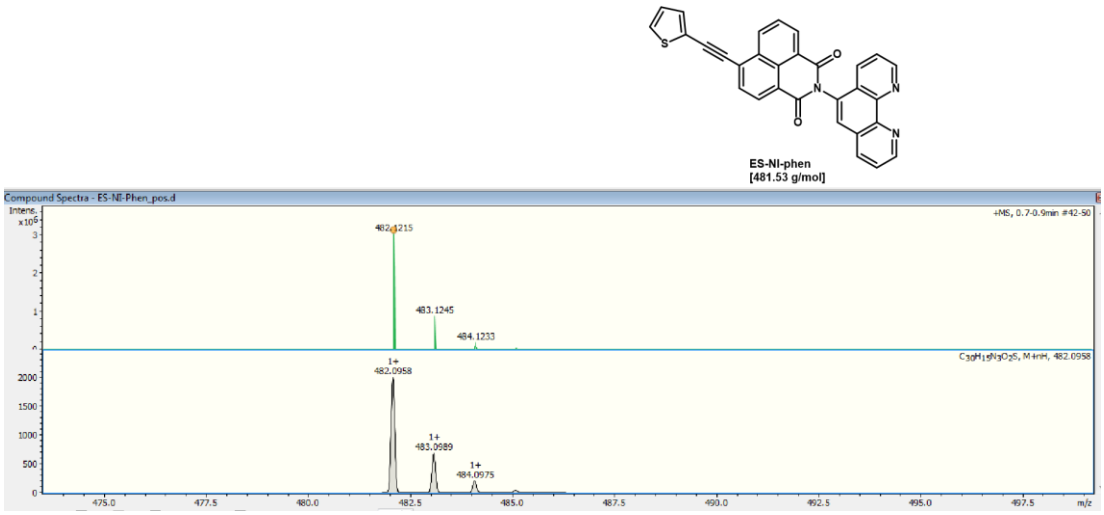


Figure S2.16. *ESI–QTOF mass spectrum of* ***ES–NI–phen*** *$[M+H]^+$ (M = 481.53 g/mol)*

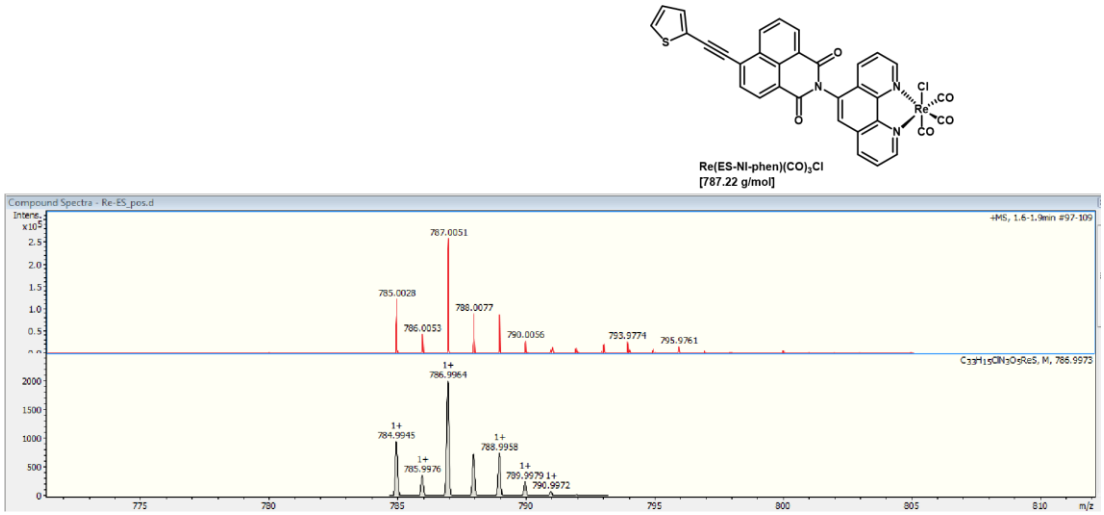


Figure S2.17. *ESI–QTOF mass spectrum of* ***Re–ES*** *[M] (M = 787.22 g/mol)*

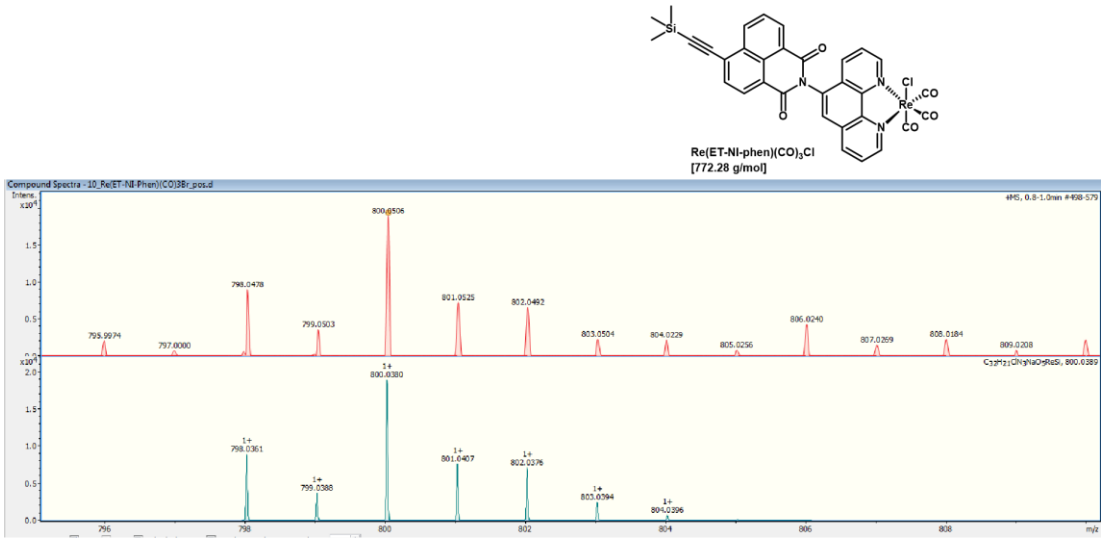


Figure S2.18. *ESI–QTOF mass spectrum of* ***Re–ET*** *$[M+Na]^+$ (M = 772.28 g/mol)*

S2.4 IR Spectra

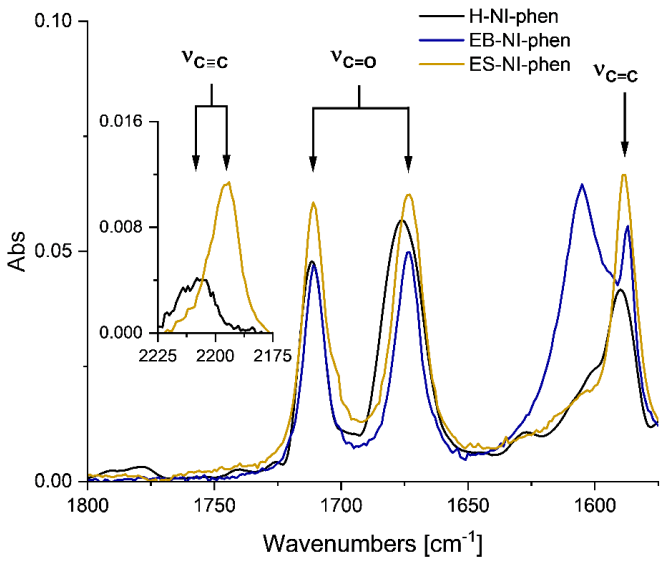


Figure S2.19. *FTIR spectra between 1750 and 1575 cm^{-1} of the **R–NI–phen** compounds in DCM. Inset: FTIR spectra between 2225 and 2175 cm^{-1} of **EB–NI–phen** and **ES–NI–phen** in DCM.*

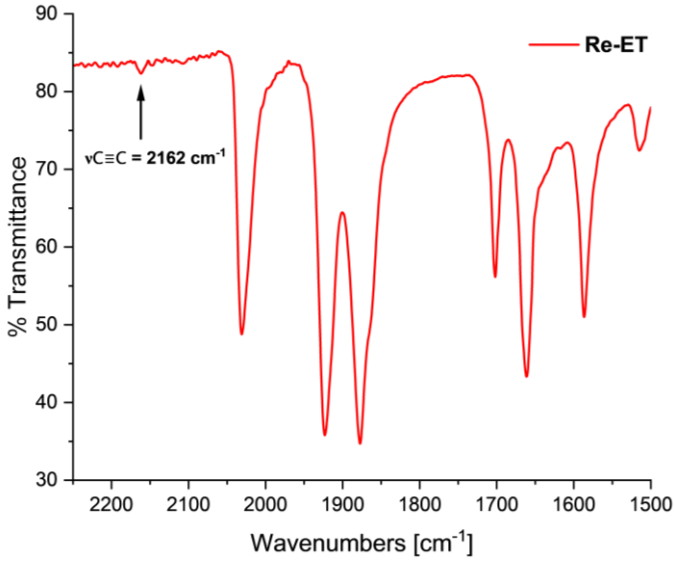


Figure S2.20. *ATR–IR spectra between 2250 and 1500 cm^{-1} of **Re–ET**. The ethynyl vibration at 2162 cm^{-1} is indicated.*

S2.5 UV-Vis Absorption and Emission Spectra

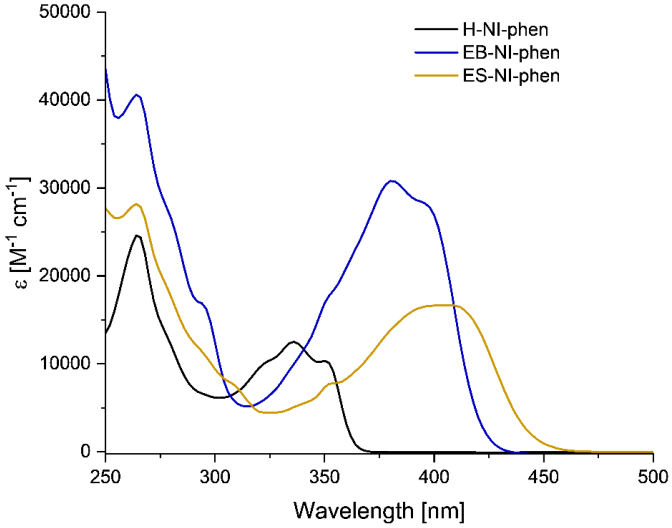


Figure S2.21. *UV-Vis absorption spectra of* ***R–NI–phen*** *in DCM solutions.*

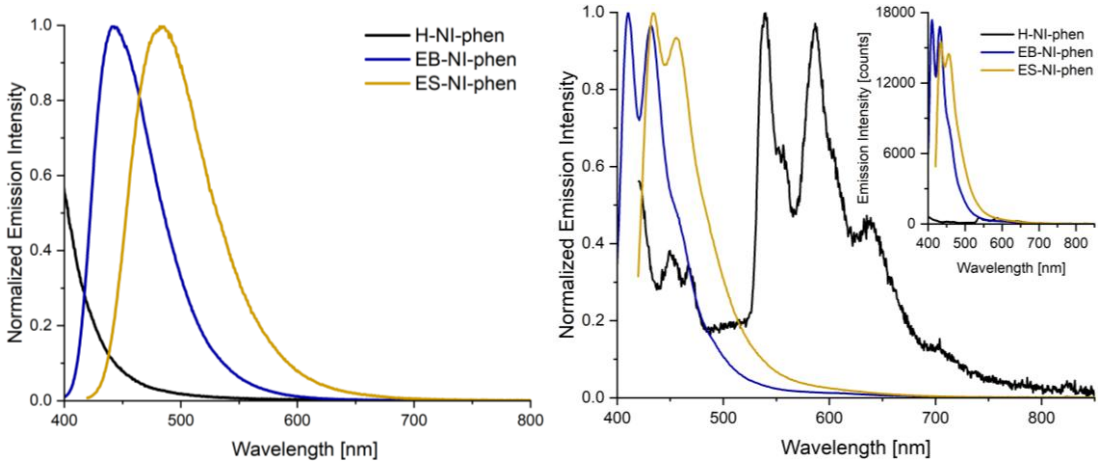


Figure S2.22. *(Left) (Right) Normalized emission spectra following excitation at 385 nm in DCM of* ***R–NI–phen****. (Right) The normalized 77 K emission spectra in 2–MeTHF of* ***R–NI–phen****. Inset – The non–normalized 77 K emission spectra of the same* ***R–NI–phen*** *compounds.*

S2.6 TRIR Spectra and Kinetic Traces

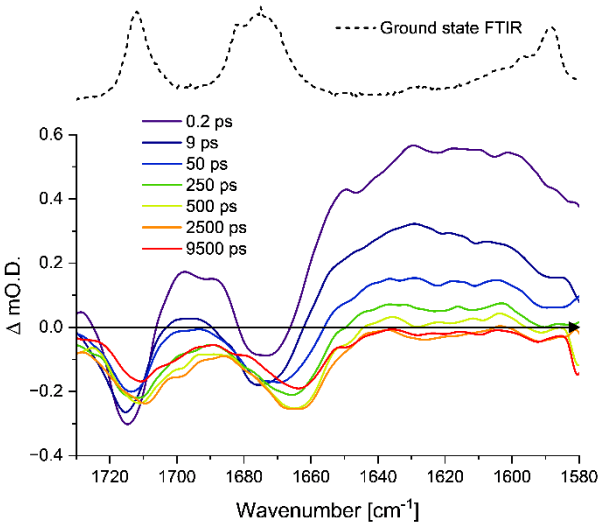


Figure S2.23. *ps–TRIR spectrum of the* $\nu_{C=O}$ *region of* ***H–NI–phen*** *in DCM following 365 nm excitation.*

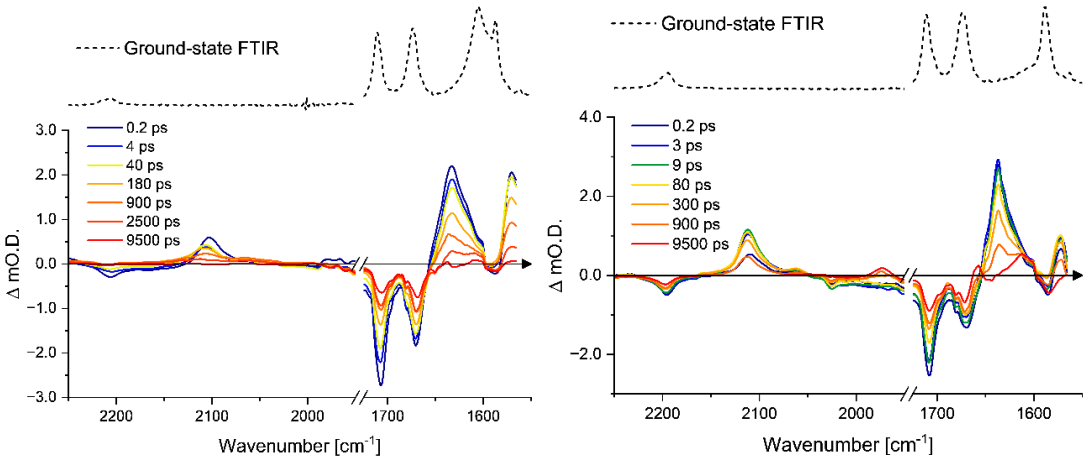


Figure S2.24. *ps–TRIR spectra displaying the ethynyl and organic carbonyl regions in DCM following 420 nm excitation of* ***EB–NI–phen*** *(Left) and* ***ES–NI–phen*** *(Right).*

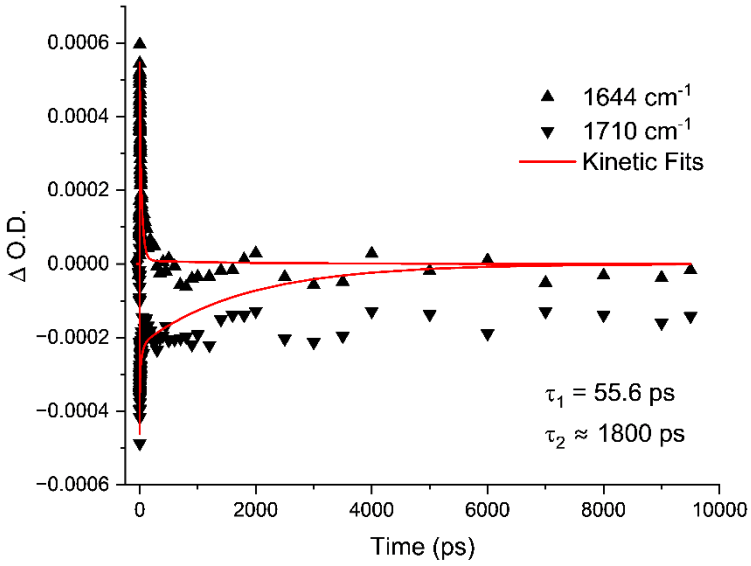


Figure S2.25. *Kinetic traces of the $\nu_{C=O}$ 1710 cm^{-1} GSB and $\nu_{C=O}$ 1644 cm^{-1} transient band of* ***H–NI–phen*** *following excitation at 365 nm.*

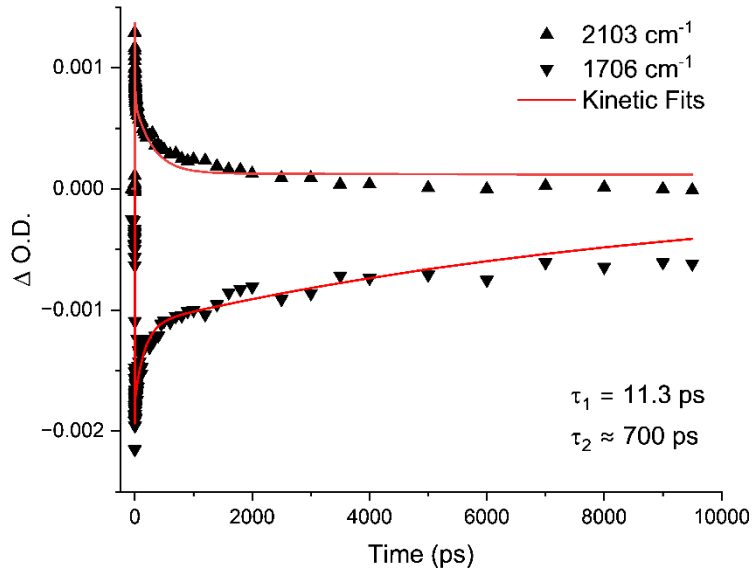


Figure S2.26. *Kinetic traces of the $\nu_{C=O}$ 1706 cm^{-1} GSB and $\nu_{C\equiv C}$ 2103 cm^{-1} transient band of* ***EB–NI–phen*** *following excitation at 420 nm.*

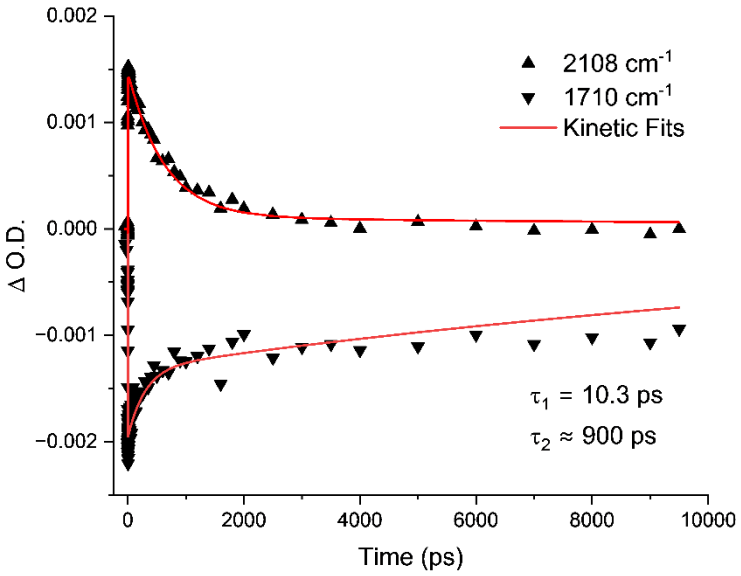


Figure S2.27. *Kinetic traces of the $\nu_{C=O}$ 1710 cm^{-1} GSB and $\nu_{C\equiv C}$ 2108 cm^{-1} transient band of* ***ES–NI–phen*** *following excitation at 420 nm.*

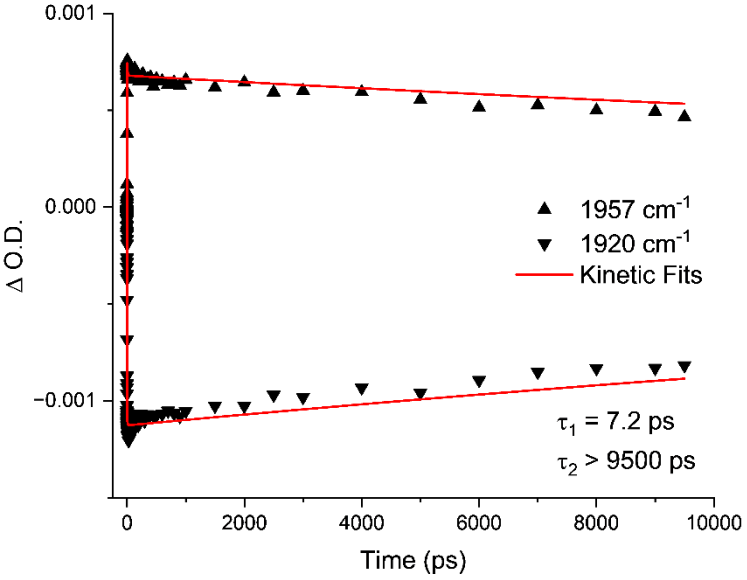


Figure S2.28. *Kinetic traces of the $\nu_{C\equiv O}$ 1920 cm^{-1} GSB and $\nu_{C\equiv O}$ 1957 cm^{-1} transient band of* ***Re–H*** *following excitation at 400 nm.*

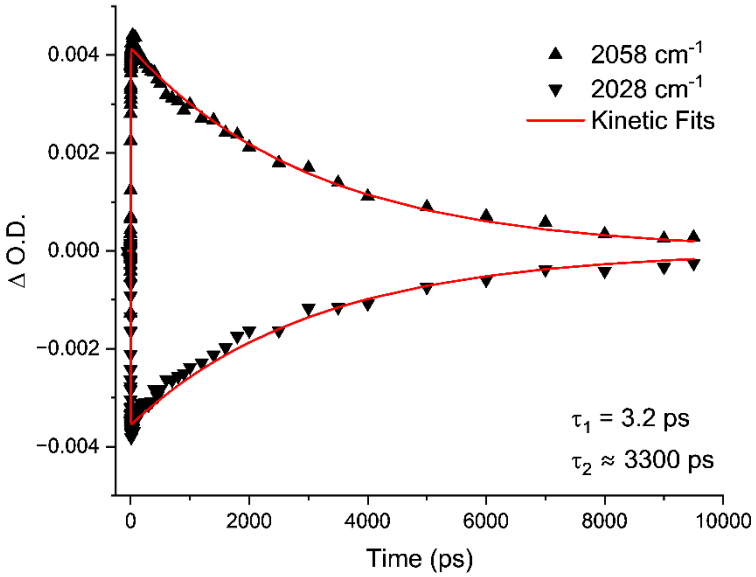


Figure S2.29. *Kinetic traces of the $\nu_{C\equiv O}$ 2028 cm^{-1} GSB and $\nu_{C\equiv O}$ 2058 cm^{-1} transient band of* ***Re–ET*** *following excitation at 420 nm.*

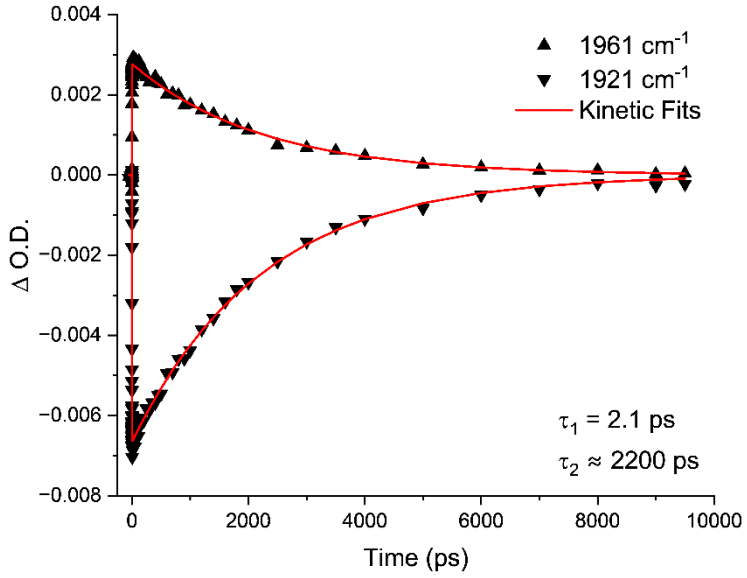


Figure S2.30. *Kinetic traces of the $\nu_{C\equiv O}$ 1921 cm^{-1} GSB and $\nu_{C\equiv O}$ 1961 cm^{-1} transient band of* ***Re–EB*** *following excitation at 420 nm.*

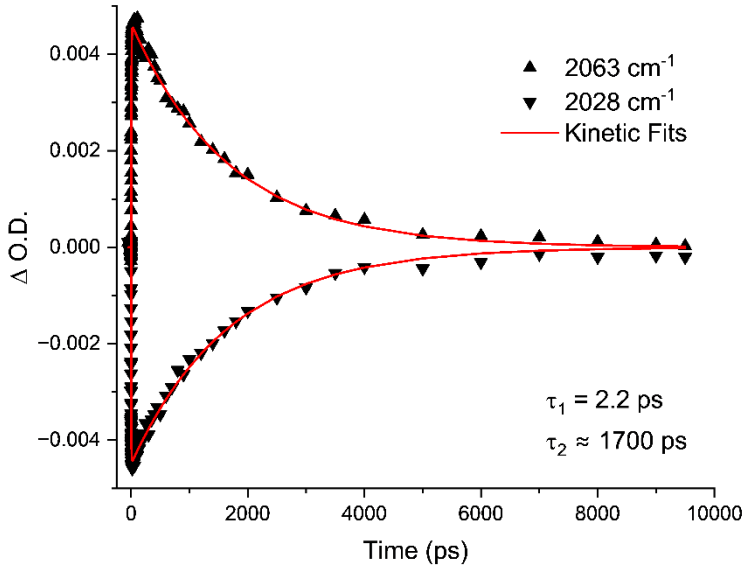


Figure S2.31. *Kinetic traces of the $\nu_{C\equiv O}$ 2028 cm^{-1} GSB and $\nu_{C\equiv O}$ 2063 cm^{-1} transient band of* ***Re–ES*** *following excitation at 420 nm.*

S2.7 TCSPC Studies

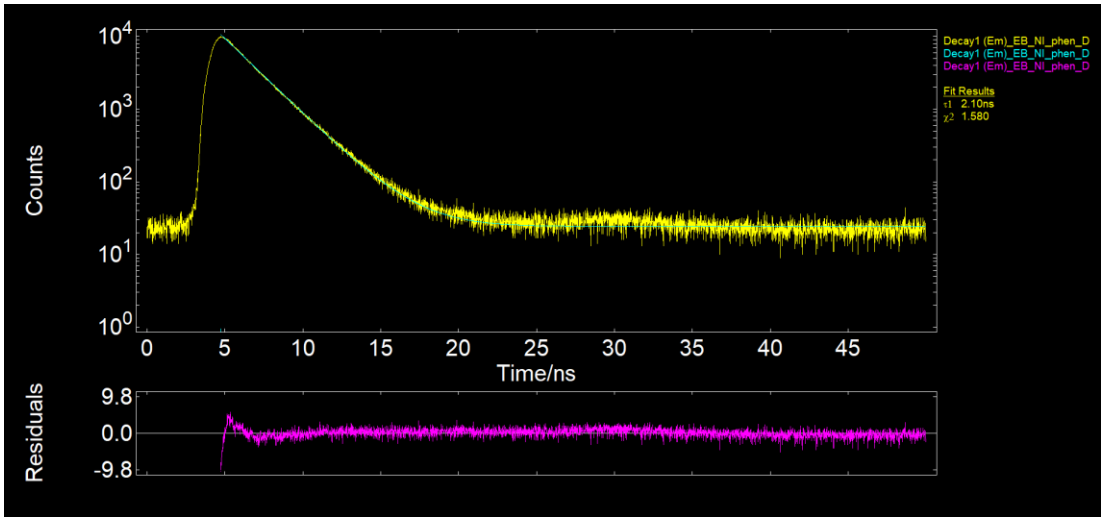


Figure S2.32. *Kinetic trace at 445 nm of* ***EB–NI–phen*** *in DCM following 375 nm excitation.*

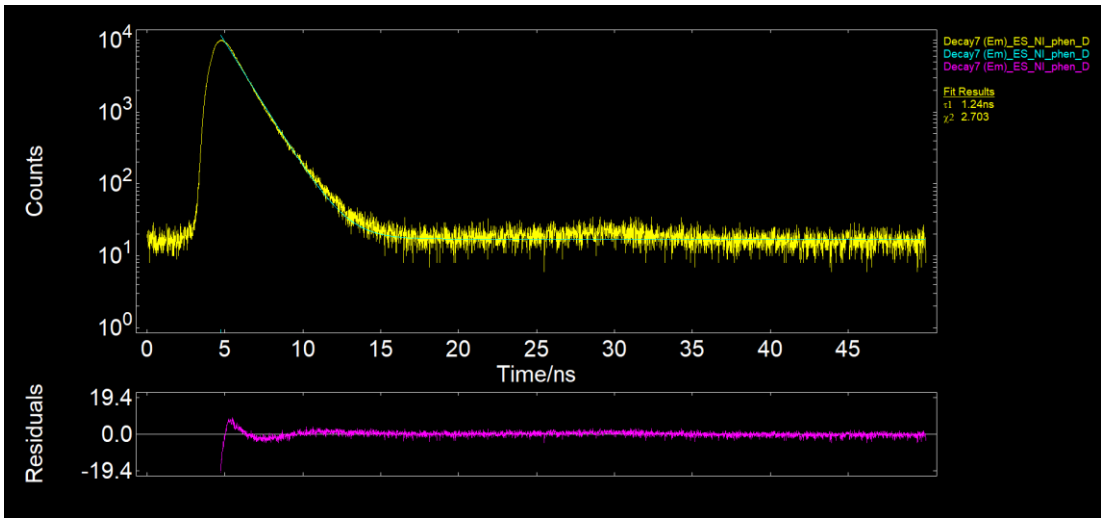


Figure S2.33. *Kinetic trace at 485 nm of* ***ES–NI–phen*** *in DCM following 375 nm excitation.*

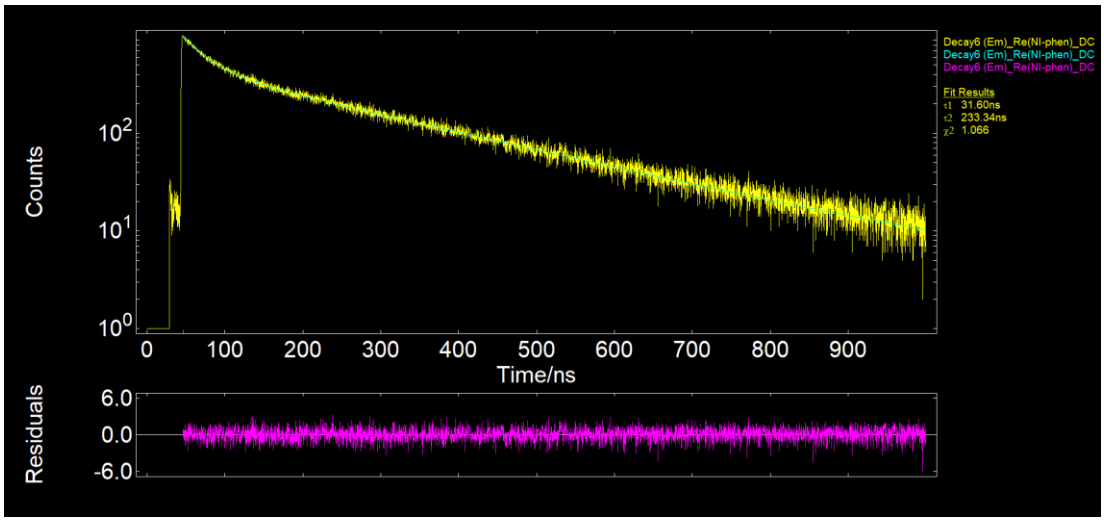


Figure S2.34. *Kinetic trace at 630 nm of* ***Re–H*** *in DCM following 375 nm excitation.*

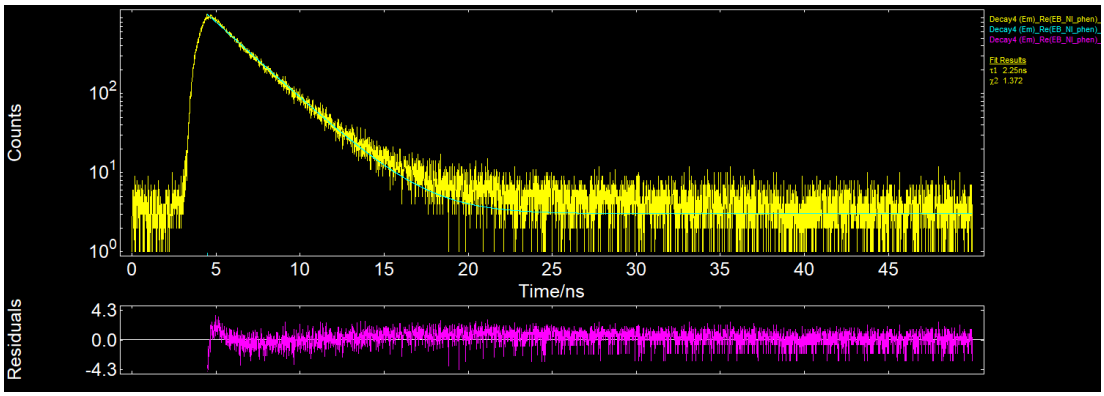


Figure S2.35. *Kinetic trace at 445 nm of* ***Re–EB*** *in DCM following 375 nm excitation.*

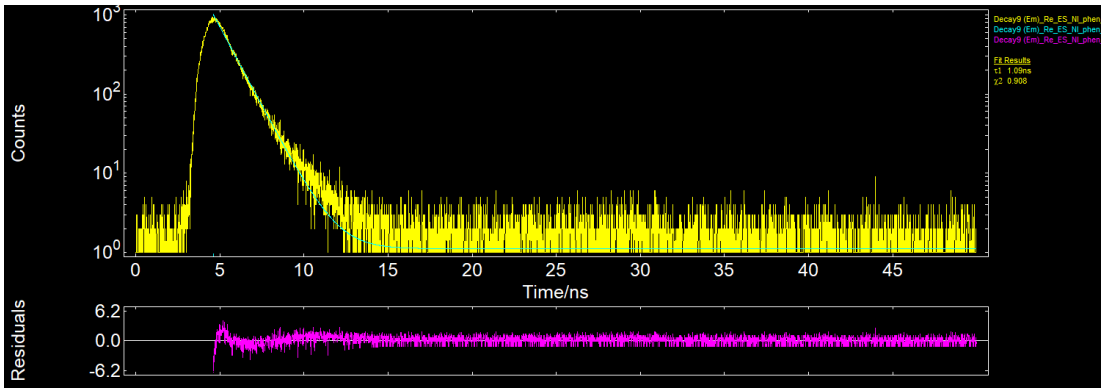


Figure S2.36. *Kinetic trace at 485 nm of* ***Re–ES*** *in DCM following 375 nm excitation.*

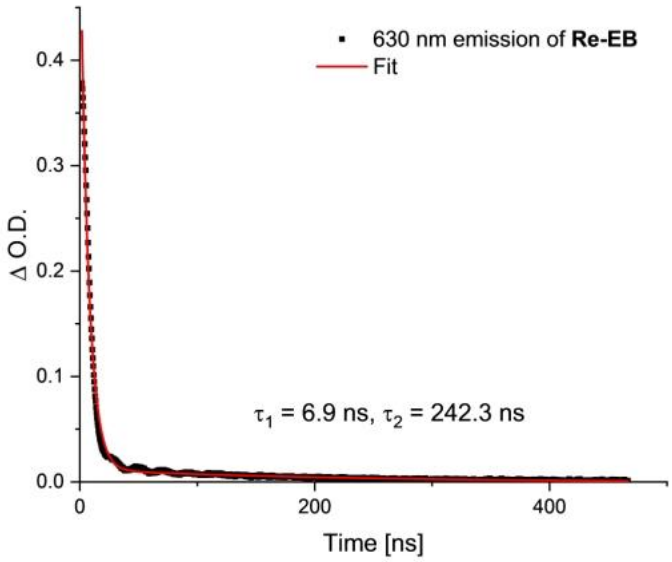


Figure S2.37. *Kinetic trace at 630 nm following 355 nm excitation of* ***Re–EB*** *in DCM.*

S2.8 TA Spectra and Kinetic Traces

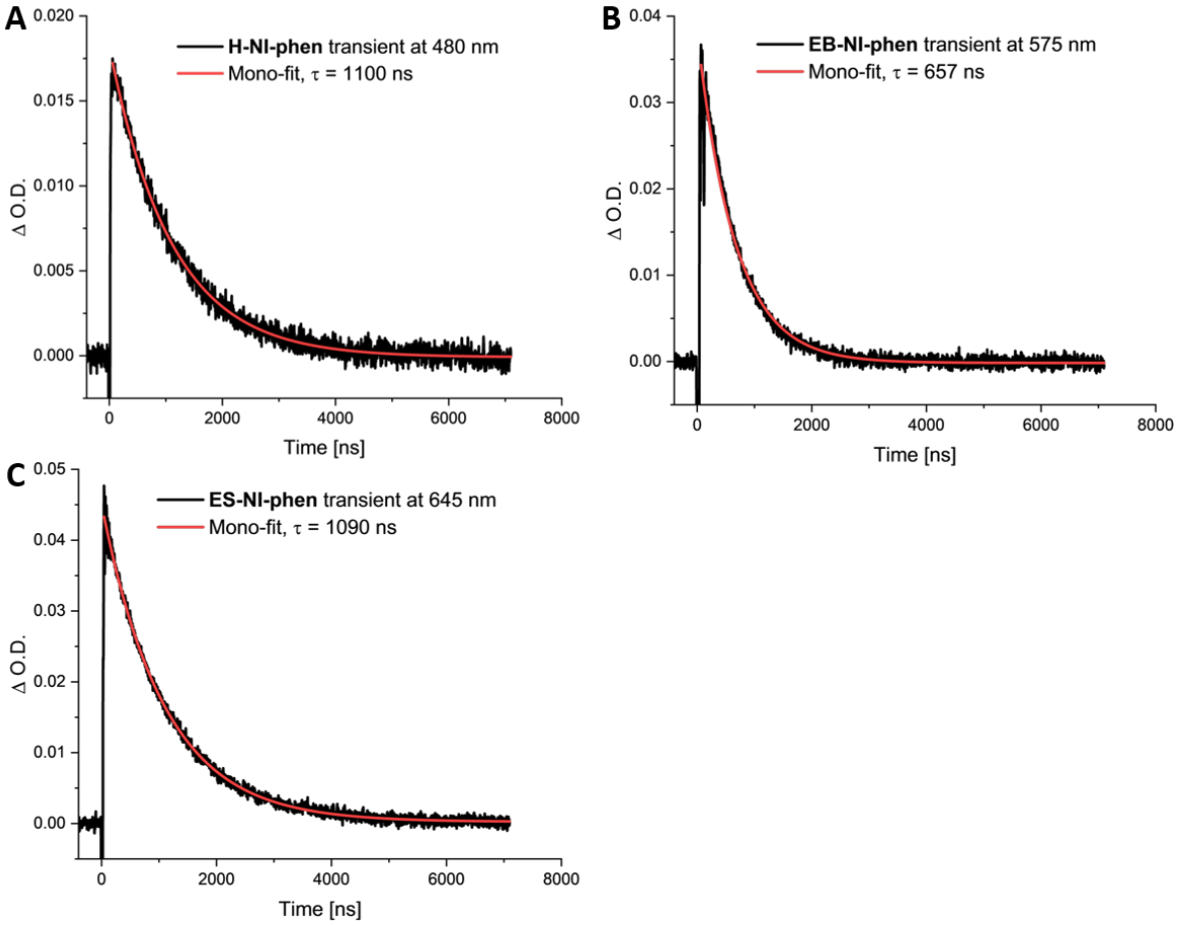


Figure S2.38. *Kinetic traces from µs-TA and µs-TRIR experiments of aerated samples of (A)* ***R–NI–phen****, (B)* ***R–NI–phen****, and (C)* ***R–NI–phen****.*

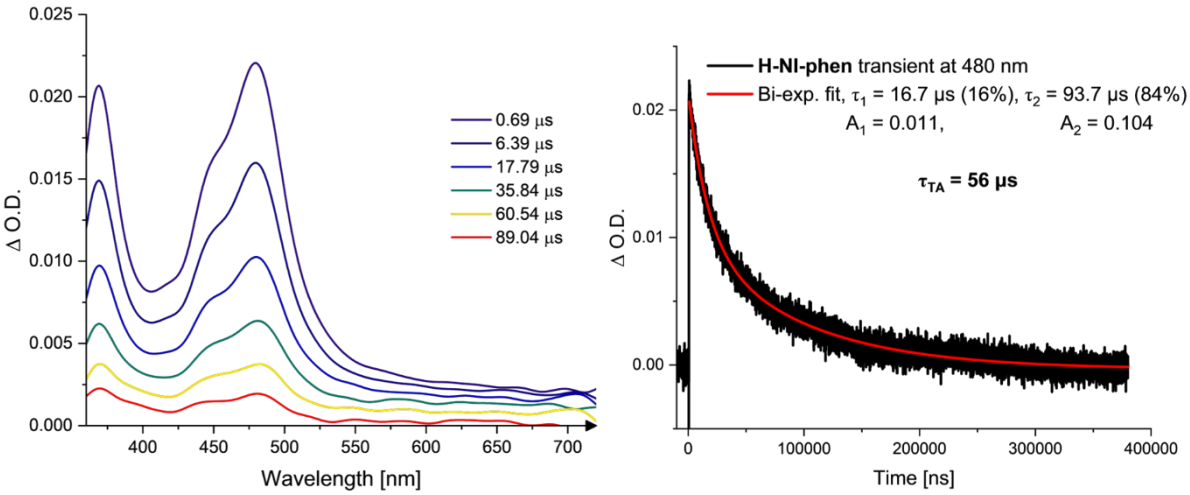


Figure S2.39. *(Left) TA spectrum of* ***H–NI–phen*** *in DCM following excitation at 355 nm. (Right) Kinetic trace displaying biexponentially fit lifetimes and average lifetime at 480 nm.*

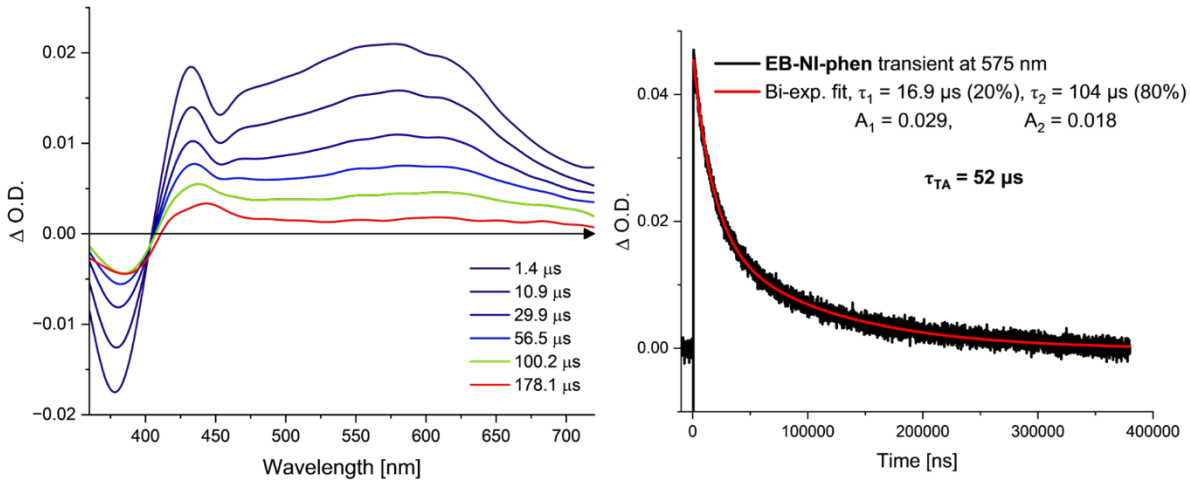


Figure S2.40. *(Left) TA spectrum of* ***EB–NI–phen*** *in DCM following excitation at 355 nm. (Right) Kinetic trace displaying biexponentially fit lifetimes and average lifetime at 575 nm.*

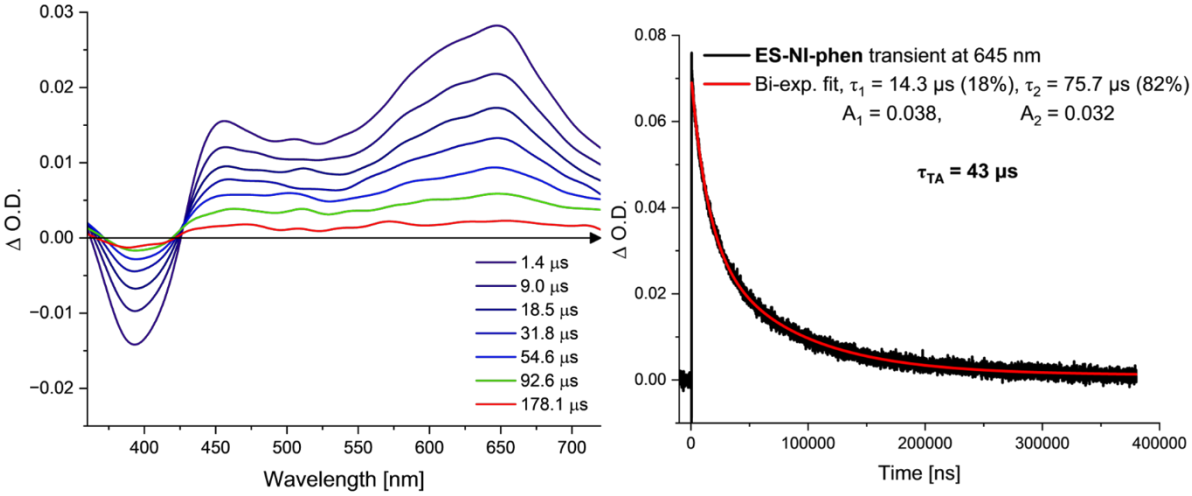


Figure S2.41. *(Left) TA spectrum of* ***ES–NI–phen*** *in DCM following excitation at 355 nm. (Right) Kinetic trace displaying biexponentially fit lifetimes and average lifetime at 645 nm.*

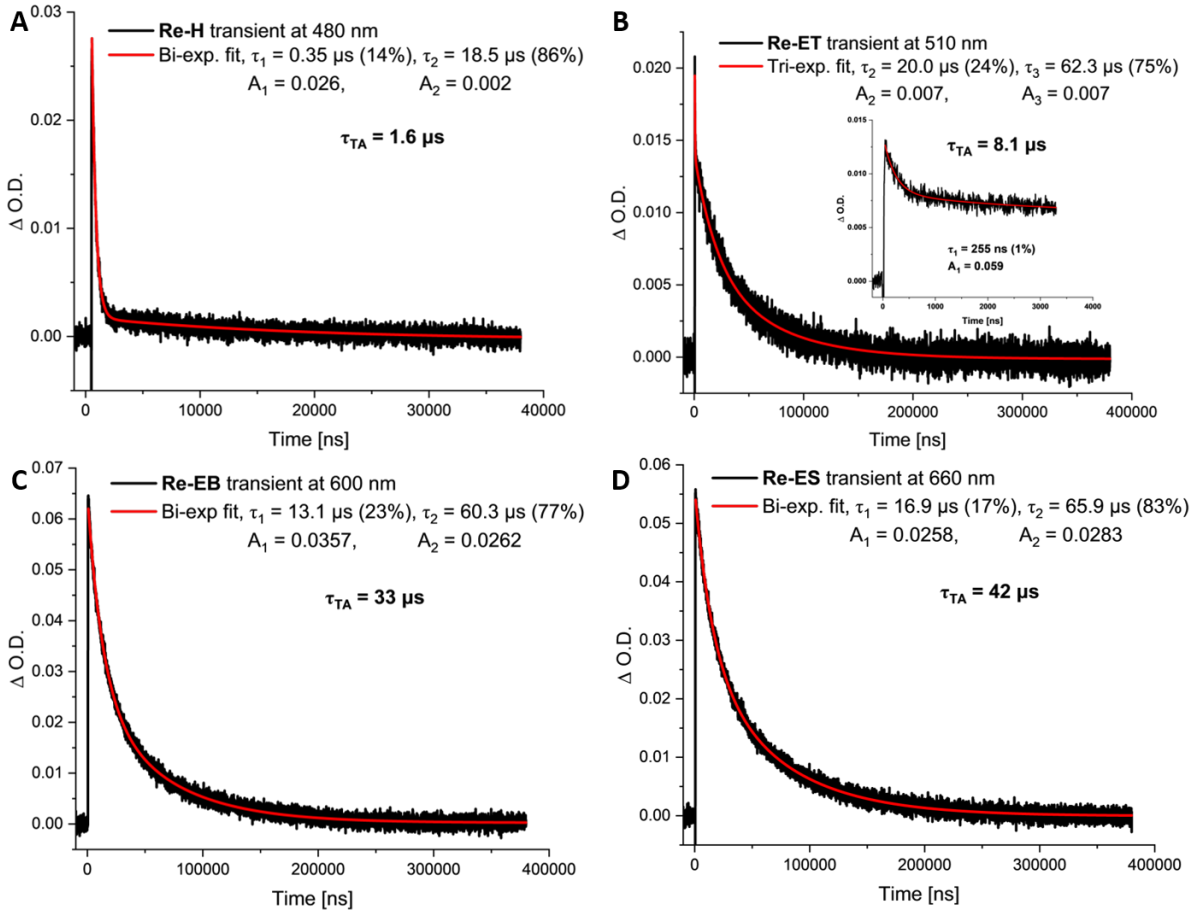


Figure S2.42. *Kinetic traces from µs–TA experiments in DCM following excitation at 355 nm of (A)* ***Re–H****, (B)* ***Re–ET****, (C)* ***Re–EB****, and (D)* ***Re–ES****.*

S2.9 DFT and TDDFT Calculations

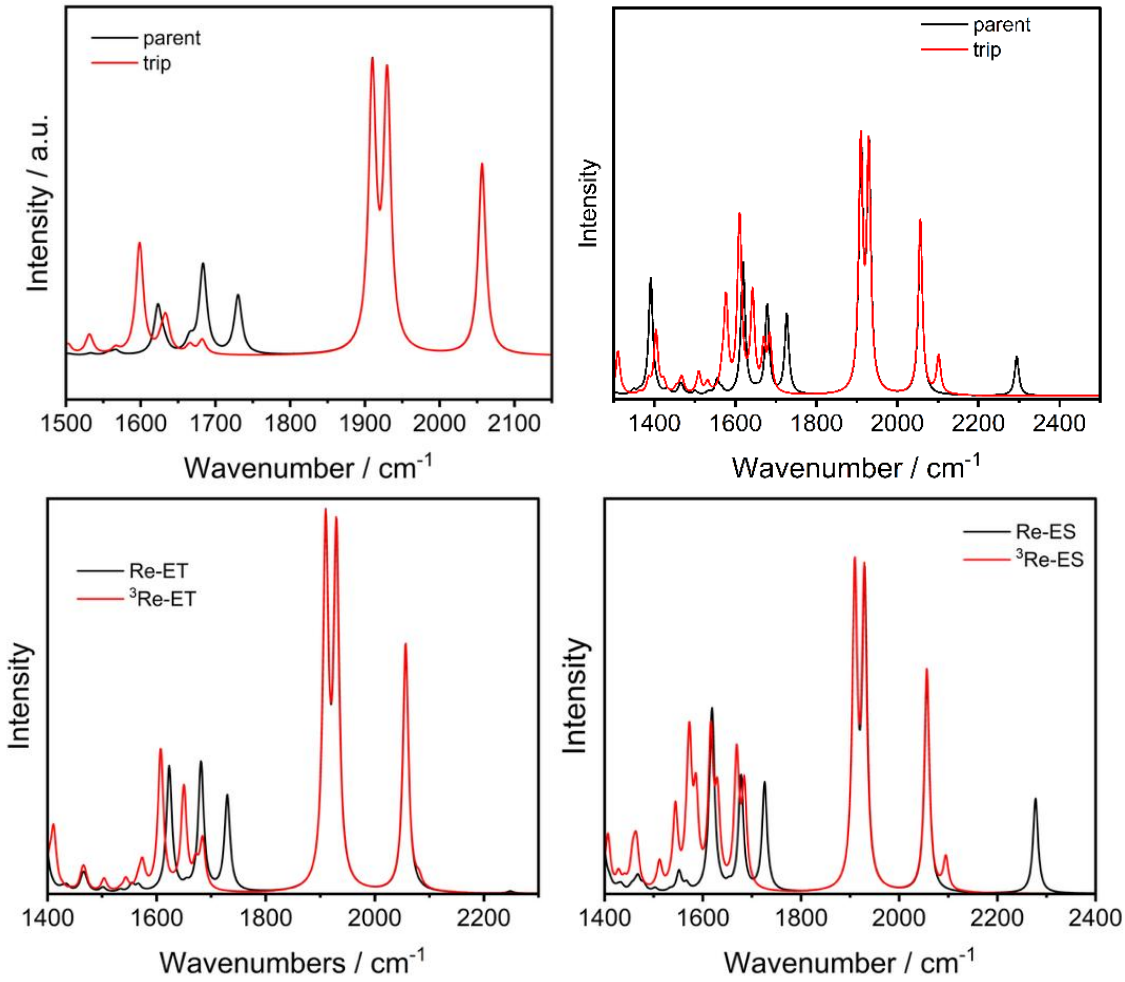


Figure S2.43. *DFT–calculated IR spectra. [Top-left]* ***Re–H*** *(black) and* ***^{3}Re–H*** *(red). [Top-right]* ***Re–EB*** *(black) and* ***^{3}Re–EB*** *(red). [Bottom-left]* ***Re–ET*** *(black) and* ***^{3}Re–ET*** *(red). [Bottom-right]* ***Re–ES*** *(black) and* ***^{3}Re–ES*** *(red).*

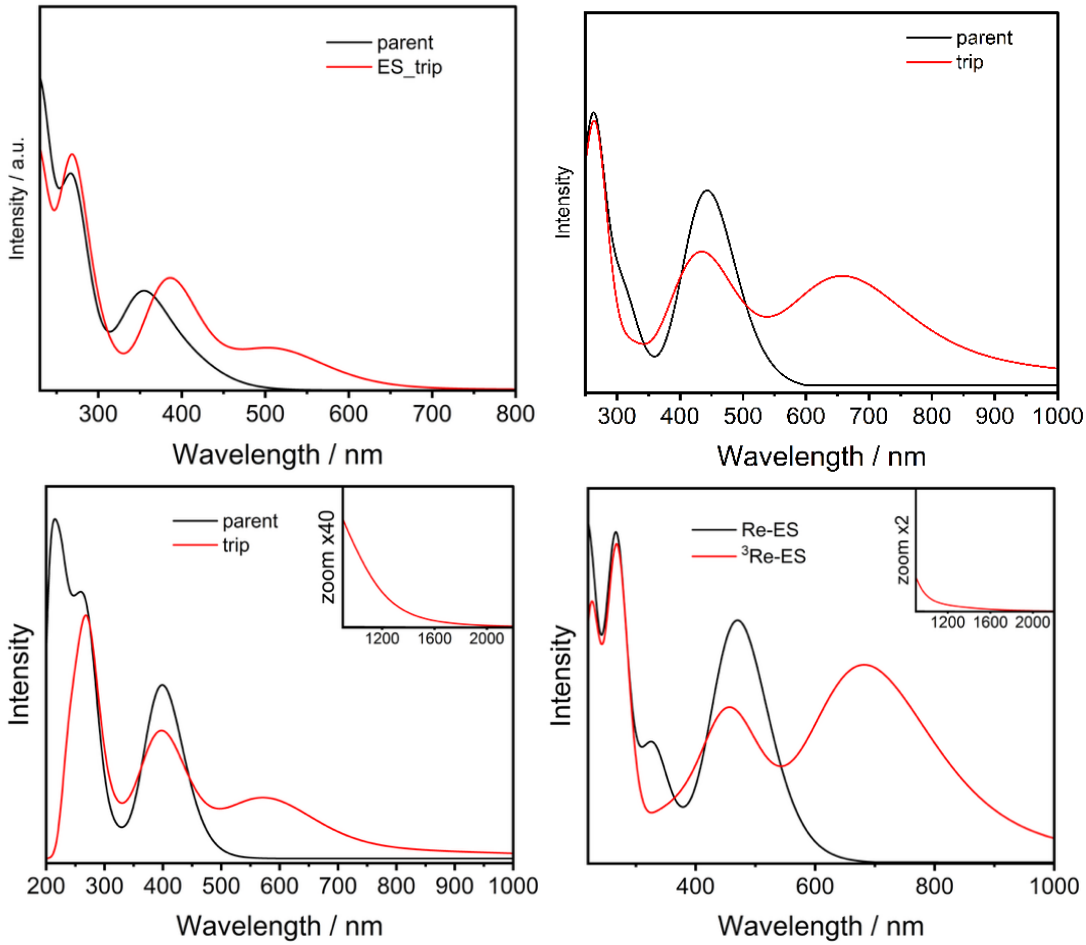


Figure S2.44. *TDDFT–calculated UV-Vis spectra. [Top-left]* ***Re–H*** *(black) and* ***^{3}Re–H*** *(red). [Top-right]* ***Re–EB*** *(black) and* ***^{3}Re–EB*** *(red). [Bottom-left]* ***Re–ET*** *(black) and* ***^{3}Re–ET*** *(red). [Bottom-right]* ***Re–ES*** *(black) and* ***^{3}Re–ES*** *(red).*

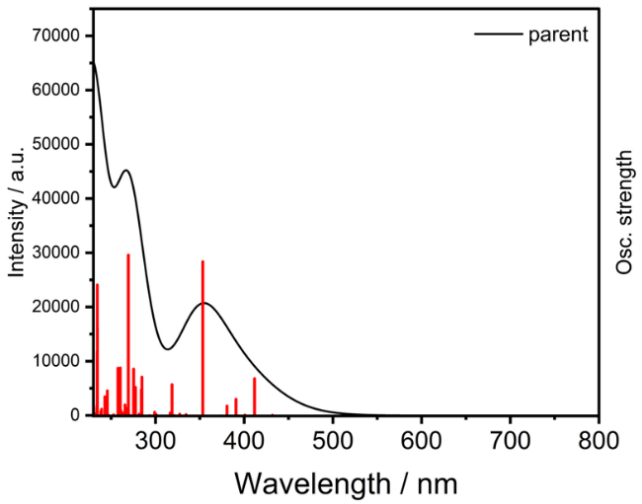


Figure S2.45. *Calculated UV-Vis spectrum of* ***Re–H****.*

Table S2.15. *Major electronic excitations in* ***Re–H*** *determined by TDDFT calculations.*

Wavelength (nm)	Osc. str (*f*)	Major contributions (%)
411.6	0.0917	HOMO–1 → LUMO+1 (68)
390.8	0.0410	HOMO → LUMO+2 (67)
353.4	0.3792	HOMO–3 → LUMO (70)
318.6	0.0769	HOMO–5 → LUMO (67) HOMO–3 → LUMO+5 (22)
284.7	0.0956	HOMO–8 → LUMO+1 (30) HOMO–7 → LUMO+1 (25) HOMO–6 → LUMO+1 (37) HOMO–4 → LUMO+2 (25) HOMO → LUMO+7 (25)
284.1	0.0644	HOMO–1 → LUMO+4 (58)
277.4	0.0704	HOMO–9 → LUMO+1 (20) HOMO–8 → LUMO+1 (42) HOMO–7 → LUMO+1 (50)
275.4	0.1151	HOMO–6 → LUMO+2 (56)
269.3	0.3950	HOMO–8 → LUMO+1 (34) HOMO–7 → LUMO+1 (21) HOMO–7 → LUMO+2 (22) HOMO–6 → LUMO+1 (29) HOMO–4 → LUMO+2 (30)
260.3	0.1181	HOMO–9 → LUMO+2 (27) HOMO–2 → LUMO+6 (42) HOMO–1 → LUMO+8 (21) HOMO–1 → LUMO+11 (25)
257.7	0.1175	HOMO–9 → LUMO+1 (25) HOMO–9 → LUMO+2 (59)
234.5	0.2167	HOMO–3 → LUMO+5 (42) HOMO → LUMO+11 (34)
234.4	0.3221	HOMO–11 → LUMO+2 (29) HOMO–3 → LUMO+5 (34) HOMO → LUMO+11 (33)
234.1	0.1576	HOMO–11 → LUMO+1 (24) HOMO–11 → LUMO+2 (54) HOMO–3 → LUMO+5 (24)
227.7	0.1538	HOMO–4 → LUMO+4 (37) HOMO–1 → LUMO+13 (23) HOMO–1 → LUMO+15 (24) HOMO–1 → LUMO+17 (22)
227.1	0.1747	HOMO–4 → LUMO+4 (47)
220.8	0.1389	HOMO–15 → LUMO+1 (33) HOMO–6 → LUMO+4 (49)
212.2	0.2286	HOMO–14 → LUMO+1 (22) HOMO–5 → LUMO+5 (24) HOMO–3 → LUMO+8 (23) HOMO–3 → LUMO+9 (41)

Wavelength (nm)	Osc. str (*f*)	Major contributions (%)
205.2	0.1368	HOMO–11 → LUMO+3 (26) HOMO–9 → LUMO+4 (25) HOMO–4 → LUMO+8 (41)

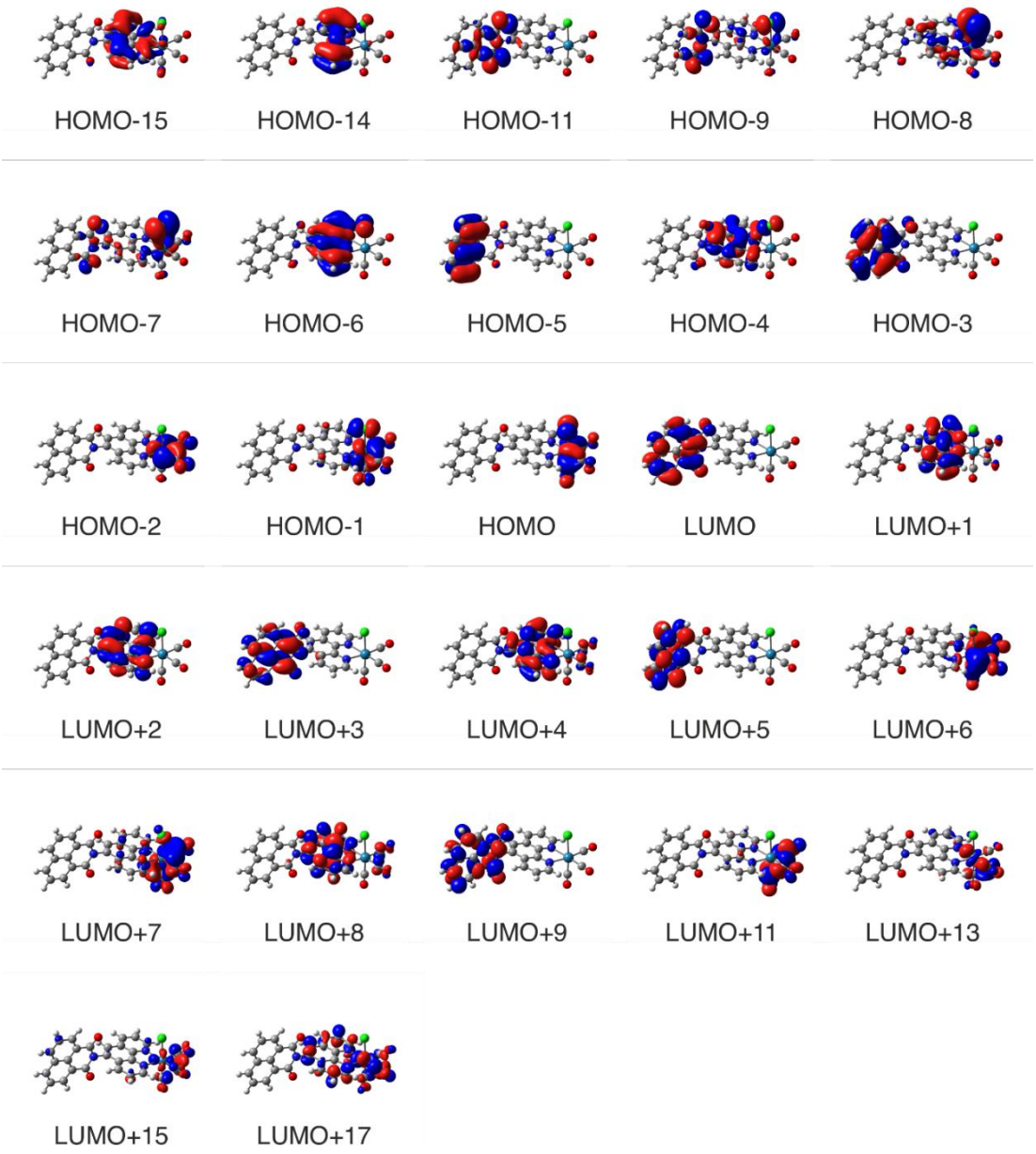


Figure S2.46. *Molecular orbitals involved in electronic transitions of* ***Re–H*** *(see* ***Table S2.1****).*

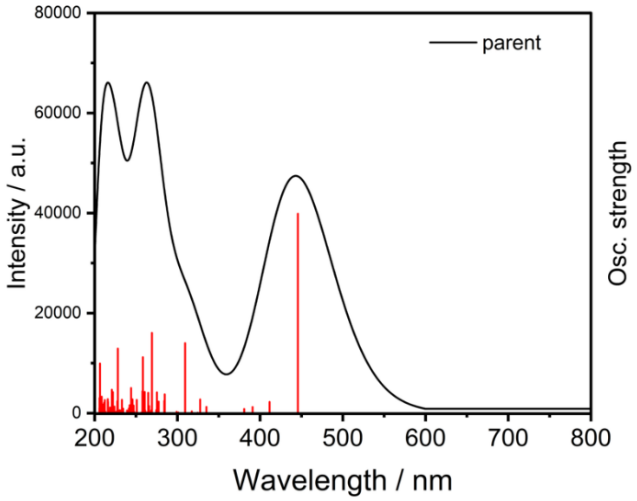


Figure S2.47. *Calculated UV-Vis spectra of* ***Re–EB****.*

Table S2.16. *Major electronic excitations in* ***Re–EB*** *determined by TDDFT calculations.*

Wavelength (nm)	Osc. str (*f*)	Major contributions (%)
445.6	0.9975	HOMO → LUMO (70)
411.5	0.0580	HOMO–2 → LUMO+1 (68)
390.9	0.0329	HOMO–1 → LUMO+2 (68)
335.0	0.0334	HOMO–5 → LUMO (58) HOMO–4 → LUMO (33)
327.6	0.0709	HOMO–7 → LUMO (65) HOMO → LUMO+5 (22)
309.4	0.3519	HOMO → LUMO+3 (68)
284.8	0.0962	HOMO–10 → LUMO+1 (30) HOMO–9 → LUMO+1 (23) HOMO–8 → LUMO+1 (39) HOMO–4 → LUMO+2 (27) HOMO–1 → LUMO+8 (23)
284.2	0.0633	HOMO–2 → LUMO+4 (60)
277.4	0.0602	HOMO–10 → LUMO+1 (37) HOMO–9 → LUMO+1 (44) HOMO–7 → LUMO+1 (30)
275.3	0.1061	HOMO–8 → LUMO+2 (54)
269.3	0.4035	HOMO–10 → LUMO+1 (34) HOMO–9 → LUMO+1 (20) HOMO–9 → LUMO+2 (23) HOMO–8 → LUMO+1 (29) HOMO–5 → LUMO+2 (26)
265.8	0.0381	HOMO–12 → LUMO+1 (33) HOMO–11 → LUMO+1 (28) HOMO–9 → LUMO+2 (45)

Wavelength (nm)	Osc. str (*f*)	Major contributions (%)
264.7	0.1042	HOMO–14 → LUMO (42) HOMO–13 → LUMO (31) HOMO → LUMO+5 (25) HOMO → LUMO+7 (30)
260.5	0.1084	HOMO–3 → LUMO+3 (32) HOMO–3 → LUMO+6 (37) HOMO–2 → 174 (22)
258.4	0.2819	HOMO–14 → LUMO (32) HOMO–13 → LUMO (32) HOMO → LUMO+5 (41)
257.8	0.1120	HOMO–12 → LUMO+2 (44) HOMO–11 → LUMO+2 (38)
250.9	0.0687	HOMO–14 → LUMO (23) HOMO–4 → LUMO+3 (36) HOMO → LUMO+7 (46)

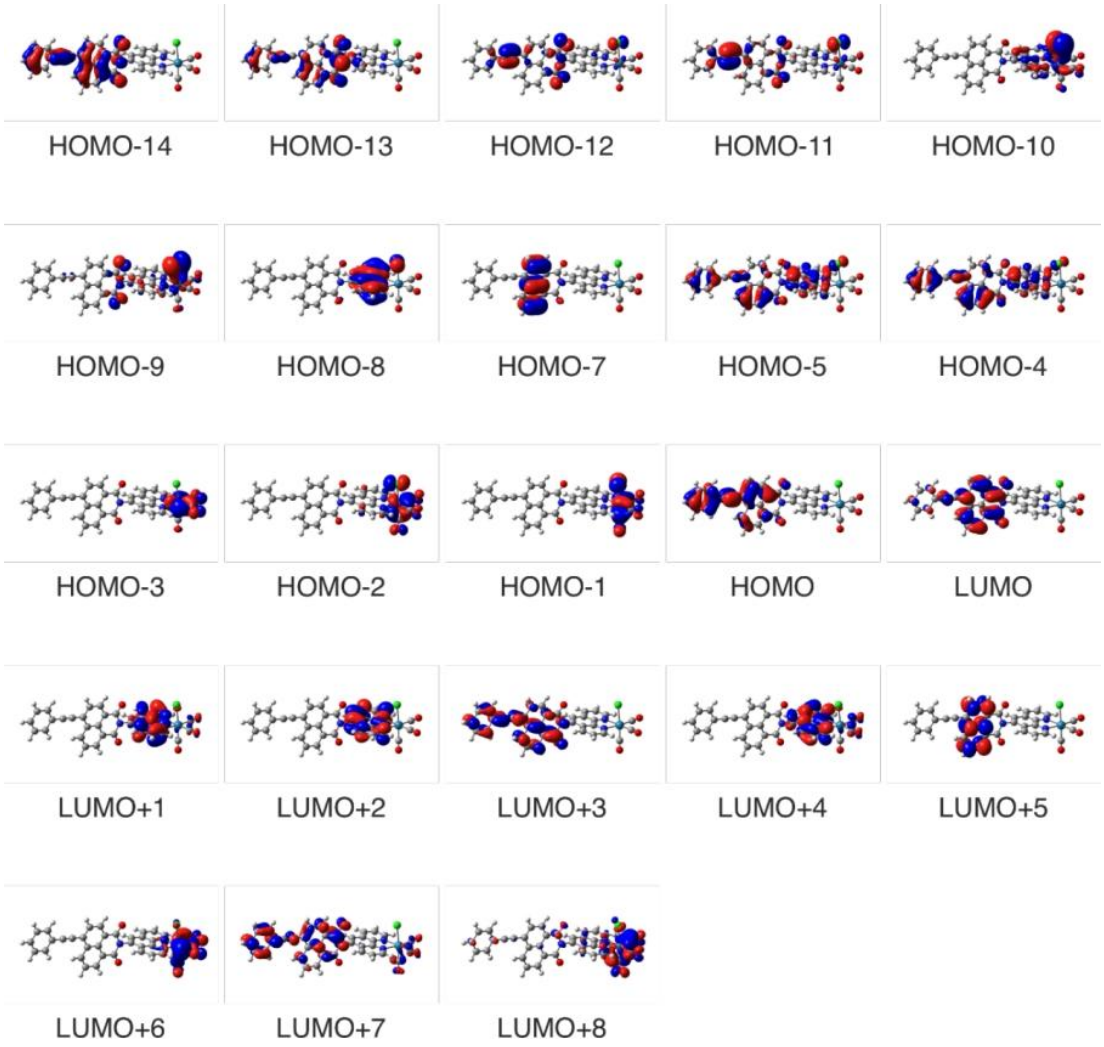


Figure S2.48. *Molecular orbitals involved in transitions of* ***Re–EB*** *(see* ***Table S2.2****).*

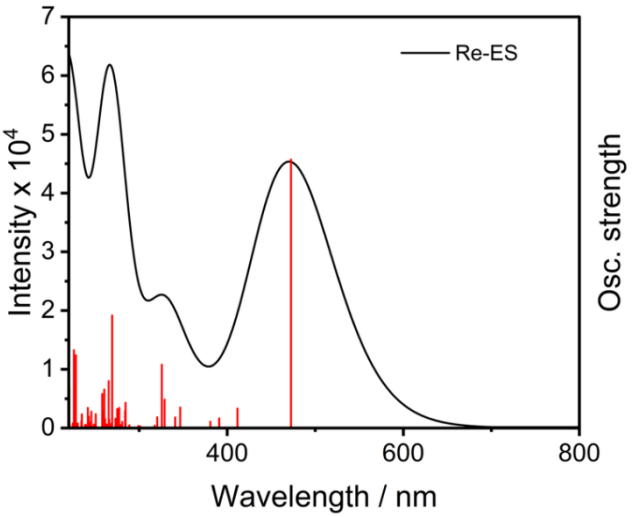


Figure S2.49. *Calculated UV-Vis spectra of* ***Re–ES****.*

Table S2.17. *Major electronic excitations in* ***Re–ES*** *determined by TDDFT calculations.*

Wavelength (nm)	Osc. str (*f*)	Major contributions (%)
472.5	0.9796	HOMO → LUMO (70)
411.6	0.0711	HOMO-2 → LUMO+1 (68)
390.9	0.0352	HOMO-1 → LUMO+2 (68)
380.8	0.0233	HOMO-2 → LUMO+2 (69)
346.5	0.0751	HOMO-4 → LUMO (65)
340.9	0.0387	HOMO-5 → LUMO (63)
328.9	0.1042	HOMO-7 → LUMO (60) HOMO → LUMO+3 (24) HOMO → LUMO+5 (21)
325.6	0.2314	HOMO-7 → LUMO (25) HOMO-6 → LUMO (21) HOMO → LUMO+3 (58)
284.5	0.0923	HOMO-10 → LUMO+1 (28) HOMO-9 → LUMO+1 (23) HOMO-8 → LUMO+1 (34) HOMO-5 → LUMO+2 (24) HOMO-2 → LUMO+4 (25) HOMO-1 → LUMO+8 (23)
284.0	0.0626	HOMO-2 → LUMO+4 (55)
277.3	0.0734	HOMO-11 → LUMO+1 (22) HOMO-10 → LUMO+1 (39) HOMO-9 → LUMO+1 (46)
275.1	0.0695	HOMO-8 → LUMO+2 (39) HOMO → LUMO+4 (51)

Wavelength (nm)	Osc. str (*f*)	Major contributions (%)
269.3	0.4109	HOMO-10 → LUMO+1 (34) HOMO-9 → LUMO+1 (20) HOMO-9 → LUMO+2 (23) HOMO-8 → LUMO+1 (29) HOMO-5 → LUMO+2 (29)
265.3	0.1713	HOMO-13 → LUMO (48) HOMO → LUMO+5 (32) HOMO → LUMO+7 (28)
260.4	0.1407	HOMO-14 → LUMO (27) HOMO-4 → LUMO+3 (44) HOMO-3 → LUMO+6 (21) HOMO → LUMO+7 (20)
258.0	0.1244	HOMO-11 → LUMO+1 (23) HOMO-11 → LUMO+2 (56)
241.7	0.0738	HOMO-6 → LUMO+3 (65)
228.1	0.2658	HOMO-5 → LUMO+4 (45) HOMO-4 → LUMO+4 (34)
227.4	0.0523	HOMO-2 → LUMO+15 (31) HOMO-2 → LUMO+19 (36) HOMO-2 → LUMO+22 (20)
225.8	0.2844	HOMO-4 → LUMO+5 (61)
220.7	0.1460	HOMO-18 → LUMO+1 (30) HOMO-8 → LUMO+4 (50)

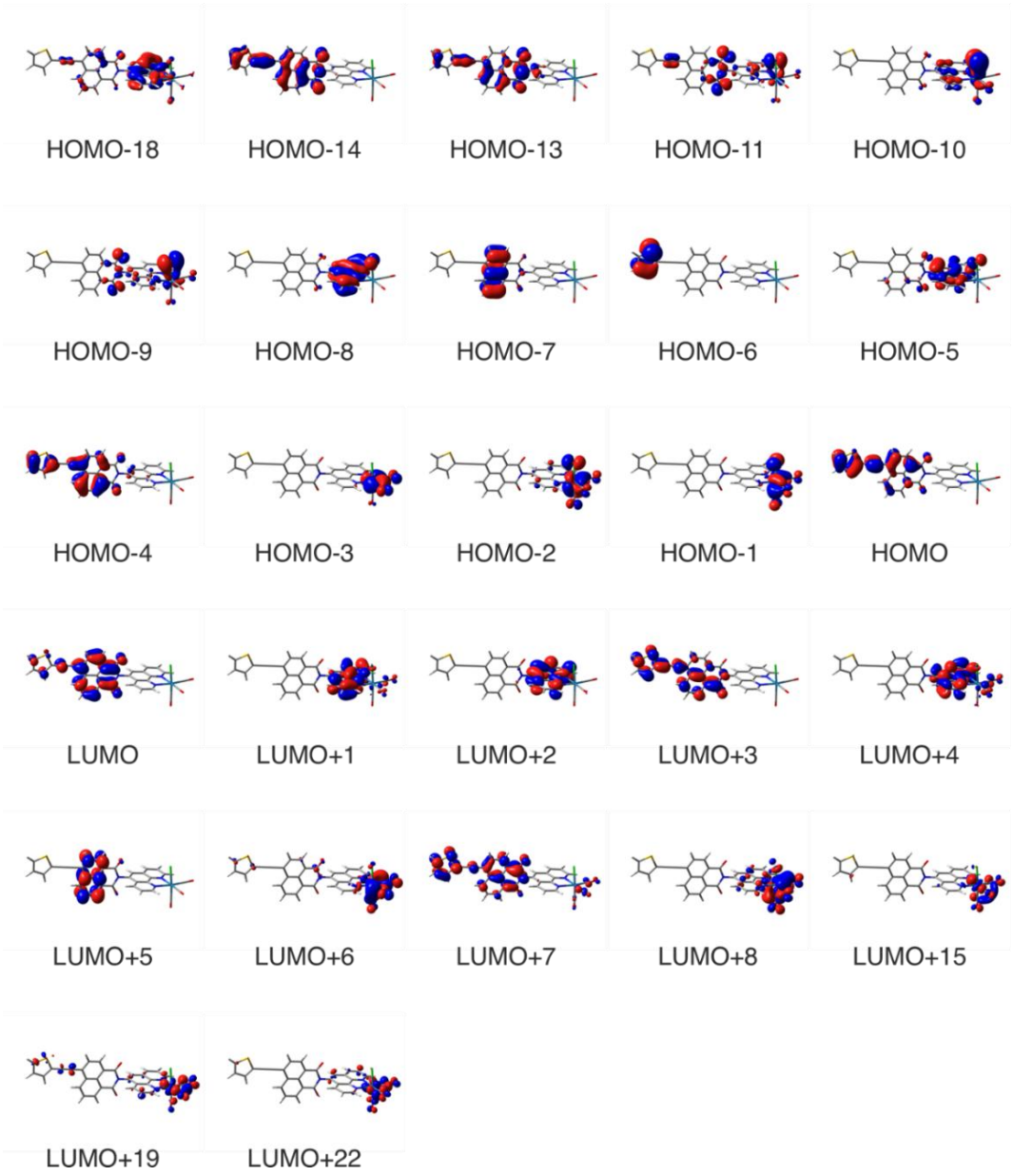


Figure S2.50. *Molecular orbitals involved in transition of* ***Re–ES*** *(see* ***Table S2.3****).*

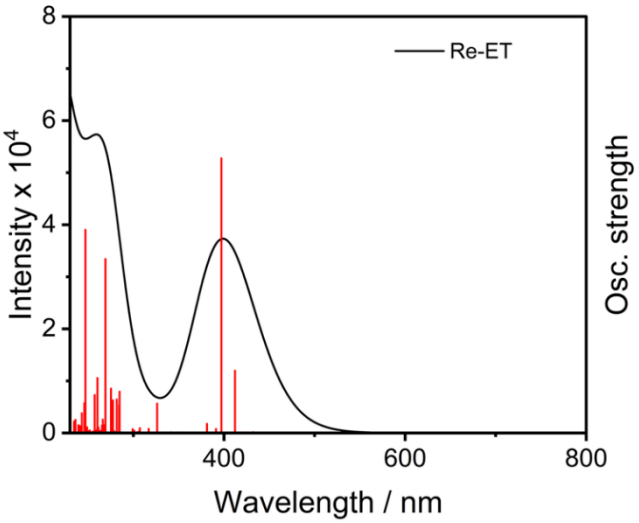


Figure S2.51. *Calculated UV-Vis spectra of* ***Re–ET****.*

Table S2.18. *Major electronic excitations in* ***Re–ET*** *determined by TDDFT calculations.*

Wavelength (nm)	Osc. str (*f*)	Major contributions (%)
412.1	0.1495	HOMO-1 → LUMO+1 (68)
397.1	0.6595	HOMO-2 → LUMO (69)
381.2	0.0221	HOMO-1 → LUMO+2 (70)
326.2	0.0707	HOMO-5 → LUMO (66) HOMO-2 → LUMO+5 (22)
284.7	0.0994	HOMO-10 → LUMO+1 (28) HOMO-9 → LUMO+1 (26) HOMO-6 → LUMO+1 (36) HOMO-4 → LUMO+2 (24) HOMO → LUMO+7 (25)
284.2	0.0665	HOMO-1 → LUMO+4 (58)
281.7	0.0805	HOMO-12 → LUMO (22) HOMO-2 → LUMO+3 (61)
277.3	0.0782	HOMO-10 → LUMO+1 (43) HOMO-9 → LUMO+1 (45)
275.3	0.1065	HOMO-6 → LUMO+2 (54)
269.2	0.4178	HOMO-10 → LUMO+1 (32) HOMO-9 → LUMO+1 (24) HOMO-6 → LUMO+1 (30) HOMO-4 → LUMO+2 (30)
260.3	0.1320	HOMO-11 → LUMO+2 (22) HOMO-3 → LUMO+6 (43) HOMO-1 → LUMO+11 (22)
257.2	0.0914	HOMO-11 → LUMO+1 (30) HOMO-11 → LUMO+2 (55)
247.1	0.4879	HOMO-12 → LUMO (32) HOMO-2 → LUMO+5 (55)

Wavelength (nm)	Osc. str (*f*)	Major contributions (%)
228.2	0.3978	HOMO-4 → LUMO+4 (48) HOMO-2 → LUMO+7 (33)
228.1	0.1305	HOMO-4 → LUMO+4 (23) HOMO-2 → LUMO+7 (62)
223.4	0.1983	HOMO-8 → LUMO+3 (53) HOMO-6 → LUMO+3 (28)
220.7	0.1182	HOMO-19 → LUMO+1 (28) HOMO-6 → LUMO+4 (48)
210.1	0.1272	HOMO-23 → LUMO (30) HOMO-8 → LUMO+5 (43) HOMO-5 → LUMO+5 (31)

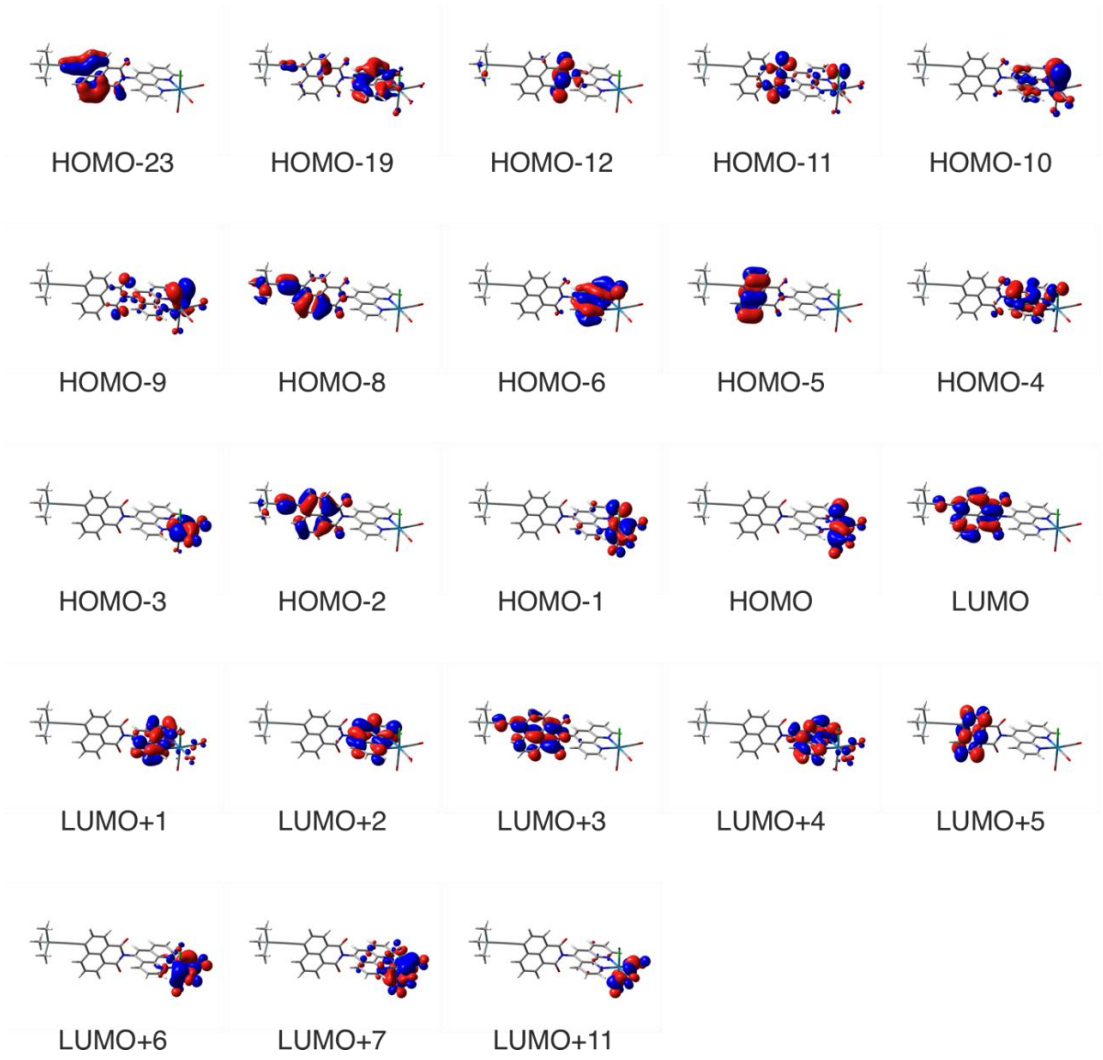


Figure S2.52. *Molecular orbitals involved in transition of* ***Re–ET*** *(see* ***Table S2.4****).*

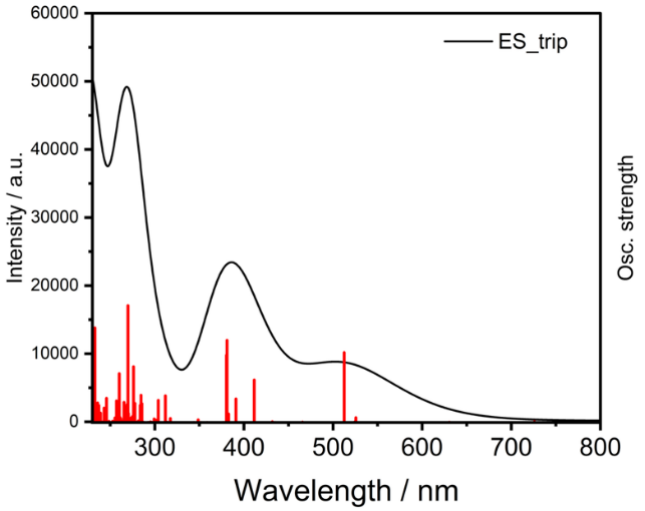


Figure S2.53. *Calculated UV-Vis spectrum of* ***^{3}Re–H****.*

Table S2.19. *Major electronic excitations in* ***^{3}Re–H*** *determined by TDDFT calculations.*

Wavelength (nm)	Osc. str (*f*)	Major contributions (%)
512.5	0.1709	α–HOSO → α–LUSO+2 (61) α–HOSO → α–LUSO+4 (40) β–HOSO–9 → β–LUSO (62)
411.6	0.1038	α–HOSO–2 → α–LUSO (68) β–HOSO–1 → β–LUSO+1 (68)
391.0	0.0578	α–HOSO–1 → α–LUSO+1 (68) β–HOSO → β–LUSO+3 (67)
381.0	0.2010	α–HOSO–2 → α–LUSO+1 (52) α–HOSO → α–LUSO+7 (50) β–HOSO–13 → β–LUSO (37) β–HOSO–1 → β–LUSO+3 (48)
380.4	0.1645	α–HOSO–2 → α–LUSO+1 (47) α–HOSO → α–LUSO+7 (54) β–HOSO–13 → β–LUSO (40) β–HOSO–1 → β–LUSO+3 (48)
276.2	0.1363	α–HOSO–6 → α–LUSO+1 (51) β–HOSO–8 → β–LUSO+1 (34) β–HOSO–5 → β–LUSO+3 (48)
270.0	0.2855	α–HOSO–9 → α–LUSO (34) α–HOSO–6 → α–LUSO (22) β–HOSO–8 → β–LUSO+1 (24) β–HOSO–7 → β–LUSO+1 (31) β–HOSO–6 → β–LUSO+1 (33) β–HOSO–6 → β–LUSO+3 (27) β–HOSO–5 → β–LUSO+1 (27) β–HOSO–3 → β–LUSO+3 (25)

Wavelength (nm)	Osc. str (*f*)	Major contributions (%)
260.1	0.1194	α–HOSO–10 → α–LUSO+1 (22) α–HOSO–9 → α–LUSO+1 (23) α–HOSO–3 → α–LUSO+5 (35) β–HOSO–10 → β–LUSO+1 (33) β–HOSO–10 → β–LUSO+3 (21) β–HOSO–7 → β–LUSO+3 (25) β–HOSO–2 → β–LUSO+6 (35) β–HOSO–1 → β–LUSO+9 (25) β–HOSO–1 → β–LUSO+11 (25)
232.8	0.2312	α–HOSO–5 → α–LUSO+4 (54) α–HOSO–4 → α–LUSO+4 (47) α–HOSO → α–LUSO+25 (34) α–HOSO → α–LUSO+26 (30) α–HOSO → α–LUSO+27 (34)
227.9	0.2026	α–HOSO–4 → α–LUSO+3 (44) β–HOSO–3 → β–LUSO+4 (47)
227.3	0.1017	α–HOSO–4 → α–LUSO+3 (33) α–HOSO–2 → α–LUSO+12 (21) α–HOSO–2 → α–LUSO+14 (23) α–HOSO–2 → α–LUSO+16 (20) β–HOSO–3 → β–LUSO+4 (36) β–HOSO–1 → β–LUSO+14 (21) β–HOSO–1 → β–LUSO+16 (23) β–HOSO–1 → β–LUSO+18 (21)
220.8	0.1470	α–HOSO–16 → α–LUSO (31) α–HOSO–6 → α–LUSO+3 (44) β–HOSO–15 → β–LUSO+1 (27) β–HOSO–5 → β–LUSO+4 (45)

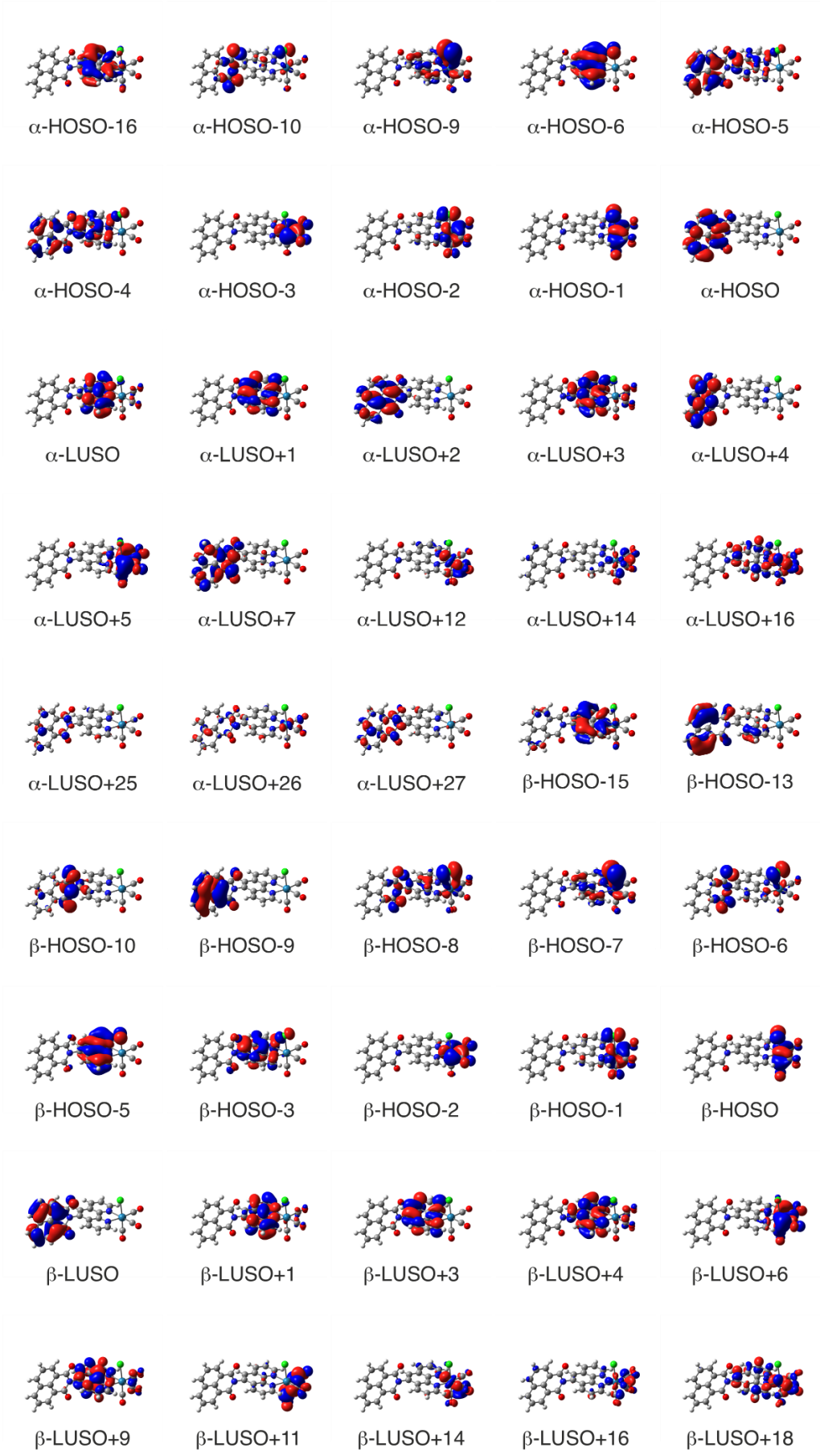


Figure S2.54. *Molecular orbitals involved in transition of* ***^{3}Re–H*** *(see* ***Table S2.5****).*

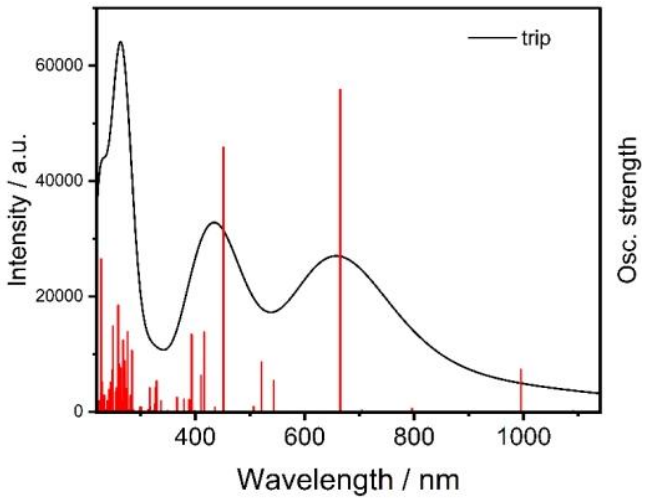


Figure S2.55. *Calculated UV-Vis spectrum of* ***^{3}Re–EB****.*

Table S2.20. *Major electronic excitations in* ***^{3}Re–EB*** *determined by TDDFT calculations.*

Wavelength (nm)	Osc. str (*f*)	Major contributions (%)
995.1	0.0741	α–HOSO → α–LUSO+2 (49) β–HOSO–3 → β–LUSO (85)
664.8	0.5587	α–HOSO → α–LUSO+2 (81) α–HOSO → α–LUSO+4 (22) β–HOSO–3 → β–LUSO (47)
543.1	0.0544	α–HOSO → α–LUSO+2 (27) α–HOSO → α–LUSO+4 (47) β–HOSO–13 → β–LUSO (78)
521.4	0.0868	α–HOSO → α–LUSO+4 (23) α–HOSO → α–LUSO+5 (21) α–HOSO → α–LUSO+6 (32) β–HOSO–13 → β–LUSO (24) β–HOSO–12 → β–LUSO (82)
451.6	0.4589	α–HOSO → α–LUSO+4 (68) α–HOSO → α–LUSO+9 (26) β–HOSO–16 → β–LUSO (31) β–HOSO–13 → β–LUSO (43) β–HOSO–12 → β–LUSO (28)
416.3	0.1387	α–HOSO → α–LUSO+4 (31) α–HOSO → α–LUSO+9 (49) α–HOSO → α–LUSO+10 (24) β–HOSO–16 → β–LUSO (53) β–HOSO–13 → β–LUSO (22) β–HOSO–3 → β–LUSO+1 (34)
410.7	0.0639	α–HOSO–2 → α–LUSO (68) β–HOSO–1 → β–LUSO+2 (68)
393.3	0.1351	α–HOSO–1 → α–LUSO+1 (23) β–HOSO–16 → β–LUSO (48) β–HOSO–3 → β–LUSO+1 (56) β–HOSO → β–LUSO+1 (46)

Wavelength (nm)	Osc. str (*f*)	Major contributions (%)
329.5	0.0543	α–HOSO–3 → α–LUSO+1 (27) α–HOSO–3 → α–LUSO+2 (50) β–HOSO–20 → β–LUSO (39) β–HOSO–18 → β–LUSO (28) β–HOSO–17 → β–LUSO (31) β–HOSO–6 → β–LUSO+1 (41) β–HOSO–3 → β–LUSO+1 (25)
327.7	0.0428	α–HOSO–3 → α–LUSO+2 (21) β–HOSO–17 → β–LUSO (32) β–HOSO–6 → β–LUSO+1 (75) β–HOSO–3 → β–LUSO+4 (20)
317.1	0.0422	α–HOSO–6 → α–LUSO+2 (21) α–HOSO–3 → α–LUSO+2 (46) β–HOSO–20 → β–LUSO (54) β–HOSO–3 → β–LUSO+1 (26) β–HOSO–3 → β–LUSO+4 (27)
284.5	0.1070	α–HOSO–11 → α–LUSO (25) α–HOSO–10 → α–LUSO (25) α–HOSO–7 → α–LUSO (35) α–HOSO–5 → α–LUSO+1 (24) α–HOSO–2 → α–LUSO+3 (25) α–HOSO–1 → α–LUSO+3 (20) α–HOSO–1 → α–LUSO+7 (25) β–HOSO–9 → β–LUSO+2 (37) β–HOSO–7 → β–LUSO+2 (37) β–HOSO–4 → β–LUSO+3 (25) β–HOSO → β–LUSO+8 (21)
283.9	0.0635	α–HOSO–2 → α–LUSO+3 (56) β–HOSO–1 → β–LUSO+5 (55)
276.6	0.1392	α–HOSO–12 → α–LUSO (23) α–HOSO–11 → α–LUSO (25) α–HOSO–10 → α–LUSO (28) α–HOSO–7 → α–LUSO+1 (33) β–HOSO–10 → β–LUSO+2 (54) β–HOSO–8 → β–LUSO+3 (21) β–HOSO–7 → β–LUSO+3 (36)
274.8	0.0410	α–HOSO–12 → α–LUSO (36) α–HOSO–10 → α–LUSO (21) α–HOSO–10 → α–LUSO+1 (30) α–HOSO–7 → α–LUSO+1 (28) β–HOSO–10 → β–LUSO+2 (29) β–HOSO–8 → β–LUSO+3 (46) β–HOSO–7 → β–LUSO+3 (29)
271.8	0.0724	α–HOSO–10 → α–LUSO (21) β–HOSO–10 → β–LUSO+2 (29) β–HOSO–9 → β–LUSO+2 (25) β–HOSO–8 → β–LUSO+2 (43) β–HOSO–8 → β–LUSO+3 (45) β–HOSO–6 → β–LUSO+3 (23)

Wavelength (nm)	Osc. str (*f*)	Major contributions (%)
271.0	0.0890	α–HOSO–11 → α–LUSO (25) α–HOSO–10 → α–LUSO (25) α–HOSO–10 → α–LUSO+1 (48) β–HOSO–10 → β–LUSO+3 (30) β–HOSO–8 → β–LUSO+3 (22) β–HOSO–6 → β–LUSO+3 (22) β–HOSO–4 → β–LUSO+3 (25)
268.5	0.1245	α–HOSO–12 → α–LUSO (28) α–HOSO–10 → α–LUSO (25) α–HOSO–5 → α–LUSO+1 (22) α–HOSO–5 → α–LUSO+2 (24) β–HOSO–10 → β–LUSO+3 (20) β–HOSO–9 → β–LUSO+2 (23) β–HOSO–8 → β–LUSO+3 (31) β–HOSO–7 → β–LUSO+5 (28)
264.3	0.0766	α–HOSO–12 → α–LUSO (34) α–HOSO–10 → α–LUSO+1 (39) α–HOSO–7 → α–LUSO+3 (22) β–HOSO–9 → β–LUSO+1 (22) β–HOSO–8 → β–LUSO+3 (32) β–HOSO–2 → β–LUSO+6 (22)
261.5	0.0823	α–HOSO–3 → α–LUSO+4 (55) α–HOSO–3 → α–LUSO+5 (25) α–HOSO–3 → α–LUSO+6 (35) α–HOSO → α–LUSO+24 (23) β–HOSO–27 → β–LUSO (21) β–HOSO–13 → β–LUSO+4 (20) β–HOSO–3 → β–LUSO+10 (20)
260.2	0.0543	α–HOSO–12 → α–LUSO+1 (46) α–HOSO–4 → α–LUSO+5 (28) β–HOSO–12 → β–LUSO+2 (24) β–HOSO–10 → β–LUSO+3 (35) β–HOSO–2 → β–LUSO+6 (32)
259.4	0.1852	α–HOSO–12 → α–LUSO+1 (47) α–HOSO–11 → α–LUSO+1 (36) α–HOSO–4 → α–LUSO+5 (21) β–HOSO–10 → β–LUSO+3 (22) β–HOSO–9 → β–LUSO+3 (40) β–HOSO–2 → β–LUSO+6 (23)
256.6	0.0425	α–HOSO–12 → α–LUSO+2 (36) α–HOSO–10 → α–LUSO+2 (42) α–HOSO–6 → α–LUSO+2 (20) α–HOSO–5 → α–LUSO+2 (42) α–HOSO → α–LUSO+29 (25) β–HOSO–3 → β–LUSO+4 (24)

Wavelength (nm)	Osc. str (*f*)	Major contributions (%)
249.6	0.1494	α–HOSO–6 → α–LUSO+2 (44) α–HOSO → α–LUSO+29 (32) β–HOSO–31 → β–LUSO (21) β–HOSO–28 → β–LUSO (20) β–HOSO–27 → β–LUSO (29) β–HOSO–13 → β–LUSO+1 (26) β–HOSO–6 → β–LUSO+7 (26) β–HOSO–3 → β–LUSO+4 (28)
248.2	0.0734	α–HOSO–14 → α–LUSO+2 (24) α–HOSO–6 → α–LUSO+2 (23) α–HOSO–3 → α–LUSO+3 (28) α–HOSO → α–LUSO+28 (26) α–HOSO → α–LUSO+30 (24) β–HOSO–29 → β–LUSO (25) β–HOSO–16 → β–LUSO+1 (23) β–HOSO–3 → β–LUSO+4 (21) β–HOSO–3 → β–LUSO+7 (21)
245.2	0.0526	α–HOSO–1 → α–LUSO+9 (38) α–HOSO–1 → α–LUSO+10 (54) β–HOSO → β–LUSO+11 (68)
230.4	0.0515	α–HOSO–3 → α–LUSO+9 (24) α–HOSO → α–LUSO+33 (56) β–HOSO–16 → β–LUSO+1 (33) β–HOSO–3 → β–LUSO+10 (21) β–HOSO–1 → β–LUSO+10 (27)
228.2	0.2655	α–HOSO–5 → α–LUSO+3 (49) β–HOSO–4 → β–LUSO+5 (51)
220.6	0.1451	α–HOSO–19 → α–LUSO (34) α–HOSO–7 → α–LUSO+3 (49) β–HOSO–18 → β–LUSO+2 (33) β–HOSO–7 → β–LUSO+5 (50)
218.5	0.0516	α–HOSO–17 → α–LUSO (26) α–HOSO–6 → α–LUSO+4 (40) α–HOSO–6 → α–LUSO+6 (23) α–HOSO–5 → α–LUSO+4 (28) α–HOSO → α–LUSO+43 (25) β–HOSO–3 → β–LUSO+7 (34)
216.8	0.0530	α–HOSO–5 → α–LUSO+7 (65) β–HOSO–4 → β–LUSO+8 (59)

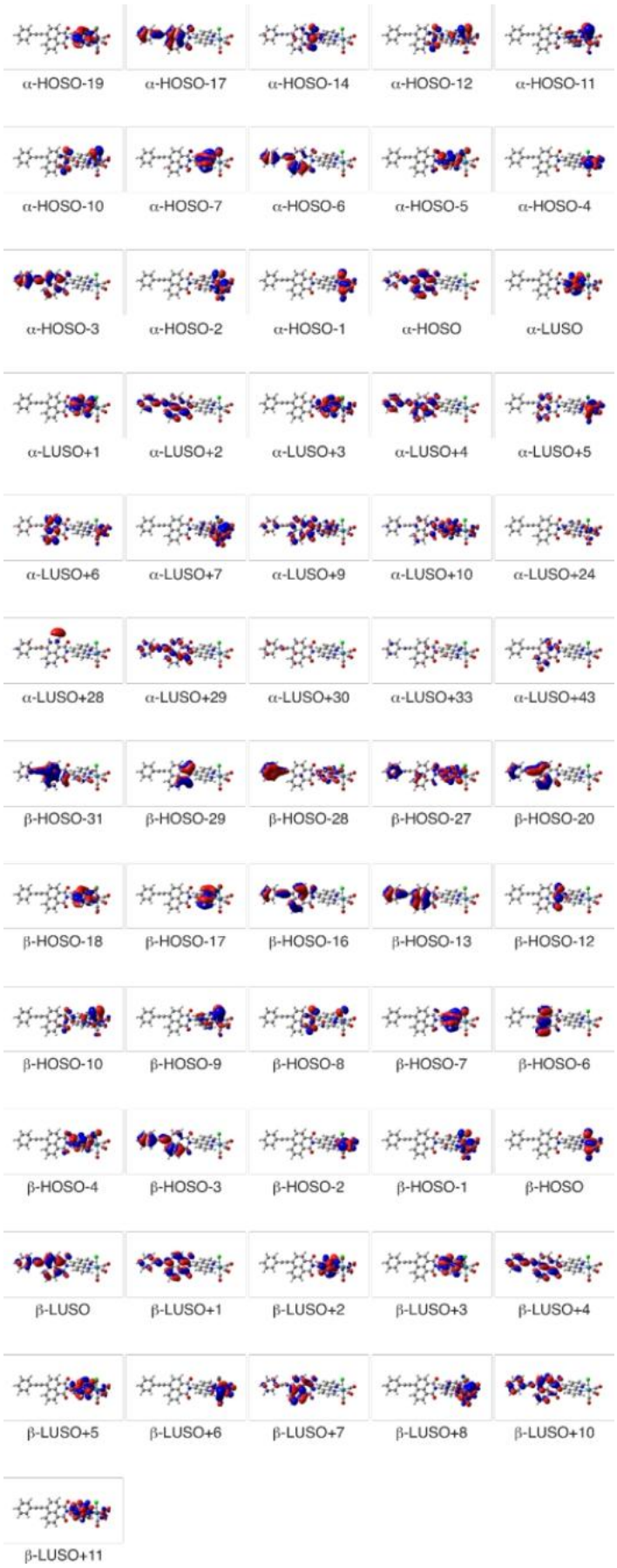


Figure S2.56. *Molecular orbitals involved in transitions of* ^{3}***Re–EB*** *(see* ***Table S2.6****).*

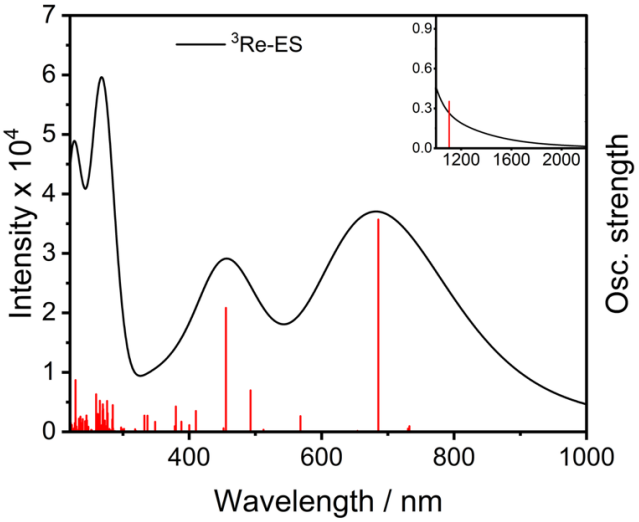


Figure S2.57. *Calculated UV-Vis spectra of* ***^{3}Re–ES****.*

Table S2.21. *Major electronic excitations in* ***^{3}Re–ES*** *determined by TDDFT calculations.*

Wavelength (nm)	Osc. str (*f*)	Major contributions (%)
1105.3	0.0353	α-HOSO → α-LUSO+2 (58) β-HOSO-3 → β-LUSO (80)
732.6	0.0205	β-HOSO-5 → β-LUSO (81) β-HOSO-2 → β-LUSO (52)
685.6	0.7647	α-HOSO → α-LUSO+2 (77) α-HOSO → α-LUSO+3 (23) β-HOSO-3 → β-LUSO (54)
568.0	0.0565	α-HOSO → α-LUSO+3 (67) β-HOSO-12 → β-LUSO (60) β-HOSO-11 → β-LUSO (29)
492.7	0.1493	α-HOSO → α-LUSO+6 (25) β-HOSO-12 → β-LUSO (20) β-HOSO-11 → β-LUSO (87)
455.4	0.4467	α-HOSO → α-LUSO+3 (61) β-HOSO-12 → β-LUSO (71)
410.1	0.0753	α-HOSO-2 → α-LUSO (68) β-HOSO-1 → β-LUSO+2 (68)
400.2	0.0243	α-HOSO-3 → α-LUSO+2 (22) α-HOSO → α-LUSO+8 (28) β-HOSO-16 → β-LUSO (52) β-HOSO-3 → β-LUSO+1 (64)
388.2	0.0364	α-HOSO-1 → α-LUSO+1 (64) β-HOSO → β-LUSO+1 (20) β-HOSO → β-LUSO+3 (69)
379.9	0.0914	α-HOSO-3 → α-LUSO+2 (53) α-HOSO → α-LUSO+8 (53) β-HOSO-16 → β-LUSO (44) β-HOSO-3 → β-LUSO+4 (21)

Wavelength (nm)	Osc. str (*f*)	Major contributions (%)
378.3	0.0205	α-HOSO-2 → α-LUSO+1 (71) β-HOSO-1 → β-LUSO+3 (66)
348.6	0.0362	α-HOSO-6 → α-LUSO+2 (34) α-HOSO-3 → α-LUSO+2 (31) α-HOSO → α-LUSO+8 (24) α-HOSO → α-LUSO+10 (23) β-HOSO-20 → β-LUSO (20) β-HOSO-16 → β-LUSO (54) β-HOSO-3 → β-LUSO+4 (35)
337.1	0.0583	α-HOSO-6 → α-LUSO+2 (25) α-HOSO-3 → α-LUSO+2 (58) α-HOSO-3 → α-LUSO+3 (26) α-HOSO → α-LUSO+18 (22) β-HOSO-20 → β-LUSO (25) β-HOSO-12 → β-LUSO+1 (22) β-HOSO-5 → β-LUSO+1 (25) β-HOSO-3 → β-LUSO+1 (37) β-HOSO-3 → β-LUSO+4 (26)
332.3	0.0584	α-HOSO-3 → α-LUSO+2 (20) β-HOSO-5 → β-LUSO+1 (91)
284.5	0.0963	α-HOSO-11 → α-LUSO (30) α-HOSO-7 → α-LUSO (31) α-HOSO-6 → α-LUSO (22) α-HOSO-5 → α-LUSO+1 (21) α-HOSO-1 → α-LUSO+7 (21) α-HOSO → α-LUSO+15 (20) β-HOSO-9 → β-LUSO+2 (25) β-HOSO-8 → β-LUSO+2 (20) β-HOSO-6 → β-LUSO+2 (31) β-HOSO-4 → β-LUSO+3 (21) β-HOSO-1 → β-LUSO+4 (21) β-HOSO-1 → β-LUSO+5 (22)
276.8	0.0670	α-HOSO-11 → α-LUSO (29) α-HOSO-10 → α-LUSO (46) β-HOSO-10 → β-LUSO+2 (62) β-HOSO-8 → β-LUSO+3 (36)
275.9	0.1112	α-HOSO-12 → α-LUSO (48) α-HOSO-10 → α-LUSO+1 (26) α-HOSO-7 → α-LUSO+1 (39) β-HOSO-8 → β-LUSO+3 (21) β-HOSO-6 → β-LUSO+3 (39)
270.2	0.0819	α-HOSO-3 → α-LUSO+3 (56) α-HOSO-3 → α-LUSO+6 (48) β-HOSO-12 → β-LUSO+1 (29) β-HOSO-3 → β-LUSO+4 (23)

Wavelength (nm)	Osc. str (*f*)	Major contributions (%)
269.6	0.0992	α-HOSO-12 → α-LUSO (48) α-HOSO-10 → α-LUSO (39) α-HOSO-7 → α-LUSO+1 (29) β-HOSO-10 → β-LUSO+2 (29) β-HOSO-8 → β-LUSO+3 (26) β-HOSO-6 → β-LUSO+3 (27)
269.2	0.0765	α-HOSO-12 → α-LUSO+1 (31) α-HOSO-10 → α-LUSO+1 (29) α-HOSO-7 → α-LUSO+4 (23) α-HOSO-5 → α-LUSO+1 (21) β-HOSO-10 → β-LUSO+3 (31) β-HOSO-9 → β-LUSO+2 (23) β-HOSO-6 → β-LUSO+5 (31)
265.1	0.1121	α-HOSO-12 → α-LUSO (23) α-HOSO-10 → α-LUSO+1 (30) α-HOSO-1 → α-LUSO+12 (28) β-HOSO-8 → β-LUSO+3 (23) β-HOSO → β-LUSO+13 (31)
259.5	0.1356	α-HOSO-12 → α-LUSO+1 (23) α-HOSO-11 → α-LUSO+1 (46) α-HOSO-4 → α-LUSO+5 (25) β-HOSO-9 → β-LUSO+3 (49) β-HOSO-2 → β-LUSO+6 (25)
228.3	0.1864	α-HOSO-12 → α-LUSO+2 (22) α-HOSO-6 → α-LUSO+3 (24) α-HOSO-5 → α-LUSO+4 (44) α-HOSO-2 → α-LUSO+8 (25) β-HOSO-4 → β-LUSO+5 (46)
220.6	0.1379	α-HOSO-19 → α-LUSO (34) α-HOSO-7 → α-LUSO+4 (49) β-HOSO-18 → β-LUSO+2 (33) β-HOSO-6 → β-LUSO+5 (50)

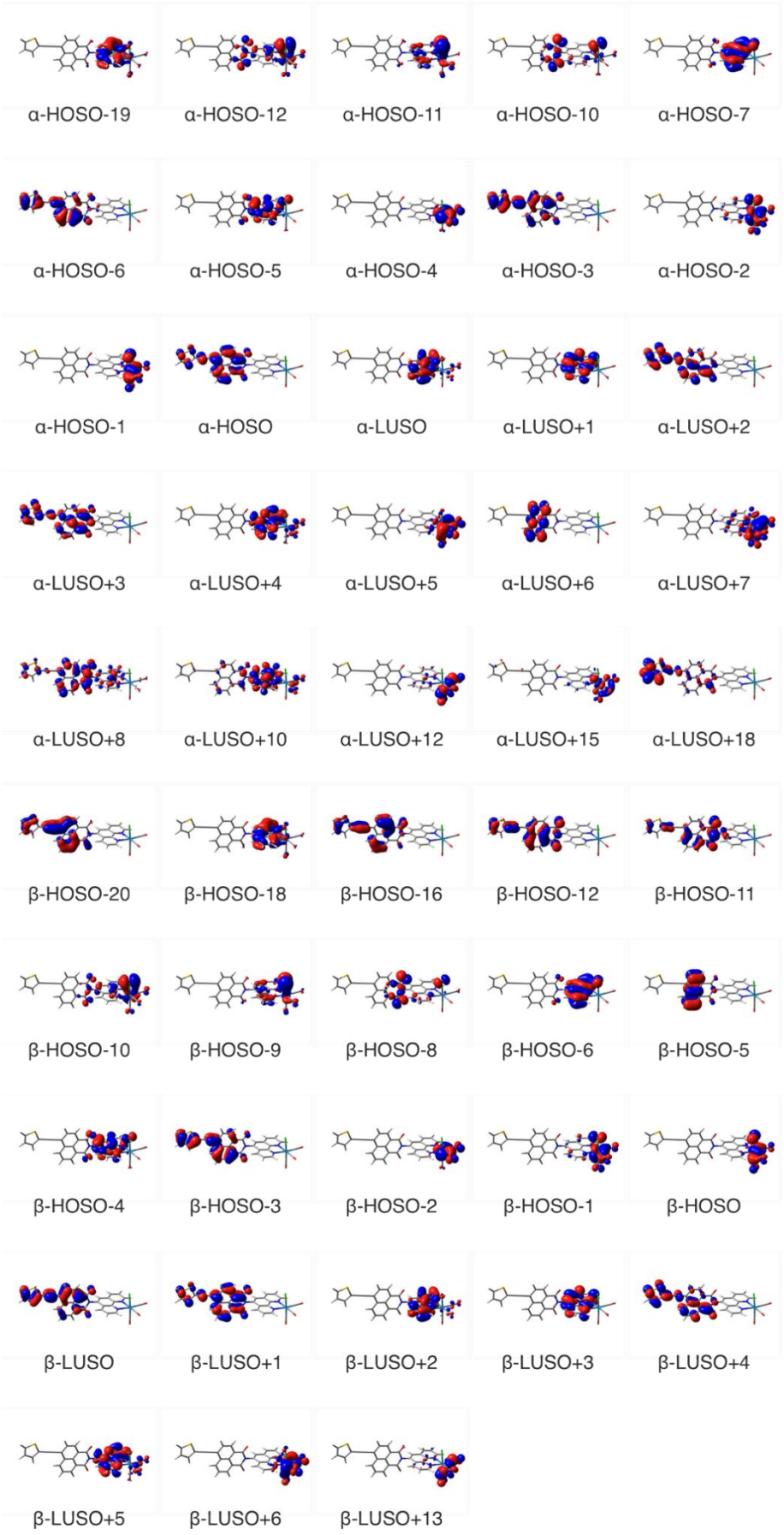


Figure S2.58. *Molecular orbitals involved in transition of* ***^{3}Re–ES*** *(see* ***Table S2.7****).*

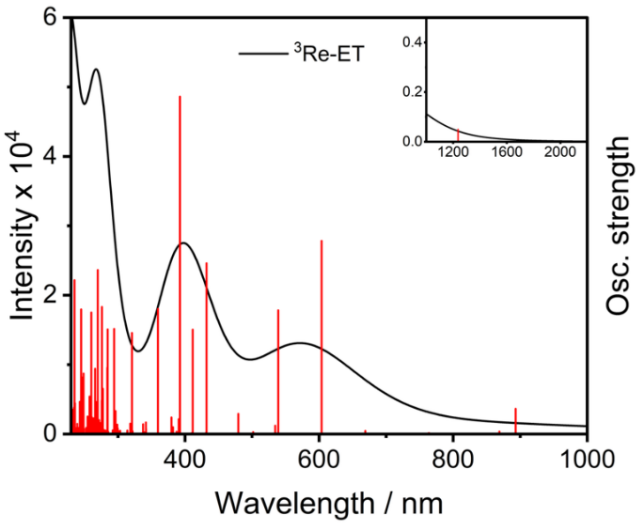


Figure S2.59. *Calculated UV-Vis spectra of* ***^{3}Re–ET****.*

Table S2.22. *Major electronic excitations in* ***^{3}Re–ET*** *determined by TDDFT calculations.*

Wavelength (nm)	Osc. str (*f*)	Major contributions (%)
893.1	0.0242	α-HOSO → α-LUSO+2 (54) β-HOSO-4 → β-LUSO (79)
603.7	0.1855	α-HOSO → α-LUSO+2 (71) β-HOSO-11 → β-LUSO (41) β-HOSO-4 → β-LUSO (51)
539.2	0.1189	α-HOSO → α-LUSO+2 (34) β-HOSO-12 → β-LUSO (25) β-HOSO-11 → β-LUSO (82) β-HOSO-4 → β-LUSO (21)
432.2	0.1640	α-HOSO → α-LUSO+6 (22) α-HOSO → α-LUSO+7 (44) β-HOSO-16 → β-LUSO (38) β-HOSO-13 → β-LUSO (70)
411.5	0.1002	α-HOSO-2 → α-LUSO (68) β-HOSO-1 → β-LUSO+2 (68)
392.5	0.3241	α-HOSO-1 → α-LUSO+1 (31) α-HOSO → α-LUSO+6 (23) α-HOSO → α-LUSO+7 (51) β-HOSO-16 → β-LUSO (57) β-HOSO → β-LUSO+3 (28)
359.6	0.1203	α-HOSO-4 → α-LUSO+2 (32) α-HOSO → α-LUSO+7 (26) β-HOSO-20 → β-LUSO (54) β-HOSO-16 → β-LUSO (20) β-HOSO-4 → β-LUSO+1 (55)
321.1	0.0971	β-HOSO-6 → β-LUSO+1 (94)

Wavelength (nm)	Osc. str (*f*)	Major contributions (%)
294.2	0.1009	α-HOSO-4 → α-LUSO+2 (37) α-HOSO → α-LUSO+16 (60) β-HOSO-11 → β-LUSO+1 (34) β-HOSO-4 → β-LUSO+1 (42)
284.6	0.1005	α-HOSO-10 → α-LUSO (26) α-HOSO-8 → α-LUSO (21) α-HOSO-6 → α-LUSO (37) α-HOSO-5 → α-LUSO+1 (25) α-HOSO-1 → α-LUSO+3 (21) α-HOSO-1 → α-LUSO+6 (23) β-HOSO-9 → β-LUSO+2 (34) β-HOSO-5 → β-LUSO+2 (36) β-HOSO-3 → β-LUSO+3 (25) β-HOSO → β-LUSO+8 (22)
276.2	0.1221	α-HOSO-6 → α-LUSO+1 (48) β-HOSO-10 → β-LUSO+2 (33) β-HOSO-6 → β-LUSO+2 (29) β-HOSO-5 → β-LUSO+3 (47)
269.9	0.1575	α-HOSO-10 → α-LUSO (23) β-HOSO-9 → β-LUSO+2 (22) β-HOSO-8 → β-LUSO+3 (22) β-HOSO-4 → β-LUSO+3 (21) β-HOSO → β-LUSO+4 (68)
269.8	0.1466	α-HOSO-10 → α-LUSO (22) β-HOSO-9 → β-LUSO+2 (22) β-HOSO-8 → β-LUSO+3 (22) β-HOSO → β-LUSO+4 (71)
260.2	0.1167	α-HOSO-11 → α-LUSO+1 (21) α-HOSO-10 → α-LUSO+1 (30) α-HOSO-8 → α-LUSO (22) α-HOSO-3 → α-LUSO+5 (36) α-HOSO-2 → α-LUSO+11 (20) β-HOSO-9 → β-LUSO+3 (26) β-HOSO-2 → β-LUSO+6 (36) β-HOSO-1 → β-LUSO+9 (23) β-HOSO-1 → β-LUSO+13 (24)
245.1	0.1197	α-HOSO-4 → α-LUSO+4 (60) β-HOSO-27 → β-LUSO (34) β-HOSO-4 → β-LUSO+4 (37)
235.0	0.1479	α-HOSO-14 → α-LUSO+2 (22) α-HOSO-13 → α-LUSO+2 (34) α-HOSO-12 → α-LUSO+2 (22) α-HOSO-11 → α-LUSO+2 (23) α-HOSO-4 → α-LUSO+7 (28) β-HOSO-32 → β-LUSO (21) β-HOSO-11 → β-LUSO+4 (32) β-HOSO-4 → β-LUSO+4 (26)

Wavelength (nm)	Osc. str (*f*)	Major contributions (%)
229.6	0.1046	α-HOSO-4 → α-LUSO+7 (30) α-HOSO → α-LUSO+30 (49) α-HOSO → α-LUSO+33 (23) β-HOSO-30 → β-LUSO (37) β-HOSO-11 → β-LUSO+4 (21)
228.6	0.4189	α-HOSO-12 → α-LUSO+2 (26) α-HOSO-11 → α-LUSO+2 (20) α-HOSO-5 → α-LUSO+3 (41) α-HOSO → α-LUSO+30 (35) β-HOSO-11 → β-LUSO+4 (21) β-HOSO-4 → β-LUSO+4 (24) β-HOSO-3 → β-LUSO+5 (40)
222.2	0.1342	α-HOSO-12 → α-LUSO+4 (24) α-HOSO-4 → α-LUSO+7 (24) α-HOSO → α-LUSO+32 (27) α-HOSO → α-LUSO+34 (33) β-HOSO-4 → β-LUSO+7 (43)
220.6	0.1349	α-HOSO-19 → α-LUSO (33) α-HOSO-6 → α-LUSO+3 (49) α-HOSO-3 → α-LUSO+7 (22) β-HOSO-18 → β-LUSO+2 (33) β-HOSO-5 → β-LUSO+5 (48)

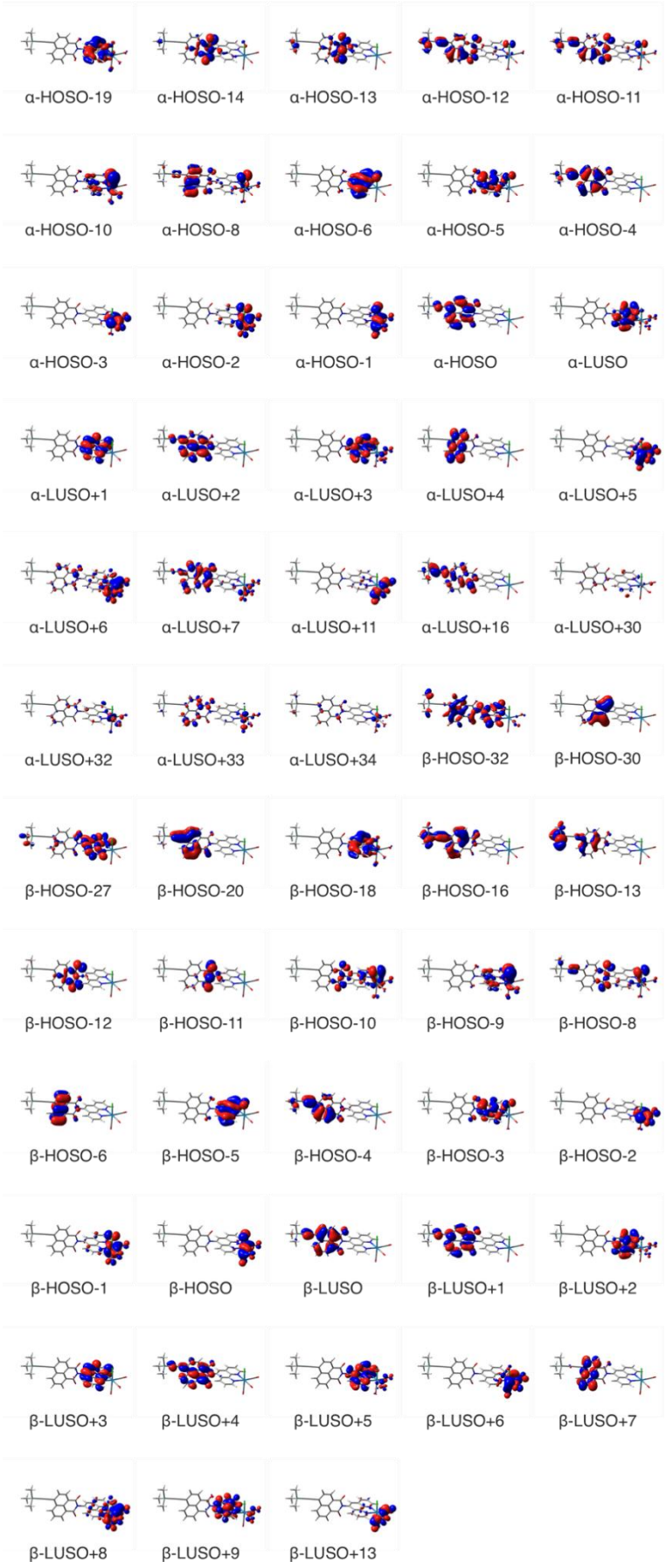


Figure S2.60. *Molecular orbitals involved in transition of* ^{3}***Re–ET*** *(see* ***Table S2.8****).*

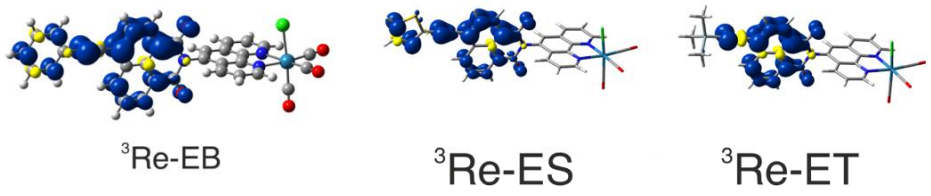


Figure S2.61. *Calculated spin density of* ***^{3}Re–EB***, ***^{3}Re–ES***, *and* ***^{3}Re–ET***.

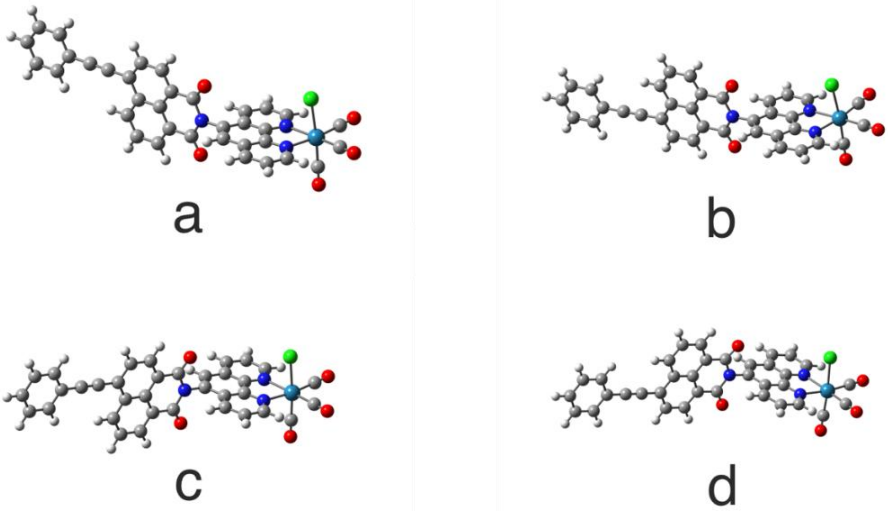


Figure S2.62. *Possible a–d structures of* ***Re–EB***.

Table S2.23. *Differential energies of structures a–d of* ***Re–EB*** *(see* ***Figure S2.62****).*

Re–EB structure	ΔE [kcal/mol]
a	0.000
b	0.093
c	0.000
d	0.094

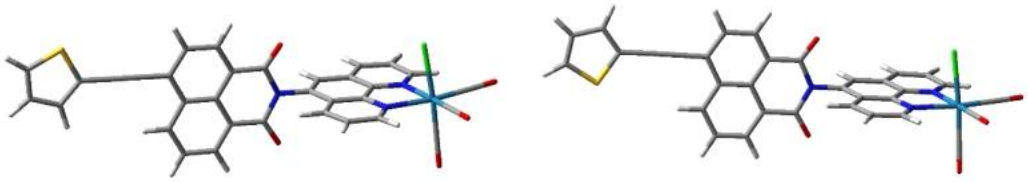


Figure S2.63. *Possible a (left) and b (right) structures of* ***Re–ES***.

Table S2.24. *Differential energies of the a and b structures of* ***Re–ES*** *(see* ***Figure S2.63****).*

Re–ES structure	ΔE [kcal/mol]
a	0.00
b	0.48

Table S2.25. *Table of triplet energy gap (ΔE_T) values.*

Re–R	State	Methods	Energy (Hartree)	Energy (eV)	Energy (kcal/mol)	ΔE (kcal/mol)	ΔE_T (kcal/mol)	ΔE_T (cm^{-1})
Re–H	GS	KS	-2115.889846	-57575.479	-1326926.686	0.00	-	-
	^{1}MLCT	TDDFT	-2115.792652	-57572.834	-1326865.733	60.95	-	-
	^{3}MLCT	TDDFT	-2115.80989	-57573.303	-1326876.544	50.14	1.51	**527**
	^{3}LC	UKS	-2115.812291	-57573.368	-1326878.049	48.64	0.00	-
Re–EB	GS	KS	-2423.066418	-65934.06	-1519564.687	0.00	-	-
	^{1}MLCT	TDDFT	-2422.96919	-65931.415	-1519503.713	60.97	-	-
	^{3}MLCT	TDDFT	-2422.986537	-65931.887	-1519514.592	50.10	9.96	**3484**
	^{3}LC	UKS	-2423.002421	-65932.319	-1519524.553	40.13	0.00	-
Re–ET	GS	KS	-2600.699027	-70767.621	-1630962.476	0.00	-	-
	^{1}MLCT	TDDFT	-2600.610821	-70765.221	-1630907.159	55.32	-	-
	^{3}MLCT	TDDFT	-2600.619655	-70765.461	-1630912.699	49.78	7.05	**2466**
	^{3}LC	UKS	-2600.630898	-70765.767	-1630919.75	42.73	0.00	-
Re–ES	GS	KS	-2743.877234	-74663.643	-1720753.059	0.00	-	-
	^{1}MLCT	TDDFT	-2743.779499	-74660.984	-1720691.767	61.29	-	-
	^{3}MLCT	TDDFT	-2743.796983	-74661.46	-1720702.732	50.33	12.61	**4411**
	^{3}LC	UKS	-2743.817093	-74662.007	-1720715.343	37.72	0.00	-

S2.10 Bibliography

1 J. E. Yarnell, K. A. Wells, J. R. Palmer, J. M. Breaux and F. N. Castellano, Excited-State Triplet Equilibria in a Series of Re(I)-Naphthalimide Bichromophores, *J. Phys. Chem. B*, 2019, **123**, 7611–7627.

2 J. E. Yarnell, J. C. Deaton, C. E. McCusker and F. N. Castellano, Bidirectional "Ping-Pong" Energy Transfer and 3000-Fold Lifetime Enhancement in a Re(I) Charge Transfer Complex, *Inorg. Chem.*, 2011, **50**, 7820–7830.

3 Y. Yang, F. Doettinger, C. Kleeberg, W. Frey, M. Karnahl and S. Tschierlei, How the Way a Naphthalimide Unit is Implemented Affects the Photophysical and -catalytic Properties of Cu(I) Photosensitizers, *Front. Chem.*, DOI:10.3389/fchem.2022.936863.

4 D. S. Tyson, C. R. Luman, X. Zhou and F. N. Castellano, New Ru(II) Chromophores with Extended Excited-State Lifetimes, *Inorg. Chem.*, 2001, **40**, 4063–4071.

5 Z. Liu, Z. Zhang, Y. Liu, Y. Mei, E. Feng, Y. Liu, T. Zheng, J. Chen, S. Zhang and Y. Tian, Raman Fiber Photometry for Understanding Mitochondrial Superoxide Burst and Extracellular Calcium Ion Influx upon Acute Hypoxia in the Brain of Freely Moving Animals, *Angew. Chem., Int. Ed.*, 2022, **61**, e202111630.

6 K. L. Wilson, A. R. Kennedy, J. Murray, B. Greatrex, C. Jamieson and A. J. B. Watson, Scope and limitations of a DMF bio-alternative within Sonogashira cross-coupling and Cacchi-type annulation, *Beilstein J. Org. Chem.*, 2016, **12**, 2005–2011.

7 S. Rykowski, D. Gurda-Woźna, M. Orlicka-Płocka, A. Fedoruk-Wyszomirska, M. Giel-Pietraszuk, E. Wyszko, A. Kowalczyk, P. Stączek, K. Biniek-Antosiak, W. Rypniewski and A. B. Olejniczak, Design of DNA Intercalators Based on 4-Carboranyl-1,8-Naphthalimides: Investigation of Their DNA-Binding Ability and Anticancer Activity, *International Journal of Molecular Sciences*, 2022, **23**, 4598.

8 G. M. Greetham, P. Burgos, Q. Cao, I. P. Clark, P. S. Codd, R. C. Farrow, M. W. George, M. Kogimtzis, P. Matousek, A. W. Parker, M. R. Pollard, D. A. Robinson, Z.-J. Xin and M. Towrie, Ultra: A Unique Instrument for Time-Resolved Spectroscopy, *Appl Spectrosc*, 2010, **64**, 1311–1319.

9 J. J. Snellenburg, S. Laptenok, R. Seger, K. M. Mullen and I. H. M. van Stokkum, Glotaran: A Java-Based Graphical User Interface for the R Package TIMP, *J. Stat. Soft.*, 2012, **49**, 1–22.

10 V. Q. Dang and T. S. Teets, A practical guide to measuring and reporting photophysical data, *Dalton Trans.*, 2025, **54**, 16268–16284.

11 M. J. Frisch, G. W. Trucks, H. B. Schlegel, G. E. Scuseria, M. A. Robb, J. R. Cheeseman, G. Scalmani, V. Barone, G. A. Petersson, H. Nakatsuji, X. Li, M. Caricato, A. V. Marenich, J.

Bloino, B. G. Janesko, R. Gomperts, B. Mennucci, H. P. Hratchian, J. V. Ortiz, A. F. Izmaylov, J. L. Sonnenberg, D. Williams-Young, F. Ding, F. Lipparini, F. Egidi, J. Goings, B. Peng, A. Petrone, T. Henderson, D. Ranasinghe, V. G. Zakrzewski, J. Gao, N. Rega, G. Zheng, W. Liang, M. Hada, M. Ehara, K. Toyota, R. Fukuda, J. Hasegawa, M. Ishida, T. Nakajima, Y. Honda, O. Kitao, H. Nakai, T. Vreven, K. Throssell, J. A. Montgomery, Jr., J. E. Peralta, F. Ogliaro, M. J. Bearpark, J. J. Heyd, E. N. Brothers, K. N. Kudin, V. N. Staroverov, T. A. Keith, R. Kobayashi, J. Normand, K. Raghavachari, A. P. Rendell, J. C. Burant, S. S. Iyengar, J. Tomasi, M. Cossi, J. M. Millam, M. Klene, C. Adamo, R. Cammi, J. W. Ochterski, R. L. Martin, K. Morokuma, O. Farkas, J. B. Foresman and D. J. Fox, Gaussian 16, Revision C.01, *Gaussian, Inc., Wallingford CT*.

12 A. D. Becke, Density-functional thermochemistry. III. The role of exact exchange, *J Chem Phys*, 1993, **98**, 5648–5652.

13 C. Lee, W. Yang and R. G. Parr, Development of the Colle-Salvetti correlation-energy formula into a functional of the electron density, *Phys. Rev. B*, 1988, **37**, 785–789.

14 D. Andrae, U. Häußermann, M. Dolg, H. Stoll and H. Preuß, Energy-adjustedab initio pseudopotentials for the second and third row transition elements, *Theoret. Chim. Acta*, 1990, **77**, 123–141.

15 R. Krishnan, J. S. Binkley, R. Seeger and J. A. Pople, Self-consistent molecular orbital methods. XX. A basis set for correlated wave functions, *J. Chem. Phys.*, 1980, **72**, 650–654.

16 M. Cossi, N. Rega, G. Scalmani and V. Barone, Energies, structures, and electronic properties of molecules in solution with the C-PCM solvation model, *J Comput Chem*, 2003, **24**, 669–681.

Appendix B

Supplementary information associated with Chapter 3

S3.1 Experimental

Synthesis and Spectral Characterisation

The synthesis and characterisation of the **Re–R** complexes is described elsewhere.[1]

All FTIR spectra were recorded on a Perkin Elmer Spectrum65 FTIR Spectrometer. Samples were prepared in spectroscopic grade DCM and THF. Experiments were conducted in a liquid-film IR cell with two CaF_2 plates, an optical pathlength of 100 μm, a resolution of 1 cm^{-1}, and 16 scans.

All UV-Vis absorption spectra were recorded on a Horiba Duetta Fluorescence and Absorbance Spectrometer. Samples were prepared in spectroscopic grade DCM or THF. The absorption spectra were collected in a 1-cm quartz fluorescence cuvette.

Electrochemistry

Cyclic voltammetry (CV) was performed under an atmosphere of dry inert N_2 or CO_2 with a V-shaped cell containing a glassy carbon working electrode, a Pt wire counter electrode, and an Ag wire pseudo-reference electrode. The cell was connected to a PalmSens4 potentiostat. The ferrocenium/ferrocene internal standard (Fc^+/Fc) was added prior to the final scans. 1 mM sample solutions (10 cm^3) were prepared using stock electrolyte solutions of 0.1 M $TBAPF_6$ in DCM, DMF, and THF.

Spectroelectrochemistry

Spectroelectrochemical (SEC) measurements were performed using an optically transparent thin-layer electrochemical (OTTLE) cell equipped with a Pt minigrid working electrode.[2] The sample solutions in spectroscopic grade DCM and THF contained 0.1 M $TBAPF_6$. IR SEC experiments were conducted at 4 mM sample concentrations, while UV-Vis SEC experiments were conducted at 2 mM sample concentrations. The course of the SEC experiment was monitored by thin-layer cyclic voltammetry (v = 2 mV s^{-1}) with a potential control by a PalmSens4 potentiostat operated with the PSTrace5 software. IR SEC was conducted with a Perkin Elmer Spectrum65 FTIR spectrometer, and UV-Vis SEC with an Agilent 8453 diode-array spectrophotometer.

Time-Resolved Infrared Spectroscopy and Time-Resolved Infrared Spectroelectrochemical Studies

Time-resolved infrared (TRIR) spectroscopy and time-resolved infrared spectroelectrochemical (TRIR SEC) experiments were conducted using the ULTRA apparatus at the Central Laser Facility (CLF), which is described in detail elsewhere.[3] Samples for TRIR SEC were excited at 420 nm in 10^{-1} M $TBAPF_6$ electrolyte solutions using spectroscopic-grade DCM and THF. Electrolysis was conducted in an optically transparent thin-layer electrochemical (OTTLE) cell equipped with a robust Pt minigrid working electrode (56 wires per cm) bearing a rectangular aperture to allow for horizontal rastering during TRIR SEC experiments. The latter was needed to avoid light scattering and minimise photodamage and re-excitation effects.

All spectra were processed using the in-house ULTRAview software provided by the CLF. Samples were calibrated from pixels into wavenumbers using the in-house ULTRAcal software provided by the CLF. The ethynyl, metal carbonyl, and organic carbonyl stretching-mode regions (2300–1500 cm^{-1}) were calibrated by fitting the absorption bands of polystyrene. All experiments were carried out at 298 K and samples were checked before and after the experiment for photodegradation by UV-Vis absorption spectroscopy in a PerkinElmer Lambda 950 spectrophotometer and FTIR in a Nicolet Avatar spectrometer. The kinetic fitting of all spectra from the TRIR and TRIR SEC experiments was conducted with global fit analysis using the Glotaran 1.5.1 software.[4]

The course of TRIR SEC experiments was monitored by thin-layer cyclic voltammetry (v = 2 mV s^{-1}) with a potential control by a PalmSens4 potentiostat operated with PSTrace5 software. Reduction was performed *in situ* within the TRIR setup, allowing for the monitoring of spectral features to identify conversion progress from parent to product species. Care was taken to approach the target redox potentials slowly and prevent potential drift by maintaining low faradaic currents.

DFT Calculations

DFT calculations were performed with Gaussian 16, Revision C01 (G16)[5], using the three-parameterized Becke, Lee, Yang, and Park (B3LYP) functional.[6,7] For the Re atom, a quasi-relativistic effective-core pseudopotential and a corresponding optimized basis set[8] was used, and for non-metal atoms, the 6–31+G(d) basis set.[9] Solvent effects (DCM) were described by the conductor-like polarisable continuum model (CPCM).[10]

Photocatalytic Studies

Solutions for photocatalysis contained 0.1 mM photocatalyst dissolved in a DMF/TEOA (5:1, v/v) solution prepared in a Schlenk tube and sealed with a Versilic silicone septum. The sample was degassed by three freeze-pump-thaw cycles and subsequently, CO_2 was added before commencing irradiation. The prepared sample was placed into an Evoluchem PhotoRedox Box, fitted with a 450 nm LED, positioned over a stirring plate. The solution was stirred and irradiated for the indicated time intervals. After this time elapsed, 1 cm^3 of the headspace was injected into a Shimadzu GC-2010 Plus gas chromatography system. Turnover numbers (TONs) were calculated by comparing the peak intensity of the photocatalysis products to those of 1000 ppm standards for H_2, CO, and CH_4.

UV-Vis Monitoring of Photocatalysis

A photocatalytic solution was prepared, as described in the preceding section, in a photolysis laser cell fitted with a Young's tap. The prepared sample was irradiated with a 450 nm Evoluchem LED and the UV-Vis spectrum collected at selected time intervals (noted as the time elapsed from the onset of irradiation) up to 24 h using an Agilent 8453 UV-Vis diode-array spectrophotometer.

S3.2 Spectral Characterisation

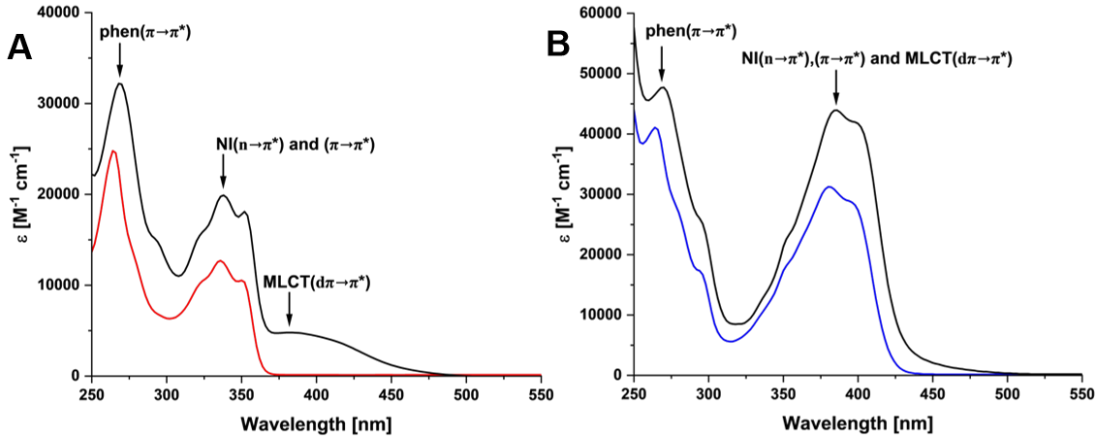


Figure S3.64. *UV-Vis absorption spectra collected in DCM of [A]* ***H–NI–phen*** *(red) and* ***Re–H*** *(black) and [B]* ***EB–NI–phen*** *(blue) and* ***Re–EB*** *(black).*

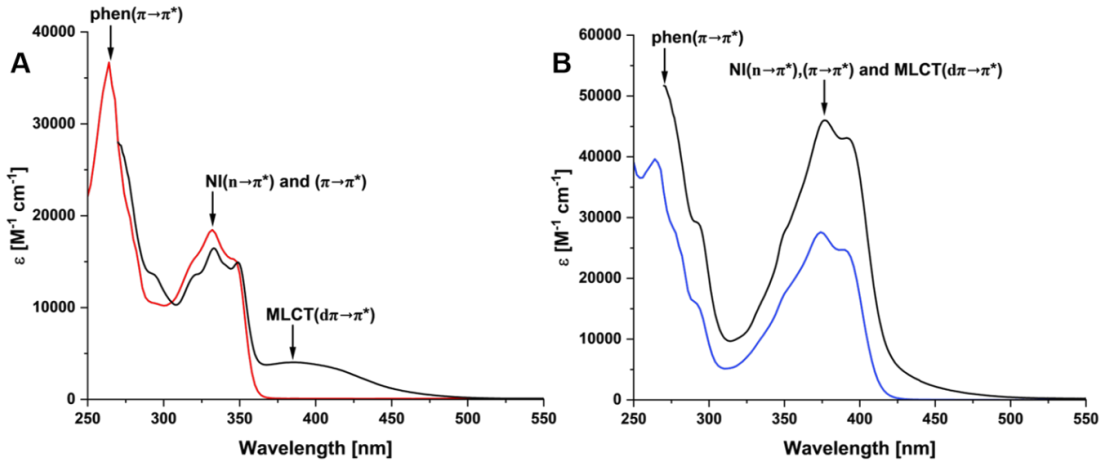


Figure S3.65. *UV-Vis absorption spectra of [A]* ***H–NI–phen*** *(red) and* ***Re–H*** *(black) and [B]* ***EB–NI–phen*** *(blue) and* ***Re–EB*** *(black) collected in THF.*

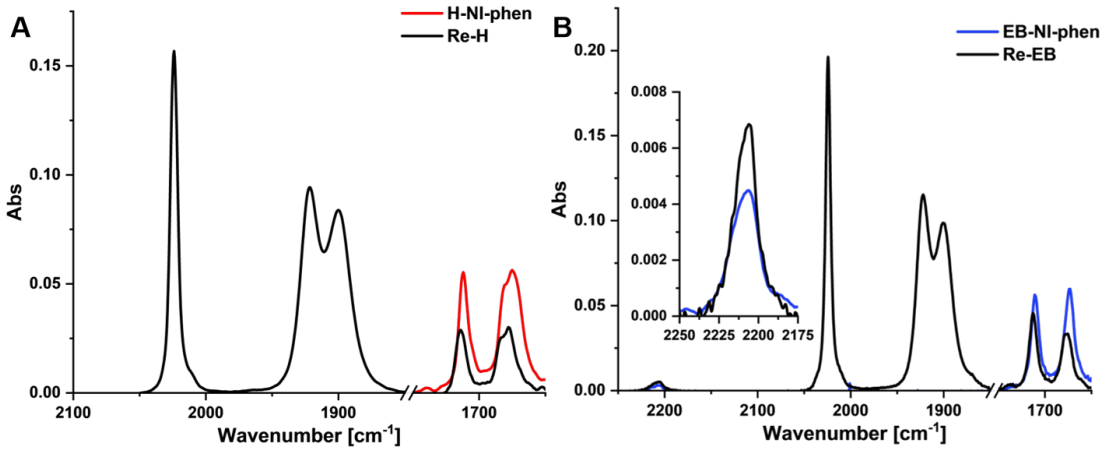


Figure S3.66. *IR spectra of [A]* ***H–NI–phen*** *and* ***Re–H****, and [B]* ***EB–NI–phen*** *and* ***Re–EB*** *with an inset of the ethynyl stretching vibration, collected in DCM.*

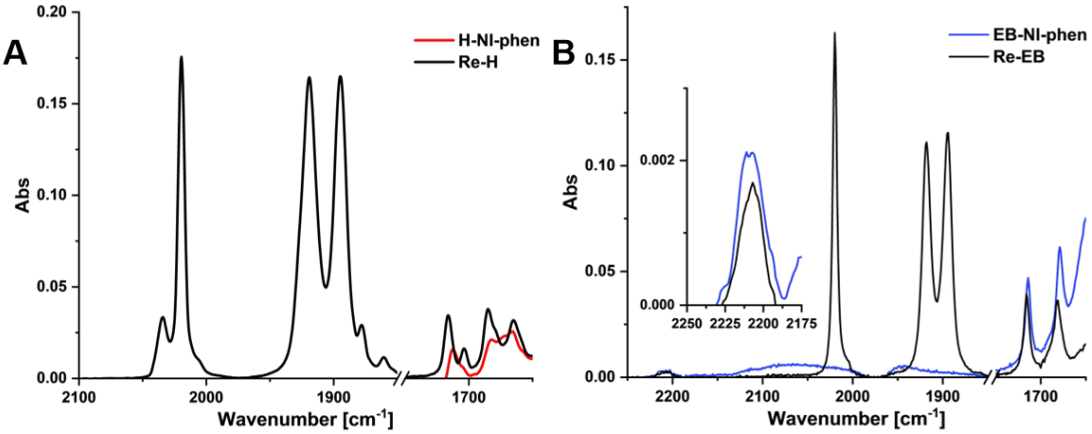


Figure S3.67. *IR spectra of [A]* ***H–NI–phen*** *and* ***Re–H****, and [B]* ***EB–NI–phen*** *and* ***Re–EB*** *with an inset of the ethynyl stretching vibration collected in THF.*

S3.3 Cyclic Voltammetry

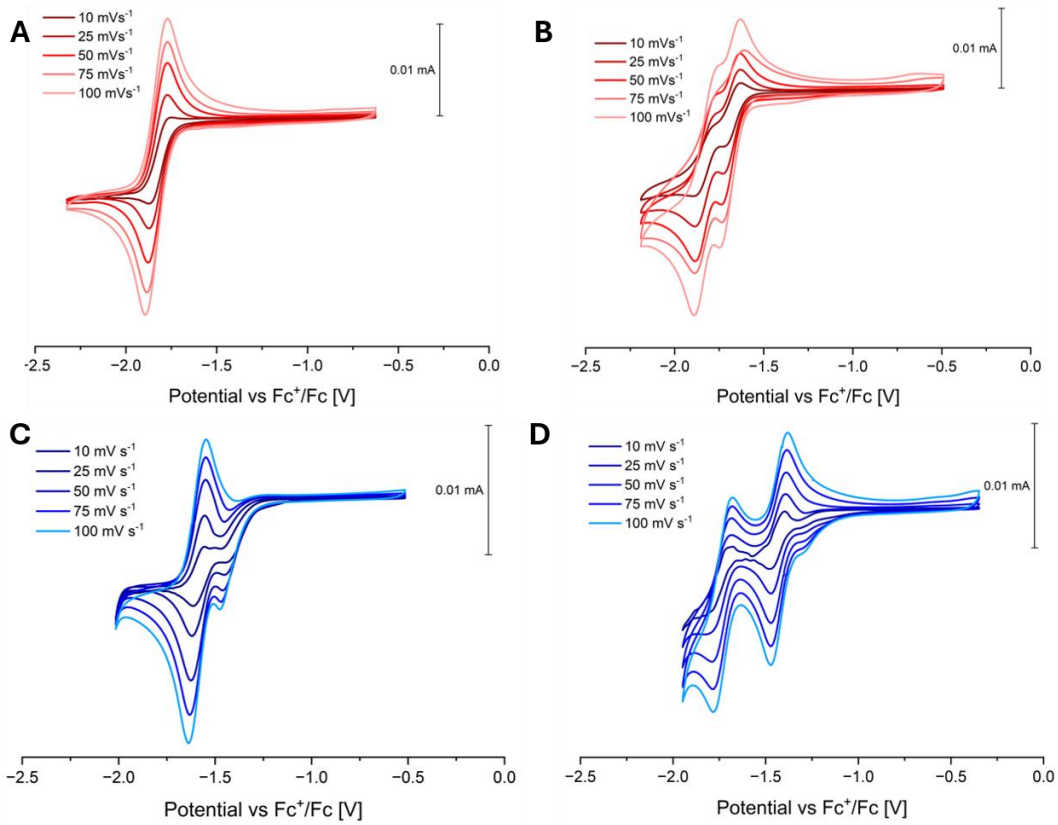


Figure S3.68. *CVs showing the reversibility of the R1 and R2 reduction waves of 1 mM [A]* ***H–NI–phen****, [B]* ***Re–H****, [C]* ***EB–NI–phen****, and [D]* ***Re–EB*** *in DCM/TBAH electrolyte solutions under N_2 atmosphere. Scan rates between 10 and 100 mV s^{-1}.*

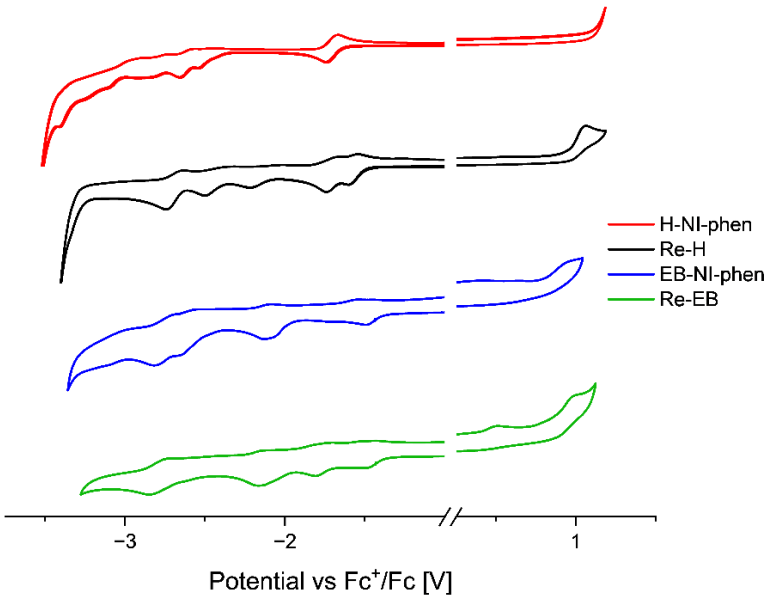


Figure S3.69. *CVs of 1 mM [red]* ***H–NI–phen****, [black]* ***Re–H****, [blue]* ***EB–NI–phen****, and [green]* ***Re–EB*** *samples in DMF/TBAH electrolyte solutions under N_2 atmosphere.*

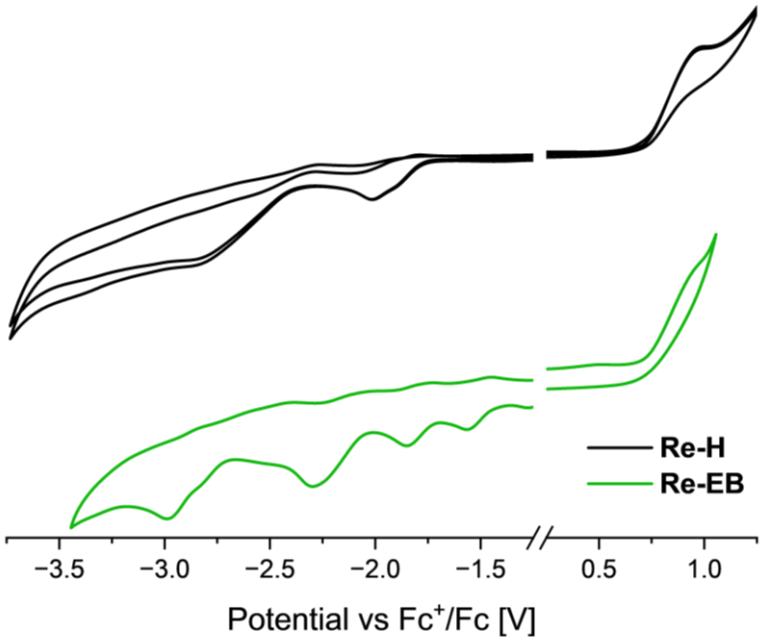


Figure S3.70. *CVs of 1 mM [black]* ***Re–H*** *and [green]* ***Re–EB*** *samples in THF/TBAH electrolyte solutions under N_2 atmosphere.*

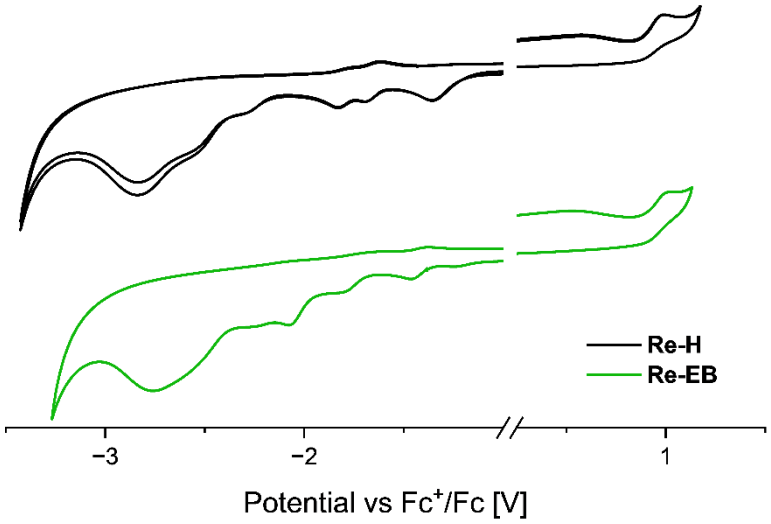


Figure S3.71. *CVs of 1 mM [black]* ***Re–H*** *and [green]* ***Re–EB*** *samples in DMF/TBAH electrolyte solution under CO_2 atmosphere.*

S3.4 Spectroelectrochemistry

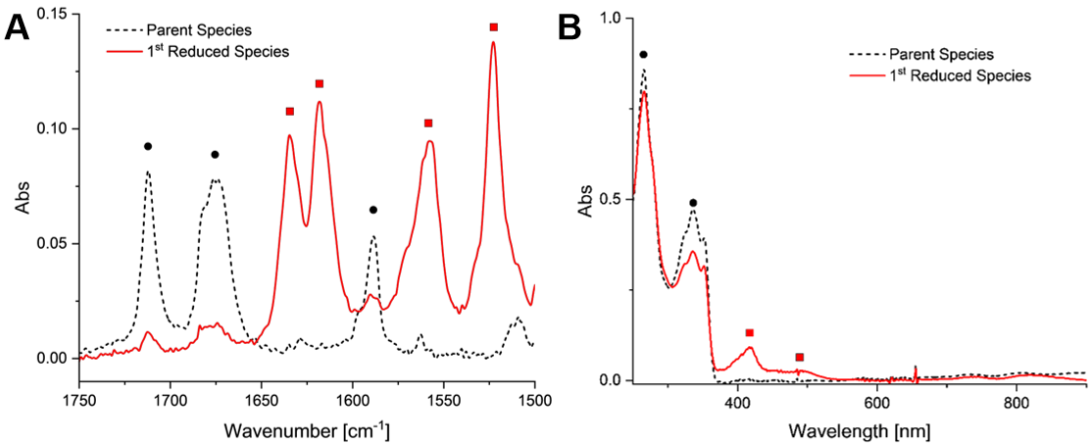


Figure S3.72. *4 mM IR SEC (A) and 2 mM UV-Vis SEC (B) spectra of* ***H–NI–phen*** *in a DCM electrolyte solution.*

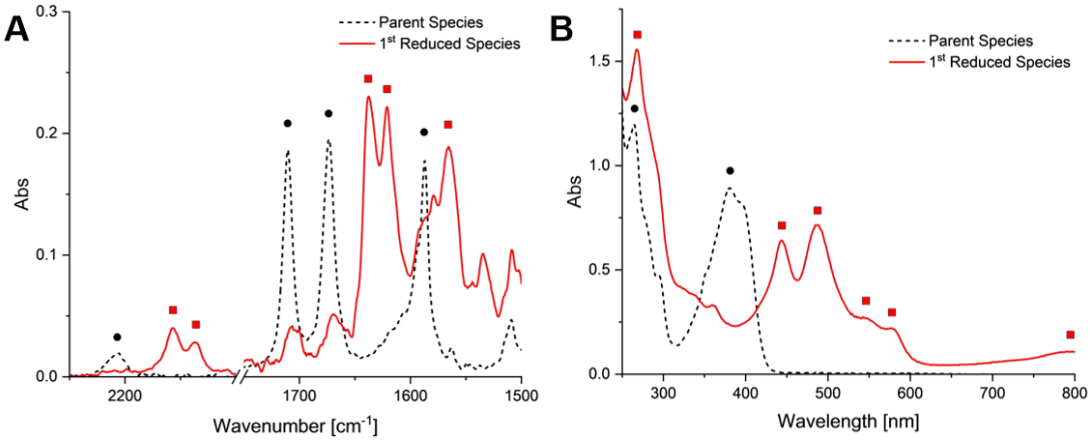


Figure S3.73. *4 mM IR SEC (A) and 2 mM UV-Vis SEC (B) spectra of* ***EB–NI–phen*** *in a DCM electrolyte solution.*

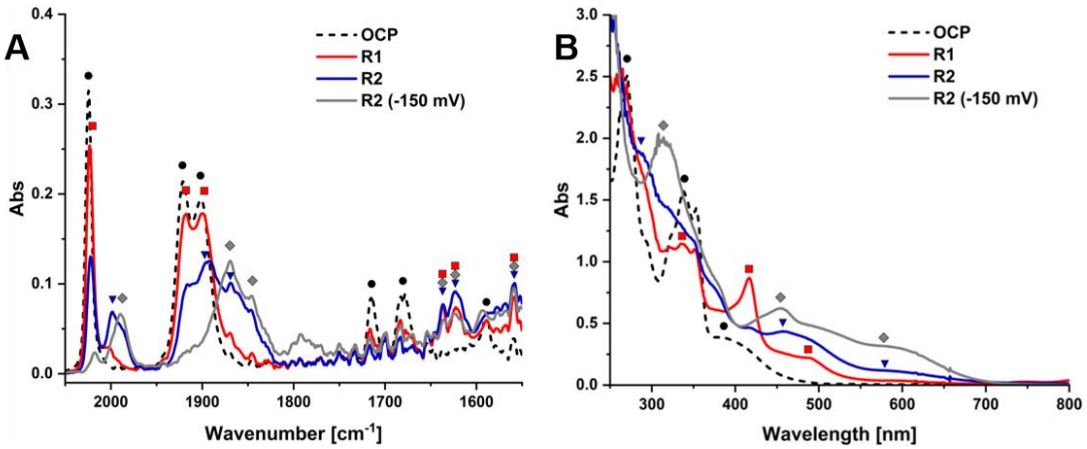


Figure S3.74. *4 mM IR SEC (A) and 2 mM UV-Vis SEC (B) spectra of* ***Re–H*** *in the DCM electrolyte solution.* ● = ***Re–H***, ■ = ***[Re–H]***$^{-}$, ▼ = ^{3}***[Re–H]***$^{2-}$, ◆ = ^{3}***5–MA***.

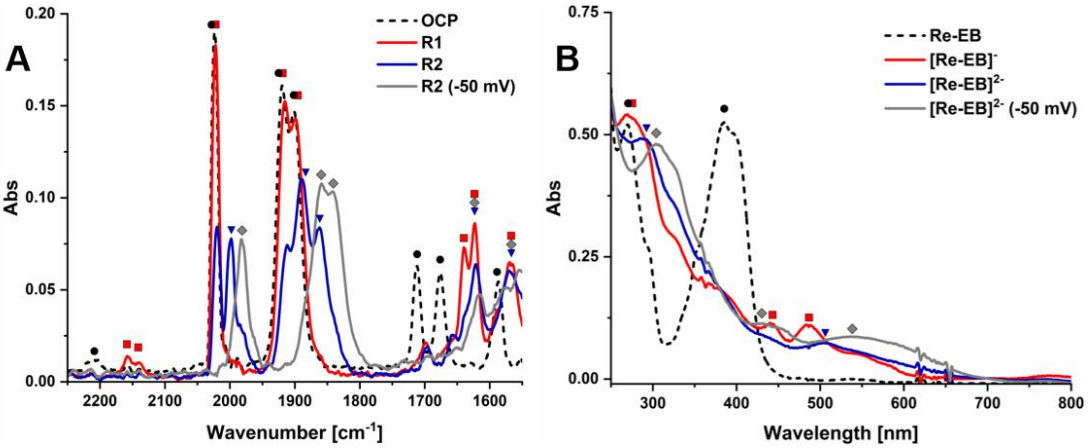


Figure S3.75. *4 mM IR SEC (A) and 1 mM UV-Vis SEC (B) spectra of* ***Re–EB*** *in the DCM electrolyte solution.* ● = ***Re–EB***, ■ = ***[Re–EB]***$^{-}$, ▼ = ^{3}***[Re–EB]***$^{2-}$, ◆ = ^{3}***5–MA***.

S3.5 TRIR Spectra and Kinetic Traces

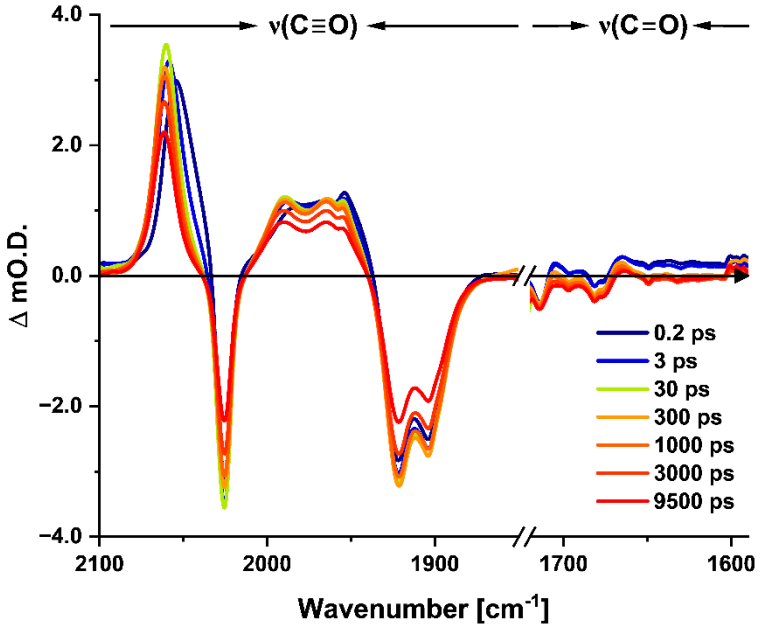


Figure S3.76. *TRIR spectrum of* ***Re–H*** *in a DCM electrolyte solution following 420 nm excitation.*

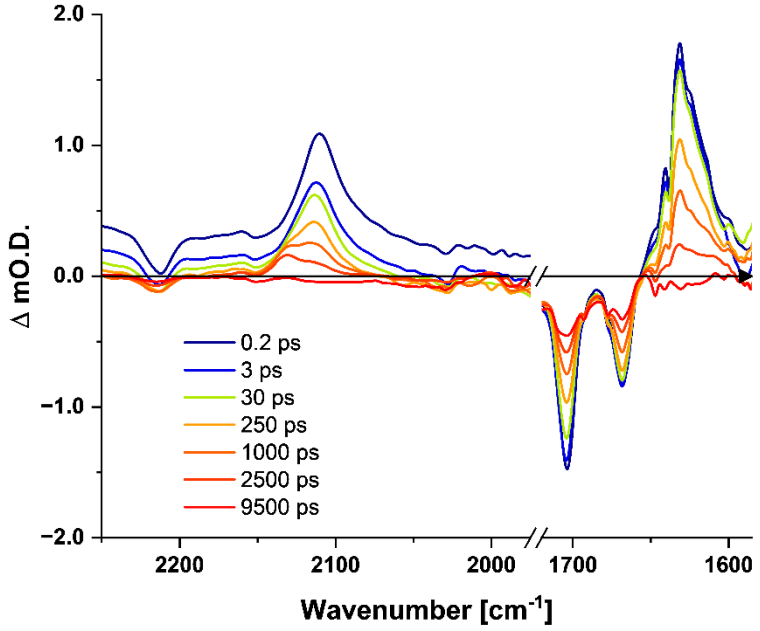


Figure S3.77. *TRIR spectra of* ***EB–NI–phen*** *in a DCM electrolyte solution following 420 nm excitation.*

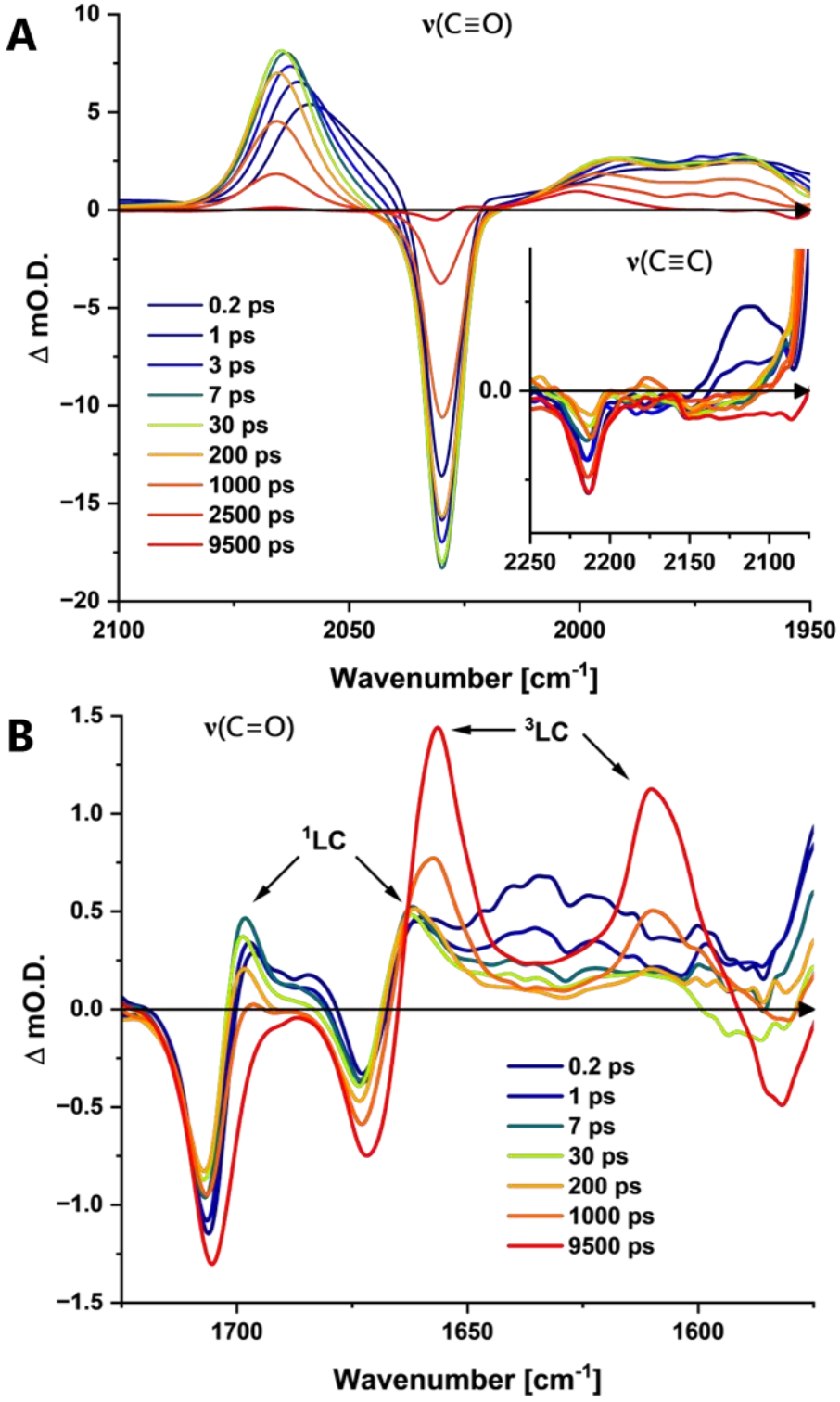


Figure S3.78. *TRIR spectrum of* ***Re–EB*** *in a DCM electrolyte solution following 420 nm excitation. A: ethynyl and metal carbonyl regions. B: organic carbonyl region.*

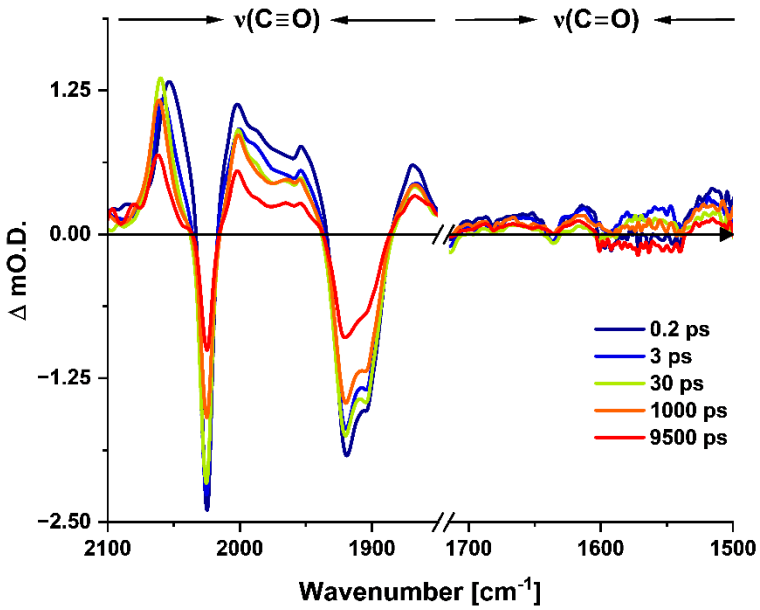


Figure S3.79. *TRIR spectrum of* ***[Re–H]⁻*** *in the DCM electrolyte solution following 420 nm excitation. The metal and organic carbonyl regions are highlighted.*

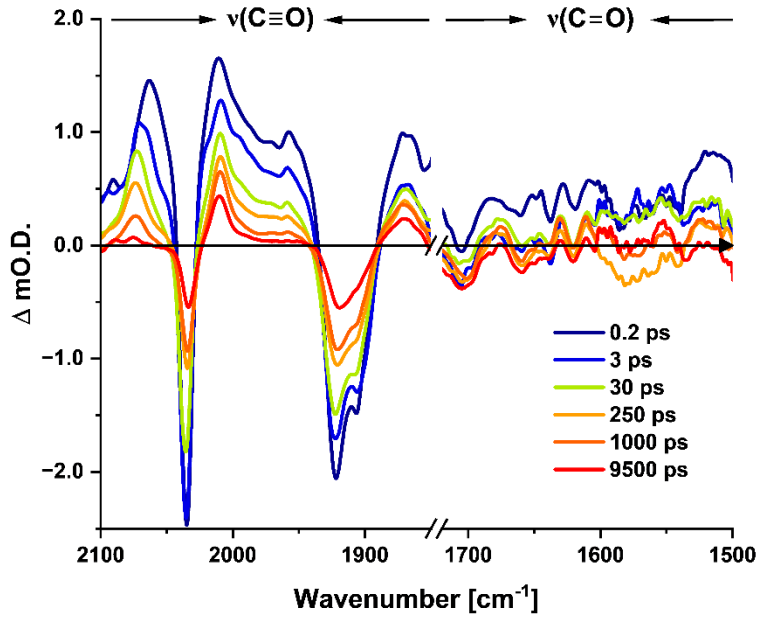


Figure S3.80. *TRIR spectrum of* ***[Re–EB]⁻*** *in the DCM electrolyte solution following 420 nm excitation. The metal and organic carbonyl regions are highlighted.*

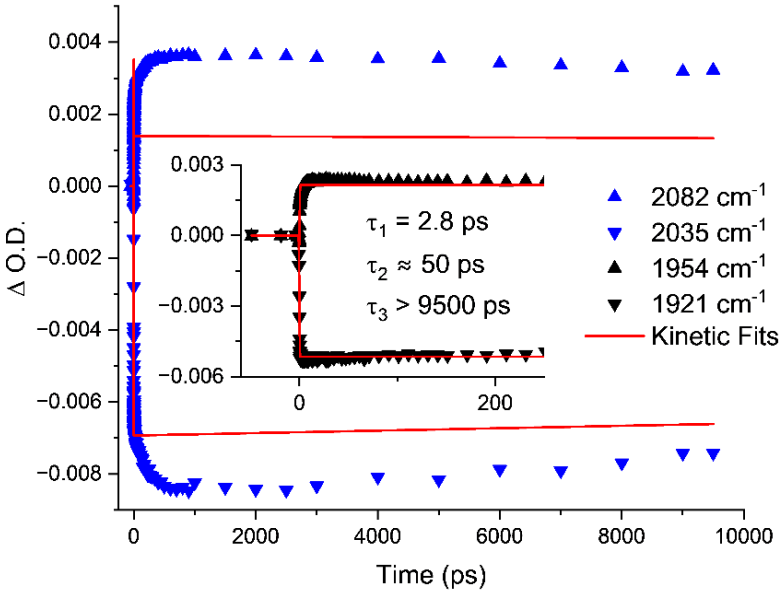


Figure S3.81. *Kinetic traces of the $\nu_{C\equiv O}$ 2035 cm^{-1} GSB and $\nu_{C\equiv O}$ 2082 cm^{-1} transient band of* ***Re–H*** *in THF following excitation at 420 nm. Inset: Kinetic traces of the $\nu_{C\equiv O}$ 1921 cm^{-1} GSB and $\nu_{C\equiv O}$ 1954 cm^{-1} transient band of* ***Re–H*** *in THF following excitation at 420 nm.*

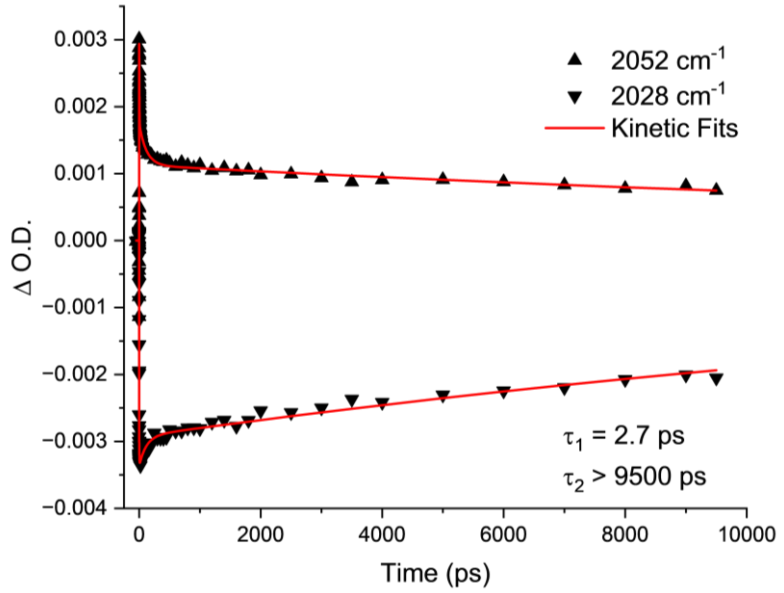


Figure S3.82. *Kinetic traces of the $\nu_{C\equiv O}$ 2028 cm^{-1} GSB and $\nu_{C\equiv O}$ 2052 cm^{-1} transient band of* ***Re–H*** *in DCM following excitation at 420 nm.*

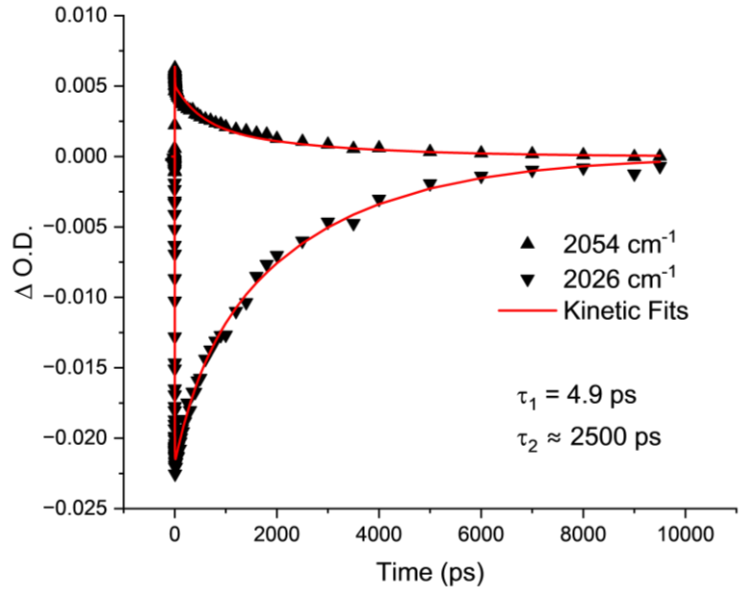


Figure S3.83. *Kinetic traces of the* $\nu_{C\equiv O}$ *= 2026 cm*$^{-1}$ *GSB and the* $\nu_{C\equiv O}$ *2054 cm*$^{-1}$ *transient band* ***Re–EB*** *in DCM following excitation at 420 nm.*

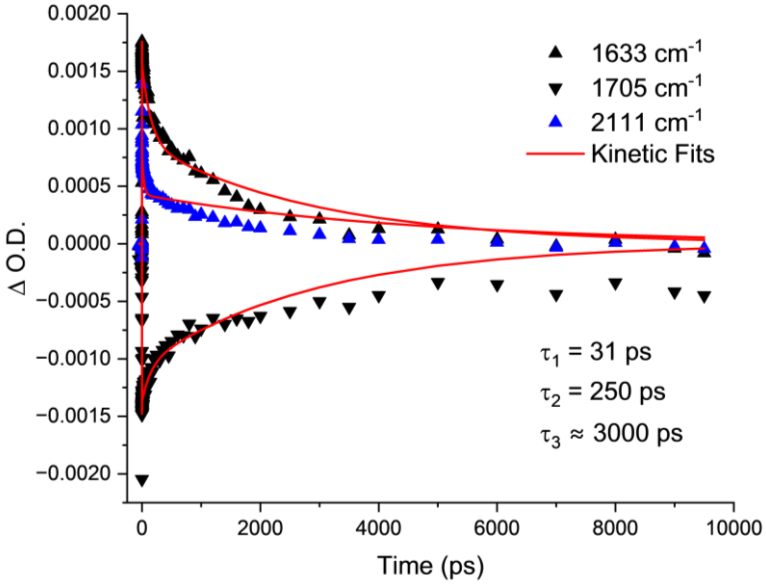


Figure S3.84. *Kinetic traces of the* $\nu_{C=O}$ *1705 cm*$^{-1}$ *GSB, the* $\nu_{C=O}$ *1633 cm*$^{-1}$ *transient band, and* $\nu_{C\equiv C}$ *2111 cm*$^{-1}$ *transient band of* ***EB–NI–phen*** *in DCM following excitation at 420 nm.*

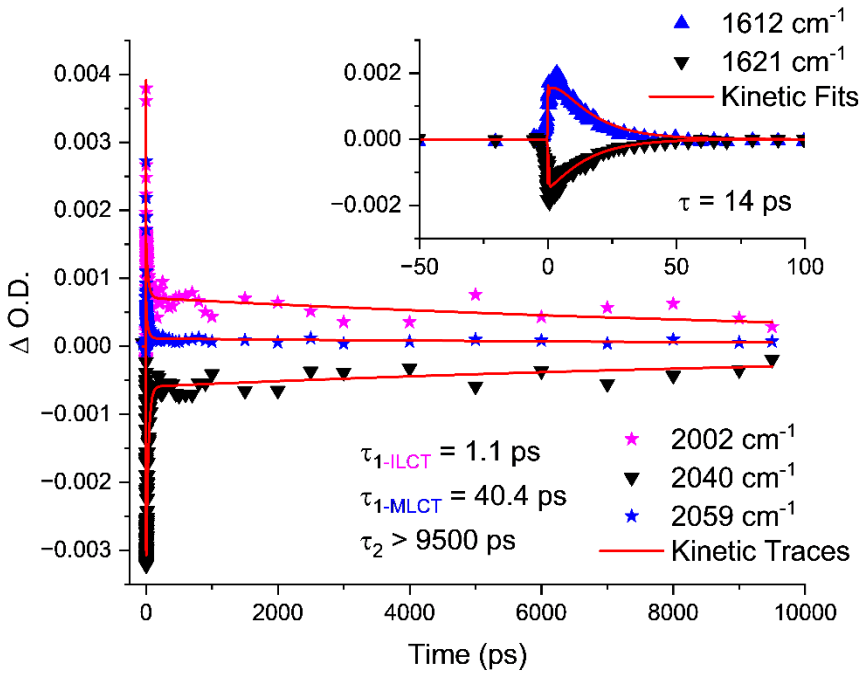


Figure S3.85. *Kinetic traces of the $\nu_{C\equiv O}$ 2040 cm^{-1} GSB and the $\nu_{C\equiv O}$ 2059 and 2002 cm^{-1} transient bands (corresponding to the ^{4}MLCT and ^{4}ILCT transient features, respectively) of* ***[Re–H]$^-$*** *in THF following excitation at 420 nm. Inset: Kinetic traces of the $\nu_{C\equiv O}$ 1621 cm^{-1} GSB and the $\nu_{C\equiv O}$ 1612 cm^{-1} transient band of* ***[Re–H]$^-$*** *in THF following excitation at 420 nm.*

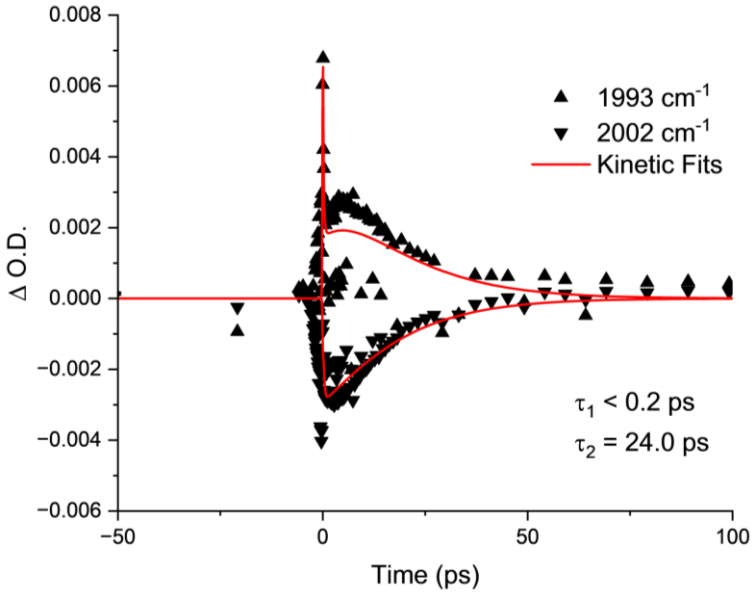


Figure S3.86. *Kinetic traces of the $\nu_{C\equiv O}$ 2002 cm^{-1} GSB and the $\nu_{C\equiv O}$ 1993 cm^{-1} transient band of* ***[Re–H]$^{2-}$*** *in THF following excitation at 420 nm.*

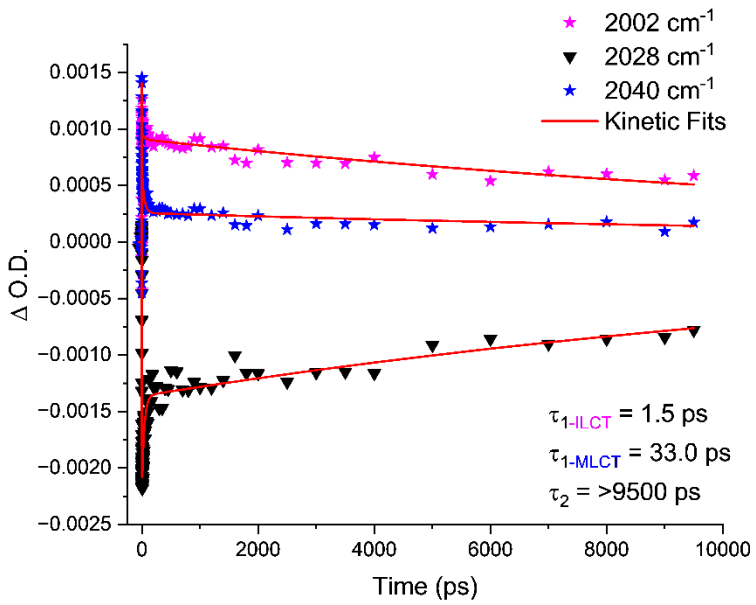


Figure S3.87. *Kinetic traces of the $\nu_{(C\equiv O)}$ 2028 cm^{-1} GSB and the $\nu_{C\equiv O}$ 2040 and 2002 cm^{-1} transient bands (corresponding to the ^{4}MLCT and ^{4}ILCT transient features, respectively) of* ***[Re–H]$^-$*** *in DCM following excitation at 420 nm.*

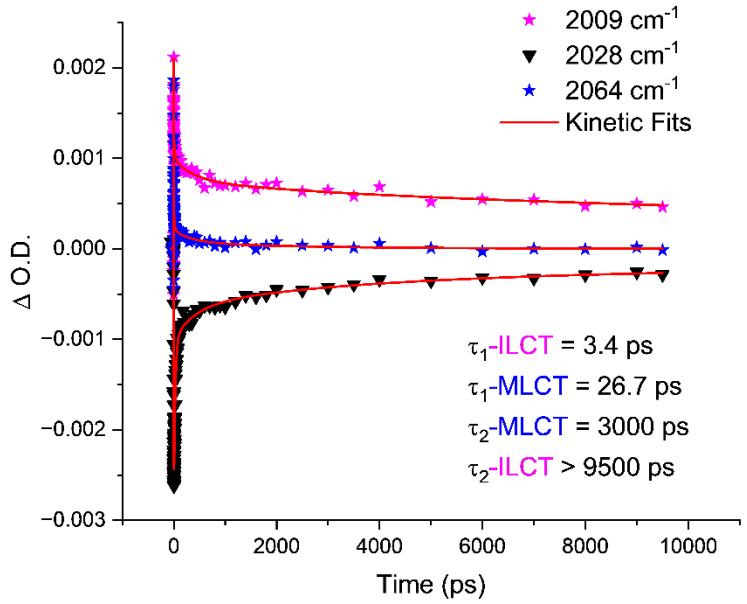


Figure S3.88. *Kinetic traces of the $\nu_{C\equiv O}$ 2028 cm^{-1} GSB and the $\nu_{C\equiv O}$ 2064 and 2009 cm^{-1} transient bands (corresponding to the ^{4}MLCT and ^{4}ILCT transient features, respectively) of* ***[Re–EB]$^-$*** *in DCM following excitation at 420 nm.*

S3.6 DFT and TDDFT calculations

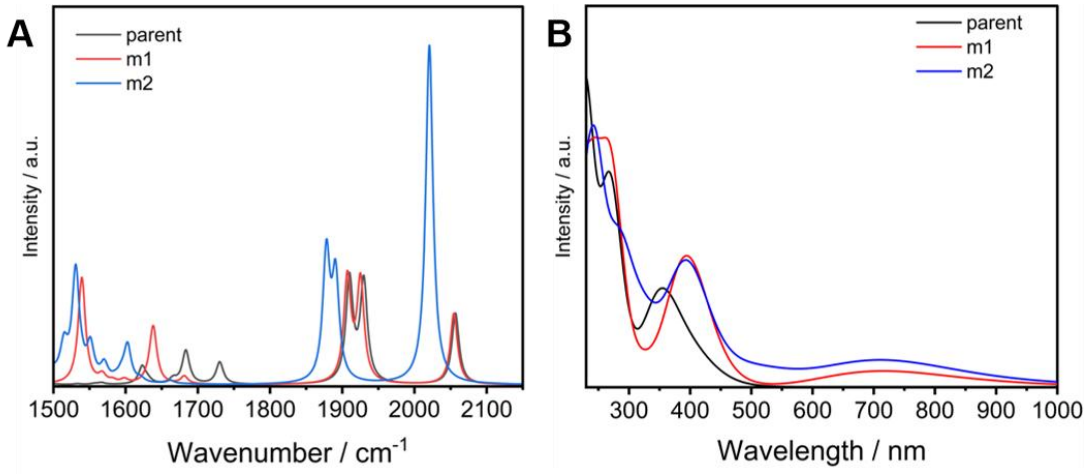


Figure S3.89. *(A) DFT calculated IR spectra and (B) TDDFT calculated UV-Vis absorption spectra of* ***Re–H*** *(black),* ***[Re–H]***$^{-}$ *(red),* ^{3}***[Re–H]***$^{2-}$ *(blue).*

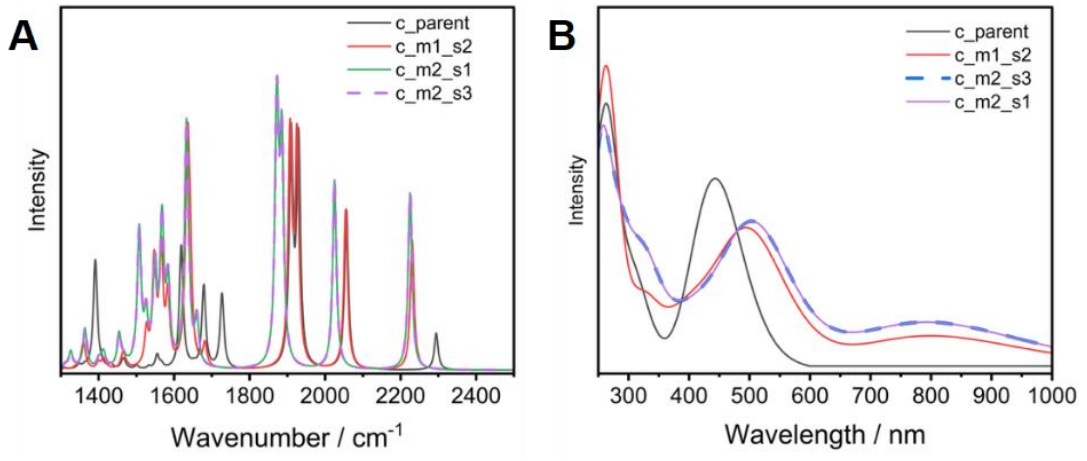


Figure S3.90. *(A) DFT calculated IR spectra and (B) TDDFT calculated UV-Vis absorption spectra of the* ***Re–EB***, ***[Re–EB]***$^{-}$, ^{3}***[Re–EB]***$^{2-}$, ^{3}***[Re–EB]***$^{2-}$ *species.*

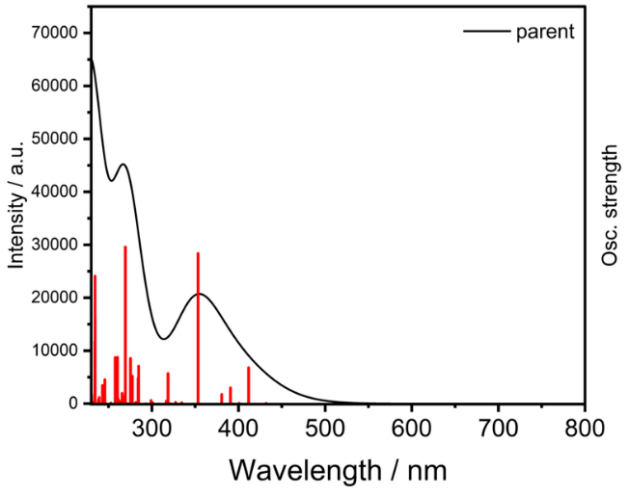


Figure S3.91. *Calculated UV-Vis absorption spectrum of* ***Re–H****.*

Table S3.26. *Major electronic excitations in* ***Re–H*** *determined by TDDFT calculations.*

Wavelength (nm)	Osc. str (*f*)	Major contributions (%)
411.6	0.0917	HOMO–1 → LUMO+1 (68)
390.8	0.0410	HOMO → LUMO+2 (67)
353.4	0.3792	HOMO–3 → LUMO (70)
318.6	0.0769	HOMO–5 → LUMO (67) HOMO–3 → LUMO+5 (22)
284.7	0.0956	HOMO–8 → LUMO+1 (30) HOMO–7 → LUMO+1 (25) HOMO–6 → LUMO+1 (37) HOMO–4 → LUMO+2 (25) HOMO → LUMO+7 (25)
284.1	0.0644	HOMO–1 → LUMO+4 (58)
277.4	0.0704	HOMO–9 → LUMO+1 (20) HOMO–8 → LUMO+1 (42) HOMO–7 → LUMO+1 (50)
275.4	0.1151	HOMO–6 → LUMO+2 (56)
269.3	0.3950	HOMO–8 → LUMO+1 (34) HOMO–7 → LUMO+1 (21) HOMO–7 → LUMO+2 (22) HOMO–6 → LUMO+1 (29) HOMO–4 → LUMO+2 (30)
260.3	0.1181	HOMO–9 → LUMO+2 (27) HOMO–2 → LUMO+6 (42) HOMO–1 → LUMO+8 (21) HOMO–1 → LUMO+11 (25)
257.7	0.1175	HOMO–9 → LUMO+1 (25) HOMO–9 → LUMO+2 (59)
234.5	0.2167	HOMO–3 → LUMO+5 (42) HOMO → LUMO+11 (34)

Wavelength (nm)	Osc. str (*f*)	Major contributions (%)
234.4	0.3221	HOMO–11 → LUMO+2 (29) HOMO–3 → LUMO+5 (34) HOMO → LUMO+11 (33)
234.1	0.1576	HOMO–11 → LUMO+1 (24) HOMO–11 → LUMO+2 (54) HOMO–3 → LUMO+5 (24)
227.7	0.1538	HOMO–4 → LUMO+4 (37) HOMO–1 → LUMO+13 (23) HOMO–1 → LUMO+15 (24) HOMO–1 → LUMO+17 (22)
227.1	0.1747	HOMO–4 → LUMO+4 (47)
220.8	0.1389	HOMO–15 → LUMO+1 (33) HOMO–6 → LUMO+4 (49)
212.2	0.2286	HOMO–14 → LUMO+1 (22) HOMO–5 → LUMO+5 (24) HOMO–3 → LUMO+8 (23) HOMO–3 → LUMO+9 (41)
205.2	0.1368	HOMO–11 → LUMO+3 (26) HOMO–9 → LUMO+4 (25) HOMO–4 → LUMO+8 (41)



Figure S3.92. *Molecular orbitals involved in electronic transitions of* ***Re–H*** *(see* ***Table S3.1****).*

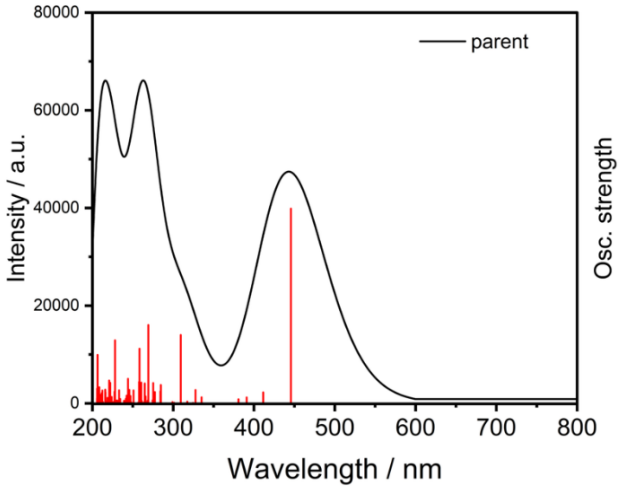


Figure S3.93. *Calculated UV-Vis absorption spectrum of* ***Re–EB.***

Table S3.27. *Major electronic excitations in* ***Re–EB*** *determined by TDDFT calculations.*

Wavelength (nm)	Osc. str (*f*)	Major contributions (%)
445.6	0.9975	HOMO → LUMO (70)
411.5	0.0580	HOMO–2 → LUMO+1 (68)
390.9	0.0329	HOMO–1 → LUMO+2 (68)
335.0	0.0334	HOMO–5 → LUMO (58) HOMO–4 → LUMO (33)
327.6	0.0709	HOMO–7 → LUMO (65) HOMO → LUMO+5 (22)
309.4	0.3519	HOMO → LUMO+3 (68)
284.8	0.0962	HOMO–10 → LUMO+1 (30) HOMO–9 → LUMO+1 (23) HOMO–8 → LUMO+1 (39) HOMO–4 → LUMO+2 (27) HOMO–1 → LUMO+8 (23)
284.2	0.0633	HOMO–2 → LUMO+4 (60)
277.4	0.0602	HOMO–10 → LUMO+1 (37) HOMO–9 → LUMO+1 (44) HOMO–7 → LUMO+1 (30)
275.3	0.1061	HOMO–8 → LUMO+2 (54)
269.3	0.4035	HOMO–10 → LUMO+1 (34) HOMO–9 → LUMO+1 (20) HOMO–9 → LUMO+2 (23) HOMO–8 → LUMO+1 (29) HOMO–5 → LUMO+2 (26)
265.8	0.0381	HOMO–12 → LUMO+1 (33) HOMO–11 → LUMO+1 (28) HOMO–9 → LUMO+2 (45)
264.7	0.1042	HOMO–14 → LUMO (42) HOMO–13 → LUMO (31) HOMO → LUMO+5 (25) HOMO → LUMO+7 (30)

Wavelength (nm)	Osc. str (*f*)	Major contributions (%)
260.5	0.1084	HOMO–3 → LUMO+3 (32) HOMO–3 → LUMO+6 (37) HOMO–2 → 174 (22)
258.4	0.2819	HOMO–14 → LUMO (32) HOMO–13 → LUMO (32) HOMO → LUMO+5 (41)
257.8	0.1120	HOMO–12 → LUMO+2 (44) HOMO–11 → LUMO+2 (38)
250.9	0.0687	HOMO–14 → LUMO (23) HOMO–4 → LUMO+3 (36) HOMO → LUMO+7 (46)

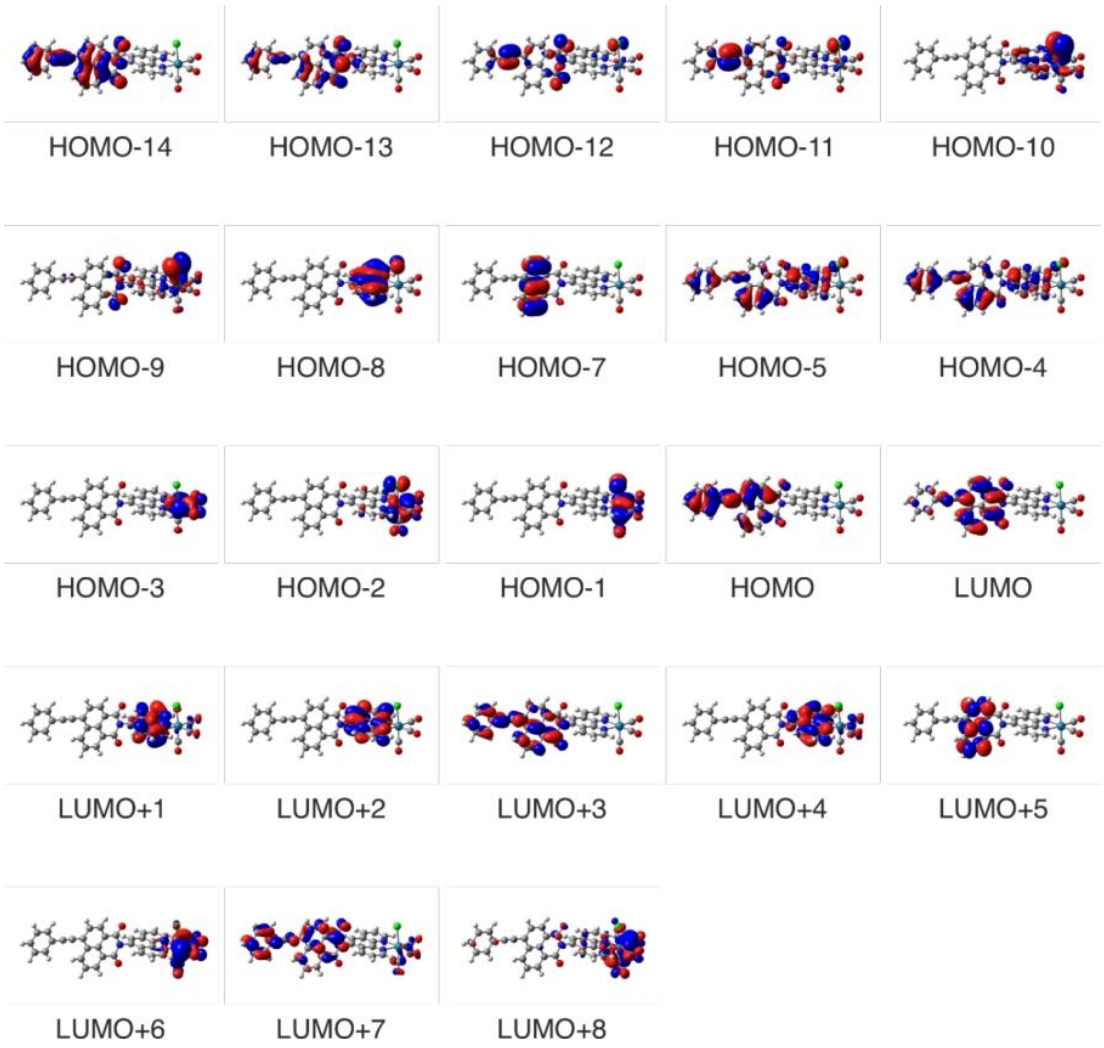


Figure S94. *Molecular orbitals involved in transitions of* ***Re–EB*** *(see* ***Table S3.2****).*

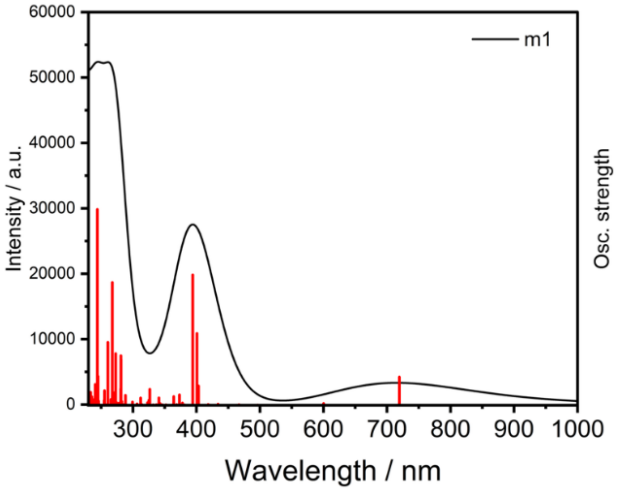


Figure S3.95. *Calculated UV-Vis absorption spectrum of* ***[Re–H]***$^{-}$.

Table S3.28. *Major electronic excitations in* ***[Re–H]***$^{-}$ *determined by TDDFT calculations.*

Wavelength (nm)	Osc. str (*f*)	Major contributions (%)
719.4	0.0716	α–HOSO → α–LUSO+4 (74) α–HOSO → α–LUSO+5 (63)
403.2	0.0489	α–HOSO–3 → α–LUSO (23) α–HOSO–1 → α–LUSO (86) β–HOSO–2 → β–LUSO (42)
400.8	0.1824	α–HOSO–3 → α–LUSO (63) α–HOSO–1 → α–LUSO (45) α–HOSO → α–LUSO+13 (22) β–HOSO–2 → β–LUSO (52)
394.1	0.3316	α–HOSO–3 → α–LUSO (21) α–HOSO → α–LUSO+13 (69) β–HOSO → β–LUSO+2 (59)
281.23	0.1163	α–HOSO–12 → α–LUSO (21) α–HOSO–8 → α–LUSO (28) α–HOSO–7 → α–LUSO+1 (22) α–HOSO–3 → α–LUSO+2 (44) α–HOSO–1 → α–LUSO+2 (20) β–HOSO–11 → β–LUSO (25) β–HOSO–10 → β–LUSO (24) β–HOSO–6 → β–LUSO+1 (22) β–HOSO–2 → β–LUSO+3 (25)
281.17	0.1258	α–HOSO–8 → α–LUSO+1 (20) α–HOSO–5 → α–LUSO+7 (34) α–HOSO–3 → α–LUSO+2 (40) β–HOSO–3 → β–LUSO+8 (38) β–HOSO–2 → β–LUSO+3 (26)
272.8	0.1313	α–HOSO–8 → α–LUSO+1 (49) β–HOSO–10 → β–LUSO+1 (43) β–HOSO–9 → β–LUSO+1 (22) β–HOSO–2 → β–LUSO+5 (22)

Wavelength (nm)	Osc. str (*f*)	Major contributions (%)
267.5	0.3122	α–HOSO–12 → α–LUSO (29) α–HOSO–8 → α–LUSO (27) α–HOSO–7 → α–LUSO+1 (27) α–HOSO–4 → α–LUSO+3 (20) β–HOSO–12 → β–LUSO+1 (20) β–HOSO–11 → β–LUSO (46) β–HOSO–10 → β–LUSO (20) β–HOSO–6 → β–LUSO+1 (20) β–HOSO–4 → β–LUSO+4 (21) β–HOSO–1 → β–LUSO+3 (23) β–HOSO–1 → β–LUSO+5 (27)
260.6	0.1599	α–HOSO–4 → α–LUSO+3 (46) α–HOSO–3 → α–LUSO+6 (21) α–HOSO–3 → α–LUSO+9 (26) β–HOSO–4 → β–LUSO+4 (48) β–HOSO–2 → β–LUSO+7 (22) β–HOSO–2 → β–LUSO+10 (25)
244.1	0.4981	α–HOSO–1 → α–LUSO+7 (72) α–HOSO → α–LUSO+39 (22) β–HOSO–7 → β–LUSO+2 (20) β–HOSO → β–LUSO+8 (45)
225.6	0.2410	α–HOSO–7 → α–LUSO+2 (35) α–HOSO–6 → α–LUSO+4 (24) α–HOSO–6 → α–LUSO+5 (29) β–HOSO–17 → β–LUSO+1 (20) β–HOSO–6 → β–LUSO+3 (44) β–HOSO–5 → β–LUSO+5 (40)
215.5	0.1879	α–HOSO–20 → α–LUSO (27) α–HOSO–4 → α–LUSO+6 (20) α–HOSO–4 → α–LUSO+9 (21) α–HOSO–1 → α–LUSO+13 (23) β–HOSO–19 → β–LUSO (29) β–HOSO–4 → β–LUSO+7 (20) β–HOSO–4 → β–LUSO+10 (23) β–HOSO → β–LUSO+19 (21)
214.6	0.1246	α–HOSO–15 → α–LUSO (28) α–HOSO–5 → α–LUSO+7 (25) α–HOSO–1 → α–LUSO+13 (41) β–HOSO–13 → β–LUSO+2 (23) β–HOSO–5 → β–LUSO+7 (23) β–HOSO–3 → β–LUSO+8 (20) β–HOSO → β–LUSO+18 (26) β–HOSO → β–LUSO+19 (33)

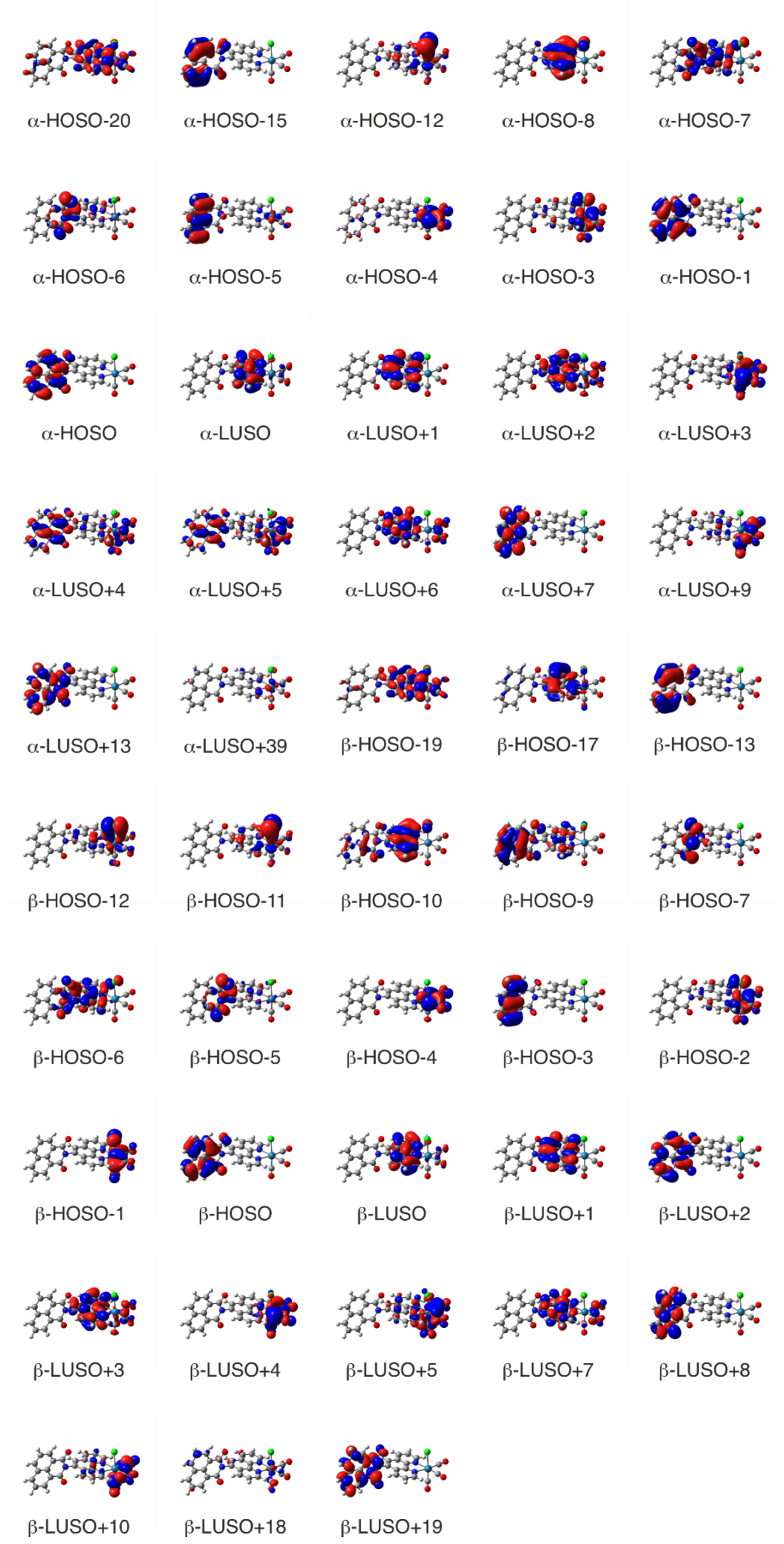


Figure S3.96. *Molecular orbitals involved in electronic transitions of* ***[Re–H]***$^{-}$ *(listed in* ***Table S3.3****).*

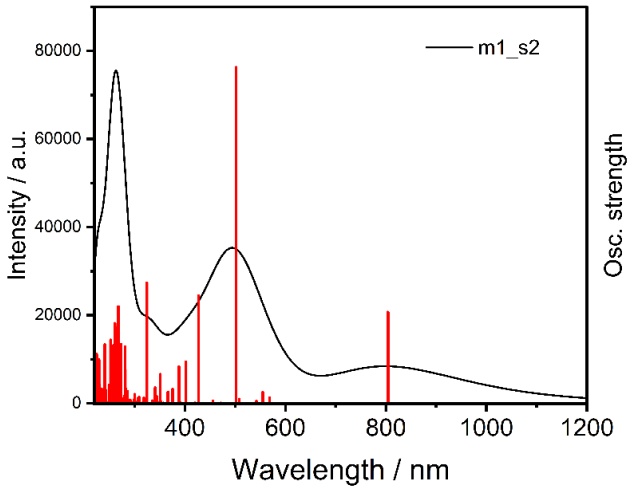


Figure S3.97. *Calculated UV-Vis absorption spectrum of* ***[Re–EB]***$^{-}$.

Table S3.29. *Major electronic excitations in* ***[Re–EB]***$^{-}$ *determined by TDDFT calculations.*

Wavelength (nm)	Osc. str (*f*)	Major contributions (%)
804.0	0.1847	α–HOSO → α–LUSO+2 (98)
501.9	0.6780	α–HOSO → α–LUSO+6 (75) β–HOSO → β–LUSO+1 (22) β–HOSO → β–LUSO+2 (54)
427.2	0.2182	α–HOSO–1 → α–LUSO+2 (35) α–HOSO → α–LUSO+14 (66) β–HOSO–3 → β–LUSO+2 (37) β–HOSO → β–LUSO+4 (37)
401.9	0.0846	α–HOSO–3 → α–LUSO (69) β–HOSO–2 → β–LUSO (69)
387.8	0.0747	α–HOSO–1 → α–LUSO+2 (44) α–HOSO → α–LUSO+11 (22) α–HOSO → α–LUSO+14 (63) β–HOSO–3 → β–LUSO+2 (31) β–HOSO → β–LUSO+4 (31)
350.8	0.0593	α–HOSO–4 → α–LUSO+2 (29) α–HOSO–1 → α–LUSO+6 (24) β–HOSO–4 → β–LUSO+1 (22) β–HOSO–4 → β–LUSO+2 (59) β–HOSO–3 → β–LUSO+2 (30) β–HOSO–3 → β–LUSO+4 (25) β–HOSO → β–LUSO+9 (22)
340.7	0.0323	α–HOSO–4 → α–LUSO+2 (30) α–HOSO–1 → α–LUSO+6 (33) β–HOSO–13 → β–LUSO+2 (24) β–HOSO–4 → β–LUSO+2 (48) β–HOSO–3 → β–LUSO+4 (32) β–HOSO → β–LUSO+4 (21) β–HOSO → β–LUSO+10 (27)

Wavelength (nm)	Osc. str (*f*)	Major contributions (%)
324.2	0.2434	α–HOSO–1 → α–LUSO+2 (71) β–HOSO → β–LUSO+4 (62)
281.0	0.1151	α–HOSO–14 → α–LUSO (27) α–HOSO–13 → α–LUSO (20) α–HOSO–11 → α–LUSO (30) α–HOSO–9 → α–LUSO+1 (23) α–HOSO–3 → α–LUSO+3 (30) β–HOSO–14 → β–LUSO (30) β–HOSO–11 → β–LUSO+1 (28) β–HOSO–10 → β–LUSO (27)
273.2	0.1199	α–HOSO–15 → α–LUSO (23) α–HOSO–12 → α–LUSO+1 (24) α–HOSO–11 → α–LUSO+1 (40) α–HOSO–10 → α–LUSO (44) β–HOSO–15 → β–LUSO (23) β–HOSO–10 → β–LUSO+1 (37)
267.6	0.1485	α–HOSO–15 → α–LUSO+1 (21) α–HOSO–9 → α–LUSO+1 (22) β–HOSO–15 → β–LUSO+1 (30) β–HOSO–14 → β–LUSO (42) β–HOSO–10 → β–LUSO+3 (24) β–HOSO–1 → β–LUSO+3 (20) β–HOSO–1 → β–LUSO+6 (21) β–HOSO → β–LUSO+7 (30)
267.3	0.1959	α–HOSO–15 → α–LUSO+1 (24) α–HOSO–14 → α–LUSO (41) α–HOSO–11 → α–LUSO+3 (21) α–HOSO–2 → α–LUSO+2 (21) α–HOSO–2 → α–LUSO+3 (20) α–HOSO–2 → α–LUSO+5 (22) β–HOSO–10 → β–LUSO (21) β–HOSO–8 → β–LUSO+1 (22) β–HOSO → β–LUSO+7 (39)
261.0	0.1558	α–HOSO–10 → α–LUSO+1 (28) α–HOSO–1 → α–LUSO+9 (55) α–HOSO → α–LUSO+34 (20) α–HOSO → α–LUSO+37 (23) β–HOSO–11 → β–LUSO+2 (20) β–HOSO → β–LUSO+9 (25) β–HOSO → β–LUSO+10 (23)
260.6	0.1619	α–HOSO–5 → α–LUSO+4 (46) α–HOSO–3 → α–LUSO+8 (20) α–HOSO–3 → α–LUSO+11 (25) β–HOSO–5 → β–LUSO+5 (45) β–HOSO–2 → β–LUSO+7 (20) β–HOSO–2 → β–LUSO+12 (26)

Wavelength (nm)	Osc. str (*f*)	Major contributions (%)
257.6	0.1174	α–HOSO–4 → α–LUSO+2 (23) α–HOSO–1 → α–LUSO+6 (25) α–HOSO–1 → α–LUSO+9 (26) β–HOSO–13 → β–LUSO+2 (26) β–HOSO–3 → β–LUSO+4 (48) β–HOSO → β–LUSO+10 (40)
252.8	0.0879	α–HOSO–10 → α–LUSO+2 (52) α–HOSO–4 → α–LUSO+2 (28) α–HOSO → α–LUSO+35 (22) α–HOSO → α–LUSO+40 (22) α–HOSO → α–LUSO+41 (34) β–HOSO–3 → β–LUSO+4 (26)
251.9	0.1285	α–HOSO–4 → α–LUSO+2 (27) α–HOSO → α–LUSO+37 (25) α–HOSO → α–LUSO+41 (33) α–HOSO → α–LUSO+42 (42) β–HOSO–13 → β–LUSO+1 (26) β–HOSO–3 → β–LUSO+4 (25) β–HOSO–2 → β–LUSO+4 (29)

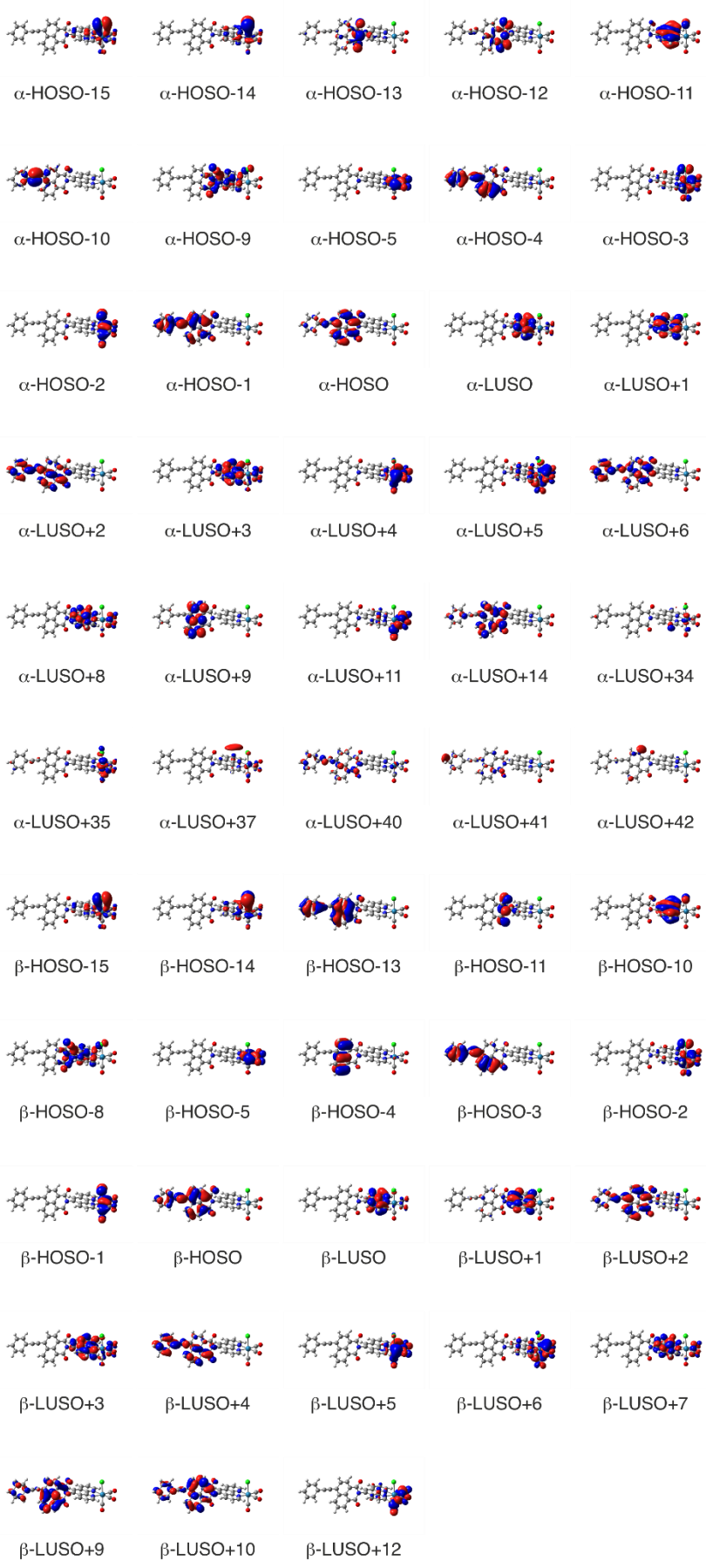


Figure S3.98. *Molecular orbitals involved in the transitions of* ***[Re–EB]⁻*** *(see* ***Table S3.4****).*

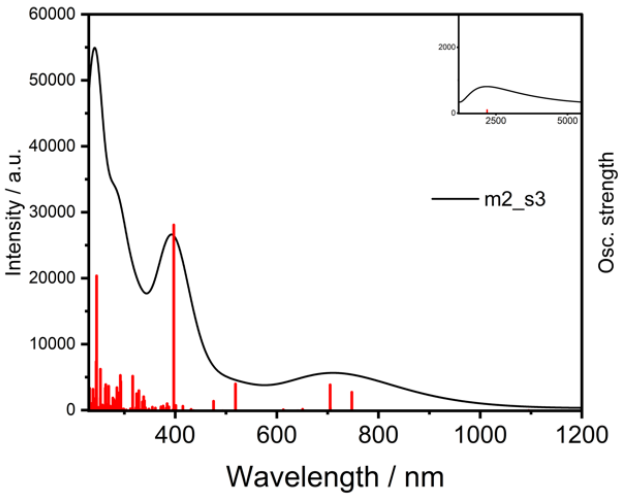


Figure S3.99. *Calculated UV-Vis absorption spectrum of* ***^{3}[Re–H]$^{2-}$****.*

Table S3.30. *Major electronic excitations in* ***^{3}[Re–H]$^{2-}$*** *determined by TDDFT calculations.*

Wavelength (nm)	Osc. str (*f*)	Major contributions (%)
704.8	0.0648	α-HOSO-1 → α-LUSO+1 (91) α-HOSO → α-LUSO+3 (33)
518.6	0.0679	α-HOSO → α-LUSO+7 (81) α-HOSO → α-LUSO+8 (53)
397.2	0.4690	α-HOSO-1 → α-LUSO+11 (53) α-HOSO-1 → α-LUSO+12 (45) β-HOSO → β-LUSO (58)
328.7	0.0510	α-HOSO-6 → α-LUSO (44) α-HOSO-4 → α-LUSO (28) α-HOSO-3 → α-LUSO (40) α-HOSO-2 → α-LUSO+2 (36) β-HOSO-5 → β-LUSO+1 (40) β-HOSO-1 → β-LUSO+4 (21)
316.5	0.0872	α-HOSO-2 → α-LUSO+2 (28) β-HOSO-5 → β-LUSO+1 (42) β-HOSO-3 → β-LUSO+2 (32) β-HOSO-2 → β-LUSO+2 (50) β-HOSO-1 → β-LUSO+4 (20)
292.9	0.0734	α-HOSO-6 → α-LUSO (33) α-HOSO → α-LUSO+31 (30) β-HOSO-5 → β-LUSO (36) β-HOSO-4 → β-LUSO (56) β-HOSO-3 → β-LUSO (35) β-HOSO-3 → β-LUSO+2 (33)
292.6	0.0632	α-HOSO-6 → α-LUSO (31) α-HOSO → α-LUSO+31 (54) β-HOSO-4 → β-LUSO (44) β-HOSO-4 → β-LUSO+2 (39) β-HOSO-3 → β-LUSO (24)

Wavelength (nm)	Osc. str (*f*)	Major contributions (%)
292.1	0.0860	α-HOSO-6 → α-LUSO (37) α-HOSO-1 → α-LUSO+24 (22) α-HOSO → α-LUSO+31 (59) β-HOSO-4 → β-LUSO+2 (27) β-HOSO-3 → β-LUSO+2 (21)
285.4	0.0586	α-HOSO-9 → α-LUSO (28) α-HOSO-7 → α-LUSO (44) α-HOSO-3 → α-LUSO+2 (20) β-HOSO-7 → β-LUSO+1 (44) β-HOSO-5 → β-LUSO+2 (37)
269.2	0.0621	α-HOSO-2 → α-LUSO+4 (31) α-HOSO → α-LUSO+33 (21) β-HOSO-7 → β-LUSO+2 (66) β-HOSO-1 → β-LUSO+6 (21) β-HOSO → β-LUSO+4 (20)
263.4	0.0662	α-HOSO-3 → α-LUSO+4 (25) β-HOSO-11 → β-LUSO+1 (36) β-HOSO-10 → β-LUSO+1 (60)
262.6	0.0575	α-HOSO-5 → α-LUSO+3 (48) α-HOSO-5 → α-LUSO+7 (20) α-HOSO-4 → α-LUSO+7 (20) α-HOSO-3 → α-LUSO+7 (43) β-HOSO-4 → β-LUSO+3 (33) β-HOSO-3 → β-LUSO+3 (29)
253.1	0.1048	α-HOSO-10 → α-LUSO (33) α-HOSO-2 → α-LUSO+4 (55) β-HOSO-11 → β-LUSO+1 (20) β-HOSO-1 → β-LUSO+6 (44)
245.5	0.3401	α-HOSO-4 → α-LUSO+5 (53) α-HOSO-3 → α-LUSO+5 (29) β-HOSO-2 → β-LUSO+5 (32) β-HOSO-1 → β-LUSO+5 (22) β-HOSO → β-LUSO+7 (37)

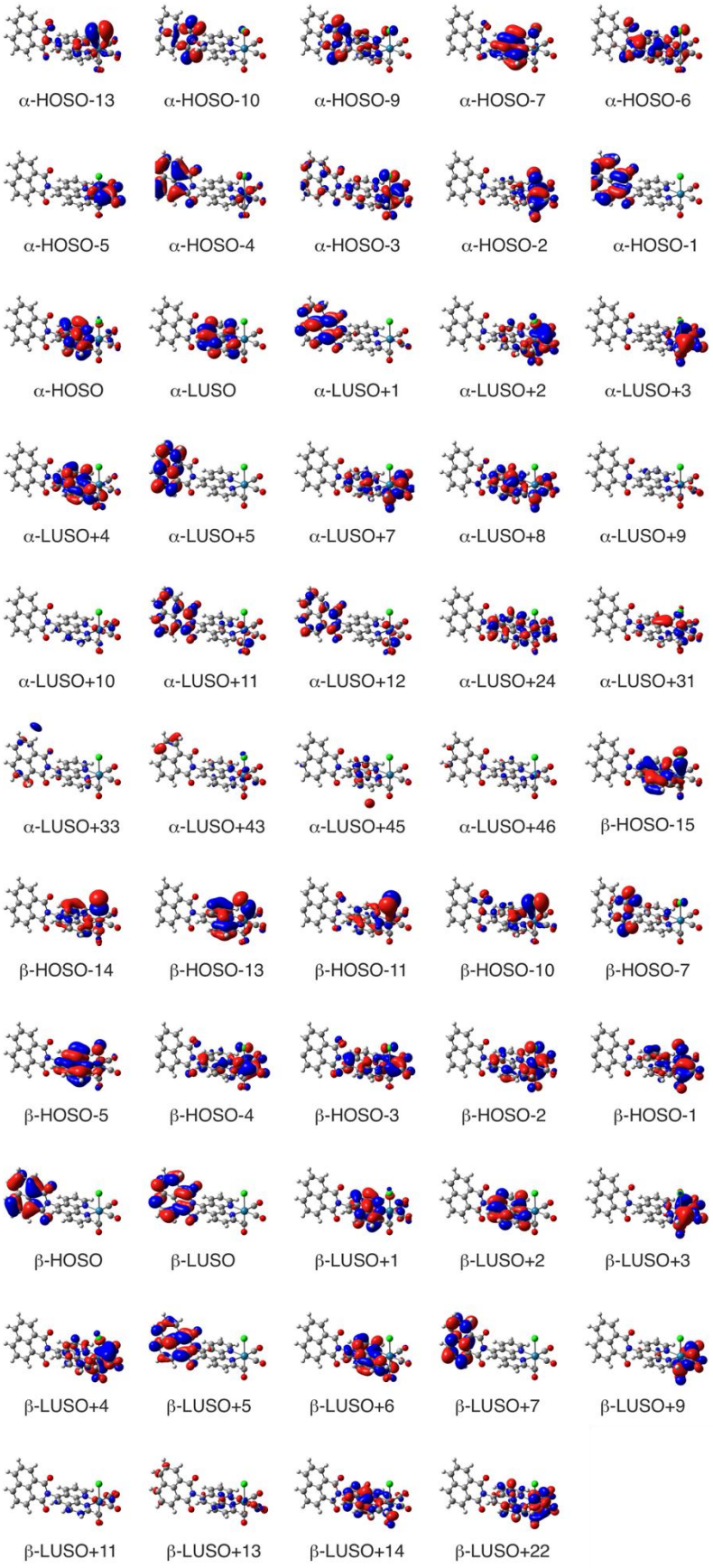


Figure S3.100. *Molecular orbitals involved in electronic transitions of* ^{3}***[Re–H]***$^{2-}$ *(see* ***Table S3.5****).*

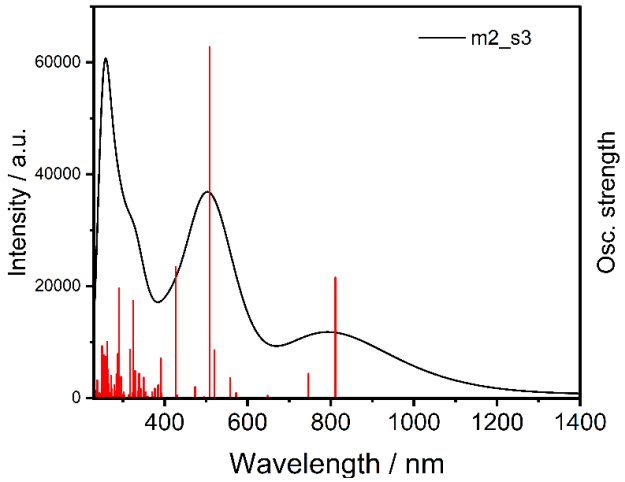


Figure S3.101. *Calculated UV-Vis absorption spectrum of* ***^{3}[Re–EB]$^{2-}$****.*

Table S3.31. *Major electronic excitations in* ***^{3}[Re–EB]$^{2-}$*** *determined by TDDFT calculations.*

Wavelength (nm)	Osc. str (*f*)	Major contributions (%)
811.1	0.2158	α–HOSO–1 → α–LUSO+1 (98)
746.2	0.0441	α–HOSO → α–LUSO+2 (89) α–HOSO → α–LUSO+7 (43)
557.9	0.0368	α–HOSO–1 → α–LUSO+5 (52) α–HOSO–1 → α–LUSO+6 (47) β–HOSO → β–LUSO (64)
519.6	0.0863	α–HOSO → α–LUSO+9 (83) α–HOSO → α–LUSO+11 (34) α–HOSO → α–LUSO+12 (39)
508.1	0.6277	α–HOSO–1 → α–LUSO+4 (26) α–HOSO–1 → α–LUSO+5 (68) β–HOSO → β–LUSO (59)
427.3	0.2351	α–HOSO–2 → α–LUSO+1 (33) α–HOSO–1 → α–LUSO+11 (51) α–HOSO–1 → α–LUSO+12 (45) β–HOSO–6 → β–LUSO (36) β–HOSO → β–LUSO+3 (37)
391.5	0.0714	α–HOSO–2 → α–LUSO+1 (44) α–HOSO–1 → α–LUSO+9 (28) α–HOSO–1 → α–LUSO+11 (48) α–HOSO–1 → α–LUSO+12 (29) β–HOSO–6 → β–LUSO (32) β–HOSO → β–LUSO+3 (32)
349.7	0.0372	α–HOSO–1 → α–LUSO+13 (36) α–HOSO–1 → α–LUSO+14 (29) α–HOSO–1 → α–LUSO+17 (20) β–HOSO–7 → β–LUSO (59) β–HOSO–6 → β–LUSO (22) β–HOSO–6 → β–LUSO+3 (20)

Wavelength (nm)	Osc. str (*f*)	Major contributions (%)
338.9	0.0445	α–HOSO–3 → α–LUSO (42) β–HOSO–4 → β–LUSO+1 (39) β–HOSO–3 → β–LUSO+1 (46) β–HOSO–1 → β–LUSO+2 (50)
329.0	0.0495	α–HOSO–6 → α–LUSO (42) α–HOSO–4 → α–LUSO (43) α–HOSO–3 → α–LUSO+2 (36) β–HOSO–5 → β–LUSO+1 (42) β–HOSO–3 → β–LUSO (22) β–HOSO–1 → β–LUSO+5 (21)
324.9	0.0301	α–HOSO–2 → α–LUSO+1 (23) β–HOSO–8 → β–LUSO (42) β–HOSO–5 → β–LUSO (63) β–HOSO–4 → β–LUSO (47)
324.6	0.1741	α–HOSO–2 → α–LUSO+1 (64) α–HOSO–1 → α–LUSO+18 (25) β–HOSO–6 → β–LUSO (23) β–HOSO → β–LUSO+3 (49)
324.2	0.0328	α–HOSO–2 → α–LUSO+1 (27) α–HOSO–1 → α–LUSO+14 (22) α–HOSO–1 → α–LUSO+18 (64) α–HOSO–1 → α–LUSO+19 (36) α–HOSO–1 → α–LUSO+21 (21) α–HOSO–1 → α–LUSO+25 (34) β–HOSO → β–LUSO+3 (21)
317.2	0.0874	α–HOSO–3 → α–LUSO+2 (32) α–HOSO–1 → α–LUSO+19 (21) β–HOSO–5 → β–LUSO+1 (45) β–HOSO–4 → β–LUSO+2 (24) β–HOSO–3 → β–LUSO+2 (24) β–HOSO–2 → β–LUSO+2 (45) β–HOSO–1 → β–LUSO+5 (20)
295.4	0.0386	α–HOSO–2 → α–LUSO+6 (24) α–HOSO–1 → α–LUSO+23 (25) β–HOSO–13 → β–LUSO (27) β–HOSO–12 → β–LUSO (40) β–HOSO–10 → β–LUSO (61)
290.6	0.0597	α–HOSO–6 → α–LUSO (26) α–HOSO → α–LUSO+27 (28) α–HOSO → α–LUSO+28 (23) α–HOSO → α–LUSO+31 (38) α–HOSO → α–LUSO+38 (51) α–HOSO → α–LUSO+40 (24) α–HOSO → α–LUSO+42 (20) β–HOSO–4 → β–LUSO+2 (24)
290.3	0.1974	α–HOSO–6 → α–LUSO (46) α–HOSO → α–LUSO+38 (26) β–HOSO–4 → β–LUSO+2 (40) β–HOSO–3 → β–LUSO+2 (22)

Wavelength (nm)	Osc. str (*f*)	Major contributions (%)
287.4	0.0797	α–HOSO–7 → α–LUSO (27) α–HOSO–6 → α–LUSO (22) β–HOSO–5 → β–LUSO+2 (50) β–HOSO–2 → β–LUSO+8 (26)
284.2	0.0433	α–HOSO–8 → α–LUSO (28) α–HOSO–7 → α–LUSO (34) α–HOSO–4 → α–LUSO+2 (25) α–HOSO–4 → α–LUSO+7 (22) β–HOSO–8 → β–LUSO+1 (24) β–HOSO–5 → β–LUSO+2 (24) β–HOSO–2 → β–LUSO+8 (20)
271.3	0.0404	α–HOSO–7 → α–LUSO+7 (20) α–HOSO–3 → α–LUSO+7 (31) α–HOSO → α–LUSO+41 (38) β–HOSO–8 → β–LUSO+1 (34) β–HOSO–5 → β–LUSO+8 (21) β–HOSO–1 → β–LUSO+8 (25)
263.2	0.0528	β–HOSO–15 → β–LUSO (20) β–HOSO–12 → β–LUSO (30) β–HOSO–12 → β–LUSO+1 (22) β–HOSO–11 → β–LUSO+1 (33) β–HOSO–10 → β–LUSO (35) β–HOSO–10 → β–LUSO+1 (24) β–HOSO–8 → β–LUSO+2 (21)
262.4	0.0573	α–HOSO–5 → α–LUSO+1 (26) α–HOSO–5 → α–LUSO+3 (46) α–HOSO–4 → α–LUSO+9 (42) β–HOSO–4 → β–LUSO+4 (23) β–HOSO–3 → β–LUSO+4 (34)
261.4	0.1011	α–HOSO–4 → α–LUSO+9 (22) α–HOSO–2 → α–LUSO+6 (47) β–HOSO–2 → β–LUSO+12 (34) β–HOSO → β–LUSO+7 (23)
257.8	0.0749	α–HOSO–2 → α–LUSO+5 (23) α–HOSO–1 → α–LUSO+36 (23) β–HOSO–15 → β–LUSO (25) β–HOSO–6 → β–LUSO+3 (29) β–HOSO–4 → β–LUSO+3 (33) β–HOSO–3 → β–LUSO+3 (35) β–HOSO → β–LUSO+9 (28)
253.5	0.0778	α–HOSO–11 → α–LUSO+1 (42) α–HOSO–3 → α–LUSO+7 (41) α–HOSO → α–LUSO+49 (21) β–HOSO–9 → β–LUSO (27) β–HOSO–9 → β–LUSO+3 (27) β–HOSO–1 → β–LUSO+8 (35)

Wavelength (nm)	Osc. str (*f*)	Major contributions (%)
251.6	0.0590	α–HOSO–16 → α–LUSO+1 (21) α–HOSO–12 → α–LUSO+1 (51) α–HOSO–9 → α–LUSO+1 (20) α–HOSO–8 → α–LUSO+1 (21) β–HOSO–7 → β–LUSO+3 (26) β–HOSO → β–LUSO+11 (26)
251.4	0.0548	α–HOSO–1 → α–LUSO+34 (25) α–HOSO–1 → α–LUSO+36 (22) α–HOSO–1 → α–LUSO+37 (51) α–HOSO–1 → α–LUSO+38 (27) α–HOSO–1 → α–LUSO+39 (20) α–HOSO–1 → α–LUSO+42 (27) β–HOSO–7 → β–LUSO+3 (23)

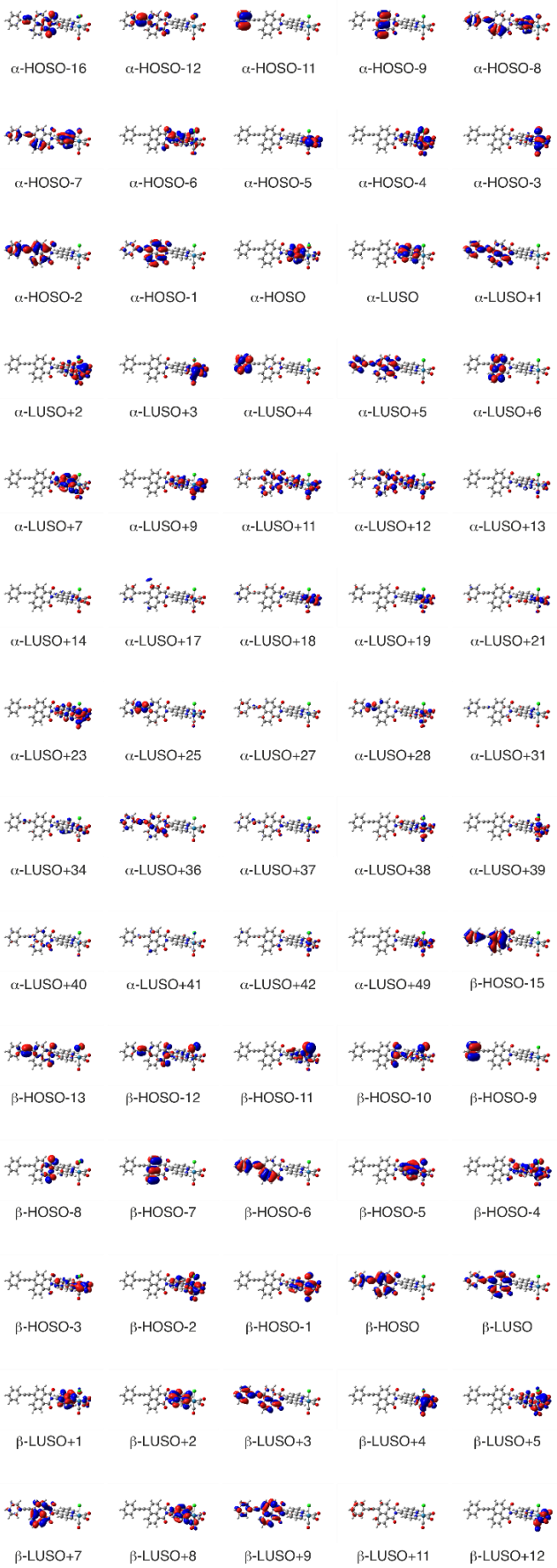


Figure S3.102. *Molecular orbitals involved in the transitions of* ***^{3}[Re–EB]$^{2-}$*** *(see* ***Table S3.6****).*

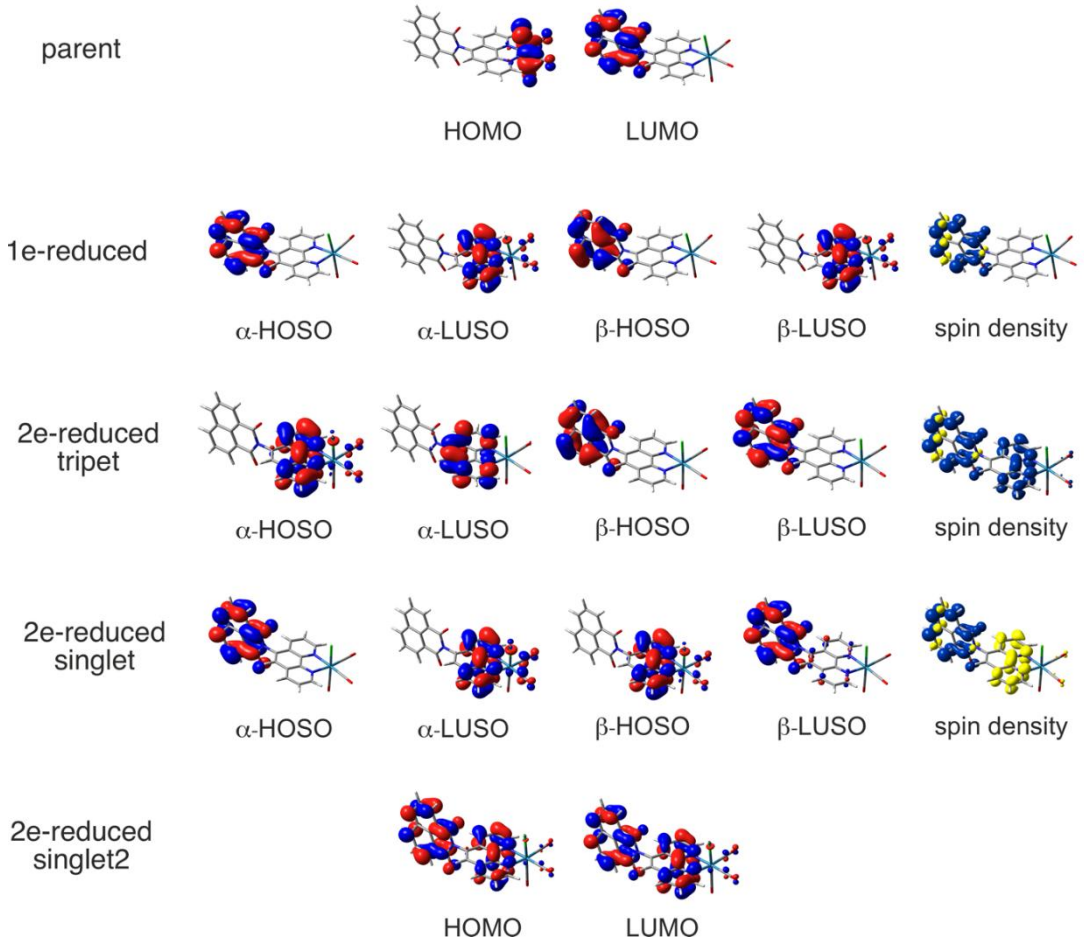


Figure S3.103. *Frontier orbitals (and the spin densities for the biradical species) of the reduced species of* ***Re–H*** *observed in SEC studies.*

Table S3.32. *Energies of different spin states of* ***[Re–H]$^{2-}$***.

state	**localised**	**Δ*E* [kcal mol^{-1}]**
singlet – biradical	phen-NI	0.65
singlet	NI	12.06
triplet – biradical	phen-NI	0.00

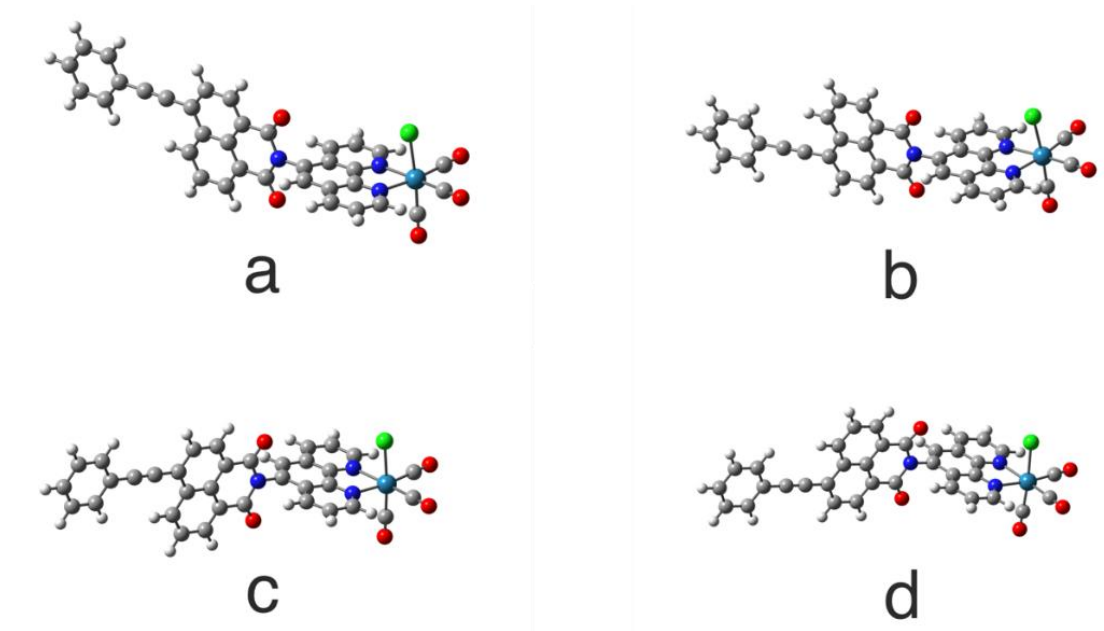


Figure S3.104. *Possible structures of* ***Re–EB****.*

Table S3.33. *Differential energies of structures a–d accompanying* ***Figure S3.41****.*

Re–EB structure	**ΔE [kcal mol^{-1}]**
a	0.000
b	0.093
c	0.000
d	0.094

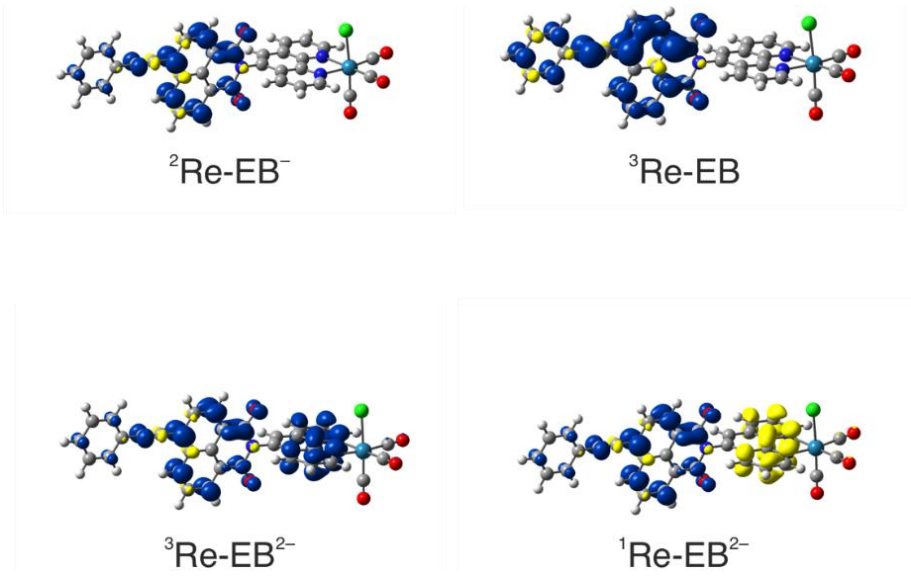


Figure S3.105. *Spin densities of doublet excited state of the 1e^{-} reduced species (*^{2}***[Re–EB]**$^{-}$*), the triplet excited state (*^{3}***Re–EB***), and the 2e^{-} reduced biradical species (*$^{3/1}$***[Re–EB]**$^{2-}$*).*

Table S3.34. *Energies of different spin states of* ***[Re–EB]$^{2-}$***.

state	localised	Δ*E* [kcal mol^{-1}]			
		a	b	c	d
singlet – biradical	NI-phen	0.66	0.66	0.38	0.66
singlets	NI	7.33	7.06	7.07	7.06
triplet – biradical	NI-phen	0.00	0.00	0.00	0.00

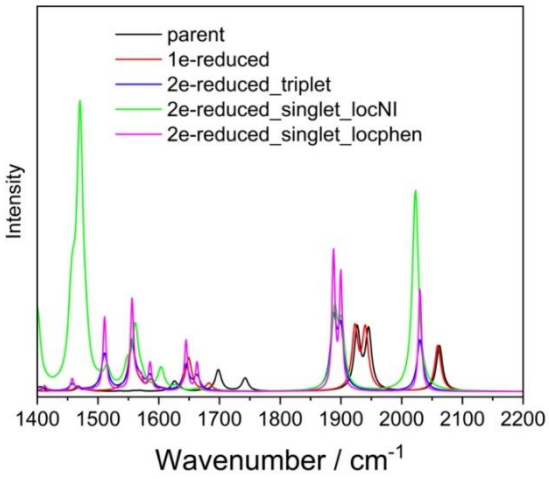


Figure S3.106. *Calculated IR spectra of* ***Re–H*** *and its reduced species.*

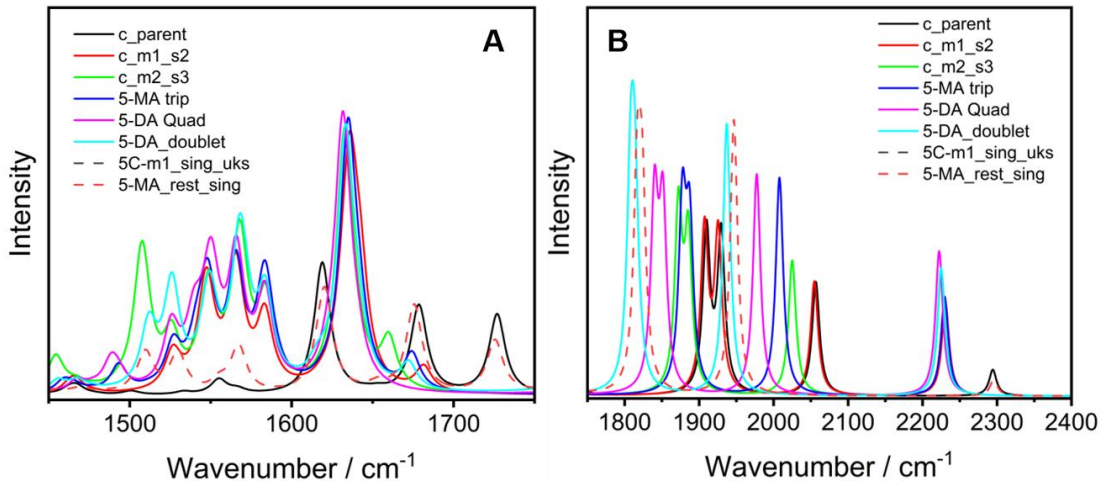


Figure S3.107. *Calculated IR spectra of* ***Re–EB*** *and its reduced species including the 5-coordinate species; parent =* ***Re–EB****, m1_s2 =* ***[Re–EB]$^{-}$****, m2_s3 =* ***^{3}[Re–EB]$^{2-}$****, 5-MA trip =* ***^{3}5–MA****, 5-DA Quad =* ***^{4}5–DA****, 5-DA doublet =* ***^{2}5–DA****, 5-MA_sing =* ***^{1}5–MA****. (A) organic carbonyl region, (B) metal carbonyl and ethynyl regions.*

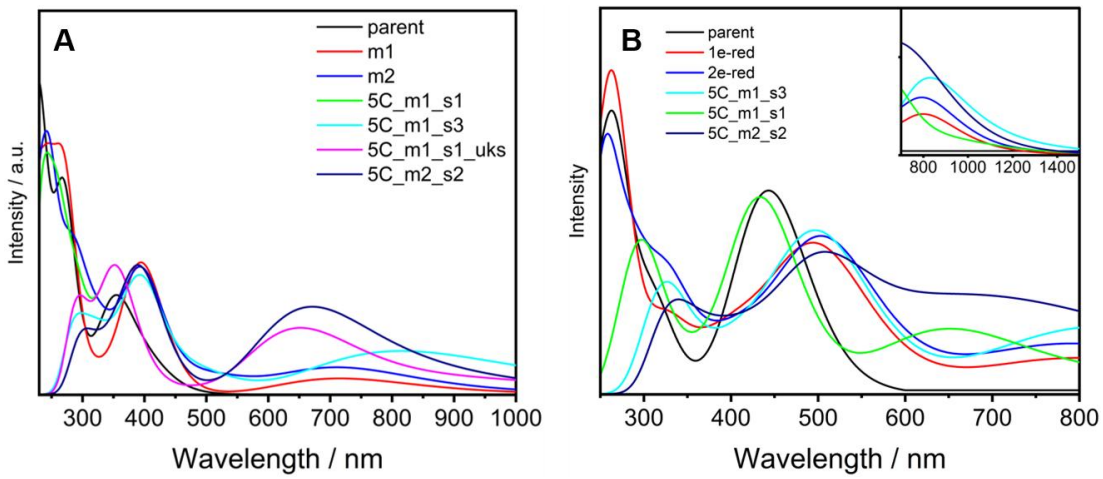


***Figure S3.108**. Calculated UV-Vis absorption spectra of **Re–R** in different redox states. (A) **Re–H** and its reduced species, (B) **Re–EB** and its reduced species; m1 = 1e-red = **[Re–R]**$^{-}$, m2 = 2e-red = **^{3}[Re–R]**$^{2-}$, 5C_m1_s1 = **^{1}5–MA**, 5C_m1_s3 = **^{3}5–MA**, 5C_m1_s2 = **^{2}5–DA**.*

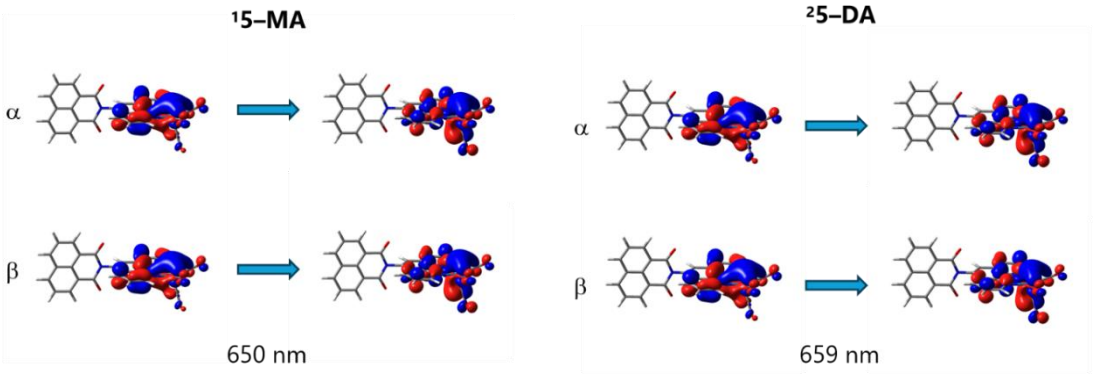


***Figure S3.109.** Visualisation of the orbitals involved in the Re^{0}-phen^{-}⟶CO$_{ax}$ π⟶π* transition of the **^{1}5–MA** and **^{2}5–DA** of **Re–H**.*

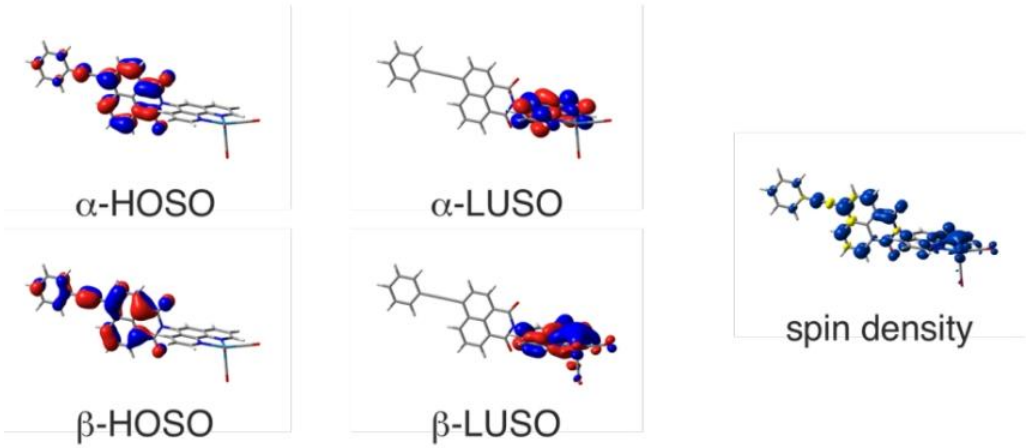


***Figure S3.110.** Frontier orbitals and spin densities of **^{3}5–MA** of **Re–EB**.*

Table S3.35. *Calculated IR modes of the 5-coordinate species of* ***Re–R****.*

IR mode	Re–H			Re–EB		
	^{1}5C–MA[a]	^{3}5C–MA	^{2}5C–DA	^{1}5C–MA[a]	^{3}5C–MA	^{2}5C–DA
$\nu_{C\equiv C}$	–	–	–	2296	2230	2225
$\nu_{C\equiv O}$	1947	2007	1936	1947	2008	1937
	1823	1886	1812	1824	1887	1814
	1817	1877	1807	1817	1878	1808
$\nu_{C=O}$	1728	1674[b]	1672[b]	1726	1674[b]	1672[b]
	1681	1636	1635	1676	1642	1641
	1668	1599	1601	1668	1635	1633
	1664	1539	1541	1654	1583	1584
					1566	1568

[a]*Calculated on UKS level.* [b]*Mostly phen character, but partially contributes to* $\nu_{C=O}$.

S3.7 UV-Vis Monitoring of Photocatalysis

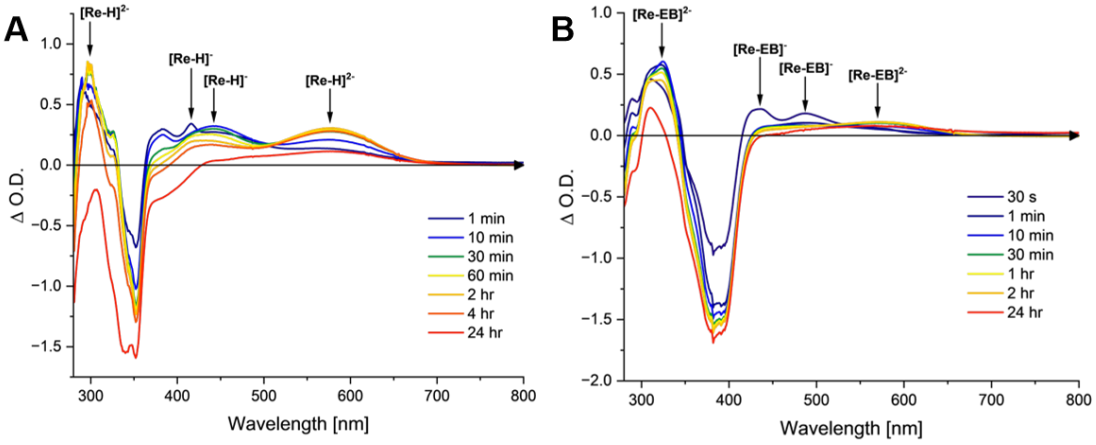


Figure S3.111. *UV-Vis absorbance-difference spectra monitored up to 24 h under photocatalytic conditions of [A]* ***Re–H*** *and [B]* ***Re–EB****.*

S3.8 Bibliography

1 J. Biddulph, M. Pižl, S. Bhattacharya, P. Malakar, G. M. Greetham, F. Hartl and M. T. Pryce, Nature and Dynamics of the Excited States of Ethynyl-Functionalized Naphthalimide–Phenanthroline Re(I) Complexes Studied by TA and TRIR Spectroscopies, *J. Phys. Chem. B*, 2026, **130**, 6383–6398.

2 M. Krejčik, M. Daněk and F. Hartl, Simple construction of an infrared optically transparent thin-layer electrochemical cell: Applications to the redox reactions of ferrocene, $Mn_2(CO)_{10}$ and $Mn(CO)_3$(3,5-di-t-butyl-catecholate)$^-$, *J. Electroanal. Chem. Interfacial Electrochem.*, 1991, **317**, 179–187.

3 G. M. Greetham, P. Burgos, Q. Cao, I. P. Clark, P. S. Codd, R. C. Farrow, M. W. George, M. Kogimtzis, P. Matousek, A. W. Parker, M. R. Pollard, D. A. Robinson, Z.-J. Xin and M. Towrie, Ultra: A Unique Instrument for Time-Resolved Spectroscopy, *Appl Spectrosc*, 2010, **64**, 1311–1319.

4 J. J. Snellenburg, S. Laptenok, R. Seger, K. M. Mullen and I. H. M. van Stokkum, Glotaran: A Java-Based Graphical User Interface for the R Package TIMP, *J. Stat. Soft.*, 2012, **49**, 1–22.

5 M. J. Frisch, G. W. Trucks, H. B. Schlegel, G. E. Scuseria, M. A. Robb, J. R. Cheeseman, G. Scalmani, V. Barone, G. A. Petersson, H. Nakatsuji, X. Li, M. Caricato, A. V. Marenich, J. Bloino, B. G. Janesko, R. Gomperts, B. Mennucci, H. P. Hratchian, J. V. Ortiz, A. F. Izmaylov, J. L. Sonnenberg, D. Williams-Young, F. Ding, F. Lipparini, F. Egidi, J. Goings, B. Peng, A. Petrone, T. Henderson, D. Ranasinghe, V. G. Zakrzewski, J. Gao, N. Rega, G. Zheng, W. Liang, M. Hada, M. Ehara, K. Toyota, R. Fukuda, J. Hasegawa, M. Ishida, T. Nakajima, Y. Honda, O. Kitao, H. Nakai, T. Vreven, K. Throssell, J. A. Montgomery, Jr., J. E. Peralta, F. Ogliaro, M. J. Bearpark, J. J. Heyd, E. N. Brothers, K. N. Kudin, V. N. Staroverov, T. A. Keith, R. Kobayashi, J. Normand, K. Raghavachari, A. P. Rendell, J. C. Burant, S. S. Iyengar, J. Tomasi, M. Cossi, J. M. Millam, M. Klene, C. Adamo, R. Cammi, J. W. Ochterski, R. L. Martin, K. Morokuma, O. Farkas, J. B. Foresman and D. J. Fox, Gaussian 16, Revision C.01, *Gaussian, Inc., Wallingford CT*.

6 A. D. Becke, Density-functional thermochemistry. III. The role of exact exchange, *J Chem Phys*, 1993, **98**, 5648–5652.

7 C. Lee, W. Yang and R. G. Parr, Development of the Colle-Salvetti correlation-energy formula into a functional of the electron density, *Phys. Rev. B*, 1988, **37**, 785–789.

8 D. Andrae, U. Häußermann, M. Dolg, H. Stoll and H. Preuß, Energy-adjustedab initio pseudopotentials for the second and third row transition elements, *Theoret. Chim. Acta*, 1990, **77**, 123–141.

9 R. Krishnan, J. S. Binkley, R. Seeger and J. A. Pople, Self-consistent molecular orbital methods. XX. A basis set for correlated wave functions, *J. Chem. Phys.*, 1980, **72**, 650–654.

10 M. Cossi, N. Rega, G. Scalmani and V. Barone, Energies, structures, and electronic properties of molecules in solution with the C-PCM solvation model, *J Comput Chem*, 2003, **24**, 669–681.

Appendix C

Supplementary information associated with Chapter 4

S4.1 Experimental

Synthesis

Naphthalic-1,8-anhydride, 4-bromo-naphthalic-1,8-anhydride, 5-amino-1,10-phenanthroline, and tetra n-butyl ammonium hexafluorophosphate ($TBAPF_6$) reagents were acquired from Fluorochem. All spectroscopic solvents were acquired from Fisher Scientific. $[Mn(CO)_5Br]$, 1,10-phenanthroline, and all other solvents were acquired from Sigma-Aldrich. The synthesis of **EB–NA**, **H–NI–phen**, and **EB–NI–phen** was conducted according to literature procedures as detailed in Appendix A.[1–3] All manganese complexes were synthesised according to a modified literature procedure for $[Mn(phen)(CO)_3Br]$ using THF the reaction solvent.[4] The **Mn–R** are characterised by FTIR and ^1H NMR spectroscopies. The novel complexes, **Mn–H** and **Mn–EB**, are further characterised by elemental analysis.

Synthesis of $[Mn(phen)(CO)_3Br]$ ***[Mn–phen]***

$[Mn(CO)_5Br]$ (0.0678 g, 0.25 mmol) and 1,10-phenanthroline (0.0451 g, 0.25 mmol) were dried under vacuum in a pre-dried Schlenk tube. After 10 minutes of drying, 4 cm^3 dry THF was added under N_2 atmosphere. The reaction solution was heated to 60 °C and stirred for ~16 hours. The solvent was removed in vacuo, then washed with 2 x 2 cm^3 pentane which was also removed in vacuo after each washing. The final drying in vacuo was performed for a further 30 minutes after solvent removal to sublimate any remaining $[Mn(CO)_5Br]$ to obtain the purified yellow product as a powder. Yield: 0.0671 g (67 %).^1H NMR ($CDCl_3$, 600 MHz): δ (ppm) = 9.56 (dd, J = 3.99, 15.57 Hz, 2H), 8.48 (d, J = 7.58 Hz, 2H), 7.99 (d, J = 2.79 Hz, 2H), 7.87 (dd, J = 7.18, 8.58 Hz, 2H). FTIR in THF calcd (found): $\nu_{C\equiv O}$ = 2024 (2024), 1956 (1937), 1946 (1915).

Synthesis of $[Mn(H\text{-}NI\text{-}phen)(CO)_3Br]$ ***[Mn–H]***

The reaction was carried out as described for **Mn–phen** with the following quantities: $[Mn(CO)_5Br]$ (0.0271 g, 0.10 mmol) and **H–NI–phen** (0.0375 g, 0.10 mmol). A yellow powder was collected as the reaction product. Yield: 0.0248 g (42%). ^1H NMR ($CDCl_3$, 600 MHz): δ (ppm) = 9.60 (d, J = 25.90 Hz, 2H), 8.77 (s, 2H), 8.52 (s, 2H), 8.73 (d, J = 20.44 Hz, 2H), 8.07 (s, 1H), 7.96 (d, J = 27.26 Hz, 2H), 7.81 (s, 1H). FTIR in THF calcd (found): $\nu_{C\equiv O}$ = 2015 (2024), 1946 (1937), 1937 (1915), $\nu_{C=O}$ = 1726 (1717), 1695 (1683). Elem. Anal. calcd (found) for $C_{27}H_{13}BrMnN_3O_5$: C, 54.57 (51.75); H, 2.21 (2.65); N, 7.07 (5.07).

Synthesis of [Mn(EB-NI-phen)(CO)$_3$Br] ***[Mn–EB]***

The reaction was carried out as described for **Mn–phen** using the following quantities: [Mn(CO)$_5$Br] (0.0506 g, 0.19 mmol) and **EB–NI–phen** (0.0476 g, 0.1 mmol). The product was analysed by FTIR spectroscopy after drying under in vacuo to determine if any unreacted [Mn(CO)$_5$Br] remained; further drying under vacuum was performed to sublime any excess remaining. This was repeated until no peaks belonging [Mn(CO)$_5$Br] were observed in the FTIR spectrum. A mustard-yellow powder was collected as the reaction product. Yield: 0.0567 g (82%). ^{1}H NMR ($CDCl_3$, 600 MHz): δ (ppm) = 9.60 (d, J = 23.17 Hz, 2H), 8.71 (m, 3H), 8.49 (s, 1H), 8.40 (s, 2H), 8.34 (s, 1H), 8.23 (s, 1H), 8.06 (s, 1H), 7.85 (m, 6H). FTIR in THF calcd (found): $\nu_{C\equiv C}$ = 2197 (2206), $\nu_{C\equiv O}$ = 2015 (2024), 1947 (1936), 1938 (1915), $\nu_{C=O}$ = 1725 (1715), 1693 (1684). Elem. Anal. calcd (found) for $C_{35}H_{17}BrMnN_3O_5$: C, 60.54 (58.55); H, 2.47 (2.94); N, 6.05 (5.25).

FTIR Spectroscopy

All FTIR spectra were recorded on a Shimadzu IRAffinity-1S FTIR Spectrometer. Samples were prepared in spectroscopic grade THF and loaded into a liquid-film IR cell with a CaF_2 window. IR spectra were obtained from a difference spectrum of the sample solution spectrum less the solvent spectrum using Spectragryph v1.2.16.1. For IR SEC studies, a Shimadzu IRAffinity-1S FTIR Spectrometer was used.

UV-Vis Absorption Spectroscopy

All UV-Vis absorption spectra were recorded on a Horiba Duetta Fluorescence and Absorbance Spectrometer. Samples were recorded in a quartz cuvette with a 1 cm path length and prepared in spectroscopic grade THF. Normalisation of spectra was completed using Spectragryph v1.2.16.1. For UV-Vis SEC studies, an Agilent 8453 UV-Visible Spectrophotometer was used.

Electrochemistry

10 cm^3 of 1 mM sample solutions were prepared using a 0.1 M electrolyte solution of $TBAPF_6$ in the solvent of choice. Samples were degassed with N_2 or CO_2 for 5 mins, experiments were carried out with a continuous flow of this gas across the surface of the solution. A PalmSens4 device was used as the potentiostat with a glassy carbon working electrode, Pt wire counter

electrode, and Ag^+/Ag wire pseudo-reference electrode in a V-shaped cell, with a ferrocene standard added as an internal reference at the end of each sample use.

Spectroelectrochemistry

1 cm^3 of 4 mM sample solutions were prepared in 0.1 M electrolyte solution of $TBAPF_6$ in solvent of choice. The electrolyte and sample were vacuum-dried prior to dissolving the sample in a Schlenk tube under a N_2 or CO_2 atmosphere. 200 µL aliquots were used to load the sample into an optically transparent, thin−layer electrochemical (OTTLE) cell. Spectroscopic results of IR SEC and UV-Vis SEC studies were collected as described for those spectroscopic techniques. A PalmSens4 electrochemical device was used as the potentiostat. Electrochemical scans were conducted with negative potential sweeps, using the corresponding potentials determined from electrochemical studies to study the observed reduction.

Controlled Potential Electrolysis

Controlled potential electrolysis was performed with 25 cm^3 of 0.8 mM samples in a 5% H_2O in THF electrolyte solution in a H-cell. The main compartment was fitted with a glassy carbon working electrode (d = 0.3 cm) and an Ag^+/Ag reference electrode. The reference electrode consisted of a Ag wire in 0.1 M $TBAPF_6$/THF supporting electrolyte isolated by a glass frit, which was calibrated *in situ* using the Fc^+/Fc redox couple as a pseudo-reference. A Pt gauze counter electrode was separated from the main compartment by a glass frit bridge. A PalmSens4 potentiostat was used to perform chronoamperometric scans; fixed to a held overpotential with constant stirring at 600 rpm and shielded from light. After 1 h, a 1 cm^3 aliquot of the headspace was analysed by gas chromatography with a Shimadzu-GC2010 fitted with a BID detector. CO and H_2 in the headspace were quantified by comparing with a 1000 ppm standard.

DFT Calculations

Structure optimisation and frequency calculations were conducted using MN15/def2TZVP for Mn, 6-31g(d) for all other atoms/smd, THF solvent continuum. Single-point energy frequency and TDDFT calculations were conducted using MN15/def2TZVP for Mn, 6-311+G(2df,p) for all other atoms/smd, THF solvent continuum. DFT-calculated IR spectra were normalised corrected

by a correction factor which was determined by calculating the ratio of both highest energy $\nu_{C\equiv O}$ stretches.

S4.2 ^{1}H NMR Spectra

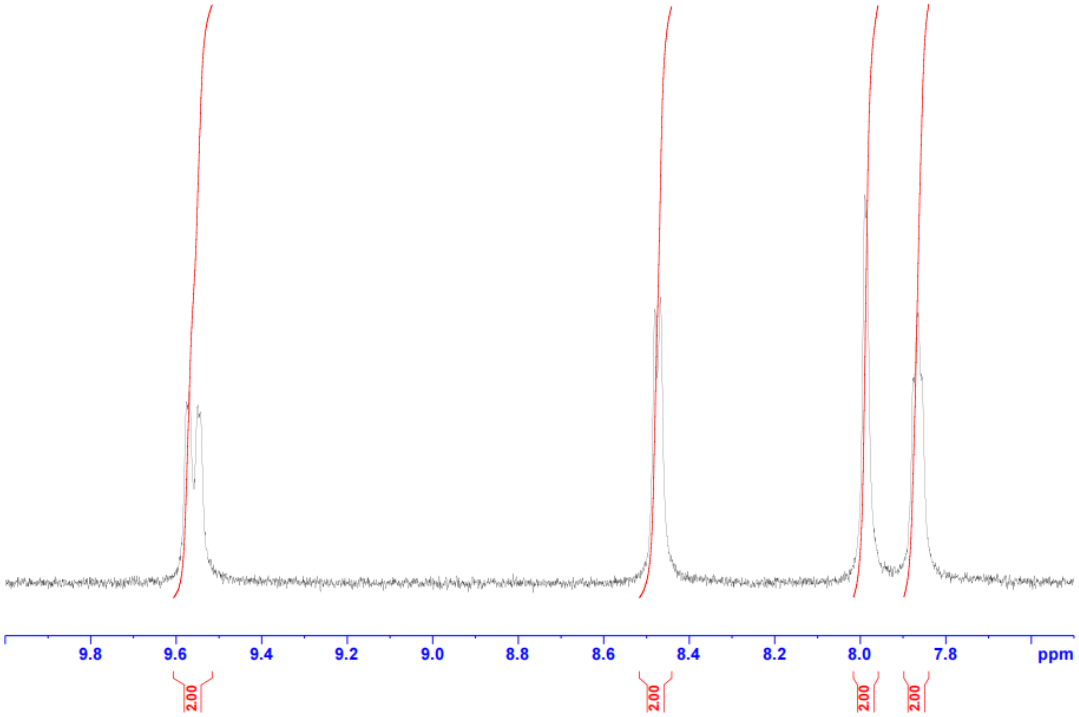


Figure S4.112. *^{1}H NMR spectrum of* ***Mn–phen*** *in $CDCl_3$.*

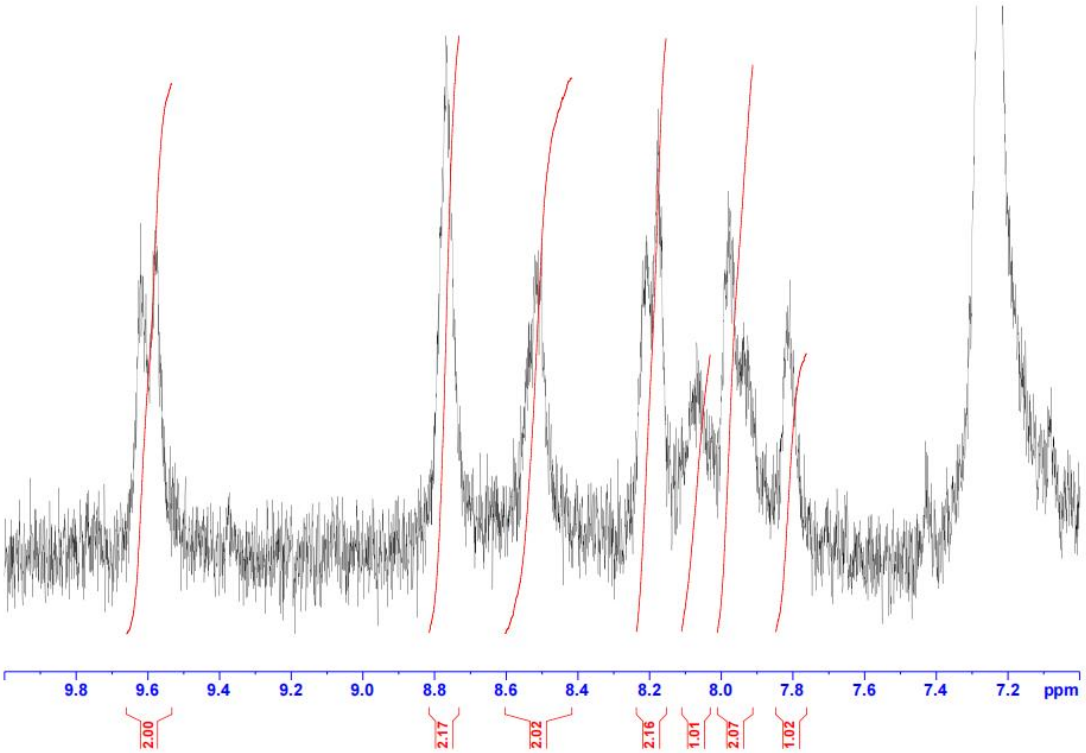


Figure S4.113. *^{1}H NMR spectrum of* ***Mn–H*** *in $CDCl_3$.*

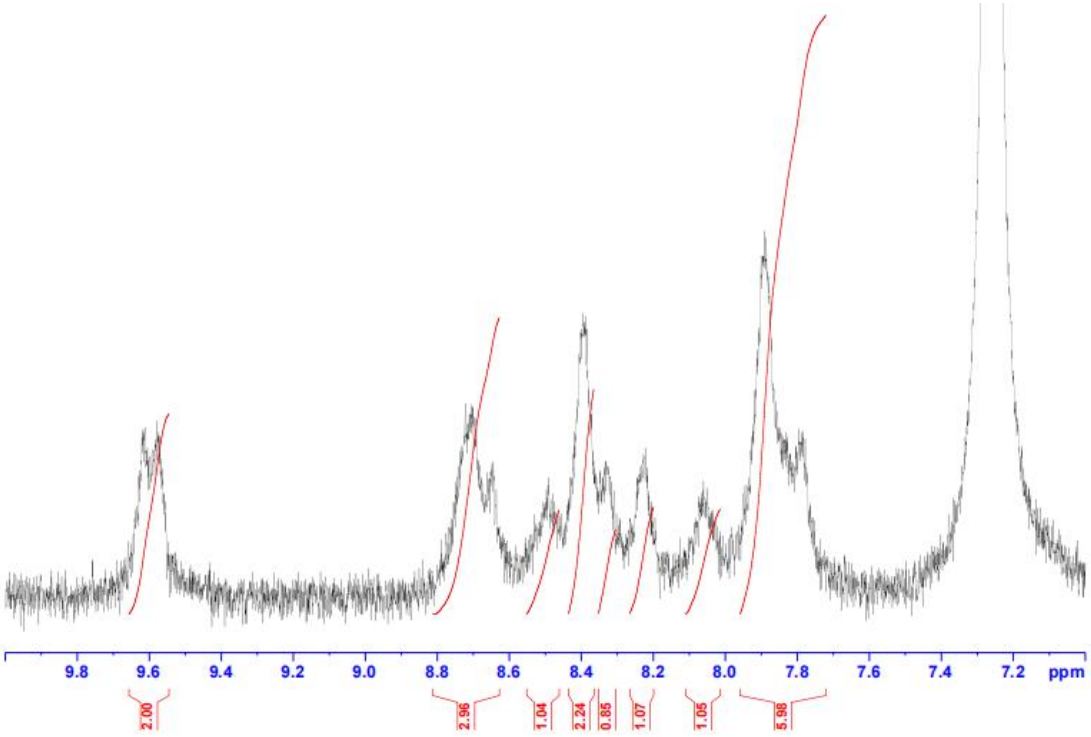


Figure S4.114. *^{1}H NMR spectrum of* ***Mn–EB*** *in $CDCl_3$.*

S4.3 Cyclic Voltammetry

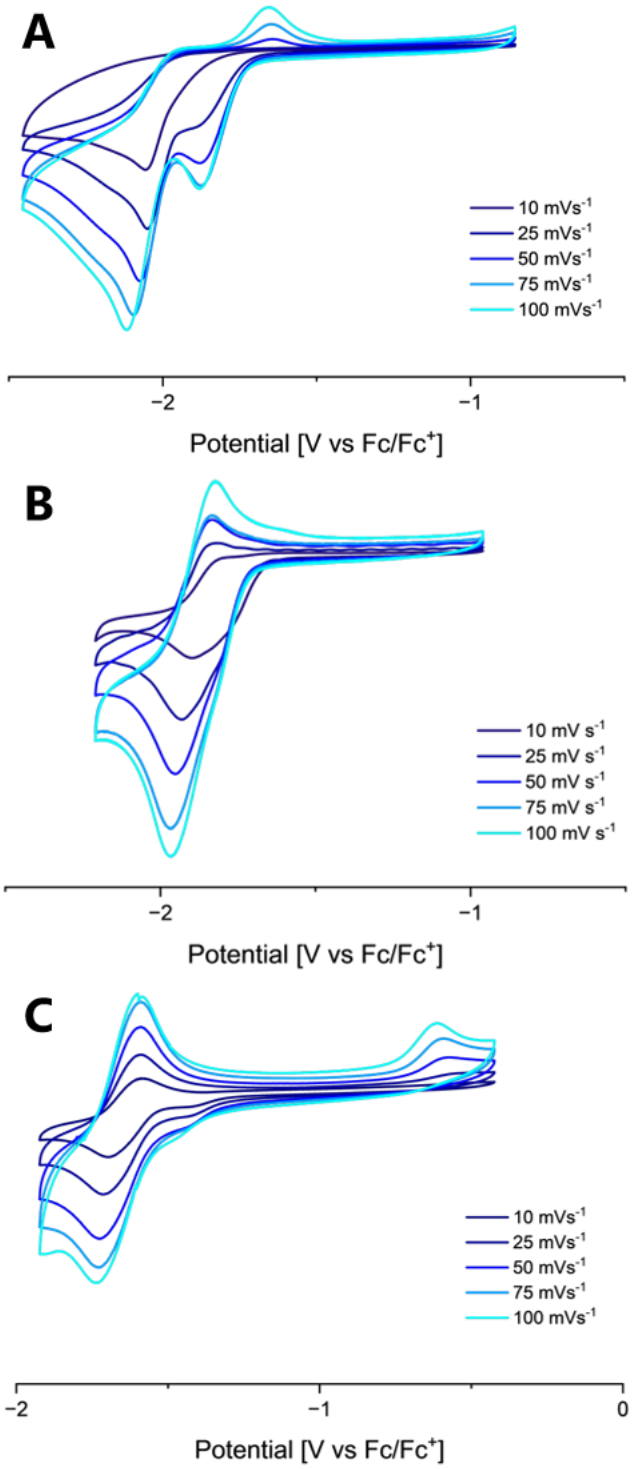


Figure S4.115. *Reversibility studies at scan rates between 10–100 mV* s^{-1} *of (A)* ***Mn–phen****, (B)* ***Mn–H****, and (C)* ***Mn–EB****.*

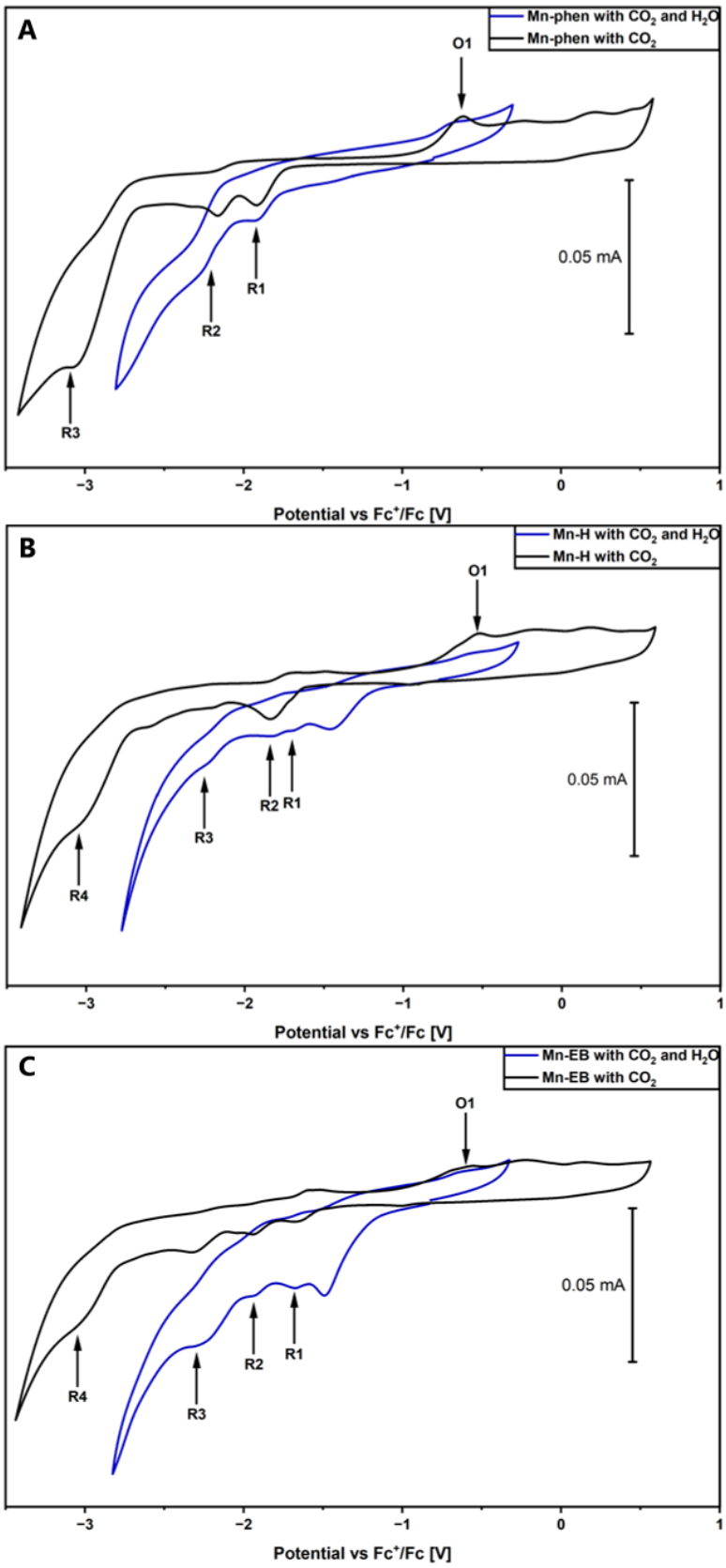


Figure S4.116. *The cyclic voltammograms of* ***Mn–R*** *in the THF electrolyte under a CO_2 atmosphere and in the 5% H_2O in THF electrolyte under a CO_2 atmosphere. (A)* ***Mn–phen****, (B)* ***Mn–H****, and (C)* ***Mn–EB****.*

S4.4 Spectroelectrochemistry

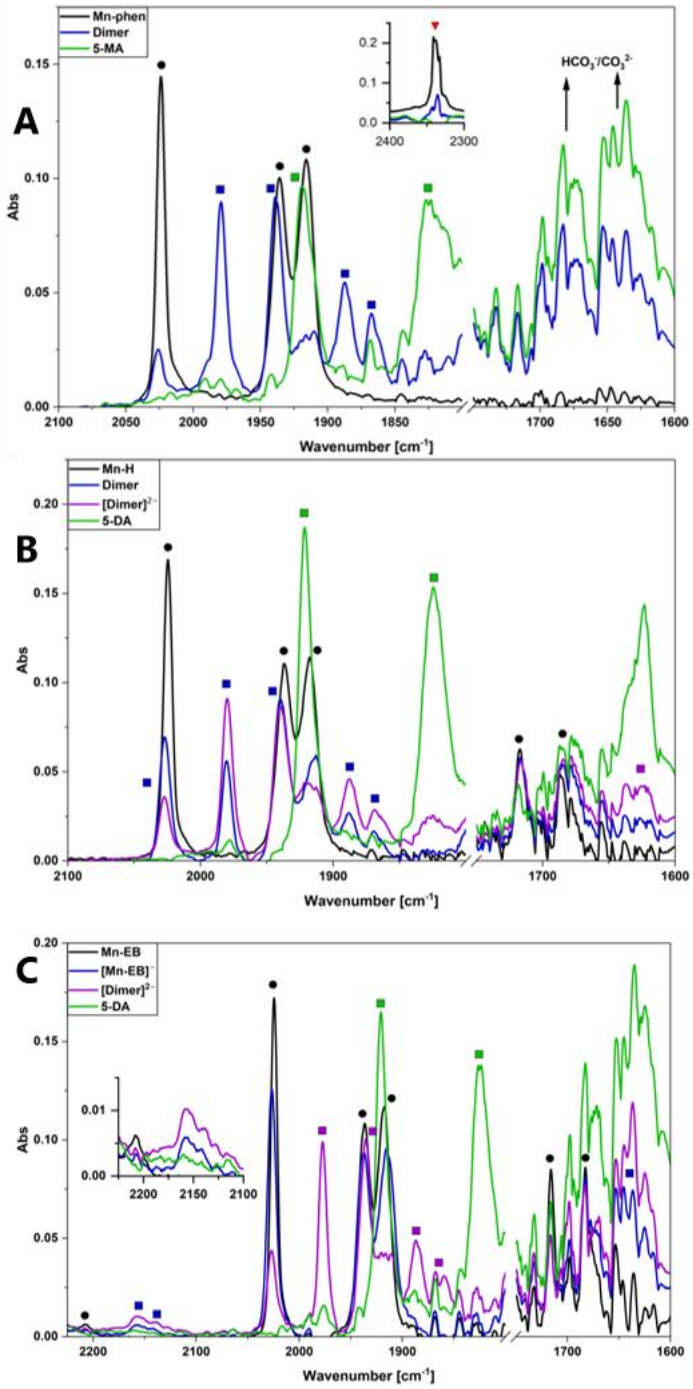


Figure S4.117. *4 mM IR spectra from SEC experiments under CO_2 of (A)* ***Mn–phen*** *with an inset showing the CO_2 band at 1340 cm^{-1}, (B)* ***Mn–H****, and (C)* ***Mn–EB*** *with an inset showing the $\nu_{C\equiv C}$ bands.*

S4.5 DFT Calculations

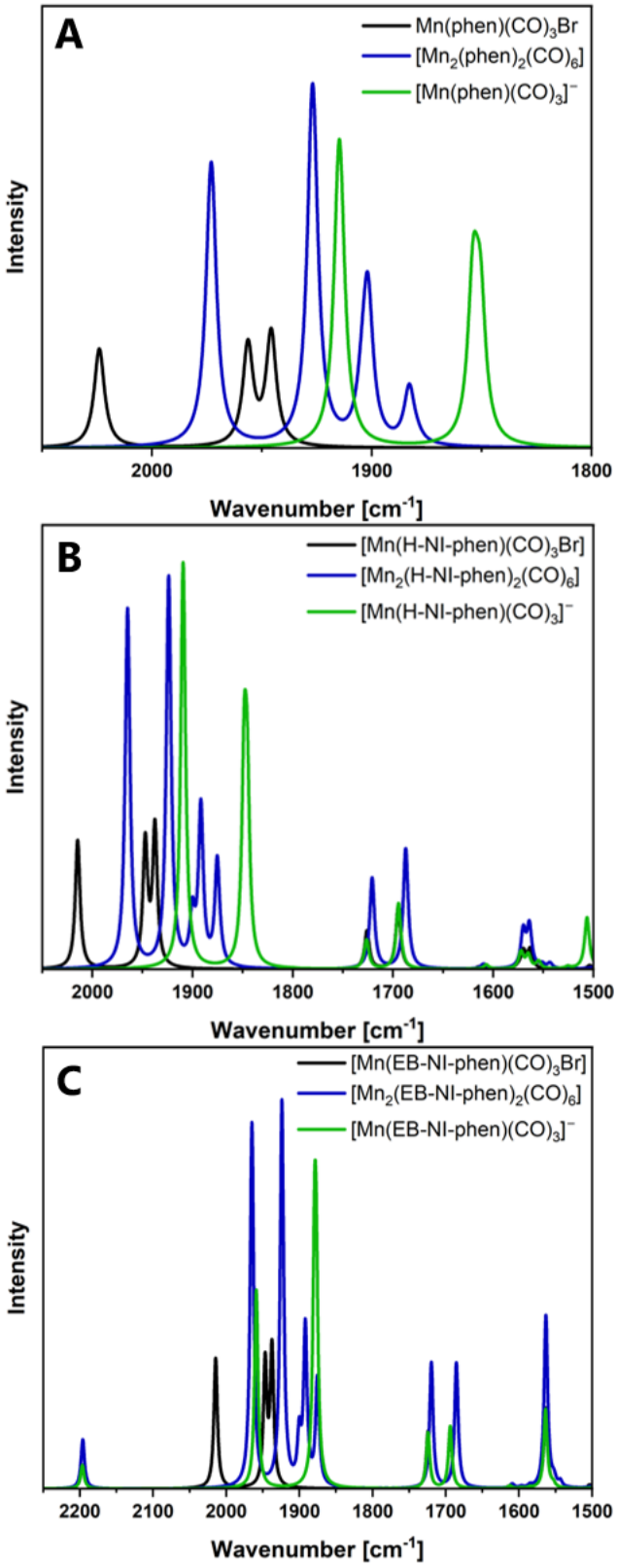


Figure S4.118. *DFT calculated IR spectra of (A)* ***Mn–phen*** *and its reduced species, (B)* ***Mn–H*** *and its reduced species, (C)* ***Mn–EB*** *and its reduced species.*

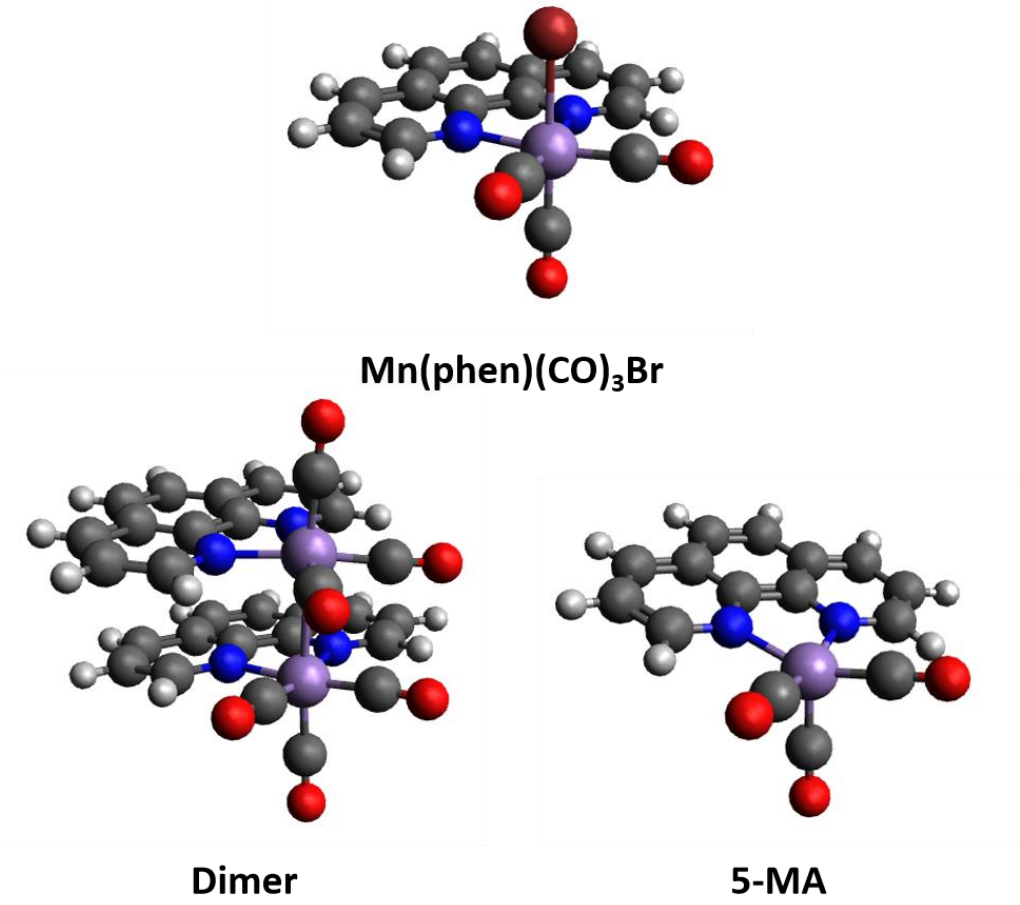


Figure S4.119. *Molecular structures of* ***Mn–phen*** *and its reduced species identified by SEC studies.*

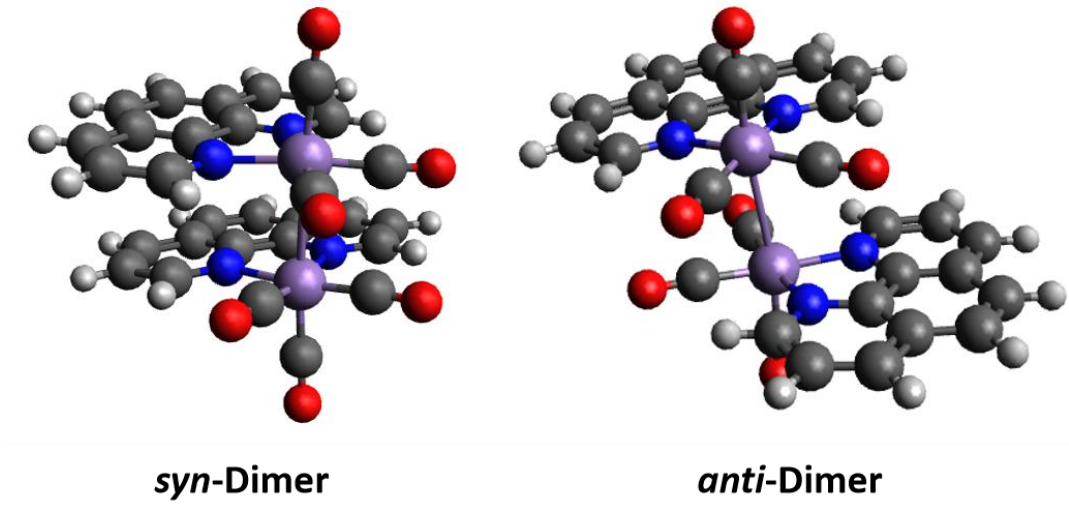


Figure S4.120. *The structures of the* ***syn-Dimer*** *and the* ***anti-Dimer*** *of* ***Mn–phen****. Only the* ***syn-Dimer*** *was observed in SEC studies of all* ***Mn–R*** *complexes.*

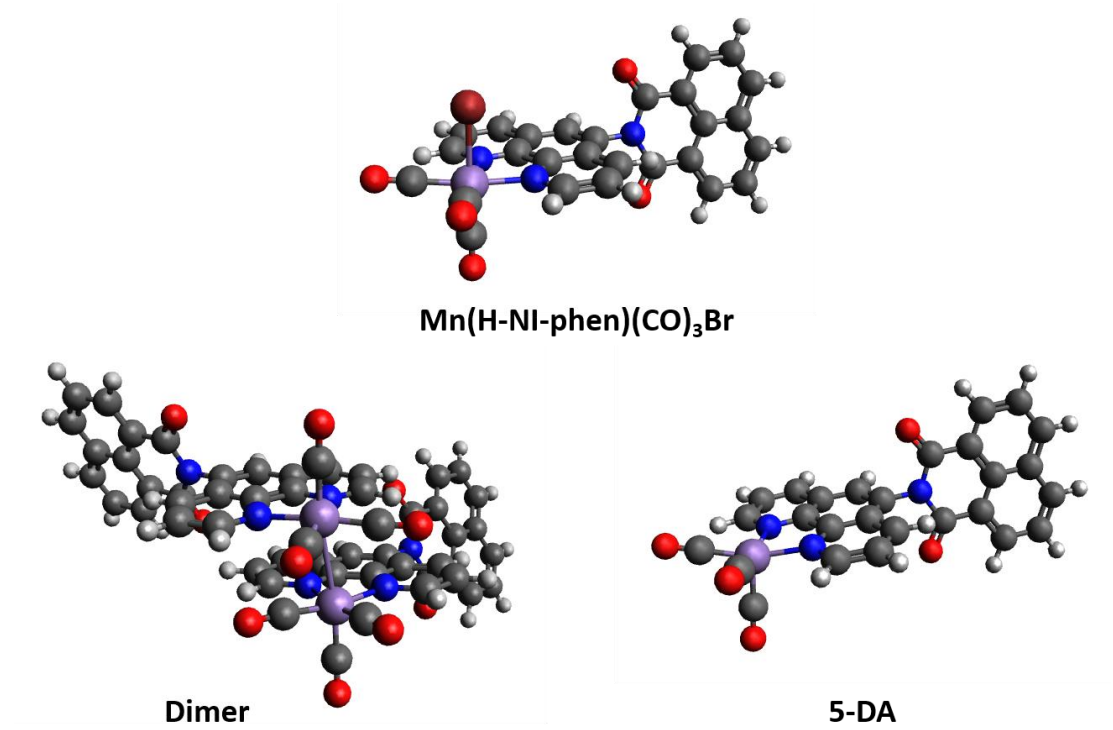


Figure S4.121. *Molecular structures of* ***Mn–H*** *and its reduced species identified by SEC studies.*

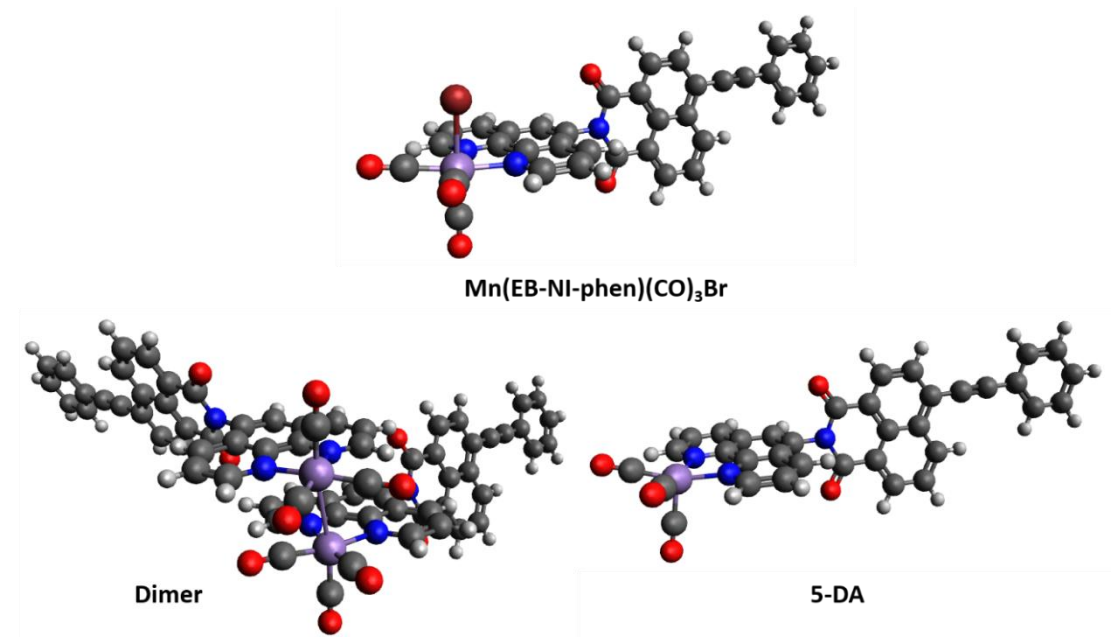


Figure S4.122. *Molecular structures of* ***Mn–EB*** *and its reduced species identified by SEC studies.*

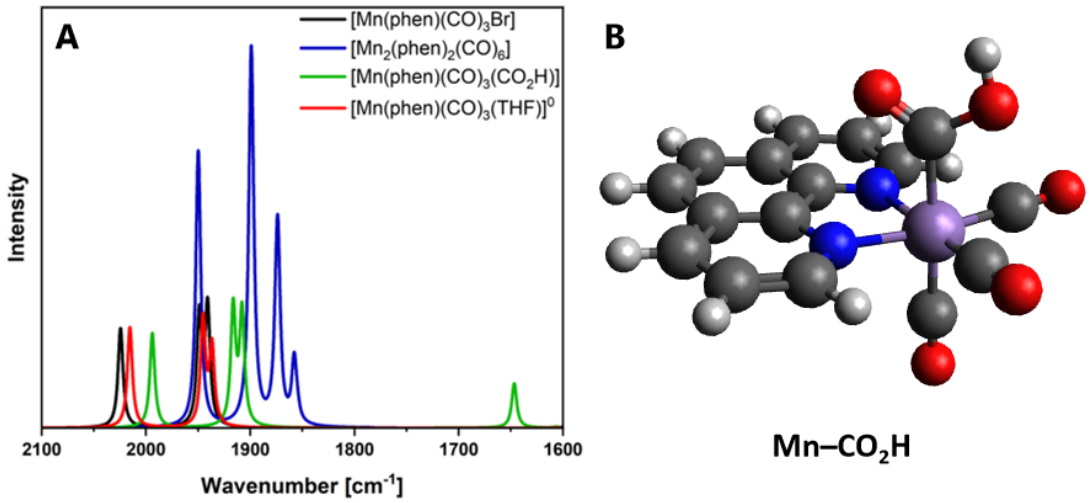


Figure S4.123. *(A) DFT calculated IR spectra in CH_3CN of key intermediate species of* ***Mn–phen*** *identified in the IR SEC experiment with CO_2 and H_2O. The THF-solvated species $[Mn(phen)(CO)_3(THF)]^0$ is included to support the assignment of a new species to the* ***Mn–CO_2H*** *(B) The molecular structure of the* ***Mn–CO_2H*** *complex.*

S4.6 Bibliography

1 J. Biddulph, M. Pižl, S. Bhattacharya, P. Malakar, G. M. Greetham, F. Hartl and M. T. Pryce, Nature and Dynamics of the Excited States of Ethynyl-Functionalized Naphthalimide–Phenanthroline Re(I) Complexes Studied by TA and TRIR Spectroscopies, *J. Phys. Chem. B*, 2026, **130**, 6383–6398.

2 J. E. Yarnell, K. A. Wells, J. R. Palmer, J. M. Breaux and F. N. Castellano, Excited-State Triplet Equilibria in a Series of Re(I)-Naphthalimide Bichromophores, *J. Phys. Chem. B*, 2019, **123**, 7611–7627.

3 Z. Liu, Z. Zhang, Y. Liu, Y. Mei, E. Feng, Y. Liu, T. Zheng, J. Chen, S. Zhang and Y. Tian, Raman Fiber Photometry for Understanding Mitochondrial Superoxide Burst and Extracellular Calcium Ion Influx upon Acute Hypoxia in the Brain of Freely Moving Animals, *Angew. Chem., Int. Ed.*, 2022, **61**, e202111630.

4 J. R. Wagner and D. G. Hendricker, Coordination of Mn(I) and Re(I) carbonyls with nitrogen heterocyclic ligands, *Journal of Inorganic and Nuclear Chemistry*, 1975, **37**, 1375–1379.

Appendix D

Supplementary information associated with Chapter 5

S5.1 Experimental

Syntheses

The malononitrile, 4-bromo naphthalic-1,8-anhydride, 5-amino-1,10-phenanthroline, and tetra n-butyl ammonium hexafluorophosphate ($TBAPF_6$) reagents were acquired from Fluorochem. The 4,4'-bis(trifluoromethyl)-2'2-bipyridine (btfmb) reagent was acquired from ABCr. All spectroscopic solvents were acquired from Fisher Scientific. 2,2'-bipyridine (bpy), $[Mn(CO)_5Br]$, $[Re(CO)_5Cl]$, $[RuCl_3.H_2O]$ and all other solvents were acquired from Sigma-Aldrich. The malononitrile-containing compounds were characterised by FTIR spectroscopy, ^1H NMR spetroscopy, high-resolution mass spectrometry, and elemental analysis. The synthesis of 4-bromo-1,8-naphthalimide-5-phenanthroline **(Br–NI–phen)** is described in Appendix A – S2.1 using the literature procedure[1,2]; the crude product was used without further purification in subsequent syntheses.

*Synthesis of 4-malononitrile-1,8-naphthalimide-5-phenanthroline **(MN–NI–phen)***

This synthesis was adapted from the literature procedure for an aromatic nucleophilic substitution reaction of a malononitrile substituent onto a NI moiety by Jeong et al.[3] Malononitrile and (0.0277 g, 0.419 mmol) and **Br–NI–phen** (0.1776 g, 0.391 mmol) were dissolved in 2 ml of DMF. NaH (0.0115 g, 0.480 mmol) was added to the stirring reaction solution resulting in the rapid formation of a purple solution. The solution was stirred for an hour at 100 °C. Upon cooling, ca. 20 ml of Et_2O was added to the solution to precipitate the product. The precipitate was collected by vacuum filtration, further washed with Et_2O and then air-dried. A purple powder was obtained. Yield: 0.01564 g (91%). ^1H NMR ($CDCl_3$, 600 MHz): δ (ppm) = 9.28 (dd, J = 4.45, 1.87 Hz, 1H), 9.24 (dd, J = 4.30, 1.56 Hz, 1H), 8.75 (dd, J = 10.97, 7.15 Hz , 2H), 8.51 (d, J = 8.09 Hz, 1H), 8.29 (d, J = 8.02, 1.59 Hz, 1H), 8.16 (d, J = 7.92 Hz, 1H), 8.02 (dd, J = 8.25, 1.54 Hz, 1H), 7.96 (dd, J = 8.79, 7.25 Hz, 1H), 7.89 (s, 1H), 7.70 (dd, J = 8.03, 4.59 Hz, 1H), 7.59 (dd, J = 8.34, 4.20 Hz 1H). MS [ESI-QTOF (THF) m/z] 462.2767 $[M+Na]^+$ and 438.10 $[M–H]^–$, calcd ($C_{27}H_{13}N_5O_2$) 439.43.

*Synthesis of [Re(MN–NI–phen)(CO)$_3$Cl] **[Re–MN]***

The reaction was carried out as described for $[Re(H–NI–phen)(CO)_3Cl]$.[1] $[Re(CO)_5Cl]$ (0.0549 g, 0.152 mmol) and **MN–NI–phen** (0.0662 g, 0.151 mmol). A red powder was collected as the reaction product. Yield: 0.0723 g (64%). ^1H NMR ($CDCl_3$, 600 MHz): δ (ppm) = 9.48 (dd, J = 5.25,

1.46 Hz, 1H), 9.44 (dd, J = 5.25, 1.46 Hz, 1H), 8.78 (m, 2H), 8.58 (d, J = 8.23 Hz, 1H), 8.53 (dd, J = 18.75, 8.00 Hz, 2H), 8.20 (dd, J = 8.33, 1.23 Hz, 1H), 8.19 (dd, J = 8.05, 3.15 Hz, 1H), 8.12 (s, 1H), 7.99 (m, 1H), 7.92 (dd, J = 8.13, 5.03 Hz, 1H), 7.80(dd, J = 8.29, 5.15 Hz, 1H). MS [ESI-QTOF (THF) m/z] 744.0043 $[M–H]^-$, calcd ($C_{30}H_{13}ClN_5O_5Re$) 745.12.

Synthesis of $[Ru(bpy)_2Cl_2]$

The synthesis of $[Ru(bpy)_2Cl_2]$ was carried out according to the literature procedure.[4] $[RuCl_3.H_2O]$ (0.1264 g, 0.485 mmol) and bpy (0.1564 g, 1.000 mmol) were dissolved in a minimum of DMF (*ca*. 1 ml) with an excess of LiCl (0.1450 g, 3.421 mmol). After heating to 160 °C for 6 h, the reaction solution was cooled to RT. Precipitation of the product was achieved by adding an excess of acetone to the solution and storing in a freezer overnight to precipitate the product. The product was collected by vacuum filtration and rinsed with Et_2O to obtain a fine black powder. Yield: 0.0750 g (32%). ^1H NMR ($CDCl_3$, 600 MHz): δ (ppm) = 10.07 (s, 2H), 8.37 (d, J = 8.21 Hz, 2H), 8.22 (d, J = 7.85 Hz, 2H), 7.99 (td, J = 8.38, 7.81, 1.41 Hz, 2H), 7.67 (t, J = 7.29, 6.36 Hz, 2H), 7.62 (m, 2H), 7.59 (t, J = 9.17, 7.82, Hz, 2H), 6.99 (td, J = 7.65, 6.12, 1.17 Hz, 2H).

Synthesis of $[Ru(MN–NI–phen)(bpy)_2](PF_6)_2$ ***[Ru–MN]***

This reaction was carried out according to the literature procedure described for rac-[Ru(4,4'-btfmb)$_3$](Cl)$_2$.[5] **MN–NI–phen** (0.0470 g, 0.107 mmol) was added to a microwave vessel with $[Ru(bpy)_2Cl_2]$ (0.0486 g, 0.112 mmol). 2 ml of ethylene glycol was used to dissolve the reagents. Following purging of the reaction solution with N_2 gas, it was subjected to microwave irradiation at 180 °C for 15 min with stirring. Following the reaction, the initially dark purple solution turned a dark red. The dark red solution was transferred to a separatory funnel with deionised water (25 ml) and CH_2Cl_2 (25 ml). The organic layer was drained after gentle agitation. The remaining aqueous layer was washed with further CH_2Cl_2 (25 ml) rinsings until the organic layer was colourless corresponding to removal of unreacted **MN–NI–phen**. Saturated aqueous KPF_6 (5 ml) was added to the aqueous layer in the separatory funnel and gently shaken. Further CH_2Cl_2 (25 ml) rinsings were used to extract the product from the aqueous layer until the aqueous layer was colourless. The organic fractions were combined and dried under vacuum to obtain the crude product.

Further purification was performed using silica gel flash column chromatography. Initially, a gradient of pure CH_3CN to a 10% water in CH_3CN mobile phase was used to remove unreacted $[Ru(bpy)_2Cl_2]$. Subsequently, a 7.5% water in CH_3CN with 0.5% KNO_3 was used to extract the

product. The product-containing fractions were then combined and concentrated under vacuum, before being transferred to a separatory funnel with CH_2Cl_2 (25 ml), deionized water (25 ml), and saturated aqueous KPF_6 (1 ml). As before, the organic layer was drained, with additional CH_2Cl_2 (25 mL) rinsing being used to extract the remaining product until the aqueous layer was colourless. The combined organic layers were then dried under vacuum to obtain the purified product as a red/brown powder. Yield: 0.0462 g (38%). ^{1}H NMR ($CDCl_3$, 600 MHz): δ (ppm) = 9.31 (ddd, J = 8.60, 3.83, 1.21 Hz, 1H), 8.68 (m, 3H), 8.51 (m, 6H), 8.39 (s, 1H), 8.15 (m, 2H), 8.10 (m, 2H), 8.03 (m, 3H), 7.85 (d, 5.63 Hz, 2H), 7.80 (dd, J = 8.37, 5.48 Hz, 1H), 7.66 (m, 3H), 7.46 (dd, J = 13.42, 5.52, 1.36 Hz, 2H), 7.31 (ddd, J = 14.21, 6.40, 1.35 Hz, 2H). MS [ESI-QTOF (THF) m/z] 438.5531 $[M+Na]^{2+}$, calcd ($[C_{47}H_{29}N_9O_2Ru]^{2+}$) 426.57.

Synthesis of $[Ru(btfmb)_2Cl_2]$

The synthesis of $[Ru(btfmb)_2Cl_2]$ was carried out according to the literature procedure.[6] $[RuCl_3.H_2O]$ (0.1264 g, 0.485 mmol) and btfmb (0.2924 g, 1.000 mmol) were dissolved in a minimum of DMF (*ca*. 1 ml) with an excess of LiCl (0.1442 g, 3.402 mmol). After heating to 160 °C for 24 h, the reaction solution was cooled to RT. Precipitation of the product was achieved by adding an excess of acetone to the solution and storing in a freezer overnight to precipitate the product. The product was collected by vacuum filtration over a sintered glass funnel and rinsed with Et_2O to obtain a fine blue/black powder. Yield: 0.1177 g (32%). ^{1}H NMR ($CDCl_3$, 600 MHz): δ (ppm) = 9.29 (d, J = 6.08 Hz, 1H), 8.85 (s, 1H), 8.68 (s, 1H), 8.01 (dd, J = 6.06, 1.59 Hz, 1H), 7.90 (d, J = 6.44 Hz, 1H), 7.39 (dd, J = 6.14, 1.63 Hz, 1H).

Synthesis of $[Ru(MN–NI–phen)(btfmb)_2](PF_6)_2$ ***[CF_3Ru–MN]***

The synthesis of **CF_3Ru–MN** was carried out using the same procedure outlined for **Ru–MN** with the following quantities; **MN–NI–phen** (0.0470 g, 0.107 mmol) and $[Ru(btfmb)_2Cl_2]$ (0.0788 g, 0.105 mmol). A red powder was obtained as the purified product. Yield: 0.0581 g (51%). ^{1}H NMR ($CDCl_3$, 600 MHz): δ (ppm) = 8.97 (dd, J = 16.15, 6.80 Hz, 4H), 8.79 (ddd, J = 8.56, 3.14, 1.14 Hz, 1H), 8.75 (dd, J = 8.40, 1.14 Hz , 1H), 8.69 (ddd, J = 26.00, 7.31, 1.14 Hz, 1H), 8.54 (dd, J = 8.67, 1.08 Hz, 1H), 8.46 (dd, J = 25.40, 7.96 Hz, 1H), 8.41 (s, 1H), 8.25 (dd, J = 9.80, 7.90 Hz, 1H), 8,12 (m, 4H), 8.04 (m, 1H), 7.91 (dd, 11.90, 7.85 Hz, 2H), 7.83 (dd, 8.32, 5.32 Hz, 1H), 7.75 (td, 5.70, 1.50 Hz, 2H), 7.71 (dd, 8.59, 5.20 Hz, 1H), 7.62 (dd, 10.24, 5.97 Hz, 2H). MS [ESI-QTOF (THF) m/z] 536.0925 $[M–CN]^{2+}$, calcd ($[C_{51}H_{25}F_{12}N_9O_2Ru]^{2+}$) 562.55.

FTIR Spectroscopy

All IR spectra were recorded on a PerkinElmer Spectrum65 FTIR Spectrometer. Samples were prepared in spectroscopic grade DMSO and loaded into a liquid–film IR cell with CaF_2 windows.

UV-Vis Absorption and Emission Spectroscopy

All UV-Vis absorption and emission spectra were recorded on a Horiba Duetta Fluorescence and Absorbance Spectrometer. Samples were recorded in a quartz cuvette with a 1 cm path length and prepared in spectroscopic grade CH_3CN. Normalisation of the emission spectra was completed using Spectragryph v1.2.16.1.

S5.2 ^{1}H NMR Spectra

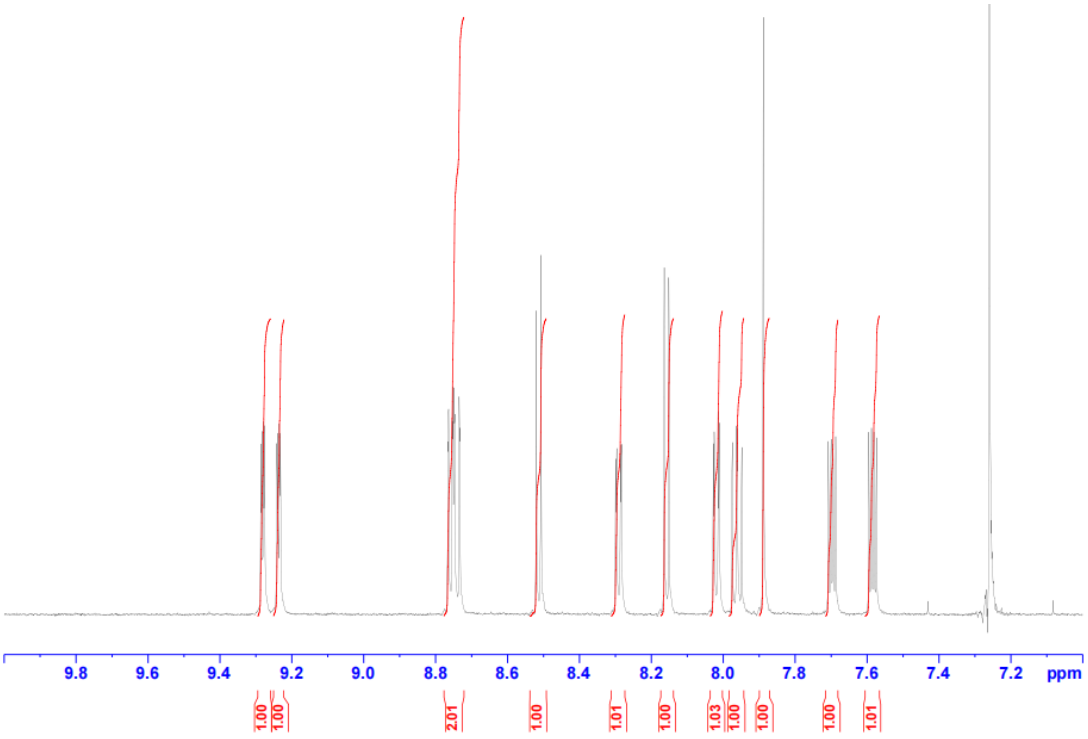


Figure S5.124. *^{1}H NMR spectrum of* ***MN–NI–phen*** *in $CDCl_3$.*

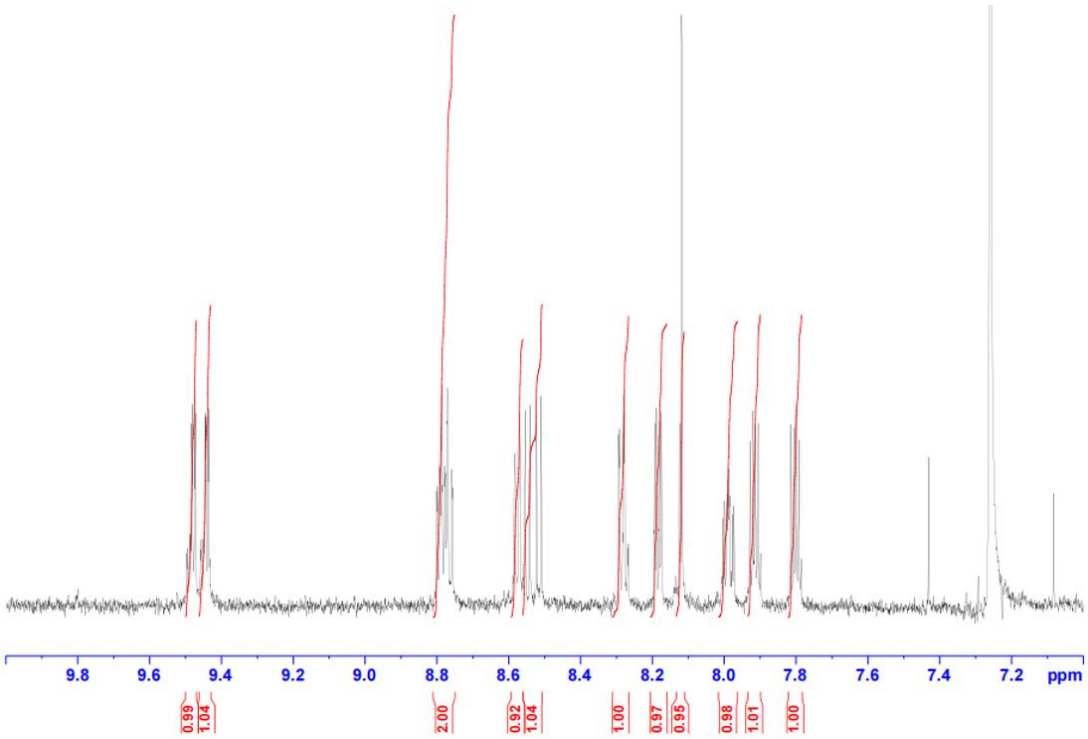


Figure S5.125. *^{1}H NMR spectrum of* ***Re–MN*** *in $CDCl_3$.*

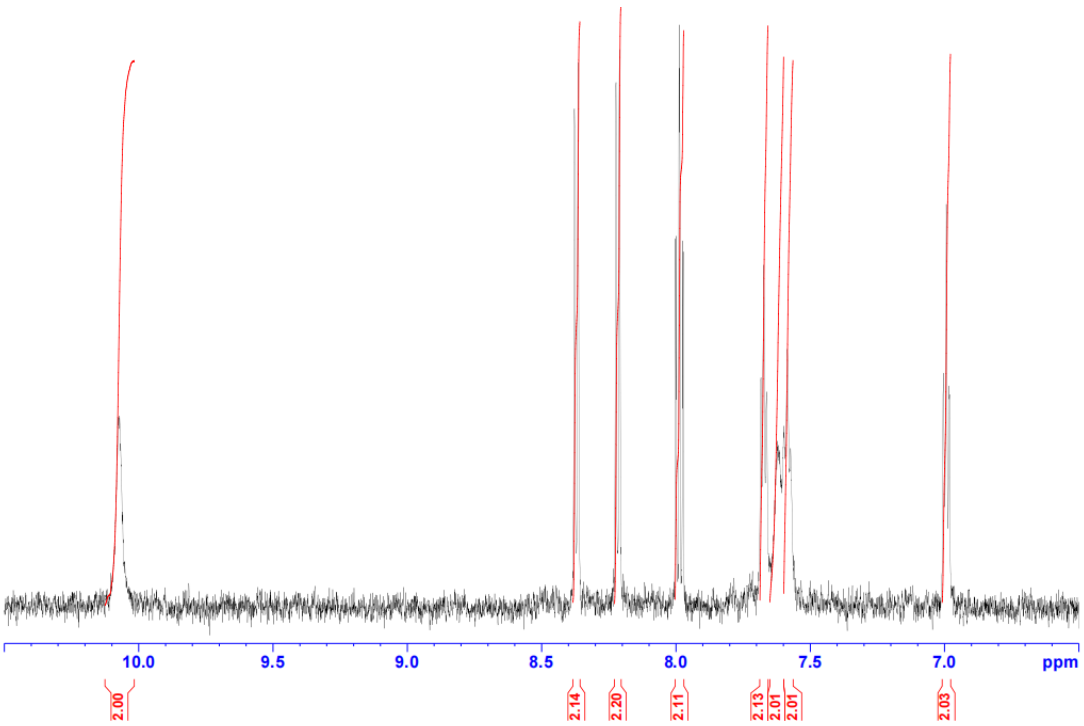


Figure S5.126. *^{1}H NMR spectrum of $[Ru(bpy)_2Cl_2]$ in CD_3CN.*

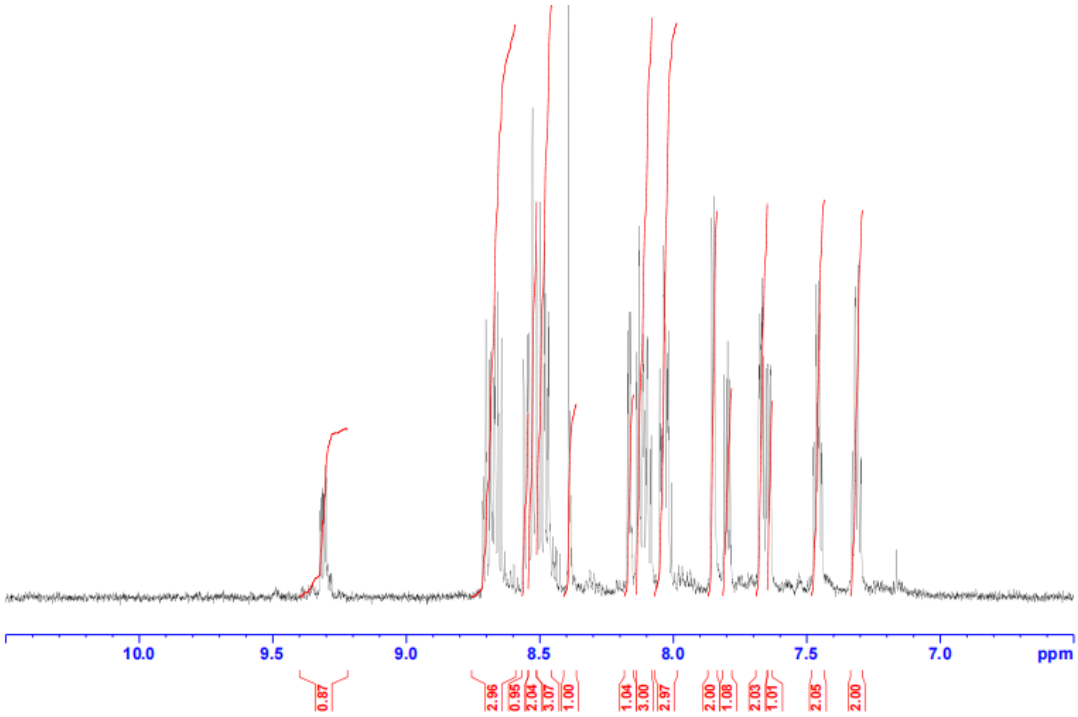


Figure S5.127. *^{1}H NMR spectrum of* ***Ru–MN*** *in CD_3CN.*

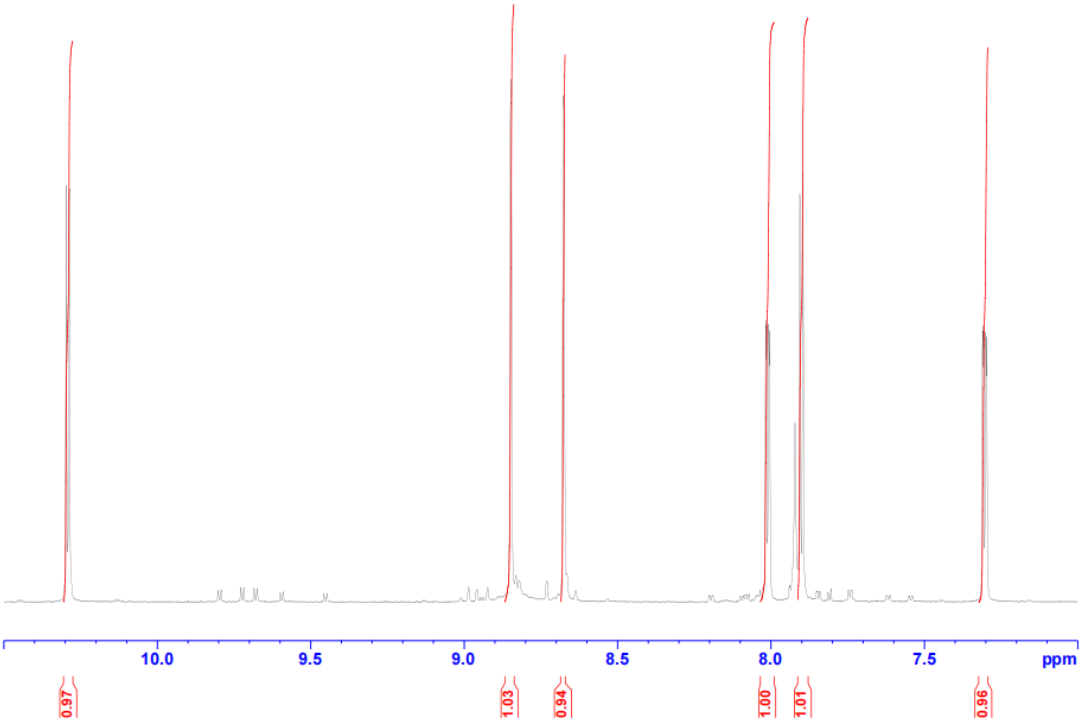


Figure S5.128. *^{1}H NMR spectrum of $[Ru(btfmb)_2Cl_2]$ in CD_3CN.*

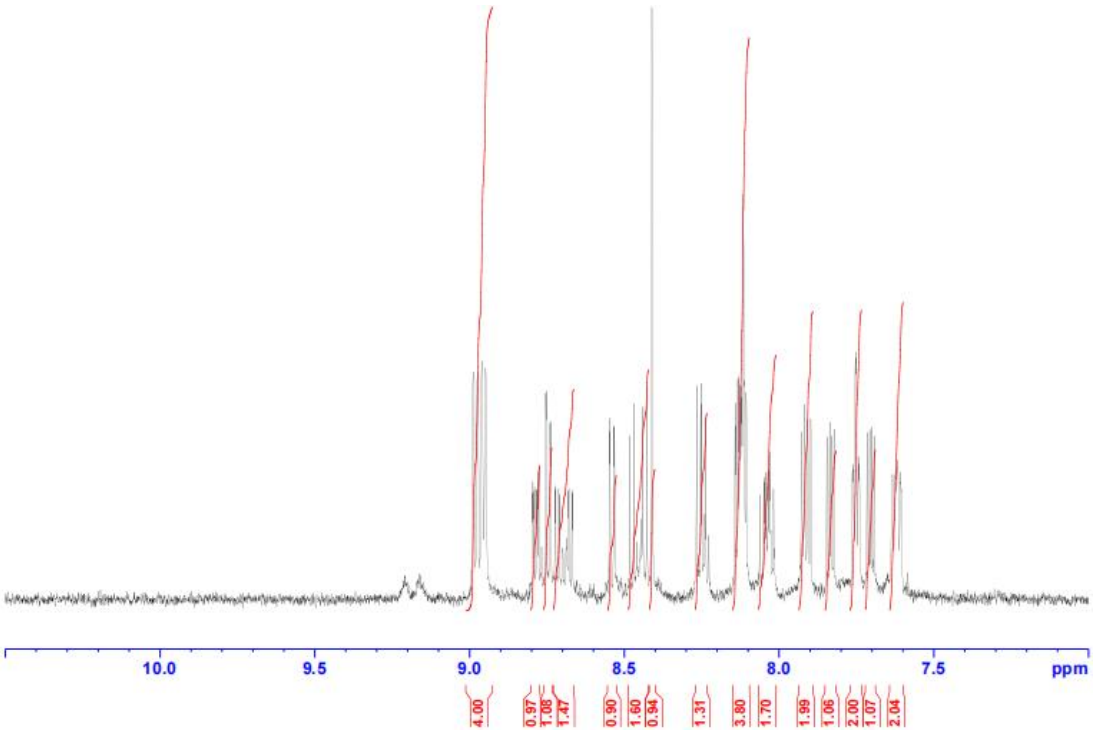


Figure S5.129. *^{1}H NMR spectrum of **CF_3Ru–MN** in CD_3CN.*

S5.3 Mass Spectrometry

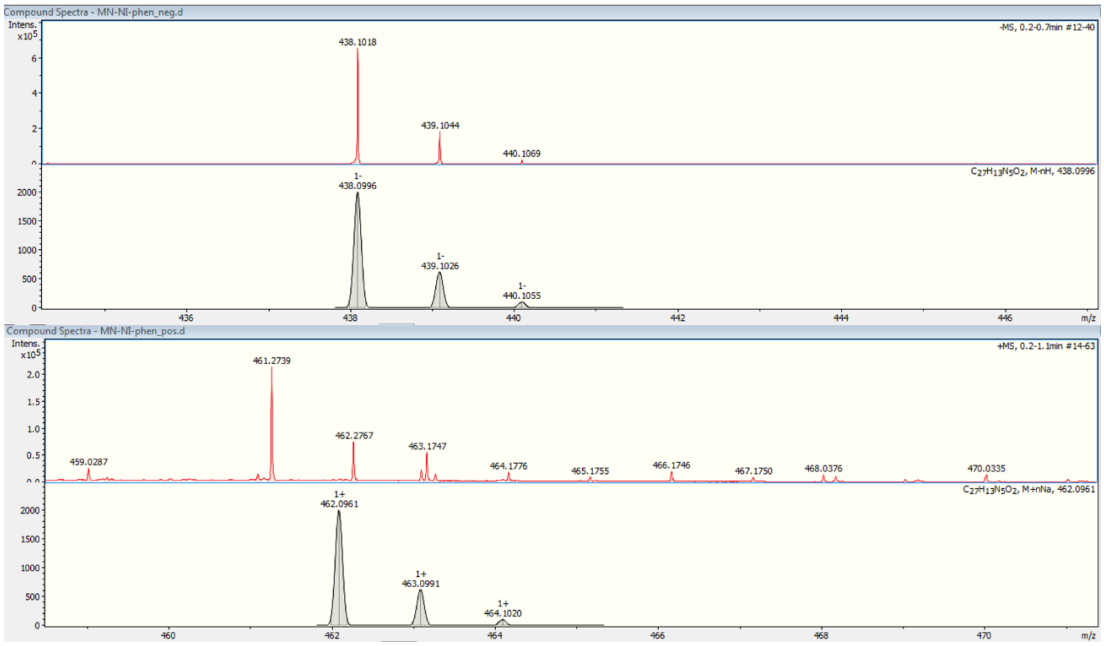


Figure S5.130. *HR-MS of **MN–NI–phen** (MW = 439.43 g/mol). Top: negative mode $[M-H]^-$, Bottom: positive mode $[M+Na]^+$.*

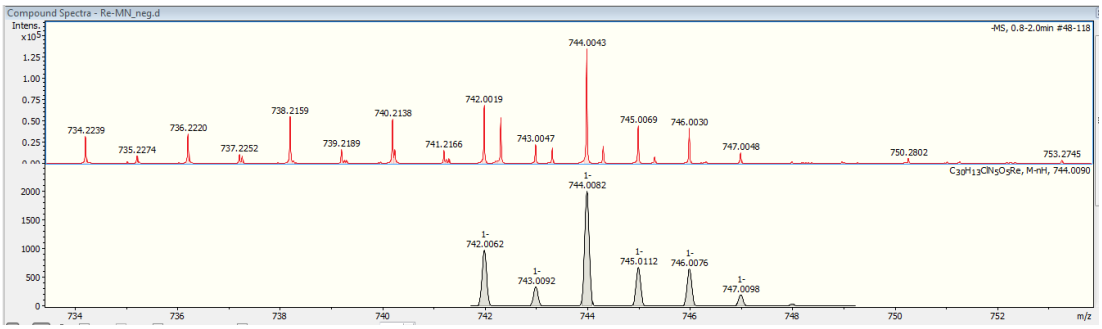


Figure S5.131. *HR-MS of* ***Re–MN*** *(MW = 745.12 g/mol) displaying the negative mode* $[M-H]^-$ *ion.*

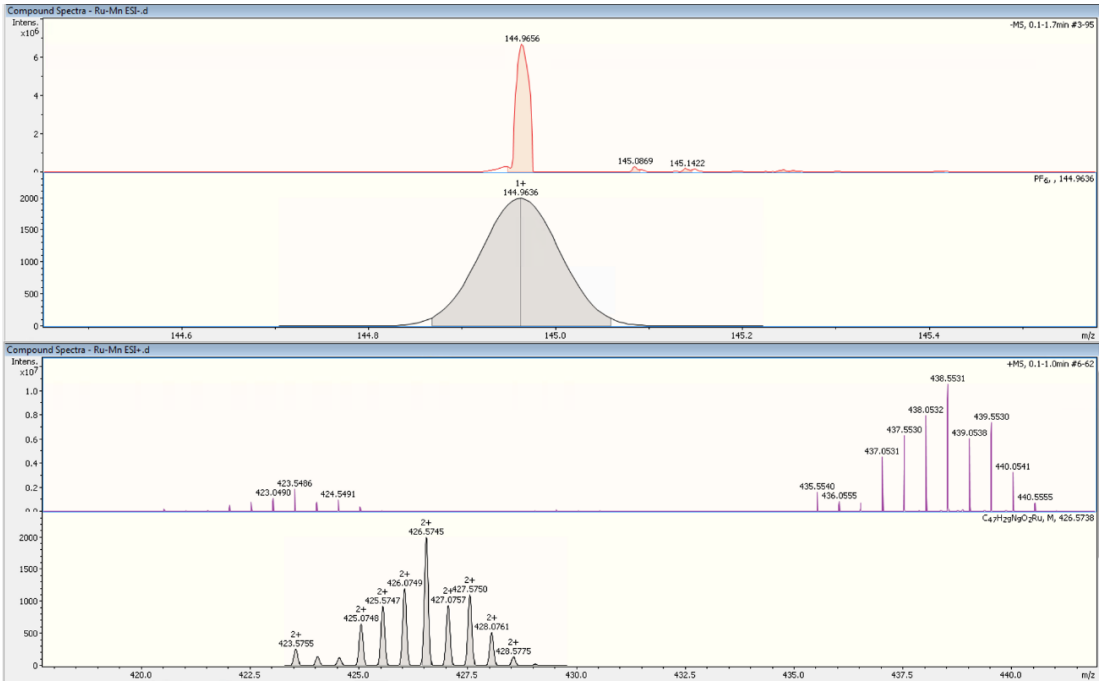


Figure S5.132. *HR-MS of* ***Ru–MN*** *(MW = 1142.81 g/mol). Top: negative mode* $[PF_6]^-$ *ion, Bottom: positive mode* $[M+Na]^{2+}$.

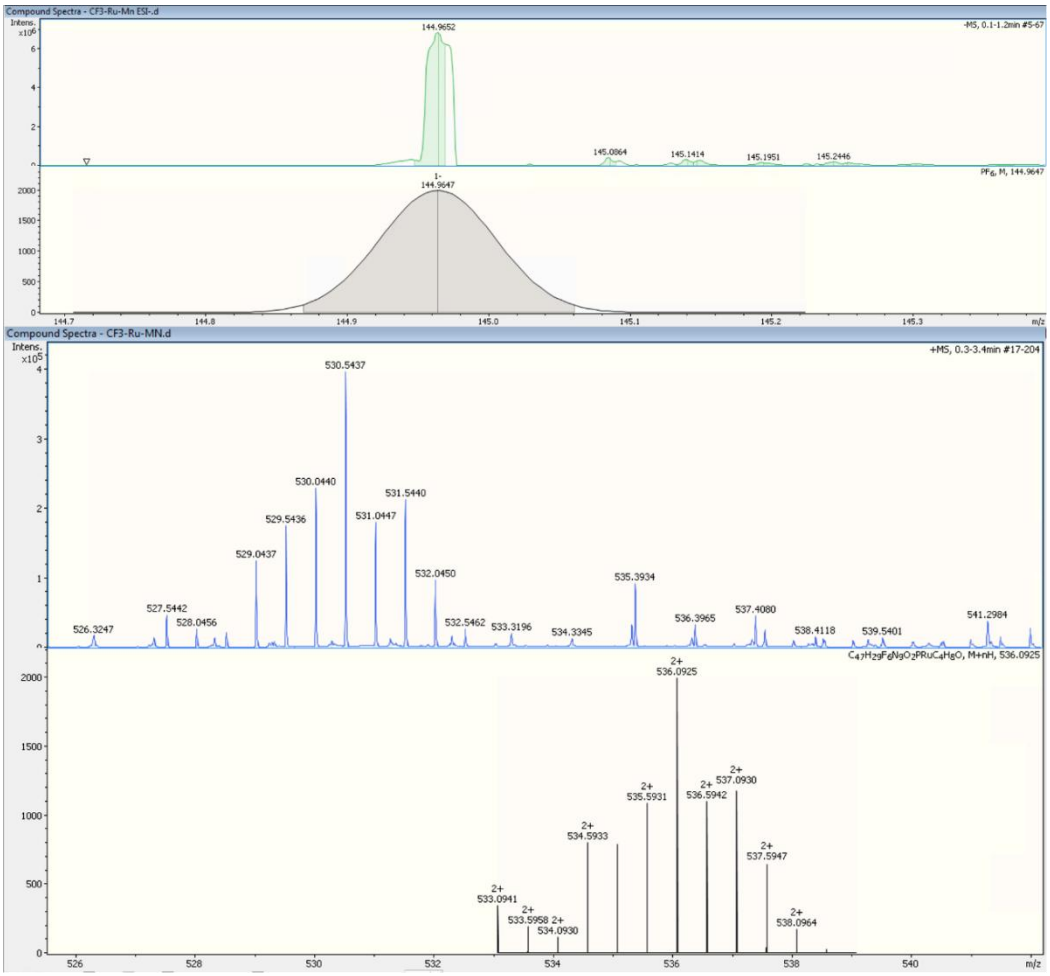


Figure S5.133. *HR-MS of* ***CF_3Ru–MN*** *(MW = 1414.80 g/mol). Top: negative mode $[PF_6]^-$, Bottom: positive mode $[M–CN]^{2+}$.*

S5.4 Bibliography

1 J. Biddulph, M. Pižl, S. Bhattacharya, P. Malakar, G. M. Greetham, F. Hartl and M. T. Pryce, Nature and Dynamics of the Excited States of Ethynyl-Functionalized Naphthalimide–Phenanthroline Re(I) Complexes Studied by TA and TRIR Spectroscopies, *J. Phys. Chem. B*, 2026, **130**, 6383–6398.

2 J. E. Yarnell, K. A. Wells, J. R. Palmer, J. M. Breaux and F. N. Castellano, *J. Phys. Chem. B*, 2019, **123**, 7611–7627.

3 C.-H. Jeong, A. Ahmad, H. C. Schmitz and H. Cao, *J Fluoresc*, 2022, **32**, 427–433.

4 B. P. Sullivan, D. J. Salmon and T. J. Meyer, *Inorg. Chem.*, 1978, **17**, 3334–3341.

5 H. D. Cole, A. Vali, J. A. I. Roque, G. Shi, A. Talgatov, G. Kaur, A. Francés-Monerris, M. E. Alberto, C. G. Cameron and S. A. McFarland, *Inorg. Chem.*, 2024, **63**, 9735–9752.

6 M. Furue, K. Maruyama, T. Oguni, M. Naiki and M. Kamachi, *Inorg. Chem.*, 1992, **31**, 3792–3795.